

Hermann Lühr
Johannes Wicht
Stuart A. Gilder
Matthias Holschneider *Editors*



Magnetic Fields in the Solar System

Planets, Moons
and Solar Wind Interactions

ASSL

 Springer

Magnetic Fields in the Solar System

Astrophysics and Space Science Library

EDITORIAL BOARD

- F. BERTOLA, *University of Padua, Italy*
C. J. CESARSKY, *Commission for Atomic Energy, Saclay, France*
P. EHRENFREUND, *Leiden University, The Netherlands*
O. ENGVOLD, *University of Oslo, Norway*
E. P. J. VAN DEN HEUVEL, *University of Amsterdam, The Netherlands*
V. M. KASPI, *McGill University, Montreal, Canada*
J. M. E. KUIJPERS, *University of Nijmegen, The Netherlands*
H. VAN DER LAAN, *University of Utrecht, The Netherlands*
P. G. MURDIN, *Institute of Astronomy, Cambridge, UK*
B. V. SOMOV, *Astronomical Institute, Moscow State University, Russia*
R. A. SUNYAEV, *Max Planck Institute for Astrophysics, Garching, Germany*

More information about this series at <http://www.springer.com/series/5664>

Hermann Lühr • Johannes Wicht • Stuart A. Gilder •
Matthias Holschneider
Editors

Magnetic Fields in the Solar System

Planets, Moons and Solar Wind Interactions



Springer

Editors

Hermann Lühr
Deutsches GeoForschungsZentrum GFZ
Potsdam, Germany

Johannes Wicht
Max Planck Institute for Solar System
Research
Göttingen, Germany

Stuart A. Gilder
Department of Earth and Environmental
Sciences
Ludwig Maximilians Universität
München, Germany

Matthias Holschneider
Institut für Mathematik
Universität Potsdam
Potsdam, Germany

ISSN 0067-0057

ISSN 2214-7985 (electronic)

Astrophysics and Space Science Library

ISBN 978-3-319-64291-8

ISBN 978-3-319-64292-5 (eBook)

DOI 10.1007/978-3-319-64292-5

Library of Congress Control Number: 2017960802

© Springer International Publishing AG 2018

This work is subject to copyright. All rights are reserved by the Publisher, whether the whole or part of the material is concerned, specifically the rights of translation, reprinting, reuse of illustrations, recitation, broadcasting, reproduction on microfilms or in any other physical way, and transmission or information storage and retrieval, electronic adaptation, computer software, or by similar or dissimilar methodology now known or hereafter developed.

The use of general descriptive names, registered names, trademarks, service marks, etc. in this publication does not imply, even in the absence of a specific statement, that such names are exempt from the relevant protective laws and regulations and therefore free for general use.

The publisher, the authors and the editors are safe to assume that the advice and information in this book are believed to be true and accurate at the date of publication. Neither the publisher nor the authors or the editors give a warranty, express or implied, with respect to the material contained herein or for any errors or omissions that may have been made. The publisher remains neutral with regard to jurisdictional claims in published maps and institutional affiliations.

Cover figure: Artists view of the planetary magnetic field, generated in the core, and its interaction with the solar wind in outer space

Credit: Cover illustration compiled by M. Rother, GFZ

Printed on acid-free paper

This Springer imprint is published by Springer Nature

The registered company is Springer International Publishing AG

The registered company address is: Gewerbestrasse 11, 6330 Cham, Switzerland

Preface

In 2009, the Deutsche Forschungsgemeinschaft (DFG, German Research Foundation) implemented “Planetary Magnetism/PlanetMag” as a nationwide Priority Program (SPP 1488).

Motivations for the priority program were manifold. For example, magnetic fields are known to play an important role for the habitability of a planet. Recent space missions to Mars and Venus indicate that the planetary magnetic fields play a vital role in preventing atmospheric erosion by the solar wind. Without the geomagnetic field, life on Earth would not be possible as we know it. However, little is known about the underlying physical processes. Space missions also reveal that planetary and lunar magnetic fields are surprisingly diverse. These distinct magnetic signatures carry invaluable information about the past and present internal structure and dynamics of their parent bodies. Harvesting this information, however, requires a better understanding of the interior dynamo processes.

The key goals of the Priority Program were as follows

- Developing new tools for satellite data analysis adapted to the specific space-time measurement geometries of the missions
- Improving computer simulations of planetary interiors and dynamos
- Building models of solar wind interactions
- Understanding the influence of the magnetic field on the planet’s environment
- Measuring magnetic properties of terrestrial rocks and meteorites and performing analog laboratory and field investigations

Many of these issues were successfully addressed in a synergetic and multidisciplinary approach, starting several new collaborations, many of which are still ongoing. During the 6-year lifetime of PlanetMag, more than 20 research groups contributed a sizable number of publications in international peer-reviewed journals.

The purpose of this book is to summarize some of the important findings from PlanetMag and to offer an up-to-date picture of the field. It is addressed to scientists and students interested in planetary studies in general and planetary magnetism in particular. The 13 chapters cover a wide variety of different topics with articles

written by several renowned experts in planetary magnetism. An introductory chapter provides an overview with short descriptions of the individual chapters.

On behalf of the scientists involved, we thank the DFG for funding the Priority Program “PlanetMag.” We appreciate the reviewers’ efforts and in particular their constructive and stimulating comments. An important success of the program is the large number of students who started their scientific careers with PlanetMag. It was inspiring to follow their progress and share their enthusiasm. Working within a group of scientists from very different fields that nevertheless use planetary magnetism as common ground was a stimulating experience for all of us. Hopefully this speaks loudly throughout the pages of this book.

Potsdam, Germany
Göttingen, Germany
München, Germany
Potsdam, Germany
June 2017

Hermann Lühr
Johannes Wicht
Stuart A. Gilder
Matthias Holschneider

Contents

| | | |
|----------|--|----------|
| 1 | General Introduction and Scientific Summary of the German Priority Program “PlanetMag” | 1 |
| | Hermann Lühr, Johannes Wicht, Stuart A. Gilder, and Matthias Holschneider | |
| 1.1 | Introduction | 2 |
| 1.2 | Planetary Interiors and Dynamos | 3 |
| 1.3 | Modeling of the Geomagnetic Field | 3 |
| 1.4 | Interaction of Planetary Magnetic Fields with the Plasma Environment | 4 |
| 1.5 | Characterizing Ancient Magnetised Rocks and Meteorites Including Laboratory Investigations | 5 |
| 1.6 | Concluding Remarks | 6 |
| | Reference | 6 |
| 2 | Modeling the Interior Dynamics of Gas Planets | 7 |
| | Johannes Wicht, Martin French, Stephan Stellmach, Nadine Nettelmann, Thomas Gastine, Lucia Duarte, and Ronald Redmer | |
| 2.1 | Introduction | 8 |
| 2.2 | Interior Structure and Properties of Jupiter and Saturn | 10 |
| 2.2.1 | Material Properties from Density Functional Theory and Molecular Dynamics | 12 |
| 2.2.2 | Properties of Hydrogen–Helium Mixtures at Conditions in the Interior of Jupiter and Saturn | 13 |
| 2.2.3 | Standard Interior Models | 16 |
| 2.2.4 | Thermal Evolution and H/He Phase Separation | 19 |
| 2.3 | Magneto-Hydrodynamic Equations and Numerics | 20 |
| 2.3.1 | Fundamental Dynamic Equations | 21 |
| 2.3.2 | Adiabatic Background State | 23 |
| 2.3.3 | Anelastic Approximation | 24 |
| 2.3.4 | Nondimensional Equations | 27 |

| | | |
|-------|---|----|
| 2.3.5 | Boundary Conditions | 29 |
| 2.3.6 | Specifying Background State and Parameters..... | 30 |
| 2.3.7 | Numerical Methods..... | 34 |
| 2.4 | Convective Flows and Zonal Jets | 35 |
| 2.4.1 | Taylor–Proudman Theorem in a Compressible Fluid | 37 |
| 2.4.2 | The β -Effect in a Compressible Fluid | 38 |
| 2.4.3 | Onset of Convection | 41 |
| 2.4.4 | Non-axisymmetric Flow Close to Onset and Beyond..... | 43 |
| 2.4.5 | Zonal Flow Generation in the Weakly Nonlinear Regime | 44 |
| 2.4.6 | Zonal Flow Generation in the Nonlinear Regime of Rapidly Rotating Convection | 46 |
| 2.4.7 | Two-Dimensional Studies of Zonal Wind Generation: The Multiple Jet Regime | 47 |
| 2.4.8 | Multiple Jets in the Case of Thin Spherical Shells | 50 |
| 2.4.9 | The Transition from Prograde to Retrograde Zonal Flows | 52 |
| 2.5 | Dynamo Simulations | 54 |
| 2.5.1 | Stress-Free Boundaries and Density Stratification..... | 54 |
| 2.5.2 | Electrical Conductivity Profile | 56 |
| 2.5.3 | Parameter Dependence | 59 |
| 2.5.4 | Toward Jupiter-Like Models | 61 |
| 2.5.5 | Jupiter’s Two Dynamos | 67 |
| 2.6 | Conclusion | 70 |
| | References | 75 |
| 3 | Global Geomagnetic Field Reconstructions from Centuries to Excursions | 83 |
| | Monika Korte, Maxwell Brown, Ute Frank, Robin Senftleben, and Norbert Nowaczyk | |
| 3.1 | Introduction | 84 |
| 3.2 | The GEOMAGIA50 Database, Application Examples, and New Holocene Data | 85 |
| 3.2.1 | Version 3 of the GEOMAGIA50 Database | 87 |
| 3.2.2 | Updating Age-Depth Models from Sediment Cores and Reconstructing Sediment Paleomagnetic Time Series | 88 |
| 3.2.3 | Historical Observations and Young Archeomagnetic Data | 92 |
| 3.2.4 | Southern Hemisphere and the South Atlantic Anomaly Region | 93 |
| 3.2.5 | Geomagnetic High-Intensity Spikes | 94 |

| | | |
|----------|--|------------|
| 3.3 | Global Holocene Field Reconstructions | 95 |
| 3.3.1 | New Millennial Scale Geomagnetic Field Models | 95 |
| 3.3.2 | A Brief Comparison of Models | 98 |
| 3.4 | A Global View on Geomagnetic Field Excursions | 100 |
| 3.4.1 | Recently Published Data Spanning the Time of the Laschamp Excursion | 101 |
| 3.4.2 | A Simple Simulation of Excursions Based on a New Holocene Field Model | 102 |
| 3.4.3 | Spherical Harmonic Models of the Laschamp and Mono Lake Excursions | 103 |
| 3.5 | Conclusions and Outlook | 103 |
| | References | 105 |
| 4 | Interannual Fluctuations of the Core Angular Momentum Inferred from Geomagnetic Field Models | 111 |
| | Seiki Asari and Ingo Wardinski | |
| 4.1 | Introduction | 111 |
| 4.2 | Magnetic Estimation of the CAM and LOD Variations | 114 |
| 4.3 | Interannual CAM Fluctuations Inferred from C ³ FM2 | 115 |
| 4.3.1 | Robust Features in CAM Fluctuations Inferred from C ³ FM2 | 115 |
| 4.3.2 | Uncertainty in CAM Fluctuations Inferred from C ³ FM2 | 117 |
| 4.4 | Interannual CAM Fluctuations Inferred from Different Magnetic Models | 118 |
| | References | 122 |
| 5 | Laboratory Experiments and Numerical Simulations on Magnetic Instabilities | 125 |
| | Frank Stefani, Marcus Gellert, Christoph Kasprzyk, Alejandro Paredes, Günther Rüdiger, and Martin Seilmayer | |
| 5.1 | Introduction | 125 |
| 5.2 | Instabilities in Cylindrical Geometry | 128 |
| 5.2.1 | Theory and Numerics | 128 |
| 5.2.2 | Experiments on HMRI | 136 |
| 5.2.3 | Experiments on AMRI | 137 |
| 5.2.4 | Experiments on TI | 140 |
| 5.3 | Instabilities in Spherical Geometry | 142 |
| 5.3.1 | Numerical Simulations | 143 |
| 5.3.2 | The HEDGEHOG Experiment | 144 |
| 5.4 | Conclusions and Outlook | 146 |
| 5.4.1 | The Large MRI/TI Experiment | 146 |
| 5.4.2 | Positive Shear Instabilities | 147 |
| | References | 148 |

| | | |
|----------|--|-----|
| 6 | Modeling Magnetospheric Fields in the Jupiter System | 153 |
| | Joachim Saur, Emmanuel Chané, and Oliver Hartkorn | |
| 6.1 | Introduction | 154 |
| 6.2 | Characterization and Description of the Interaction | 155 |
| 6.2.1 | Overview of the Interaction | 155 |
| 6.2.2 | MHD Model | 157 |
| 6.3 | Jupiter's Magnetosphere | 160 |
| 6.4 | Time-Varying Magnetosphere | 163 |
| 6.5 | Ganymede's Magnetosphere | 166 |
| 6.6 | Ganymede's Ocean | 168 |
| 6.7 | Callisto | 173 |
| 6.7.1 | Callisto's Ionosphere | 174 |
| 6.7.2 | Callisto's Plasma Interaction | 177 |
| 6.8 | Summary | 179 |
| | References | 179 |
| 7 | Empirical Modeling of Planetary Magnetospheres in Response to Solar Wind Dynamics Using EOF Analysis and Multivariate Linear Regression | 183 |
| | Maosheng He and Joachim Vogt | |
| 7.1 | Introduction | 183 |
| 7.2 | Analysis Methodology | 186 |
| 7.2.1 | Predictor Variables | 186 |
| 7.2.2 | Response Variables | 187 |
| 7.2.3 | EOF Analysis | 189 |
| 7.2.4 | Regression Analysis and Model Reconstruction | 193 |
| 7.3 | Scientific Results | 195 |
| 7.3.1 | Results of F2COSMIC | 196 |
| 7.3.2 | Results of MFACE | 197 |
| 7.3.3 | Results of EMVIM | 198 |
| 7.4 | Summary | 198 |
| | References | 199 |
| 8 | Kinetic Simulations of Electron Acceleration at Mercury | 201 |
| | Jörg Büchner, Patrick Kilian, Patricio A. Muñoz, Felix Spanier, Fabien Widmer, Xiaowei Zhou, and Neeraj Jain | |
| 8.1 | Introduction | 202 |
| 8.2 | High Mach-Number Interplanetary Shocks at the Mercury Distance from the Sun | 209 |
| 8.2.1 | Interplanetary High-mach Number Shock Formation | 211 |
| 8.2.2 | Role of the Resonant Electron-Wave Interaction | 215 |
| 8.3 | Magnetopause Electron Acceleration by Finite Guide-Field Reconnection | 217 |

| | | |
|-----------|---|------------|
| 8.4 | Particle Acceleration in Hermean Magnetotail Flux Ropes | 222 |
| 8.4.1 | Test Particle Acceleration in a Plasmoid-Unstable Hermean Magnetotail Current Sheets | 223 |
| 8.4.2 | Kinetic Physics of Electron Acceleration in Magnetotail Flux Ropes | 228 |
| 8.5 | Summary, Conclusions, and Outlook..... | 231 |
| 8.5.1 | Particle Acceleration at Strong Interplanetary Shock Waves at the Mercury Distance from the Sun | 231 |
| 8.5.2 | Electron Acceleration by Hermean Magnetopause Reconnection | 233 |
| 8.5.3 | Acceleration by Flux Ropes in the Magnetotail..... | 233 |
| 8.5.4 | Outlook..... | 234 |
| | References..... | 235 |
| 9 | Physical Processes in the Dusty Plasma of the Enceladus Plume..... | 241 |
| | Victoria Yaroshenko, Patrick Meier, Hermann Lühr, and Uwe Motschmann | |
| 9.1 | Introduction | 242 |
| 9.2 | Plasma Parameters and Dust Characteristics of the Plume | 243 |
| 9.3 | Charging Model | 246 |
| 9.4 | Stochastic Dust Charge Fluctuations | 247 |
| 9.5 | Plume Grains as Heavy Plasma Species and Their Effect on Plasma Screening | 251 |
| 9.6 | Conductivity of Dusty Plasma | 255 |
| 9.7 | Conclusions and Outlook | 259 |
| | References..... | 261 |
| 10 | Modeling of the Ionospheric Current System and Calculating Its Contribution to the Earth's Magnetic Field | 263 |
| | Boris E. Prokhorov, Matthias Förster, Vincent Lesur, Alexander A. Namgaladze, Matthias Holschneider, and Claudia Stolle | |
| 10.1 | Introduction | 264 |
| 10.2 | The Upper Atmosphere Model (UAM) | 265 |
| 10.2.1 | The Structure of the UAM-P Model | 265 |
| 10.2.2 | The New Version of the Electric Field Calculation | 267 |
| 10.3 | Ionospheric Contribution to the Earth's Magnetic Field | 275 |
| 10.3.1 | Basic Physical Equations | 275 |
| 10.3.2 | Numerical Scheme..... | 277 |
| 10.3.3 | Examples of the Additional Magnetic Field..... | 280 |
| 10.3.4 | The Equivalent Current System | 285 |
| 10.4 | Conclusions | 289 |
| | References..... | 291 |

| | |
|--|-----|
| 11 Climatology of Air Upwelling and Vertical Plasma Flow in the Terrestrial Cusp Region: Seasonal and IMF-Dependent Processes | 293 |
| Guram N. Kervalishvili and Hermann Lühr | |
| 11.1 Introduction | 294 |
| 11.2 Data Set and Observations | 296 |
| 11.2.1 CHAMP Data | 296 |
| 11.2.2 GRACE Data | 297 |
| 11.2.3 DMSP Data | 298 |
| 11.2.4 IMF Data | 298 |
| 11.3 Data Selection and Processing Approach | 299 |
| 11.3.1 Electron Temperature and Zonal Wind Velocity | 299 |
| 11.3.2 Thermospheric Density | 299 |
| 11.3.3 Field-Aligned Current | 300 |
| 11.3.4 Vertical Ion Flow | 300 |
| 11.4 Statistical Properties of Observations | 301 |
| 11.4.1 Cusp Density Anomalies in CHAMP and GRACE Observations | 303 |
| 11.4.2 The Spatial Distribution of ρ_{rel} , SSFAC, T_e , and V_z | 305 |
| 11.4.3 The Spatial Correlation of ρ_{rel} , SSFAC, T_e , and V_z | 307 |
| 11.4.4 A Linear Relationship Between V_z and ΔT_e | 309 |
| 11.4.5 The IMF B_y -Dependent Spatial Correlation of ρ_{rel} , U_{zon} , and LSFAC | 310 |
| 11.4.6 The IMF B_y -Dependent Spatial Correlation of $V_z N_i$ and LSFAC | 315 |
| 11.5 Discussion and Conclusion | 320 |
| 11.5.1 Conditions for Neutral Air Upwelling | 320 |
| 11.5.2 Conditions for Ion Upflow | 322 |
| 11.5.3 Ion Upflow Locations with Respect to Auroral Plasma Flow Topology | 323 |
| 11.6 Summary | 324 |
| References | 326 |
| 12 Mars' Crustal Magnetic Field | 331 |
| Achim Morschhauser, Foteini Vervelidou, Paul Thomas, Matthias Grott, Vincent Lesur, and Stuart A. Gilder | |
| 12.1 Mars Magnetic Field | 331 |
| 12.1.1 Current Knowledge | 332 |
| 12.1.2 Open Questions | 332 |
| 12.2 Modeling the Crustal Magnetic Field of Mars | 333 |
| 12.2.1 Data Selection | 333 |
| 12.2.2 Model Description | 334 |
| 12.2.3 The Predicted Surface Magnetic Field | 335 |
| 12.3 The Magnetization of Mars | 337 |
| 12.3.1 Method | 337 |

| | |
|--|-------------|
| Contents | xiii |
| 12.3.2 Results | 338 |
| 12.3.3 Magnetic Minerals | 340 |
| 12.4 Timing of the Core Dynamo | 341 |
| 12.4.1 Impact Craters | 342 |
| 12.4.2 Volcanoes | 343 |
| 12.5 Paleopoles | 346 |
| 12.5.1 Limits of Estimating Paleopole Positions | 346 |
| 12.5.2 Estimating Paleopole Positions on Mars | 349 |
| 12.6 Discussion and Summary | 351 |
| References | 353 |
| 13 Magnetic Signatures of Terrestrial Meteorite Impact Craters: A Summary | 357 |
| Stuart A. Gilder, Jean Pohl, and Michael Eitel | |
| 13.1 Brief Description of an Impact Event with Relevance to Magnetism | 358 |
| 13.2 Link Between Crater Structure and Local Aeromagnetic Signatures | 359 |
| 13.3 Magnetic Mineralogy | 364 |
| 13.3.1 Melt Rocks | 364 |
| 13.3.2 Target Rocks | 368 |
| 13.3.3 Shock Remanent Magnetization | 368 |
| 13.4 Paleomagnetism | 371 |
| 13.4.1 Crater Formation Processes | 371 |
| 13.4.2 Do Meteorite Impacts Influence the Geodynamo? | 373 |
| 13.5 Conclusions | 375 |
| References | 376 |
| 14 Magnetic Properties of the Iron–Nickel System: Pressure, Composition, and Grain Size | 383 |
| Michael Wack, Michael Volk, and Qingguo Wei | |
| 14.1 Introduction | 383 |
| 14.2 Magnetic Properties | 385 |
| 14.2.1 Magnetometry | 385 |
| 14.3 Studies on Synthetic Samples | 387 |
| 14.3.1 Structure | 387 |
| 14.3.2 Grain and Crystallite Size | 388 |
| 14.3.3 Chemical Synthesis | 389 |
| 14.3.4 Bulk Samples | 390 |
| 14.3.5 Mechanical Alloying | 391 |
| 14.3.6 Composition | 396 |
| 14.3.7 Pressure Cycling | 399 |
| 14.4 Conclusions | 402 |
| References | 403 |
| Index | 407 |

Contributors

Seiki Asari Institute for Mathematics, University of Potsdam, Potsdam, Germany

Maxwell Brown Helmholtz Centre Potsdam-GFZ German Research Centre for Geosciences, Potsdam, Germany

Present Address: Institute of Earth Sciences, University of Iceland, Reykjavik, Iceland

Jörg Büchner Max Planck Institute for Solar System Research, Göttingen, Germany

Emmanuel Chané Centre for Mathematical Plasma Astrophysics, KU Leuven, Leuven, Belgium

Lucia Duarte College of Engineering, Mathematics and Physical Sciences, University of Exeter, Exeter, UK

Michael Eitel Department of Earth and Environmental Sciences, Ludwig-Maximilians-Universität, Munich, Germany

Matthias Förster Helmholtz Centre Potsdam-GFZ German Research Centre for Geosciences, Potsdam, Germany

Ute Frank Helmholtz Centre Potsdam-GFZ German Research Centre for Geosciences, Potsdam, Germany

Martin French Institut für Physik, University of Rostock, Rostock, Germany

Thomas Gastine Institut de Physique du Globe de Paris, Sorbonne Paris Cité, Université Paris-Diderot, Paris, France

Marcus Gellert Leibniz Institute for Astrophysics Potsdam, Potsdam, Germany

Stuart A. Gilder Department of Earth and Environmental Sciences, Ludwig-Maximilians-Universität, München, Germany

Matthias Grott Institute of Planetary Research, German Aerospace Center, Berlin, Germany

Oliver Hartkorn Institute of Geophysics and Meteorology, University of Cologne, Cologne, Germany

Maosheng He Department of Physics and Earth Sciences, Jacobs University Bremen, Bremen, Germany

Department of Radar Soundings, Leibniz-Institute of Atmospheric Physics, University of Rostock, Kühlungsborn, Germany

Matthias Holschneider Institute of Applied Mathematics, University of Potsdam, Potsdam, Germany

Neeraj Jain Max Planck Institute for Solar System Research, Göttingen, Germany

Christoph Kasprzyk Helmholtz-Zentrum Dresden-Rossendorf, Dresden, Germany

Guram N. Kervalishvili Helmholtz Centre Potsdam-GFZ German Research Centre for Geosciences, Potsdam, Germany

Patrick Kilian Max Planck Institute for Solar System Research, Göttingen, Germany

Monika Korte Helmholtz Centre Potsdam-GFZ German Research Centre for Geosciences, Potsdam, Germany

Vincent Lesur Institut de Physique du Globe de Paris, Sorbonne Paris Cité, Université Paris-Diderot, Paris, France

Hermann Lühr Deutsches GeoForschungsZentrum GFZ, Potsdam, Germany

Patrick Meier Institute of Theoretical Physics and Institute for Geophysics and Extraterrestrial Physics, TU Braunschweig, Germany

Achim Morschhauser Helmholtz Centre Potsdam-GFZ German Research Centre for Geosciences, Potsdam, Germany

Uwe Motschmann Institute of Theoretical Physics, TU Braunschweig, Braunschweig, Germany

Patricio A. Muñoz Max Planck Institute for Solar System Research, Göttingen, Germany

Alexander A. Namgaladze Murmansk Arctic State University, Murmansk, Russia

Nadine Nettelmann Institut für Physik, University of Rostock, Rostock, Germany

Norbert Nowaczyk Helmholtz Centre Potsdam-GFZ German Research Centre for Geosciences, Potsdam, Germany

Alejandro Paredes Leibniz Institute for Astrophysics Potsdam, Potsdam, Germany

Jean Pohl Department of Earth and Environmental Sciences, Ludwig-Maximilians-Universität, Munich, Germany

Boris E. Prokhorov Helmholtz Centre Potsdam-GFZ German Research Centre for Geosciences, Potsdam, Germany

Ronald Redmer Institut für Physik, University of Rostock, Rostock, Germany

Günther Rüdiger Leibniz Institute for Astrophysics Potsdam, Potsdam, Germany

Joachim Saur Institute of Geophysics and Meteorology, University of Cologne, Cologne, Germany

Martin Seilmayer Helmholtz-Zentrum Dresden-Rossendorf, Dresden, Germany

Robin Senftleben Helmholtz Centre Potsdam-GFZ German Research Centre for Geosciences, Potsdam, Germany

Felix Spanier Centre for Space Research, North-West University, Potchefstroom, South Africa

Frank Stefani Helmholtz-Zentrum Dresden-Rossendorf, Dresden, Germany

Stephan Stellmach Institut für Geophysik, Westfälische Wilhelms-Universität Münster, Münster, Germany

Claudia Stolle Helmholtz Centre Potsdam-GFZ German Research Centre for Geosciences, Potsdam, Germany

Paul Thomas Institute of Planetary Research, German Aerospace Center, Berlin, Germany

Foteini Vervelidou Helmholtz Centre Potsdam-GFZ German Research Centre for Geosciences, Potsdam, Germany

Joachim Vogt Department of Physics and Earth Sciences, Jacobs University Bremen, Bremen, Germany

Michael Volk Department of Earth and Environmental Sciences, Ludwig-Maximilians-Universität, Munich, Germany

Michael Wack Department of Earth and Environmental Sciences, Ludwig-Maximilians-Universität, Munich, Germany

Ingo Wardinski Laboratory of Planetology and Geodynamics, University of Nantes, Nantes, France

Helmholtz Centre Potsdam-GFZ German Research Centre for Geosciences, Potsdam, Germany

Qingguo Wei Department of Earth and Environmental Sciences, Ludwig-Maximilians-Universität, Munich, Germany

Johannes Wicht Max Planck Institute for Solar System Research, Göttingen, Germany

Fabien Widmer Max Planck Institute for Solar System Research, Göttingen, Germany

Institut de Recherche sur la Fusion Magnétique, Cadarache, Saint-Paul-lez-Durance, France

Victoria Yaroshenko Helmholtz Centre Potsdam-GFZ German Research Centre for Geosciences, Potsdam, Germany

Xiaowei Zhou Max Planck Institute for Solar System Research, Göttingen, Germany

Purple Mountain Observatory of the Chinese Academy of Sciences, Nanjing, People's Republic of China

Chapter 1

General Introduction and Scientific Summary of the German Priority Program “PlanetMag”

Hermann Lühr, Johannes Wicht, Stuart A. Gilder,
and Matthias Holschneider

Abstract This book aims at understanding the diversity of planetary and lunar magnetic fields and their interaction with the solar wind. A synergistic interdisciplinary approach combines newly developed tools for data acquisition and analysis, computer simulations of planetary interiors and dynamos, models of solar wind interaction, measurement of terrestrial rocks and meteorites, and laboratory investigations. The following chapters represent a selection of some of the scientific findings derived by the 22 projects within the DFG Priority Program Planetary Magnetism” (PlanetMag).

This introductory chapter gives an overview of the individual following chapters, highlighting their role in the overall goals of the PlanetMag framework. The diversity of the different contributions reflects the wide range of magnetic phenomena in our solar system. From the program we have excluded magnetism of the sun, which is an independent broad research discipline, but include the interaction of the solar wind with planets and moons.

Within the subsequent 13 chapters of this book, the authors review the field centered on their research topic within PlanetMag. Here we shortly introduce the content of all the subsequent chapters and outline the context in which they should be seen.

H. Lühr (✉)

Deutsches GeoForschungsZentrum GFZ, 14473 Potsdam, Germany
e-mail: bluehr@gfz-potsdam.de

J. Wicht

Max Planck Institute for Solar System Research, Justus-von-Liebig-Weg 3, 37077 Göttingen,
Germany
e-mail: wicht@mps.mpg.de

S.A. Gilder

Department of Earth and Environmental Sciences, Ludwig Maximilians Universität,
Theresienstrasse 41, 80333 München, Germany
e-mail: gilder@lmu.de

M. Holschneider

Institute of Mathematics, University of Potsdam, Karl-Liebknecht-Str. 24-25, 14476 Potsdam,
Germany
e-mail: hols@uni-potsdam.de

1.1 Introduction

The results from recent space missions to Mars and Venus strongly indicate that planetary magnetic fields play a vital role in preventing atmospheric erosion by the solar wind. Without the geomagnetic field, for example, life on Earth as we know it would not be possible. However, very little is known about the underlying interaction between the solar wind and a planet's magnetic field. Space missions have also revealed that the planetary and lunar magnetic fields show surprising differences. These distinct magnetic signatures carry invaluable information about the past and present internal structure and dynamics of their parent bodies but many questions remain open. This book aims at understanding the diversity of planetary and lunar magnetic fields and their interaction with the solar wind. A synergistic interdisciplinary approach combines newly developed tools for data acquisition and analysis, computer simulations of planetary interiors and dynamos, models of solar wind interaction, measurement of terrestrial rocks and meteorites, and laboratory investigations.

Magnetic Fields in the Solar System comprises a summary of this effort on behalf of the numerous participants in the 22 projects in the Priority Program “Planetary Magnetism.” The book’s chapters are designed to introduce the reader to a variety of aspects of magnetic fields, touching many of the planets in the solar system. This includes the processes generating magnetic fields, techniques to represent the fields, and the interaction of planetary bodies with solar wind or other plasma streams.

This introductory chapter provides an overview of the individual following chapters, highlighting their role in the overall goals of the priority program Planetary Magnetism. The diversity of the different contributions reflects the wide field of magnetic phenomena in our solar system. From the program we have excluded magnetism of the sun, which is an independent broad research discipline, but include the interaction of the solar wind with planets and moons. This book represents only a selection of some of the scientific findings within the PlanetMag framework. A sizable number of articles have been published up to date and several are still expected to come.

An important issue for the Priority Program was the cooperation between groups working on different but related topics. In order to highlight the synergy effects, several groups have teamed up to write joined chapters. Additional cross-references between individual chapters are mentioned below.

The chapters are grouped into four topics, which also reflect the structure for the PlanetMag organization:

- Simulations of planetary interiors and dynamos
- Modeling of planetary magnetic fields
- Interaction of planetary magnetic fields with the plasma environment
- Characterizing ancient terrestrial rocks and meteorites, including laboratory investigations.

In the subsequent sections the following chapters are shortly introduced. At the end we provide some concluding remarks summarizing the special features of PlanetMag and touching on some emerging fields.

1.2 Planetary Interiors and Dynamos

At the time of writing, NASA's Juno mission has arrived at its target planet Jupiter, performing its extensive campaign to unravel the planet's interior structure and dynamics. And after almost 20 years in space, NASA's Cassini mission has come to a grand finale at Saturn. Its last months were devoted to following similar goals as Juno at Jupiter. In the second chapter of this book, *Wicht et al.* report on efforts within PlanetMag related to these missions. Scientists from the University Rostock, the University Münster, and the Max Planck Institute for Solar System Research teamed up their expertise to develop state-of-the-art models for the interior of gas planets in general and Jupiter in particular. One of the interesting predictions from their computer simulations is that Jupiter harbors two dynamos. The primary one in the deeper regions of the planet produces the large-scale field well known from previous missions. The secondary dynamo, however, operates at a depth of only 7000 km where Jupiter's surface zonal flow reaches down to electrical conductivities large enough for sizable induction effects to happen. The signatures of this latter dynamo are banded magnetic structures and patches at low to mid latitudes that may explain some of the unexpected measurements during the early Juno flybys.

Since numerical simulations cannot run at parameters that would realistically describe the conducting liquids of astrophysical dynamo regions, laboratory experiments provide essential counterparts. Chapter 5 (*Stefani et al.*) provides an account of several experiments that were performed at the Helmholtz Zentrum Dresden Rossendorf in collaboration with the Leibniz Institute for Astrophysics Potsdam. These experiments provide laboratory hands-on insight into several magnetic instabilities that play important roles in planets, stars, galaxies, or protoplanetary discs.

1.3 Modeling of the Geomagnetic Field

The geomagnetic field has been studied for centuries and remains a focus of intense research. Magnetizations preserved in archeological objects, sediments, or magmatic rocks provide information about the field from times up to billions of years ago. Several scientists from the Deutsches GeoForschungZentrum worked on different related problems within PlanetMag and *Korte et al.* report their progress in Chap. 3. Their contribution includes the maintenance of GEOMAGIA50, an important community database of magnetic samples, the acquisition of new data, and the development of global field models on different time scales, including detailed descriptions of the two most recent magnetic field excursions.

Global magnetic field models allow to downward continue the magnetic field to the top of Earth's core and thus to its source region. On timescale of decades to centuries, the variations of the core field are dominated by advection and can thus be inverted for the flow patterns at the top of the core. While this process provides a unique window into the core dynamics, it also has many potential pitfalls that are outlined by *Asari and Wardinski* in Chap. 4. Variations in the length of day on time scales of years to decades are thought to reflect the exchange of angular moment between the core and the mantle. They provide an important additional constraint on the core flow that is extensively discussed in Chap. 4.

1.4 Interaction of Planetary Magnetic Fields with the Plasma Environment

In this section, the diverse interactions of the planets and moons with their ionized environment are considered. It is appropriate to start this topic with the magnetosphere of Jupiter. It is by far the largest in the solar system and comprises a great variety of processes and effects. *Saur et al.* present in Chap. 6 the different kinds of interactions depending on the plasma speed (super-sonic, super-Alfvénic, or sub-Alfvénic). Furthermore, the resulting fields and currents depend on the properties of the obstacle (possessing a magnetic field, an atmosphere, or made up of an electrically conducting interior). Examples of all these types can be found in Jupiter's universe. Chapter six presents models that simulate these effects, and results are compared with observations.

Quite different are the conditions found at Venus, an unmagnetized planet. Here the interaction of the solar wind with the ionosphere generates an induced magnetosphere. In Chap. 7, *He and Vogt* describe some aspects of the magnetic field in the near Venusian space. The main emphasis of that chapter, however, is the presentation of analysis tools that identify the dependences of ionospheric-magnetospheric characteristics on controlling factors like solar wind, interplanetary magnetic field, or local time and season. The chosen approach in this case is empirical orthogonal functions. Some examples of successful application are presented.

Mercury possesses a weak intrinsic magnetic field. Combined with the enhanced solar wind pressure at its close distance to the sun (0.3 astronomical unit, AU), only a small magnetosphere forms. In spite of that, all the typical features like bow shock, magnetopause, elongated tail, and a cross-tail current sheet can be observed. The lack of an essential atmosphere and ionosphere, however, prevents the formation of a radiation belt and the display of auroras. In spite of these conditions satellite missions to Mercury have detected energetic electrons up to several hundred keV. With the help of numerical simulations, *Büchner et al.* explored in Chap. 8 the conditions for acceleration of solar wind electrons in several regions like the bow shock, magnetopause, and tail current sheet. Most favorable are the conditions in the thin tail current sheet, which is breaking up into multiple flux ropes.

Enceladus, one of Saturn’s moons, has been identified as the most important plasma source in the Saturnian magnetosphere. This geologically active moon blows out jets of water vapor and dust mainly in the South Pole region. The ejected material interacts with Saturn’s corotating magnetospheric plasma and forms a so-called dusty plasma plume. The physical properties of this mixture of electrons, ions, neutral and charged dust grains are described by *Yaroshenko et al.* in Chap. 9. Of particular interest is the modification of electric conductivity by the contamination of classical plasma by an admixture of small dust grains.

In the Priority Program PlanetMag, the Earth was included in the series of studied planets. Many of the effects observed here have been searched for on other planets. The much more complete observational coverage of our home planet has often successfully been used as a blueprint for the interpretation of the partly sparse data from other planets. For example, *Prokhorov et al.* simulated in Chap. 10 the distribution of ionospheric currents on Earth. Based on their results they computed the generated magnetic field, both on ground and at satellite altitudes. Alternatively, they forced all currents to flow in the ionospheric E-layer and calculated again the magnetic field. The differences between the two results show how important the current geometry is for properly interpreting magnetic field recordings in terms of electric currents.

Another topic of relevance for the terrestrial planets is the escape of the atmosphere, in particular the non-thermal escape of atoms and molecules that are too heavy to leave the gravity field. Here the intrinsic magnetic field plays an important role. It helps to deflect the solar wind around the planet and prevents it from directly eroding the atmosphere. As part of the Priority Program two independent studies were performed, one for Mars (no main field, only patchy crustal magnetic fields) and another one for Earth. The main results of the Mars study were published in Wei et al. (2012). Ion outflow on Earth was investigated by *Kervalishvili and Lühr* and described in Chap. 11. Recent observations in the magnetosphere inferred that the large majority of escaping ionospheric ions have low energy. Therefore, the focus in Chap. 11 is to identify mechanisms that lift the atmospheric particles out of the gravity field without heating them too much.

1.5 Characterizing Ancient Magnetised Rocks and Meteorites Including Laboratory Investigations

While Mars has no global magnetic field at present, the signature of an ancient dynamo is preserved in the form of a complex and surprisingly strong crustal magnetizations. In Chap. 12, *Morschhauser et al.* present a detailed global model for the crustal magnetic field, which indicates that the dynamo ceased to operate about 4.1 Gyr ago since younger large impact craters or volcanic edifices show clear signals of demagnetization. Deducing the structure of the ancient magnetic field, however, remains difficult.

Meteorite impacts have profoundly influenced the evolution of planets and moons in our solar system. Seismic waves generated by the shock can potentially influence the geodynamo when reaching the Earth's core. Cessation of the Martian dynamo was proposed to have been caused by a large meteorite impact. Chapter 13 (*Gilder et al.*) addresses whether shock waves generated during impact influenced the geodynamo. From a study of terrestrial craters up to 90 km in diameter, no evidence was found that the impact event disturbed the dynamo process. That paleomagnetic directions are well clustered at each crater suggests that building of the structures was completed before the ferrimagnetic minerals cooled through their Curie temperatures.

Several workers have studied meteorites to measure the range in magnetic field intensities present in the early solar system. The study of magnetic field intensity in rocks necessitates the presence of ideal “single-domain” sized magnetic recorders in the meteorites, which commonly contain Fe–Ni alloys as their main remanence-carrying minerals. However, the single domain threshold sizes of Fe–Ni alloys were unknown. In Chap. 14, *Wack et al.* introduce the magnetic properties of the Fe–Ni alloys and explain a unique way to synthesize Fe–Ni alloys in discrete size fractions to better understand how their magnetic properties vary as a function of grain size and pressure.

1.6 Concluding Remarks

Many important and new results have been achieved in the PlanetMag Priority Program. The performed in-depth studies were able to answer several of the open issues. At the same time new questions arose. In particular, new aspects are expected from the recent satellite measurements at Jupiter (Juno) and Saturn (Cassini, Grand Final). Observations from such low orbiting spacecrafts have never been available before. The detailed magnetic field data will certainly challenge our present understanding of the respective dynamo mechanisms. This national PlanetMag program has brought together expertise from a wide range of communities, including space science, geomagnetism, paleomagnetism, mathematics, modelers, and even solid-state physics. Several of the results are made possible by the synergy effects of interdisciplinary research. The German planetary community has greatly benefitted from this DFG priority program. The acquired momentum should definitely be used in future projects with national or international partners.

Reference

- Wei, Y., Fraenz, M., Dubinin, E., Woch, J., Lühr, H., Wan, W., Zong, Q.-G., Zhang, T.L., Pu, Z.Y., Fu, S.Y., Barabash, S., Lundin, R., Dandouras, I.: Enhanced atmospheric oxygen outflow on Earth and Mars driven by a corotating interaction region. *J. Geophys. Res.* **117**, A03208 (2012)

Chapter 2

Modeling the Interior Dynamics of Gas Planets

Johannes Wicht, Martin French, Stephan Stellmach, Nadine Nettelmann,
Thomas Gastine, Lucia Duarte, and Ronald Redmer

Abstract With NASA’s Juno mission having arrived at its target and ESA’s JUICE mission in planning, the interest in state-of-the-art models for the interior structure and dynamics of Jupiter is increasing. This chapter reports on the related attempts within the Special Priority Program PlanetMag of the German Science Foundation and provides an up-to-date review of the topic. Refined interior models are discussed that are based on new ab initio calculations for the equations of state for hydrogen and helium. For the first time, the depth-dependent transport properties have also been calculated, most notably an electrical conductivity profile that captures the transition from the molecular outer to the metallic inner hydrogen-rich envelopes. Anelastic simulations of convection show that the strong density stratification causes flow amplitudes to increase with radius while the flow scale decreases. Zonal jet systems very similar to those observed on Jupiter or Saturn are found in simulations of the molecular hydrogen envelope. Dynamo simulations that include the whole gaseous envelope show strikingly Jupiter-like magnetic field configurations when the strong density stratification is combined with an electrical conductivity profile that includes the significant drop in the molecular layer. While the dipole-dominated large-scale field is produced at depth, the equatorial jet can give rise to a secondary dynamo process where it reaches down to regions of sizable electrical conductivity. The magnetic surface signatures of this secondary dynamo are banded but also have

J. Wicht (✉)

Max Planck Institute for Solar System Research, Justus-von-Liebig-Weg 3, 37077 Göttingen, Germany

e-mail: wicht@mps.mpg.de

M. French • N. Nettelmann • R. Redmer

Institut für Physik, Universität Rostock, Rostock, Germany

S. Stellmach

Institut für Geophysik, Westfälische Wilhelms-Universität Münster, Münster, Germany

T. Gastine

Institut de Physique du Globe de Paris, Sorbonne Paris Cité, Université Paris-Diderot, UMR 7154 CNRS, 1 rue Jussieu, F-75005 Paris, France

L. Duarte

University of Exeter, Exeter, UK

more localized wave number $m = 1$ and $m = 2$ concentrations at lower latitudes. By detecting these features, the Juno mission should be able to constrain the deep dynamics of the equatorial jet.

2.1 Introduction

NASA's spacecraft Juno arrived at its target planet Jupiter in summer 2016. The main scope of the mission lies in the exploration of the planet's deep atmosphere and interior by measuring the magnetic and gravity fields to high precision. While the gravity data will constrain the interior structure and major wind system (Kaspi 2013), the magnetic field measurements will reveal the dynamics of the deep dynamo process. The "Grand Finale" of NASA's Cassini mission, which ended in September 2017, pursues similar goals for Saturn. The European space agency is preparing the Juice mission to the Jupiter system with an anticipated launch date in 2022. While the main motivation for all these activities is our very limited knowledge of the Solar System gas giants, the discovery of giant gas planets outside of the Solar system further stimulates interest in understanding these objects.

This chapter reports recent efforts to develop new models for Jupiter and Saturn in order to improve our understanding of their internal structure and dynamics, such as the generation of their magnetic fields. The models will be important for the interpretation of the Juno and also the Cassini Grand Finale data and may serve as a framework for future refinements suggested by the mission results. While most of the work discussed here was conducted within the Special Priority Program 1448 "PlanetMag" of the German Science Foundation, we also provide a more general overview on the topic.

The construction of new planetary models requires several steps that feed back on each other. First, ab initio simulations are used to explore the equations of state of the major constituents in the relevant pressure and temperature range. This forms the basis for constructing interior models that obey the measured gravity moments up to spherical harmonic degree $\ell = 6$, planetary rotation rate, radius, and the atmospheric chemical composition. Here we assume three layers: a rocky core and a two-part gas envelope. Both parts mainly consist of hydrogen and helium, but the inner part contains more helium and more heavy elements (Guillot 2005; Nettelmann et al. 2013). The interior models and transport properties provide essential input for the dynamo simulations. And since different input can lead to quite different results, the comparison of the simulated magnetic fields and flows with observations offers valuable constraints on the planetary interior.

Though the structure of both gas giants is thought to be similar, Saturn's core may be much larger and its gas envelope could be cold enough for hydrogen–helium demixing to occur. A consequence of the demixing is that helium forms droplets, which rain into the deep interior (Stevenson and Salpeter 1977a,b) and provide additional energy by converting gravitational energy into heat. This may lead to a negative outward helium gradient and thus a stable stratification, which

would prevent convection in deeper regions of Saturn’s envelope. Qualitatively, the extra energy can explain why Saturn emits much more heat than predicted by standard planetary evolution models (Fortney and Hubbard 2003). Hydrogen–helium demixing may also be related to the question of why Saturn’s magnetic field is strongly axisymmetric (Stevenson 1982). The stably stratified layer would filter out the more time-dependent non-axisymmetric field contributions due to the magnetic skin effect.

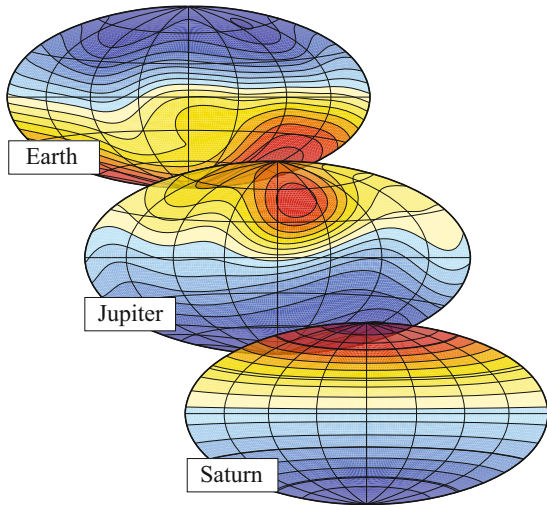
Once the temperature, density, and pressure profiles are established, which are typically assumed to be adiabats (isentropes), advanced ab initio methods are used to calculate transport properties (French et al. 2012). Of particular interest for the internal dynamo process is the electrical conductivity profile. When pressures are high enough (at about 90% of Jupiter’s radius), hydrogen undergoes a phase transition from the molecular to a metallic state (Chabrier et al. 1992; Fortney and Nettelmann 2010; Nettelmann et al. 2012). Since this transition lies beyond the critical point (Weir et al. 1996; French et al. 2012), however, there is no sharp change in the physical properties, such as the electrical conductivity, except perhaps for the onset of hydrogen–helium demixing triggered by hydrogen metallization.

Traditional fluid dynamics simulations were focused either on modeling the observed zonal wind systems in the upper part of the planetary envelope or the dynamo process in the deeper metallic envelope. The zonal winds have been successfully simulated with various approaches, among them are shallow “weather layer” models (Scott and Polvani 2008; Lian and Showman 2010) and “deep models” that represent the whole molecular layer (Heimpel et al. 2005; Gastine et al. 2013). However, replicating the wind structure in a deep layer that includes the metallic region proves difficult, as we will further discuss below.

Dynamo simulations aim at reproducing the measured planetary fields. Magnetic field models for Jupiter from the pre-Juno era rely on a few flybys and sometimes auroral information to constrain spherical harmonic surface field contributions up to degree $\ell = 4$ (Connerney et al. 1998; Grodent et al. 2008; Hess et al. 2011) or $\ell = 7$ at best (Ridley and Holme 2016). Due to its dedicated polar orbit, Juno is expected to constrain models up to $\ell = 15$ or higher. This even exceeds the resolution available for Earth where the crustal field shields harmonics beyond $\ell \simeq 14$. Saturn’s field can be reasonably constrained up to degree $\ell = 5$ (Cao et al. 2012) and Cassini’s Grand Final mission is expected to considerably improve this current limit.

While Jupiter’s magnetic field looks Earth-like with a clear dipole dominance and a dipole tilt of 10°, Saturn’s field seems perfectly axisymmetric and is concentrated at higher latitudes (see Fig. 2.1). This is incompatible with Cowling’s theorem, which states that a perfectly axisymmetric magnetic field cannot be maintained by dynamo action. A possible stably stratified layer could provide a viable explanation (Stevenson 1982): It would act as a filter that prevents non-axisymmetric or otherwise complex and fast-varying field contributions to reach the planetary surface (Cao et al. 2012). While simplified dynamo simulations support this view (Christensen and Wicht 2008), implementing the stratified layer in a more realistic manner is rather challenging. Thus, we will mainly report on efforts to model Jupiter’s dynamo.

Fig. 2.1 Comparison of the radial surface field model GRIM (Lesur et al. 2008) for Earth, VIP4 (Connerney et al. 1998) for Jupiter, and the spherical harmonic degree $\ell = 5$ model (Cao et al. 2012) for Saturn



Since Jupiter’s magnetic field has a very Earth-like configuration, it is tempting to assume that numerical geodynamo simulations capture the appropriate dynamics. However, more recent simulations have shown that it becomes increasingly difficult to maintain dipole-dominated fields when modifying the geodynamo models to better represent gas planets.

This chapter is organized as follows: In Sect. 2.2 we discuss the new interior structure models that rely on ab initio simulations. Section 2.3 then introduces the mathematical formulation and numerical methods for the simulations of the interior dynamics. Section 2.4 concentrates on nonmagnetic simulations with a special focus on reproducing the observed zonal jets in “deep models.” In Sect. 2.5 we then discuss the development from Earth-like dynamo simulations to the most realistic integrated Jupiter models. A discussion on our combined efforts in Sect. 2.6 closes the chapter.

2.2 Interior Structure and Properties of Jupiter and Saturn

Gas giants like Jupiter and Saturn contain mainly hydrogen and helium plus smaller amounts of heavier elements. The calculation of interior models for these planets requires accurate information on the properties, first and foremost the equation of state (EOS), of the relevant materials inside the planet. In Jupiter, for example, the thermodynamic conditions change significantly with depth because pressure and temperature increase from 1 bar and about 170 K at the surface to extreme values of up to about 70 Mbar and 20,000 K in the center. Therefore, most of the planet’s interior consists of a dense multi-component plasma with high electrical

conductivity, which is surrounded by an outer envelope of molecular and atomic gases.

So far, it is not possible to determine the material properties of such hydrogen–helium mixtures across the entire pressure–temperature domain experimentally. Experiments in the 1 Mbar pressure range but nevertheless relatively low temperatures are one of the great challenges in high-pressure physics. Static pressures of a few Mbar can be realized in solid hydrogen in diamond anvil cells (DACs) at relatively low temperatures. The location of the high-pressure phases I, II, and III and of the melting line up to 1000 K has been studied in depth (McMahon et al. 2012). New high-pressure phases IV, V, and VI have been predicted, and metallization of solid hydrogen was reported recently at about 5 Mbar (Dias and Silvera 2017). Higher pressures can be reached with dynamic experiments using shock waves driven by, e.g., gas guns, high explosives, high-power lasers, or pulsed power. While single-shock-wave experiments probe thermodynamic states along the Hugoniot curve, other dynamic compression techniques are more suitable for reaching states that occur in the deep interior of gas giant planets. Examples for such techniques are reverberating shocks in sandwich targets (with gas guns) (Weir et al. 1996), spherical implosions driven by high explosives (Fortov et al. 2007), and quasi-isentropic ramp compression using pulse-shaped high-power optical lasers (Moses 2011). Strong evidence for an abrupt insulator-to-metal transition in liquid hydrogen at about 3 Mbar and very few 1000 K has been deduced from experiments using Sandia’s Z machine (pulsed power) (Knudson et al. 2015). Another option in this context is the use of precompressed targets in the gaseous or liquid state up to about 0.1 GPa or in small DACs up to few GPa (Holst et al. 2012). Alternatively, new static compression techniques, such as double-stage or laser-heated dynamic DACs, will enable the study of pressures well beyond 3–4 Mbar and above temperatures of 5000 K (Dubrovinsky et al. 2012). Using such high-pressure platforms at free electron lasers as, e.g., LCLS in Stanford, SACLA in Japan, or the European XFEL in Hamburg will allow probing extreme states of matter with so far unprecedented accuracy.

Despite the recent progress on experiments, it is necessary to develop wide-range material models based on theoretical many-particle physics that cover states from the surface of a planet to its deep interior. For instance, wide-range EOSs were designed by Kerley (Sesame) (Kerley and Christian-Frear 1993; Lyon and Johnson 1992), Saumon, Chabrier, and Van Horn (SCvH) (Saumon et al. 1995), and Juraneck et al. (2002) based on chemical models and then applied successfully in astrophysics. The accuracy of such EOS models can be improved considerably by using ab initio simulations for conditions where strong correlations are dominant and chemical plasma models usually fail (McMahon et al. 2012). Ab initio EOSs (Caillabet et al. 2011; Militzer and Hubbard 2013; Becker et al. 2014) are validated against available experimental data and applied to predict planetary interiors and evolution scenarios (Guillot and Gautier 2015).

2.2.1 Material Properties from Density Functional Theory and Molecular Dynamics

A powerful theoretical framework for calculating material properties under extreme conditions is based on density functional theory (DFT). In DFT, the electronic structure of matter is calculated on a quantum-statistical level that allows one to take the Coulomb interactions between the electrons into account in an efficient way (Dreizler and Gross 1990; Kohanoff 2006). DFT reformulates the quantum many-particle problem of interacting electrons into an effective one-particle problem that can be solved on modern computers. The central quantity in DFT is the electron density

$$n(\mathbf{r}) = \sum_i f_i |\psi_i(\mathbf{r})|^2 , \quad (2.1)$$

where $\psi_i(\mathbf{r})$ is the wavefunction of Kohn–Sham state i and f_i is its Fermi occupation number. The Kohn–Sham states are determined by solving the effective Schrödinger equation

$$\left[-\frac{\hbar^2}{2m_e} \nabla^2 + V_{\text{KS}}(\mathbf{r}) \right] \psi_i(\mathbf{r}) = E_i \psi_i(\mathbf{r}) , \quad (2.2)$$

where m_e is the electron mass and E_i the eigenvalue of state i . The Kohn–Sham potential $V_{\text{KS}}(\mathbf{r})$ is the effective many-particle potential of the electrons which contains their mutual interaction and is defined as:

$$V_{\text{KS}}(\mathbf{r}) = -\frac{e^2}{4\pi\epsilon_0} \sum_n \frac{Z_n}{|\mathbf{r} - \mathbf{R}_n|} + \frac{e^2}{4\pi\epsilon_0} \int d^3\mathbf{r}' \frac{n(\mathbf{r}')}{|\mathbf{r} - \mathbf{r}'|} + V_{\text{XC}}(\mathbf{r}) . \quad (2.3)$$

The first term is the potential energy of an electron in the Coulomb field of the nuclei (external potential), where Z_n and \mathbf{R}_n are their charge numbers and position vectors, respectively. The second term describes the classical electron–electron interaction (Hartree potential) and the third term is the exchange correlation (XC) potential $V_{\text{XC}}(\mathbf{r})$, which contains exchange contributions and correlation effects from interactions between the electrons.

Equations (2.1)–(2.3) are solved self-consistently, which results in the minimization of the total energy of the electron system (Hohenberg and Kohn 1964; Kohn and Sham 1965; Mermin 1965) represented by an energy density functional $E[n(\mathbf{r})]$, which also includes terms that correspond to those in Eq. (2.3).

The XC term is not exactly known and has to be approximated. In most cases here, the approximation of Perdew, Burke, and Ernzerhof (PBE) (Perdew et al. 1996) is used, which can reproduce the atomization energies of many molecules and lattice constants of solids to an accuracy of very few percent (Haas et al. 2009).

After converging the electronic structure calculation, the force on each individual nucleus is calculated via the Hellmann–Feynman theorem (Feynman 1939). In a subsequent molecular dynamics (MD) step, all nuclei are moved according to Newton’s equation of motion, which changes their positions \mathbf{R}_n . By alternating DFT and MD-step calculations, the electronic wave functions $\psi_i(\mathbf{r})$ and nuclear coordinates \mathbf{R}_n are propagated in time, which results in the DFT-MD simulation method (Marx and Hutter 2009).

On parallel high-performance computers, one can simulate ensembles of few hundred nuclei (plus their electrons) for time scales of about 10 ps (several 10,000 time steps of 0.2–0.5 fs) with DFT-MD. This is sufficient to calculate well-converged thermodynamic equilibrium quantities like pressure p and internal energy u at many different densities ϱ and temperatures T , so that corresponding EOS tables can be generated.

Moreover, one can derive transport properties using expressions from linear response theory. For example, viscosity, diffusion coefficients, and the electrical and thermal conductivity from the nuclei can be derived via autocorrelation functions of the pressure tensor, particle velocities, electric current, or heat current (Allen and Tildesley 1989), respectively.

Electronic transport coefficients are derived from current–current correlation functions, like the Kubo–Greenwood formula for the electronic conductivity (Kubo 1957; Greenwood 1958; Desjarlais 2003)

$$\sigma_e = \lim_{\omega \rightarrow 0} \frac{\pi e^2}{3V\omega} \sum_{ij} |\langle i | \hat{\mathbf{v}} | j \rangle|^2 (f_i - f_j) \delta(E_j - E_i - \hbar\omega), \quad (2.4)$$

where $\langle i | \hat{\mathbf{v}} | j \rangle$ are matrix elements of the velocity operator with the electronic states i and j . Similar expressions for related quantities, like the electronic heat conductivity, are known as well (Holst et al. 2011).

2.2.2 Properties of Hydrogen–Helium Mixtures at Conditions in the Interior of Jupiter and Saturn

At about 90% of Jupiter’s radius (about $p \approx 0.5$ Mbar, $T \approx 4300$ K), the hydrogen–helium mixture becomes metallic as the hydrogen molecules dissociate and ionize. This metallization transition is continuous at such high temperature, similar as in pure hydrogen. Figure 2.2 displays the phase diagram of hydrogen predicted by DFT-MD at high pressures, including a Jupiter isentrope (Nettelmann et al. 2012). The flattening of the isentrope in the transition region is caused by an enhanced heat capacity of the H/He mixture due to the dissociation and ionization of hydrogen. It has long been argued that this transition from a molecular, nonconducting fluid to a conducting plasma is of first order below a critical temperature of about 10,000 K (McMahon et al. 2012). Recent measurements using Sandia’s Z machine

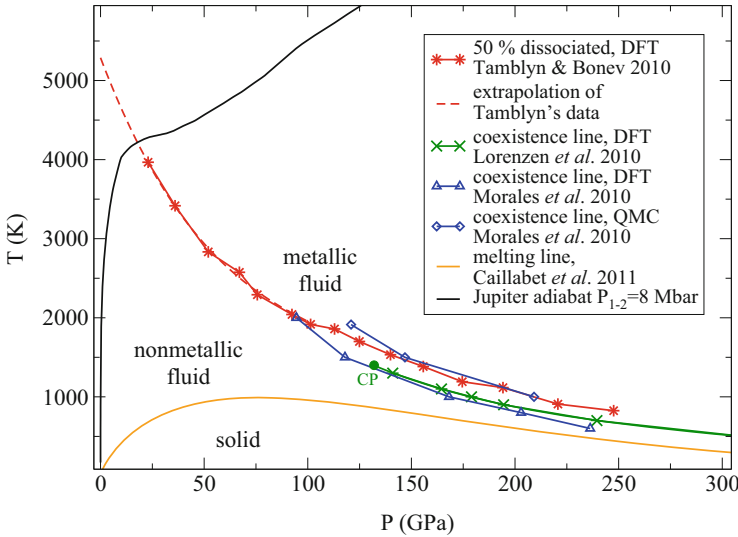


Fig. 2.2 Theoretical phase diagram of hydrogen including the Jupiter adiabat from French et al. (2012). The data are taken from Tamblyn and Bonev (2010), Lorenzen et al. (2010), Morales et al. (2010), and Caillabet et al. (2011). Recent experiments (Knudson et al. 2015) indicate that, at temperatures below the critical point (CP), the insulator-to-metal transition occurs at somewhat higher pressures (~ 300 GPa) than predicted by the DFT-MD calculations

(Knudson et al. 2015) indeed strongly indicate that this insulator-to-metal transition is a first-order liquid-liquid phase transition, but only at temperatures of about 2000 K or lower. The exact transition pressure is still subject of discussion though (Pierleoni et al. 2016).

For the modeling of gas giants, EOS tables for hydrogen and helium have been constructed using DFT-MD simulation data. These tables span several orders of magnitude in density and temperature (Becker et al. 2014), which is achieved by combining DFT-MD data for the dense gas and plasma with simpler chemical EOS models (Saumon et al. 1995; Juranek et al. 2002) at low densities that describe the weakly interacting plasma and gas well.

Along almost the entire Jupiter isentrope, the EOS of the hydrogen–helium mixture can be approximated well by the EOS of the pure substances using linear mixing rules (Militzer and Hubbard 2013; Becker et al. 2014). However, in specific p - T regions, hydrogen and helium can demix and macroscopically separate from each other (Lorenzen et al. 2009; Morales et al. 2009). This effect is especially strong in the cooler planet Saturn and it may lead to helium rain and the formation of a stably stratified zone.

The calculation of a hydrogen–helium demixing phase diagram is challenging with DFT-MD. It requires to determine the Gibbs free energy $g(T, p, x) = u + p/\rho - Ts$ of mixing for several molar fractions x of helium in hydrogen (Lorenzen et al. 2009; Morales et al. 2009) and performing double-tangent constructions with

$\Delta g(x)$ for various pressures and temperatures. Especially, the Gibbs free energy contains the entropy s as an additional thermodynamic quantity, which is not directly accessible in DFT-MD simulations and requires more elaborate simulation techniques (Morales et al. 2009; Desjarlais 2013).

According to the two most recent DFT-MD studies (Lorenzen et al. 2011; Morales et al. 2013), H-He demixing occurs across a large portion of Saturn's interior but may not happen in Jupiter. Respective consequences are discussed below.

In contrast to many thermodynamic properties, the transport properties are usually much more sensitive to the concentration of the hydrogen–helium mixture. Large efforts have been made to calculate the electrical conductivity, thermal conductivity, diffusion coefficients, and viscosity in a hydrogen–helium mixture along the Jovian isentrope (French et al. 2012). Especially, the radial dependence of the electrical conductivity is strongly influenced by the metallization transition near $0.9R_J$, see Fig. 2.7 in Sect. 2.3. The kinematic shear viscosity, on the other hand, is almost constant throughout the interior of Jupiter, whereas the dynamic shear viscosity is not, see Fig. 2.3.

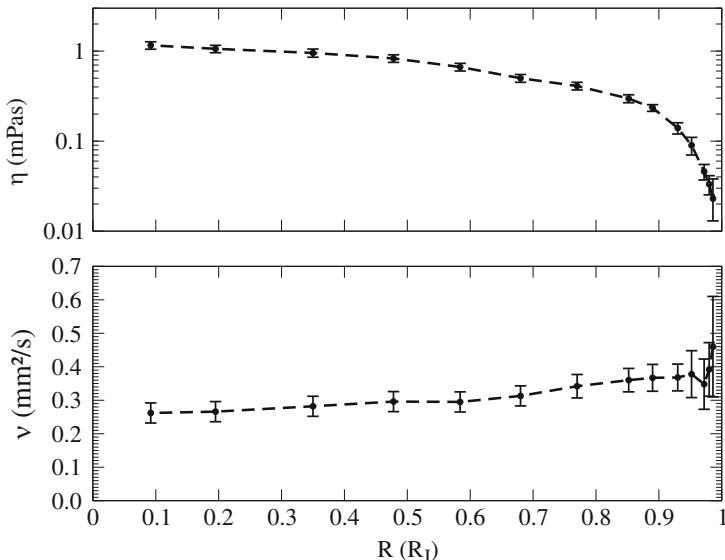


Fig. 2.3 Dynamic shear viscosity η (upper panel) and kinematic shear viscosity ν (lower panel) of the hydrogen–helium mixture inside Jupiter (French et al. 2012)

2.2.3 Standard Interior Models

Interior structure models of Jupiter and Saturn are required in this context in order to obtain internal density-temperature-pressure profiles. Those provide not only the background state for the flow, see Sect. 2.5, but also the conditions for which the thermodynamic and transport coefficients (electrical conductivity, viscosity, specific heat, etc.) are computed, which in turn enter the MHD equations for the dynamo modeling. Here we describe how planetary profiles are generated under standard assumptions for the internal structure. More detailed descriptions can be found in Guillot (2005) and Nettelmann et al. (2012).

Interior structure models for Jupiter and Saturn rest on four columns: observational data, constituent physics, physical laws, and assumptions.

While the mean density, derived from measured mass (M) and radius (R), allows an estimate of the bulk composition, i.e., H/He-dominated for gas giant planets, detailed internal properties can only be derived indirectly from the constraints observed at the planetary surface, for gas giants commonly taken to be the 1-bar pressure level. It is foremost the low-order gravitational harmonics J_2 and J_4 that respond to the internal density distribution $\rho(r)$, while the heat flow contains clues on the internal temperature profile and thus the dynamic state. J_2 and J_4 have been observed for all four giant planets in the Solar system, and the Juno mission is designed to increase the accuracy from about $1 : 10^6$ to $1 : 10^9$ for Jupiter's gravity field. In particular, we have

$$J_{2n} = -\frac{1}{MR_{\text{eq}}^{2n}} \int_V r^2 \sin \theta \rho(r, \theta) r^{2n} P_{2n}(\cos \theta) d\phi d\theta dr \quad (2.5)$$

for the even gravitational harmonics, where P_{2n} denote Legendre polynomials and r, ϕ, θ spherical coordinates. For an isolated, nonrotating fluid planet in hydrostatic equilibrium, $\rho = \rho(r)$ and the integration over the polar angle θ can be performed separately, yielding $J_{2n} = 0$ for $n > 0$. However, Jupiter and Saturn are rotating which leads to a flattening of their equipotential surfaces $r_l(\theta)$, including the surface itself, and thus to $J_{2n} \neq 0$. The density profile, which is constant on equipotential surfaces, can then be adjusted to reproduce the observed J_2 and J_4 values.

Assuming the planet has three distinct layers, the mean densities of two compositionally different H/He-rich envelope layers are adjusted by an appropriate choice of their respective heavy-element mass fractions Z_1 and Z_2 . The rocky core mass is then obtained as the remaining mass, $M_{\text{core}} = M - M_{\text{env}}$. Assuming the planet has only two layers (envelope+core), the envelope Z is typically adjusted to match J_2 , while the resulting deviation between the model- J_4 and the observed J_4 value can be used to estimate the presence of further effects, such as differential rotation (Militzer et al. 2008), EOS uncertainties (Saumon and Guillot 2004), or uncertainties in the bulk helium abundance (Miguel et al. 2016). In this work, we have adopted the three-layer assumption, which raises the fundamental question of

what may cause and maintain a compositional gradient within the H/He-dominated envelope, and if this assumption is consistent with the results from dynamo models for Jupiter and Saturn. This is a topic of ongoing research.

We fix the He mass fraction in the outer envelope to the observed value and chose a heavy-element mass fraction Z_1 that is consistent with the observed enrichment in C, N, and heavy noble gases over the solar value (Nettelmann et al. 2012). The transition to the deeper envelope is assumed to be sharp and is located within the metallic region at 4 Mbar or deeper. The heavy-element mass fraction Z_1 of the outer envelope is then consistent with the observed atmospheric enrichment in C, N, and heavy noble gases over the solar value (Nettelmann et al. 2012). We employ versions 2 and 3 of our ab initio H/He-EOS (Nettelmann et al. 2012; Becker et al. 2014), which yield small changes in our resulting planetary profiles. Typical three-layer models for Jupiter and Saturn are displayed in Fig. 2.4, while the interior density, pressure, and temperature profiles of the respective Jupiter model are shown in Fig. 2.5.

Using our ab initio H/He EOS, we find that the fraction of heavy elements must increase with depth in Jupiter (Nettelmann et al. 2012), but might be constant throughout the envelope in Saturn if the boundary between the envelope is put at not too high pressures of about $P_{\text{sep}} \sim 3$ Mbar (Nettelmann et al. 2013).

The chosen value of the layer boundary pressure P_{sep} also influences the resulting size of the rocky core significantly. This induces an additional uncertainty in the determination of the core mass even if the low-order gravitational harmonics would be precisely known. Within the adiabatic three-layer model approach, resulting

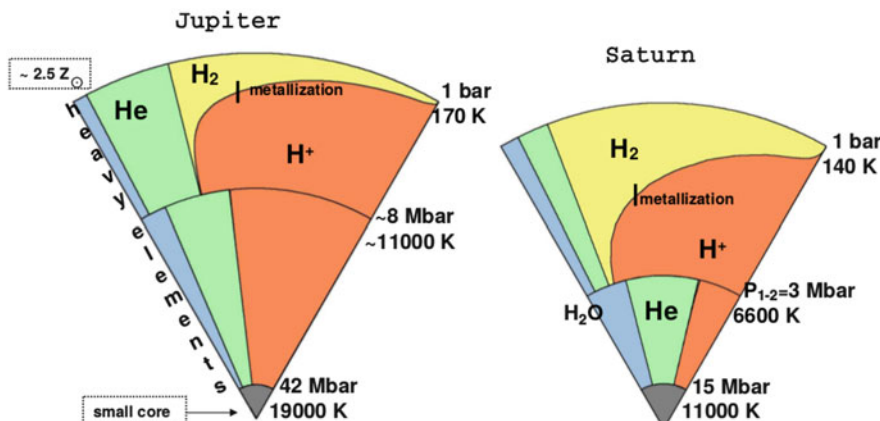


Fig. 2.4 Three-layer models for Jupiter (left) (Nettelmann et al. 2012) and Saturn (right) (Nettelmann et al. 2013). Their internal profiles are used as input for thermophysical property calculations and dynamo models. Colors code the different assumed constituents, blue: water as a representative for heavy elements, green: helium, yellow: molecular hydrogen, orange: atomic hydrogen. The black bar indicates the region where hydrogen metallizes. In these depicted models, the boundaries between the two H/He-rich envelopes are chosen to be located at $P_{\text{sep}} = 8$ Mbar for Jupiter and $3 \lesssim$ Mbar in Saturn

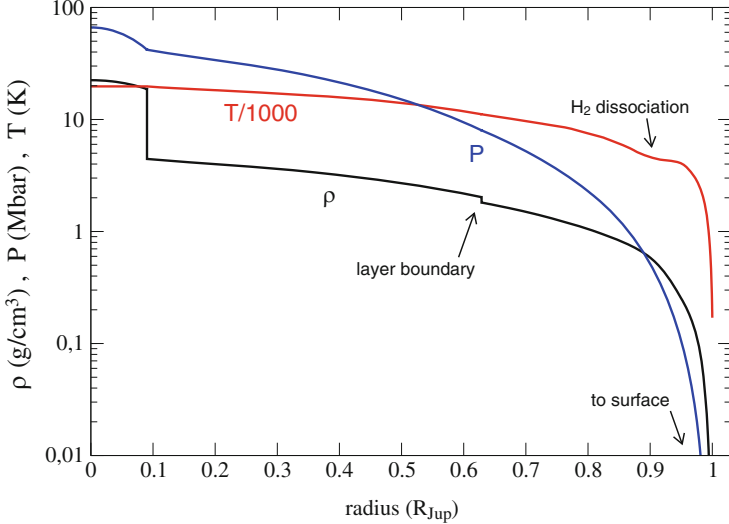


Fig. 2.5 Interior profiles of density (black), pressure (blue), and temperature (red) of our three-layer Jupiter model shown in Fig. 2.4. The separation between the He-poor outer and the He-rich inner envelope, which also contains more heavier elements, is modeled by a sharp change in composition that explains the small jump in density. Note the flattening of the T -profile due to H_2 dissociation (French et al. 2012)

core masses are typically below $10 M_E$ and decrease with increasing P_{sep} value (Miguel et al. 2016; Nettelmann et al. 2012). Moreover, the real interior structure of Jupiter and Saturn may be different from the simple adiabatic few-layer assumption due to the unknown efficiency of convective mixing (Helled and Stevenson 2017). Therefore, the size of the heavy-element-rich central region, i.e., the inner core, may be larger than predicted so far. One goal of the Juno mission is to determine that size. Combined efforts from internal structure modeling and from flow and magnetic field modeling may be necessary to reach that goal.

In agreement with previous work (e.g., Stevenson and Salpeter 1977b; Fortney and Hubbard 2003), we find that such adiabatic structure models yield too low luminosities for present Saturn. This well-known deviation is generally attributed to the assumption of homogeneous thermal evolution where the local mean molecular weight stays constant with time. This precludes physical processes, such as sedimentation and erosion. On the other hand, sedimentation of a major species could significantly change the gravitational energy of the planet and thus have a strong effect on the thermal evolution. We discuss this issue in Sect. 2.2.4.

2.2.4 Thermal Evolution and H/He Phase Separation

Helium is predicted to phase separate from hydrogen under certain conditions, which may occur in cool gas giant planets (Stevenson and Salpeter 1977b). Thus, sedimentation of helium as a result of phase separation has long been suggested to explain Saturn's high luminosity and perhaps also the depletion in helium in the atmospheres of both Jupiter and Saturn (Wilson and Militzer 2010). Moreover, the dipolarity of Saturn's magnetic field and its alignment with the rotation axis can hardly be explained without invoking the presence of a differentially rotating and/or stably stratified, nonadiabatic zone atop the dynamo region (Cao et al. 2012; Christensen and Wicht 2008). Helium sedimentation could possibly provide the reason for such a zone, as the sunken helium naturally leads to a mean molecular gradient which can suppress convective motion. Important questions in this regard are the location and thickness of such a zone and whether or not the additional gravitational energy can quantitatively explain Saturn's excess luminosity.

Lorenzen et al. (2011) calculated the H/He miscibility gap at pressures of a few Mbars using DFT-MD simulations. It was found that at pressures $P \ll 1$ Mbar the demixing temperature drops steeply, while at pressures $P > 10$ Mbar it stays nearly constant with pressure but increases strongly with helium mass fraction Y , see Fig. 2.6. According to these results, the adiabats of Jupiter and Saturn would enter the H/He demixing region at $P \sim 1$ Mbar. The corresponding point of exit needs to be determined self-consistently by taking into account the amount of helium that has settled down. For Jupiter, Y values around 0.3 are found for the helium-rich, metallic inner envelope compared to the measured value of 0.238 in its very outer

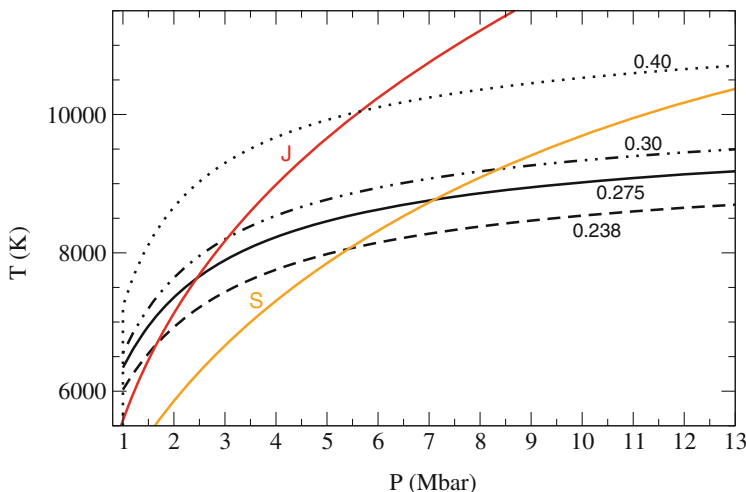


Fig. 2.6 H/He demixing curves $T(P)$ for different helium mass fractions as labeled (*black*) according to the Lorenzen H/He phase diagram (Lorenzen et al. 2009); *colored curve*: the adiabats of the Jupiter and Saturn structure models from Fig. 2.4

atmosphere. Values of up to $Y = 0.4$ may be reached in Saturn's inner envelope, assuming standard models. The protosolar value is 0.275 so that Jupiter's outer envelope is clearly depleted in comparison.

In line with that, Püstow et al. (2016) find that Saturn's envelope—if adiabatic—would not exit the demixing region (Fig. 2.6) so that helium droplets would fall all the way down to the core and form a He layer on top of it. Therefore, in case that hydrogen–helium demixing causes the existence of a stably stratified zone and if that zone remains of nearly adiabatic temperature profile, it would persist down to the core and not stop atop the respective dynamo region. However, we also found that the H/He phase diagram by Lorenzen et al. (2009, 2011) yields to high luminosities for Saturn by allowing too much He rain out. We also caution that Saturn's H/He demixing zone may not be adiabatic, which potentially has a larger impact on the amount of He that has rained down during the planet's evolution and also on the thickness of the He rain layer.

Our results suggest that small uncertainties in the H/He demixing diagram can have significant effects on the planetary luminosity, the atmospheric helium abundance, and the thickness of the He rain zone in Jupiter and Saturn. Further work will include the systematic investigation of the interplay between modifications to the Lorenzen H/He phase diagram, the internal structure and thermal evolution of Jupiter and Saturn, as well as the magnetic field generation.

2.3 Magneto-Hydrodynamic Equations and Numerics

Self-consistent approaches geared to model planetary dynamo action simultaneously solve for the convective fluid flow and magnetic field generation in a rotating spherical shell. The shell is confined by an outer boundary at radius r_o , which may represent the transition to the molecular hydrogen envelope in the gas planets or the outer boundary of the considered atmosphere in the integrated models. An inner boundary at $r = r_i$ models the surface of the rocky core. The convective motion is driven by gravity acting on density differences. These differences are caused by temperature variations due to the secular cooling of the planet. The heating and compositional fractionation associated with helium separation and sedimentation provide another potential driving mechanism not discussed further here. While this process may play a key role in Saturn, it may not even have started in the much hotter planet Jupiter.

Only temperature variations that exceed the adiabatic gradient give rise to destabilizing effects and have to be considered. The simulations thus solve for a small disturbance around a hydrostatic, adiabatic, and nonmagnetic background state. When simulating the dynamics in the iron cores of terrestrial planets, the density and temperature gradients are typically ignored in the so-called Boussinesq approximation (Braginsky and Roberts 1995). For gas planets, the anelastic formulation allows including radial gradients in the background density, temperature, and pressure while filtering out sound waves that would require a significantly smaller

time step (Glatzmaier 1984; Braginsky and Roberts 1995; Lantz and Fan 1999). This chapter explains the mathematical formulation of dynamo dynamics in the anelastic approximation.

We start with discussing the fundamental fluid dynamic equations for describing convection in Sect. 2.3.1. Section 2.3.2 is then devoted to deriving the properties of the background state, while Sect. 2.3.3 explains the first-order dynamical equations. These are transformed into a dimensionless form in Sect. 2.3.4 where we also finally introduce the dynamo equation that describes the magnetic field evolution. Boundary conditions and the radial dependence of the background state are discussed in Sects. 2.3.5 and 2.3.6. We close the derivation of the anelastic formulation with a brief outline of the numeric strategy used in the MHD-code MagIC in Sect. 2.3.7. MagIC contributed to the benchmark study for anelastic convective dynamos simulations. More details on the theoretical background and on the methods used by other codes can be found in the respective publication (Jones et al. 2011).

2.3.1 Fundamental Dynamic Equations

We start with introducing the equations for the convective problem. Changes in the convective flow are described by the Navier–Stokes equation that formulates the conservation of momentum in a frame of reference rotating with rate Ω :

$$\rho \frac{d\mathbf{U}}{dt} = -\nabla p + \rho\mathbf{g} + 2\rho\Omega\mathbf{U} \times \hat{\mathbf{z}} + \mathbf{J} \times \mathbf{B} + \rho\mathbf{F}_v. \quad (2.6)$$

Here \mathbf{U} is the flow, \mathbf{B} the magnetic induction, \mathbf{g} the gravity acceleration, $\hat{\mathbf{z}}$ the unit vector in the direction of the planetary rotation axis, and $\hat{\mathbf{r}}$ the unit vector in radial direction. The modified pressure p contains the non-hydrostatic pressure, the centrifugal effects, and may also account for variations of the gravity potential (Braginsky and Roberts 1995). We have used the substantial time derivative that combines the effects of local changes and advection: $d/dt = (\partial/\partial t + \mathbf{U} \cdot \nabla)$. The forces on the right-hand side of Eq. (2.6) are, in this order, pressure gradient, buoyancy, Coriolis force, Lorentz force, and viscous force. The viscous forces have the components

$$F_{vi} = \frac{\partial}{\partial x_j} V_{ij}, \quad (2.7)$$

where

$$V_{ij} = 2\nu \left(e_{ij} - \frac{1}{3} \nabla \cdot \mathbf{U} \right) \quad (2.8)$$

are the elements of the viscous stress tensor that depends on the rate of strain tensor

$$e_{ij} = \frac{1}{2} \left(\frac{\partial U_i}{\partial x_j} + \frac{\partial U_j}{\partial x_i} \right). \quad (2.9)$$

Here x_i denotes the three spatial directions and ν is the kinematic shear viscosity.

The second equation is the continuity equation,

$$\frac{\partial \rho}{\partial t} = -\nabla \cdot (\rho \mathbf{U}), \quad (2.10)$$

which guarantees conservation of mass and describes the dynamic density changes due to the flow. The flow itself is driven by buoyancy, i.e., by gravity acting on thermodynamic density variations. When expressing density in terms of specific entropy S and pressure p , evolution equations for both of these quantities are required to close the description of the dynamo problem.

The Navier–Stokes equation can be used to solve for the pressure evolution (see Sect. 2.3.7). A general evolution equation for specific entropy reads

$$\rho \frac{dS}{dt} = -\nabla \cdot \mathbf{I}^S + q^S, \quad (2.11)$$

where \mathbf{I}^S is an entropy flux and q^S an entropy source. Rewriting this in terms of a heat or energy equation yields

$$\rho T \frac{dS}{dt} = -\nabla \cdot (T \mathbf{I}^S) + q, \quad (2.12)$$

with heat flux $T \mathbf{I}^S$ and heat sources q (Braginsky and Roberts 1995). We will consider two heat sources: viscous heating

$$q_v = \rho V_{ij} e_{ij} \quad (2.13)$$

and Ohmic heating

$$q_J = \frac{1}{\mu_0^2 \sigma} (\nabla \times \mathbf{B})^2, \quad (2.14)$$

where μ_0 is the magnetic permeability and σ the electrical conductivity. In Eq. (2.13) the sum convention over identical indices is assumed. The entropy flux is classically simply related to the heat diffusion:

$$\mathbf{I}^S = -\frac{1}{T} k \nabla T, \quad (2.15)$$

where k is the thermal conductivity. However, we chose a different formulation further discussed below.

Instead of an explicit equation of state we use a simplified version that describes the dependence of density on specific entropy and pressure:

$$\frac{1}{\rho} d\rho = -\alpha_S dS + \beta_S dp. \quad (2.16)$$

The two thermodynamic properties are the compressibility at constant entropy,

$$\beta_S = \frac{1}{\rho} \left(\frac{\partial \rho}{\partial p} \right)_S \quad (2.17)$$

and the quantity α_S that obeys the relation

$$\alpha_S = -\frac{1}{\tilde{\rho}} \left(\frac{\partial \rho}{\partial S} \right)_p = \left(\frac{\partial T}{\partial p} \right)_S = \frac{\alpha T}{c_p}, \quad (2.18)$$

with the isobaric heat capacity

$$c_p = \frac{1}{T} \left(\frac{\partial S}{\partial T} \right)_p \quad (2.19)$$

and thermal expansivity

$$\alpha = \frac{1}{\rho} \left(\frac{\partial \rho}{\partial T} \right)_p. \quad (2.20)$$

Some authors use the adiabatic sound velocity $u_s^2 = 1/(\rho\beta_S)$, Grüneisen parameter $\gamma = \alpha/(\rho c_p \beta_S)$, or isentropic bulk modulus $K_s = \beta_S^{-1}$ as alternative properties.

2.3.2 Adiabatic Background State

While flow and magnetic field are obviously considered as disturbances of the hydrostatic and nonmagnetic background state, we explicitly decompose the thermodynamic variables into the two respective contributions:

$$T = \widetilde{T} + T' , \rho = \widetilde{\rho} + \rho' , S = \widetilde{S} + S' , p = \widetilde{p} + p' \quad (2.21)$$

with

$$\epsilon = \frac{T'}{\widetilde{T}} \approx \frac{\rho'}{\widetilde{\rho}} \approx \dots \ll 1. \quad (2.22)$$

Here tilde and prime indicate the background state and dynamic disturbance, respectively.

For the adiabatic background state, Eq. (2.16) yields

$$\frac{1}{\tilde{\rho}} d\tilde{\rho} = \beta_s d\tilde{\rho}, \quad (2.23)$$

while the dynamic disturbances follow

$$\frac{1}{\tilde{\rho}} \rho' = -\alpha_s S' + \beta_s p'. \quad (2.24)$$

When neglecting the tiny velocities describing the contraction of a cooling planet, the zero order Navier–Stokes equation (2.6) for the background state reduces to the hydrostatic condition

$$\frac{\partial \tilde{p}}{\partial r} = \tilde{\rho} \tilde{g}. \quad (2.25)$$

Since the deviations from spherical symmetry are very small, the background state is assumed to depend only on radius. Plugging this into Eq. (2.23) yields the density gradient

$$\frac{1}{\tilde{\rho}} \frac{\partial \tilde{\rho}}{\partial r} = \beta_s \frac{\partial \tilde{p}}{\partial r} = \beta_s \tilde{\rho} \tilde{g} \quad (2.26)$$

and the temperature gradient

$$\frac{1}{\tilde{T}} \frac{\partial \tilde{T}}{\partial r} = \left(\frac{\partial T}{\partial p} \right)_S \frac{1}{\tilde{T}} \frac{\partial \tilde{p}}{\partial r} = \frac{\alpha}{c_p} \tilde{g}, \quad (2.27)$$

where we have used Eq. (2.18).

2.3.3 Anelastic Approximation

To simplify the notation we drop the prime indicating the disturbances around the background state in the following. When taking only first order terms in ϵ into account, the continuity equation (2.10) assumes the simplified anelastic form

$$\nabla \cdot (\tilde{\rho} \mathbf{U}) = 0. \quad (2.28)$$

This only holds when the flow velocities remain small enough so that

$$\frac{\partial \rho / \partial t}{\nabla \cdot (\tilde{\rho} \mathbf{U})} \approx \frac{\rho}{\tilde{\rho}} \approx \epsilon. \quad (2.29)$$

The Navier–Stokes equation for the first-order thermodynamic disturbances is

$$\tilde{\rho} \frac{d\mathbf{U}}{dt} = -\nabla p + \rho \tilde{\mathbf{g}} + \tilde{\rho} \mathbf{g} - 2\tilde{\rho} \Omega \mathbf{U} \times \hat{\mathbf{z}} + \mathbf{J} \times \mathbf{B} + \tilde{\rho} \mathbf{F}_v. \quad (2.30)$$

The first three contributions on the right-hand side can be rewritten in terms of an effective pressure (Braginsky and Roberts 1995):

$$p_e = p + \tilde{\rho} \Phi, \quad (2.31)$$

where Φ is the convective disturbance of the gravity potential with $\mathbf{g} = -\nabla \Phi$. Using the background gradient (2.26) leads to:

$$-\nabla p + \rho \tilde{\mathbf{g}} + \tilde{\rho} \mathbf{g} = -\tilde{\rho} \nabla \left(\frac{p_e}{\tilde{\rho}} \right) - p \frac{\nabla \tilde{\rho}}{\tilde{\rho}} + \rho \tilde{\mathbf{g}}. \quad (2.32)$$

Plugging in the background density gradient Eq. (2.26) and using the equation of state (2.24) in combination with Eq. (2.18) yield:

$$-\nabla p + \rho \tilde{\mathbf{g}} + \tilde{\rho} \mathbf{g} = -\tilde{\rho} \nabla \left(\frac{p_e}{\tilde{\rho}} \right) - \frac{\alpha \tilde{\rho} \tilde{T}}{c_p} S \tilde{\mathbf{g}}. \quad (2.33)$$

The Navier–Stokes equation then reads

$$\tilde{\rho} \frac{d\mathbf{U}}{dt} = -\tilde{\rho} \nabla \frac{p}{\tilde{\rho}} - \frac{\alpha \tilde{\rho} \tilde{T}}{c_p} S \tilde{\mathbf{g}} - 2\tilde{\rho} \Omega \mathbf{U} \times \hat{\mathbf{z}} + \mathbf{J} \times \mathbf{B} + \tilde{\rho} \mathbf{F}_v, \quad (2.34)$$

where we have dropped the index e from the effective pressure for simplicity.

This modification has two advantages. For one, the convective variations of the gravity potential are included implicitly and do not have to be calculated. The second advantage becomes apparent when approximating the entropy flux by an entropy diffusion term. The modified heat equation then reads

$$\tilde{\rho} \tilde{T} \frac{dS}{dt} = \nabla (\tilde{\rho} \tilde{T} \kappa_S \nabla S) + q_v + q_J + q_s, \quad (2.35)$$

with the entropy diffusivity κ_S . Since any explicit dependence on the temperature disturbance T has now vanished from the system of equations, there is no need to actually solve for T .

While numerical efficiency is the main reason for adopting entropy diffusion, there is also a possible physical justification. Since the numerical simulations cannot resolve the smallest scale turbulent flows, the fluxes may represent turbulent mixing rather than molecular diffusion. The parametrization of the mixing resembles (to first order) molecular diffusion but with much larger diffusivities that reflect the increased efficiency of the process (Braginsky and Roberts 1995). When κ_S

represents a turbulent value, however, the same should also hold for kinematic viscosity ν and magnetic diffusivity λ since turbulence should mix all physical quantities with similar efficiency. The result would be that the diffusivity ratios, i.e., the Prandtl numbers we will introduce in Sect. 2.3.4, are of order one. Note that preferred directions due to Coriolis or Lorentz forces may lead to anisotropic turbulence and thus anisotropic diffusivity tensors.

The heat equation (2.35) has gained an additional source q_s that describes the effects of secular cooling of the background state. Since both viscous and Ohmic heating result from convective disturbances, q_s is the only term that provides a net driving force. It combines the two contributions involving the background entropy that result from going with ansatz (2.21) into the heat equation:

$$q_s = -\tilde{\rho}\tilde{T}\frac{\partial\tilde{S}}{\partial t} + \nabla \cdot (k \nabla \tilde{T}). \quad (2.36)$$

This can be further constrained by integrating the heat equation (2.12) over the spherical shell and averaging over time scales long enough to get rid of convective variations. The procedure yields

$$\overline{\langle \tilde{\rho}\tilde{T} \rangle} \frac{\partial\tilde{S}}{\partial t} = - (Q_o^{\text{sa}} - Q_i^{\text{sa}}) / V_{\text{oc}} + \langle \overline{q_v} \rangle + \langle \overline{q_J} \rangle, \quad (2.37)$$

where the overbar denotes the temporal and angular brackets the volume average. The contributions Q_o^{sa} and Q_i^{sa} are the super-adiabatic heat flux through the outer and inner boundaries, respectively. For example, for the outer boundary this reads:

$$Q_o = \frac{r_o^2}{F_o} \int_0^{2\pi} d\phi \int_{-1}^1 d\cos\theta \left(\tilde{T}_o \hat{\mathbf{r}} \cdot \mathbf{I}^S - k \frac{\partial \tilde{T}}{\partial r} \right). \quad (2.38)$$

Note that we have used Gauss' theorem to convert the volume integrals over the divergence of the fluxes into surface integrals. F_o is the outer boundary surface while V_{oc} denotes the shell volume. Plugging Eq. (2.37) into Eq. (2.36) shows that q_s is the net volumetric heat source due to the background state evolution, corrected by the conduction down the background adiabat:

$$q_s = \frac{\overline{\tilde{\rho}\tilde{T}}}{\overline{\langle \tilde{\rho}\tilde{T} \rangle}} (q_n - \langle \overline{q_v} \rangle - \langle \overline{q_J} \rangle) + \nabla \cdot (k \nabla \tilde{T}). \quad (2.39)$$

Here

$$q_n = -(Q_o^{\text{sa}} - Q_i^{\text{sa}}) / V_{\text{oc}} \quad (2.40)$$

is the effective homogeneous heat source due to secular cooling.

2.3.4 Nondimensional Equations

The last steps in deriving the system of equations that we will finally solve numerically are the conversion to a dimensionless formulation by choosing appropriate scales and the definition of the radial dependencies in the background state and the physical properties. We start with discussing the latter.

Taking the radial profiles of background density and temperature into account is of obvious interest, but what about the other physical properties? Choosing $\tilde{\rho}(r)$ and $\tilde{T}(r)$ also fixes the radial dependence of the buoyancy term in the Navier–Stokes equation (2.34) since

$$\frac{\alpha \tilde{T}}{c_p} \tilde{g} = \frac{\partial \tilde{T}}{\partial r}, \quad (2.41)$$

according to Eq. (2.27). There is thus no need to detail the radial dependence of α , c_p , or \tilde{g} separately. Since the ab initio calculations discussed in Sect. 2.2 indicate only a mild variation (see Fig. 2.3), we assume that the kinematic viscosity ν is constant. The entropy diffusivity κ_s is a theoretical construct and therefore more difficult to pin down. Using the variations in the ab initio derived molecular thermal diffusivity as a proxy seems questionable. If we think of κ_s as a turbulent value, its variation should rather reflect variations in the efficiency of turbulent mixing. Since it seems reasonable to assume a roughly homogeneous efficiency, we assume a constant κ_s . The radial variation of the electrical conductivity is a different matter, however, since it defines fundamentally different dynamical regions. We will further discuss this issue in Sect. 2.3.6.

The radial dependent background density and background temperature are nondimensionalized by using their outer boundary values $\tilde{\rho}_o$ and \tilde{T}_o as reference. Instead of the electrical conductivity we use the magnetic diffusivity $\lambda(r) = 1/\sigma(r)\mu$ with the inner core value λ_i as reference. The shell thickness $d = r_o - r_i$ serves as a length scale, viscous diffusion time $\tau_v = d^2/\nu$ as a timescale, and $\sqrt{\Omega\mu_0\lambda_i\tilde{\rho}_o}$ as a magnetic scale. The entropy scale S_s depends on the entropy boundary condition, as we will outline below.

The nondimensional Navier–Stokes, heat, and continuity equations then read:

$$\begin{aligned} E \tilde{\rho} \frac{d\mathbf{U}}{dt} &= -\tilde{\rho} \nabla \left(\frac{p}{\tilde{\rho}} \right) + 2\tilde{\rho} \mathbf{U} \times \hat{\mathbf{z}} - \frac{Ra' E}{Pr Di} \tilde{\rho} \frac{\partial \tilde{T}}{\partial r} S \hat{\mathbf{r}} \\ &\quad + \frac{1}{Pm_i} (\nabla \times \mathbf{B}) \times \mathbf{B} + E \tilde{\rho} \mathbf{F}_v, \end{aligned} \quad (2.42)$$

$$\tilde{\rho} \tilde{T} \frac{dS}{dt} = \frac{1}{Pr} \nabla \cdot (\tilde{\rho} \tilde{T} \nabla S) + \frac{Pr Di}{Ra'} \left(q_v + \frac{1}{Pm_i^2 E} q_J \right) + q_s, \quad (2.43)$$

$$\nabla \cdot (\tilde{\rho} \mathbf{U}) = 0. \quad (2.44)$$

The magnetic field evolution is described by the nondimensional dynamo equation

$$\frac{\partial \mathbf{B}}{\partial t} = \nabla \times (\mathbf{U} \times \mathbf{B}) - \frac{1}{\text{Pm}_i} \nabla \times (\tilde{\lambda} \nabla \times \mathbf{B}). \quad (2.45)$$

Naturally, the magnetic field also has to obey

$$\nabla \cdot \mathbf{B} = 0. \quad (2.46)$$

Equations (2.42)–(2.46) define the dynamical system to be solved numerically. This system is controlled by five dimensionless parameters: the Ekman number

$$E = \frac{\nu}{\Omega d^2}, \quad (2.47)$$

the modified Rayleigh number

$$\text{Ra}' = \frac{\alpha_o \tilde{g}_o d^3 \tilde{T}_o}{\nu \kappa} \frac{S_s}{c_p} = \text{Ra} \frac{S_s}{c_p}, \quad (2.48)$$

the Prandtl number

$$\text{Pr}_S = \frac{\nu}{\kappa_S}, \quad (2.49)$$

the magnetic Prandtl number

$$\text{Pm}_i = \frac{\nu}{\lambda_i}, \quad (2.50)$$

and the aspect ratio

$$a = \frac{r_i}{r_o}. \quad (2.51)$$

The modified Rayleigh number Ra' is the product of the classical Rayleigh number Ra and the dimensionless entropy scale S_s/c_p . The dissipation number

$$\text{Di} = \frac{d}{\tilde{T}_o} \left(\frac{\partial \tilde{T}}{\partial r} \right)_{r_o} = \frac{d \alpha_o \tilde{g}_o}{c_p} \quad (2.52)$$

is simply the dimensionless radial derivative of the background temperature at the outer boundary and is thus defined once \tilde{T} has been chosen (see Sect. 2.3.6).

The remaining quantities with a tilde, namely $\tilde{\rho}$, \tilde{T} , and $\tilde{\lambda}$, now contain all the information about the radial dependencies of the background state which, in addition to the dimensionless parameters, define a given model. The volumetric heat sources

in Eq. (2.43) also depend on radius. Viscous heating q_v is proportional to $\tilde{\rho}(r)$, while Ohmic heating q_J is proportional to $\tilde{\sigma}(r)$. Equation (2.36) demonstrates that the radial dependence of q_s is determined by the background temperature and density profiles and can thus be written in the form

$$q_s(r) = \tilde{\rho}(r) \tilde{T}(r) H, \quad (2.53)$$

where H is an additional dimensionless heating parameter. We have assumed here that convective transport dominates the diffusion down the background adiabat, which is a safe bet, at least for the strongly driven convection in Jupiter.

Duarte et al. (2018) explore the two alternatives of a constant heat source,

$$q_s = H, \quad (2.54)$$

and a source that is proportional to density,

$$q_s(r) = \tilde{\rho}(r) H. \quad (2.55)$$

Most of the dynamo simulations presented here, however, are driven by bottom heating with $q_s = 0$. All the heat that leaves the simulated domain through the outer boundary thus comes in through the lower. Though less realistic, this heating mode helps to guarantee dipole dominated dynamos, as we will discuss in Sect. 2.5.3.

2.3.5 Boundary Conditions

Stress-free conditions,

$$\frac{\partial}{\partial r} \left(\frac{\hat{\mathbf{r}} \times \mathbf{U}}{r} \right) = 0 \text{ and } \hat{\mathbf{r}} \cdot \mathbf{U} = 0, \quad (2.56)$$

are an appropriate choice for the outer boundary. At the interface to a rocky inner core, rigid flow conditions,

$$\mathbf{U} = 0, \quad (2.57)$$

are more realistic. Stress-free conditions are nevertheless sometimes used to avoid a strong braking of the zonal winds due to the unrealistically thick Ekman boundary layers in numerical simulations. This becomes more of an issue for larger inner cores, for example in Saturn, and also in simulations modeling the zonal wind dynamics in the thinner molecular outer layer.

We employ either constant entropy or constant heat flux boundary conditions. In the former case, the super-adiabatic contrast ΔS imposed across the shell serves as the specific entropy scale S_s . The heat fluxes through both boundaries are then

determined by the internal volumetric heat sources and dynamics. The alternative is to impose a boundary heat flux density, for example $q_o = Q_o/F_o$ at the outer boundary.

Since the turbulent mixing vanishes as the boundaries are approached, molecular heat diffusion rather than turbulent entropy diffusion should be used. This suggests that

$$q_o = -\frac{1}{\text{Pr}} \frac{c_p}{S_s} \left(\frac{\partial T}{\partial r} - \frac{\partial \tilde{T}}{\partial r} \right), \quad (2.58)$$

where $\text{Pr} = k/\tilde{\rho}_o c_p$ is the classical thermal Prandtl number. However, since the details of the thermal boundary layer are of little interest for the dynamo process, we simply use a diffusive entropy flux

$$q_o = -\frac{1}{\text{Pr}_s} \frac{\partial S_o}{\partial r} \quad (2.59)$$

which is more consistent with the entropy diffusion used in the heat equation (2.43) and allows prescribing a radial entropy gradient. The role of the very steep temperature gradient in transporting heat through the boundaries is then at least partially taken over by the increased turbulent entropy diffusivity, which certainly saves numerical costs. In the case of a flux boundary condition, the entropy scale is given by $S_s = q_o d / \tilde{\rho}_o \tilde{T}_o v$.

The magnetic field is matched to a potential field at both boundaries. The matching conditions can be formulated in terms of a boundary condition in spherical harmonic space once the magnetic field has been decomposed into its poloidal and toroidal contribution (Christensen and Wicht 2015).

2.3.6 Specifying Background State and Parameters

We explore two types of background states: simple models assuming an ideal gas and more Jupiter-like models based on the profiles discussed in Sect. 2.2. For an ideal gas, the thermal expansivity is simply $\alpha = 1/T$ so that the background temperature gradient becomes

$$\frac{\partial \tilde{T}}{\partial r} = -\text{Di} \tilde{g}. \quad (2.60)$$

Two end members have been explored for the dimensionless gravity profile \tilde{g} . When the mass is concentrated below the shell of interest, gravity decays away from the lower boundary like $1/r^2$ and $\tilde{g} = r_o^2/r^2$. The other end member is a homogeneous density which yields $\tilde{g} = r/r_o$. Integration of Eq. (2.60) then gives either

$$\tilde{T} = 1 + \frac{\text{Di}}{2r_o} (r_o^2 - r^2) \quad (2.61)$$

for $\tilde{g} = r/r_o$ or

$$\tilde{T} = 1 + \text{Di } r_o \left(\frac{r_o}{r} - 1 \right) \quad (2.62)$$

for $\tilde{g} = r_o^2/r^2$. The density gradient is defined by assuming a polytropic behavior

$$\tilde{\rho} = \tilde{T}^n, \quad (2.63)$$

where $n = 1/(\gamma - 1)$ is the polytropic index and $\gamma = c_p/c_v$. We chose a value of $n = 2$, which is a compromise between $n = 3/2$ for monatomic and $n = 5/2$ for a diatomic ideal gas and more appropriate for Jupiter's very outer molecular envelope than for most of the planet's interior, where $n = 1$ provides a much better fit.

While we keep the polytropic index fixed, we vary the second parameter defining the ideal gas background state: the number of density scale heights

$$N_\rho = \ln \left(\frac{\rho_i}{\rho_o} \right). \quad (2.64)$$

For $N_\rho = 5$, a value frequently used in the models discussed here, the total density contrast amounts to $\rho_i/\rho_o \approx 150$. The dissipation number is then given by

$$\text{Di} = \frac{r_o}{r_i} \left(\exp(N_\rho/n) - 1 \right). \quad (2.65)$$

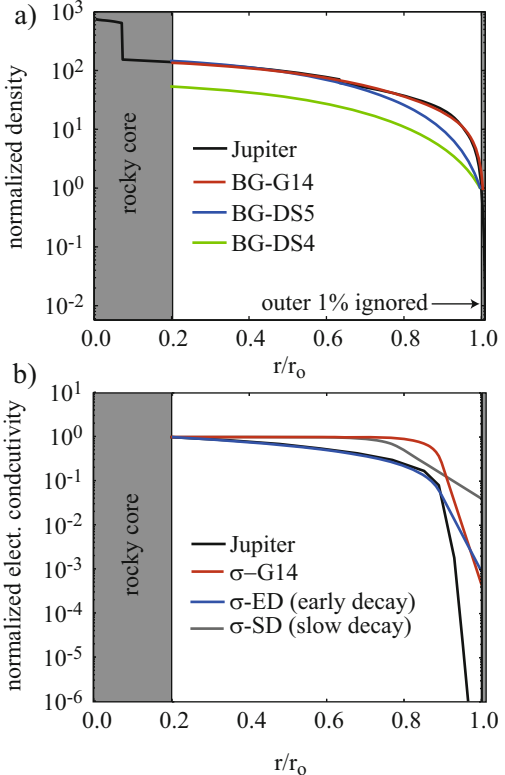
We will refer to these ideal gas background models as BG-DS x in the following, where the x stands for the number of density scale heights N_ρ .

The more Jupiter-like background models adopt the density profile discussed in Sect. 2.2. Because of numerical limitations, the very outer region of the shell where the density gradient becomes most extreme must be neglected. The most advanced models discussed here use a cutoff radius of $r_c = 0.99 R_J$. The numerical code MagIC approximates the density profile below r_c by a polynomial of degree seven and the temperature profile is then fitted with a power law $\tilde{T}(r) = \text{const. } \tilde{\rho}(r)(1/m)$ to the polynomial density model. We find that $m = 2.22$ provides the best fit while the density model closely obeys a polytrope with index $n = 1$:

$$\tilde{\rho} \approx \text{const. } \tilde{\rho}^{(n+1)/n} = \text{const. } \tilde{\rho}^2. \quad (2.66)$$

The difference of the two exponents n and m demonstrates that Jupiter's interior strongly deviates from an ideal gas, where both would agree. Using Eq. (2.41) guarantees that gravity obeys the consistent hydrostatic profile of the interior model. Gastine et al. (2014b) were the first to follow this approach. We will refer to this article as G14 in the following and to the respective background model as BG-G14. A very similar model was used by Jones (2014). Figure 2.7a illustrates that the respective density profiles are steeper at larger radii than the BG-DS4 or BG-DS5 profiles, respectively.

Fig. 2.7 Comparison of background models used in the simulations with the Jupiter interior model discussed in Sect. 2.2 (black lines). Panel (a): in red the normalized density profile for background model BG-G14, in blue model BG-DS5 ($N_\rho = 5$), and in green model BG-DS4 ($N_\rho = 4$), all spanning 99% of Jupiter's radius R_J and assuming an inner core with radius $r_i = 0.2(0.99 R_J)$. Panel (b): in red the normalized electrical conductivity profile σ -G14 used in Gastine et al. (2014b) ($a = 13.0$, $\sigma_m = 0.2$, $\chi_m = 0.9$), in blue an early decaying profile σ -ED ($a = 1.0$, $\sigma_m = 0.03$, $\chi_m = 0.9$), and in dark grey the weakly decaying profile σ -SD ($a = 9$, $\sigma_m = 0.5$, $\chi_m = 0.8$)



The other property that varies with radius in our model is the electrical conductivity $\sigma(r)$. The ab initio simulations discussed in Sect. 2.2 suggest the profile illustrated in Fig. 2.7b. A super-exponential increase in the molecular layer until about $0.9R_J$ smoothly transitions into a much shallower gradient in the metallic layer. Since the super-exponential increase causes numerical difficulties, we use several simplified conductivity profiles with a constant interior conductivity branch that is matched to an exponentially decaying outer branch via a polynomial that assures a continuous first derivative (Gómez-Pérez et al. 2010):

$$\tilde{\sigma}(r) = \begin{cases} 1 + (\tilde{\sigma}_m - 1) \left(\frac{r-r_i}{r_m-r_i} \right)^a & r < r_m \\ \tilde{\sigma}_m \exp \left(a \frac{r-r_m}{r_m-r_i} \frac{\tilde{\sigma}_m - 1}{\tilde{\sigma}_m} \right) & r \geq r_m \end{cases}. \quad (2.67)$$

Free parameters are the rate of the exponential decay a and the radius r_m and conductivity value σ_m for the transition between both branches. For convenience we also define the relative transition radius

$$\chi_m = r_m / r_o. \quad (2.68)$$

The electrical conductivity enters the calculation as a nondimensional magnetic diffusivity profile $\tilde{\lambda}(r) = 1/\tilde{\sigma}(r)$ in the dynamo equation (2.45). As discussed above, the diffusivities used in the simulations may be interpreted as turbulent rather than molecular. Turbulence would increase and homogenize λ in the dynamo region but would have no effect in the weakly conducting outer region where Ohmic diffusion anyway dominates advection effects. This suggests that the primary dependence modeled by the $\sigma(r)$ profile should capture the drop in conductivity from the metallic to the molecular layer, whereas the details of the profile and also the extreme drop in the very outer part of the shell may not matter.

Figure 2.7b compares the electrical conductivity profiles mostly used in this study with the ab initio profile. The profile $\sigma\text{-G14}$ (red) used by Gastine et al. (2014b) and most of the Jupiter-like simulations discussed in Sect. 2.5.4 has a rather shallow transition radius at $\chi_m = 0.87$ and decays by about four orders of magnitude in the weakly conducting outer region. The “early decay” profile $\sigma\text{-ED}$ (blue) captures the slower conductivity decrease predicted for the inner metallic layer with a linear decay rate. The third model profile $\sigma\text{-SD}$ (gray) is a slowly decaying example that combines a deeper transition at $\chi_m = 0.8$ with a total decay by only about two orders of magnitude.

For reference, Fig. 2.8 shows the radial profiles of the parameters that the ab initio simulations suggest for Jupiter. Since the kinematic viscosity changes only mildly with depth, the Ekman number varies only between 5×10^{-19} and 8×10^{-19} . Assuming a constant value thus seems indeed reasonable. The small absolute value reflects the minuscule viscosity and fast planetary rotation that both promote very tiny flow length scales. Numerical limitations dictate to adopt considerable larger Ekman number values that still allow to resolve the flow and the simulations discussed below use $E \geq 10^{-5}$.

Since the Ekman number is not realistic, other system parameters also have to be adjusted to yield Jupiter-like solutions, as we will discuss in more detail in Sect. 2.5. While their absolute values are thus of little importance, the radial variation may still be essential. Panel (b) in Fig. 2.8 shows the normalized radial gradient of the background temperature suggested for Jupiter. This determines the radial variation in buoyancy that could be cast into a radially dependent Rayleigh number and obviously increases considerably in the outer 10% of the shell but remains roughly constant deeper down. Since the kinematic viscosity varies so little, the magnetic Prandtl number profile shown in Fig. 2.8c is dictated by the electrical conductivity profile. Absolute values range from 10^{-19} at R_J to about 10^{-4} at the rocky core boundary, but much larger values of about order one have to be chosen for the simulations to guarantee dynamo action.

Figure 2.8d shows the Prandtl number profile which basically reflects the thermal diffusivity variations. In the metallic hydrogen region, the thermal conductivity is dominated by electronic transport and thermal and electrical conductivities are proportional to each other according to the Wiedemann–Franz law. The Prandtl number increases from $Pr = 10^{-2}$ at $0.2 R_J$ to about $Pr = 1$ at the transition radius $0.9 R_J$. In the molecular region, however, the ionic contribution dominates and the Prandtl number once more drops to lower values (French et al. 2012). Though the

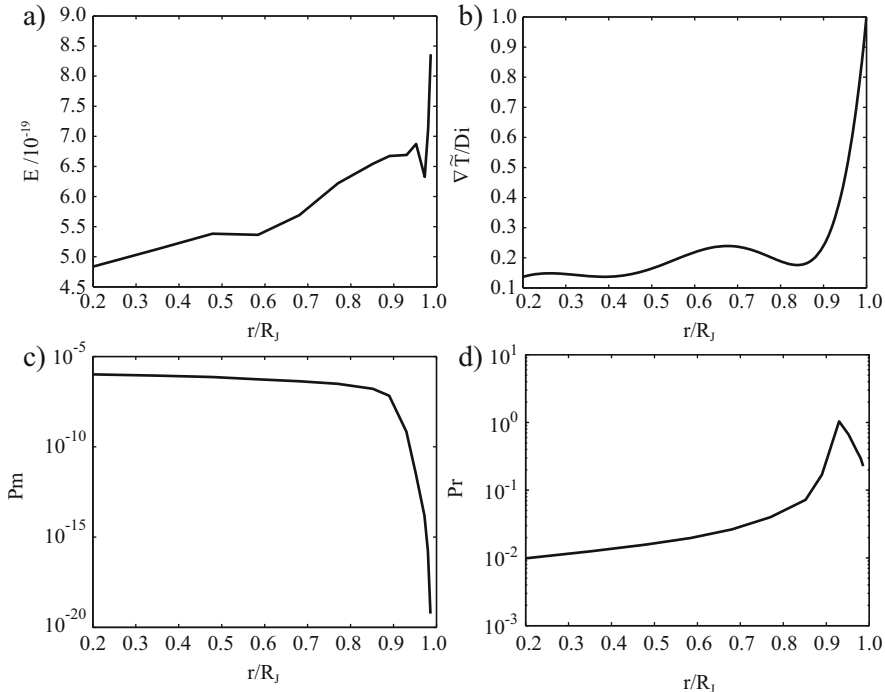


Fig. 2.8 Ekman number, normalized buoyancy, magnetic Prandtl number, and Prandtl number profiles as suggested by the ab initio simulations

numerical model has been formulated based on a turbulent entropy diffusivity rather than the thermal diffusivity, it remains interesting to explore the possible impact of the smaller Prandtl number values.

2.3.7 Numerical Methods

We briefly outline the numerical methods employed to solve the anelastic equations. A more in-depth description can be found in Glatzmaier (1984), Christensen and Wicht (2015), and the MagIC online manual. The MHD code MagIC (Wicht 2002; Gastine and Wicht 2012) and its manual are freely available online at <https://github.com/magic-sph/magic>. Since MagIC uses a poloidal/toroidal composition of mass flux,

$$\tilde{\rho} \mathbf{U} = \nabla \times (\nabla \times W \hat{\mathbf{r}}) + \nabla \times Z \hat{\mathbf{r}}, \quad (2.69)$$

and magnetic field,

$$\mathbf{B} = \nabla \times (\nabla \times G\hat{\mathbf{r}}) + \nabla \times H\hat{\mathbf{r}}, \quad (2.70)$$

the continuity equations (2.44) and (2.46) are automatically fulfilled. The six unknown flow and field components are replaced by the two poloidal potentials W and G and the two toroidal counterparts Z and H . The radial components of the Navier–Stokes equation (2.42) and the dynamo equation (2.45) provide evolution equations for the poloidal potentials. For the toroidal potentials, the radial components of the curled equations are used. The remaining additional two unknowns are pressure and entropy. The horizontal divergence of the Navier–Stokes equation (2.42) and the heat equation (2.43) provide the respective evolution equations.

MagIC uses pseudospectral methods where each variable is either represented on a physical grid or in spectral space. Expansions in Chebyshev polynomials for radius and spherical harmonics functions for longitude and latitude provide the spectral representations. Nonlinear terms are solved on the physical grid, while all derivatives are calculated in spectral space. Fast-Fourier transforms in radius and longitude and a Gauss–Legendre transform in latitude allow switching between both representations.

Minimal dealiasing is used in radius where the number of radial grid points N_r is typically only by two larger than the number of Chebyshev modes. Full dealiasing is guaranteed in longitude and latitude, however, by using a maximum spherical harmonic degree which obeys $L = (N_\phi - 1)/3$. Here N_ϕ is the number of longitudinal grid points, which is always twice the number of latitudinal grid points N_θ .

Time integration follows a mixed scheme where nonlinear terms and the Coriolis force are treated explicitly with a Crank–Nicolson step, while an explicit Adams–Bathforth method is used for the remaining contributions.

2.4 Convective Flows and Zonal Jets

In this section, we focus on the dynamics of the outer, electrically nonconducting portion of the planetary atmosphere. Models of this region often assume that Lorentz forces in deeper layers largely decouple the dynamics of this outer region from the deeper parts, such that the outer layer can be studied in isolation. While the most advanced numerical models now aim to simulate both regions simultaneously (see Sect. 2.5), the decoupled approach provides valuable insight into the nature of rotating, compressible convection and its ability to generate zonal flows.

The available flow observations on Jupiter and Saturn are largely limited to their surfaces. Strong zonal winds alternating in direction dominate the velocity field, with a strong prograde equatorial jet being flanked by weaker and narrower mid-to-high latitude jets. Figure 2.9 shows velocity profiles as a function of latitude

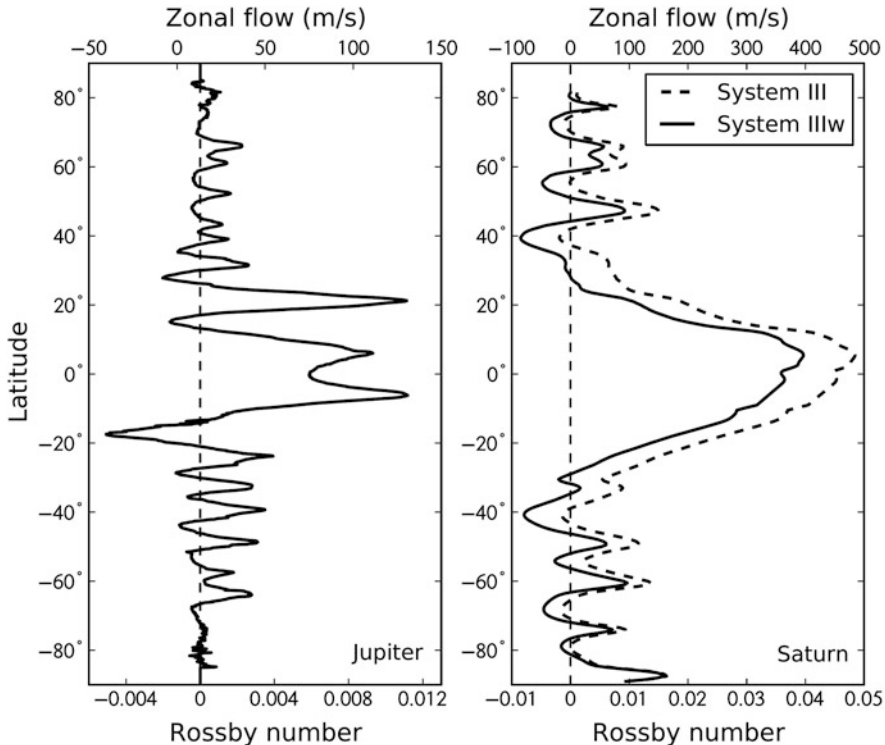


Fig. 2.9 Observed surface zonal flow profiles for Jupiter (left) and Saturn (right). Jupiter's zonal flow profiles come from Cassini's data by Porco et al. (2003) and Vasavada and Showman (2005). Saturn's profiles in the two rotation systems have been derived by Read et al. (2009). The conversion between zonal wind velocities in m/s and Rossby numbers is given by $U/\Omega r_o$ with r_o being the planetary radius at the 1 bar level. From Gastine et al. (2014a)

obtained by tracking cloud features on Jupiter and Saturn. Saturn's equatorial jet exhibits higher velocities, extends to higher latitudes, and is more symmetric with respect to the equator. The wind speeds need to be measured relative to an assumed average rotation rate of the planet. For Saturn, two curves are plotted in Fig. 2.9. For the first one, the so-called System III rotation period was used that is based on Saturn's kilometric radio emissions. System IIIw is based on potential vorticity analysis and yields a profile which is more balanced between pro- and retrograde winds (Read et al. 2009).

The question of whether these zonal jets are constrained to a relatively shallow weather layer close to the planetary surface or are expressions of the deep convective dynamics remains unresolved. Both the “shallow” and “deep” models are capable of reproducing alternating zonal flow patterns (see e.g. Vasavada and Showman 2005). Detailed measurement of the planetary gravity field, as carried out by the Juno spacecraft for Jupiter, are expected to constrain the depth to which the zonal winds

extend (Kaspi et al. 2010, 2016; Kaspi 2013; Kong et al. 2012, 2013, 2014, 2016, 2017; Galanti and Kaspi 2017). As the focus of this review is on the convection dynamics in giant planets, we do not discuss the shallow models here.

Instead, we focus on the dynamics of convective flows in spherical shells. We neglect the influence of a magnetic field in this section, but include the effects of rotation and of a strong density stratification. Rotating convection in spherical shells has been studied extensively in the framework of the Boussinesq approximation where the increase of density with depth is neglected. Excellent reviews are available for this case (Busse 2002; Jones 2015). In the following, we will therefore largely focus on the dynamical changes induced by the compressibility of the fluid in planetary atmospheres. The anelastic approximation will be used throughout. From the anelastic continuity Eq. (2.44) it follows that

$$\nabla \cdot \mathbf{U} = -(\mathbf{U} \cdot \nabla) \ln \tilde{\rho}, \quad (2.71)$$

which shows that the only form of compression or expansion allowed by the governing equations arises from fluid motion along the background density gradient. Especially in a rapidly rotating environment, the volume changes expressed by Eq. (2.71) can have significant dynamical effects.

2.4.1 Taylor–Proudman Theorem in a Compressible Fluid

We begin with a discussion of the Taylor-Proudman Theorem. When dividing Eq. (2.42) by $\tilde{\rho}$ and taking the curl, the vorticity field $\boldsymbol{\omega} := \nabla \times \mathbf{U}$ is found to develop according to

$$E \frac{d\boldsymbol{\omega}}{dt} = 2 \left[\frac{\partial \mathbf{U}}{\partial z} - (\nabla \cdot \mathbf{U}) \hat{\mathbf{z}} \right] + E [(\boldsymbol{\omega} \cdot \nabla) \mathbf{U} - \boldsymbol{\omega} (\nabla \cdot \mathbf{U}) + \nabla \times \mathbf{F}_v + \nabla \times \mathbf{F}_B], \quad (2.72)$$

where \mathbf{F}_v and \mathbf{F}_B denote the respective viscous and buoyancy terms. At low Ekman and Rossby numbers, the leading order balance is expected to be geostrophic. If inertial, viscous, and buoyancy forces are neglected completely, this would imply

$$\frac{\partial \mathbf{U}}{\partial z} = (\nabla \cdot \mathbf{U}) \hat{\mathbf{z}} = -(\mathbf{U} \cdot \nabla) \ln \tilde{\rho} \hat{\mathbf{z}}, \quad (2.73)$$

where Eq. (2.71) has been used in the last step. From this, the Taylor–Proudman-Theorem for a compressible fluid follows in the form

$$\frac{\partial \mathbf{U}_\perp}{\partial z} = 0, \quad \text{and} \quad \frac{\partial U_z}{\partial z} = -(\mathbf{U} \cdot \nabla) \ln \tilde{\rho}, \quad (2.74)$$

where \mathbf{U}_\perp represents the velocity component perpendicular to the rotation axis $\hat{\mathbf{z}}$. While \mathbf{U}_\perp remains constant along the rotation axis, just as in the incompressible case, the background density field $\tilde{\rho}$ is found to induce variations in U_z along the rotation axis. Eq. (2.73) further implies

$$\nabla_\perp \cdot \mathbf{U}_\perp = 0, \quad (2.75)$$

where $\nabla_\perp = \nabla - \hat{\mathbf{z}}(\partial/\partial z)$ denotes the gradient perpendicular to the rotation axis. Local volume changes by expansion or contraction of fluid particles perpendicular to the rotation axis are therefore suppressed. The compressibility is accommodated purely by expansion or contraction parallel to the rotation axis, i.e., by a finite divergence $\partial U_z / \partial z$.

The leading order geostrophic balance represents a purely diagnostic condition without any predictive power. Higher order contributions need to be considered in order to calculate the flow behavior. In the Boussinesq case, the flow at onset can be interpreted as a thermal Rossby wave (Busse 1970). The associated vorticity oscillations are a consequence of the varying vertical depth of the spherical shell with distance from the rotation axis, which gives rise to a so-called topographic β -effect. The nature of this β -effect can change in a compressible fluid, which we discuss next.

2.4.2 The β -Effect in a Compressible Fluid

We consider a compressible fluid enclosed by impenetrable top and bottom boundaries at $z_t(s), z_b(s)$. In a spherical shell, using cylindrical coordinates (s, ϕ, z) , $z_t = (r_o^2 - s^2)^{1/2}$, and $z_b = -z_t$ outside the tangent cylinder, while inside the northern tangent cylinder $z_b = (r_i^2 - s^2)^{1/2}$. The tangent cylinder is an imaginary surface that connects the inner core equator with the outer boundary. However, we keep the analysis general in the following without assuming a spherical geometry from the outset.

We begin by showing that the vertically integrated mass flux $\tilde{\rho}U_\perp$ has to be divergence free,

$$\nabla_\perp \cdot \int_{z_b}^{z_t} \tilde{\rho} \mathbf{U}_\perp dz = 0, \quad (2.76)$$

in order to ensure mass conservation. Formally, this can be shown by integrating the anelastic continuity equation $\nabla_\perp \cdot (\tilde{\rho} \mathbf{U}_\perp) = -\partial(\tilde{\rho} U_z)/\partial z$ over the entire fluid depth using the Leibniz rule, which reveals

$$\begin{aligned} \int_{z_b}^{z_t} \nabla_\perp \cdot (\tilde{\rho} \mathbf{U}_\perp) dz &= \nabla_\perp \cdot \int_{z_b}^{z_t} \tilde{\rho} \mathbf{U}_\perp dz + (\nabla_\perp z_b) \cdot [\tilde{\rho} \mathbf{U}_\perp]_{z_b} - (\nabla_\perp z_t) \cdot [\tilde{\rho} \mathbf{U}_\perp]_{z_t} \\ &= -[\tilde{\rho} U_z]_{z_b}^{z_t}. \end{aligned}$$

Impenetrability of the boundaries implies $\tilde{\rho} \mathbf{U} \cdot \mathbf{n}_{b,t} = 0$ at z_b and z_t , where $\mathbf{n}_{b,t} := -\nabla_{\perp} z_{b,t} + \hat{\mathbf{z}}$ are suitable vectors normal to the top and bottom boundary. This causes cancellation of the last three terms in the equation above, which proves Eq. (2.76).

In order to illustrate the β -effect in a compressible fluid, we consider solutions for which \mathbf{U}_{\perp} is independent of z . In such a flow, vertical columns of fluid move in directions perpendicular to the rotation axis. Defining the vertically integrated density as

$$M = \int_{z_b}^{z_t} \tilde{\rho} dz, \quad (2.77)$$

this results in

$$\nabla_{\perp} \cdot (M \mathbf{U}_{\perp}) = 0 \quad \text{or} \quad \nabla_{\perp} \cdot \mathbf{U}_{\perp} = -(\mathbf{U}_{\perp} \cdot \nabla_{\perp}) \ln M. \quad (2.78)$$

For a purely geostrophic flow, which by definition always satisfies $\nabla_{\perp} \cdot \mathbf{U}_{\perp} = 0$ according to Eq. (2.75), \mathbf{U}_{\perp} must therefore be directed along lines of constant M . In the case of a perfect spherical shell and a spherically symmetric background density $\tilde{\rho} = \tilde{\rho}(r)$, this implies that geostrophic flows are purely azimuthal and therefore cannot transport heat radially. Note that in assuming a z -independent flow we have effectively neglected the Ekman boundary layers, which are generally very thin for planetary applications and absent in the stress-free case.

Rossby waves can arise from oscillations of fluid columns about a geostrophic state. If \mathbf{U}_{\perp} remains independent of z , linearizing Eq. (2.72) in the absence of buoyancy and friction effects reveals

$$\frac{\partial \xi}{\partial t} = \frac{2}{E} \left(\frac{\partial \mathbf{U}_z}{\partial z} - \nabla \cdot \mathbf{U} \right) = -\frac{2}{E} (\nabla_{\perp} \cdot \mathbf{U}_{\perp}) = \mathbf{U}_{\perp} \cdot \boldsymbol{\beta} \quad (2.79)$$

where $\xi = \hat{\mathbf{z}} \cdot \boldsymbol{\omega}$ is the vertical vorticity and

$$\boldsymbol{\beta} := \frac{2}{E} \nabla_{\perp} \ln M. \quad (2.80)$$

Any vertically invariant flow \mathbf{U}_{\perp} along which the vertically integrated mass M varies thus generates vertical vorticity, which can result in Rossby wave propagation. Eq. (2.80) generalizes previous results derived specifically for spherical shell geometries (Ingersoll and Pollard 1982; Gastine et al. 2014a) to a wide range of model configurations. Two limiting cases are of particular importance. The first one is the well-studied Boussinesq case $\tilde{\rho} = 1$, in which we have a purely *topographic* β -effect with

$$\boldsymbol{\beta} = \boldsymbol{\beta}_t := \frac{2}{Eh} \nabla_{\perp} h, \quad (2.81)$$

where $h = z_t - z_b$ is the local height. The other one is a case with flat parallel boundaries $z_b, z_t = \text{const}$, where we have a purely *compressional* β -effect with

$$\boldsymbol{\beta} = \boldsymbol{\beta}_c := \frac{2}{EM} \int_{z_b}^{z_t} \nabla_{\perp} \tilde{\rho} dz, \quad (2.82)$$

which vanishes in the Boussinesq case. Furthermore, when $\tilde{\rho}(z_B) = \tilde{\rho}(z_T)$ it follows that

$$\boldsymbol{\beta} = \frac{2}{EM} \nabla_{\perp} \int_{z_b}^{z_t} \tilde{\rho} dz = \frac{2}{EM} \left[\tilde{\rho}(r_o) \nabla_{\perp} h + \int_{z_b}^{z_t} \nabla_{\perp} \tilde{\rho} dz \right] = \frac{h \tilde{\rho}(z_T)}{M} \beta_t + \boldsymbol{\beta}_c, \quad (2.83)$$

such that the β -effect can be interpreted as a weighted sum of a purely topographic and a purely compressional part.

For the important case of a spherical shell with $\tilde{\rho} = \tilde{\rho}(r)$, Eqs. (2.80) and (2.81) give

$$\boldsymbol{\beta} = \frac{2}{EM} \frac{\partial M}{\partial s} \hat{\mathbf{s}} \quad \text{and} \quad \beta_t = \frac{2}{Eh} \frac{dh}{ds} \hat{\mathbf{s}} = \frac{\hat{\mathbf{s}}}{E} \begin{cases} \frac{-2s}{r_o^2 - s^2} & \text{for } s > r_i \\ \frac{2s}{\sqrt{(r_o^2 - s^2)(r_i^2 - s^2)}} & \text{for } s < r_i \end{cases}. \quad (2.84)$$

Note that both $\boldsymbol{\beta}$ and β_t exhibit a singularity at $s = r_i$ and $s = r_o$. For the region outside the tangent cylinder, Eq. (2.83) results in

$$\boldsymbol{\beta} = \frac{h \tilde{\rho}(r_o)}{M} \beta_t + \boldsymbol{\beta}_c \quad \text{for} \quad s > r_i. \quad (2.85)$$

A strong density stratification thus not only leads to a significant value of β_c outside the tangent cylinder, but also diminishes the prefactor $h \tilde{\rho}(r_o)/M$. The density stratification thus reduces the influence of the topographic β -effect in comparison to the well-studied Boussinesq case.

The fact that the compressibility influences the nature of the β -effect might have important consequences, in particular in highly turbulent flow regimes where the global velocity correlations along the rotation axis break down. In compressible flows, this happens particularly easily close to the outer boundary, where the density gradient is large and the flow is so vigorous that the ordering influence of rotation and thus the geostrophy is lost (Jones and Kuzanyan 2009; Gastine and Wicht 2012). In essence, the vorticity generation associated with the compressible β -effect is due to the fact that fluid particles moving along the density gradient expand or contract, as described by the term $-2\nabla \cdot \mathbf{U}$ in Eq. (2.72) in combination with Eq. (2.71). As pointed out by Glatzmaier et al. (2009), this is a purely local process that does not require that \mathbf{U}_{\perp} is independent of z as assumed above.

2.4.3 Onset of Convection

In order to get a conceptual picture of the dynamics close to onset, simplified model geometries provide considerable insight. Figure 2.10 illustrates such geometrical configurations. We focus on the region outside the tangent cylinder ($s > r_i$) here, because this is where convection sets in first.

In panel (a), a cylindrical section of the full sphere of thickness D is shown. For a Boussinesq fluid, Busse (1970) showed that a simplified model for the dynamics in this region can be constructed by considering a fluid filled annulus bounded by coaxial cylinders, as shown in panel (b). The end caps are approximated by planar surfaces tilted by a small angle η with respect to the equatorial plane. Gravity points in $-\hat{s}$ direction and a fixed temperature (or equivalently entropy) drop between the cylinders drives the convective flow. In the asymptotic case of small η , the flow at onset can be shown to be dominated by a z -independent horizontal flow component \mathbf{U}_\perp . While a perfectly geostrophic flow would be purely azimuthal, convective heat transfer requires that \mathbf{U}_\perp also has an \hat{s} component. In the Boussinesq case, this gives rise to a purely topographic β -effect.

In the compressible case, a similar model can be constructed by considering an annulus geometry with flat and parallel end caps (Busse and Simitev 2014), as shown in Fig. 2.10c. As before, gravity points in $-\hat{s}$ direction, which causes a background density field $\tilde{\rho} = \tilde{\rho}(s)$. Convection is again driven by a constant entropy difference between the cylindrical surfaces. In this case, it is assumed that $D/H \ll 1$, where $H = -(\partial \ln \tilde{\rho} / \partial s)^{-1}$ is the density scale height. The flow in this model experiences a purely compressible β -effect.

If the annulus is assumed to be thin, the dynamics can be analyzed in terms of local Cartesian coordinates x, y, z as indicated in Fig. 2.10. When, following Busse (2002) and Busse and Simitev (2014), we assume that to leading order

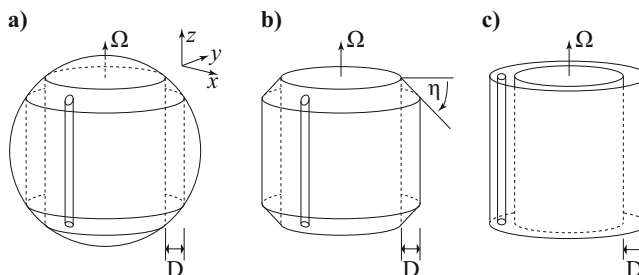


Fig. 2.10 Simplified models providing insight into the convection dynamics close to onset. (a) Cylindrical section of the region outside the tangent cylinder, (b) the classical Busse annulus where compressibility and the curvature of the spherical boundaries is neglected and gravity points in $-\hat{s}$ direction, and (c) a cylindrical model with parallel end caps that takes the compressibility of the fluid into account. A fluid column moved in \hat{s} direction generates vertical vorticity ζ by a topographic β -effect in the classical Busse annulus (b) and by the compressible β effect in (c). The inner sphere $r = r_i$ is hidden in all these sketches within the inner cylindrical surface

$\mathbf{U} = \mathbf{U}_\perp(x, y, t) = \tilde{\rho}^{-1} \nabla \times (\psi(x, y, t) \hat{\mathbf{z}})$, where ψ denotes the stream function, it follows from Eq. (2.72) that the vertical vorticity ζ is governed by

$$\frac{\partial \zeta}{\partial t} + \frac{1}{\tilde{\rho}} \left[\frac{\partial \zeta}{\partial x} \frac{\partial \psi}{\partial y} - \frac{\partial \zeta}{\partial y} \frac{\partial \psi}{\partial x} - \left(1 + \frac{E}{2} \zeta \right) \frac{\partial \psi}{\partial y} \beta \right] = \hat{\mathbf{z}} \cdot \nabla \times (\mathbf{F}_v + \mathbf{F}_B). \quad (2.86)$$

For the classical Busse annulus shown in Fig. 2.10b and the compressible version shown in Fig. 2.10c, from Eqs. (2.82) and (2.84) we have

$$\beta = \hat{\mathbf{x}} \cdot \beta_t = \frac{2}{Eh} \frac{dh}{dx} \quad \text{and} \quad \beta = \hat{\mathbf{x}} \cdot \beta_c = \frac{2}{E\tilde{\rho}} \frac{\partial \tilde{\rho}}{\partial x}, \quad (2.87)$$

respectively. A combined model can be constructed using Eq. (2.85). Note that Eq. (2.86) has a mathematical form that is similar to the vorticity equation used in studies of beta-plane turbulence (Vallis 2006). It is also similar to the Hasegawa–Mima equation governing drift wave turbulence in plasma physics (e.g. Connaughton et al. 2015).

The onset of convection in the different annulus models can be investigated using linear theory. The starting point is the linearized version of the vorticity Eq. (2.86) and of an entropy equation similar to Eq. (2.43) or its Boussinesq equivalent, respectively. For the anelastic case, the analysis becomes essentially identical to the classical Busse annulus when viscous stresses generated by volume changes are neglected and the entropy diffusion term is restricted to its main contributor. Because of space restrictions, we omit the details here which may be found in the original literature. In both the Boussinesq and the compressible case, convection is found to set in as a thermal Rossby wave propagating in azimuthal direction. Rotation, which enters the problem through the respective β terms, considerably delays the onset of convective instabilities and enforces increasingly small spatial scales.

The results from the annulus models can be used to formulate predictions for the onset of convection in spherical shells. In the Boussinesq case, such predictions compare quite well (Simitov and Busse 2003) with numerical solutions of the full eigenvalue problem for the onset of convection in spherical geometry (e.g. Dormy et al. 2004; Jones et al. 2000), even though the analysis for the annulus is mathematically rigorous only in the limit of small η . In the compressible case, a similar comparison between results obtained by an appropriate annulus model (Busse and Simitov 2014) and by numerical solutions of the full linear problem in a spherical shell (Jones et al. 2009) reveals poorer quantitative agreement. The main dynamical effects, however, still appear to be captured reasonably well, confirming the conceptional value of the annulus model in this case. In particular, both models find that the onset location moves outward from the tangent cylinder and becomes increasingly localized close to the outer boundary with increasing density stratification. Interestingly, the annulus model predicts that the onset location returns to the interior of the shell for very strong density stratifications in a parameter regime

that has not been reached in numerical solutions of the full eigenvalue problem (Glatzmaier and Gilman 1981; Drew et al. 1995; Jones et al. 2009) so far.

2.4.4 Non-axisymmetric Flow Close to Onset and Beyond

The main features found in the linear case persist into the weakly nonlinear regime, as illustrated in Fig. 2.11. In particular, increasing compressibility tends to move the convective structures away from the tangent cylinder toward the outer shell. It also tends to increase the azimuthal wavenumber and wave frequency at onset when all other parameters are fixed. This behavior may be interpreted physically as largely being caused by the fact that the purely conductive entropy gradient is steepest at the outer boundary. For a sufficiently strong density stratification, its destabilizing effect overcompensates the stabilizing effect of the radial decrease in gravity, such that convection is most easily generated close to the outer boundary (Jones et al. 2009; Gastine and Wicht 2012). Figure 2.12 compares radial velocity contours at different depths for a strongly stratified background model with $N_p = 5$ and a more supercritical Rayleigh number. The outward decrease in length scale illustrated here persists even into the strongly nonlinear regime. The velocity amplitude, on the other hand, increases with radius because of the growing buoyancy (Gastine and Wicht 2012). These effects make simulations of strongly stratified flows numerically very challenging.

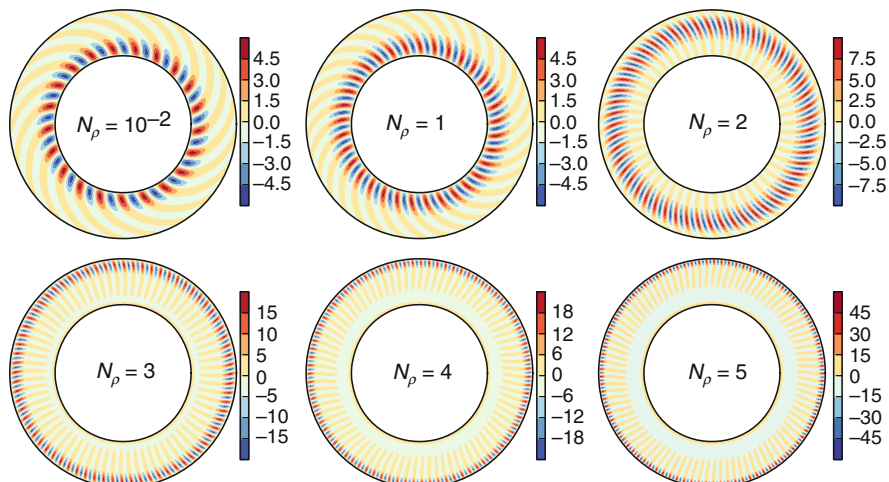
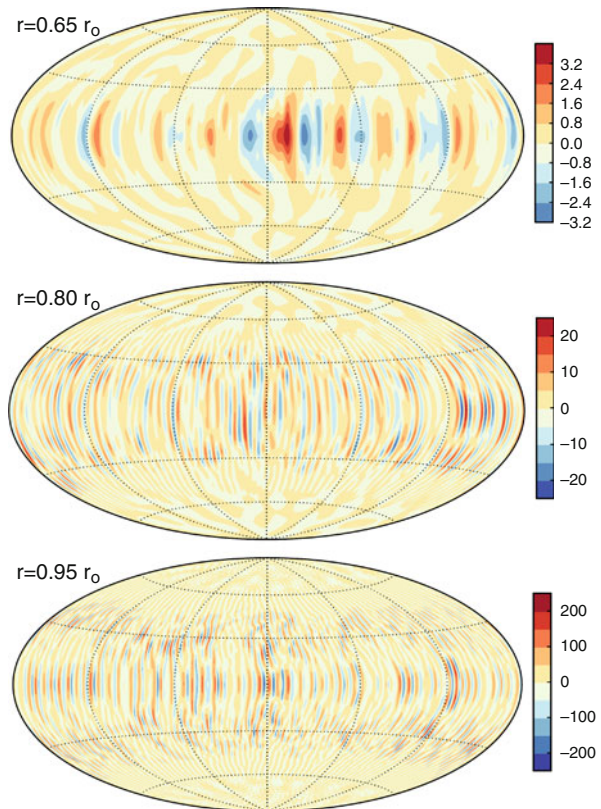


Fig. 2.11 Radial component of the velocity field U_r at $E = 10^{-4}$, $\text{Pr} = 1$, $a = r_i/r_o = 0.6$, $n = 2$ and a Rayleigh number that exceeds its critical value by less than 5%. The dimensionless velocity values are expressed in terms of a Reynolds number based on the shell thickness. From Gastine and Wicht (2012)

Fig. 2.12 Radial velocity contours at different depth in a convection simulation with $E = 10^{-4}$, $\text{Ra} = 3.41\text{Ra}_c$, $\text{Pr} = 1$, $a = 0.6$ and background model BG-DS5. Modified from Gastine and Wicht (2012)

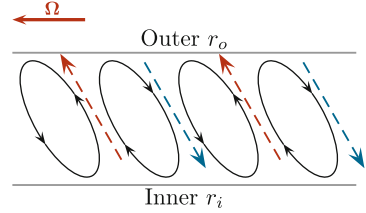


The flow at onset consists of drifting columnar structures, which develop a spiraling character for the moderately small Prandtl numbers characteristic for giant planet interiors. This spiraling effect, which tilts the fluid columns in prograde direction, is well known from the Boussinesq case (Zhang 1992) and results from the variation of the β parameter with distance from the rotation axis. In the compressible case, it is therefore caused by both the height change of the spherical container and the density stratification. As the Rayleigh number is increased, the drifting columns observed close to onset typically first begin to vacillate in time. A further sequence of dynamical transitions, which depend on the model parameters, then leads to chaotic and finally turbulent flows.

2.4.5 Zonal Flow Generation in the Weakly Nonlinear Regime

For stress-free boundary conditions, strong azimuthal mean flows can be generated by the tilted convection columns. The consistent tilt creates systematic correlations

Fig. 2.13 Sketch that illustrates the tilt of the convective columns and the net outward transport of angular momentum in spherical shells



between the horizontal velocity components U_ϕ and U_s and thus causes Reynolds stresses $\langle U_\phi U_s \rangle_\phi$, where the brackets indicate an azimuthal average. A positive flux of angular momentum away from the rotation axis results that generates a pair of geostrophic zonal flows, as illustrated in Fig. 2.13. The interaction of this mean zonal flow with the convective eddies then becomes an important dynamical effect. Depending on the parameters, chaotic or intermittent relaxation oscillations can occur. The zonal flow grows in strength until it shears apart the convective eddies by which it is generated. Deprived of its driving mechanism, the zonal flow decays until convection bursts again and the dynamics enters a new cycle. This behavior is well known from the Boussinesq case (e.g. Busse 2002). At even higher Rayleigh numbers, the relaxation dynamics ceases and the flow enters a chaotic regime characterized by a coexistence of zonal flow and convective eddies. The exact path to this regime depends on the control parameters and the shell thickness and has not been fully explored yet. For the particular case $E = 10^{-4}$, $\text{Pr} = 1$ and $a = r_i/r_o = 0.6$, the simulations of Gastine and Wicht (2012) show that the relaxation oscillations cease to exist for $N_\rho > 4$, where the system transitions directly from vacillating columns into a chaotic regime.

To explore in more detail how the strong zonal flows are generated and maintained, we analyze the azimuthal component of the Navier–Stokes Eq. (2.42) integrated over cylindrical surfaces of radius s . The Coriolis term is proportional to the net mass flux across these surfaces and therefore vanishes. The integrated Navier–Stokes equation thus simplifies to

$$\int_S \tilde{\rho} \frac{\partial U_\phi}{\partial t} s d\phi dz = - \int_S \frac{1}{s^2} \frac{\partial}{\partial s} [s^2 \tilde{\rho} U_s U_\phi] s d\phi dz + \int_S \frac{1}{s^2} \frac{\partial}{\partial s} \left[s^2 \tilde{\rho} s \frac{\partial}{\partial s} \left(\frac{U_\phi}{s} \right) \right] s d\phi dz. \quad (2.88)$$

In a statistically stationary state the two terms on the right-hand side, Reynolds and viscous stresses, should balance on time average. This leads to the condition

$$\int_h \tilde{\rho} s \frac{\partial}{\partial s} \left(\overline{\frac{U_\phi}{s}} \right) dz = \int_h \tilde{\rho} \overline{U_s U_\phi} dz, \quad (2.89)$$

where the overbars indicate a temporal and azimuthal average and h corresponds to the height of the container. As long as the convective columns keep their integrity along the rotation axis, the consistent tilt guarantees a good correlation between the

convective flow components U_s (in the cylindrically radial direction) and U_ϕ (in the azimuthal direction), defined by

$$\mathcal{C}_{s\phi} = \frac{\overline{U_s U_\phi}}{\sqrt{\overline{U_\phi^2} \overline{U_s^2}}}. \quad (2.90)$$

Since the columns are tilted in the prograde direction, $\overline{U_s U_\phi} > 0$ and the mean zonal flow $\overline{u_\phi}$ increases with distance from the rotation axis s . Close to onset, $\mathcal{C}_{s\phi} \sim 1$ and the r.m.s. zonal flow amplitude thus increase quadratically with the convective flow amplitude (Christensen 2002; Showman et al. 2011; Gastine and Wicht 2012), i.e.,

$$\text{Re}_{\text{zon}} \sim \text{Re}_c^2. \quad (2.91)$$

Note that since we have used a viscous time scale in our dimensionless equations, the flow amplitude always corresponds to a Reynolds number.

2.4.6 Zonal Flow Generation in the Nonlinear Regime of Rapidly Rotating Convection

At larger Rayleigh numbers, the convective columns are disrupted and loose their integrity along z and turbulent effects rather than the boundary curvature start to influence the flow. When convection is strongly driven, the role played by Reynolds stresses remains in a statistical sense though $\mathcal{C}_{s\phi}$ becomes much smaller than unity and actually decreases with the convective Reynolds number (Christensen 2001). This implies that the energy transfer between the small scale convective structures and the large scale zonal flow becomes less and less efficient when the turbulence increases, yielding

$$\text{Re}_{\text{zon}} \sim \text{Re}_c^\alpha, \quad (2.92)$$

where $\alpha < 2$ is a decreasing function of Re_c .

Figure 2.14 compares the zonal flows for different density contrasts for numerical models with similar convective power input. It demonstrates that the zonal flow structure actually changes very little for $N_\rho \leq 3$. In the two cases with $N_\rho \geq 4$, the high-latitude jets are still weak but this difference can be attributed to the weaker supercriticality employed in these two numerically demanding cases. The background density contrast has an impact on the ratio between the main prograde equatorial jet and the secondary jets: while they are of comparable amplitude in the nearly-Boussinesq cases, the strongly stratified models have a much stronger equatorial jet.

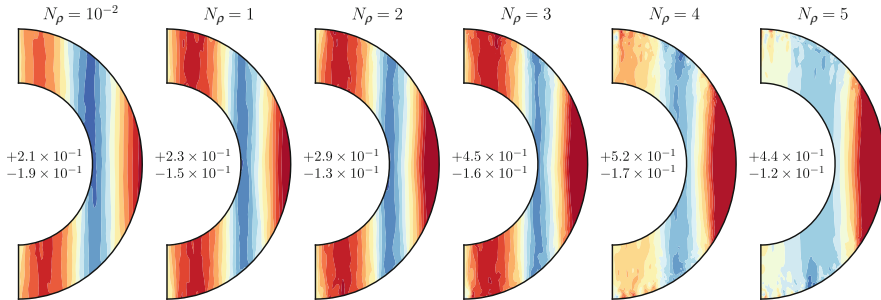


Fig. 2.14 Snapshots of zonally averaged azimuthal velocity in the meridian plane for simulations with increasing density stratifications (from left to right) for numerical models with $a = r_i/r_o = 0.6$, $E = 10^{-4}$, and $\text{Pr} = 1$. Color scales are centered around zero: prograde jets are rendered in red, retrograde jets in blue. Prograde contours have been truncated in amplitude to emphasize the structure of the retrograde flows. Dimensionless azimuthal velocities are expressed here in terms of Rossby numbers $\bar{U}_\phi / \Omega d$. The extrema of the zonal flow velocity are indicated in the center of each panel. Details concerning those simulations can be found in Gastein and Wicht (2012)

Except for this amplitude difference and the requirement for larger supercriticalities at stronger stratifications, the zonal flow structure is relatively unaffected by the density stratification (see also Jones and Kuzanyan 2009).

2.4.7 Two-Dimensional Studies of Zonal Wind Generation: The Multiple Jet Regime

Additional insight into zonal wind generation can be obtained from two-dimensional models. Evonuk and Glatzmaier (2006), Evonuk (2008), Glatzmaier et al. (2009), and Evonuk and Samuel (2012) studied rotating, density-stratified convection in the equatorial plane of a giant planet. Even though these models are two-dimensional, the compressible β -effect is naturally retained, as fluid parcels moving along the density gradient expand or contract and therefore change their vorticity. In fact, because of the assumed two-dimensionality, this model is similar to the compressible annulus model with flat end caps described in Sect. 2.4.3 and illustrated in Fig. 2.10c, with the β -parameter being given by $\beta = \beta_c = 2H^{-1}E^{-1}\hat{s}$. Radial variations of the density scale height H lead to a radial change in β_c , which tilts the convective structures and generates flow correlations and Reynolds stresses that can drive zonal flows, just as in the mechanism sketched in Fig. 2.13. Numerical simulations indeed reveal the generation of strong zonal flows in these two-dimensional models. In most cases, two jets are found in the papers cited above, with the direction of the jets largely depending on the assumed radial variation of the inverse density scale height H^{-1} , which determines the radial variation of β_c .

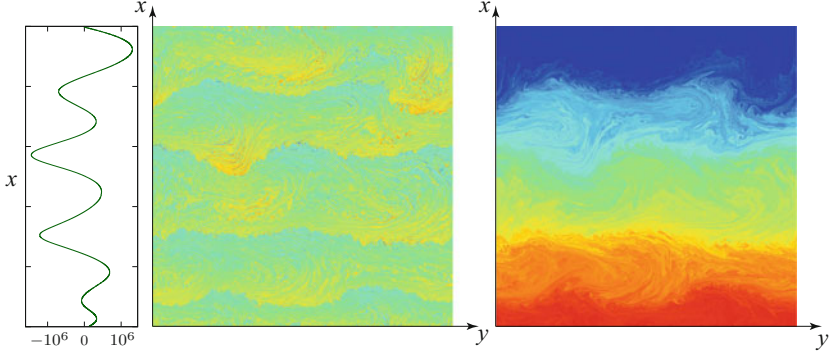


Fig. 2.15 Mean horizontal flow velocity $\langle U_x \rangle$ (left), vorticity field (middle), and entropy field (right) in a two-dimensional simulation of rapidly rotating compressible convection in a Cartesian domain. This model may be interpreted as representing a part of the equatorial plane of a giant planet. The rotation vector Ω points into the plane of the paper, with the x and y direction chosen as indicated in Fig. 2.10. Periodicity is assumed in the horizontal direction. The background density $\tilde{\rho}$ increases by only 20% from the top to the bottom of the layer. Gravity, kinematic viscosity, and entropy diffusivity are assumed to be constant, while a simple, diatomic ideal gas is considered. A constant entropy drop between stress-free inner and outer boundaries drives convection. The control parameters in this case are $\text{Pr} = 1$, $E = 5 \cdot 10^{-10}$, $\text{Ra} = 4 \times 10^{13}$. Details concerning these simulations can be found in Verhoeven and Stellmach (2014)

The authors, however, also report the occurrence of more than two jets in rapidly rotating cases.

Such multiple jet states were investigated in detail by Verhoeven and Stellmach (2014). They further simplified the two-dimensional model by neglecting curvature effects and by considering a local Cartesian geometry as shown in Fig. 2.15. This model may be interpreted as representing a part of the equatorial plane. Convection in a density stratified fluid is driven by a fixed entropy difference imposed across a plane layer. The whole system rotates about an axis pointing into the plane of the paper. Again, there is a close connection to the compressible annulus model discussed in Sect. 2.4.3, where the properties were also analyzed in a local Cartesian coordinate frame. Indeed, the vorticity equation for the model shown in Fig. 2.15 is identical to Eq. (2.86).

The turbulent flow field shown in Fig. 2.15 is dominated by multiple alternating jets. Interfaces characterized by pronounced jumps in both vorticity and entropy are found in the cores of the westward propagating jets, giving the system a layered appearance. Large-scale Rossby waves propagate along the interfaces in an eastward direction and cause undulating structures clearly discernible in both the entropy and vorticity field. In between the interfaces, the entropy field is homogenized by intense convection, resulting in layers of dense material overlying less dense fluid, suggesting a competition between the jet generation mechanism and the tendency of the buoyancy field to cause cross-interfacial mixing. Depending on the parameters, the interface sharpness, jet thickness, and Rossby wave activity vary. Relaxation

oscillations and intermittent convective bursts are also observed. In addition to the time scales associated with the Rossby waves, the zonal flows, and the turbulence, the system also tends to evolve on a much slower time scale on which the kinetic energy gradually increases. In the early stages of a simulation started from rest, thin jets tend to merge to form thicker ones, while such events become rare at later times. Due to computational constraints, Verhoeven and Stellmach (2014) were unable to determine the ultimate fate of the system.

The behavior found in this model appears reasonable in view of Eq. (2.86), which has the same mathematical form as the vorticity equation considered in two-dimensional beta-plane turbulence (Rhines 1975; Williams 1978; Vallis and Maltrud 1993; Chekhlov et al. 1996; Danilov and Gryanik 2004; Sukoriansky et al. 2007; Dritschel and McIntyre 2008). Numerical solutions of this equation for an incompressible fluid and a prescribed, typically bandwidth-limited small-scale forcing indeed reveal many of the features seen in Fig. 2.15. Furthermore, two-dimensional, quasi-geostrophic models of incompressible convection under the influence of a prescribed topographic β -effect also show zonal wind generation, convective bursts, and a multiple-jet regime for suitable control parameters and boundary conditions (Jones et al. 2003; Rotvig and Jones 2006; Teed et al. 2012). An additional scale-independent damping term is often also included in these models in order to model the effects of Ekman pumping for sloping top and bottom boundaries of no-slip type. This so-called Ekman-friction reduces the kinetic energy and makes it much easier to achieve persistent multiple jet solutions. Unfortunately, the assumption of no-slip boundaries seems highly artificial in the context of giant planets.

Of particular interest is the process determining the jet thickness. A simple scale analysis reveals that the term $\beta \partial \psi / \partial y$ in Eq. (2.86) becomes negligible on small scales, such that we expect this part of the spectrum to be dominated by two-dimensional turbulence. On large scales, the term involving β can become dominant and Rossby waves must be expected to play a major dynamical role. The crossover between both regimes is expected to occur at a scale where the eddy turnover time equals the Rossby wave time scale, the so-called Rhines length

$$l_R = \sqrt{U_\beta / \beta}, \quad (2.93)$$

where U_β denotes a typical velocity amplitude at that scale. Energy initially injected into the system at the small convective forcing scale then moves up the spectrum in an inverse cascade until it is channeled into zonal modes. Indeed, approximate Rhines scaling is found in the simulations by Verhoeven and Stellmach (2014) when U_β is taken to be the typical jet velocity. For large density stratification, β_c strongly depends on depth, but still the underlying process robustly generates jets of a thickness that is reasonably well approximated by Eq. (2.93). The inclusion of a scale-independent Ekman friction term would tend to diminish U_β and therefore the Rhines length, which generally aids multiple jet formation (e.g. Teed et al. 2012).

In planetary applications, the β -effect is caused by both compressibility and spherical topography of the boundaries. The β parameter entering the expression for the Rhines length in Eq. (2.93) may then be expected to be given by Eq. (2.80), at least as long as vertical correlations remain strong enough for the analysis to be applicable. Multiple jets may then also be generated by the β -effect within the tangent cylinder, a region that is not considered in the simple 2D models discussed above.

2.4.8 Multiple Jets in the Case of Thin Spherical Shells

Numerical models in relatively deep layers and moderately small Ekman numbers (i.e., aspect ratio $a \leq 0.6$ and $E \geq 10^{-5}$) typically only produce a pair of jets in each hemisphere, as shown in Fig. 2.14 (see also Christensen 2001; Jones and Kuzanyan 2009; Gastine and Wicht 2012). The pioneering 3-D models of Heimpel et al. (2005) were computed with lower Ekman numbers and larger aspect ratio ($a \geq 0.85$). These Boussinesq simulations show clear evidence of multiple jets inside the tangent cylinder. Using stress-free conditions at both boundaries becomes mandatory for larger aspect ratios, since the viscous friction would otherwise prevent strong jets from developing. While these simulations produce fewer bands than observed in Jupiter, the width of each zonal band follows the Rhines scaling with a purely topographical β -effect (Heimpel and Aurnou 2007).

Reaching the multiple-jets regime in a compressible 3-D model of rotating convection in thin spherical shells is numerically very demanding. Figure 2.16 shows the zonal flow structure for five numerical models with decreasing Ekman

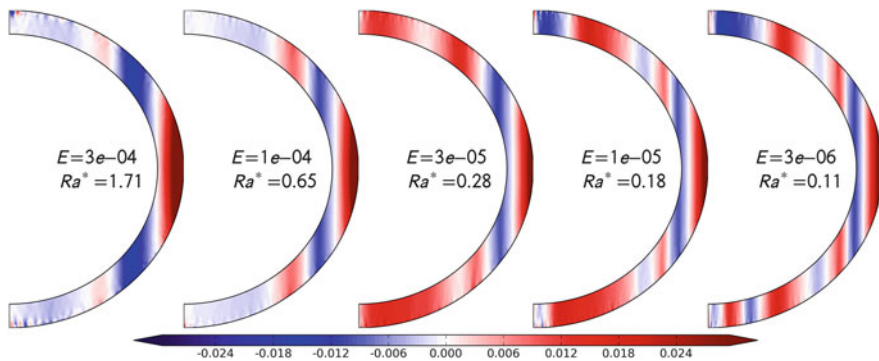


Fig. 2.16 Snapshots of zonally averaged azimuthal velocity in the meridian plane. Velocities are expressed in Rossby number units (i.e., $\bar{u}_\phi/\Omega r_o$) and color scales are centered around zero: prograde (retrograde) jets are rendered in red (blue). In all cases, the prograde contours have been truncated in amplitude to emphasize the structure of the secondary jets. The parameter Ra^* is defined as $Ra^* = Ra E^2 / Pr$. Details concerning these simulations can be found in Gastine et al. (2014b). The simulations used background model BG-DSS and gravity proportional to $1/r^2$.

number, $a = r_i/r_o = 0.85$ and a strong density contrast $N_\rho = 5$. Only the lowest Ekman numbers ($E \leq 10^{-5}$) allow for strong multiple jets at high latitudes. Similar to the thicker shells, the latitudinal extent of those jets was found to be again very similar to the previous Boussinesq results (Heimpel and Aurnou 2007; Gastine et al. 2014a).

These similarities can be explained when comparing the profiles of the purely topographic with the full β -effect. Figure 2.17 shows some examples of β for different spherical shell geometries and density contrasts. Outside the tangent

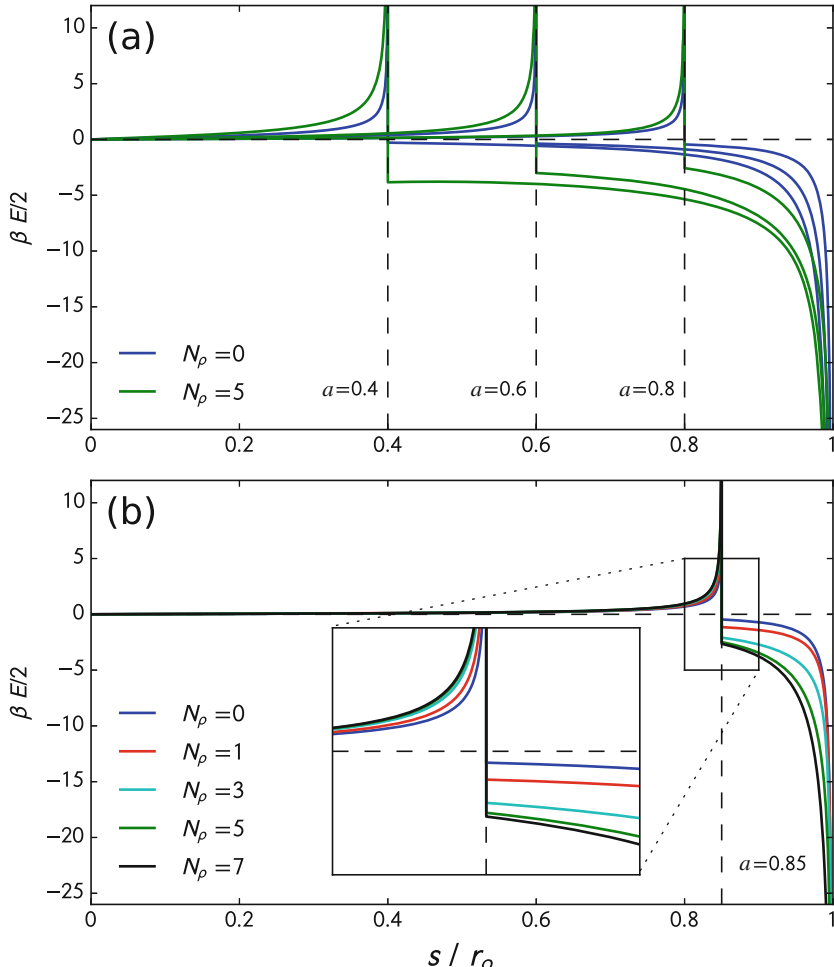


Fig. 2.17 β as a function of the normalized cylindrical radius s/r_o for different spherical shell geometries $a = r_i/r_o = [0.4, 0.6, 0.8]$ with $N_\rho = 0$ and $N_\rho = 5$ (a). β as a function of s/r_o for different density stratifications $N_\rho = [0, 1, 3, 5, 7]$ with $a = r_i/r_o = 0.85$ (b). On each panel, the location of the tangent cylinder is marked by a vertical dashed line

cylinder, the integrated mass decreases when going away from the rotation axis, resulting in $\beta < 0$. The opposite happens inside the tangent cylinder. The differences with the purely topographic β_t profiles (blue curves in Fig. 2.17a) are more pronounced in the case of a relatively thick spherical shell ($a = 0.4$ or $a = 0.6$). For a thinner shell ($a = 0.8$), this difference fades away for $s < r_i$ but β is still significantly larger in amplitude than β_t outside the tangent cylinder due to the strong density gradient in the equatorial region (Fig. 2.17b), as predicted by Eq. (2.85).

This explains the similarities of the high-latitude jets observed in Boussinesq and anelastic models (Fig. 2.16). The main differences between topographic and compressional β -effects occur outside the tangent cylinder where the density gradient is mainly perpendicular to the rotation axis. However, the Rhines scaling does not seem to be applicable there as there is only one single equatorial jet which seems to be rather controlled by the geometry of the spherical shell (Heimpel and Aurnou 2007; Gastine et al. 2014a).

2.4.9 The Transition from Prograde to Retrograde Zonal Flows

Differential rotation maintained in 3-D spherical shells is expected to be sensitive to the relative contribution of buoyancy and Coriolis force in the global force balance. The ratio between these two forces can be roughly assessed by the so-called *convective Rossby number*, defined by $Ro_c = \sqrt{Ra E^2 / Pr}$ (Gilman 1977). Figure 2.18 shows the surface zonal flow amplitude α_e at the equator as a function of Ro_c for a huge ensemble of numerical models. When Coriolis forces dominate the force balance (i.e., $Ro_c \ll 1$, regime I), the equatorial zonal flow is prograde and its amplitude increases with Ro_c . A relatively sharp transition to retrograde zonal winds then occurs close to $Ro_c \sim 1$. Despite differences in size of the convective layer, values of the control parameters, definition of the Rayleigh number, choice of thermal boundary conditions, and so on, the transition between regimes I and II is well captured by Ro_c .

As long as the convective flow is dominated by rotation, $Ro_c \ll 1$ and the main equatorial jet remains prograde or eastward. In contrast, when buoyancy becomes a first-order contribution in the force balance (i.e., when $Ro_c \sim 1$), the convective features lose their preferred alignment with the rotation axis and the zonal flow direction reverses. The equatorial jet becomes retrograde and is flanked by two prograde zonal winds inside the tangent cylinder. The formation of a retrograde equatorial jet, which is observed in the ice giants Uranus and Neptune, can be attributed to the mixing of angular momentum by the turbulent convective motions (Gilman and Foukal 1979; Aurnou et al. 2007; Gastine et al. 2013). The angular momentum per unit mass \mathcal{M} is a physical quantity that becomes homogenized by turbulence such that

$$\mathcal{M} = \bar{u}_\phi s + \Omega_0 s^2 = \text{const.} = \zeta(\eta, N_\rho) \Omega_0 r_o^2, \quad (2.94)$$

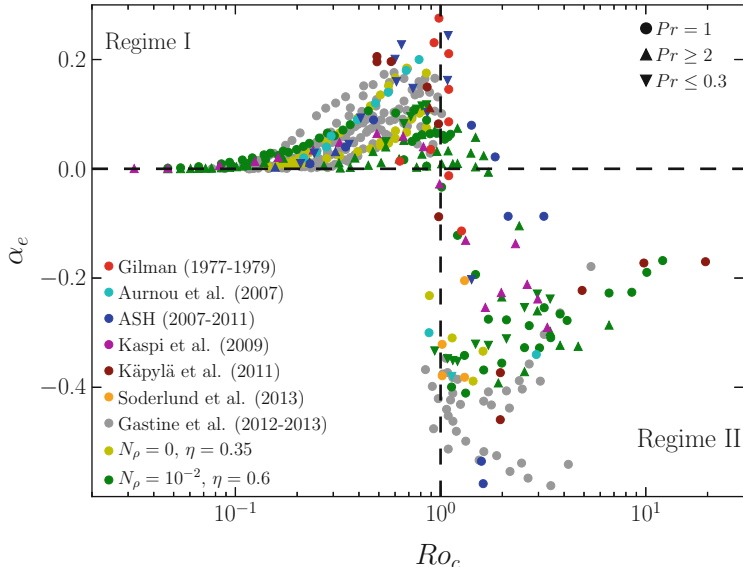


Fig. 2.18 Amplitude of the surface zonal flows at the equator in units of $\alpha_e = \overline{u_\phi}(r = r_o, \theta = \pi/2)/\Omega r_o$ as a function of $Ro_c = \sqrt{\text{Ra} E^2 / \text{Pr}}$. Data have been gathered and adapted from Gilman (1977, 1979), from simulations computed using the ASH code (Ballot et al. 2007; Browning 2008; Brun and Palacios 2009; Brown 2009; Matt et al. 2011; Bessolaz and Brun 2011), from numerical simulations by Kaspi et al. (2009), from simulations computed with the Pencil-Code (Käpylä et al. 2011), and from simulations obtained with MagIC (Aurnou et al. 2007; Soderlund et al. 2013; Gastine and Wicht 2012; Gastine et al. 2013)

where s is the cylindrical radius and $0 < \zeta(\eta, N_\rho) < 1$ depends on the background density stratification, the thickness of the convective layer, and the efficiency of the angular momentum mixing. Using $\Omega_0 r_o^2$ to nondimensionalize this equation leads to the following formulation of the zonal flow in this regime:

$$Ro = \frac{\overline{u_\phi}}{\Omega_0 r_o} = \zeta(\eta, N_\rho) \frac{r_o}{s} - \frac{s}{r_o}. \quad (2.95)$$

Comparisons between the zonal flow profiles and this theoretical prediction give a good agreement for models with $Ro_c > 1$ (Aurnou et al. 2007; Gastine et al. 2013, 2014c).

Estimates for both ice giants indicate that Ro_c is likely several orders of magnitude lower than one. While this suggests that the scenario developed above may not apply, several authors argue that the transition to 3d turbulent flow and thus to efficient angular momentum mixing is also controlled by other criteria that are more likely met in the ice giants (Soderlund et al. 2013). For example, King et al. (2012) report that the transition happens when the thermal boundary layer becomes unstable. This condition seems to be fulfilled in the ice but not in the gas giants, mostly because of the larger Prandtl number in the former planet family.

2.5 Dynamo Simulations

The starting points for most of the numerical dynamo models presented here were simulations mostly geared towards terrestrial planets. Adopting the Boussinesq approximation, these simulations ignore the background density and temperature gradients and assume that all properties are homogeneous throughout the core. Moreover, rigid rather than stress-free flow boundary conditions are typically used. In the following, we demonstrate how the adaptation of the numerical model to represent gaseous planets changes the dynamo mechanism.

We start by discussing the first-order field geometry quantified by the relative strength of the axial dipole field

$$f_{\text{dip}} = \frac{\langle \mathbf{B}_{1,0}^2 \rangle}{\langle \mathbf{B}^2 \rangle} \quad (2.96)$$

that we will refer to as dipolarity. The angular brackets refer to the average over the outer boundary and $\mathbf{B}_{\ell,m}$ stands for the magnetic field contribution of spherical harmonic degree ℓ and order m . Solutions with $f_{\text{dip}} \geq 0.4$ are considered dipolar with a clearly dominant axial dipole that changes rather slowly in time. For $f_{\text{dip}} < 0.4$, the axial dipole typically loses its special role and the geometry appears to be multipolar and also more time dependent.

2.5.1 Stress-Free Boundaries and Density Stratification

Earth-like Boussinesq simulations with rigid flow boundary conditions remain dipole-dominated when the system is not driven too strongly, i.e., when the Rayleigh number remains in a range where inertial effects are small. Christensen and Aubert (2006) quantify the relative importance of inertia with a local Rossby number,

$$\text{Ro}_\ell = \frac{U}{d_\ell \Omega}, \quad (2.97)$$

and report that dipolar solutions can only be found for Ro_ℓ values smaller than a critical value of $\text{Ro}_{\ell_c} \approx 0.1$. Here U is the mean flow velocity and

$$d_\ell = \frac{\pi}{\ell_U} \quad (2.98)$$

a typical flow length scale defined via the mean spherical harmonic degree

$$\ell_U = \frac{(\sum_\ell \ell U_\ell)}{(\sum_\ell U_\ell)}, \quad (2.99)$$

where U_ℓ is the amplitude of the degree ℓ contribution.

Stress-free flow boundary conditions promote the strong geostrophic zonal wind systems described in Sect. 2.4. The competition between these winds and a strong dipolar field seems decisive for determining whether the magnetic field is dipole dominated (Grote and Busse 2000; Busse and Simitev 2006; Simitev and Busse 2009; Sasaki et al. 2011; Schrinner et al. 2012; Gastine et al. 2012). Non-axisymmetric flows can produce both poloidal and toroidal fields in a so-called α -mechanism. The zonal wind shear, however, produces only an azimuthal toroidal magnetic field by shearing radial poloidal field in a so-called Ω -mechanism. We distinguish between α^2 and $\alpha\Omega$ -dynamos depending on whether the toroidal field is predominantly produced by an α -process or an Ω -process. More often than not, $\alpha\Omega$ -dynamos that involve a strong zonal flow and thus an Ω -effect end up being multipolar. Dipolar magnetic field configurations, however, result in strong Lorentz forces that brake the zonal winds, reduce the Ω -effect, and are more likely connected to α^2 -dynamos.

A consequence of this competition is the bistability found at not too large Rayleigh numbers where dipolar and multipolar solutions coexist at identical parameters (Gastine et al. 2012). The multipolar branch is reached when starting a simulation with a weak dipole field. Establishing a solution on the dipolar branch, on the other hand, requires starting with a strong dipole that sufficiently suppresses the zonal flows. Dipolar solutions indeed have rather slow zonal flows, while the zonal winds in the multipolar solutions can be much faster.

Even for stress-free boundary conditions, the local Rossby number criterion still seems to hold in the sense that only the multipolar branch remains once Ro_ℓ exceeds $\text{Ro}_{\ell_c} \approx 0.1$. However, Fig. 2.19 illustrates that when adopting the anelastic approach, this also depends on the density stratification. For $N_\rho > 1.0$, the critical local Rossby number seems to decrease and once $N_\rho \geq 2.0$, the dipolar branch has vanished altogether. The simulations compiled in Fig. 2.19 are all bottom heated, use homogeneous electrical conductivity, an Ekman number of $E = 10^{-4}$, and an aspect ratio of $a = 0.2$. The background states are the polytropic ideal gas variant for linear gravity introduced as BG-DBx in Sect. 2.3.6. More details and a similar figure for $a = 0.6$ can be found in Gastine et al. (2012).

Examples of the radial surface field for a bistable pair and two multipolar solutions at larger N_ρ are shown in Fig. 2.20. The multipolar magnetic fields can be highly hemispherical (panel c), highly equatorially symmetric (panel d), or more complex. Often smaller wave numbers $m = 1$ or $m = 2$ dominate the azimuthal structure. As the stratification increases, both zonal flow shear and non-axisymmetric flow components are progressively concentrated in the outer part of the shell around the equator. This results in a localized $\alpha\Omega$ -dynamo which, according to several mean field dynamo studies (Rüdiger et al. 2003; Jiang and Wang 2006; Bassom et al. 2005), is likely to produce the multipolar low-wave-number fields we observe at stronger stratifications.

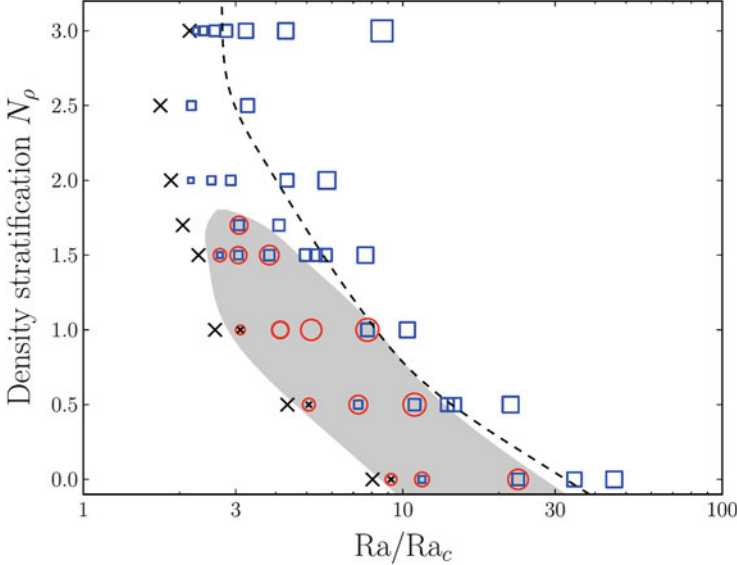


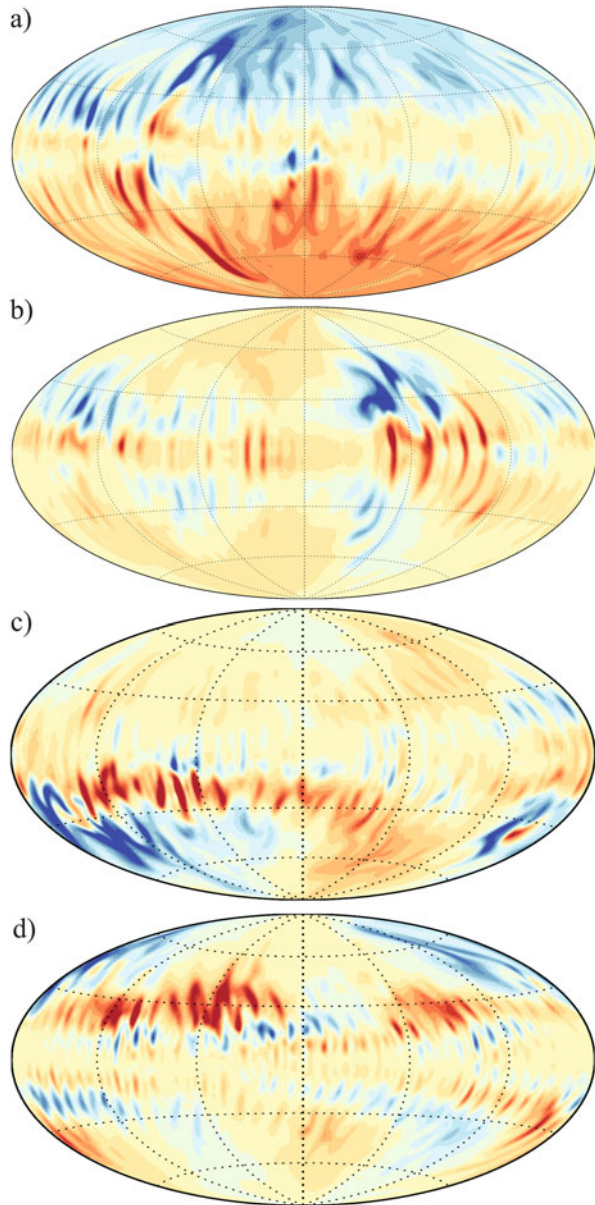
Fig. 2.19 Dependence of the time averaged magnetic field geometry on density stratification N_p and super-criticality Ra/Ra_c . Red circles indicate dipole-dominated solutions while blue boxes indicate multipolar magnetic fields. The symbol size is scaled with the magnetic energy. Crosses mark simulations where an initial magnetic field decayed. The shaded area shows the bistability regime where dipolar and multipolar solutions coexist. Parameters are $a = 0.2$, $E = 10^{-4}$, $\text{Pr}_S = 1$ and $\text{Rm} = 2$. The figure is taken from Gastine et al. (2012) where also a comparable diagram for the larger aspect ratio of $a = 0.6$ can be found

2.5.2 Electrical Conductivity Profile

Beyond the radius where the electrical conductivity becomes negligible in the molecular hydrogen layer, dynamo processes and Lorentz forces cease to play a role. When the zonal wind shear is mostly concentrated in this region, the localized $\alpha\Omega$ -dynamo that proved problematic for dipole-dominated dynamo solutions should be rendered largely ineffective. Implementing an appropriate electrical conductivity profile could thus help to reestablish dipole dominance.

Figure 2.21 shows how various electrical conductivity profiles influence the dipolarity and basically confirms this scenario. Thin weakly conducting shells, where the relative transition radii between the smoother inner and the exponentially decaying outer conductivity branch is larger than $\chi_m = r_m/r_o \geq 0.9$, have no effect and we still find the regimes outlined above: bistability for smaller stratification and only multipolar solutions for $N_p \geq 2$. For $\chi_m = 0.8$, however, we indeed recover dipolar solutions at $N_p \geq 5$. Somewhat surprisingly, the solutions at smaller stratifications are now multipolar and for intermediate stratifications the dynamo seems to switch between dipolar and multipolar solutions, sometimes in a rather regular, nearly oscillatory fashion (Duarte et al. 2013). This results in the strong time

Fig. 2.20 Radial magnetic field at the outer boundary for snapshots of some of the simulations shown in Fig. 2.19. Panels (a) and (b) show an example for bistability at $N_\rho = 1.7$ and $\text{Ra} = 9 \times 10^6$. Panels (c) and (d) depict multipolar solutions at $(N_\rho = 2.0, \text{Ra} = 1 \times 10^7)$ and $(N_\rho = 3.0, \text{Ra} = 1.1 \times 10^7)$. Yellow/red (blue) colors indicate outward (inward) directed field. Modified from Gastine et al. (2012)



dependence indicated by the vertical lines in Fig. 2.21. All simulations compared here use ideal gas background states with linear gravity (see Sect. 2.3.6), assume conductivity profiles of the form given by Eq. (2.67), and are driven by bottom heating. The Ekman number is $E = 10^{-4}$ and the aspect ratio is $a = 0.2$. For more details see Duarte et al. (2013).

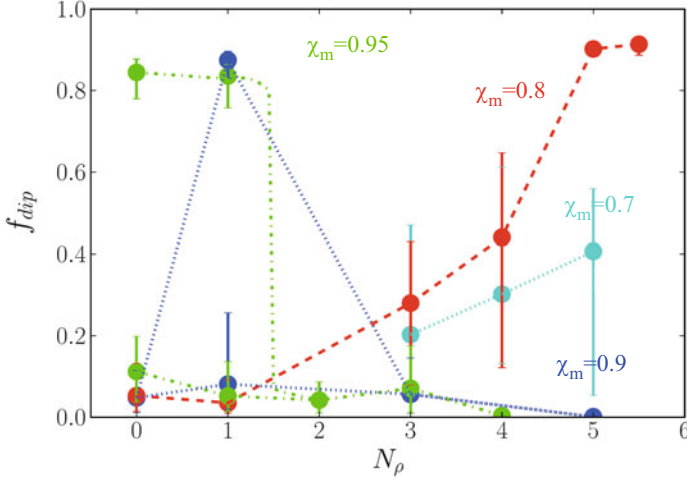
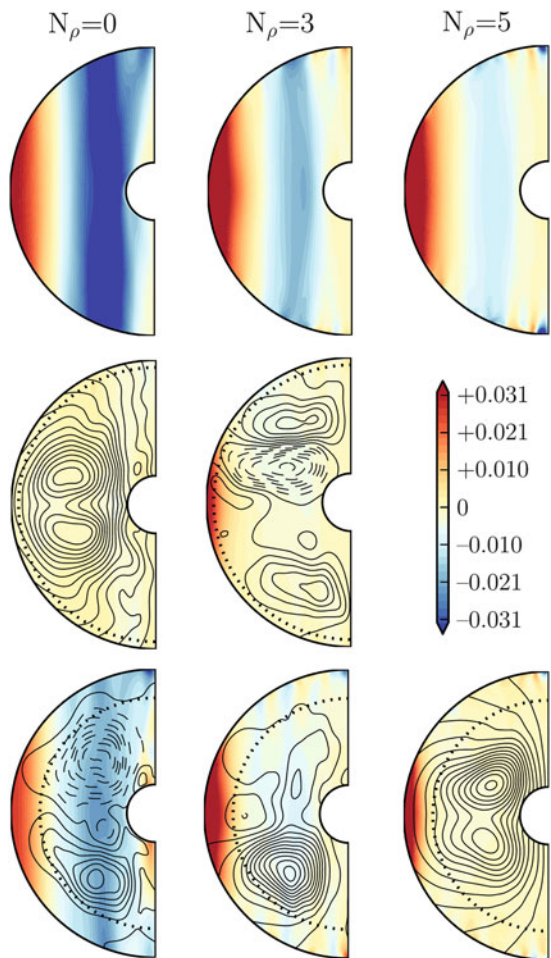


Fig. 2.21 Dipolarity for different density stratifications and electrical conductivity profiles. Dots represent time averaged values while vertical lines with a length corresponding to the standard deviation provide an idea of the variability. Parameters are $E = 10^{-4}$, $Pr_S = 1$, $Pm = 2$, and moderate Raleigh numbers that should guarantee dipolar dynamo solutions. Modified from Duarte et al. (2013)

Example of zonal winds and axisymmetric poloidal field contributions for different stratifications and χ_m values and an Ekman number of $E = 10^{-4}$ are compared in Fig. 2.22. The key questions regarding the field geometry seem to be whether the Lorentz forces associated with the dipole field can sufficiently brake the zonal winds and whether the strongly localized kinetic power at larger stratifications significantly contributes to dynamo action. For weak stratifications and thin (or nonexistent) weakly conducting layers, we find dipolar solutions in the bistable regime where the Lorentz force manages to restrain the zonal winds; see the middle panel in the left column of Fig. 2.22. However, when the weakly conducting layer becomes thicker, the region where Lorentz forces act shrinks, while the Reynolds stresses that drive the zonal winds still act (more or less) globally. The lower panel of the left column in Fig. 2.22 illustrates a respective example where dipolar solutions cease to exist for a Boussinesq simulation with $\chi_m = 0.8$. The same effect is likely responsible for the fact that dipolar solutions are generally missing for stronger stratifications and $\chi_m = 0.7$ (see Fig. 2.21).

At an intermediate stratification, the increasing localization of dynamo action at the equatorial region tends to promote multipolar solutions. The lower two panels in the middle column of Fig. 2.22 demonstrate that at $N_\rho \geq 3$ the Lorentz forces push the prograde equatorial jet to the weakly conducting region and damp the deeper retrograde jet, but the effect is not sufficient to establish dipolar solutions. At $N_\rho = 5$ (right column of Fig. 2.22), however, the inner retrograde jet is already quite weak

Fig. 2.22 Zonal flow and axisymmetric poloidal field lines for three different density stratifications. Red/yellow (blue) colors indicate prograde (retrograde) flow. The top row shows nonmagnetic solutions. Dotted half circles mark the transition radius $\chi_m = 0.95$ in the second row and $\chi_m = 0.80$ in the third row. Solutions with $\chi_m = 0.95$ are practically identical to those for homogeneous electrical conductivity. Modified from Duarte et al. (2013)



in the nonmagnetic case (top panel). Lorentz forces have a better chance of reducing the amplitude of the retrograde jet to a rather low level. In addition, the equatorial jet is pushed out even farther, which diminishes its role in the dynamo process.

2.5.3 Parameter Dependence

Even the dipolar solutions that combine a stronger stratification with a sufficient weakly conducting layer eventually become multipolar when the Rayleigh number is increased beyond a critical value Ra_{cm} that depends on the other system parameters. There is a certain tradeoff between Rayleigh number and magnetic Prandtl number in the sense that Ra_{cm} increases with Pm (Duarte et al. 2013; Schrinner et al.

2014; Jones 2014; Raynaud et al. 2015; Duarte et al. 2018). However, this effect only mildly extends the regime of dipolar solutions, increasing Ra_{cm} by perhaps 50% at best. Decreasing the Ekman number also seems to help, likely because the ratio of magnetic to kinetic energy tends to increase (Christensen and Aubert 2006; Gastine et al. 2012) and the stronger Lorentz forces can more easily balance the zonal flows. However, for the explored Ekman number range $E \geq 10^{-5}$, this effect remains rather limited and is therefore hard to quantify.

The simulations discussed so far used Prandtl numbers $\text{Pr}_S = 1$. Since the thermal Prandtl number may be as small as 10^{-2} at depth, Jones (2014) and Duarte et al. (2018) also explore models with $\text{Pr}_S = 0.1$ and find interesting new effects. For small Rayleigh numbers, the convection is more evenly distributed throughout the shell at $\text{Pr}_S = 0.1$ than at $\text{Pr}_S = 1.0$, even at strong stratifications. The magnetic field, however, is multipolar for $\text{Pr}_S = 0.1$ and dipolar for $\text{Pr}_S = 1.0$ which confirms the findings in Boussinesq simulations (Simitev and Busse 2005). When the Rayleigh number is increased, the situation reverses, and the magnetic field becomes dipolar for the smaller but multipolar for the larger Prandtl number. The reason remains unclear and the respective effect needs to be explored further in the future. When increasing Ra even more, the $\text{Pr} = 0.1$ simulations should also become multipolar again.

Gastine et al. (2012) compare bottom heated dynamos with constant electrical conductivity for a thicker Jupiter-like shell with an aspect ratio of $a = 0.2$ and linear gravity with simulations at $a = 0.6$ and gravity proportional to $1/r^2$ (see Sect. 2.3.6). All simulations use polytropic ideal-gas background states and show the same dipolar and multipolar regimes outlined in Sect. 2.5.1. They also find that using rigid rather than stress-free lower boundary conditions in the $a = 0.2$ setup has little impact. For thinner shells, however, rigid lower boundary conditions tend to suppress zonal winds and fundamentally change the overall behavior.

Most of the simulations reported above used pure bottom heating with $q_s = 0$ (see Sect. 2.3). Only Jones (2014) and Duarte et al. (2018) explore some models with dominant volumetric heating, testing radial dependencies like Eq. (2.53), Eq. (2.54), or Eq. (2.55). They report that it becomes generally much more difficult to find dipole-dominated solutions for either radial dependency. Only a combination of a heating term following Eq. (2.53), a relatively low Ekman number ($E = 1.5 \times 10^{-5}$ to 2.4×10^{-5}), a larger magnetic Prandtl number, and a low Prandtl number $\text{Pr}_S = 0.1$ proved successful (Jones 2014). Since this kind of internal heating that parameterizes the cooling of an adiabatic planet is likely the dominant driving force for Jupiter's dynamo, it seems essential to further explore this scenario. Jones (2014) also reports that there seems to be no bistable regime in his lower Ekman number cases at $E = 1.5 \times 10^{-5}$. The solutions are either dipolar at lower or multipolar at higher Rayleigh numbers.

2.5.4 Toward Jupiter-Like Models

A closer comparison of the simulation results with the Jupiter field models VIP4 and JCF helps to constrain which of the dipole-dominated solutions yield more realistic field details. VIP4 is based on data from the Pioneer and Voyager space crafts and from the Io auroral footprint to provide Gauss coefficients g_ℓ^m and h_ℓ^m up to degree $\ell = 4$ and order $m = 4$. Ridley and Holme (2016) use all available mission data, which in addition to Pioneer and Voyager also comprise Ulysses and Galileo measurements and cover a period of 30 years. Their JCF variant fits these data with a Jupiter Constant Field model of degree and order seven. Regularization helps to constrain smaller scale JCF contributions in regions of insufficient data coverage.

Duarte et al. (2018) use a misfit measure M to judge how close a particular simulation comes to replicating VIP4. The misfit is based on relative deviations in the axial dipole, equatorial dipole, quadrupole, and octopole surface field contributions:

$$M = \sqrt{\frac{(b_{10} - b_{10J})^2 + (b_{11} - b_{11J})^2 + (b_2 - b_{2J})^2 + (b_3 - b_{3J})^2}{4}}, \quad (2.100)$$

with

$$b_{10} = \frac{B_{\ell=1,m=0}}{B_{\ell \leq 4}}, \quad (2.101)$$

$$b_{11} = \frac{B_{\ell=1,m=1}}{B_{\ell \leq 4}}, \quad (2.102)$$

$$b_2 = \frac{B_{\ell=2}}{B_{\ell \leq 4}}, \quad (2.103)$$

and

$$b_3 = \frac{B_{\ell=3}}{B_{\ell \leq 4}}. \quad (2.104)$$

The normalization with the rms field strength $B_{\ell \leq 4}$ allows for a comparison without the need to rescale the dimensionless simulations to absolute field amplitudes. Gastine et al. (2014b) confirm that such a rescaling process based on the available convective power (Yadav et al. 2013) can indeed yield Jupiter-like values as we will also show in Sect. 2.5.5. Values with subindex J in Eq. (2.100) refer to VIP4. For more discussion on the rescaling see Duarte et al. (2018).

Figure 2.23 illustrates how close some of the simulations come to the Jupiter values b_{10J} to b_{3J} . Considered are simulations for different background states, electrical conductivity profiles, Ekman numbers, Rayleigh numbers, magnetic

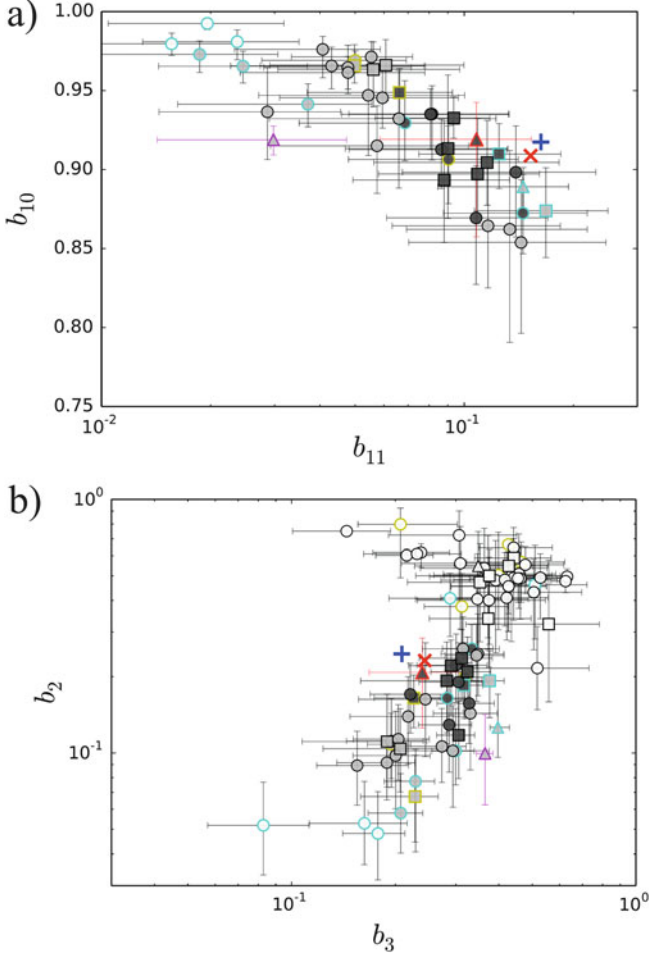


Fig. 2.23 Comparison of relative field contributions in dynamo simulations with those in the VIP4 and JCP Jupiter field models. VIP4 and JCP values are shown as red crosses and blue plusses, respectively. Other symbols represent time averages of various numerical simulations, while the error bars show the standard deviation to provide an idea of the variability. Symbol colors indicate the VIP4 misfit: $M < 0.08$ dark grey, $0.08 \leq M \leq 0.12$ light grey, $M > 0.12$ white. The rim color indicates the background model: BG-G14 in black, BG-IP4 in yellow, and BG-IP5 in cyan. The symbol type codes the Ekman number: $E = 10^{-4}$ circles, $E = 3 \times 10^{-5}$ squares, $E = 10^{-5}$ triangles. The red-rimmed and magenta-rimmed triangles pick out solutions by Gastine et al. (2014b) and Heimpel and Gómez Pérez (2011), respectively. Panel (a) shows only dipole-dominated solutions while panel (b) shows all 66 simulations considered by Duarte et al. (2018). The white (open) symbols in the upper part of panel (b) are multipolar solutions

Prandtl numbers, and Prandtl numbers. Table 2.1 lists parameters and properties for some of the models discussed in more detail in the following. All simulations use an aspect ratio of $a = 0.2$.

Table 2.1 Comparison of several numerical models of Gastine et al. (2014b) (model G14) and Duarte et al. (2018) with Jupiter field models VIP4 and JCF

| Model | BG | $\sigma(r)$ | E | $\frac{R_a}{Ra_c}$ | Pm_i | P_{TS} | χ_{50} | f_{dip} | θ ($^{\circ}$) | b_{11} | b_2 | b_3 | M |
|-------|--------|---------------------|--------------------------|--------------------|--------|----------|-------------|------------------|-------------------------|----------|-------|-------|-------|
| VIP4 | – | – | $\sim 5 \times 10^{-19}$ | – | – | – | – | 0.83 | 9.6 | 0.152 | 0.232 | 0.244 | 0 |
| JCF | – | – | $\sim 5 \times 10^{-19}$ | – | – | – | – | 0.84 | 10.2 | 0.163 | 0.246 | 0.209 | 0.021 |
| 2 | BG-ND4 | $\sigma\text{-SD}$ | 3×10^{-5} | 5.6 | 1.03 | 1.0 | 0.89 | 0.90 | 4.0 | 0.066 | 0.165 | 0.227 | 0.065 |
| 60 | BG-G14 | $\sigma\text{-ED}$ | 3×10^{-5} | 9.6 | 0.74 | 1.0 | 0.86 | 0.93 | 3.4 | 0.056 | 0.104 | 0.207 | 0.095 |
| 4 | BG-G14 | $\sigma\text{-G14}$ | 10^{-4} | 7.4 | 2.0 | 1.0 | 0.89 | 0.89 | 2.5 | 0.037 | 0.102 | 0.300 | 0.096 |
| 20 | BG-G14 | $\sigma\text{-G14}$ | 10^{-4} | 11.7 | 1.27 | 0.1 | 0.91 | 0.88 | 4.6 | 0.081 | 0.171 | 0.221 | 0.064 |
| 44 | BG-G14 | $\sigma\text{-G14}$ | 10^{-4} | 7.4 | 6.39 | 1.0 | 0.92 | 0.76 | 7.2 | 0.108 | 0.222 | 0.301 | 0.067 |
| G14 | BG-G14 | $\sigma\text{-G14}$ | 10^{-5} | 12.3 | 0.37 | 1.0 | 0.90 | 0.85 | 7.0 | 0.108 | 0.208 | 0.240 | 0.063 |

The second column gives the background model while the third column details the electrical conductivity profile

Within the limited set of models, neither the Ekman number nor the Prandtl number or the details of the background model seem to matter much in the sense that similarly Jupiter-like solutions can be found by adjusting Rayleigh number and magnetic Prandtl number along the lines discussed above. While a too large Rayleigh number always yields multipolar solutions, a too small Rayleigh number results in an unrealistically simplistic field where the axial dipole and often also the axial quadrupole are too dominant, while the equatorial dipole and other contributions are far too weak. The reason is the lack of equatorially symmetric magnetic field contributions, which are only more efficiently produced at larger Rayleigh numbers (Wicht and Christensen 2010). These cases are represented by the white (open) symbols with larger misfit values $M > 0.12$ located in the upper left corner of Fig. 2.23a and lower left part of Fig. 2.23b. Typical for the best fitting solutions with misfits below $M < 0.08$ (dark gray symbols) are a too small equatorial dipole and a too large quadrupole.

Figure 2.24 compares magnetic power spectra (Mauersberger-Lowes) for various simulations with those for VIP4 and JCF. The steeper decay of magnetic energy beyond degree $\ell = 5$ in JCF is likely owed to the model regularization (Ridley and Holme 2016). Models 20 and 44 from Duarte et al. (2018) and model G14 from Gastine et al. (2014b) are among the best fitting models with $M < 0.08$ and nicely agree with VIP4 and JCF. Model 4 is an example for a simulation with a small Rayleigh number and illustrates the too low relative quadrupole but also $\ell > 3$ contributions.

A second property that influences the Jupiter-likeness of dipolar solutions is the form of the electrical conductivity profile $\tilde{\sigma}(r)$, which determines the depth where dynamo action starts or Lorentz forces are efficient enough to contain the zonal winds. Model 60 in Fig. 2.24 uses the early decaying profile σ -ED illustrated in Fig. 2.7, which promotes a very dominant axial dipole contribution, a steeper decaying spectrum, and an unfavorable misfit of $M = 0.095$. The reason for this magnetic field configuration is likely the deeper dynamo action. Beyond a radius r_D where the electrical conductivity becomes small enough, the magnetic field approaches a potential field that decays like $(r_D/r)^{\ell+2}$. What “small enough” actually means and how r_D can be pinned down, in particular when the transition to a potential field is gradual, remains unclear for the moment. However, the misfit strongly indicates that r_D is obviously too small in model 60 and more reasonable in models 20, 44, and G14.

The lower panel of Fig. 2.24 compares the spherical harmonic order spectra. Both Jupiter field models show a particularly strong decay at their smaller scales, which is likely caused by the respective regularizations. At $m = 4$ the difference between VIP4 and JCF is more than one order of magnitude, demonstrating the effects of the different modeling approaches. The numerical models predict a continuous smooth decay, much larger $m = 4$ contributions than in VIP4, and much larger $m = 5$ and 6 contributions than JCF.

More decisive for dynamo action than the electrical conductivity alone is the magnetic Reynolds number

$$\text{Rm}_r(r) = U(r)\sigma(r)\mu d, \quad (2.105)$$

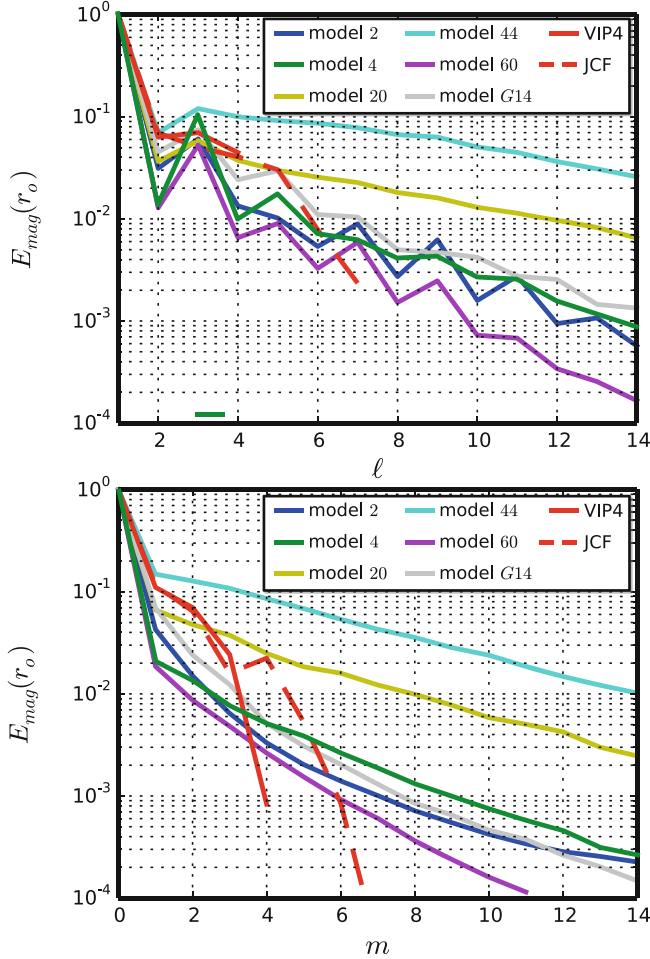


Fig. 2.24 Energy spectra (Mauersberger-Lowes) of the magnetic surface field for the VIP4 (*solid red*) and JCF (*dashed red*) Jupiter field models and several numerical dynamo simulations. The *top* and *bottom* panels show the spectra for spherical harmonic degree ℓ and order m respectively. All numerical simulations depicted here are driven by bottom heating

an estimate for the ratio between magnetic field production to diffusion. Here $U(r)$ is the rms amplitude of non-axisymmetric flows at radius r . Note that Rm_r defines a radial profile while other authors more typically cite the volume average equivalent

$$Rm = \frac{4\pi}{V} \int_{r_i}^{r_o} dr r^2 Rm_r(r), \quad (2.106)$$

where V is the volume of the shell. Being based on the non-axisymmetric flows, Rm_r also excludes the potential dynamo action of the equatorial zonal flow jet, which we will further discuss in the next section.

To guarantee dynamo action, the field production obviously has to exceed diffusion, but since Rm only provides a crude estimate, the true value of the critical magnetic Reynolds number Rm_c beyond which self-consistent dynamo action becomes possible is always significantly larger than one. Christensen and Aubert (2006) analyze a suite of Boussinesq dynamo simulations geared to model the geodynamo and find a value of $Rm_c \approx 50$. Figure 2.25 shows the magnetic Reynolds number profile for the Jupiter dynamo simulations already depicted in Fig. 2.24. The relative radius $\chi_{50} = r(Rm_r = 50)/r_o$ where the profiles first exceeds $Rm_r = 50$ likely marks the depth where self-consistent dynamo action becomes possible, assuming that the findings by Christensen and Wicht (2015) still apply (Duarte et al. 2018).

Figure 2.25 demonstrates that the Rm profiles are clearly shaped by the conductivity model, in particular in the outer region where the conductivity drops strongly with radius, while the flow amplitude increases more mildly. This leads to a smaller χ_{50} value of 0.86 in model 60, while values larger than 0.89 are typical for the more successful simulations. Model 2 is an example for the slowly decaying conductivity profile σ -SD illustrated in Fig. 2.7 (dark gray line). Since the conductivity drops by only two orders of magnitude, Rm_c remains sizable throughout the shell and the magnetic field never comes close to a potential field, except at r_o . While the small misfit values would still classify this as one of the most Jupiter-like simulations, the respective spectrum in Fig. 2.24 shows that the $\ell = 4$ to $\ell = 6$ contributions are too

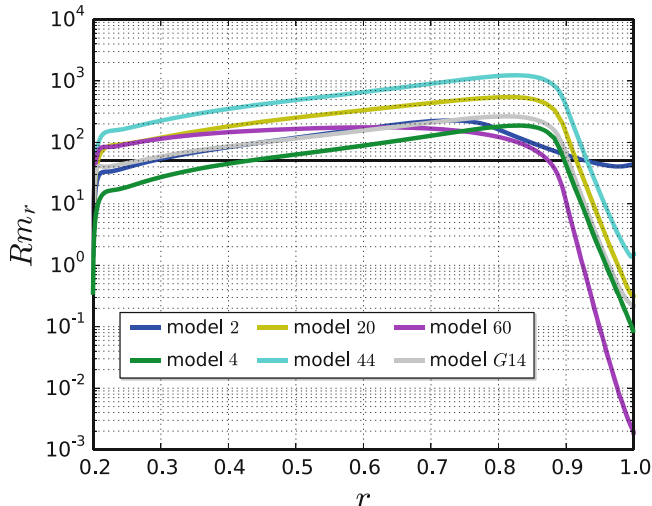


Fig. 2.25 Magnetic Reynolds number profiles for several numerical simulations by Duarte et al. (2018) and Gastine et al. (2014b). The model names refer to Duarte et al. (2018) and Table 2.1

low. These models will likely have to be dismissed once the Juno mission data will allow us to formulate a refined misfit.

The $Rm_c = 50$ criterion only concerns a global value for self-consistent dynamo action of non-axisymmetric flows. Local dynamo action may be possible at much smaller values $Rm_c > 1$, for example where the equatorial jet acts on the dipolar magnetic field that is produced at greater depth. In addition, magnetic diffusion may be enhanced where the electrical conductivity gradient is steep and the conductivity scale height rather than the scale of magnetic field determines the diffusive process (Liu et al. 2008). More research is obviously required to determine where Jupiter's observed surface field truly originates from.

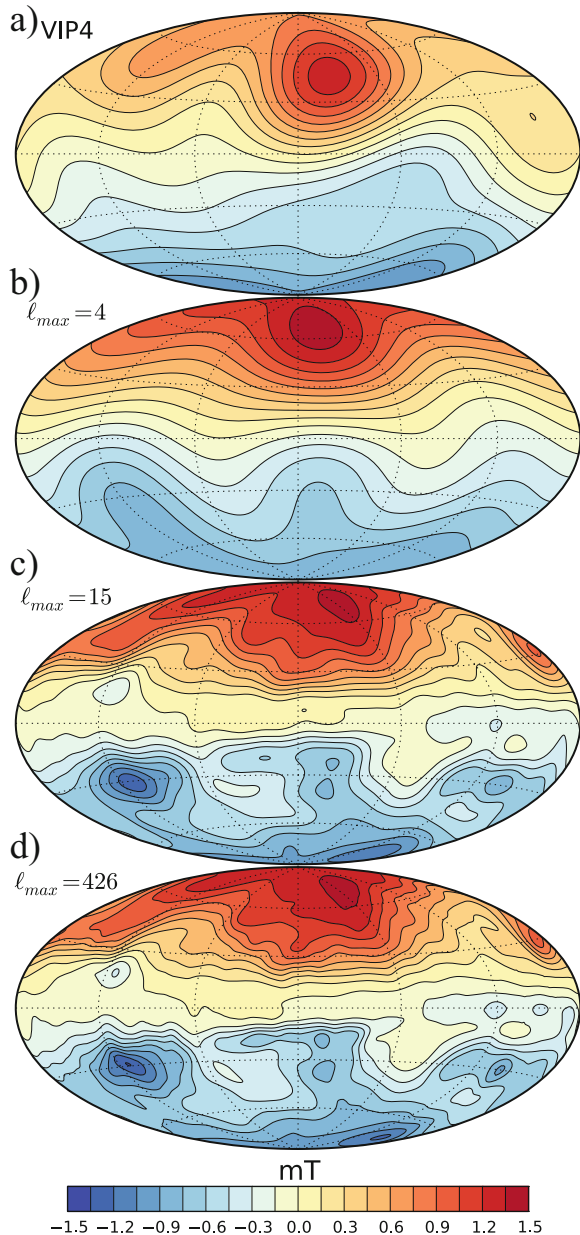
The magnetic Reynolds number can reach values around 10^6 in Jupiter's dynamo region but it never significantly exceeds 10^3 in our simulations. Larger values will likely be reached at smaller Ekman numbers where the stronger Coriolis force should guarantee dipolar dynamo action at larger Rayleigh numbers. Model 44 reaches particularly large Rm values, as illustrated in Fig. 2.25, because the magnetic Prandtl number of $Pm = 10$ is high. While the misfit still classifies model 44 as one of the most VIP4-like simulations, the spectra in Fig. 2.24 also show particularly large small scale contributions and a smoother decay than for the other models. This can only partly be explained with a shallower dynamo region indicated by $\chi_{50} = 0.92$. The reason for the smooth decay in model 20, however, could be the smaller Prandtl number of $Pr = 0.1$. The Juno mission data should reveal whether these spectra are particularly realistic.

All simulations discussed in this section are driven by bottom heating. While the more realistic volumetric heating (see Sect. 2.3.4) makes finding dipole dominated solutions more difficult, Jones (2014) demonstrates that very Jupiter-like solutions can nevertheless be found.

2.5.5 Jupiter's Two Dynamos

Figure 2.26 compares the radial surface field of a snapshot from the G14 simulation (Gastine et al. 2014b) with VIP4. The field amplitude has been rescaled from the dimensionless simulation using the available convective power as suggested by Yadav et al. (2013). This process results in very Jupiter-like field strengths. The misfit discussed above addressed only four relative field contributions in an average sense. The visual comparison additionally confirms that the simulations can also reproduce details of the observed field geometry, for example the presence of only one strong large scale field patch in the northern hemisphere at a comparable location. Panel (c) displays the field filtered to resolution $\ell \leq 15$ in order to illustrate the level of detail the Juno mission should be able to resolve. A comparison with the full resolution field in panel (d) predicts that Juno would likely capture all the important features, since even smaller scale contributions have already decayed significantly over the weakly conducting molecular envelope.

Fig. 2.26 Comparison of a snapshot from the dynamo model G14 by Gastine et al. (2014b) with VIP4 (Connerney et al. 1998) radial surface field in panel (a). Panel (b) shows the numerical model field filtered to the same spherical harmonic resolution $\ell = 4$ used in VIP4. Panel (c) filters to the resolution likely achieved by the Juno mission while panel (d) shows the full numerical resolution $\ell = 426$. Red/yellow (blue) colors indicate outward (inward) directed radial magnetic field. Taken from Gastine et al. (2014b)



Particularly interesting are the stronger spots and banded features that appear at low latitudes. Figure 2.27 demonstrates that the dipole-dominated large-scale magnetic field is produced by a primary dynamo operating in the deeper interior where electrical conductivities are high. However, the equatorial jet gives rise to

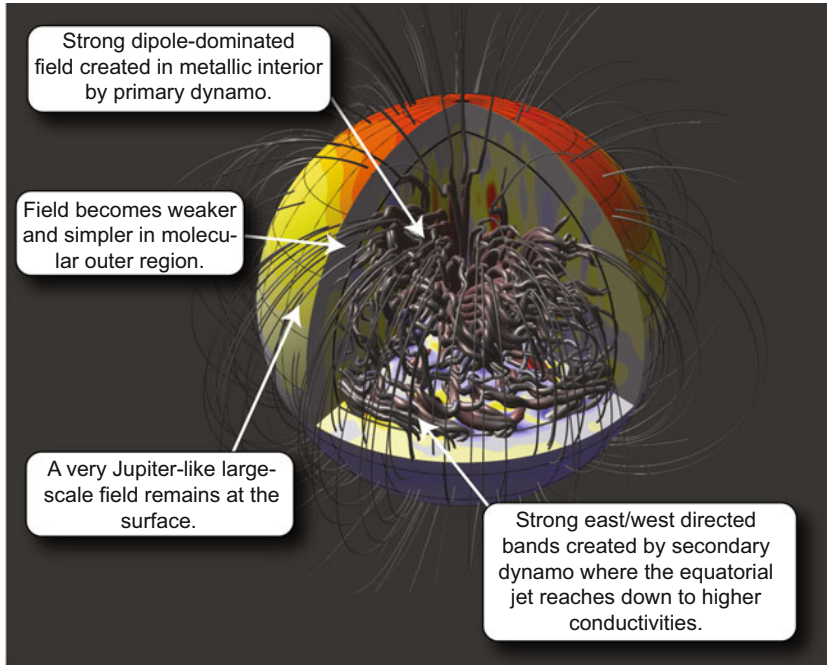


Fig. 2.27 The dynamo process in a Jupiter-like simulation. The thickness of the field lines is scaled with the local magnetic field strength. The *black line* at 87% of the radius marks the transition from the higher conducting (metallic) interior to the weakly conducting (molecular) outer envelope

a secondary dynamo close to the transition to the weakly conducting outer layer. The strong flux bundles indicate the efficient Ω -mechanism operating here. This secondary dynamo is of the $\alpha\Omega$ -type already discussed above, while the primary deeper dynamo is of α^2 -type according to the classical mean field categorization.

Figure 2.28 shows the full-resolution surface field and the axisymmetric field in meridional cuts for two additional snapshots from simulations G14, about 360 years and 680 years later than the one in Fig. 2.26. Time has been rescaled by estimating an rms flow amplitude of 3 cm/s based on the convective power (Yadav et al. 2013; Gastine et al. 2014b). The strong inverse axisymmetric band just north of the equator in Fig. 2.28a is clearly correlated to a strong toroidal flux bundle just below the transition radius $r_m = 0.87r_o$. A second feature with opposite magnetic field direction is just developing south of the equator. About 320 years later, both features seem to have drifted northward. The southern band has intensified and developed a wave number $m = 1$ contribution, while the northern band is now clearly dominated by $m = 2$ with two distinct inverse field patches. As already mentioned above, low wave number contributions seem typical for this type of shallow $\alpha\Omega$ -dynamos.

The dynamics of the equatorial features can partly be described by a Parker dynamo wave mechanism, which explains the poleward propagation and reversal

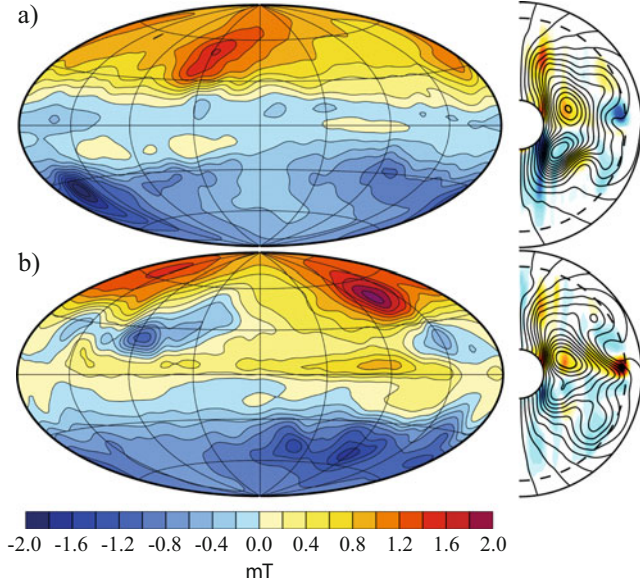


Fig. 2.28 Magnetic field in two other snapshots of the simulation G14 by Gastine et al. (2014b), about 360 years (**a**) and 680 years (**b**) later than the snapshot depicted in Fig. 2.26. The *left column* shows the full resolution radial surface field. Red/yellow (blue) colors indicate radial outward (inward) field. The *right column* shows the axisymmetric azimuthal toroidal field as colored contours and the axisymmetric poloidal field as fieldlines. The red/yellow (blue) colors indicate prograde (retrograde) field. The *dashed line* in the *right panels* marks the transition radius at $r_m = 0.87 r_o$. See caption of Fig. 2.26 for additional explanation

of the field direction over time scales of centuries (Gastine et al. 2012). Additional effects, like the dynamics of the low wave number instabilities but also smaller wave number disturbances, complicate the evolution (Duarte et al. 2018).

2.6 Conclusion

We have outlined above the path toward an up-to-date model for the interior dynamics of gas planets in general and Jupiter in particular. New ab initio simulations do not only provide the equations of state for hydrogen and helium but also the transport properties, most notably the electrical conductivity with its pronounced increase from the molecular outer to the metallic inner envelope. The updated MHD-code MagIC includes the effects of the background density and temperature stratification in the anelastic formulation developed by Braginsky and Roberts (1995). Additionally, a radial electrical conductivity profile allows to model the differences between the metallic and molecular envelopes. This chapter reported on the attempts to explore not only the dynamo effect but also the nonmagnetic flows

under Jupiter-like conditions with a wealth of MagIC simulations. The following provides a brief summary, discussion, and outlook.

New and accurate equations of state for hydrogen–helium mixtures at planetary interior conditions were calculated using ab initio simulations based on density functional theory. These equations of state were used to derive new interior structure models for Jupiter and Saturn, which yield the internal profiles for density, pressure, and temperature, respectively. The ab initio demixing diagram of hydrogen and helium indicates that helium sedimentation is likely to occur in Saturn, which might lead to a stably stratified zone. Several evolution scenarios of Saturn were investigated to estimate the size of the demixing region and its contribution to Saturn’s luminosity. Future research will explore to which extent such a demixing region plays a role in the generation of Saturn’s axisymmetric magnetic field. In addition, major efforts were made to calculate a set of transport properties (electrical and thermal conductivity, viscosity) for the interior of Jupiter using the ab initio simulation technique (French et al. 2012). For instance, the conductivity data indicate that metallization of the hydrogen–helium mixture occurs at about 90% of Jupiter’s radius at a pressure of about 0.5 Mbar and a temperature of 4500 K. Together with the interior structure model, this consistent set of thermodynamic and transport properties served as prerequisites for performing extensive MHD simulations for Jupiter’s internal flow dynamics and its dynamo.

Nonmagnetic convection simulations have shown that the flow speed increases with radius while the flow scale decreases. Jupiter or Saturn-like zonal wind systems develop in a spherical shell that models only the molecular outer layer. These jets are driven by Reynolds stresses, a statistical correlation of non-axisymmetric flow contributions. While both the β -effect due to the background density stratification or the β -effect due to the topography of the spherical container could cause the required correlation, only the latter effect seems to be important in the more realistic spherical shell simulations. The width of the multiple jets forming inside the tangent cylinder, an imaginary cylinder touching the inner core equator, seems to obey the Rhines scaling. The region outside the tangent cylinder, however, always harbors a dominant prograde equatorial jet and two flanking retrograde jets that are part of the same geostrophic zonal flow structure.

This poses a problem when extending the simulated region to also include the metallic envelope. The region inside the tangent cylinder then shrinks to an insignificant size in the Jupiter models where the rocky core occupies only 20% in radius. Since only the prograde equatorial jet and the two flanking retrograde jets remain, the zonal flow system seems not very Jupiter-like.

Several dynamo simulations come nevertheless very close to replicating magnetic field models that are based on the available pre-Juno data. A weakly conducting outer layer is required to minimize the dynamo action of the strong prograde equatorial zonal jet and the powerful small scale convection in the very outer part of the convective shell. This particular flow combination drives an $\alpha\Omega$ -dynamo mechanism that tends to produce non-dipolar magnetic fields. In simulations that closely reproduce Jupiter’s known magnetic field, Lorentz forces manage to push the zonal jet to the weakly conducting outer region so that the

$\alpha\Omega$ -dynamo assumes a secondary role. The primary magnetic field, however, is produced by an α^2 -dynamo at depth, where variations in density and electrical conductivity are only mild. Since this resembles the situation characteristic for many successful geodynamo simulations (Christensen and Wicht 2015), the similarity of Jupiter's and Earth's large scale fields may not be a coincidence.

These results suggest that only Jupiter's equatorial jet may be geostrophic in the sense that it reaches through the whole planet. The flanking mid-to-high latitude jets, on the other hand, must remain confined to the weaker conducting outer region by an effect that is obviously not correctly captured in the simulations. The limited depth of these jets is supported by several observation-based arguments. Liu et al. (2008) constrain the depth based on the argument that the heat produced by the dissipation of the jet-induced electric currents cannot exceed the observed luminosity. Assuming a magnetic diffusivity profile similar to the one discussed above, they estimate that the jets observed at the surface cannot penetrate deeper than $0.96 R_J$.

Ridley and Holme (2016) invert for possible flows on the top of Jupiter's dynamo region by assuming that variations in the magnetic field observations are explained by advection. They find a flow pattern devoid of strong zonal flows with a maximum flow amplitude of only about 1 cm/s and thus orders of magnitude slower than the observed zonal surface jets (up to 150 m/s). This suggested that the jets cannot reach down to sizable conductivities where larger magnetic Reynolds numbers would facilitate field advection and radii much below $0.96 R_J$ therefore seem unlikely.

The width of the equatorial jet may provide additional information. While it remains an open question which effects would prevent the jets from penetrating deeper, Lorentz forces seem a likely candidate but would only start to become significant where the increasing conductivity permits sizable electric currents. This would result in a “magnetic tangent cylinder” which could take over the role in determining the width of the equatorial jet from the tangent cylinder imposed by the rocky core in nonmagnetic simulations. Adjusting the radius of the cylinder to match the observed jet width yields a radius of $0.96 R_J$ (Gastine et al. 2013).

The simulation results of Duarte et al. (2018) discussed above suggest that the dynamo region would start where the magnetic Reynolds number based on the non-axisymmetric flows exceeds 50. This argument excludes possible effects of the equatorial zonal jet present in the simulations. Using a mean flow speed of 3 cm/s and the ab initio magnetic diffusivity profile (Sect. 2.2) predicts that this particular Rm threshold is exceeded at $0.95 R_J$ in Jupiter.

While the various depth estimates address somewhat different questions, they are all tied to dynamo effects and lead to quite similar values. Because the flow speeds are so large in Jupiter, Rm and therefore any magnetic effect will only become negligible where the gradient in the electrical conductivity is already very steep. This steepness explains why the depth estimate is not very sensitive to the particularities of the criterion (Duarte et al. 2018).

An analysis of magnetic spectra from simulations and Jupiter field models suggests that the top of the dynamo cannot be located much deeper than $0.90 R_J$ and demonstrates that the Juno mission will certainly help to address this question. The magnetic energy spectrum should decay like $(r_D/R_J)^{\ell+2}$, where r_D is the depth

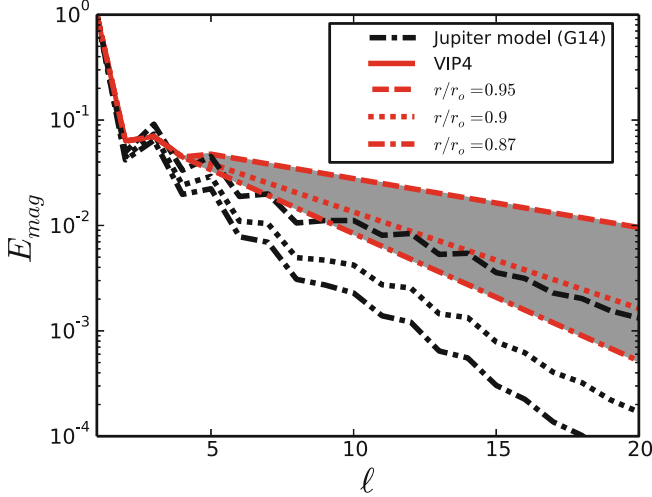


Fig. 2.29 Magnetic power spectra for G14 (black) and VIP4 (red). VIP4 has been extended by assuming a potential field above the top of the dynamo region at $0.95 R_J$ (red dashed), $0.90 R_J$ (red dotted), and $0.87 R_J$ (red dashed-dotted), respectively. Black lines show model G14 extrapolated to the different dynamo depths. We assume that the G14 dynamo starts at the radius suggested by $r_{50} = 0.87$ and use potential field extrapolation to predict the spectra at the other two radii. Modified from Duarte et al. (2018)

where dynamo effects cease and the field approaches a potential field (Duarte et al. 2018). The Juno mission will be able to constrain the field to at least degree $\ell = 15$, which should be sufficient to determine the slope of the spectrum with some confidence. Figure 2.29 illustrates the spectral differences for three values of r_D . VIP4 spectra have been extended from $\ell = 4$ to $\ell = 20$ by assuming a white spectrum at the top of dynamo regions at depths $r_D = 0.95, 0.90$, or 0.87 . While the white spectrum assumption is roughly warranted for Earth, its applicability remains unclear for Jupiter. If true, the Juno measurements would allow to constrain the top of the dynamo region. However, comparison of the extrapolated VIP4 lines with the respective lines from simulation G14 in Fig. 2.29 suggests a more complex behavior and a more detailed analysis is required to establish the limitation of this approach.

The idea that Lorentz forces would prevent the flanking zonal jets from penetrating into the regions of higher conductivity is certainly attractive but never seemed to work in the simulations where all jets remained geostrophic. The scenario may only be correct at lower Ekman numbers where viscous forces are smaller while Lorentz forces increase, but first test runs at $E = 10^{-6}$ have not confirmed this. Another possibility is that the mechanism that drives the flanking jets has not been captured in the numerical simulations. Even the most advanced run covers only the region up to $0.99 R_J$ which would translate to a pressure of about 1.7 kbar. Any effects promoted by the extremely steep very outer density gradient and phenomena like insolation, radiation, or moist convection have thus been neglected. Lian and

Showman (2010), for example, show that moist convection in a thin shell can indeed drive Jupiter-like zonal wind systems.

Another discrepancy to the planetary situation is the too small magnetic Reynolds number. The numerical simulations suggest that dipole-dominated dynamo solutions can only be retained at larger flow velocities and thus larger magnetic Reynolds numbers when the Ekman number is decreased (Christensen and Aubert 2006). The numerical costs, however, have so far prevented conclusive Jupiter simulations below $E = 10^{-5}$. Problems in finding dipole dominated solutions for the more realistic internal driving that mimics the secular cooling of Jupiter are also a concern and need to be explored further. While the recent models discussed here are a significant step toward more realistic Jupiter dynamo simulations, there is certainly ample room for improvement.

While the Juno data will prove essential for guiding the development of future models for Jupiter's interior dynamics, the up-to-date simulations already make interesting predictions that may help to interpret the mission data. Should, for example, the magnetic measurements identify banded or more localized wave number $m = 1$ or $m = 2$ structures at low latitudes, they could be a signature of the secondary $\alpha\Omega$ dynamo operating at the transition region around $0.95 R_J$. There also seems to be a chance that Juno may detect magnetic field variations which could then be inverted for the interior dynamics (Gastine et al. 2014b; Ridley and Holme 2016).

It has been suggested that magnetic field measurements may also help to constrain the size of Jupiter's rocky core (Stanley et al. 2007). Geomagnetic field models and geodynamo simulations indicate that the surface field inside the tangent cylinder is often particularly weak, while stronger magnetic flux patches tend to cluster just outside or at the tangent cylinder. A possible explanation is the flow into largely geostrophic anti-cyclonic convective columns located just outside the rocky core. This flow weakens the field closer to the poles but concentrates and thus amplifies the field where the columns touch the outer boundary (Aubert et al. 2008). Since Jupiter's rocky core is likely rather small with a relative radius below $0.2 R_J$, resolving the respective magnetic features will prove difficult. The simulations discussed here also suggest that the surface field structure is often dominated by patches at low to mid latitudes.

While we mostly focused on Jupiter, the results presented here have also implications for other gas planets. The discussion of the nonmagnetic zonal wind system also applies to Saturn. Like on Jupiter, deep rooted Reynolds stresses that rely on topographic β -effects could drive Saturn's zonal jet system (Gastine et al. 2014a). The magnetic field, however, is so different that we have to evoke additional effects that could not play any significant role in Jupiter. A stably stratified conducting layer, left behind by the hydrogen–helium demixing process acting over a significant part of the planet's history, could explain why the field seems to be perfectly axisymmetric. The layer would simply filter out any non-axisymmetric contributions produced at depth by a magnetic skin effect (Christensen and Wicht 2008). However, why Saturn's magnetic field is significantly concentrated at higher latitudes remains an open question (Cao et al. 2012).

The inverse direction of the zonal jets on Uranus and Neptune suggests that their driving must be different. Angular momentum mixing caused by a smaller impact of rotation and thus a more three-dimensional turbulent convection, provides a possible explanation (Aurnou et al. 2007; Gastine et al. 2013). Recently, Dietrich et al. (2017) show that insolation-driven thermal winds could significantly change the Reynolds stress and would also promote an inverse jet direction, at least on Neptune.

Several scenarios have been studied to explain the multipolar nature of the magnetic fields, for example a dynamo operating in a thin shell (Stanley and Bloxham 2004) or a smaller impact of rotation (Soderlund et al. 2013). So far, the exploration of both models ignore the effects of background density stratification and radial electrical conductivity variations. The simulations discussed above have shown that both density and conductivity variations tend to promote multipolar magnetic field configurations. It would be interesting to explore whether the respective solutions provide appropriate models for the magnetic fields of the ice giants.

Acknowledgements The work presented here was extensively supported by the German Science Foundation within the Special Priority Program 1488 “PlanetMag.” Most of the numerical dynamo and flow simulations have been performed at the “Gesellschaft für Wissenschaftliche Datenverarbeitung” in Göttingen and the “Max Planck Computing and Data Facility” in Garching.

References

- Allen, M.P., Tildesley, D.J.: Computer Simulation of Liquids. Oxford University Press, Oxford (1989)
- Aubert, J., Aurnou, J., Wicht, J.: The magnetic structure of convection-driven numerical dynamos. *Geophys. J. Int.* **172**, 945 (2008)
- Aurnou, J., Heimpel, M., Wicht, J.: The effects of vigorous mixing in a convective model of zonal flow on the ice giants. *Icarus* **190**, 110 (2007)
- Ballot, J., Brun, A.S., Turck-Chièze, S.: Simulations of turbulent convection in rotating young solarlike stars: differential rotation and meridional circulation. *Astrophys. J.* **669**, 1190 (2007)
- Bassom, A.P., Kuzanyan, K.M., Sokoloff, D., Soward, A.M.: Non-axisymmetric $\alpha^2\Omega$ -dynamo waves in thin stellar shells. *Geophys. Astrophys. Fluid Dyn.* **99**, 309 (2005)
- Becker, A., Lorenzen, W., Fortney, J.J., Nettelmann, N., Schöttler, M., Redmer, R.: Ab initio equations of state for hydrogen (H-REOS.3) and helium (HE-REOS.3) and their implications for the interior of brown dwarfs. *Astrophys. J. Suppl. Ser.* **215**, 14 (2014)
- Bessolaz, N., Brun, A.S.: Hunting for giant cells in deep stellar convective zones using wavelet analysis. *Astrophys. J.* **728**, 115 (2011)
- Braginsky, S.I., Roberts, P.H.: Equations governing convection in Earth’s core and the geodynamo. *Geophys. Astrophys. Fluid Dyn.* **79**, 1 (1995)
- Brown, B.P.: Convection and dynamo action in rapidly rotating suns. Ph.D. thesis, University of Colorado (2009)
- Browning, M.K.: Simulations of dynamo action in fully convective stars. *Astrophys. J.* **676**, 1262 (2008)
- Brun, A.S., Palacios, A.: Numerical simulations of a rotating red giant star. I. Three-dimensional models of turbulent convection and associated mean flows. *Astrophys. J.* **702**, 1078 (2009)
- Busse, F.H.: Thermal instabilities in rapidly rotating systems. *J. Fluid Mech.* **44**, 441 (1970)

- Busse, F.H.: Convective flows in rapidly rotating spheres and their dynamo action. *Phys. Fluids* **14**, 1301 (2002)
- Busse, F.H., Simitev, R.D.: Parameter dependences of convection-driven dynamos in rotating spherical fluid shells. *Geophys. Astrophys. Fluid Dyn.* **100**, 341 (2006)
- Busse, F.H., Simitev, R.D.: Quasi-geostrophic approximation of anelastic convection. *J. Fluid Mech.* **751**, 216 (2014)
- Caillabet, L., Mazevert, S., Loubeyre, P.: Multiphase equation of state of hydrogen from ab initio calculations in the range 0.2 to 5 g/cc up to 10 eV. *Phys. Rev. B* **83**, 094101 (2011)
- Cao, H., Russell, C.T., Wicht, J., Christensen, U.R., Dougherty, M.K.: Saturn's high-degree magnetic moments: evidence for a unique planetary dynamo. *Icarus* **221**, 388 (2012)
- Chabrier, G., Saumon, D., Hubbard, W.B., Lunine, J.I.: The molecular-metallic transition of hydrogen and the structure of Jupiter and Saturn. *Astrophys. J.* **391**, 817 (1992)
- Chekhlov, A., Orszag, S.A., Sukoriansky, S., Galperin, B., Staroselsky, I.: The effect of small-scale forcing on large-scale structures in two-dimensional flows. *Physica D* **98**, 321 (1996)
- Christensen, U.R.: Zonal flow driven by deep convection in the major planets. *Geophys. Res. Lett.* **28**, 2553 (2001)
- Christensen, U.R.: Zonal flow driven by strongly supercritical convection in rotating spherical shells. *J. Fluid Mech.* **470**, 115 (2002)
- Christensen, U., Aubert, J.: Scaling properties of convection-driven dynamos in rotating spherical shells and applications to planetary magnetic fields. *Geophys. J. Int.* **116**, 97 (2006)
- Christensen, U.R., Wicht, J.: Models of magnetic field generation in partly stable planetary cores: applications to Mercury and Saturn. *Icarus* **196**, 16 (2008)
- Christensen, U., Wicht, J.: Numerical dynamo simulations. In: Olson, P. (ed.) *Core Dynamics. Treatise on Geophysics*, vol. 8, p. 245. Elsevier, Amsterdam (2015)
- Connaughton, C., Nazarenko, S., Quinn, B.: Rossby and drift wave turbulence and zonal flows: the Charney-Hasegawa-Mima model and its extensions. *Phys. Rep.* **604**, 1 (2015)
- Connerney, J.E.P., Acuña, M.H., Ness, N.F., Satoh, T.: New models of Jupiter's magnetic field constrained by the Io flux tube footprint. *J. Geophys. Res.* **103**, 11929 (1998)
- Danilov, S., Gryankin, V.M.: Barotropic beta-plane turbulence in a regime with strong zonal jets revisited. *J. Atmos. Sci.* **61**, 2283 (2004)
- Desjarlais, M.P.: Density-functional calculations of the liquid deuterium Hugoniot, reshock, and reverberation timing. *Phys. Rev. B* **68**, 064204 (2003)
- Desjarlais, M.P.: First-principles calculation of entropy for liquid metals. *Phys. Rev. E* **88**, 062145 (2013)
- Dias, R.P., Silvera, I.F.: Observation of the Wigner-Huntington transition to metallic hydrogen. *Science* (2017). ISSN:0036-8075
- Dietrich, W., Gastine, T., Wicht, J.: Reversal and amplification of zonal flows by boundary enforced thermal wind. *Icarus* **282**, 380 (2017)
- Dormy, E., Soward, A.M., Jones, C.A., Jault, D., Cardin, P.: The onset of thermal convection in rotating spherical shells. *J. Fluid Mech.* **501**, 43 (2004)
- Dreizler, R.M., Gross, E.K.U.: *Density Functional Theory*. Springer, Berlin (1990)
- Drew, S.J., Jones, C.A., Zhang, K.: Onset of convection in a rapidly rotating compressible fluid spherical shell. *Geophys. Astrophys. Fluid Dyn.* **80**, 241 (1995)
- Dritschel, D.G., McIntyre, M.E.: Multiple jets as PV staircases: the Phillips effect and the resilience of eddy-transport barriers. *J. Atmos. Sci.* **65**, 855 (2008)
- Duarte, L.D.V., Gastine, T., Wicht, J.: Anelastic dynamo models with variable electrical conductivity: an application to gas giants. *Phys. Earth Planet. Inter.* **222**, 22 (2013)
- Duarte, L.D.V., Wicht, J., Gastine, T.: Physical properties for Jupiter-like dynamo models. *Icarus* **229**, 206–221 (2018)
- Dubrovinsky, L., Dubrovinskaia, L.N., Prakapenka, V.B., Abakumov, A.M.: Implementation of micro-ball nanodiamond anvils for high-pressure studies above 6 Mbar. *Nat. Commun.* **3**, 1163 (2012)
- Evonuk, M.: The role of density stratification in generating zonal flow structures in a rotating fluid. *Astrophys. J.* **673**, 1154 (2008)

- Evonuk, M., Glatzmaier, G.A.: A 2D study of the effects of the size of a solid core on the equatorial flow in giant planets. *Icarus* **181**, 458 (2006)
- Evonuk, M., Samuel, H.: Simulating rotating fluid bodies: when is vorticity generation via density-stratification important? *Earth Planet. Sci. Lett.* **317**, 1 (2012)
- Feynman, R.P.: Forces in molecules. *Phys. Rev.* **56**, 340 (1939)
- Fortney, J.J., Hubbard, W.B.: Phase separation in giant planets: inhomogeneous evolution of Saturn. *Icarus* **164**, 228 (2003)
- Fortney, J.J., Nettelmann, N.: The interior structure, composition, and evolution of giant planets. *Space Sci. Rev.* **152**, 423 (2010)
- Fortov, V.E., Ilkaev, R.I., Arinin, V.A., Burtzev, V.V., Golubev, V.A., Iosilevskiy, I.L., Khrustalev, V.V., Mikhailov, A.L., Mochalov, M.A., Ternovoi, V.Y., Zhernkletov, M.V.: Phase transition in a strongly nonideal deuterium plasma generated by quasi-isentropical compression at megabar pressures. *Phys. Rev. Lett.* **99**, 185001 (2007)
- French, M., Becker, A., Lorenzen, W., Nettelmann, N., Bethkenhagen, M., Wicht, J., Redmer, R.: Ab initio simulations for material properties along the Jupiter adiabat. *Astrophys. J. Suppl. Ser.* **202**, 5 (2012)
- Galanti, E., Kaspi, Y.: Decoupling Jupiter's deep and atmospheric flows using the upcoming Juno gravity measurements and a dynamical inverse model. *Icarus* **286**, 46 (2017)
- Gastine, T., Wicht, J.: Effects of compressibility on driving zonal flow in gas giants. *Icarus* **219**, 428 (2012)
- Gastine, T., Duarte, L., Wicht, J.: Dipolar versus multipolar dynamos: the influence of the background density stratification. *Astron. Astrophys.* **546**, A19 (2012)
- Gastine, T., Wicht, J., Aurnou, J.M.: Zonal flow regimes in rotating anelastic spherical shells: an application to giant planets. *Icarus* **225**, 156 (2013)
- Gastine, T., Heimpel, M., Wicht, J.: Zonal flow scaling in rapidly-rotating compressible convection. *Phys. Earth Planet. Inter.* **232**, 36 (2014a)
- Gastine, T., Wicht, J., Duarte, L.D.V., Heimpel, M., Becker, A.: Explaining Jupiter's magnetic field and equatorial jet dynamics. *Geophys. Res. Lett.* **41**, 5410 (2014b)
- Gastine, T., Yadav, R.K., Morin, J., Reiners, A., Wicht, J.: From solar-like to antisolar differential rotation in cool stars. *Mon. Not. R. Astron. Soc.* **438**, L76 (2014c)
- Gilman, P.A.: Nonlinear dynamics of Boussinesq convection in a deep rotating spherical shell. I. *Geophys. Astrophys. Fluid Dyn.* **8**, 93 (1977)
- Gilman, P.A.: Model calculations concerning rotation at high solar latitudes and the depth of the solar convection zone. *Astrophys. J.* **231**, 284 (1979)
- Gilman, P.A., Foukal, P.V.: Angular velocity gradients in the solar convection zone. *Astrophys. J.* **229**, 1179 (1979)
- Glatzmaier, G.: Numerical simulation of stellar convective dynamos. I. The model and methods. *J. Comput. Phys.* **55**, 461 (1984)
- Glatzmaier, G.A., Gilman, P.A.: Compressible convection in a rotating spherical shell. II. A linear anelastic model. *Astrophys. J. Suppl. Ser.* **45**, 351 (1981)
- Glatzmaier, G.A., Evonuk, M., Rogers, T.M.: Differential rotation in giant planets maintained by density-stratified turbulent convection. *Geophys. Astrophys. Fluid Dyn.* **103**, 31 (2009)
- Gómez-Pérez, N., Heimpel, M., Wicht, J.: Effects of a radially varying electrical conductivity on 3D numerical dynamos. *Phys. Earth Planet. Inter.* **181**, 42 (2010)
- Greenwood, D.A.: The Boltzmann equation in the theory of electrical conduction in metals. *Proc. Phys. Soc.* **71**, 585 (1958)
- Grodent, D., Bonfond, B., GéRard, J.-C., Radioti, A., Gustin, J., Clarke, J.T., Nichols, J., Connerney, J.E.P.: Auroral evidence of a localized magnetic anomaly in Jupiter's northern hemisphere. *J. Geophys. Res.* **113**, A09201 (2008)
- Grote, E., Busse, F.: Hemispherical dynamos generated by convection in rotating spherical shells. *Phys. Rev. E* **62**, 4457 (2000)
- Guillot, T.: The interior of giant planets: models and outstanding questions. *Annu. Rev. Earth Planet. Sci.* **33**, 493 (2005)

- Guillot, T., Gautier, D.: Giant planets. In: Spohn, T., Schubert, G. (eds.) *Treatise on Geophysics*, vol. 10, 2nd edn., p. 529. Elsevier, Amsterdam (2015)
- Haas, P., Tran, F., Blaha, P.: Calculation of the lattice constant of solids with semilocal functionals. *Phys. Rev. B* **79**, 085104 (2009)
- Heimpel, M., Aurnou, J.: Turbulent convection in rapidly rotating spherical shells: a model for equatorial and high latitude jets on Jupiter and Saturn. *Icarus* **187**, 540 (2007)
- Heimpel, M., Gómez Pérez, N.: On the relationship between zonal jets and dynamo action in giant planets. *Geophys. Res. Lett.* **381**, L14201 (2011)
- Heimpel, M., Aurnou, J., Wicht, J.: Simulation of equatorial and high-latitude jets on Jupiter in a deep convection model. *Nature* **438**, 193 (2005)
- Helled, R., Stevenson, D.: The fuzziness of giant planets' cores. *Astrophys. J. Lett.* **L840**, L4 (2017)
- Hess, S.L.G., Bonfond, B., Zarka, P., Grodent, D.: Model of the Jovian magnetic field topology constrained by the Io auroral emissions. *J. Geophys. Res.* **116**, A05217 (2011)
- Hohenberg, P., Kohn, W.: Inhomogeneous electron gas. *Phys. Rev.* **136**, B864 (1964)
- Holst, B., French, M., Redmer, R.: Electronic transport coefficients from ab initio simulations and application to dense liquid hydrogen. *Phys. Rev. B* **83**, 235120 (2011)
- Holst, B., Redmer, R., Gryaznov, V.K., Fortov, V.E., Iosilevskiy, I.L.: Hydrogen and deuterium in shock wave experiments, ab initio simulations and chemical picture modeling. *Eur. Phys. J. D* **66**, 104 (2012)
- Ingersoll, A.P., Pollard, D.: Motion in the interiors and atmospheres of Jupiter and Saturn: scale analysis, anelastic equations, barotropic stability criterion. *Icarus* **52**, 62 (1982)
- Jiang, J., Wang, J.: A non-axisymmetric spherical α^2 -dynamo. *Chin. J. Astron. Astrophys.* **6**, 227 (2006)
- Jones, C.A.: A dynamo model of Jupiter's magnetic field. *Icarus* **241**, 148 (2014)
- Jones, C.A.: Thermal and compositional convection in the outer core. In: Olson, P. (ed.) *Treatise on Geophysics*, 2nd edn., p. 115. Elsevier, Oxford (2015)
- Jones, C.A., Kuzanyan, K.M.: Compressible convection in the deep atmospheres of giant planets. *Icarus* **204**, 227 (2009)
- Jones, C.A., Soward, A.M., Mussa, A.I.: The onset of thermal convection in a rapidly rotating sphere. *J. Fluid Mech.* **405**, 157 (2000)
- Jones, C.A., Rotvig, J., Abdulrahman, A.: Multiple jets and zonal flow on Jupiter. *Geophys. Res. Lett.* **30**, 1731 (2003)
- Jones, C.A., Kuzanyan, K.M., Mitchell, R.H.: Linear theory of compressible convection in rapidly rotating spherical shells, using the anelastic approximation. *J. Fluid Mech.* **634**, 291 (2009)
- Jones, C.A., Boronski, P., Brun, A.S., Glatzmaier, G.A., Gastine, T., Miesch, M.S., Wicht, J.: Anelastic convection-driven dynamo benchmarks. *Icarus* **216**, 120 (2011)
- Juranek, H., Redmer, R., Rosenfeld, Y.: Fluid variational theory for pressure dissociation in dense hydrogen: multicomponent reference system and nonadditivity effects. *J. Chem. Phys.* **117**, 1768 (2002)
- Käpylä, P.J., Mantere, M.J., Guerrero, G., Brandenburg, A., Chatterjee, P.: Reynolds stress and heat flux in spherical shell convection. *Astron. Astrophys.* **531**, A162 (2011)
- Kaspi, Y.: Inferring the depth of the zonal jets on Jupiter and Saturn from odd gravity harmonics. *Geophys. Res. Lett.* **40**, 676 (2013)
- Kaspi, Y., Flierl, G.R., Showman, A.P.: The deep wind structure of the giant planets: results from an anelastic general circulation model. *Icarus* **202**, 525 (2009)
- Kaspi, Y., Hubbard, W.B., Showman, A.P., Flierl, G.R.: Gravitational signature of Jupiter's internal dynamics. *Geophys. Res. Lett.* **37**, L01204 (2010)
- Kaspi, Y., Davighi, J.E., Galanti, E., Hubbard, W.B.: The gravitational signature of internal flows in giant planets: comparing the thermal wind approach with barotropic potential-surface methods. *Icarus* **276**, 170 (2016)
- Kerley, G.I., Christian-Frear, T.L.: Sandia Report No. SAND93-1206. Technical report, Sandia National Laboratories (1993)

- King, E.M., Stellmach, S., Aurnou, J.M.: Heat transfer by rapidly rotating Rayleigh-Bénard convection. *J. Fluid Mech.* **691**, 568 (2012)
- Knudson, M.D., Desjarlais, M.P., Becker, A., Lemke, R.W., Cochrane, K.R., Savage, M.E., Bliss, D.E., Mattsson, T.R., Redmer, R.: Direct observation of an abrupt insulator-to-metal transition in dense liquid deuterium. *Science* **348**, 1455 (2015)
- Kohanoff, J.: Electronic Structure Calculations for Solids and Molecules. Cambridge University Press, Cambridge (2006)
- Kohn, W., Sham, L.J.: Self-consistent equations including exchange and correlation effects. *Phys. Rev.* **140**, A1133 (1965)
- Kong, D., Zhang, K., Schubert, G.: On the variation of zonal gravity coefficients of a giant planet caused by its deep zonal flows. *Astrophys. J.* **748**, 143 (2012)
- Kong, D., Liao, X., Zhang, K., Schubert, G.: Gravitational signature of rotationally distorted Jupiter caused by deep zonal winds. *Icarus* **226**, 1425 (2013)
- Kong, D., Liao, X., Zhang, K., Schubert, G.: Equatorial zonal jets and Jupiter's gravity. *Astrophys. J. Lett.* **791**, L24 (2014)
- Kong, D., Zhang, K., Schubert, G.: Odd gravitational harmonics of Jupiter: effects of spherical versus nonspherical geometry and mathematical smoothing of the equatorially antisymmetric zonal winds across the equatorial plane. *Icarus* **277**, 416 (2016)
- Kong, D., Zhang, K., Schubert, G.: On the gravitational signature of zonal flows in Jupiter-like planets: an analytical solution and its numerical validation. *Phys. Earth Planet. Inter.* **263**, 1 (2017)
- Kubo, R.: Statistical-mechanical theory of irreversible processes. I. General theory and simple applications to magnetic and conduction problems. *J. Phys. Soc. Jpn.* **12**, 570 (1957)
- Lantz, S.R., Fan, Y.: Anelastic magnetohydrodynamic equations for modeling solar and stellar convection zones. *Astrophys. J. Suppl. Ser.* **121**, 247 (1999)
- Lesur, V., Wardinski, I., Rother, M., Mandea, M.: GRIMM: the GFZ Reference Internal Magnetic Model based on vector satellite and observatory data. *Geophys. J. Int.* **173**, 382 (2008)
- Lian, Y., Showman, A.P.: Generation of equatorial jets by large-scale latent heating on the giant planets. *Icarus* **207**, 373 (2010)
- Liu, J., Goldreich, P.M., Stevenson, D.J.: Constraints on deep-seated zonal winds inside Jupiter and Saturn. *Icarus* **196**, 653 (2008)
- Lorenzen, W., Holst, B., Redmer, R.: Demixing of hydrogen and helium at megabar pressures. *Phys. Rev. Lett.* **102**, 115701 (2009)
- Lorenzen, W., Holst, B., Redmer, R.: First-order liquid-liquid phase transition in dense hydrogen. *Phys. Rev. B* **82**, 195107 (2010)
- Lorenzen, W., Holst, B., Redmer, R.: Metallization in hydrogen-helium mixtures. *Phys. Rev. B* **84**, 235109 (2011)
- Lyon, S.P., Johnson, J.D.: Los Alamos Report No. LA-UR-92-3407. Technical report, Los Alamos National Lab (1992)
- Marx, D., Hutter, J.: Ab Initio Molecular Dynamics. Cambridge University Press, Cambridge (2009)
- Matt, S.P., Do Cao, O., Brown, B.P., Brun, A.S.: Convection and differential rotation properties of G and K stars computed with the ASH code. *Astron. Nachr.* **332**, 897 (2011)
- McMahon, J.M., Morales, M.A., Pierleoni, C., Ceperley, D.M.: The properties of hydrogen and helium under extreme conditions. *Rev. Mod. Phys.* **84**, 1607 (2012)
- Mermin, N.D.: Thermal properties of the inhomogeneous electron gas. *Phys. Rev.* **137**, A1441 (1965)
- Miguel, Y., Guillot, T., Fayon, L.: Jupiter internal structure: the effect of different equations of state. *Astron. Astrophys.* **596**, A114 (2016)
- Militzer, B., Hubbard, W.B.: Ab initio equation of state for hydrogen–helium mixtures with recalibration of the giant-planet mass–radius relation. *Astrophys. J.* **774**, 148 (2013)
- Militzer, B., Hubbard, W.B., Vorberger, J., Tamblyn, I., Bonev, S.A.: A massive core in Jupiter predicted from first-principles simulations. *Astrophys. J.* **688**, L45 (2008)

- Morales, M.A., Schwegler, E., Ceperley, D., Pierleoni, C., Hamel, S., Caspersen, K.: Phase separation in hydrogen–helium mixtures at Mbar pressures. *Proc. Natl. Acad. Sci. USA* **106**, 1324 (2009)
- Morales, M.A., Pierleoni, C., Schwegler, E., Ceperley, D.M.: Evidence for a first-order liquid–liquid transition in high-pressure hydrogen from ab initio simulations. *Proc. Natl. Acad. Sci. USA* **107**, 12799 (2010)
- Morales, M.A., Hamel, S., Caspersen, K., Schwegler, E.: Hydrogen–helium demixing from first principles: from diamond anvil cells to planetary interiors. *Phys. Rev. B* **87**, 174105 (2013)
- Moses, E.: The National Ignition Facility: an experimental platform for studying behavior of matter under extreme conditions. *Astrophys. Space Sci.* **336**, 3 (2011)
- Nettelmann, N., Becker, A., Holst, B., Redmer, R.: Jupiter models with improved hydrogen EOS (H-REOS.2). *Astrophys. J.* **750**, 52 (2012)
- Nettelmann, N., Püstow, R., Redmer, R.: Saturn structure and homogeneous evolution models with different EOS. *Icarus* **225**, 548 (2013)
- Perdew, J.P., Burke, K., Ernzerhof, M.: Generalized gradient approximation made simple. *Phys. Rev. Lett.* **77**, 3865 (1996)
- Pierleoni, C., Morales, M.A., Rillo, G., Holzmann, M., Ceperley, D.M.: Liquid–liquid phase transition in hydrogen by coupled electron–ion Monte Carlo simulations. *Proc. Natl. Acad. Sci. USA* **113**, 4953 (2016)
- Porco, C.C., West, R.A., McEwen, A., Del Genio, A.D., Ingersoll, A.P., Thomas, P., Squyres, S., Dones, L., Murray, C.D., Johnson, T.V., Burns, J.A., Brahic, A., Neukum, G., Veverka, J., Barbara, J.M., Denk, T., Evans, M.L., Ferrier, J.J., Geissler, P., Helfenstein, P., Roatsch, T., Throop, H., Tiscareno, M., Vasavada, A.R.: Cassini imaging of Jupiter’s atmosphere, satellites, and rings. *Science* **299**, 1541 (2003)
- Püstow, R., Nettelmann, W., Lorenzen, N., Redmer, R.: H/He demixing and the cooling behavior of Saturn. *Icarus* **267**, 323 (2016)
- Raynaud, R., Petitdemange, L., Dormy, E.: Dipolar dynamos in stratified systems. *Mon. Not. R. Astron. Soc.* **448**, 2055 (2015)
- Read, P.L., Dowling, T.E., Schubert, G.: Saturn’s rotation period from its atmospheric planetary-wave configuration. *Nature* **460**, 608 (2009)
- Rhines, P.B.: Waves and turbulence on a beta-plane. *J. Fluid Mech.* **69**, 417 (1975)
- Ridley, V.A., Holme, R.: Modeling the Jovian magnetic field and its secular variation using all available magnetic field observations. *J. Geophys. Res.* **121**, 309 (2016)
- Rotvig, J., Jones, C.: Multiple jets and bursting in the rapidly rotating convecting two-dimensional annulus model with nearly plane-parallel boundaries. *J. Fluid Mech.* **567**, 117 (2006)
- Rüdiger, G., Elstner, D., Ossendrijver, M.: Do spherical α^2 -dynamos oscillate? *Astron. Astrophys.* **406**, 15 (2003)
- Sasaki, Y., Takehiro, S.-I., Kuramoto, K., Hayashi, Y.-Y.: Weak-field dynamo emerging in a rotating spherical shell with stress-free top and no-slip bottom boundaries. *Phys. Earth Planet. Inter.* **188**, 203 (2011)
- Saumon, D., Guillot, T.: Shock compression of deuterium and the interiors of Jupiter and Saturn. *Astrophys. J.* **609**, 1170 (2004)
- Saumon, D., Chabrier, G., van Horn, H.M.: An equation of state for low-mass stars and giant planets. *Astrophys. J. Suppl. Ser.* **99**, 713 (1995)
- Schrinner, M., Petitdemange, L., Dormy, E.: Dipole collapse and dynamo waves in global direct numerical simulations. *Astrophys. J.* **752**, 121 (2012)
- Schrinner, M., Petitdemange, L., Raynaud, R., Dormy, E.: Topology and field strength in spherical, anelastic dynamo simulations. *Astron. Astrophys.* **564**, A78 (2014)
- Scott, R.K., Polvani, L.M.: Equatorial superrotation in shallow atmospheres. *Geophys. Res. Lett.* **35**, L24202 (2008)
- Showman, A.P., Kaspi, Y., Flierl, G.R.: Scaling laws for convection and jet speeds in the giant planets. *Icarus* **211**, 1258 (2011)
- Simeitev, R., Busse, F.: Patterns of convection in rotating spherical shells. *New J. Phys.* **5**, 97 (2003)

- Simitev, R., Busse, F.: Prandtl-number dependence of convection-driven dynamos in rotating spherical fluid shells. *J. Fluid Mech.* **532**, 365 (2005)
- Simitev, R.D., Busse, F.H.: Bistability and hysteresis of dipolar dynamos generated by turbulent convection in rotating spherical shells. *Europhys. Lett.* **85**, 19001 (2009)
- Soderlund, K.M., Heimpel, M.H., King, E.M., Aurnou, J.M.: Turbulent models of ice giant internal dynamics: dynamos, heat transfer, and zonal flows. *Icarus* **224**, 97 (2013)
- Stanley, S., Bloxham, J.: Convective-region geometry as the cause of Uranus' and Neptune's unusual magnetic fields. *Nature* **428**, 151 (2004)
- Stanley, S., Zuber, M.T., Bloxham, J.: Using reversed magnetic flux spots to determine a planet's inner core size. *Geophys. Res. Lett.* **34**, 19205 (2007)
- Stevenson, D.J.: Reducing the non-axisymmetry of a planetary dynamo and an application to Saturn. *Geophys. Astrophys. Fluid Dyn.* **21**, 113 (1982)
- Stevenson, D., Salpeter, E.: The phase diagram and transport properties for hydrogen-helium fluid planets. *Astrophys. J. Suppl. S.* **35**, 221 (1977a)
- Stevenson, D., Salpeter, E.: The dynamics and helium distribution in hydrogen-helium fluid planets. *Astrophys. J. Suppl. S.* **35**, 221 (1977b)
- Sukoriansky, S., Dikovskaya, N., Galperin, B.: On the arrest of inverse energy cascade and the Rhines scale. *J. Atmos. Sci.* **64**, 3312 (2007)
- Tamblyn, I., Bonev, S.A.: Structure and phase boundaries of compressed liquid hydrogen. *Phys. Rev. Lett.* **104**, 065702 (2010)
- Teed, R.J., Jones, C.A., Hollerbach, R.: On the necessary conditions for bursts of convection within the rapidly rotating cylindrical annulus. *Phys. Fluids* **24**, 066604 (2012)
- Vallis, G.K.: *Atmospheric and Oceanic Fluid Dynamics: Fundamentals and Large-Scale Circulation*. Cambridge University Press, Cambridge (2006)
- Vallis, G.K., Maltrud, M.E.: Generation of mean flows and jets on a beta plane and over topography. *J. Phys. Oceanogr.* **23**, 1346 (1993)
- Vasavada, A.R., Showman, A.P.: Jovian atmospheric dynamics: an update after Galileo and Cassini. *Rep. Prog. Phys.* **68**, 1935 (2005)
- Verhoeven, J., Stellmach, S.: The compressional β -effect: a source of zonal winds in planets? *Icarus* **237**, 143 (2014)
- Weir, S.T., Mitchell, A.C., Nellis, W.J.: Metallization of fluid molecular hydrogen at 140 GPa (1.4 Mbar). *Phys. Rev. Lett.* **76**, 1860 (1996)
- Wicht, J.: Inner-core conductivity in numerical dynamo simulations. *Phys. Earth Planet. Inter.* **132**, 281 (2002)
- Wicht, J., Christensen, U.R.: Torsional oscillations in dynamo simulations. *Geophys. J. Int.* **181**, 1367 (2010)
- Williams, G.P.: Planetary circulations: I. Barotropic representation of Jovian and terrestrial turbulence. *J. Atmos. Sci.* **35**, 1399 (1978)
- Wilson, H.F., Militzer, B.: Sequestration of noble gases in giant planet interiors. *Phys. Rev. Lett.* **104**, 121101 (2010)
- Yadav, R.K., Gastine, T., Christensen, U.R., Duarte, L.D.V.: Consistent scaling laws in anelastic spherical shell dynamos. *Astrophys. J.* **774**, 6 (2013)
- Zhang, K.: Spiralling columnar convection in rapidly rotating spherical fluid shells. *J. Fluid Mech.* **236**, 535 (1992)

Chapter 3

Global Geomagnetic Field Reconstructions from Centuries to Excursions

Monika Korte, Maxwell Brown, Ute Frank, Robin Senftleben,
and Norbert Nowaczyk

Abstract Three projects within the SPP Planetary Magnetism dealt with reconstructing past geomagnetic field morphology and variations based on paleo- and archeomagnetic data in order to better understand global field characteristics and underlying processes. Their aims were as follows: (1) Obtaining a detailed reconstruction of the field for the past ten centuries, particularly focussing on the reliable reconstruction of the dipole moment prior to the invention of direct absolute intensity observations in 1833. The combination of direct historical observations and young archeomagnetic results with very different uncertainty characteristics and global distributions is a challenge. (2) Improving Holocene geomagnetic field models and (3) developing global reconstructions of the Laschamp (~ 41 ka) and Mono Lake (~ 33 ka) magnetic field excursions. High-quality data and a good understanding of data and age uncertainties are the prerequisite for long-term geomagnetic field models. Upgrading the GEOMAGIA50 database for archeomagnetic and volcanic data spanning the past 50 ka years and adding a new part for sediments were important achievements in this regard. The database now offers possibilities to update age-depth models of individual records or reassess multiple core correlations. Additionally, new sediment records were obtained from African and American low latitudes and from lava flows on Fogo, Cape Verde Islands, in order to better constrain the region of the present-day South Atlantic Anomaly. The projects are presented in the context of reviewing recent international progress towards better understanding of the geomagnetic field evolution on centennial to millennial timescales.

M. Korte (✉) • U. Frank • R. Senftleben • N. Nowaczyk
Deutsches GeoForschungsZentrum GFZ, Telegrafenberg, 14473 Potsdam, Germany
e-mail: monika@gfz-potsdam.de; nowa@gfz-potsdam.de

M. Brown
Deutsches GeoForschungsZentrum GFZ, Telegrafenberg, 14473 Potsdam, Germany
Present Address: Institute of Earth Sciences, University of Iceland, Sturlugata 7, 101 Reykjavik, Iceland
e-mail: maxwell@hi.is

3.1 Introduction

The geomagnetic main field, originating in Earth's outer core, shields our habitat against solar wind and radiation from space. Understanding the geodynamo processes that generate the field is not only of scientific interest but may also allow us to estimate the future development of this magnetic shield. At present, the geomagnetic field is anomalously weak in a region around the South Atlantic known as the South Atlantic Anomaly (SAA), and the global dipole moment has decreased by nearly 10% since direct measurements of field intensity became possible in 1832. Discussions on whether these two characteristics might indicate an impending field reversal or excursion are ongoing (Laj and Kissel 2015; Pavon-Carrasco and De Santis 2016). It has been suggested that this weak field anomaly may originate from core flux expulsion linked to unusual core-mantle boundary composition and structure in this region, which is manifested as a large low-shear wave velocity province (LLSVP) in seismic tomography, and a recurrence of this anomaly over millions of years might have acted as a trigger for geomagnetic field reversals (Gubbins 1987; Tarduno et al. 2015).

Global inverse models of the geomagnetic field are powerful tools for studying the spatial and temporal evolution of the field at Earth's surface and core-mantle boundary (CMB). Studying field evolution on timescales of centuries to millennia is essential to detect any recurrent, periodic, or asymmetric field behavior, which gives insights into dynamo processes. Global field reconstructions can also be used in calculations of the shielding effect of the geomagnetic field and the interaction of galactic cosmic rays or the solar wind with our planet's environment. Two recent examples are a new solar activity reconstruction (Usoskin et al. 2014) and a study that uses the dependence on the orientation of the dipole field over the past 10 ka to estimate variations in the location of the auroral oval (Korte and Stolze 2016). Moreover, global field models may be used as dating tools for archeological artifacts, sediments, or volcanics that carry a magnetic signature, some of which cannot be dated by other methods (e.g., Pavón-Carrasco et al. 2011). Studies from diverse areas, such as archeology, climate reconstructions from sediments, or volcanology, can thus benefit from geomagnetic field models. Further applications are described in Brown et al. (2015b). Three projects within the SPP "Planetary Magnetism" dealt with reconstructing past geomagnetic field morphology and variations, with the aim of understanding the global character of the geomagnetic field and its underlying processes. This included obtaining new paleomagnetic data from sediments and volcanics.

The most important ingredients for global inverse models are good spatial and temporal data coverage and an understanding of any data uncertainties. In Sect. 3.2, we describe an upgrade to the GEOMAGIA50 database for archeomagnetic and volcanic data and the new development of an addition for paleomagnetic and chronological data from sediments. We summarize recent work on obtaining new data to better constrain the Southern Hemisphere field and in particular the evolution of the SAA. We also review evidence for the occurrence of geomagnetic high-intensity spikes (Ben-Yosef et al. 2009). We discuss methods to reconstruct or

update previously published paleomagnetic records from sediments, with the aim of incorporating new chronological data and removing methodological differences between studies. Moreover, we discuss the challenges of combining historical and archeomagnetic data in order to better understand the field evolution over the past centuries.

Section 3.3 puts our work in the context of recent developments in millennial scale geomagnetic field modeling with a particular focus on the robustness of models and influences of data distribution and dating uncertainties.

In Sect. 3.4 we report on work in progress to gain a better global understanding of geomagnetic field excursions, in particular the most recent ones, i.e., the Laschamp and Mono Lake excursions.

Two of our projects were still in progress at the time of writing and Sect. 3.5 contains not only a summary and conclusions, but also an outlook based on this ongoing work.

3.2 The GEOMAGIA50 Database, Application Examples, and New Holocene Data

Data are the foundation of inverse modeling. Information about geomagnetic field evolution over the past millennia comes from burnt archeological artifacts, volcanic rocks, and sediments. Two sets of data have notably different characteristics (see, e.g., Constable and Korte 2015):

- *Archeological artifacts and volcanics:* A thermoremanent magnetization (TRM) is acquired on cooling through the Curie temperature of assemblages of magnetic iron oxides within these materials. These assemblages have the potential to preserve the direction and strength of the magnetic field on timescales up to billions of years. A TRM can be acquired by an archeological material during the time of its last firing and cooling (e.g., clay in an oven). The most common source of paleomagnetic data from volcanics are lavas, which acquire their TRM when the source magma cools after extrusion. When the archeological or volcanic materials have been sampled *in situ*, the full vector field can be recovered through laboratory measurements. However, for many archeological artifacts, e.g., potsherds, the orientation during firing is not known and declination and inclination cannot be determined. Furthermore, experiments to estimate the past strength of the field (archeointensity, paleointensity) are challenging with low success rates (Tauxe and Yamazaki 2007; Dunlop 2011). Volcanic and archeological data are discrete and often lack a stratigraphic context. Rarely does a time series from an individual location exist. They are scattered in time and unevenly distributed geographically. Archeomagnetic data are dominantly from Europe or other regional centers, such as Japan (Fig. 3.1). They can be dated by a wide variety of methods, e.g., typology or radiometric methods, resulting in a range of age uncertainties and confidence in their age. Volcanic data are

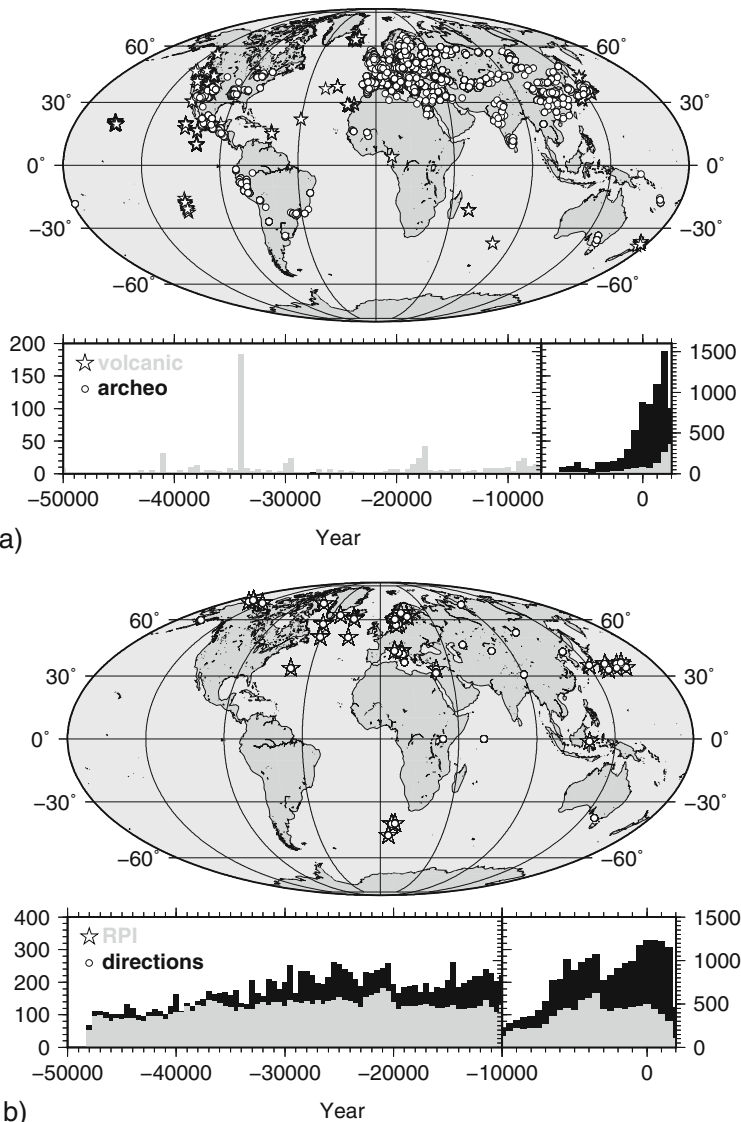


Fig. 3.1 Location and temporal distribution (in 500-year bins) of (a) archeomagnetic (circles and black bars) and volcanic (stars and gray bars) data, and of (b) sediment directional (circles and black bars) and relative paleointensity (stars and gray bars) data currently included in the GEOMAGIA50.v3 database. For sediments, individual core results are counted when available and composite/smoothed results if not. Note the change of scale at 7000 and 10,000 BC in the temporal distribution histograms, respectively, to accommodate the higher number of Holocene data

confined to a limited number of volcanic regions that have been active over the past 50 ka (Fig. 3.1) and their age is commonly estimated through radiometric means, sometimes with large uncertainties. However, new efforts are under way to expand the global coverage of archeological and volcanic data.

- *Sediments:* The remanence acquisition process within sediments is complex and not fully understood (Roberts et al. 2013; Egli and Zhao 2015). However, in general terms a remanent magnetization is acquired through the reorientation of magnetic particles within a sediment suspension by the ambient magnetic field as they fall through the water column, through processes close to the sediment surface and during consolidation of the sediment. Sediments can provide long and quasi-continuous time series; however, the paleomagnetic record is often smoothed by filtering effects during remanence acquisition and laboratory measurement. Sediments from low sedimentation rate environments may strongly average the paleomagnetic field recorded over each unit of depth and this may correspond to a significant amount of time. The amplitude of the variations is reduced and rapid variations are suppressed. The methods used to measure remanence in the laboratory also result in smoothing. Two methods are commonly used: (1) discrete 8 cm³ plastic cubes, which are measured individually, and (2) long tubes of sediments known as U-channels, which are passed through the magnetometer and measured at set intervals. For discrete samples the signal will be averaged over the length of the sample cube and the corresponding time is determined by the sedimentation rate (e.g., 2 cm sample length over a sediment deposited at 50 cm/ka would correspond to a signal averaged over 40 years per sample). Smoothing during U-channel measurement results from nonindependent measurement of remanence at each core depth. As the sediment is continuous, the magnetometer measures a portion of sediment on either side of the central measurement point and this contribution to the remanence signal is governed by the response function of the sensor (Jackson et al. 2010). Unlike fired archeological materials or volcanics, sediments cannot be used to estimate absolute intensity; however, through careful normalization of the natural remanent magnetization for concentration and grain-size variations relative paleointensity (RPI) variations can be estimated (Tauxe and Yamazaki 2007; Roberts et al. 2013).

3.2.1 Version 3 of the GEOMAGIA50 Database

Good global coverage and an understanding of data quality and accuracy of related age information are prerequisites for reliable global geomagnetic field reconstructions. This need was the driving force for the development of the online GEOMAGIA50 database, a global database of paleomagnetic data, chronological data, and metadata from archeological artifacts, volcanics, and sediments spanning the past 50 ka. It began purely as a database of paleointensity data from archeological artifacts and volcanic rocks (Donadini et al. 2006; Korhonen et al. 2008) but was

later expanded to include directional results (Donadini et al. 2009). The database has always contained a large amount of metadata, ranging from the locations and ages of the data to materials, experimental methods, and numbers of samples and specimens used. This detailed information can be used, e.g., for comparing data obtained from different materials or experimental techniques in order to assess the reliability of data (Donadini et al. 2007). All metadata have recently been carefully reviewed and partly revised for version 3 of the database (GEOMAGIA50.v3) (see Brown et al. 2015b, where further details on the history of the database can also be found). The terminology used in the database has been aligned with the MAGIC database (Tauxe et al. 2016) that archives all kinds of paleo- and archeomagnetic results down to experiment level.

The recent addition of paleomagnetic and chronological data from lake and marine sediments to GEOMAGIA50.v3 (Brown et al. 2015a) required a new subsection of the database to be developed to accommodate the greater range and different types of data that are acquired from sediments compared with archeological and volcanic materials. The sediment database contains individual paleomagnetic and rock magnetic results at the specimen or stratigraphic level, averaged or smoothed paleomagnetic results from composite records, detailed age information from radiocarbon and other dating methods, and an option to add reconstructed paleomagnetic data that have, e.g., been updated in terms of creating a new composite record from multiple cores or placed on a new timescale through the creation of a new age-depth model (Brown et al. 2015a) (an example is given in Sect. 3.2.2). As it is common for multiple papers to be written on a sediment core, the sediment database attempts to coherently combine paleomagnetic, rock magnetic, and chronological data appearing in more than one publication.

At the time of writing, GEOMAGIA50.v3 contains 7101 archeomagnetic and 1916 volcanic data entries (of one to three field vector components for a location and time) from 460 published studies. Data from 103 studies on sediments are currently included and further studies will be added (see Brown et al. 2015a), as a large amount of published sediment data is not yet included in the database. Currently, sediment data come from 60 sites. Approximately 32,000 entries have directions and 19,000 entries have RPI from individual cores from 52 sites. Approximately 4700 entries have directions and 1000 entries have RPI from the composite records of 16 sites. Some sites have individual core data and composite records. An overview of the spatial and temporal distributions of the data currently included in GEOMAGIA50.v3 is given in Fig. 3.1.

3.2.2 *Updating Age-Depth Models from Sediment Cores and Reconstructing Sediment Paleomagnetic Time Series*

Published paleomagnetic records from sediments have been used for a variety of scientific aims. Their method of construction may have varied depending on (1)

the goal of the original study and (2) improvements to methods over time. The GEOMAGIA50.v3 database includes information that allows any researcher to update or unify several aspects of earlier analyses of the data.

Two further problems in incorporating sediment data in geomagnetic field models are the inclusion of smoothed and unsmoothed paleomagnetic time series and the range of approaches used to smooth time series. Smoothing is often performed to isolate a stronger signal from a noisy data set, so that broader patterns in directional or RPI variations are easier to discern. However, smoothed data series may remove information useful for modeling (e.g., suppressing amplitude variations) and different approaches will result in differing amounts of smoothing, e.g., if smoothing employed moving averages, discrete means, interpolation at set time steps, or splines. Differences between time series may merely result from the chosen method of smoothing. Furthermore, there is currently a mix of smoothed and unsmoothed data used for modeling, which results in an inconsistent weighting of data in the inversion, e.g., a smoothed record with a data point every 50 years may have been calculated from multiple cores with vastly more data, and this is not accounted for during modeling. It is desirable to use unsmoothed data and apply a consistent approach to its processing within the modeling strategy (e.g., Nilsson et al. 2014). GEOMAGIA50.v3 was designed to accommodate all sediment data at the core level.

Transferring sediment records from a depth scale to a timescale is most commonly done using an age-depth model derived from radiocarbon-dated materials within the sediment; however, numerous sources of uncertainty exist in radiocarbon dating (see the comprehensive review of Björck and Wohlfahrt 2001). Some of them, such as $\delta^{13}\text{C}$ fractionation or reservoir effects, are commonly addressed by corrections, which have been improved and updated over time. GEOMAGIA50.v3 contains all original measured ^{14}C ages and available metadata for a core or a set of cores. This includes data that have been published subsequently to the publication of the paleomagnetic time series. This allows corrections to be applied or updated, e.g., if new measurements or estimates of ^{13}C fractionation or reservoir effects become available. It also allows new ^{14}C ages to be added to a revised age-depth model.

Two more aspects influence the creation of age-depth models. Firstly, as a result of variations in atmospheric radiocarbon through time, experimentally derived radiocarbon ages require calibration. Calibration curves were developed in the 1970s (e.g., Clark 1975) and have been refined numerous times to improve their resolution and accuracy, and their geographic and temporal extent. Separate curves are now available for Northern and Southern Hemispheres and for the oceans (IntCal13, SHCal13, MarineCal13), respectively, (Reimer et al. 2013; Hogg et al. 2013) and extend to 50 ka. Global models of the Holocene geomagnetic field include paleomagnetic time series published in the 1980s, which used inferior radiocarbon calibration curves in their creation. It is therefore desirable to recalibrate radiocarbon ages from older paleomagnetic studies and develop new age-depth models. However, the creation of age-depth models using calibrated radiocarbon ages is nontrivial. Atmospheric radiocarbon does not vary linearly through time and this results in multimodal probability distribution functions for the calibrated ^{14}C ages.

Choosing the most probable age from this distribution is not straightforward. A range of ages may be equally probable and a weighted mean or median may lie in part of the distribution that may not have a high probability.

Secondly, often only a few horizons within a sediment core may have been dated, leaving the majority of horizons without age control. To create a temporally continuous age-depth model both of these issues must be addressed. A variety of methods have been used previously, e.g., using the median ages of the calibrated radiocarbon probability distribution and interpolating (linearly or with a function of another form) through these ages, sometimes without considering the ages' uncertainties. However, in recent years Bayesian age-depth modeling approaches have been developed that consider (1) the multimodal nature of the calibrated ^{14}C age distribution and (2) how to model the age of depths between ^{14}C ages (e.g., Parnell et al. 2008; Bronk Ramsey 2009; Blaauw and Christen 2011).

An important advantage in taking a Bayesian approach is that age uncertainties can be assigned to the final age-depth model. Such age uncertainties could be incorporated in future inversions of paleomagnetic data from sediments and may produce more robust models of the geomagnetic field. For example, in Nilsson et al. (2014) sediment records were iteratively adjusted within a ± 500 year limit to improve their fit to an initial model. The ± 500 year limit could be replaced with variable limits from the uncertainties calculated by a Bayesian age-depth model. Alternatively, the age uncertainties could be used as a basis to weight data within the inversion.

An example of creating an age-depth model with a Bayesian approach and the resulting paleomagnetic time series is shown in Fig. 3.2 for Loch Lomond, Scotland. The original paleomagnetic data and radiocarbon ages were published by Turner and Thompson (1981) and were provided by one of the authors (*pers. comm.* Gillian Turner, University of Wellington). The new age-depth model was made using the *Bacon* Bayesian algorithm of Blaauw and Christen (2011).

To reconstruct this record we started from the raw data on the original depths of the four cores. As sedimentation rates can vary across a lake, it is necessary to correlate like features in the core data (e.g., magnetic, chemical, lithological) to account for sedimentation rate variations and place all cores on a common composite depth scale. For this reconstruction we manually picked new correlation ties using the natural remanent magnetization (NRM) and magnetic susceptibility of the cores and linearly interpolated between core and composite depth to place the paleomagnetic data on the composite depth scale.

Thirteen uncalibrated radiocarbon ages were published by Turner and Thompson (1981); however, we rejected five dates, following the approach of Turner and Thompson (1981) (GU900; GU901; GU902; GU903; GU911), although we retained one originally rejected date (GU906) to demonstrate the ability of the modeling algorithm to cope with outlying data (Fig. 3.2a). We included a new average uncalibrated ^{14}C age for the elm decline in the UK ($5036 \pm 247 (\sigma)$ yr BP (Parker et al. 2002)) published after the study of Turner and Thompson (1981).

Turner and Thompson (1981) used the radiocarbon calibration curve of Clark (1975) to determine calendar ages and created a preferred timescale by combining

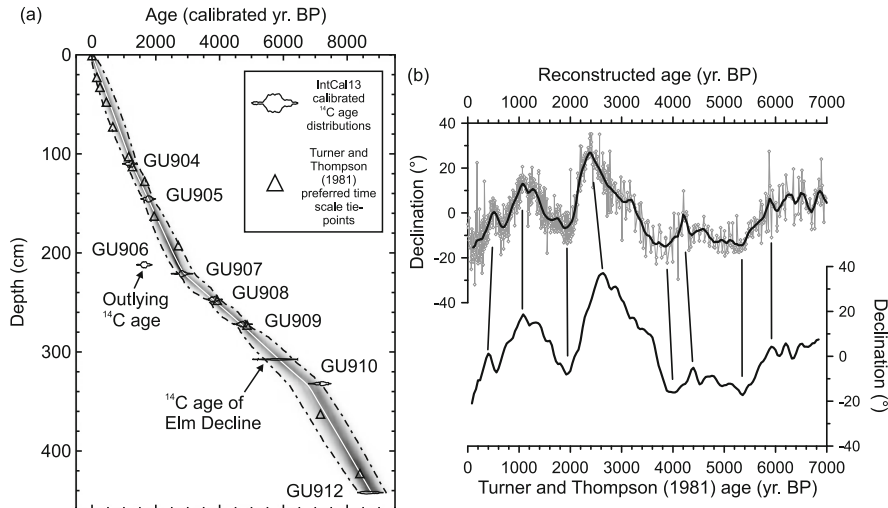


Fig. 3.2 An example of reconstructing a directional record from a series of sediment cores from Loch Lomond, using data originally published by Turner and Thompson (1981). **(a)** Age-depth model created using the Bayesian algorithm of Blaauw and Christen (2011). Grayscale shading is the posterior age-depth model (dark is more probable); the solid white line joins the weighted means of the probability distributions at each depth; the black dot-dashed lines are the 95% limit of the probability distributions; ^{14}C ages are shown as their calibrated distributions using the IntCal13 atmospheric radiocarbon calibration curve of Reimer et al. (2013) and Turner and Thompson (1981) preferred timescale ages are given as triangles. **(b)** A comparison of the average declination record of Turner and Thompson (1981) (lower panel) with the declination record reconstructed using all core data (gray diamonds, upper panel), placed on the weighted mean age-depth model of **(a)**. The black line in the upper panel is a trigonal weighted mean using a 200-year sliding window. Black lines between panels link common features between the original and reconstructed declination records

these dates with the age of directional features determined from observatory, archeomagnetic and other UK sediment records (Windermere, Llyn Geirionydd and Loch Shiel). To retain the temporal independence of the directional features determined from this record, we used only the uncalibrated ^{14}C ages to create an age-depth model. The *Bacon* age-depth model was calculated using ^{14}C ages calibrated against the IntCal13 atmospheric radiocarbon calibration curve of Reimer et al. (2013). The weighted mean of the model iterations was used to transfer the paleomagnetic data on depth to a timescale.

The most notable time differences between the Turner and Thompson (1981) declination record and our reconstructed record are between 2000 and 5000 yr BP with a maximum difference of ~ 300 years (Fig. 3.2b). This results from (1) the different calibration of the ^{14}C ages using the IntCal13 calibration curve compared with the Clark (1975) curve, (2) the addition of a new age for the elm decline, and (3) removal of additional temporal constraints from other UK sediment cores. This example shows that even minor additions of new data, the application of a new

calibration curve, or a reappraisal of which age data to incorporate in an age-depth model can result in a few hundreds of years' difference in the paleomagnetic time series.

3.2.3 *Historical Observations and Young Archeomagnetic Data*

Reconstructions of past changes in geomagnetic dipole moment indicate a maximum about 2–3 kyr ago. However, the reconstructions vary in detail and it is not clear, e.g., for how long the truly uninterrupted, rather strong, decay of the dipole moment existed prior to \sim 1840. In the 400-year field model gufm1 (Jackson et al. 2000), constructed from historical and modern observations, axial dipole strength was linearly extrapolated from 1840 to 1590, owing to the lack of historical intensity observations during this time. However, Gubbins et al. (2006), Finlay (2008), and Sutcliffe et al. (2011), using archeomagnetic and volcanic results from historical times, inferred a range of linear dipole decay rates for this time interval. Their results ranged from no change to similar rates as seen today.

Work in progress aims at deriving a global field model for the interval 1000 AD to 2000 AD, combining all available historical, archeomagnetic, and volcanic data, with a special focus on a robust reconstruction of dipole strength. Work on the CALSxk series of millennial scale geomagnetic field models (see Sect. 3.3), which were forced to agree with gufm1 for recent times, indicated some inconsistencies between archeomagnetic/volcanic data and the historical model. This was also noted by Lodge and Holme (2009), raising the question whether any systematic bias exists in the historical model or the archeomagnetic data. Pavón-Carrasco et al. (2014b) compared archeomagnetic and volcanic directional data from the GEOMAGIA50.v2 database with the gufm1 model and found a general statistical agreement between the data and the model. However, they also found systematically shallow inclinations for volcanic data, an effect also noted earlier in young lavas from Italy (e.g., Lanza et al. 2005) and Hawaii (Castro and Brown 1987).

Directly combining historical and archeomagnetic/volcanic data in one model is not straightforward. This is mainly a result of the much larger amount of historical data and differences in global distributions and accuracy of the two data types. The historical data set contains a large number of declinations (Table 3.1), mostly due to measurements carried out on ships for navigational purposes. Inclination data are available from ship logbooks or land surveys, but with a good coverage only from 1800 AD onwards. The directional historical data, described in detail by

Table 3.1 Numbers of data in the time interval 800–2000 AD

| Data type | Declination | Inclination | Horizontal intensity | Total intensity |
|---------------------|-------------|-------------|----------------------|-----------------|
| Archeomag./volcanic | 1845 | 3053 | – | 1646 |
| Historical | 197,176 | 47,729 | 59,015 | 29,105 |

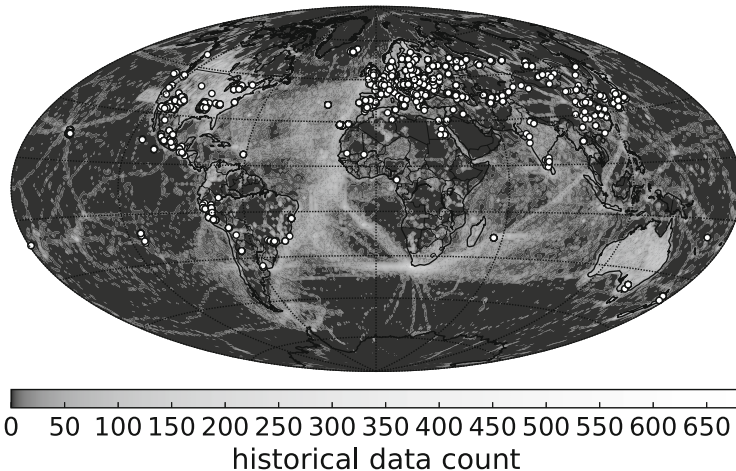


Fig. 3.3 Global historical data count of the last 400 years with overlying locations of archeomagnetic/volcanic data (*circles*). The grayscale is logarithmic and shows the number of data for all magnetic field components binned in 1×1 degree areas

Jonkers et al. (2003), provide a good coverage of the oceans for the last 400 years (Fig. 3.3). Historical absolute intensity data of the magnetic field are only available from 1832 AD onwards with a good continental coverage especially over Australia, North America, Japan, and Europe.

Archeomagnetic and volcanic data in general come from continents and a few islands and are mostly concentrated in the Northern Hemisphere (Fig. 3.3). They only make up about 2% of the combined data set with the historical data (Table 3.1) for the past 1200 years. The modeling method has to be adapted to this imbalance. In order to consider any biases in the archeomagnetic and volcanic data, statistical analyses of the influence of differently weighting subsets of these data based on metadata information from GEOMAGIA50.v3 were performed. A preliminary 1 kyr model was presented by Senftleben et al. (2016).

3.2.4 Southern Hemisphere and the South Atlantic Anomaly Region

Global geomagnetic field modeling has highlighted the scarcity of archeomagnetic and volcanic data from the Southern Hemisphere (see Fig. 3.1) (Korte et al. 2009; Licht et al. 2013). Archeomagnetic and volcanic data should be able to describe the past field evolution with higher temporal resolution than sediments, where the signal is inevitably smoothed. Spherical harmonic (SH) field models built purely from archeomagnetic and volcanic data, however, cannot be at present considered truly global and should not be applied to, e.g., studies of field morphology at the core-mantle boundary, as they lack sufficient information from the Southern Hemisphere (see also Sect. 3.3).

Moreover, the broader region surrounding the present-day SAA (including low northern latitudes around Africa and the Americas) is sparsely covered by archeo- or paleomagnetic data. Such data are of importance in investigating whether the SAA is a unique feature of the present-day field or a recurring structure.

A growing number of studies aim at improving global data coverage of archeomagnetic and volcanic data from southern latitudes and the African region. Recently published data come from, e.g., Argentina (Goguitchaichvili et al. 2015), Brazil (Poletti et al. 2016), West Africa (Mitra et al. 2013; Donadini et al. 2015), Ethiopia (Osepe et al. 2015), and South Africa (Tarduno et al. 2015). Work in progress includes data from SW Pacific Islands (Hill et al. 2014), New Zealand (Kinger et al. 2014; Greve et al. 2014), and Fogo, Cape Verde Islands (Senftleben et al. 2016).

In terms of sediment records, a full vector time series has recently been published from Lake Mavora, New Zealand (Turner et al. 2015). The excellent age control of that record indicates that ages of the only previously published directional record from New Zealand, Lake Pounui (Turner and Lillis 1994), are up to 400 years too old. Modifications to geomagnetic field models due to this update are expected in this region as a result of including the Lake Mavora record. The first full-vector paleomagnetic records from Africa come from Lake Malawi in East Africa (Lund et al. 2016). Work in progress will provide new high-resolution records from lakes Chamo and Chew Bahir in Ethiopia (Brown et al. 2012) and from the Congo Fan (Frank et al. 2016b). A new full-vector sediment record from low latitudes in the Caribbean (Frank et al. 2016a) will also help to constrain the SAA region in future global Holocene field models.

3.2.5 *Geomagnetic High-Intensity Spikes*

Rapidly varying high-intensity values recently found in slag mound data from the Levant (Israel and Jordan) in the tenth and ninth centuries BC by Ben-Yosef et al. (2009) and Shaar et al. (2011) have been termed “geomagnetic spikes.” Unusually high-intensity values for similar ages have subsequently also been found in new archeomagnetic data from Turkey (Ertepinar et al. 2012), Georgia (Shaar et al. 2013), the Canary Islands (de Groot et al. 2015), and as far away as South Korea (Hong et al. 2013) and Texas (Bourne et al. 2016). Shaar et al. (2016) argue for a regional nature of the spike with unknown eastward extent, while the South Korean and Texan data might hint at a global character. More data from regions further from the Levant are necessary to resolve this question. Livermore et al. (2014) investigated whether core-flow models with realistic velocities are capable of generating rapid and extreme intensity changes at Earth’s surface and conclude that they do not seem compatible with our current understanding of the core dynamics and the geodynamo process. Presently available global geomagnetic field models do not produce the geomagnetic spikes. This, however, might be due to lack of temporal and/or spatial resolution in the models or simply to the fact that most of the data showing the spike have not been included in these models yet.

3.3 Global Holocene Field Reconstructions

A recent review by Constable and Korte (2015) offers a comprehensive overview of regional and global Holocene geomagnetic field models and dipole reconstructions published up to 2012. However, several new models have been derived since then. All models so far use essentially the same modeling techniques of SH basis functions in space and cubic B-splines in time as previously used for the historical gufm1 model (Jackson et al. 2000). The method was first adapted to millennial scales and archeo- and paleomagnetic data for the CALSxk (Continuous model of Archeomagnetic and Lake Sediment data of the past x kyrs) model series (Korte and Constable 2003). Recently published models are based on similar starting data sets; in particular, no additions have been made to the sediment compilation used in CALS10k.1b (Korte et al. 2011). The majority of recently published archeomagnetic and volcanic data were included at the time of development of more recent models, but the influence of these data is limited in any model using both data types. Differences between models lie in the SH truncation degree, spline knot point spacing, temporal and spatial regularizations, and, mainly, treatment and selection of data and their uncertainties. Table 3.2 gives an overview over the new models. Most of them are freely available from the Internet under the URLs given in the appendix. The most recent previously published 3 and 10 kyr models from the CALSxk series and their derivates based only on archeomagnetic and volcanic (ARCH10k.1) or only on sediment data (SED3k.1) are included in the table as well as the first models (Panovska 2012; Panovska et al. 2015; Constable et al. 2016).

3.3.1 New Millennial Scale Geomagnetic Field Models

Licht et al. (2013) derived models for the past three millennia based on three datasets: A_FM is based purely on archeomagnetic and volcanic data, ASD_FM additionally uses directional sediment records, and ASDI_FM also uses RPI records. In contrast to other models where the SH basis is expanded to degree and order 10, these models are truncated at degree and order 5 and a modeling error is introduced to account for unmodeled higher degree contributions. Nevertheless, both a spatial and a temporal regularization are applied similarly to the other SH models. Outliers in the data are not discarded but iteratively re-weighted. Licht et al. (2013) used a bootstrap where paleomagnetic values and ages are randomly varied within their error estimates. The method follows Korte et al. (2009), but modified uncertainty estimates were used. In particular, sediments were assigned smaller age uncertainties, which were then used as limits between which the whole records were randomly shifted. The full ensembles of 1000 models were published together with initial and average models for all three data sets (A_FM, ASD_FM and ASDI_FM). This allows the non-diagonal elements of Gauss coefficient covariance matrices to be obtained, in addition to uncertainty estimates on coefficients and on site-dependent field predictions.

Table 3.2 Recently published Holocene geomagnetic field models

| Model | Reference | Time (AD) | Data type | No. of data | Notes |
|-------------|-------------------------------|-----------------|-------------|-------------|--------------|
| ARCH3k.1 | Korte et al. (2009) | -1000 to 1990 | AM | 9605 | |
| SED3k.1 | Korte et al. (2009) | -1000 to 1990 | LS, RPI | 20,375 | |
| CALS3k.4 | Korte and Constable (2011) | -1000 to 1990 | AM, LS, RPI | 35,777 | |
| CALS3k.4b | Korte and Constable (2011) | -1000 to 1990 | AM, LS, RPI | ~35,800 | BA(2000) |
| CALS10k.1b | Korte et al. (2011) | -8000 to 1990 | AM, LS, RPI | ~87,000 | BA(2000) |
| HFM | Panovska (2012) | -8000 to 1990 | AM, LS, RPI | ~85,000 | Four models |
| A_FM | Licht et al. (2013) | -1000 to 2000 | AM | 9660 | BA + 1000 |
| ASD_FM | Licht et al. (2013) | -1000 to 2000 | AM, LS | 29,660 | BA + 1000 |
| ASDL_FM | Licht et al. (2013) | -1000 to 2000 | AM, LS, RPI | 34,020 | BA + 1000 |
| pfm9k.1 | Nilsson et al. (2014) | -7000 to 1900 | AM, LS, RPI | 29,051 | |
| pfm9k.1a | Nilsson et al. (2014) | -7000 to 1900 | AM, LS, RPI | 29,422 | AA |
| pfm9k.1b | Nilsson et al. (2014) | -7000 to 1900 | AM, LS, RPI | 29,207 | BA(2000) |
| SHA,DIF,14k | Pavón-Carrasco et al. (2014a) | -12,000 to 1900 | AM | 12,779 | |
| CALSI10k.* | Panovska et al. (2015) | -8000 to 1990 | AM, LS, RPI | ~82,500 | Three models |
| HFM.* | Panovska et al. (2015) | -8000 to 1990 | AM, LS, RPI | ~85,000 | Three models |
| ARCH10k.1 | Constable et al. (2016) | -8000 to 1990 | AM | 12,504 | |
| CALSI10k.2 | Constable et al. (2016) | -8000 to 1990 | AM, LS, RPI | 77,075 | L1 |
| HFM,OL1.A1 | Constable et al. (2016) | -8000 to 1990 | AM, LS, RPI | 79,722 | L1 |

AM: archeomagnetic and volcanic data; LS: (mainly lacustrine) sediment directional data; RPI: sediment relative intensity; BA(2000): bootstrap average of 2000 individual models; BA + 1000: bootstrap average of 1000 models, all published; AA: age adjustments made to sediment records during modeling; L1: L₁ norm used for outlier rejection instead of L₂ norm; CALSI10k.OL2, CALSI10k.OL2c, CALS10k.OL2w; HFM.*: models CALS10k.OL2, CALS10k.OL2c, HFM.OL1c, HFM.OL2

Nilsson et al. (2014) presented three new models named pfm9k (paleomagnetic field model for 9 kyrs) for the time interval 7000 BC to 1900 AD. Slight changes were made to the sediment data compilation. Reasoning that fast decadal variation cannot be resolved by millennial scale field models that include sediment data, all data were binned in 50-yr bins to give equal weight to each record independent of sedimentation and sampling rate. Consequently, the number of data appears notably reduced in these models (Table 3.2) compared with CALSxk or HFM models of similar duration. Sediment RPI and declinations were initially calibrated by a prior dipole model using a dipole moment estimate based on cosmogenic radionuclides and absolute archeointensity data and a dipole tilt reconstruction based on five selected sediment records (Nilsson et al. 2011). Nilsson et al. (2014) also reassessed all data uncertainties and most data were weighted somewhat differently from the CALSxk or the Licht et al. (2013) models. Model pfm9k.1 is based on this final dataset with iterative outlier rejection. To address sediment age uncertainties, all records were then stretched and compressed randomly between piecewise limits and obeying the stratigraphy, and the best-fit adjustment to the original pfm9k.1 model was found. Model pfm9k.1a is based on a new data set consisting of these age-adjusted sediment cores together with the original archeomagnetic and volcanic data. The third model, pfm9k.1b, is the average of 2000 magnetic error and age bootstrap models. Random piecewise stretching and compressing were also used here, in contrast to the approach of shifting whole sediment records in other bootstrap-averaged SH models. The three pfm9k models suggest a more dominant westward motion of northern high-latitude high-intensity flux patches than seen in previous Holocene models.

Pavón-Carrasco et al. (2014a) derived the longest Holocene model yet (SHA.DIF.14k), a 14 kyr model based only on archeomagnetic and lava flow data. However, the resolution and reliability of this model vary more strongly than in other models in space and time. The Southern Hemisphere field is only weakly constrained as 97% of the total data are from the Northern Hemisphere. Similarly, the global field for ages older than 3 ka is weakly constrained as only 17% of the data are older than 1000 BC and only 3% older than 6000 BC. Uncertainty estimates used for weighting the data are similar to those used in the CALSxk series and outlier rejection is applied by prior statistics and iteratively during modeling.

Panovska et al. (2015) derived and compared six new field models to assess the influence of modeling strategies, such as different starting models for RPI and declination calibration, and approaches to the treatment of outliers and data weighting. Three models are of the CALSxk type, and three of the HFM type. The main difference between these model series is that calibration factors are co-estimated initially and iteratively in the HFM models, while they are determined prior to and between model iterations in the CALSxk series. Five of the models use nearly the same data set as CALS10k.1b, but with improved uncertainty estimates for the sediment records. They take into account sedimentation rates and the level of smoothing according to the method of Panovska et al. (2012). One of the six models uses exactly the same data set as the others but with uncertainty estimates as used previously in CALS10k.1b; that is, the data are given different relative

weights compared to the five other models. Further differences were (1) the use of either a simple axial dipole or a previous model (CALS10k.1b or CALS3k.3) as starting model for RPI and declination calibration, and (2) the use of the L_1 (minimum absolute deviation) instead of the mostly used L_2 (least squares) norm for outlier rejection. The former seems more suitable given the non-Gaussian, long-tailed residual distribution, but the effect on the resulting models was found to be minor. In general, the study of Panovska et al. (2015) showed that Holocene field models are most sensitive to changes in relative weighting of the data and scaling of RPI, and less so to variations in modeling strategy. This confirms that good data coverage, data quality, and an understanding of data uncertainties are the most important ingredients to obtain reliable field reconstructions.

Constable et al. (2016) presented the latest versions of the CALSxk and HFM models, i.e., CALS10k.2 and HFM.OL1.A1. They were obtained considering the results from the comparative study of Panovska et al. (2015), by implementing the improved sediment data weighting scheme by Panovska et al. (2012), and by using starting model from archeomagnetic and volcanic data only (ARCH10k.1) for initial RPI and declination calibration. Constable et al. (2016) used these models to investigate persistent asymmetries in the geomagnetic field. They found that lower secular variation in the Pacific Hemisphere compared with the Atlantic Hemisphere as observed in the modern field extends back for the past 10 kyr. Moreover, on average the field has been stronger in the Northern than the Southern Hemisphere, but with higher variability and stronger secular variation in the Southern Hemisphere.

3.3.2 A Brief Comparison of Models

When the most recently published models are compared it is not surprising that they agree best for times and regions where high numbers of data exist, very generally speaking the Northern Hemisphere and the past 3 kyr. Differences are more significant at times and in areas less well constrained by data, and it is hard to decide which model is most accurate given the currently available data. Convergence or divergence among different models' quantities and predictions seem good indicators of how reliably the field evolution is recovered by the models.

Figures 3.4 and 3.5 compare some global quantities of several of the most recently published models. Models ASD_FM, pfm9k.1, and pfm9k.1b are not included in the comparison. Differences between ASD_FM and ASDI_FM and among the pfm9k family of models, respectively, are in general smaller than differences between the different types of models.

The dipole moment in Fig. 3.4 shows rather good agreement among all models over the past 2 kyr and increasing differences further back in time. Differences in quadrupole and octupole evolution (Fig. 3.4) are larger, but show the same trend. The models including sediment data (all black lines) tend to show less variability than models based on archeomagnetic and volcanic data only (gray lines). This is reasonable given the stronger smoothing in sedimentary records, but also depends

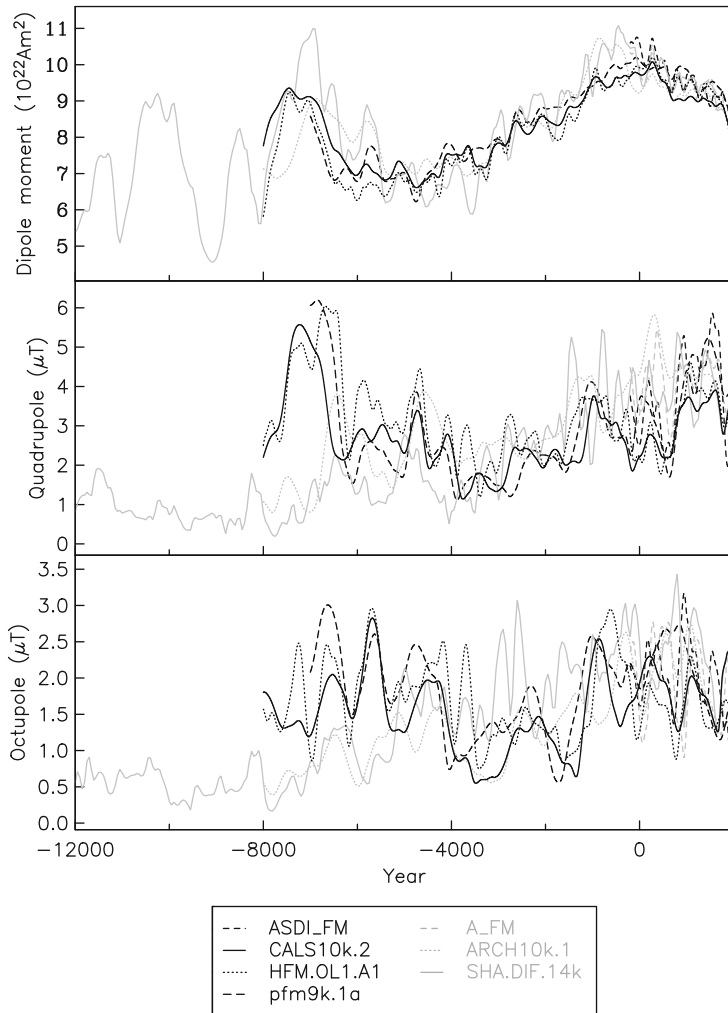


Fig. 3.4 Dipole moment (*top*) and quadrupole (*middle*) and octupole (*bottom*) field contributions for several Holocene geomagnetic field models over their validity time spans. Models based only on archeomagnetic and volcanic data are in gray

on the choice of temporal regularization in the modeling. Given the small amounts of archeomagnetic and volcanic data prior to 1000 BC, some of the variability seen in ARCH10k.1 and SHA.DIF.14k in those times might not be robust. Moreover, the archeomagnetic and volcanic data-only models become more and more dipolar back in time, as seen in the comparison of geomagnetic power spectra for two time intervals in Fig. 3.5. While the spectra of all models are rather similar when averaged over the time interval 1000 BC to 1500 AD, the models including sediment data (black symbols) clearly resolve more spatial structure in earlier epochs, here

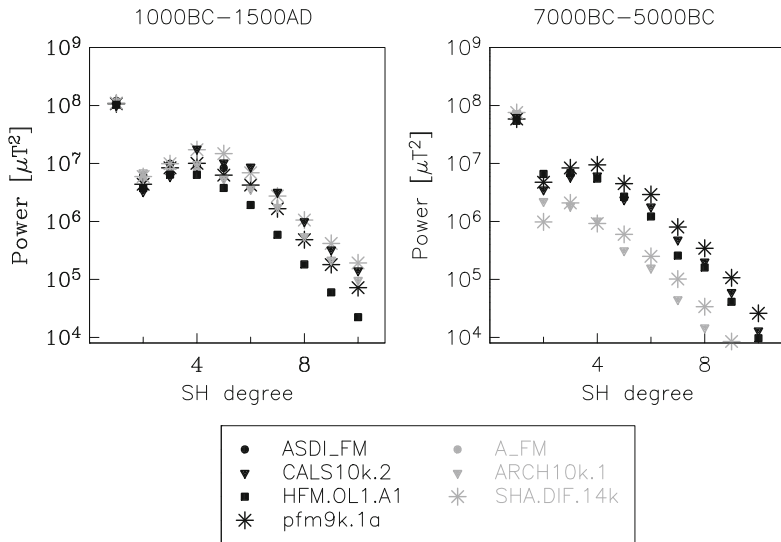


Fig. 3.5 Geomagnetic power spectra at the core-mantle boundary averaged over the time intervals 1000 BC to 1500 AD (*left*) and 7000 BC to 5000 BC (*right*) for several Holocene field models. Models based only on archeomagnetic and volcanic data are in gray

averaged over 7000 BC to 5000 BC. Note that the time interval from 1600 AD to recent times is constrained to agree with the gufm1 model (Jackson et al. 2000) in CALS10k.2 and ARCH10k.1, increasing spatial resolution compared with other Holocene models over that time interval. The stronger drop-off in power with increasing SH degree in HFM.OL1.A1 than in the other models is a consequence of stronger spatial regularization in this model.

Model pfm9k.1a is the only one that attempts to adjust sediment age scales that might be offset or distorted (e.g., Licht et al. 2013) as a result of the intrinsic challenges of dating sediments (e.g., by radiocarbon dating (Björck and Wohlfahrt 2001)). Indeed, the phase of variations in the quantities shown in Fig. 3.4 occasionally seems slightly offset compared with other models that include sediments. However, pfm9k.1a does not always appear to be in better agreement with models using only archeomagnetic and volcanic data.

3.4 A Global View on Geomagnetic Field Excursions

Centennial-to-millennial scale geomagnetic field models have proven useful tools for studying the geomagnetic field and the geodynamo process on timescales longer than covered by modern geomagnetic observatory and satellite observations. However, on even longer periods normal geomagnetic secular variation has frequently been disrupted by extreme changes in the directions and strength of the

field, i.e., reversals and excursions. During reversals, the field changes its polarity and then remains in the opposing polarity for a sustained period of time. During excursions, the field briefly departs from its dipole-dominated configuration, with either transitional or fully reversed directions observed at Earth's surface, and returns to its original polarity. Intervals of stable polarity vary greatly in length (see, e.g., Laj and Channell 2015), and in general the processes behind reversals and excursions are not fully understood (e.g., Roberts 2008; Amit et al. 2011; Laj and Channell 2015; Valet and Fournier 2016). In particular global characteristics of reversals and excursions are hard to constrain as a result of the limited number of available records. The Laschamp excursion, arguably the best documented excursion, is dated at about 41 ka BP and thus falls within the time interval covered by the GEOMAGIA50.v3 database. The same is true for the less well-documented Mono Lake excursion (\sim 33 ka).

3.4.1 Recently Published Data Spanning the Time of the Laschamp Excursion

Several new data records spanning the time of the Laschamp and Mono Lake excursions have been published recently. A new volcanic compilation from the Chaîne de Puys, France, by Laj et al. (2013) contains results from 35 lava flows spanning the interval 75–10 ka and clearly documents the Laschamp excursion in both direction and absolute intensity. It provides an estimate for the duration of the directional excursion of 640 years. A very-high-resolution full-vector record documenting fast directional field changes during the Laschamp excursion (<200 years from normal to reverse and back, respectively) comes from Black Sea sediments (Nowaczyk et al. 2012, 2013). The short duration of less than 500 years for the excursion is confirmed for the western North Atlantic by new data from the Bermuda Rise (Channell et al. 2012a) and the Blake-Bahama Outer Ridge (Bourne et al. 2013). Several new records from further north (50 to 70°N) in the Atlantic (Channell et al. 2012b; Mazaud et al. 2012; Simon et al. 2012), however, do not show a clear and rapid directional excursion signal as observed earlier somewhat further east, i.e., north-west of Iceland (Laj et al. 2000, 2006) and in the Irminger Basin (Channell 2006). The geographic distances among these sites seem too small to explain these differences by variations in regional geomagnetic field morphology. More likely the rather fast geomagnetic signal is not resolved due to sediment properties and/or a lack of temporal resolution due to low sedimentation rates and limits in experimental methods (see Roberts and Winklhofer 2004; Valet et al. 2016). Recent studies that have observed the Laschamp and Mono Lake excursion in the Southern Hemisphere come from Lake Pupuke, New Zealand (Nilsson et al. 2011) and the high southern latitude Scotia Sea (Xiao et al. 2016).

3.4.2 A Simple Simulation of Excursions Based on a New Holocene Field Model

Brown et al. (2007) and Valet and Plenier (2008) used the CALS7K.2 (Korte and Constable 2005) geomagnetic field model for simple global simulations of geomagnetic field reversals or excursions, manipulating the axial dipole component and letting all other field contributions vary unmodified according to the secular variation of the model. For reversals, the axial dipole was linearly scaled with time through zero to reverse strength over the duration of the model (Brown et al. 2007) and over four 1500-year intervals separated by 500 years within the most recent 3 kyr of the model (Valet and Plenier 2008). Valet and Plenier (2008) also simulated excursions by linearly decreasing the axial dipole to zero or reversed it to a range of values up to 20% of its original strength and then increased it back to pre-excursion strength. Comparison of data and characteristics of simple models like this are useful to test, e.g., how complex the surface field might be during even simple scenarios and whether manipulating only the axial dipole might produce geomagnetic field variations similar to those observed in paleomagnetic records of reversals and excursions without smaller scale secular variation playing a significant role. For example, Brown et al. (2007) concluded that non-dipole field could add significant structure to the field at Earth's surface during reversals and excursions and that reversal records could be significantly site dependent, especially in regard to the timing of directional changes. Valet and Plenier (2008) concluded that their simple simulations can account for many characteristics reported in detailed reversal records regarding virtual geomagnetic pole (VGP) trajectories.

Brown and Korte (2016) expanded upon these earlier studies by using the new CALS10k.2 model to explore a range of excursion behavior caused solely by varying the axial dipole. They linearly scaled the axial dipole to decrease and increase by a range of values, reaching between 50% of its original strength and fully reversed strength at the excursion midpoint in the middle of the model time interval. When the axial dipole was decreased, but was not reversed, field directions varied significantly across Earth's surface at the excursion midpoint and the timing of the maximum directional change depended on location (Fig. 3.6a). To produce globally reversed directions the axial dipole needed to be negatively increased by $\sim 20\%$ of its original strength (Fig. 3.6b). The increase in reversed strength resulted in small maxima in the intensity records in many regions at the excursion midpoint. The directional field behavior is more globally uniform when the axial dipole is reversed by greater amounts, with longer lasting reversed directions and an intensity maximum everywhere at the excursion midpoint (Fig. 3.6c). Interestingly, two recent high-resolution records from two different excursions, the Laschamp excursion record of Nowaczyk et al. (2013) and the Iceland Basin excursion record of Channell (2014), hint at a double dip in intensity with a brief maximum coincident with the major directional changes of the excursions. Both these excursion have been identified in directional records from many locations worldwide.

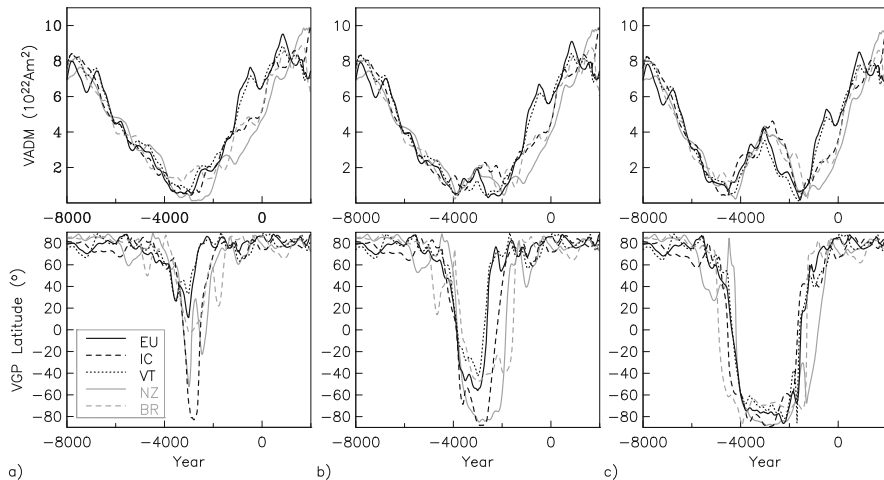


Fig. 3.6 Virtual axial dipole moment (*top*) and virtual geomagnetic pole latitude (*bottom*) for three of the simulations based on CALS10k.2, with the axial dipole linearly scaled to (a) zero, (b) reversed to 20% of its original value, and (c) reversed to 50% of its original value in the middle of the time interval. Time series are shown for five globally dispersed locations similar to those shown by Brown and Korte (2016), i.e., Central Europe (EU), Iceland (IC), Vietnam (VT), New Zealand (NZ), and Brazil (BR)

3.4.3 Spherical Harmonic Models of the Laschamp and Mono Lake Excursions

A handful of SH models have been attempted for different geomagnetic reversals and excursions so far (Mazaud 1995; Shao et al. 1999; Ingham and Turner 2008; Leonhardt and Fabian 2007; Lenci et al. 2008; Leonhardt et al. 2009). However, they use either very low SH truncation degrees and strong prior assumptions or very few data records. The only published model of the Laschamp excursion is the IMOLee model by Leonhardt et al. (2009), which is built from four sediment records from the northern Atlantic, one from the southern Indian Ocean, and a volcanic record from Iceland for the calibration of intensity. With strongly improved data coverage including the new data described above (Sect. 3.4.1) we are working towards a new SH model spanning both the Laschamp and Mono Lake excursions, using up to 30 directional and 36 RPI sediment records (Brown et al. 2016).

3.5 Conclusions and Outlook

In recent years, substantial progress has been made towards a better understanding of global geomagnetic field evolution over past millennia. Most importantly, new high-quality archeo- and paleomagnetic data from archeological artifacts, volcanics,

and sediments have been produced with a particular focus on gaps in global data coverage, e.g., the Southern Hemisphere, and to better characterize the field in regions around the present-day SAA or geomagnetic intensity spikes. Many of the data are now readily available through the GEOMAGIA50.v3 database, enabling easy access not only to regional and global data compilations, but also to a wealth of metadata to assess the reliability of records or to update, e.g., outdated age information. Secondly, a growing number of millennial scale geomagnetic field models are being produced with different modeling strategies and variations in assessment of the reliability of individual data. These models provide estimates of global field characteristics, e.g., dipole moment and dipole tilt over time, as well as descriptions of regional field variations. All models tend to agree relatively well for the past 3 kyr. This indicates a convergence in our understanding of the field characteristics for this time interval due to the improving data coverage, particularly in archeomagnetic data. Open questions regarding, e.g., the history of the SAA prior to 1600 or whether intensity spikes are regional or global features, might be answered by the next generations of models as more and more data are published that will help to constrain these features. The presently available models tend to diverge more further back in time, indicating a persistent need for more data for older periods, in particular including absolute intensity information from archeological and volcanic materials.

The DFG priority program “Planetary Magnetism” contributed notably to this progress. We upgraded the GEOMAGIA50 database and produced several new paleomagnetic sediment records from Ethiopia, off the coast of West Africa, and from the Caribbean, i.e., from areas sparsely covered by data before. Extensive rock magnetic studies confirmed the quality of the new data. Ongoing work on historical lava flows from Fogo, Cape Verde Islands, is expected to give new paleointensity information to help constrain the past history of the SAA. We were involved in producing several new Holocene field models and in particular in studying the robustness of models depending on modeling strategy and data treatment. New findings from our latest field models suggest that secular variation has been persistently higher in the Southern than the Northern Hemisphere, and in the Atlantic compared with the Pacific Hemisphere over the past 10 kyr, with weaker fields in the Southern than the Northern Hemisphere.

Two of our projects were still ongoing at the time of writing. Regarding the recent past and the Holocene, two new models are under construction. A model spanning the last 1000 yrs will provide insights into the detailed evolution of the dipole moment prior to 1840 and give new information about the history of the SAA. A Holocene model including our new Southern Hemisphere and low-latitude sediment data will focus on recurrence of SAA-like structures over the past 10 kyr.

Moreover, we took advantage of data spanning back to 50 ka in GEOMAGIA50.v3 to build SH models that include the times of the Laschamp and Mono Lake excursions. The models are based on a much larger number of sediment records than the only published global model of the Laschamp excursion, and a preferred model version is in its final stages of preparation. By comparing this model to our simple empirical simulation of excursions (Sect. 3.4.2), which we

created based on one of the latest Holocene field models, we will be able to infer the importance of the axial dipole in driving excursion behavior.

Acknowledgements All authors acknowledge funding from Deutsche Forschungsgemeinschaft within the priority program SPP 1488 Planetary Magnetism.

Appendix

This appendix contains lists of URLs where the databases and models that are discussed in the text can be accessed or downloaded. Both databases listed here contain online query forms. All models come with some forward modeling code in Matlab or Fortran to obtain, e.g., field predictions for any location on Earth or spherical harmonic coefficients for any time. Moreover, field predictions from some of the models can be obtained directly from the query form of the GEOMAGIA50.v3 database.

Recent Archeo-, Paleo-, and Rock Magnetic Databases

- GEOMAGIA50.v3: <http://geomagia.gfz-potsdam.de/index.php>
- MagIC: <https://earthref.org/MagIC/>

Archeo- and Paleomagnetic Global Models

- CALS10k.2 and HFM.OL1.A1: <https://earthref.org/ERDA/2207/>
- CALS10k.* and HFM.*: <https://earthref.org/ERDA/2102/>
- All CALSxk and ARCHxk models: <http://www.gfz-potsdam.de/magmodels/calsxk>
- The pfm9k models: <https://earthref.org/ERDA/1951/>
- A_FM, ASD_FM, ASDI_FM: http://geomag.ipgp.fr/download/ARCHEO_FM.zip
- SHA.DIF.14k: <https://earthref.org/ERDA/1897/>

References

- Amit, H., Leonhardt, R., Wicht, J.: Polarity reversals from paleomagnetic observations and numerical dynamo simulations. In: Hulot, G., Balogh, A., Christensen, U.R., Constable, C., Mandea, M. (eds.) *Terrestrial Magnetism*, pp. 293–336. Springer, New York (2011)

- Ben-Yosef, E., Tauxe, L., Levy, T.E., Shaar, R., Ron, H., Najjar, M.: Geomagnetic intensity spike recorded in high resolution slag deposit in Southern Jordan. *Earth Planet. Sci. Lett.* **287**(3), 529–539 (2009)
- Björck, S., Wohlfahrt, B.: ¹⁴C chronostratigraphic techniques in paleolimnology. In: Last, W.M., Smol, J.P. (eds.) *Tracking Environmental Change Using Lake Sediments*, vol. 1, pp. 205–245. Springer, New York (2001)
- Blaauw, M., Christen, J.A.: Flexible paleoclimate age-depth models using an autoregressive gamma process. *Bayesian Anal.* **6**, 457–474 (2011)
- Bourne, M.D., Mac Niocaill, C., Thomas, A.L., Henderson, G.M.: High-resolution record of the Laschamp geomagnetic excursion at the Blake-Bahama Outer Ridge. *Geophys. J. Int.* **195**, 1519–1533 (2013)
- Bourne, M.D., Feinberg, J.M., Stafford, T.W., Waters, M.R., Lundelius, E., Forman, S.L.: High-intensity geomagnetic field ‘spike’ observed at ca. 3000 cal BP in Texas, USA. *Earth Planet. Sci. Lett.* **442**, 80–92 (2016)
- Bronk Ramsey, C.: Bayesian analysis of radiocarbon dates. *Radiocarbon* **51**, 337–360 (2009)
- Brown, M.C., Korte, M.: A simple model for geomagnetic field excursions and inferences for palaeomagnetic observations. *Phys. Earth Planet. Int.* **254**, 1–11 (2016)
- Brown, M.C., Holme, R., Bargery, A.: Exploring the influence of the non-dipole field on magnetic records for field reversals and excursions. *Geophys. J. Int.* **168**, 541–550 (2007)
- Brown, M.C., Frank, U., Foerster, V.E., Gebru, T., Nowaczyk, N., Schaebitz, F., Korte, M.C.: Holocene paleomagnetic field variations recorded in lake sediments from Southern Ethiopia. Abstract GP33B-01 presented at 2012 Fall Meeting, AGU, San Francisco, CA (2012)
- Brown, M., Donadini, F., Nilsson, A., Panovska, S., Frank, U., Korhonen, K., Schubert, M., Korte, M., Constable, C.G.: Geomagia50.v3: 2. a new paleomagnetic database for lake and marine sediments. *Earth Planets Space* **67**, 70 (2015a). doi:10.1186/s40623-015-0233-z
- Brown, M.C., Donadini, F., Korte, M., Nilsson, A., Korhonen, K., Lodge, A., Lengyel, S.N., Constable, C.G.: Geomagia.v3: 1. general structure and modifications to the archeological and volcanic database. *Earth Planets Space* **67**, 83. doi:10.1186/s40623-015-0232-0 (2015b)
- Brown, M.C., Korte, M., Wardinski, I.: The global character of excursions: insights from empirical and dynamo models. *Geophys. Res. Abstr.* **18**, EGU2016-3080-1 (2016)
- Castro, J., Brown, L.: Shallow paleomagnetic directions from historical lava flows, Hawaii. *Geophys. Res. Lett.* **14**, 1203–1206 (1987)
- Channell, J.E.T.: Late Brunhes polarity excursions (Mono Lake, Laschamp, Iceland Basin and Pringle Falls) recorded at ODP Site 911 (Irminger Basin). *Earth Planet. Sci. Lett.* **171**, 489–502 (2006)
- Channell, J.E.T.: The Iceland Basin excursion: age, duration, and excursion field geometry. *Geochim. Geophys. Geosys.* **15**, 4920–4935 (2014)
- Channell, J.E.T., Hodell, D.A., Curtis, J.H.: ODP site 1063 (Bermuda Rise) revisited: oxygen isotopes, excursions and paleointensity in the Brunhes chron. *Geochim. Geophys. Geosys.* **13**, Q02001 (2012a). doi:10.1029/2011GC003897
- Channell, J.E.T., Hodell, D.A., Romero, O., Hillaire-Marcel, C., de Vernal, A., Stoner, J.S., Mazaud, A., Röhl, U.: 750-kyr detrital-layer stratigraphy for the North Atlantic (IODP sites U1302-U1303, Orphan Knoll, Labrador Sea). *Earth Planet. Sci. Lett.* **317–318**, 218–230 (2012b)
- Clark, R.M.: A calibration curve for radiocarbon dates. *Antiquity* **49**, 251–266 (1975)
- Constable, C., Korte, M.: Centennial- to millennial-scale geomagnetic field variations. In: Schubert, G. (ed.) *Treatise on Geophysics*, vol. 5, pp. 309–341. Elsevier, Amsterdam (2015)
- Constable, C., Korte, M., Panovska, S.: Persistent high paleosecular variation activity in southern hemisphere for at least 10 000 years. *Earth Planet. Sci. Lett.* **453**, 78–86 (2016)
- de Groot, L.V., Béguin, A., Kosters, M.E., van Rijsingen, E.M., Struijk, E.L.M., Biggin, A.J., Hurst, E.A., Langereis, C.G., Dekkers, M.J.: High paleointensities for the Canary Islands constrain the Levant geomagnetic high. *Earth Planet. Sci. Lett.* **419**, 154–167 (2015)
- Donadini, F., Korhonen, K., Riisager, P., Pesonen, L.J.: Database for Holocene geomagnetic intensity information. *EOS Trans. Am. Geophys. Soc.* **87**(14), 92–93 (2006)

- Donadini, F., Riisager, P., Korhonen, K., Kahma, K., Pesonen, L.J., Snowball, I.: Holocene geomagnetic paleointensities: A blind test of absolute paleointensity techniques and materials. *Phys. Earth Planet. Inter.* **161**, 19–35 (2007)
- Donadini, F., Korte, M., Constable, C.: Geomagnetic field for 0–3 ka: 1. new data sets for global modeling. *Geochem. Geophys. Geosys.* **10**, Q06007 (2009). doi:10.1029/2008GC002295
- Donadini, F., Serneels, V., Kapper, L., El Kateb, A.: Directional changes of the geomagnetic field in West Africa: insights from the metallurgical site of Korsimoro. *Earth Planet. Sci. Lett.* **430**, 349–355 (2015)
- Dunlop, D.J.: Physical basis of the Thellier-Thellier and related paleointensity methods. *Phys. Earth. Planet. Inter.* **187**, 118–138 (2011)
- Egli, R., Zhao, X.: Natural remanent magnetization acquisition in bioturbated sediment: general theory and implications for relative paleointensity reconstructions. *Geochem. Geophys. Geosys.* **16**, 995–1016 (2015)
- Ertepınar, P., Langereis, C.G., Biggin, A.J., Frangipane, M., Matney, T., Ökse, T., Engin, A.: Archaeomagnetic study of five mounds from Upper Mesopotamia between 2500 and 700 BCE: further evidence for an extremely strong geomagnetic field ca. 3000 years ago. *Earth Planet. Sci. Lett.* **357**, 84–98 (2012)
- Finlay, C.C.: Historical variations of the geomagnetic axial dipole. *Phys. Earth Planet. Inter.* **170**, 1–14 (2008)
- Frank, U., Nowaczyk, N.R., Frederichs, T., Korte, M.: Paleo- and rock magnetic investigations on Late Quaternary sediments from low latitudes I: the record from the Tobago Basin, Southern Caribbean. *Geophys. J. Int.* **208**, 1740–1755 (2017)
- Frank, U., Nowaczyk, N.R., Frederichs, T., Korte, M.: Paleo- and rock magnetic investigations on Late Quaternary sediments from low latitudes II: magnetic mineralogy and paleomagnetic secular variation records from the Congo deep-sea fan (in preparation)
- Goguitchaichvili, A., Morales, J., Schavelzon, D., Vásquez, C., Gogorza, C.S.G., Loponte, D., A. Rapalini, A.: Variation of the Earth's magnetic field strength in South America during the last two millennia: new results from historical buildings of Buenos Aires and re-evaluation of regional data. *Phys. Earth Planet. Int.* **245**, 15–25 (2015)
- Greve, A., Turner, G.M., Hodgson, E., Nilsson, A., Hill, M.J.: Palaeomagnetic secular variation from Holocene lava flows of the Taupo Volcanic Zone (TVZ0), New Zealand. Abstract GP53A-3759 presented at 2014 Fall Meeting, AGU, San Francisco, CA, 15–19 December (2014)
- Gubbins, D.: Mechanism for geomagnetic polarity reversals. *Nature* **326**, 167–169 (1987)
- Gubbins, D., Jones, A.L., Finlay, C.C.: Fall in Earth's magnetic field is erratic. *Science* **312**, 900–902 (2006)
- Hill, M.J., Nilsson, A., Holme, R.T., Thomas, M.L., Hurst, E., Turner, G.M., Sheppard, P.: New archeointensity data from the SW Pacific: towards better constrained global geomagnetic field models. Abstract GP51C-06 presented at 2014 Fall Meeting, AGU, San Francisco, CA, 15–19 December (2014)
- Hogg, A.G., Hua, Q., Blackwell, P.G., Niu, M., Buck, C.E., Guilderson, T.P., Heaton, T.J., Palmer, J.G., Reimer, P.J., Reimer, R.W., Turney, C.S.M., Zimmerman, S.R.H.: SHCal13 Southern Hemisphere calibration, 0–50,000 years cal BP. *Radiocarbon* **55**, 1–15 (2013)
- Hong, H., Yu, Y., Lee, C.H., Kim, R.H., Park, J., Doh, S.J., Kim, W., Sung, H.: Globally strong geomagnetic field intensity circa 3000 years ago. *Earth Planet. Sci. Lett.* **383**, 142–152 (2013)
- Ingham, M., Turner, G.: Behaviour of the geomagnetic field during the Matuyama-Brunhes polarity transition. *Phys. Earth Planet. Int.* **168**, 163–178 (2008)
- Jackson, A., Jonkers, A.R.T., Walker, M.R.: Four centuries of geomagnetic secular variation from historical records. *Phil. Trans. R. Soc. Lond. A* **358**, 957–990 (2000)
- Jackson, M., Bowles, J., Lascau, I., Solheid, P.: Deconvolution of u channel magnetometer data: experimental study of accuracy, resolution and stability of different inversion methods. *Geochem. Geophys. Geosys.* **11**, Q07Y10 (2010). doi:10.1029/2009GC002991
- Jonkers, A.R.T., Jackson, A., Murray, A.: Four centuries of geomagnetic data from historical records. *Rev. Geophys.* **41**, 957–990 (2003)

- Kinger, R., Turner, G.M., McFadgen, B.: Archaeomagnetic studies of Maori hangi stones from New Zealand. Abstract GP53A-3756 presented at 2014 Fall Meeting, AGU, San Francisco, CA, 15–19 December (2014)
- Korhonen, K., Donadini, F., Riisager, P., (2008), L.P.: Geomagia50: an archeointensity database with PHP and MySQL. *Geochem., Geophys., Geosys.* **9**, Q04029 (2008). doi:10.1029/2007GC001893
- Korte, M., Constable, C.G.: Continuous global geomagnetic field models for the past 3000 years. *Phys. Earth Planet. Interiors* **140**, 73–89 (2003)
- Korte, M., Constable, C.G.: Continuous geomagnetic field models for the past 7 millennia: 2. CALS7K. *Geochem. Geophys. Geosys.* **6**, Q02H16 (2005). doi:10.1029/2004GC000801
- Korte, M., Constable, C.: Improving geomagnetic field reconstructions for 0–3 ka. *Phys. Earth Planet. Int.* **188**, 247–259 (2011)
- Korte, M., Stolze, S.: Variations in mid-latitude auroral activity during the Holocene. *Archaeometry* **58**, 159–176 (2016)
- Korte, M., Donadini, F., Constable, C.: Geomagnetic field for 0–3 ka: 2. A new series of time-varying global models. *Geochem. Geophys. Geosys.* **10**, Q06008 (2009). doi:10.1029/2008GC002297
- Korte, M., Constable, C., Donadini, F., Holme, R.: Reconstructing the Holocene geomagnetic field. *Earth Planet. Sci. Lett.* **312**, 497–505 (2011)
- Laj, C., Channell, J.E.T.: Geomagnetic excursions. In: Schubert, G. (ed.) *Treatise on Geophysics*, 2nd edn., vol. 5, pp. 343–363. Elsevier, Amsterdam (2015)
- Laj, C., Kissel, C.: An impending geomagnetic transition? Hints from the past. *Front. Earth Sci.* **3**(61) (2015). doi:10.3389/feart.2015.00061
- Laj, C., Kissel, C., Mazaud, A., Channell, J.E.T., Beer, J.: North Atlantic palaeointensity stack since 75 ka (NAPIS-75) and the duration of the Laschamp event. *Phi. Trans. R. Soc. Lond. A* **358**, 1009–1025 (2000)
- Laj, C., Kissel, C., Roberts, A.P.: Geomagnetic field behaviour during the Iceland Basin and Laschamp geomagnetic excursions: a simple transitional field geometry? *Geochem. Geophys. Geosys.* **7**, Q03004 (2006). doi:10.1029/2005GC001122
- Laj, C., Guillou, H., Kissel, C.: Dynamics of the Earth magnetic field in the 10–75 kyr period comprising the Laschamp and Mono Lake excursions: new results from the French Caïne des Puys in a global perspective. *Earth Planet. Sci. Lett.* **387**, 184–197 (2013)
- Lanci, L., Kissel, C., Leonhardt, R., Laj, C.: Morphology of the Iceland Basin Excursion from a spherical harmonic analysis and an iterative Bayesian inversion procedure of sedimentary records. *Phys. Earth Planet. Int.* **169**, 131–139 (2008)
- Lanza, R., Meloni, A., Tema, E.: Historical measurements of the Earth's magnetic field compared with remanence directions from lava flows in Italy over the last four centuries. *Phys. Earth Planet. Int.* **148**, 97–107 (2005)
- Leonhardt, R., Fabian, K.: Paleomagnetic reconstruction of the global geomagnetic field evolution during the Matuyama–Brunhes transition: iterative Bayesian inversion and independent verification. *Earth Planet. Sci. Lett.* **253**, 172–195 (2007)
- Leonhardt, R., Fabian, K., Winklhofer, M., Ferk, A., Laj, C., Kissel, C.: Geomagnetic field evolution during the Laschamp excursion. *Earth Planet. Sci. Lett.* **278**, 87–95 (2009)
- Licht, A., Hulot, G., Gallet, Y., Thébault, E.: Ensembles of low degree archeomagnetic field models for the past three millennia. *Phys. Earth Planet. Int.* **224**, 38–67 (2013)
- Livermore, P.W., Fournier, A., Gallet, Y.: Core-flow constraints on extreme archeomagnetic intensity changes. *Earth Planet. Sci. Lett.* **387**, 145–156 (2014)
- Lodge, A., Holme, R.: Towards a new approach to archaeomagnetic dating in Europe using geomagnetic field modelling. *Archaeometry* **50**(3), 309–322 (2009)
- Lund, S., Platzman, E., Johnson, T.: Full-vector paleomagnetic secular variation records from latest Quaternary sediments of Lake Malawi (10°S, 34.3°E). *Quat. Sci. Rev.* **144**, 16–27 (2016)
- Mazaud, A.: An attempt at reconstructing the geomagnetic field at the core-mantle boundary during the upper Olduvai polarity transition. *Phys. Earth Planet. Int.* **90**, 211–219 (1995)

- Mazaud, A., Channell, J.E.T., Stoner, J.S.: Relative paleointensity and environmental magnetism since 1.2 ma at IODP site U1305 (Eirik Drift, NW Atlantic). *Earth Planet. Sci. Lett.* **357–358**, 137–144 (2012)
- Mitra, R., Tauxe, L., McIntosh, S.K.: Two thousand years of archeointensity from West Africa. *Earth Planet. Sci. Lett.* **364**, 123–133 (2013)
- Nilsson, A., Muscheler, R., Snowball, I.: Millennial scale cyclicity in the geodynamo inferred from a dipole tilt reconstruction. *Earth Planet. Sci. Lett.* **311**, 299–205 (2011)
- Nilsson, A., Holme, R., Korte, M., Sutcliffe, N., Hill, M.: Reconstructing Holocene geomagnetic field variations: new methods, models and implications. *Geophys. J. Int.* **198**, 229–248 (2014)
- Nowaczyk, N.R., Arz, H.W., Frank, U., Kind, J., Plessen, B.: Dynamics of the Laschamp geomagnetic excursion from Black Sea sediments. *Earth Planet. Sci. Lett.* **351–352**, 54–69 (2012)
- Nowaczyk, N.R., Frank, U., Kind, J., Arz, H.: A high-resolution paleointensity stack of the past 13 to 68 ka from Black Sea sediments. *Earth Planet. Sci. Lett.* **384**, 1–16 (2013)
- Oseote, M.L., Catanzariti, G., Chauvin, A., Pavón-Carrasco, F.J., Roperch, P., Fernández, V.M.: First archaeomagnetic field intensity data from Ethiopia, Africa (1615 ± 12 ad). *Phys. Earth Planet. Int.* **242**, 24–35 (2015)
- Panovska, S.: Modelling Holocene geomagnetic field evolution. Ph.D. thesis, ETH Zürich (2012)
- Panovska, S., Finlay, C.C., Donadini, F., Hirt, A.M.: Spline analysis of Holocene sediment magnetic records: uncertainty estimates for field modeling. *J. Geophys. Res.* **117**, B02101 (2012). doi:10.1029/2011JB008813
- Panovska, S., Korte, M., Finlay, C.C., Constable, C.G.: Limitations in paleomagnetic data and modelling techniques and their impact on Holocene geomagnetic field models. *Geophys. J. Int.* **202**, 402–418 (2015)
- Parker, A.G., Goudie, A.S., Anderson, D.E., Robinson, M.A., Bonsall, C.: A review of the mid-Holocene elm decline in the British Isles. *Prog. Phys. Geog.* **26**, 1–45 (2002)
- Parnell, A., Haslett, J., Allen, J., Buck, C., Huntley, B.: A flexible approach to assessing synchronicity of past events using Bayesian reconstruction of sedimentation history. *Quat. Sci. Rev.* **27**, 1827–1885 (2008)
- Pavón-Carrasco, J.F., DeSantis, A.: The South Atlantic Anomaly: the key for a possible geomagnetic reversal. *Front. Earth Sci.* **4**(40) (2016). doi:10.3389/feart.2016.00040
- Pavón-Carrasco, F.J., González, J.R., Oseote, M.L., Torta, J.M.: A Matlab tool for archaeomagnetic dating. *J. Archaeol. Sci.* **38**, 408–419 (2011)
- Pavón-Carrasco, F.J., Oseote, M.L., Torta, J.M., De Santis, A.: A geomagnetic field model for the Holocene based on archeomagnetic and lava flow data. *Earth Planet. Sci. Lett.* **388**, 98–109 (2014a)
- Pavón-Carrasco, F.J., Tema, E., Oseote, M.L., Lanza, R.: Statistical analysis of palaeomagnetic data from the last four centuries: evidence of systematic inclination shallowing in lava flow records. *Pure Appl. Geophys.* **173**, 839–848 (2014b)
- Poletti, W., Trindade, R.I.F., Hartmann, G.A., Damiani, N., Rech, R.M.: Archeomagnetism of Jesuit missions in South Brazil (1657–1706 AD) and assessment of the South American database. *Earth Planet. Sci. Lett.* **445**, 36–47 (2016)
- Reimer, P.J., Bard, E., Bayliss, A., Beck, J.W., Blackwell, P.G., Bronk Ramsey, C., Buck, C.E., Cheng, H., ad M. Friedrich, R.L.E., Grootes, P.M., Guilderson, T.P., Haflidason, H., an C. Hatté, I.H., Heaton, T.J., Hoffmann, D.L., Hogg, A.G., Hughen, K.A., Kaiser, K.F., Kromer, B., Manning, S.W., Niu, M., Reimer, R.W., Richards, D.A., Scott, E.M., Southon, J.R., Staff, R.A., Turney, C.S.M., van der Plicht, J.: IntCal13 and Marine13 radiocarbon age calibration age curves 0–50,000 years cal BP. *Radiocarbon* **55**, 1869–1887 (2013)
- Roberts, A.: Geomagnetic excursions: knowns and unknowns. *Geophys. Res. Lett.* **35**, L17307 (2008). doi:10.1029/2008GL034719
- Roberts, A.P., Winklhofer, M.: Why are geomagnetic excursions not always recorded in sediments? Constraints from post-depositional remanent magnetization lock-in modelling. *Earth Planet. Sci. Lett.* **227**(3), 345–359 (2004)

- Roberts, A.P., Tauxe, L., Heslop, D.: Magnetic paleointensity stratigraphy and high-resolution Quaternary geochronology: successes and future challenges. *Quat. Sci. Rev.* **61**, 1–16 (2013)
- Senftleben, R., Korte, M., Finlay, C.: Global magnetic field modelling with archeomagnetic and historical data. *Geophys. Res. Abstr.* **18**, EGU2016-13059 (2016)
- Shaar, R., Ben-Yosef, E., Ron, H., Tauxe, L., Agnon, A., Kessel, R.: Geomagnetic field intensity: how high can it get? How fast can it change? Constraints from Iron age copper slag. *Earth Planet. Sci. Lett.* **301**(1), 297–306 (2011)
- Shaar, R., Tauxe, L., Gogichaishvili, A., Rathert, M.C., Devidze, M., Licheli, V.: Absolute geomagnetic field intensity in Georgia during the past 6 millennia. *Latinmag Lett.* **3**, 1–4 (2013)
- Shaar, R., Tauxe, L., Ron, H., Ebert, Y., Zuckerman, S., Finkelstein, I., Agnon, A.: Large geomagnetic field anomalies revealed in Bronze to Iron Age archeomagnetic data from Tel Megiddo and Tel Hazor, Israel. *Earth Planet. Sci. Lett.* **442**, 173–185 (2016)
- Shao, J.C., Fuller, M., Tanimoto, T., Dunn, J.R., Stone, D.B.: Spherical harmonic analyses of paleomagnetic data: The time-averaged geomagnetic field for the past 5 Myr and the Brunhes/Matuyama reversal. *J. Geophys. Res.* **104**, 5015–5030 (1999)
- Simon, Q., St-Onge, G., Hillaire-Marcel, C.: Late Quaternary chronostratigraphic framework of deep Baffin Bay glaciomarine sediments from high-resolution paleomagnetic data. *Geochem. Geophys. Geosyst.* **13**, Q0AO03 (2012). doi:10.1029/2012GC004272
- Sutte, N., Holme, R., Hill, M.J., Shaw, J.: Consistent treatment of errors in archaeointensity implies rapid decay of the dipole. *Earth Planet. Sci. Lett.* **304**, 13–21 (2011)
- Tarduno, J.A., Watkeys, M.K., Huffman, T.N., Cottrell, R.D., Blackman, E.G., Wendt, A., Scribner, C.A., Wagner, C.L.: Antiquity of the South Atlantic Anomaly and evidence for top-down control on the geodynamo. *Nat. Commun.* **6** (2015). doi:10.1038/ncomms8865
- Tauxe, L., Yamazaki, T.: Paleointensities. In: Kono, M. (ed.) *Treatise on Geophysics*, vol. 5. Elsevier, Amsterdam (2007)
- Tauxe, L., Shaar, R., Jonestrask, L., Swanson-Hysell, N.L., Minnett, R., Koppers, A.A.P., Constable, C.G., Jarboe, N., Gaastra, K., Fairchild, L.: PmagPy: Software package for paleomagnetic data analysis and a bridge to the MagNETics Information Consortium (MagIC) database. *Geochem. Geophys. Geosyst.* **17**, 2450–2463 (2016)
- Turner, G.M., Lillis, D.A.: A palaeomagnetic secular variation record for New Zealand during the past 2500 years. *Phys. Earth Planet. Inter.* **83**, 265–282 (1994)
- Turner, G.M., Thompson, R.: Lake sediment record of the geomagnetic secular variation in Britain during Holocene times. *Geophys. J. R. Astron. Soc.* **65**, 703–725 (1981)
- Turner, G.M., Howarth, J.D., de Gelder, G.I.N.O., Fitzsimons, S.J.: A new high-resolution record of Holocene geomagnetic secular variation from New Zealand. *Earth Planet. Sci. Lett.* **430**, 296–307 (2015)
- Usoskin, I., Hulot, G., Gallet, Y., Roth, R., Licht, A., Joos, F., Kovaltsov, G.A., Thébault, E., Khokhlov, A.: Evidence for distinct modes of solar activity. *Astron. Astrophys.* **562**, L10 (2014). doi:10.1051/0004-6361/201423391
- Valet, J.P., Fournier, A.: Deciphering records of geomagnetic reversals. *Rev. Geophys.* **54** (2016). doi:10.1002/2015RG000506
- Valet, J.P., Plenier, G.: Simulations of a time-varying non-dipole field during geomagnetic reversals and excursions. *Phys. Earth Planet. Int.* **169**, 178–193 (2008)
- Valet, J.P., Meynadier, L., Simon, Q., Thouveny, N.: When and why sediments fail to record the geomagnetic field during polarity reversals. *Earth Planet. Sci. Lett.* **453**, 96–107 (2016)
- Xiao, W., Frederichs, T., Gersonde, R., Kuhn, G., Esper, O., Zhang, X.: Constraining the dating of late Quaternary marine sediment records from the Scotia Sea (Southern Ocean). *Quat. Geochron.* **31**, 97–118 (2016)

Chapter 4

Interannual Fluctuations of the Core Angular Momentum Inferred from Geomagnetic Field Models

Seiki Asari and Ingo Wardinski

Abstract Recent models of Earth’s core magnetic field based on geomagnetic satellite data suggest an existence of interannual core dynamics. The related magnetic signal of the interannual core dynamics is found to be small, which makes an observational detection of interannual variations of the core flow and the associated oscillations of the core angular momentum (CAM) difficult. However, it has been shown that the phase of the interannual oscillation is robustly determined, according to numerous CAM computations from diverse core flow models that are all estimated as a result of inverting a single geomagnetic model C³FM2. Here, we show that the phase identification depends on the secular acceleration (SA) of a geomagnetic model. Estimates of the phase still vary with geomagnetic models, C3FM2, gufm1, and COV-OBS, for the pre-satellite era, whose differences are readily recognisable in their SA representations. None of them may be an optimal model for describing the SA. Compared with the SA of a satellite model GRIMM3, C³FM2 is overdamped in time, but it may be improved for resolving the interannual CAM oscillations by properly modifying its temporal smoothness in reference to the SA of satellite models.

4.1 Introduction

Recent satellite geomagnetic field models provide an increasing precision for describing the core field, the magnetic field component arising as a consequence of the dynamo action in Earth’s fluid outer core. These models include the GRIMM series (Lesur et al 2010) based on data from the CHAMP satellite (Reigber et al

S. Asari (✉)

Institute for Mathematics, University of Potsdam, Karl-Liebknecht-Strasse 24-25, D14476
Potsdam Golm, Germany
e-mail: asari@gfz-potsdam.de

I. Wardinski

Laboratory of Planetology and Geodynamics, University of Nantes, Nantes, France
e-mail: ingo.wardinski@univ-nantes.fr

2002) and the CHAOS series (Finlay et al 2016) based additionally on those from other satellites, Ørsted (Neubert et al 2001), SAC-C, and Swarm (Friis-Christensen et al 2006). The latest version of CHAOS supports the core field expressed in terms of the Gauss coefficients up to spherical harmonics (SH) degree of 18, and their time dependences are further expanded in the quartic B-spline function with knot points at intervals of 0.5 year. They can reliably image the core field at spatial and temporal scales much finer than models for the era before the advent of these satellites.

Envisaged by the satellite models, rapid variations of the core field have received much attention. Posterior to the launch of Ørsted satellite in 1999, geomagnetic jerks (sudden change in the secular variation trend) have been detected successively at 2003, 2007, 2010, and 2014 with alternating polarity (Chulliat and Maus 2014; Torta et al 2015). The origin of those rapid variations may be explained by different hypotheses, such as outward expulsions of magnetic field through the core surface (Chulliat et al 2010), oscillations of the magnetic field due to hydromagnetic waves in the stratified layer near the core surface (Chulliat and Maus 2014) and the torsional oscillations of the outer core fluid (also referred to as torsional Alfvén waves) (Gillet et al 2015). The last hypothesis is of particular interest in that the waves may cause changes in the core angular momentum (CAM) about the Earth rotation axis. A 6-year oscillation has been clearly extracted from the observed length-of-day (LOD) series for the last half century (Holme and de Viron 2013).

From a point of view of the core dynamics, it is worth attempting to identify the fundamental period of torsional oscillations from observations because this may be utilised as a constraint on the magnetic field intensity within the outer core (Zatman and Bloxham 1997; Gillet et al 2010). For example, an estimate of some tenths of mT (the magnitude comparable to the radial magnetic field at the core surface) follows from assuming the fundamental period to be approximately 60 years (Zatman and Bloxham 1997) at which prominent variations have actually been observed in both the magnetic field and LOD. The intensity estimate increases by an order of magnitude for a fundamental period of 6 years (Gillet et al 2010). Due to small amplitudes of the corresponding waves, detecting the core field 6-year signal is not an unambiguous matter and requires a rather careful analysis. Nevertheless, interannual behaviours of the core field have been better resolved by the recent satellite models. Estimated from these high-precision magnetic models, core flow models involve rapid flow variations that are correlated with the interannual LOD variations (Wardinski et al 2008) and indicative of the 6-year torsional oscillations (Asari and Lesur 2011).

Unfortunately, the length of satellite era is still inadequate to perform a substantial analysis of the rapid core flow variations. Considering the enhanced uncertainty of satellite magnetic models near the either end of their valid periods, time sections available for the analysis may be as short as some two cycles of the 6-year oscillation. The investigation should necessarily rely on a core field model extending back in time. For the pre-Ørsted era, however, magnetic data are limited in quantity, mostly supplied by ground-based measurements with sparse and uneven distribution over the globe. There have still been attempts to detect the 6-year signal in the pre-Ørsted era, with some findings in favour of 6-year core field variations. Fourier

Table 4.1 B-splines used to expand geomagnetic field models in time

| Model | Period | Degree | Knot spacing (yr) |
|--------------------|---------------|---------|-------------------|
| C ³ FM2 | 1957.0–2008.4 | Quartic | 1.4 |
| gufm1 | 1590.0–1990.0 | Cubic | 2.5 |
| COV-OBS | 1838.0–2012.0 | Cubic | 2.0 |
| GRIMM3 | 2000.0–2011.4 | Quartic | 0.5 |

analysing second-order time derivatives¹ of a geomagnetic field model as well as observatory records, Silva et al (2012) identified a peak at the vicinity of the period of 6 years in their power spectra. Even more powerful arguments for the 6-year torsional oscillations have been invoked from long time-series core flow models; Gillet et al (2010) found a surprisingly high coherence between interannual variations of the observed LOD and its prediction associated with the CAM variation estimated from the historical core field model gufm1 (Jackson et al 2000). More recently (Gillet et al 2015) have shown the coherence by using another centennial magnetic model named COV-OBS (Gillet et al 2013). These studies imply the possibility that the small signals of the 6-year torsional oscillations are indeed captured by the pre-Ørsted magnetic models, despite the fact that their temporal behaviours are strongly regularised and sparsely parametrised (Table 4.1).

This chapter is dedicated to discussing the pre-Ørsted resolution of the interannual CAM fluctuations provided by different geomagnetic field models. Among these models, C³FM2² is rather unique in regard to the dataset used for its construction (Wardinski and Lesur 2012). The model is constructed exclusively from ground-based observatory SV data (even for the recent satellite era), except for satellite field measurements at a single epoch 2004. Parametrised in time more densely than the centennial models (Table 4.1), C³FM2 can, in principle, better describe rapid behaviours of the core field, and may be more appropriate for resolving the interannual CAM fluctuations. Deriving a wide variety of core flow models from C³FM2, Asari and Wardinski (2015) have already reached an important conclusion: the phase of computed CAM fluctuations is relatively robust and hardly affected by the ambiguity of the flow modelling as far as a certain specific magnetic field model is used.

In the next section, the method of Asari and Wardinski (2015) to estimate the CAM variations from a magnetic model is succinctly reviewed. In Sect. 4.3, the key results of Asari and Wardinski (2015) are presented: the robust features and uncertainty in the estimations of the interannual CAM fluctuations from a

¹The second-order time derivative of core field time series is commonly referred to as secular acceleration (SA) such as in Wardinski et al (2008), while the first-order time derivative as secular variation (SV).

²This time-dependent geomagnetic field model consists of two variants, each constructed with and without the frozen-flux constraint (Lesur et al 2010). In this chapter, ‘C³FM2’ always refers to the latter only.

single core field model C³FM2. In Sect. 4.4, we compare estimates of the CAM fluctuations from different core field models, with particular attention to their SAs.

4.2 Magnetic Estimation of the CAM and LOD Variations

CAM changes about Earth rotation axis, or z -axis, are attributed to every azimuthal fluid acceleration within the whole core. It is, however, possible to compute CAM variation from flow at the core surface alone, by assuming that fluctuating flows on decadal or interannual timescales are geostrophic. It follows that such flow fluctuations are invariant in z -direction (Bloxham 1998), and due to the spherical geometry of the boundary, these flows are restricted to rotations of rigid fluid annuli about the z -axis (also referred to as ‘Taylor cylinders’). By analytically integrating their angular momentum variations with respect to the whole core, the time derivative of the CAM is eventually given in terms of accelerations of zonal toroidal and equatorially symmetric flows (Jault et al 1988). The predicted time derivative of the LOD, $\dot{\Lambda}_J$, in millisecond/year is formulated as (Jackson 1997)

$$\dot{\Lambda}_J = 1.138 \left(i_1^0 + \frac{12}{7} i_3^0 \right),$$

where i_1^0 and i_3^0 (in km/year) are the coefficients for the zonal toroidal flow accelerations of SH degree 1 and 3, respectively. All the results for $\dot{\Lambda}_J$ presented here are calculated with this formula from time-dependent core flow models.

The core flow inversion relying on the radial component of the frozen-flux induction equation has been performed in many previous studies (Holme 2015). In principle, no unique solution can be obtained for this problem, and resulting flow models vary significantly with additional constraints imposed subjectively. The interest being how $\dot{\Lambda}_J$ vary with flow models, we change additional constraints and controlling parameters in the inversion, to obtain various solutions. Here, we refer to Sect. 3 of Asari and Wardinski (2015) for details of the inversion method. All the results shown here are obtained after their method. We just raise the points below, and list the statistics of the reference solutions in Table 4.2.

- Inversion method for systematically varying flow models
 - Least-squares inversion is adopted in the spectral domain in space, with regularisations for smoothing in both space and time.
 - Different physical constraints are imposed in the weak form: tangential geostrophy (TG) (Le Mouël 1984), tangential magnetostrophy (TM) (Asari and Lesur 2011), and quasi-geostrophy (QG) (Pais and Jault 2008).
 - Variance of model SV is pre-evaluated (Table 1 of Asari and Lesur (2011)).
 - Misfit to magnetic models are evaluated in the form of root-mean-square (RMS) SV misfit at the Earth surface (denoted by $\langle \Delta \dot{B} \rangle$).

Table 4.2 Statistics of the reference flow models

| Model | RMS misfit ^a | RMS velocity ^b |
|---------------|-------------------------|---------------------------|
| $C^3FM2.TG^c$ | 5.7 | 10.9 |
| $C^3FM2.TM^c$ | 5.3 | 9.5 |
| $C^3FM2.QG$ | 19.2 | 20.4 |
| $COV-OBS.TG$ | 5.1 | 10.0 |
| $COV-OBS.TM$ | 4.9 | 9.3 |
| $COV-OBS.QG$ | 17.7 | 18.9 |

^aUnit in nT/year^bUnit in km/year

^c $C^3FM2.TG$ and $C^3FM2.TG$ are identical to $TG27-1.0^*$ and $TM27+1.0^*$ in Asari and Wardinski (2015), respectively

- Regularisation for temporal smoothness is fixed at a weight just enough to damp spurious undulations near either end of model period.
- Regularisation for spatial smoothness is such that the flow kinetic spectrum follows the power-law $\propto l^{-p}$ for the SH degree l , with the variable p .
- Data and model parametrisations
 - Geomagnetic field model up to SH degree and order 14 is used.
 - Flow model is spatially parametrised by SH expansion of toroidal and poloidal scalar functions truncated at degree 27.
 - Flow model covers the same period as C³FM2 (1957.0–2008.4).
 - All SH coefficients are expanded temporally in the quartic B-spline function with the same knot points as for C³FM2.

4.3 Interannual CAM Fluctuations Inferred from C³FM2

According to the analysis by Asari and Wardinski (2015), some periodic behaviours are present in the interannual variations of the predictions $\dot{\Lambda}_J$. Despite the extensive diversity of flow models derived from C³FM2, the associated $\dot{\Lambda}_J$ are obviously in coherence with one another (Sect. 4.3.1). Care needs to be taken, however, for the resolution that the magnetic model provides, when interpreting $\dot{\Lambda}_J$ to discuss the rapid core dynamics (Sect. 4.3.2).

4.3.1 Robust Features in CAM Fluctuations Inferred from C³FM2

Figure 4.1 shows $\dot{\Lambda}_J$ for three C³FM2 flow models with different levels of the misfit $\langle \Delta \dot{B} \rangle$: overfitting (~ 2.0 nT/year), moderate (~ 5.5 nT/year), and underfitting

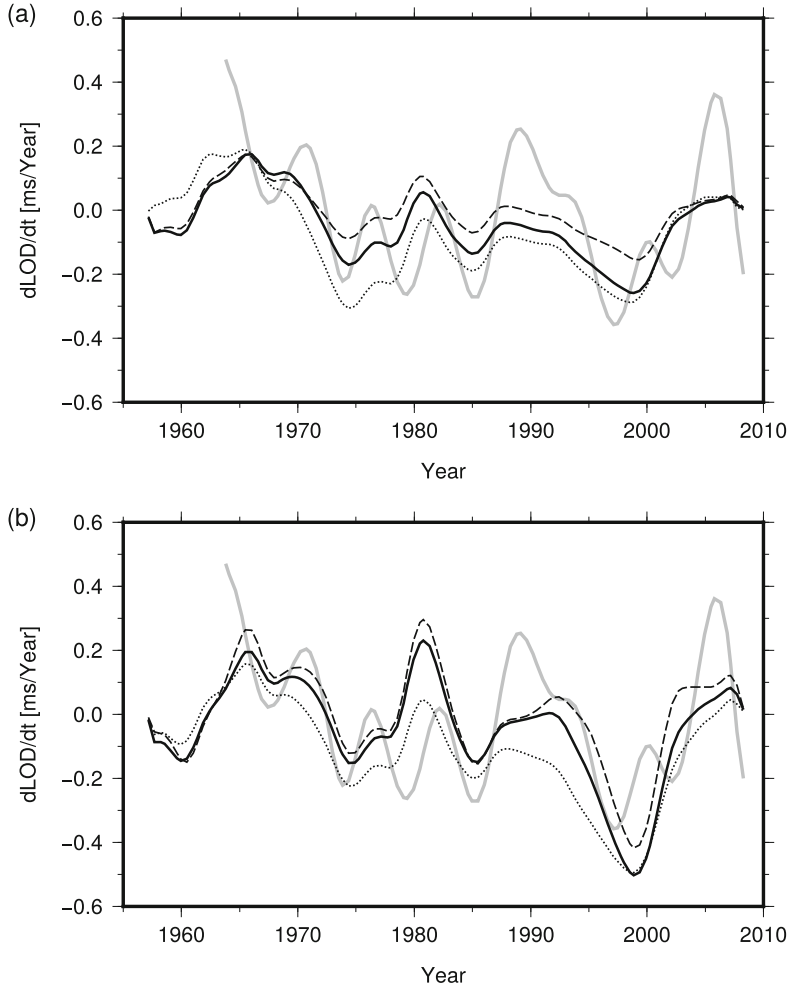


Fig. 4.1 Time-derivatives $\dot{\Lambda}_J$ of LOD predicted from the reference flow models in Table 4.2: (a) $C^3\text{FM2.TG}$ and (b) $C^3\text{FM2.TM}$ (black solid). $\dot{\Lambda}_J$ from the overfitting models (dotted) and underfitting models (dashed) are also plotted in each panel. The misfits $\langle \Delta \dot{B} \rangle$ of the overfitting models are (a) 2.0 and (b) 2.2 nT/yr, and of the underfitting models (a) 17.3 and (b) 15.6 nT/yr. The time derivative $\dot{\Lambda}_o$ of the observed LOD is shown as well (grey solid)

(~ 16 nT/year). For all the six predictions, regardless of the misfit levels and the additional constraints imposed (tangential geostrophy (TG) or tangential magnetostrophy (TM)), $\dot{\Lambda}_J$ apparently have interannual fluctuations that are in phase. For instance, the peaks shortly after 1980 and the troughs around 1985 can obviously be recognised in all of the computed $\dot{\Lambda}_J$. Furthermore, the peaks and troughs of the interannual fluctuations in these $\dot{\Lambda}_J$ seem to have one-to-one correspondences to those of the time derivative of the observed LOD $\dot{\Lambda}_o$.

It follows from the above results that the coherently estimated phase of $\dot{\Lambda}_J$ interannual variations does not depend on the subjective factors in the inversion setting but on the magnetic model used. This is confirmed in Fig. 8 of Asari and Wardinski (2015), where the coherence is also seen in $\dot{\Lambda}_J$ associated with flow models estimated with an even larger variety of physical constraints. We thus argue that the phase of $\dot{\Lambda}_J$ is robustly determined by the variability of the magnetic field model on corresponding timescales. Moreover, the $\dot{\Lambda}_J$ phase depends mostly on temporal behaviours of the large-scale magnetic field (SH degrees 4 and lower), as shown by Fig. 9 of Asari and Wardinski (2015) where the coherent phase is still seen for $\dot{\Lambda}_J$ derived from C³FM2 truncated at as low a SH degree as 4. This finding is important because it indicates that the interannual phase in CAM estimates or LOD predictions remains robust, even in circumstances where significant observational or modelling errors cause a larger misfit (Hulot et al 1992).

4.3.2 Uncertainty in CAM Fluctuations Inferred from C³FM2

There is still uncertainty in the rapid components of $\dot{\Lambda}_J$. The amplitude of its interannual fluctuations is hardly determinable. From one flow model to another the amplitude varies considerably (see Fig. 4.1 and Figs. 8 and 9 of Asari and Wardinski (2015)). The tighter the additionally imposed constraints are, the larger the estimated amplitude of $\dot{\Lambda}_J$ tends to be. The estimates can even be several times larger than the interannual variations in the observation $\dot{\Lambda}_o$ (see Figs. 8 and 9 of Asari and Wardinski (2015)). One could possibly utilise this amplitude to evaluate a posteriori the flow model from which $\dot{\Lambda}_J$ is calculated; a flow model may be preferred which has an amplitude of $\dot{\Lambda}_J$ comparable to that of $\dot{\Lambda}_o$.

The uncertainty in the estimation of interannual CAM variations is due to the lack of resolution. This is a serious issue in the sense it cannot be overcome within the relevant inversion framework. It has to be noted that even the phase of $\dot{\Lambda}_J$ interannual variations (apparently robustly determined from a magnetic model, as shown in Sect. 4.3.1) may not fully represent those of the true Earth's core. This has been demonstrated by Asari and Wardinski (2015) following the steps below.

- Step 1 Construct a flow model *virtual core* such that it accounts for both C³FM2 and $\dot{\Lambda}_o$ by inverting for both in the same inversion setting for either C³FM2.TG or C³FM2.TM.
- Step 2 Calculate a SV prediction from *virtual core*.
- Step 3 Invert the SV produced in Step 2 with the same inversion setting as in Step 1, to obtain a test flow model.
- Step 4 Examine $\dot{\Lambda}_J$ for the test flow obtained in Step 3 to evaluate if the $\dot{\Lambda}_J$ for *virtual core* is retrieved.

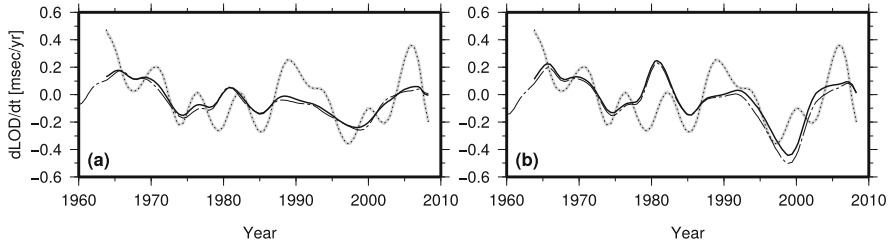


Fig. 4.2 Time derivatives of the observed LOD $\dot{\Lambda}_o$ (thick grey curve) and predictions $\dot{\Lambda}_J$ from (a) $C^3FM2.TG$ flow model and (b) $C^3FM2.TM$ flow model (black dash-dotted line). Also plotted are $\dot{\Lambda}_J$ from *virtual core* built with the same inversion settings as used to derive the C^3FM2 flow models (black dotted line), and from the test flow retrieved from *virtual core* SV up to SH degree 14 (black solid line)

Figure 4.2 shows the results of the above resolution test performed with the two inversion settings for $C^3FM2.TG$ and $C^3FM2.TM$. As a consequence of Step 1, $\dot{\Lambda}_J$ for *virtual core* (black dotted curves) perfectly fits $\dot{\Lambda}_o$ (thick grey curves). However, $\dot{\Lambda}_J$ for the test flows (black solid curves) are significantly apart from $\dot{\Lambda}_o$ in both their phases and amplitudes, but rather similar for $C^3FM2.TG$ and $C^3FM2.TM$ (black dash-dotted curves). This indicates that a full image of the interannual fluctuations in the CAM of true Earth is unavailable due to the limited resolution. Conceivably, apparently robust estimates for the phase of $\dot{\Lambda}_J$ in Sect. 4.3.1 may still have some (if not much) shifts with respect to the true interannual CAM phase.

4.4 Interannual CAM Fluctuations Inferred from Different Magnetic Models

It remains to be investigated how the estimation of the $\dot{\Lambda}_J$ interannual variations depends on geomagnetic field models used for the flow inversion. For consistency we compare $\dot{\Lambda}_J$ derived from C^3FM2 and COV-OBS with identical flow inversion setting. Here, results are shown from three COV-OBS flow models, *COV-OBS.TG*, *COV-OBS.TM* and *COV-OBS.QG*, which are obtained by inverting COV-OBS with the same settings as for $C^3FM2.TG$, $C^3FM2.TM$ and $C^3FM2.QG$, respectively (Table 4.2).

The predictions $\dot{\Lambda}_J$ from the corresponding pairs of *COV-OBS.XX* and $C^3FM2.XX$ do not agree with each other (Fig. 4.3). There are noticeable differences even in the phases of their interannual variations, although correlations are still noticeable between them outside the first and last decade of the model period. Also, there are substantial discrepancies in their amplitudes, with tendencies for those of the COV-OBS flow models to be much larger. $\dot{\Lambda}_J$ for *COV-OBS.QG* show the best coherence with the observation $\dot{\Lambda}_o$. This is consistent with results of Gillet et al (2015), although their QG flow model is not built with a temporal spline expansion.

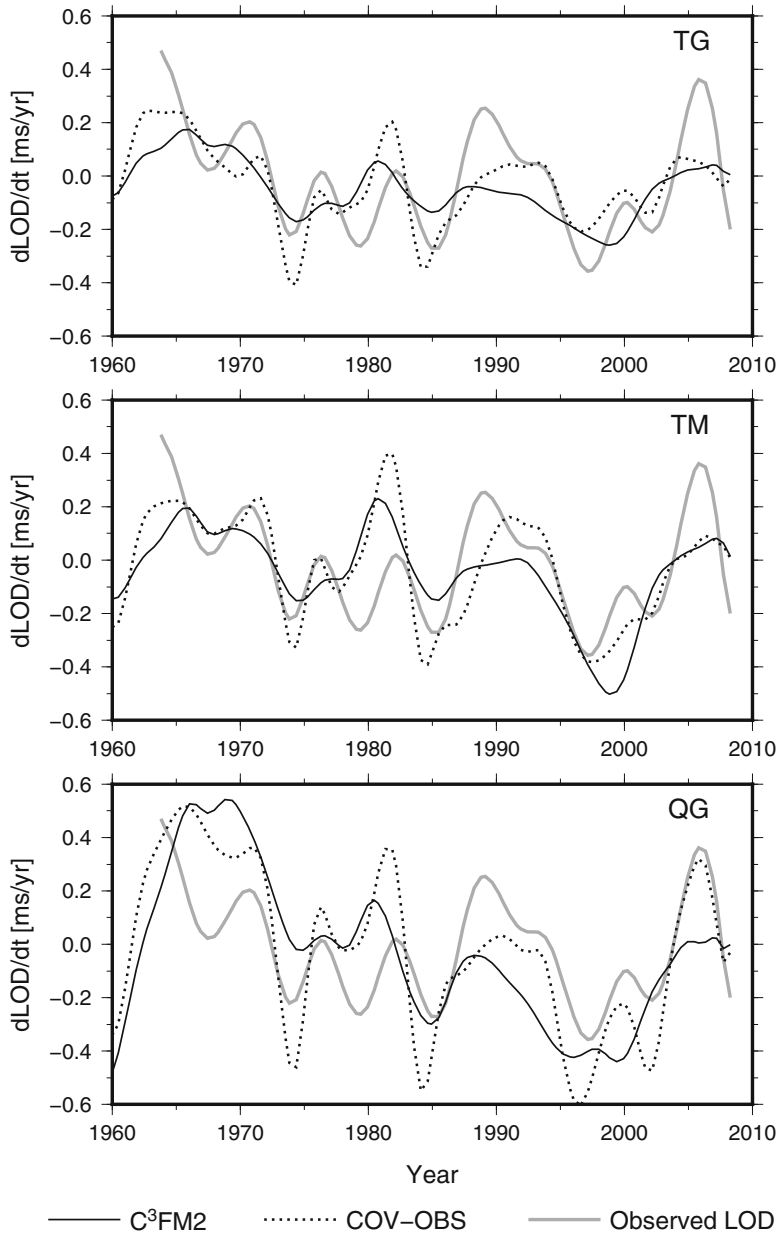


Fig. 4.3 Time derivatives of the observed LOD $\dot{\Lambda}_o$ (thick grey curve) and predictions $\dot{\Lambda}_J$ from (top) $C^3\text{FM2.TG}$ and COV-OBS.TG , (middle) $C^3\text{FM2.TM}$ and COV-OBS.TM , (bottom) $C^3\text{FM2.QG}$ and COV-OBS.QG . In each panel, $\dot{\Lambda}_J$ from $C^3\text{FM2}$ and COV-OBS flow models are plotted in black solid line and black dotted line, respectively

The dependence of the $\dot{\Lambda}_J$ phase on the magnetic models contrasts with its insensitivity to the flow inversion settings illustrated in Sect. 4.3.1. For making a more reliable estimate of interannual CAM variations as well as interannual flow fluctuations, it would then be essential to refine time-dependences of core field models on the relevant timescales, perhaps rather than to elaborate the inversion method for the core flow. Particularly, a knowledge of SA is crucially important for determining $\dot{\Lambda}_J$, because SA is associated predominantly with core flow acceleration (Lesur et al 2010), which includes i_1^0 and i_3^0 in the formulation of $\dot{\Lambda}_J$ (Sect. 4.2).

Actually, the varying behaviours of $\dot{\Lambda}_J$ for the C³FM2 and COV-OBS flow models are likely associative with their differences eminently seen in their SAs. In Fig. 4.4 we plot time evolutions of the SA Gauss coefficients of various magnetic models. Only the sectorial modes are shown here in view of their causal relations to i_1^0 and i_3^0 , but we have confirmed that the current discussion applies to other modes, too. On interannual timescales, the COV-OBS SA is allowed a higher power than the C³FM2 SA (and the gufm1 SA); while the amplitudes are still comparable at SH degree 1, the disparity grows rapidly with increasing degree. For example, the C³FM2 SA exhibits almost no interannual fluctuations at SH degree 5 and higher, whereas the COV-OBS SV has vigorous interannual oscillation. This is particularly eminent in the GRIMM3 epochs; constructed from satellite data, COV-OBS is superior in mimicking the GRIMM3 SA at every SH degree. Accordingly, the COV-OBS flow models are estimated to have relatively large amplitudes of $\dot{\Lambda}_J$ on relevant timescales (see Fig. 4.3).

The phase differences observed between the $\dot{\Lambda}_J$ interannual variations for C³FM2 and COV-OBS flow models are correspondingly present in some of the individual SA coefficients. For instance, the peaks of $\dot{\Lambda}_J$ for C³FM2 flow models right after 1980 lead those for COV-OBS flow models by approximately 1 year (Fig. 4.3). These may be related to the contemporary leads of troughs in the C³FM2 \ddot{h}_1^1 and \ddot{h}_3^3 relative to those in COV-OBS (Fig. 4.4).

The differences between C³FM2 and COV-OBS are so minor that they both are acknowledgeable as appropriate models to describe the core field. When it comes to probing the interannual CAM variations, however, even such marginal differences (as are evidently illustrated only when differentiated twice in time) can indeed matter, adding to the uncertainty of interannual CAM variations together with the theoretical lack of resolution (Sect. 4.3.2). Furthermore, neither of the two core field models may be built optimally for revealing the interannual CAM variations or torsional oscillations. C³FM2 is obtained by imposing a damping for temporal smoothness, but it could be so strong that it prevents tiny signals of the interannual core flow fluctuations from being adequately modelled. In fact, the amplitudes of the C³FM2 interannual SA fall short of those of COV-OBS and GRIMM3 SAs even at as low a SH degree as 2 (Fig. 4.4). In contrast, the amplitudes of the COV-OBS interannual SA are comparable to those of GRIMM3 (COV-OBS is constructed without temporal damping (Gillet et al 2013)). Designed to uniformly parametrise

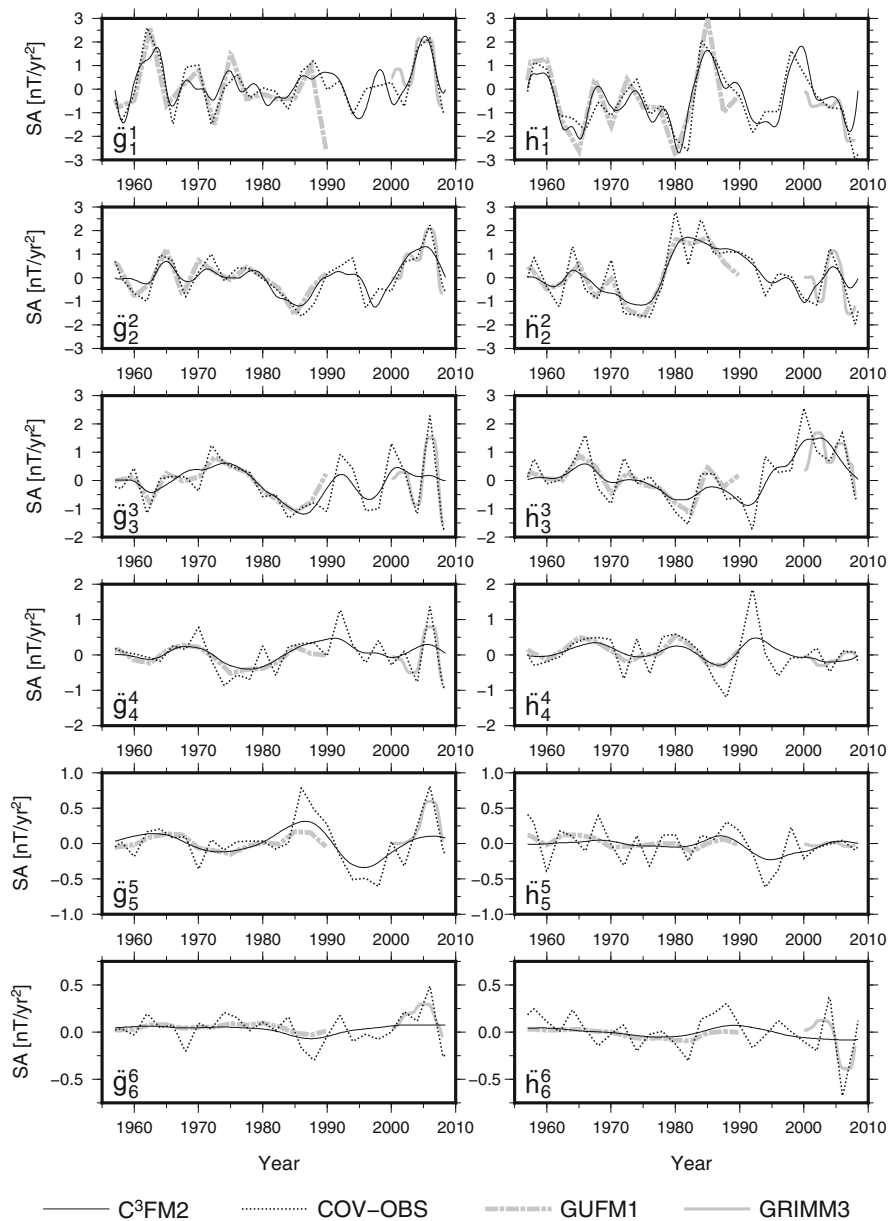


Fig. 4.4 Second order time derivatives of sectorial Gauss coefficients from C³FM2 (black solid line), COV-OBS (black dotted line), gufm1 (grey dash-dotted line) and GRIMM3 (grey solid line)

the core field over a much longer period of time (Table 4.2), however, the temporal description of COV-OBS (and gufm1 as well) may be too coarse to resolve the interannual SA adequately. The COV-OBS SA coefficients have indifferentiable points every 2 years at the nodes for its cubic B-spline basis (Fig. 4.4).

There is still a room to improve C³FM2 so that it is optimised for reliable detection of the interannual CAM fluctuations and also the fast torsional waves. We argue that the model time range and the temporal parametrisation of C³FM2 are already appropriate, based on the quartic B-spline functions with the knot points distributed densely enough. It is still necessary to define which kind of and how much temporal smoothing should be applied. This could be evaluated by testing different regularisations for the smoothing, while modelling the core field exclusively from ground-based magnetic data for epochs in common with the latest satellite model like CHAOS-6 (Finlay et al 2016). Based on the optimal temporal smoothing for the core field specified in reference to the interannual SA of a satellite model, the pre-Ørsted geomagnetic modelling should be performed so that the constructed model is particularly tuned for studying the interannual core flow variations. It would also yield insights on the extent to which the interannual SA is resolved by ground-based data alone.

References

- Asari, S., Lesur, V.: Radial vorticity constraint in core flow modeling. *J. Geophys. Res.* **116** (2011). doi:10.1029/2011JB008267
- Asari, S., Wardinski, I.: On magnetic estimation of Earth's core angular momentum variation. *J. Geophys. Res.* **120** (2015). doi:10.1002/2014JB011458
- Bloxham, J.: Dynamics of angular momentum in the Earth's core. *Ann. Rev. Earth Planet. Sci.* **26**, 501–517 (1998)
- Chulliat, A., Maus, S.: Geomagnetic secular acceleration, jerks, and a localized standing wave at the core surface from 2000 to 2010. *J. Geophys. Res.* **119** (2014). doi:10.1002/2013JB010604
- Chulliat, A., Hulot, G., Newitt, L.R.: Magnetic flux expulsion from the core as a possible cause of the unusually large acceleration of the north magnetic pole during the 1990s. *J. Geophys. Res.* **115** (2010). doi:10.1029/2009JB007143
- Finlay, C.C., Olsen, N., Kotsiaros, S., Gillet, N., Tøffner-Clausen, L.: Recent geomagnetic secular variation from Swarm and ground observatories as estimated in the CHAOS-6 geomagnetic field model. *Earth Planets Space* **68**(1), 112 (2016). doi:10.1186/s40623-016-0486-1. <http://dx.doi.org/10.1186/s40623-016-0486-1>
- Friis-Christensen, E., Lühr, H., Hulot, G.: Swarm: a constellation to study the earth's magnetic field. *Earth Planets Space* **58**, 351–358 (2006). doi:10.1186/BF03351933
- Gillet, N., Jault, D., Canet, E., Fournier, A.: Fast torsional waves and strong magnetic field within the Earth's core. *Nature* **465**, 74–77 (2010)
- Gillet, N., Jault, D., Finlay, C., Olsen, N.: Stochastic modelling of the Earth's magnetic field: inversion for covariances over the observatory era. *Geochem. Geophys. Geosyst.* **14**, 766–786 (2013). doi:10.1002/ggge.20041
- Gillet, N., Jault, D., Finlay, C.C.: Planetary gyre, time-dependent eddies, torsional waves, and equatorial jets at the Earth's core surface. *J. Geophys. Res.* **120** (2015). doi:10.1002/2014JB011786
- Holme, R.: Large scale flow in the core. In: Schubert, G. (ed.) *Treatise in Geophysics, Core Dynamics*, Elsevier, vol. 8, pp. 91–113 (2015)

- Holme, R., de Viron, O.: Characterization and implications of intradecadal variations in length of day. *Nature* **499**, 202–204 (2013)
- Hulot, G., Le Mouël, J.L., Wahr, J.: Taking into account truncation problems and geomagnetic model accuracy in assessing computed flows at the core-mantle boundary. *Geophys. J. Int.* **108**, 224–246 (1992)
- Jackson, A.: Time-dependency of tangentially geostrophic core surface motions. *Phys. Earth Planet. Inter.* **103**, 293–311 (1997)
- Jackson, A., Jonker, A.R.T., Walker, M.R.: Four centuries of geomagnetic secular variation from historical records. *Philos. Trans. R. Soc. Lond. A* **358**, 957–990 (2000)
- Jault, D., Gire, C., Le Mouël, J.L.: Westward drift, core motion and exchanges of angular momentum between core and mantle. *Nature* **333**, 353–356 (1988)
- Le Mouël, J.L.: Outer-core geostrophic flow and secular variation of Earth's geomagnetic field. *Nature* **311**, 734–735 (1984)
- Lesur, V., Wardinski, I., Asari, S., Minchev, B., Mandea, M.: Modelling the Earth's core magnetic field under flow constraint. *Earth Planets Space* **62**, 503–516 (2010)
- Neubert, T., Mandea, M., Hulot, G., von Frese, R., Primdahl, F., Jørgensen, J.L., Friis-Christensen, E., Stauning, P., Olsen, N., Risbo, T.: Ørsted satellite captures high-precision geomagnetic field data. *Eos, Transactions American Geophysical Union*, vol. **82**(7), pp. 81–88 (2001). doi:10.1029/01EO00043. <http://dx.doi.org/10.1029/01EO00043>
- Pais, M.A., Jault, D.: Quasi-geostrophic flows responsible for the secular variation of the Earth's magnetic field. *Geophys. J. Int.* **173**, 421–443 (2008)
- Reigber, C., Lühr, H., Schwintzer, P.: CHAMP mission status. *Adv. Space Res.* **30**, 129–134 (2002). doi:10.1016/S0273-1177(02)00276-4
- Silva, L., Jackson, L., Mound, J.: Assessing the importance and expression of the 6 year geomagnetic oscillation. *J. Geophys. Res.* **117** (2012). doi:10.1029/2012JB009405
- Torta, J.M., Pavón-Carrasco, F.J., Marsal, S., Finlay, C.C.: Evidence for a new geomagnetic jerk in 2014. *Geophys. Res. Lett.* **42**(19), 7933–7940 (2015). doi:10.1002/2015GL065501, 2015GL065501
- Wardinski, I., Lesur, V.: An extended version of the C³FM geomagnetic field model: application of a continuous frozen-flux constraint. *Geophys. J. Int.* **189**, 1409–1429 (2012)
- Wardinski, I., Holme, R., Asari, S., Mandea, M.: The 2003 geomagnetic jerk and its relation to the core surface flows. *Earth Planet. Sci. Lett.* **267**, 468–481 (2008)
- Zatman, S., Bloxham, J.: Torsional oscillations and the magnetic field within the Earth's core. *Nature* **388**, 760–763 (1997)

Chapter 5

Laboratory Experiments and Numerical Simulations on Magnetic Instabilities

Frank Stefani, Marcus Gellert, Christoph Kasprzyk, Alejandro Paredes,
Günther Rüdiger, and Martin Seilmayer

Abstract Magnetic fields of planets, stars, and galaxies are generated by self-excitation in moving electrically conducting fluids. Once produced, magnetic fields can play an active role in cosmic structure formation by destabilizing rotational flows that would be otherwise hydrodynamically stable. For a long time, both hydromagnetic dynamo action and magnetically triggered flow instabilities had been the subject of purely theoretical research. Meanwhile, however, the dynamo effect has been observed in large-scale liquid sodium experiments in Riga, Karlsruhe, and Cadarache. In this chapter, we summarize the results of some smaller liquid metal experiments devoted to various magnetic instabilities, such as the helical and the azimuthal magnetorotational instability, the Tayler instability, and the different instabilities that appear in a magnetized spherical Couette flow. We conclude with an outlook on a large scale Tayler-Couette experiment using liquid sodium, and on the prospects to observe magnetically triggered instabilities of flows with positive shear.

5.1 Introduction

Magnetic fields of planets and stars are known to be produced by the homogeneous dynamo effect (Jones 2011; Wicht and Tilgner 2010). After decades of mainly theoretical and numerical work, the last years have seen tremendous progress in complementary experimental studies devoted to a better understanding of self-excitation in homogeneous fluids (Gailitis and Lielausis 2002; Lathrop and Forest 2011; Stefani et al. 2008). Following the pioneering Riga and Karlsruhe dynamo experiments (Gailitis et al. 2000; Stieglitz and Müller 2001), it was in particular

F. Stefani (✉) • C. Kasprzyk • M. Seilmayer
Helmholtz-Zentrum Dresden-Rossendorf, Bautzner Landstr. 400, 01328 Dresden, Germany
e-mail: F.Stefani@hzdr.de

M. Gellert • A. Paredes • G. Rüdiger
Leibniz-Institut für Astrophysik Potsdam, An der Sternwarte 16, 14482 Potsdam, Germany
e-mail: mgellert@aip.de

the rich dynamics observed in the French von Kármán Sodium (VKS) experiment (Berhanu et al. 2010) that has provoked interest throughout the dynamo community. The observed reversals, excursions, bursts, hemispherical fields, etc. have boosted considerable research directed to a deeper physical understanding of the corresponding geomagnetic phenomena (Benzi and Pinton 2010; Mori et al. 2013; Petrelis et al. 2009; Sorriso-Valvo et al. 2007; Stefani et al. 2006a).

While realistic “bonsai” models of planetary dynamos, with all dimensionless numbers matching those of planets, will never be possible in the laboratory (Lathrop and Forest 2011), there is still ongoing effort to explore the technical limits of dynamo experiments. This applies to the 3 m diameter spherical Couette experiment presently being spun at the University of Maryland (Adams et al. 2015; Zimmermann et al. 2010), to the 2 m diameter precession dynamo experiment (Stefani et al. 2012, 2015) that is under construction at Helmholtz-Zentrum Dresden-Rossendorf (HZDR), as well as to the 3 m diameter plasma dynamo experiment in Madison (Cooper et al. 2014). One of the characteristics of those “second generation” dynamo experiments is a larger degree of uncertainty of success. Whereas the Riga and Karlsruhe experiments had turned out to be well predictable by kinematic dynamo codes and simplified saturation models (Stefani et al. 2009) (and even the unexpected VKS dynamo results can be explained when correctly including the high permeability disks (Giesecke et al. 2010, 2012; Nore et al. 2016)), the outcomes of the Maryland, HZDR, and Madison experiments are much harder to predict. In either case, this uncertainty follows directly from the ambition to construct a truly homogeneous dynamo, neither driven by pumps or propellers, nor influenced by guiding blades or gradients of magnetic permeability. This higher degree of freedom makes those experiments prone to emerging medium-size flow structures and waves. Actually, it is the influence of such waves that might foster, or inhibit, dynamo action in a much stronger way than any quasi-stationary analysis would suggest (Reuter et al. 2009; Tilgner 2008). A closely related aspect here is the possibility of subcritical dynamo action under the influence of magnetic fields (as discussed, e.g., for rapidly rotating convection problems (Dormy 2016; Sreenivasan and Jones 2011)).

Apart from this connection to dynamo action, instabilities and wave phenomena that appear under the common influence of rotation and magnetic fields are interesting in their own right, in particular with respect to the angular momentum transport in planetary cores (Petitdemange et al. 2008; Petitdemange 2010) and in active galactic nuclei and proto-planetary disks (Balbus 2003) by virtue of the magneto-rotational instability (MRI). The fluctuations, arising from this and related magnetic flow instabilities, correlate and amplify the eddy viscosity of the fluid. The magnetic resistivity and the transport coefficients for temperature and mixing of chemicals, however, are less influenced by the magnetic fluctuations. Consequently, the magnetic Prandtl number and the Schmidt number (i.e. the ratio of viscosity and diffusion coefficient) are enhanced under the presence of turbulent magnetic field components which are due to the instability of the magnetic background fields (Paredes et al. 2016). This effect is supposed to explain the rigid rotation of the

stellar interiors (Spada et al. 2016) but may also play a role for the amplification of the fluid viscosity by magnetic instabilities in planetary cores.

It is for good reasons, therefore, that a number of medium-size liquid metal experiments are dedicated mainly to those instabilities, without ambition to reproduce the very dynamo effect. This applies, in particular, to the DTS experiment in Grenoble where a variety of magneto-inertial waves have been identified (Schmitt et al. 2013), to the spherical Couette experiment in Maryland which has shown coherent velocity/magnetic field fluctuations quite reminiscent of MRI (Sisan et al. 2004), as well as to the Taylor-Couette experiment in Princeton which has shown evidence for slow magneto-Coriolis waves (Nornberg et al. 2010) and a free-Shercliff layer instability (Roach et al. 2012). Despite these preliminary successes, the latter experiments have made it clear that for liquid metal flows the unambiguous identification of the standard MRI (SMRI), with a purely axial field being applied, is extremely complicated due to the key role of boundary effects (e.g., Ekman pumping) on the flow structure at those high Reynolds numbers ($\sim 10^6$) that are inevitably connected with the need to obtain magnetic Reynolds numbers of order unity.

These sobering prospects for studying MRI in the lab suddenly brightened up with the numerical prediction (Hollerbach and Rüdiger 2005) of a very special, essentially inductionless, version of MRI whose onset does not depend on crossing certain critical magnetic Reynolds and Lundquist numbers, but only on crossing certain critical Reynolds and Hartmann numbers, which makes its experimental identification much easier. Since, in its axisymmetric form initially studied, this MRI version requires the application of axial and azimuthal magnetic field of comparable strengths, it was coined helical MRI (HMRI) (Liu et al. 2006). In 2006, a swiftly designed experiment at the PROMISE facility at HZDR had given first evidence for the onset of this HMRI, with roughly correct wave frequencies observed in the predicted parameter regions of the Hartmann number (Stefani et al. 2006, 2007). In 2009, an improved version of this experiment—using split end-rings installed at the top and bottom of the cylinder in order to minimize the global Ekman pumping—allowed to observe the onset and cessation of HMRI for a number of parameter variations in much better agreement with numerical predictions (Stefani et al. 2009a). After some preceding dispute about the (noise-triggered) convective or global character of the observed instability (Liu et al. 2007; Priede and Gerbeth 2009), the results gave now strong arguments in favor of the latter.

In parallel with these experimental works, Hollerbach et al. (2010) had identified a further inductionless MRI version that appears for strongly dominant azimuthal fields in form of a non-axisymmetric ($m = 1$) mode, which is now called azimuthal MRI (AMRI). When further relaxing the demand that the azimuthal field should be current-free, one enters the realm of current-driven instabilities, including the Tayler instability (TI) (Tayler 1973), a kink-type instability in current-carrying conductors, whose ideal counterpart has been known for a long time from plasma z-pinch experiments (Bergerson et al. 2006). Interestingly, the TI has been intensely discussed as a main ingredient of the Tayler-Spruit dynamo model (Spruit 2002; Gellert et al. 2008; Rüdiger et al. 2011)). The first experimental investigation of

the AMRI and the TI was the central goal of the project within the DFG focus programme “PlanetMag.” The corresponding numerical and experimental results for cylindrical geometry will be the content of section Sect. 5.2.

A further topic was related to the different types of non-axisymmetric instabilities in spherical Couette flow that appear in dependence on the strength of an applied axial magnetic field (Hollerbach 2009). Corresponding numerical predictions, and first experimental results, will be reported in Sect. 5.3.

The paper closes with an outlook on the large-scale combined MRI/TI experiment as it is planned in the framework of the DRESDYN project at HZDR, and on the prospects to observe magnetically triggered instabilities of flows with positive shear.

5.2 Instabilities in Cylindrical Geometry

In this section, we will present various numerical and experimental results on magnetically triggered flow instabilities in cylindrical geometry. These comprise the AMRI and the TI, which are both non-axisymmetric instabilities with azimuthal wavenumber $m = 1$ that appear under the influence of a purely (or dominantly) azimuthal magnetic field. While AMRI draws its energy from the shear of the flow and requires the current-free azimuthal field only as a trigger, the kink-type TI draws its energy from the electric current that is passing through the fluid. The axisymmetric HMRI, which becomes dominant when the azimuthal magnetic field is complemented by a vertical magnetic field of comparable magnitude, will also be discussed.

5.2.1 Theory and Numerics

During the last decade, the theory of HMRI, AMRI, and TI has been developed in a rather comprehensive manner. This development was ignited by the observation of Hollerbach and Rüdiger (Hollerbach and Rüdiger 2005) that the combination of an axial and an azimuthal magnetic field leads to an essentially inductionless version of the axisymmetric MRI which does not scale with the magnetic Reynolds and the Lundquist number, but rather with the Reynolds and Hartmann number. It is important to note that SMRI and HMRI are continuously and monotonically connected (Hollerbach and Rüdiger 2005), although the transition involves an exceptional point of the spectrum where a slow magneto-Coriolis mode and an inertial mode coalesce (Kirillov and Stefani 2010). Later it was also shown that the scaling properties of AMRI are essentially the same as those of HMRI (Kirillov et al. 2012, 2014).

These instabilities can be treated with analytical and numerical methods of increasing complexity. In the following, we will present in some detail the short-wavelength, or Wentzel-Kramers-Brillouin (WKB) method. It allows for analytical solutions in quite a couple of circumstances, and it provides easily a general overview about many parameter dependencies and the transitions between different instabilities. Then we give illustrating examples of 1D modal stability analyses and of 3D simulations which are necessary for quantitative predictions of real-world experiments. We also discuss some recent results explaining turbulent angular momentum transport and turbulent diffusion in stars in a consistent manner.

5.2.1.1 Basic Equations

For the direct numerical simulations the MHD equations for an incompressible and electrically conduction fluid are solved. These are the coupled Navier-Stokes equation for the velocity field \mathbf{u} and the induction equation for the magnetic field \mathbf{B} ,

$$\frac{\partial \mathbf{u}}{\partial t} + \mathbf{u} \cdot \nabla \mathbf{u} - \frac{1}{\mu_0 \rho} \mathbf{B} \cdot \nabla \mathbf{B} + \frac{1}{\rho} \nabla P - \nu \nabla^2 \mathbf{u} = 0, \quad (5.1)$$

$$\frac{\partial \mathbf{B}}{\partial t} + \mathbf{u} \cdot \nabla \mathbf{B} - \mathbf{B} \cdot \nabla \mathbf{u} - \eta \nabla^2 \mathbf{B} = 0, \quad (5.2)$$

where $P = p + \mathbf{B}^2/(2\mu_0)$ is the total pressure, ρ the density, ν the kinematic viscosity, $\eta = (\mu_0 \sigma)^{-1}$ the magnetic diffusivity, σ the conductivity of the fluid, and μ_0 the magnetic permeability constant. This set is complemented by the continuity equation for incompressible flows and the solenoidal condition for the magnetic induction:

$$\nabla \cdot \mathbf{u} = 0, \quad (5.3)$$

$$\nabla \cdot \mathbf{B} = 0. \quad (5.4)$$

For treating instabilities of flows in cylindrical geometry under the influence of an external magnetic field, this equation system can conveniently be re-written in dimensionless form using the Reynolds number $\text{Re} = \Omega_i L^2 / \nu$, the Hartmann number $\text{Ha} = B_0 L / \sqrt{\mu_0 \rho \nu \eta}$, and the magnetic Prandtl number $\text{Pm} = \nu / \eta$, where B_0 denotes the external field amplitude, Ω_i the angular frequency of an inner cylinder, and L the gap width $L = r_o - r_i$ between an inner radius r_i and an outer radius r_o .

To study the mixing properties the diffusion equation for a passive scalar,

$$\frac{\partial C}{\partial t} + \nabla \cdot (\mathbf{u} C) = \frac{1}{\text{Sc}} \Delta C \quad (5.5)$$

is additionally solved. Here $\text{Sc} = v/D^*$ is the Schmidt number and $D^* = D_{\text{mol}} + D_{\text{turb}}$ the effective diffusion coefficient with a molecular and a turbulent contribution.

5.2.1.2 Short Wavelength Approximation

The short-wavelength, or WKB, approximation provides a unified and comprehensive framework for the investigation of the HMRI, AMRI, and TI. In its simplest version, restricted to the axisymmetric HMRI, it traces back to the work of Liu et al. (2006), which was later corroborated in more detail and extended to the non-axisymmetric case by Kirillov and Stefani (2010, 2011, 2013) and Kirillov et al. (2012, 2014).

Following Kirillov et al. (2014), the theory starts from the set of equations (1)–(4) as described above. Here we consider the stability of a rotating conducting fluid exposed to a magnetic field sustained by electrical currents outside and/or inside the fluid. Introducing cylindrical coordinates (r, ϕ, z) , we assume a steady-state background liquid flow with the angular velocity profile $\Omega(r)$ in a (in general) helical background magnetic field with constant axial and radially varying azimuthal components:

$$\mathbf{u}_0(r) = r\Omega(r)\mathbf{e}_\phi, \quad p = p_0(r), \quad \mathbf{B}_0(r) = B_\phi^0(r)\mathbf{e}_\phi + B_z^0\mathbf{e}_z. \quad (5.6)$$

In the particular case that the azimuthal component is produced by an axial current I confined to $r < r_i$, the azimuthal field becomes

$$B_\phi^0(r) = \frac{\mu_0 I}{2\pi r}. \quad (5.7)$$

It is convenient to characterize the shear of the background field by the hydrodynamic Rossby number (Ro),

$$\text{Ro} := \frac{r}{2\Omega}\partial_r\Omega, \quad (5.8)$$

which gives $\text{Ro} = 0$ for solid body rotation, $\text{Ro} = -3/4$ for Keplerian rotation, and $\text{Ro} = -1$ for the Couette flow profile $\Omega(r) \sim r^{-2}$. In close correspondence to Ro , we also define the *magnetic* Rossby number

$$\text{Rb} := \frac{r}{2B_\phi^0 r^{-1}}\partial_r(B_\phi^0 r^{-1}). \quad (5.9)$$

Then, $\text{Rb} = 0$ results from a linear dependence of the magnetic field on the radius, $B_\phi^0(r) \propto r$, as it would be produced by a homogeneous axial current in the fluid, while $\text{Rb} = -1$ characterizes the limit of a current-free field in the liquid that is produced solely by an axial current confined to $r < r_i$.

The linearization around this steady state leads, after some algebra, to a fourth order secular equation

$$p(\gamma) = \det(\mathbf{H} - \gamma\mathbf{I}) = 0 \quad (5.10)$$

for the complex spectral parameter γ whose real and imaginary parts are the growth rate and the angular frequency of the perturbation. Here, \mathbf{I} is the 4×4 identity matrix and \mathbf{H} is

$$\mathbf{H} = \begin{pmatrix} -in\text{Re} - 1 & 2\alpha\text{Re} & \frac{i\text{Ha}(1+n\beta)}{\sqrt{\text{Pm}}} & -\frac{2\alpha\beta\text{Ha}}{\sqrt{\text{Pm}}} \\ -\frac{2\text{Re}(1+\text{Ro})}{\alpha} & -in\text{Re} - 1 & \frac{2\beta\text{Ha}(1+\text{Rb})}{\alpha\sqrt{\text{Pm}}} & \frac{i\text{Ha}(1+n\beta)}{\sqrt{\text{Pm}}} \\ \frac{i\text{Ha}(1+n\beta)}{\sqrt{\text{Pm}}} & 0 & -in\text{Re} - \frac{1}{\text{Pm}} & 0 \\ -\frac{2\beta\text{Ha}\text{Rb}}{\alpha\sqrt{\text{Pm}}} & \frac{i\text{Ha}(1+n\beta)}{\sqrt{\text{Pm}}} & \frac{2\text{Re}\text{Ro}}{\alpha} & -in\text{Re} - \frac{1}{\text{Pm}} \end{pmatrix}, \quad (5.11)$$

where we use the magnetic Prandtl number (Pm), the ratio of the Alfvén frequencies (β), the Reynolds (Re) and Hartmann (Ha) numbers as well as the modified azimuthal wavenumber n according to

$$\text{Pm} = \frac{\omega_v}{\omega_\eta}, \quad \beta = \alpha \frac{\omega_{A_\phi}}{\omega_{A_z}}, \quad \text{Re} = \alpha \frac{\Omega}{\omega_v}, \quad \text{Ha} = \frac{\omega_{A_z}}{\sqrt{\omega_v \omega_\eta}}, \quad n = \frac{m}{\alpha}. \quad (5.12)$$

Note the definitions for the viscous, resistive and the two Alfvén frequencies:

$$\omega_v = v|\mathbf{k}|^2, \quad \omega_\eta = \eta|\mathbf{k}|^2, \quad \omega_{A_z} = \frac{k_z B_z^0}{\sqrt{\rho \mu_0}}, \quad \omega_{A_\phi} = \frac{B_\phi^0}{R \sqrt{\rho \mu_0}}, \quad (5.13)$$

with $\mathbf{k} = (k_z^2 + k_r^2)^{1/2}$ and $\alpha = k_z/|\mathbf{k}|$.

The secular equation (5.10) has been analyzed in much detail using Bilharz' stability criterion (Kirillov and Stefani 2013; Kirillov et al. 2014). One of the most important results refers to the limiting stability curve (see Fig. 5.1) in the $\text{Ro}-\text{Rb}$ plane, which obeys the analytical equation

$$\text{Rb} = -\frac{1}{8} \frac{(\text{Ro} + 2)^2}{\text{Ro} + 1}. \quad (5.14)$$

The crossing points of this curve with the abscissa ($\text{Rb} = -1$) recover the original result of Liu et al. (2006) that for $\text{Pm} = 0$, and optimal values of β , the instability domains lie outside the stratum

$$2 - 2\sqrt{2} =: \text{Ro}_{\text{LLL}} < \text{Ro} < \text{Ro}_{\text{ULL}} := 2 + 2\sqrt{2},$$

where $\text{Ro}_{\text{LLL}} = 2(1 - \sqrt{2}) \approx -0.828$ denotes the lower Liu limit (LLL), as we call it now, and $\text{Ro}_{\text{ULL}} = 2(1 + \sqrt{2}) \approx 4.828$ the upper Liu limit (ULL).

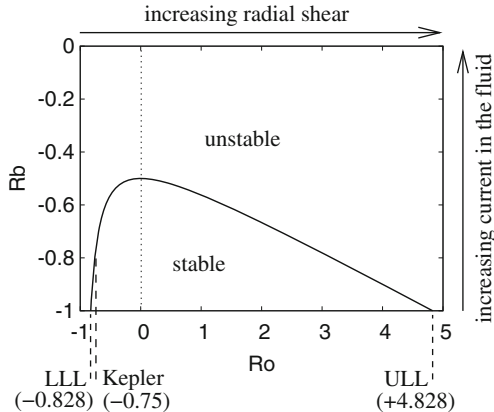


Fig. 5.1 Stability chart in the Ro - Rb plane, for $\text{Pm} = 0$, Ha and Re tending to infinity, and optimized values of β (for HMRI) or α (for AMRI). Stability and instability corresponds to a negative or a positive real part of γ , respectively. The Liu limits LLL and ULL apply only for $\text{Rb} = -1$, while for $\text{Rb} > -1$ shallower shear profiles can also be destabilized (including Kepler rotation starting at $\text{Rb} = 0.78125$). The *dotted line* separates flows with negative shear (to the *left*) and positive shear (to the *right*)

Figure 5.1 shows that the LLL and ULL are just the endpoints of a quasi-hyperbolic curve. At $\text{Rb} = -1/2$ the branches for negative shear $\text{Ro} < 0$ and positive shear $\text{Ro} > 0$ meet each other. We find that in the inductionless case $\text{Pm} = 0$, when the Reynolds and Hartmann numbers tend to infinity in a well-defined manner (Kirillov et al. 2014) and β or n are optimized, the maximum achievable critical Rossby number Ro_{extr} increases with the increase of Rb . At $\text{Rb} \geq -25/32 = -0.78125$, Ro_{extr} would even exceed the critical value for the Keplerian flow. Therefore, the very possibility for $B_\phi(r)$ to depart from the profile $B_\phi(r) \propto r^{-1}$ allows us to break the conventional lower Liu limit and extend the inductionless versions of MRI to velocity profiles $\mathcal{Q}(r)$ as flat as the Keplerian one and even to less steep profiles.

One might ask whether there is any deeper physical sense behind the two Liu limits and the line connecting them. In order to clarify this point, we have investigated in Mamatsashvili and Stefani (2016) the non-modal dynamics of HMRI. This consists in calculating the optimal initial perturbations that lead to the maximum possible linear amplification during some finite time. While in self-adjoint problems the perturbations that undergo the largest amplification are also the most unstable normal modes, in non-self-adjoint shear flow problems, as represented by the operator \mathbf{H} of Eq. (5.11), the normal mode eigenfunctions are nonorthogonal due to the non-normality, resulting in transient, or nonmodal growth of perturbations. For $\text{Pm} \ll 1$ we traced the entire time evolution of the optimal growth of the perturbation energy and demonstrated how the non-modal growth smoothly carries over to the modal behavior at large times. At small and intermediate times, HMRI undergoes a transient amplification. It turned out

that the modal growth rate of HMRI displays a very similar dependence on Ro as the maximum non-modal growth of the purely hydrodynamic shear flow. In particular, the optimized non-modal growth rate G_m turned out to be *identical* at the two Liu limits, namely $G_m = (1 + \text{Ro})^{\text{sign}(\text{Ro})} = 5.828!$ This indicates a fundamental connection between non-modal dynamics and dissipation-induced modal instabilities, such as HMRI. Despite the latter being magnetically triggered, both rely on hydrodynamic means of amplification, i.e., they extract energy from the background flow mainly by Reynolds stress.

5.2.1.3 1D and 3D Simulations

Actually, the apparently simpler WKB analysis of HMRI, AMRI, and TI, as sketched above, was preceded by many detailed 1D and 3D simulations (Hollerbach and Rüdiger 2005; Hollerbach et al. 2010; Rüdiger et al. 2005, 2007). Specifically, the first predictions of HMRI (Hollerbach and Rüdiger 2005; Rüdiger et al. 2005) and AMRI (Hollerbach et al. 2010; Rüdiger et al. 2007) were done with 1D codes solving a linear eigenvalue problem for determining the stability thresholds.

Figure 5.2 shows a recent example for predicting the AMRI experiment at the PROMISE facility (to be discussed below). For the experimentally relevant values $\text{Pm} = 10^{-6}$, $\text{Re} = 3000$, a ratio of outer to inner boundary rotation rates $\mu := f_o/f_i = 0.26$, and varying Ha , the left column shows the normalized growth rate (a), the normalized drift rate (b), and the normalized wave number (c), all obtained with the linear eigenvalue solver (Rüdiger et al. 2014). Evidently, the unstable region extends from $\text{Ha} \approx 80$ to $\text{Ha} \approx 400$. The right column (d) shows the radial magnetic field component of the AMRI pattern, which was computed with the 3D fully non-linear code described in Gellert et al. (2007).

More recent numerical results include the proof that Chandrasekhar's supposedly stable solution (Chandrasekhar 1956), in which the Alfvén velocity of the azimuthal field equals the rotation velocity of the background flow, becomes unstable against non-axisymmetric perturbations when at least one of the diffusivities is finite (Rüdiger et al. 2015). Another example of such (double-)diffusive instabilities is the magnetic destabilization of flows with positive shear (Rüdiger et al. 2016).

5.2.1.4 Turbulent Diffusion

Observations of the present sun with its nearly rigidly rotating core, and of main-sequence stars at late evolutionary stages, lead to the conclusion that a mechanism must exist that transports angular momentum rather effectively outwards. Since the radiative cores are stably stratified, convection is most probably not relevant here. Furthermore, the sought-after mechanism should enhance the transport of chemicals only mildly, with an effective diffusion coefficient D_{turb} exceeding the molecular viscosity by one or two orders of magnitude (Schatzman 1977). The authors of Lebreton and Maeder (1987) considered a relation $D_{\text{turb}} = \text{Re}^* v$ for the diffusion coefficient (after the notation of Schatzman, see Zahn (1990)) with $\text{Re}^* \simeq 100$.

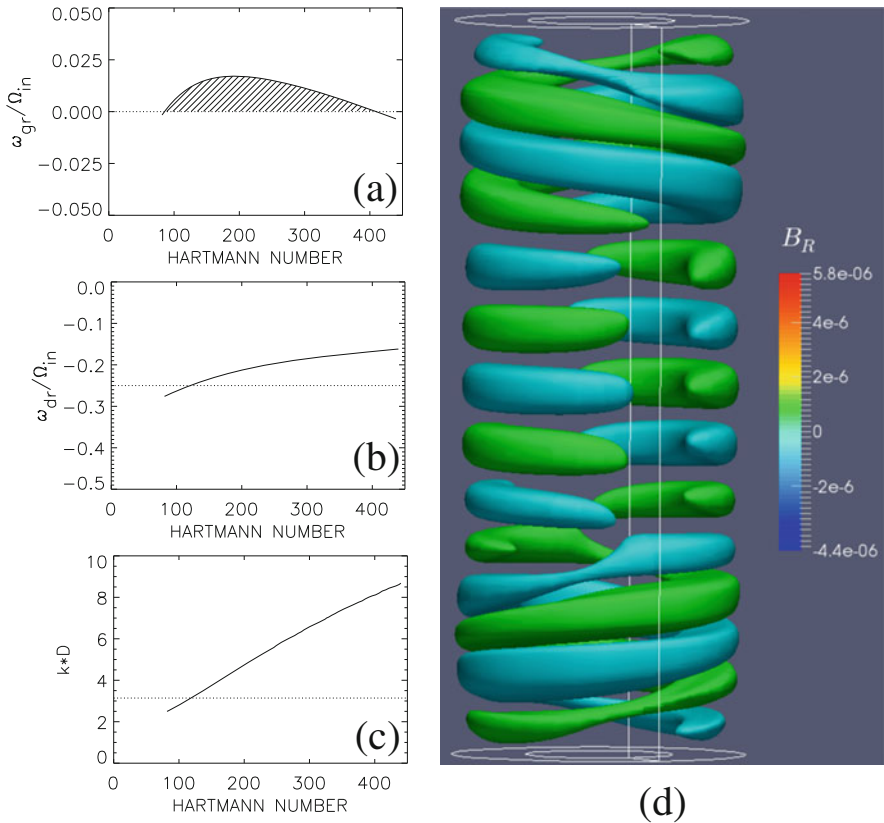


Fig. 5.2 Numerical simulations for the AMRI experiment. *Left:* Results of a 1D linear eigenvalue solver giving the normalized growth rate **(a)**, the normalized drift frequency **(b)**, and the normalized wave number **(c)**. **(d)** Radial magnetic field computed with a 3D nonlinear code, at $Re = 1500$, $Ha = 100$, $\mu = 0.26$, and $Pm = 10^{-5}$ with split end-plates, in units of the applied external field

While it has been known for some time that magnetic instabilities could provide enhanced angular momentum transport (see Rüdiger et al. (2009) and Spada et al. (2016)), we show in the following that it also leads to a Schatzman number Re^* of the correct magnitude.

The numerical model is based on a Taylor-Couette setup with a current-driven magnetic field that becomes unstable due to the Tayler instability. The whole system rotates differentially with a quasi-Keplerian rotation profile ($\mu = 0.354$ for a radius ratio of $r_i/r_o = 0.5$). The most unstable mode is the $m = 1$ that grows and saturates. Now the additional diffusion equation (5.5) is switched on, and the enhanced or turbulent diffusion coefficient D_{turb} due to the TI is measured (in units of the molecular diffusion coefficient D_{mol}) (Paredes et al. 2016).

The resulting ratio D_{turb}/D_{mol} for a fixed Hartmann number is shown in Fig. 5.3a. In the slow rotation regime (with a magnetic Mach number $Mm = Rm/S < 1$, where $S = Pm^{1/2}Ha$ is the Lundquist number), the effective diffusivity hardly

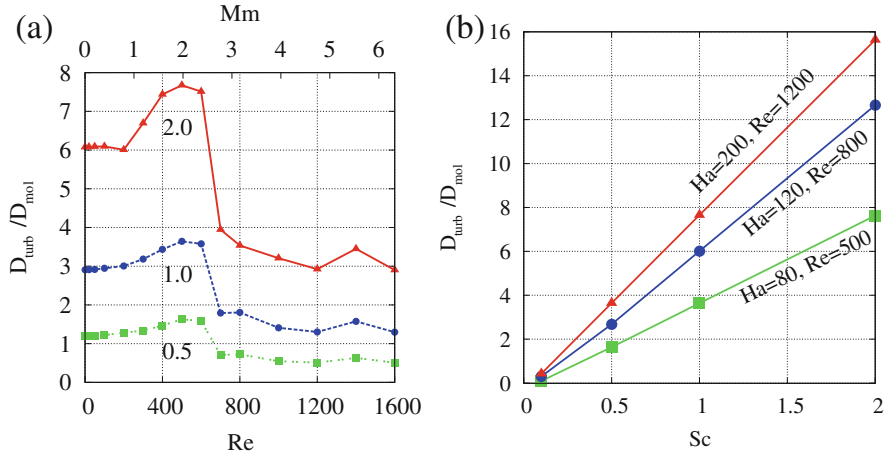


Fig. 5.3 Turbulent contribution to the diffusivity or mixing of TI-unstable flows. (a) Reynolds number dependence of D_{turb} for three values of the Schmidt number $Sc = 0.1/1/2$ with $Ha = 80$, $Pm = 0.1$. The value $Mm = 1$ (top horizontal axis) separates the regimes of slow and fast rotation. Note the reduction of $D_{\text{turb}}/D_{\text{mol}}$ for $Mm > 2$. (b) Schmidt number dependence with increasing slope or Schatzman Re^* . Always $\mu = 0.35$

changes and is very close to the molecular value. In the fast rotation regime, the ratio $D_{\text{turb}}/D_{\text{mol}}$ increases monotonically until it reaches a maximum at about $Mm \simeq 2$. Finally, for faster rotation ($Mm > 2$), the effective diffusivity decreases rapidly due to the usual rotational quenching of non-axisymmetric instabilities and reaches a rather constant value. Nevertheless, the effective normalized diffusivity always increases with increasing Schmidt numbers so that the Schatzman relation $D_{\text{turb}} \propto \nu$ is valid without any influence from the microscopic diffusivity.

Figure 5.3b shows the normalized diffusivity as a function of Sc in the range $0.1 \leq Sc \leq 2$ (for the plasma of the solar tachocline, Gough had estimated a value of $Sc \approx 3$ (Gough 2007)). For all Reynolds numbers, the induced diffusivities D_{turb} are different from zero, and the ratio $D_{\text{turb}}/D_{\text{mol}}$ scales linearly with Sc . The figure only shows the relation for those Reynolds numbers for which the diffusivities reach their maximum at $Mm \approx 2$. For $Sc \rightarrow 0$, the diffusivity D_{turb} vanishes as well. However, the essential result is the linear relation between $D_{\text{turb}}/D_{\text{mol}}$ and Sc for molecular Schmidt numbers $Sc > 0.1$. In the notation of Schatzman this means $D_{\text{turb}} = Re^* \nu$ with the scaling factor Re^* (which indeed forms some kind of Reynolds number). This linear relation holds for all considered Reynolds and Hartmann numbers.

The scaling or *Schatzman* factor Re^* increases with increasing Ha , while for all three shown parameter sets the magnetic Mach number is nearly the same. We find $Re^* \sim 4$ for $Ha = 80$, increasing to $Re^* \sim 8$ for $Ha = 200$. A saturation for larger Ha is indicated by the results presented in Fig. 5.3 and would be of the order of 50, which is indeed the right magnitude of the additional diffusion process acting in

the sun. A more detailed discussion of the applicability of our simulations to solar parameters can be found in Paredes et al. (2016).

5.2.2 Experiments on HMRI

Shortly after the theoretical prediction of HMRI (Hollerbach and Rüdiger 2005) the PROMISE experiment was setup at HZDR. Its heart is a cylindrical vessel made of copper (Fig. 5.4). The inner wall extends in radius from 22 to 32 mm; the outer wall extends from 80 to 95 mm. This vessel is filled with the alloy GaInSn, which is a most convenient medium as it is liquid at room temperatures. The physical properties of GaInSn at 25 °C are: density $\rho = 6.36 \times 10^3 \text{ kg/m}^3$, kinematic viscosity $\nu = 3.40 \times 10^{-7} \text{ m}^2/\text{s}$, electrical conductivity $\sigma = 3.27 \times 10^6 \text{ S/m}$. The magnetic Prandtl number Pm is therefore 1.4×10^{-6} .

The copper vessel is fixed via a spacer on a precision turntable. Hence, the outer wall of the vessel serves also as the outer cylinder of the Taylor-Couette flow. The inner cylinder of the Tayler-Couette flow is fixed to an upper turntable, and is immersed into the GaInSn from above. It has a thickness of 4 mm, extending from 36 to 40 mm. The actual Taylor-Couette flow then extends between $r_i = 40 \text{ mm}$ and $r_o = 80 \text{ mm}$. In the very first setup, PROMISE 1 (Stefani et al. 2006, 2007), the upper end-plate was a plexiglass lid fixed to the frame while the bottom was simply

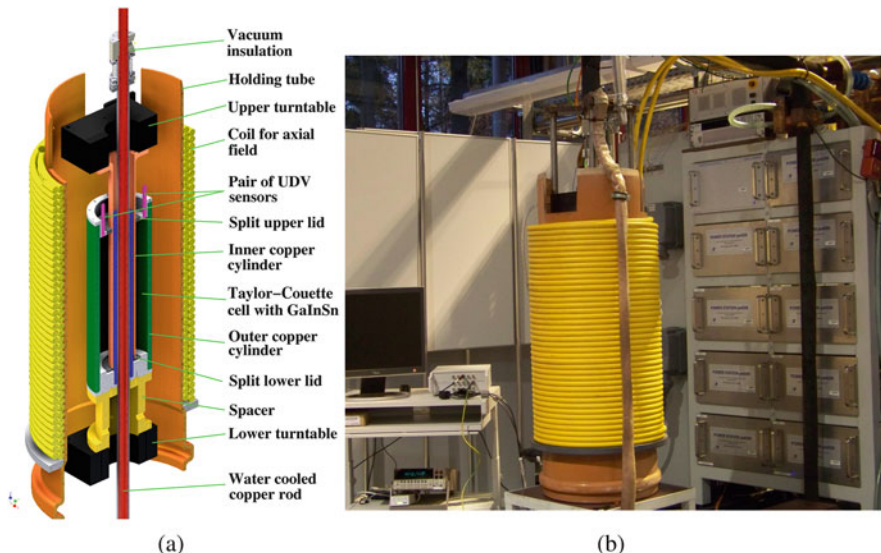


Fig. 5.4 The PROMISE experiment: (a) Schematic sketch of the central Taylor-Couette setup and the coil for producing the axial field. (b) Photograph of the installation, with the 20 kA power supply visible on the right

part of the copper vessel, and hence rotated with the outer cylinder. There was thus a clear asymmetry in the end-plates, with respect to both their rotation rates and electrical conductivity.

In the second version, PROMISE 2 (Stefani et al. 2009), the lid-configuration was significantly improved by using insulating rings both on top and bottom, and by splitting them at a well-defined intermediate radius of 56 mm which had been found in Szklarski (2007) to minimize the Ekman pumping.

With this setup, HMRI has been comprehensively characterized by varying various parameters and comparing the observed travelling wave structure with numerical predictions. The variations included those of the Reynolds number Re , of the ratio $\mu = f_o/f_i$ of rotation rates, of the Hartmann number Ha , and of the ratio β of azimuthal to axial field. Figure 5.5 illustrates a typical result for the latter variation. Fixing $f_i = 0.06\text{ Hz}$, $\mu = 0.26$, $I_{\text{coil}} = 76\text{ A}$, we varied the axial current between 0 and 8.2 kA . Using Ultrasonic Doppler Velocimetry (UDV), we observe a travelling HMRI wave only above 4 kA (Fig. 5.5a). The comparison with numerical predictions is shown in Fig. 5.5b. The two triangles indicate the numerically determined thresholds for the convective and the absolute instability. The match between the experimental and theoretical curves suggests that the observed instability is indeed a global one.

5.2.3 *Experiments on AMRI*

What happens in the PROMISE experiment when we switch off the axial magnetic field? The theoretical predictions for this case have been given in Hollerbach et al. (2010). The axisymmetric ($m = 0$) HMRI is then replaced by the non-axisymmetric ($m = 1$) AMRI. At the same time, the threshold of the Hartmann number increases to 80 which requires a central current of approximately 10 kA (Seilmayer et al. 2014).

In order to explore that parameter region, the power supply for the central rod, restricted previously to 8 kA , was replaced by a new one which is able to deliver 20 kA . Connected with this enhancement of the switching mode power supply, significant effort had to be spent on various issues of electromagnetic interference (Seilmayer et al. 2016) before the (initially extremely noisy) UDV data could be utilized for characterizing the AMRI.

Another problem that became evident when analyzing the data was the factual slight asymmetry of the allegedly axisymmetric field, which results from the one-sided wiring of the central vertical current (Fig. 5.4b). While the observable AMRI structure was originally expected to be similar to that shown in Fig. 5.2d, a more sophisticated numerical analysis revealed the specific effect of the slight symmetry breaking. This is illustrated in Fig. 5.6a, which shows the spatio-temporal structure of the AMRI wave as it would be expected for a perfectly symmetric, purely azimuthal magnetic field produced by infinitely long wire at the central axis. The parameters for this simulations are $Re = 1479$, $Ha = 124$. What comes out here is

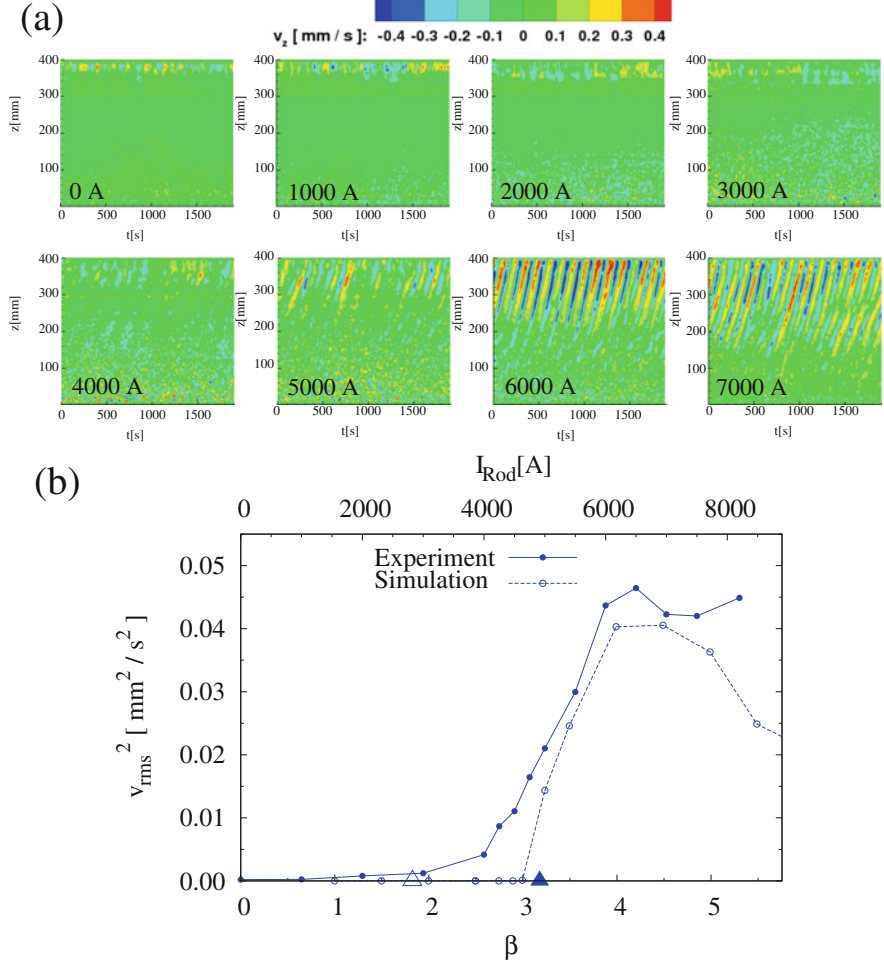


Fig. 5.5 Results of the PROMISE experiment, when varying the axial current. The fixed parameters are $f_i = 0.06 \text{ Hz}$, $f_o = 0.0156 \text{ Hz}$, resulting in $\text{Re} = 1775$ and $\mu = 0.26$, $I_{\text{coil}} = 76 \text{ A}$, giving $\text{Ha} = 12$. **(a)** Measured UDV signals in dependence on time (abscissa) and vertical position (ordinate axis), for eight different axial currents I_{rod} . **(b)** Rms of the perturbation of the axial velocity at the UDV sensor position, in dependence on I_{rod} . The dashed line shows the numerical predictions, the full line shows the experimental results. The triangles give the numerical prediction for the onset of the convective instability (empty triangle) and the absolute instability (full triangle)

a very regular “butterfly” diagram of downward and upward traveling waves, which are concentrated in the upper and lower half of the cylinder, respectively. While in an infinitely long cylinder upward and downward travelling waves should be equally likely, it is the breaking of axial symmetry due to the effect of the end-caps that

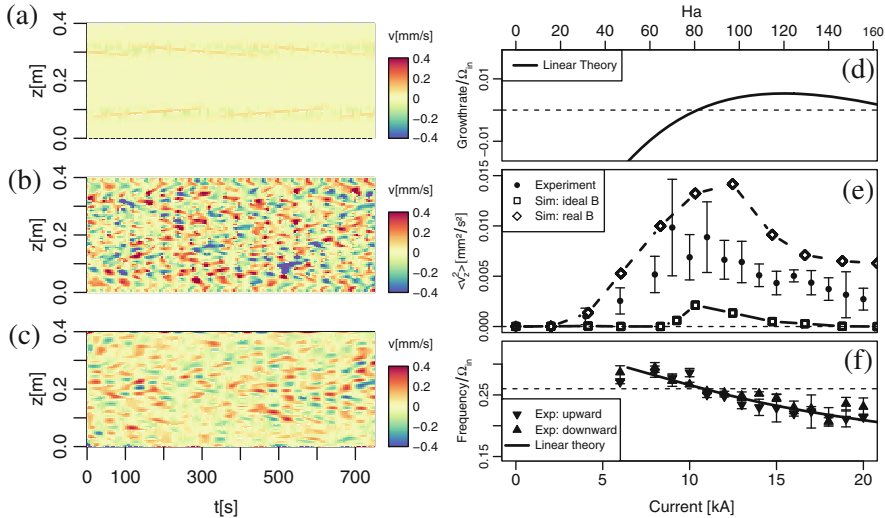


Fig. 5.6 Results of the AMRI experiment. *Left:* Velocity perturbation $v_z(m = 1, z, t)$ for $\mu = 0.26$, $\text{Re} = 1480$, and $\text{Ha} = 124$. (a) Simulation for ideal axisymmetric field. (b) Simulation for realistic field. (c) Experimental results. *Right:* Dependence of various quantities on Ha : (d) Numerically determined growth rate. (e) Mean squared velocity perturbation. (f) Angular drift frequency. In the frequency plot, “upward” and “downward” refer to the travel direction of the AMRI wave. After Seilmayer et al. (2014)

induces a preference for upward or downward travelling waves in the two halves of the vessel.

Interestingly, the effect of this first symmetry breaking in axial direction (due to the end-caps) is neutralized by the second symmetry breaking in azimuthal direction (due to the one sided wiring). As a result, the upward and downward travelling waves interpenetrate each other in the two halves of the cylinder. This effect has been revealed both in a numerical simulation which respects the correct geometry (Fig. 5.6b), and in the experiment (Fig. 5.6c). In Fig. 5.6d–e we summarize the results for varying Hartmann numbers, including the simulated growth rate (d), the measured and predicted rms of the velocity perturbation (e), and the measured and simulated drift frequencies (f).

While the observed and numerically confirmed effects of the double symmetry breaking on the AMRI are interesting in their own right, we have decided to improve the experiment in such a way that the azimuthal symmetry breaking is largely avoided. This is accomplished by a new system of wiring of the central current, comprising now a “pentagon” of five back-wires situated around the experiment. First experiments with this setup show encouraging results. Any details, in particular on the transitions between AMRI and HMRI when cranking up the axial magnetic field, are left for future publications.

5.2.4 Experiments on TI

Imagine the central current used in the AMRI experiment to be complemented, or completely replaced, by a parallel current guided through the fluid column. This current provides a further energy source for instabilities that adds to any prevailing differential rotation. In the limiting case of vanishing differential rotation, the purely current-driven, kink-type Tayler instability (TI) will arrive for sufficiently large currents.

In principle, this effect has been known for a long time in plasma physics, where the (compressible and non-dissipative) counterpart of TI is better known as the kink instability in a z -pinch (Bergerson et al. 2006). In astrophysics, TI has been discussed as a possible ingredient of an alternative, nonlinear stellar dynamo mechanism (Tayler-Spruit dynamo (Spruit 2002; Stefani et al. 2016a)), as a mechanism for generating helicity (Gellert et al. 2008), and as a possible source of helical structures in galactic jets and outflows (Moll et al. 2008). A particular, though non-astrophysical, motivation to study the TI in liquid metals arises from the growing interest in large-scale liquid metal batteries as supposedly cheap storages for renewable energies. Such a battery would consist of a self-assembling stratification of a heavy liquid half-metal (e.g., Bi, Sb) at the bottom, an appropriate molten salt as electrolyte in the middle, and a light alkaline or earth alkaline metal (e.g. Na, Mg) at the top. While small versions of this battery have already been tested (Kim et al. 2013), for larger versions the occurrence of TI could represent a serious problem for the integrity of the stratification (Stefani et al. 2011, 2016; Weber et al. 2013, 2014, 2015).

For liquid metals, TI is expected to set in at an electrical current in the order of one kA. The precise value is a function of various material parameters, since for viscous and resistive fluids the TI is known (Montgomery et al. 2013; Rüdiger et al. 2011; Spies 1988) to depend effectively on the Hartmann number $\text{Ha} = B_\varphi(R)R(\sigma/(\rho v))^{1/2}$, where R is the radius of the column.

Here, we summarize experimental results (Seilmayer et al. 2012) that confirm the numerically determined growth rates of TI (Rüdiger et al. 2011; Stefani et al. 2011) as well as the corresponding prediction that the critical current increases monotonically with the radius of an inner cylinder.

The central part of our TI experiment (Fig. 5.7) is an insulating cylinder of length 75 cm and inner diameter 10 cm, filled again with the eutectic alloy GaInSn. At the top and bottom, the liquid metal column is contacted by two massive copper electrodes of height 9 cm, which are connected by water cooled copper tubes to a DC power supply that is able to provide electrical currents of up to 8 kA. By intensively rubbing the GaInSn into the copper, we have provided a good wetting, making the electrical contact as homogeneous as possible.

For the identification of TI we exclusively relied on the signals of 14 external fluxgate sensors that measure the vertical component B_z of the magnetic field. Eleven of these sensors were aligned along the vertical axis (with a spacing of 7.5 cm), while the remaining three sensors were positioned along the azimuth in

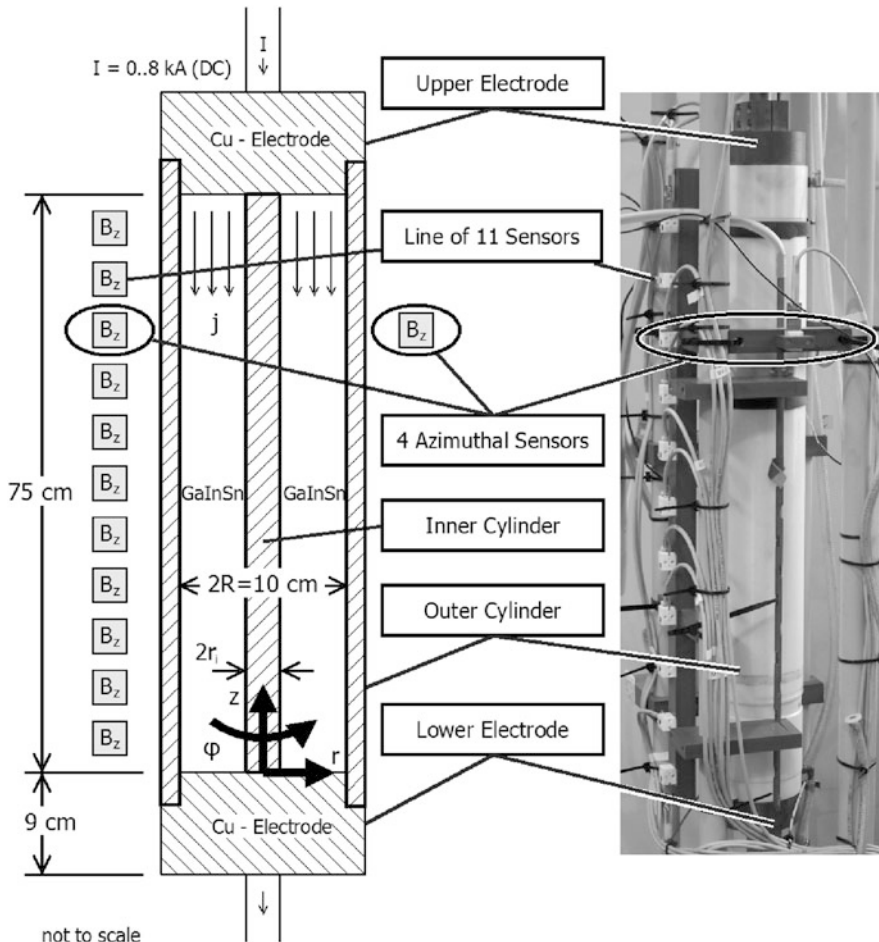
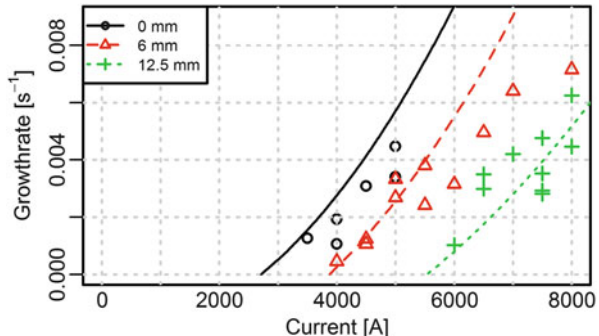


Fig. 5.7 Setup of the TI-experiment. *Left:* Scheme with liquid metal column and fluxgate sensors positioned along the vertical axis and the azimuth. *Right:* Photograph of the central part of the experiment

the upper part, approximately at 15 cm from the top electrode. The distance of the sensors from the outer rim of the liquid metal column was 7.5 cm. This rather large value, which is certainly not ideal to identify small wavelength perturbations, has been chosen in order to prevent saturation of the fluxgate sensors in the strong azimuthal field of the axial current.

One of the main goals of the experiment was to study the influence of the electric current through the fluid on the growth rate and on the amplitude of the magnetic field perturbations. This was done without any insert, as well as for two different radii of an inner non-conducting cylinder, $r_i=6$ mm and 12.5 mm, for which we expect a monotonic increase of the critical current with the radius.

Fig. 5.8 Growth rates of the TI in dependence on the current for three different radii (0, 6, and 12.5 mm) of a central insulating cylinder. The *lines* give the numerical results, the *symbols* show the values inferred from the experiment. After Seilmayer et al. (2012)



In Fig. 5.8 we compile the dependence of the growth rate of the TI on the radius of the inner cylinder and on the current through the fluid, and compare them with the numerically determined growth rates (Rüdiger et al. 2011) for the mode with optimum wavelength (appr. 13 cm). Despite some scatter of the data, we observe a quite reasonable agreement with the numerical predictions.

We have to admit that the realization and the data analysis of the TI experiment was significantly harder than originally envisioned. The main reason is the indirect identification of the TI by the fluxgate sensors along the height of the column and the azimuth. The very weak induced magnetic fields, the slightly under-critical number of sensors, but also the Joule heating due to the high current densities were main obstacles for a clear identification of the TI.

We note that some later experiments using UDV in order to measure directly the axial velocity component along the z -axis did not really solve the problems (Starace et al. 2015). Actually, they even lead to strong electro-vortex flows driven by the inhomogeneous current distribution at the sensor positions which spoiled significantly the previous TI results obtained with a more homogeneous interface between fluid and copper electrodes.

5.3 Instabilities in Spherical Geometry

The terminus spherical Couette flow refers to the fluid motion between two differentially rotating spherical shells. If the liquid is electrically conducting and exposed to an external magnetic field, the setup is sometimes called magnetized spherical Couette flow (MSCF). For resting outer sphere, the system is completely defined by three dimensionless parameters (Rüdiger et al. 2013): the Reynolds number $\text{Re} = \Omega_i r_i^2 / v$ as a measure of the rotation (with angular velocity Ω_i of the inner sphere with radius r_i), the Hartmann number $\text{Ha} = B_0 r_i \sqrt{\sigma / \rho v}$ with B_0 denoting the strength of the applied axial magnetic field, and the geometric aspect ratio $\eta = r_i / r_o$ with the outer sphere radius r_o .

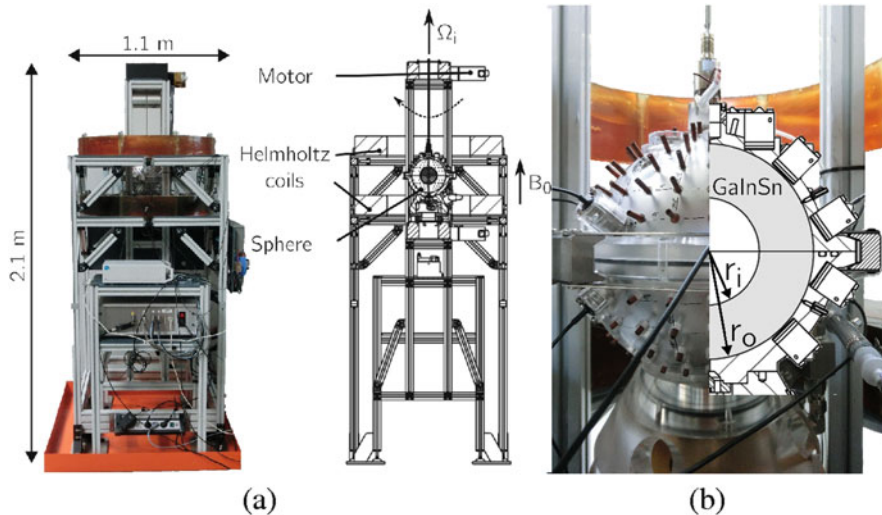


Fig. 5.9 The HEDGEHOG experiment: (a) Photograph and drawing of the facility. (b) Zoom on the spherical Couette module, showing the mountings for the UDV probes and the copper electrodes for electric potential measurements. $r_i = 4.5\text{ cm}$, $r_o = 9\text{ cm}$

Besides its paradigmatic character, the MSCF gained new attention in the astrophysical community as Sisan et al. (2004) had claimed the observation of the MRI on the background of a fully turbulent flow. Later, however, Hollerbach (2009) and Gissinger et al. (2011) interpreted the observed fluctuations just as turbulent analogues of various well-known MSCF instabilities.

In order to clarify this point, the new apparatus HEDGEHOG (*Hydromagnetic Experiment with Differentially Gyrating sphEres HOLDing GaInSn*) has been installed at HZDR (see Fig. 5.9). In contrast to Sisan et al. (2004), HEDGEHOG works in a quasi-laminar regime for which numerical reference data is available for the two particular aspect ratios $\eta = 0.35$ (Hollerbach 2009) and $\eta = 0.5$ (Travnikov et al. 2011).

5.3.1 Numerical Simulations

The experiment has been numerically simulated by two different codes. One is the code described in Hollerbach (2000), which solves for a flow, driven by the rotating inner sphere, according to the incompressible Navier-Stokes Equation including a Lorentz force term. The steady states of the full three-dimensional calculation have the practical use of guiding diagnostic design and expectations for the low Re case. They also demonstrate a saturation mechanism for the instabilities (Kaplan 2014). Complementary to that code, we have also used the Magic code (Wicht 2014),

which has a long and very successful record of simulating dynamos in spherical geometry.

Figure 5.10 shows the stability boundaries and illustrates two typical instabilities, for an MSCF with aspect ratio $\eta = 0.5$. First, Fig. 5.10a shows the boundaries for the different types of instability in dependence on Ha . Actually, the lines have been replotted from Travnikov et al. (2011), although large parts of the diagram were reproduced by Hollerbach's code. The two full circles represent the two distinct types of instability, which are separated by a region of stability. Their spatial character, as simulated by the MagIC code, is illustrated in Fig. 5.10b–e.

At low $\text{Ha} = 5$, the instability arises in the equatorial jet, see Fig. 5.10b, d. It is anti-symmetric with respect to the equator, and characterized by an $m = 3$ azimuthal dependence. At higher $\text{Ha} = 30$, the instability arises along the Shercliff layer, see Fig. 5.10c, e, it is symmetric with respect to the equator, and has an $m = 4$ azimuthal dependence.

5.3.2 The HEDGEHOG Experiment

HEDGEHOG (see Fig. 5.9) consists of one of two optional inner spheres ($r_i = 3$ cm or 4.5 cm) held in the center of an outer sphere ($r_o = 9$ cm). The outer sphere is a Polymethyl Methacrylate (PMMA) acrylic with 30 cylindrical holders for ultrasonic Doppler velocimetry (UDV), and 168 copper electrodes for electric potential measurement.

The space between the spheres is filled with GaInSn. Because of the high density of this medium, each optional inner sphere holds a lead weight to counter the significant buoyancy force which would otherwise require a thicker, flow-disturbing shaft. The axial magnetic field is provided by a pair of copper electromagnets with central radii of 30 cm, with a vertical gap of 31 cm between them (a near Helmholtz configuration). The spheres can be driven with a minimum rotation frequency $f_i = 0.02$ Hz by 90 W electromotors.

The data presented here are based on the velocity acquired from six equally spaced UDV sensors on the northern hemisphere (NH), and from one UDV sensor on the southern hemisphere (SH). This sensor configuration allows to identify (roughly) the azimuthal dependence of the modes and their symmetry properties with respect to the equator.

For low Ha the UDV sensors show an outward directed velocity around the depth of the equatorial plane. This is the radial jet whose instability is known from the purely hydrodynamic case (Hollerbach 2006). Increasing Ha further, the jet is suppressed and a growing area with zero velocity values comes up. At still higher Ha new velocity fluctuations occur close to the tangential cylinder, i.e., at greater depth of the UDV beam.

Using six sensor data in azimuthal direction, according to the Nyquist-Shannon criterion a maximum wave number $m = 3$ can be resolved by Fourier transform. Further to this, the frequency of the equatorially symmetric and anti-symmetric

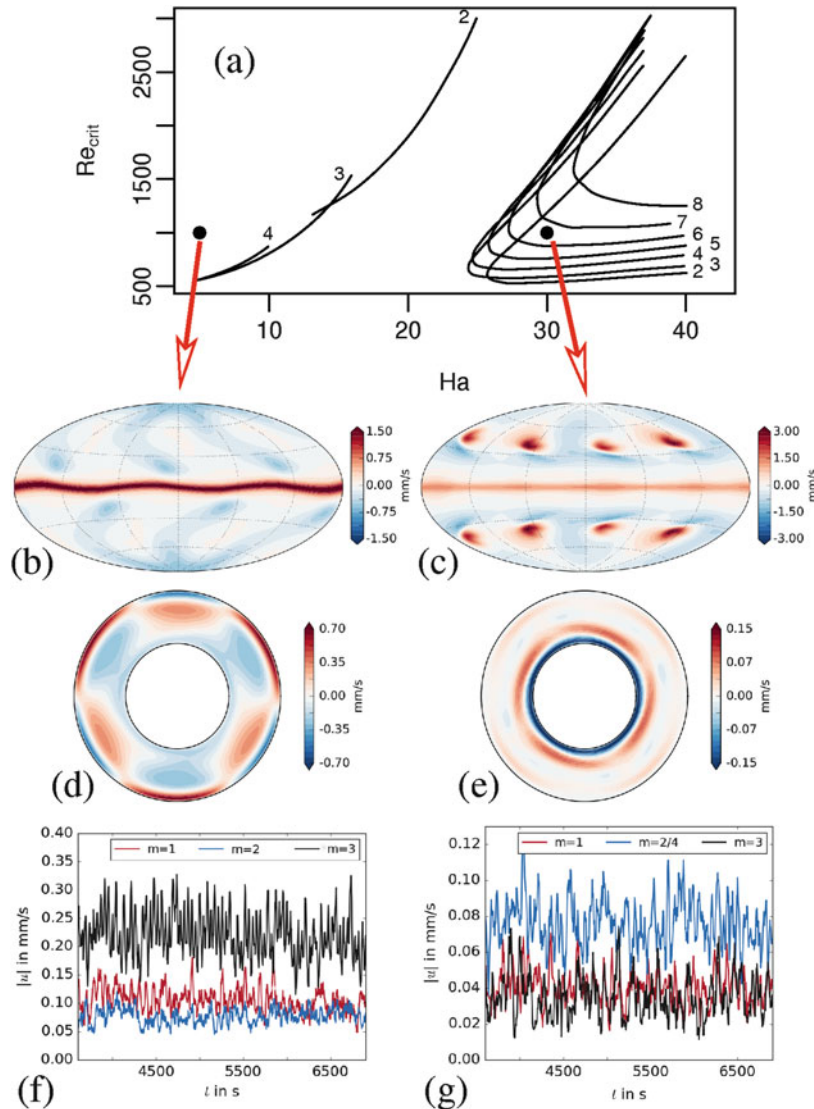


Fig. 5.10 Numerical simulations and experimental results of the HEDGEHOG experiment. (a) Boundaries of instabilities in dependence on Ha and Re , reproduced from Travnikov et al. (2011). Lower left: Jet instability at $Rm = 1000$ and $Ha = 5$. (b) Meridional view of the simulated radial velocity component at $r = 0.85r_o$, showing the anti-symmetric character with respect to the equator. (d) Polar view of the meridional velocity component at $\theta = \pi/2$, showing an $m = 3$ azimuthal dependence. (f) Azimuthal Fourier components of the UDV measured velocity taken at a depth of 25 mm, showing the expected dominance of the $m = 3$ mode. Lower right: Return flow instability at $Rm = 1000$ and $Ha = 30$. (c) Meridional view of the simulated radial velocity component at $r = 0.6r_o$, showing the symmetric character with respect to the equator. (e) Polar view of the meridional velocity component at $\theta = \pi/2$, showing an $m = 4$ azimuthal dependence. (g) Azimuthal Fourier components of the UDV measured velocity taken at a depth of 36 mm, showing the expected dominance of the $m = 4$ mode

velocity parts can be inferred from spectrograms. Using the data from the facing NH and SH UDV pair, the equatorial symmetric part is computed as $(u_{\text{NH}} + u_{\text{SH}})/2$, and the anti-symmetric part as $(u_{\text{NH}} - u_{\text{SH}})/2$. Figure 5.10f shows the Fourier transform of the anti-symmetric part taken at a depth of 25 mm. For this low $\text{Ha} = 5$ we clearly recognize a dominating azimuthal $m = 3$ mode, also with the numerically predicted frequency (not shown here).

At $\text{Ha} = 30$ the instability is distinctly shifted towards the inner sphere and acquires an equatorially symmetric character, which indicates the onset of the return flow instability. Figure 5.10g shows the Fourier transform of the symmetric part taken at a depth of 36 mm. We clearly recognize a dominating azimuthal $m = 4$ mode, also with the numerically predicted frequency.

The wave number and frequency observations at the chosen $\text{Re} = 1000$ and increasing values of Ha are in good agreement with numerical predictions. In future, electric potential measurements will help to resolve the remaining ambiguities with respect to the azimuthal wave number of the observed modes.

5.4 Conclusions and Outlook

Despite the significant theoretical and experimental achievements on the various inductionless forms of shear- or current-driven instabilities, the unambiguous laboratory proof of SMRI is still elusive. In the following we will sketch our plans for a large-scale liquid sodium experiment which is supposed to allow for studying the transition between the inductionless versions such as HMRI and AMRI to SMRI.

Further to this, we will also delineate the prospects for laboratory studies of instabilities of rotating flows with positive shear.

5.4.1 The Large MRI/TI Experiment

The DREsdan Sodium facility for DYNamo and thermohydraulic studies (DRES-DYN) is intended as a platform both for large-scale experiments related to geo- and astrophysics and for experiments related to thermohydraulic and safety aspects of liquid metal batteries and liquid metal fast reactors. The most ambitious project in the framework of DRESDyn is a homogeneous hydromagnetic dynamo driven solely by precession (Stefani et al. 2012, 2015).

A second large-scale experiment relevant to geo- and astrophysics will investigate combinations of different versions of the MRI with the current-driven TI (see Fig. 5.11). Basically, the setup is designed as a Taylor-Couette experiment with 2 m height, an inner radius $r_i = 20$ cm and an outer radius $r_o = 40$ cm. Rotating the inner cylinder at up to 20 Hz, we plan to reach $\text{Rm} \sim 40$, while the maximum axial magnetic field $B_z = 120$ mT will correspond to a Lundquist number

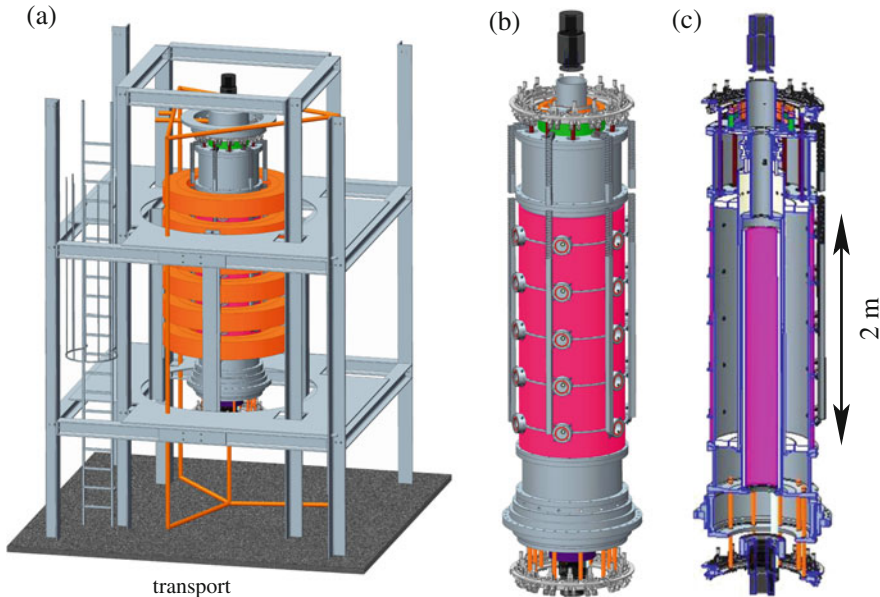


Fig. 5.11 Drawings of the combined MRI/TI experiment as planned in the framework of the DRESDYN project. (a) Total view. (b) Central module from outside. (c) Central module from inside

$S := Pm^{1/2}Ha \sim 8$. Both values are about twice their respective critical values for SMRI as they were derived in Rüdiger and Shalybkov (2003).

Below those critical values, we plan to investigate how the helical version of MRI approaches the limit of SMRI (Hollerbach and Rüdiger 2005). To this end, we will use a strong central current, as it was already done in the PROMISE experiment (Seilmayer et al. 2014; Stefani et al. 2009). This insulated central current can be supplemented by another axial current guided through the (rotating) liquid sodium, which will then allow to investigate arbitrary combinations of MRI and TI. As discussed in Sect. 5.2, theoretical studies (Kirillov and Stefani 2013; Kirillov et al. 2014) have shown that even a slight addition of current through the liquid would extend the range of application of the helical and azimuthal MRI to Keplerian flow profiles.

5.4.2 Positive Shear Instabilities

The last remarks refer to flows with positive Ro , i. e. flows whose angular velocity (not only the angular momentum) is increasing outward. From the purely hydrodynamic point of view, such flows are linearly stable (while non-linear instabilities

were actually observed in experiments (Tsukahara et al. 2010)). Flows with positive Ro are indeed relevant for the equator-near strip (approximately between $\pm 30^\circ$) of the solar tachocline (Parfrey and Menou 2007), which is, interestingly, also the region of sunspot activity (Charbonneau 2010).

As discussed in Sect. 5.2, a first hint on a magnetic destabilization of flows with $\text{Ro} > \text{Ro}_{\text{ULL}}$ was given in the paper Liu et al. (2006) for the case of a helical magnetic field. For a purely azimuthal field, a similar effect was found both in the framework of WKB approximation (Stefani and Kirillov 2015) as well as by a 1D modal stability analysis (Rüdiger et al. 2016).

What are the prospects for an experiment that could show a magnetic destabilization of positive shear flows? The WKB analysis in Stefani et al. (2015) has revealed the need for a rather narrow gap flow which necessarily leads to comparable high axial currents. For a prospective Taylor-Couette experiment using Na with an outer diameter of $r_o = 0.25$ m, and choosing $\eta = 0.85$, those values would be $\text{Re} = 1898$, $\text{Ha} = 892$ which amounts to physical values of $f_o = 0.022$ Hz, and $B_\phi(r_i) = 77$ mT, requiring a central current of 82 kA !

The 1D simulations of Rüdiger et al. (2016) predicted more optimistic values in the order of 30 kA when the radial boundaries were considered as ideally conducting. It remains to be shown by careful numerical studies what are the real critical currents for an optimized laboratory implementation when realistic conductivity ratios between the liquid (sodium) and the wall material (copper) are taken into account.

Acknowledgements This work was supported by Deutsche Forschungsgemeinschaft in the frame of the focus programme 1488 (PlanetMag). Intense collaboration with Rainer Hollerbach on the theory and numerics of the different instabilities is gratefully acknowledged. We thank Thomas Gundrum for his contributions in setting up and running the experiments, and Elliot Kaplan for his numerical and experimental work on the HEDGEHOG experiment. We are grateful to Johannes Wicht for the introduction into the MagIC code. F.S. likes to thank Oleg Kirillov for his efforts to establish a comprehensive WKB theory of the magnetically triggered instabilities, and George Mamatsashvili for his work on non-modal aspects of MRI.

References

- Adams, M.M., Stone, D.R., Zimmerman, D.S., Lathrop, D.P.: Liquid sodium models of the Earth's core. *Prog. Earth Planet. Sci.* **29**, 1–18 (2015).
- Balbus, S.A.: Enhanced angular momentum transport in accretion disks. *Ann. Rev. Astron. Astrophys.* **41**, 555–597 (2003)
- Benzi, R., Pinton, J.-F.: Magnetic reversals in a simple model of magnetohydrodynamics. *Phys. Rev. Lett.* **105**, 024501 (2010)
- Bergerson, W.F., Hannum, D.A., Hegna, C.C., Kendrick, R.D., Sarff, J.S., Forest, C.B.: Onset and saturation of the kink instability in a current-carrying line-tied plasma. *Phys. Rev. Lett.* **96**, 015004 (2006)
- Berhanu, M., et al.: Dynamo regimes and transitions in the VKS experiment. *Eur. Phys. J. B* **77**, 459–468 (2010)

- Chandrasekhar, S.: On the stability of the simplest solution of the equations of hydromagnetics. *Proc. Natl. Acad. Sci. U. S. A.* **42**, 273–276 (1956)
- Charbonneau, P.: Dynamo models of the solar cycle. *Liv. Rev. Sol. Phys.* **7**, 3 (2010)
- Cooper, C.M., et al.: The Madison plasma dynamo experiment: a facility for studying laboratory plasma astrophysics. *Phys. Plasmas* **21**, 013505 (2014)
- Dormy, E.: Strong-field spherical dynamos. *J. Fluid Mech.* **789**, 500–513 (2016)
- Gailitis, A., Lielausis, O., Dement'ev, S., Platacis, E., Cifersons, A., Gerbeth, G., Gundrum, T., Stefani, F., Christen, M., Hänel, H., Will, G.: Detection of a flow induced magnetic field eigenmode in the Riga dynamo facility. *Phys. Rev. Lett.* **84**, 4365–4369 (2000)
- Gailitis, A., Lielausis, O., Platacis, E., Gerbeth, G., Stefani, F.: Laboratory experiments on hydromagnetic dynamos, *Rev. Mod. Phys.* **74**, 973–990 (2002)
- Gellert, M., Rüdiger, G., Fournier, A.: Energy distribution in nonaxisymmetric magnetic Taylor-Couette flow. *Astron. Nachr.* **328**, 1162–1165 (2007)
- Gellert, M., Rüdiger, G., Elstner, D.: Helicity generation and alpha-effect by Tayler instability with z-dependent differential rotation. *Astron. Astrophys.* **479**, L33–L36 (2008)
- Giesecke, A., Stefani, F., Gerbeth, G.: Role of soft-iron impellers on the mode selection in the von-Karman-sodium dynamo experiment. *Phys. Rev. Lett.* **104**, 044503 (2010)
- Giesecke, A., Nore, C., Stefani, F., Gerbeth, G., Léorat, J., Herremans, W., F., Guermond, J.-L.: Influence of high-permeability discs in an axisymmetric model of the Cadarache dynamo experiment. *New J. Phys.* **14**, 053005 (2012)
- Gissinger, C., Ji, H., Goodman, J.: Instabilities in magnetized spherical Couette flow. *Phys. Rev. E* **84**, 026308 (2011)
- Gough, D.: An introduction to the solar tachocline. In: Hughes, D.W., Rosner, R., Weiss, N.O. (eds.) *The Solar Tachocline*, pp. 3–30. Cambridge University Press, Cambridge (2007)
- Hollerbach, R.: A spectral solution of the magneto-convection equations in spherical geometry. *Int. J. Num. Meth. Fluids* **32**, 773–797 (2000)
- Hollerbach, R.: Non-axisymmetric instabilities in basic state spherical Couette flow. *Fluid. Dyn. Res.* **38**, 257–273 (2006)
- Hollerbach, R.: Non-axisymmetric instabilities in magnetic spherical Couette flow. *Proc. R. Soc. A* **465**, 2003–2013 (2009)
- Hollerbach, R., Rüdiger, G.: New type of magnetorotational instability in cylindrical Taylor-Couette flow. *Phys. Rev. Lett.* **95**, 124501 (2005)
- Hollerbach, R., Teeluck, V., Rüdiger, G.: Nonaxisymmetric magnetorotational instabilities in cylindrical Taylor-Couette flow. *Phys. Rev. Lett.* **104**, 044502 (2010)
- Jones, C.A.: Planetary magnetic fields and dynamos. *Ann. Rev. Fluid Mech.* **43**, 583–614 (2011)
- Kaplan, E.: Saturation of nonaxisymmetric instabilities of magnetized spherical Couette flow. *Phys. Rev. E* **89**, 063016 (2014)
- Kim, H. et al.: Liquid metal batteries: past, present, and future. *Chem. Rev.* **113**, 2075–2099 (2013)
- Kirillov, O.N., Stefani, F.: On the relation of standard and helical magnetorotational instability. *Astrophys. J.* **712**, 52–68 (2010)
- Kirillov, O.N., Stefani, F.: Paradoxes of magnetorotational instability and their geometrical resolution. *Phys. Rev. E* **84**, 036304 (2011)
- Kirillov, O.N., Stefani, F.: Extending the range of the inductionless magnetorotational instability. *Phys. Rev. Lett.* **111**, 061103 (2013)
- Kirillov, O.N., Stefani, F., Fukumoto, Y.: A unifying picture of helical and azimuthal magnetorotational instability, and the universal significance of the Liu limit. *Astrophys. J.* **756**, 83 (2012)
- Kirillov, O.N., Stefani, F., Fukumoto, Y.: Local instabilities in magnetized rotational flows: a short-wavelength approach. *J. Fluid Mech.* **760**, 591–633 (2014)
- Lathrop, D.P., Forest, C.B.: Magnetic dynamos in the lab. *Phys. Today* **64**, 40–45 (2011)
- Lebreton, Y., Maeder, A.: Stellar evolution with turbulent diffusion mixing. VI - The solar model, surface Li-7, and He-3 abundances, solar neutrinos and oscillations. *Astron. Astrophys.* **175**, 99 (1987)
- Liú, W., Goodman, J., Herron, I., Ji, H.: Helical magnetorotational instability in magnetized Taylor-Couette flow. *Phys. Rev. E* **74**, 056302 (2006)

- Liu, W., Goodman, J., Ji, H.: Traveling waves in a magnetized Taylor-Couette flow. *Phys. Rev. E* **76**, 016310 (2007)
- Mamatsashvili, G., Stefani, F.: Linking dissipation-induced instabilities with nonmodal growth: the case of helical magnetorotational instability. *Phys. Rev. E* **76**, 016310 (2016)
- Moll, R., Spruit, H.C., Obergaulinger, M.: Kink instabilities in jets from rotating magnetic fields. *Astron. Astrophys.* **492**, 621–630 (2008)
- Montgomery, D.: Hartmann, Lundquist, and Reynolds: the role of dimensionless numbers in nonlinear magnetofluid behavior. *Phys. Rev. E* **87**, 012108 (2013)
- Mori, N., Schmitt, D., Wicht, J., Ferriz-Mas, A., Mouri, H., Nakamichi, A., Morikawa, M.: Domino model for geomagnetic field reversals. *Phys. Rev. E* **87**, 012108 (2013)
- Nore, C., Quiroz, D.C., Cappanera, L., Guermond, J.L.: Direct numerical simulation of the axial dipolar dynamo in the Von Kármán Sodium experiment. *Europhys. Lett.* **114**, 65002 (2016)
- Nornberg, M.D., Ji, H., Schartman, E., Roach, A., Goodman, J.: Observation of magnetocoriolis waves in a liquid metal Taylor-Couette experiment. *Phys. Rev. Lett.* **104**, 074501 (2010)
- Paredes, A., Gellert, M., Rüdiger, G.: Mixing of a passive scalar by the instability of a differentially rotating axial pinch. *Astron. Astrophys.* **588**, A147 (2016)
- Parfrey, K.P., Menou, K.: The origin of solar activity in the tachocline: *Astrophys. J. Lett.* **667**, L207 (2007)
- Petitdemange, L.: Two-dimensional non-linear simulations of the magnetostrophic magnetorotational instability. *Geophys. Astrophys. Fluid Dyn.* **104**, 287–299 (2010)
- Petitdemange, L., Dormy, E., Balbus, S.A.: Magnetostrophic MRI in the Earth's outer core. *Geophys. Res. Lett.* **35**, L15305 (2008)
- Petrelis, F., Fauve, S., Dormy, E., Valet, J.-P.: Simple mechanism for reversals of Earth's magnetic field. *Phys. Rev. Lett.* **102**, 144503 (2009)
- Priede, J., Gerbeth, G.: Absolute versus convective helical magnetorotational instability in a Taylor-Couette flow. *Phys. Rev. E* **79**, 046310 (2009)
- Reuter, K., Jenko, F., Tilgner, A., Forest, C.B.: Wave-driven dynamo action in spherical magnetohydrodynamic systems. *Phys. Rev. E* **80**, 056304 (2009)
- Roach, A.H., Spence, E.J., Gissinger, C., Edlund, E.M., Sloboda, P., Goodman, J., Ji, H.: Observation of a free-Shercliff-layer instability in cylindrical geometry. *Phys. Rev. Lett.* **108**, 154502 (2012)
- Rüdiger, G., Shalybkov, D.: Linear magnetohydrodynamic Taylor-Couette instability for liquid sodium. *Phys. Rev. E* **67**, 046312 (2003)
- Rüdiger, G., Hollerbach, R., Schultz, M., Shalybkov, D.: The stability of MHD Taylor-Couette flow with current-free spiral magnetic fields between conducting cylinders. *Astron. Nachr.* **326**, 409–413 (2005)
- Rüdiger, G., Hollerbach, R., Schultz, M., Elstner, D.: Destabilization of hydrodynamically stable rotation laws by azimuthal magnetic fields. *Mon. Not. R. Astron. Soc.* **377**, 1481–1487 (2007)
- Rüdiger, G., Gellert, M., Schultz, M.: Eddy viscosity and turbulent Schmidt number by kink-type instabilities of toroidal magnetic fields. *Mon. Not. R. Astron. Soc.* **399**, 996–1004 (2009)
- Rüdiger, G., Schultz, M., Gellert, M.: The Tayler instability of toroidal magnetic fields in a columnar gallium experiment. *Astron. Nachr.* **332**, 17–23 (2011)
- Rüdiger, G., Hollerbach, R., Kitchatinov, L.L.: *Magnetic Processes in Astrophysics: Theory, Simulations, Experiments*. Wiley-VCH, Weinheim (2013)
- Rüdiger, G., Gellert, M., Schultz, M., Hollerbach, R., Stefani, F.: Astrophysical and experimental implications from the magnetorotational instability of toroidal fields. *Mon. Not. R. Astron. Soc.* **438**, 271–277 (2014)
- Rüdiger, G., Schultz, M., Stefani, F., Mond, M.: Diffusive magnetohydrodynamic instabilities beyond the Chandrasekhar theorem. *Astrophys. J.* **811**, 84 (2015)
- Rüdiger, G., Schultz, M., Gellert, M., Stefani, F.: Subcritical excitation of the current-driven Tayler instability by super-rotation. *Phys. Fluids* **28**, 014105 (2016)
- Schatzman, E.: Turbulent transport and lithium destruction in main sequence stars. *Astron. Astrophys.* **56**, 211 (1977)

- Schmitt, D., Cardin, P., La Rizza, P., Nataf, H.C.: Magneto-Coriolis waves in a spherical Couette flow experiment. *Eur. J. Phys. B - Fluids* **37**, 10–22 (2013)
- Seilmayer, M., Stefani, F., Gundrum, T., Weier, T., Gerbeth, G.: Experimental evidence for a transient Tayler instability in a cylindrical liquid-metal column. *Phys. Rev. Lett.* **108**, 244501 (2012)
- Seilmayer, M., Galindo, V., Gerbeth, G., Gundrum, T., Stefani, F., Gellert, M., Rüdiger, G., Schultz, M.: Experimental evidence for nonaxisymmetric magnetorotational instability in a rotating liquid metal exposed to an azimuthal magnetic field. *Phys. Rev. Lett.* **113**, 024505 (2014)
- Seilmayer, M., Gundrum, T., Stefani, F.: Noise reduction of ultrasonic Doppler velocimetry in liquid metal experiments with high magnetic fields. *Flow Meas. Instrum.* **48**, 74–80 (2016)
- Sisan, D.R., Mujica, N., Tillotson, W.A., Huang, Y.M., Dorland, W., Hassam, A.B., Lathrop, D.P.: Experimental observation and characterization of the magnetorotational instability. *Phys. Rev. Lett.* **93**, 114502 (2004)
- Sorriso-Valvo, L., Stefani, F., Carbone, V., Nigro, G., Lepreti, F., Vecchio, A., Veltri, P.: A statistical analysis of polarity reversals of the geomagnetic field. *Phys. Earth Planet. Inter.* **164**, 197–207 (2007)
- Spada, F., Gellert, M., Arlt, R., Deheuvels, S.: Angular momentum transport efficiency in post-main sequence low-mass stars. *Astron. Astrophys.* **589**, A23 (2016)
- Spies, G.O.: Visco-resistive stabilization of kinks with short wavelengths along an elliptic magnetic stagnation line. *Plasma Phys. Controlled Fusion* **30**, 1025–1037 (1988)
- Spruit, H.C.: Dynamo action by differential rotation in a stably stratified stellar interior. *Astron. Astrophys.* **381**, 923–932 (2002).
- Sreenivasan, B., Jones, C.A.: Helicity generation and subcritical behaviour in rapidly rotating dynamos. *J. Fluid Mech.* **688**, 5–30 (2011)
- Starace, M., Weber, N., Seilmayer, M., Kasprzyk, C., Weier, T., Stefani, F., Eckert, S.: Ultrasound Doppler flow measurement in a liquid metal columns under the influence of a strong axial electric current. *Magnetohydrodynamics* **51**, 249–256 (2015)
- Stefani, F., Kirillov, O.N.: Destabilization of rotating flows with positive shear by azimuthal magnetic fields. *Phys. Rev. E* **92**, 051001 (2015)
- Stefani, F., Gundrum, T., Gerbeth, G., Rüdiger, G., Schultz, M., Szklarski, J., Hollerbach, R.: Experimental evidence for magnetorotational instability in a Taylor-Couette flow under the influence of a helical magnetic field. *Phys. Rev. Lett.* **97**, 184502 (2006)
- Stefani, F., Gerbeth, G., Günther, U., Xu, M.: Why dynamos are prone to reversals. *Earth Planet. Sci. Lett.* **243**, 828–840 (2006)
- Stefani, F., Gundrum, T., Gerbeth, G., Rüdiger, G., Szklarski, J., Hollerbach, R.: Experiments on the magnetorotational instability in helical magnetic fields. *New J. Phys.* **9**, 295 (2007)
- Stefani, F., Gailitis, A., Gerbeth, G.: Magnetohydrodynamic experiments on cosmic magnetic fields. *Zeitschr. Angew. Math. Mech.* **88**, 930–954 (2008)
- Stefani, F., Giesecke, A., Gerbeth, G.: Numerical simulations of liquid metal experiments on cosmic magnetic fields. *Theor. Comp. Fluid Dyn.* **23**, 405–429 (2009)
- Stefani, F., Gerbeth, G., Gundrum, T., Hollerbach, R., Priede, J., Rüdiger, G., Szklarski, J.: Helical magnetorotational instability in a Taylor-Couette flow with strongly reduced Ekman pumping. *Phys. Rev. E* **80**, 066303 (2009)
- Stefani, F., Weier, T., Gundrum, T., Gerbeth, G.: How to circumvent the size limitation of liquid metal batteries due to the Tayler instability. *Energy Convers. Manage.* **52**, 2982–2986 (2011)
- Stefani, F., Eckert, S., Gerbeth, G., Giesecke, A., Gundrum, T., Steglich, C., Wustmann, B.: DRESDYN - a new facility for MHD experiments with liquid sodium. *Magnetohydrodynamics* **48**, 103–113 (2012)
- Stefani, F., Albrecht, T., Gerbeth, G., Giesecke, A., Gundrum, T., Herault, J., Nore, C., Steglich, C.: Towards a precession driven dynamo experiment. *Magnetohydrodynamics* **51**, 275–284 (2015)
- Stefani, F., Galindo, V., Kasprzyk, C., Landgraf, S., Seilmayer, M., Starace, M., Weber, N., Weier, T.: Magnetohydrodynamic effects in liquid metal batteries. *IOP Conf. Ser.: Mater. Sci. Eng.* **143**, 012024 (2016)

- Stefani, F., Giesecke, A., Weber, N., Weier, T.: Synchronized helicity oscillations: a link between planetary tides and the solar cycle? *Solar Phys.* **291**, 2197–2212 (2016)
- Stieglitz, R., Müller, U.: Experimental demonstration of a homogeneous two-scale dynamo. *Phys. Fluids* **13**, 561–564 (2001)
- Szklarski, J.: Reduction of boundary effects in the spiral MRI experiment PROMISE. *Astron. Nachr.* **328**, 499–506 (2007)
- Taylor, R.J.: Adiabatic stability of stars containing magnetic fields. I. Toroidal fields. *Mon. Not. R. Astron. Soc.* **161**, 365–380 (1973)
- Tilgner, A.: Dynamo action with wave motion. *Phys. Rev. Lett.* **100**, 128501 (2008)
- Travnikov, V., Eckert, K., Odenbach, S.: Influence of an axial magnetic field on the stability of spherical Couette flows with different gap widths. *Acta Mech.* **219**, 255–268 (2011)
- Tsukahara, T., Tillmark, N., Alfredsson, P.H.: Flow regimes in a plane Couette flow with system rotation. *J. Fluid Mech.* **648**, 5–33 (2010)
- Weber, N., Galindo, V., Stefani, F., Weier, T.: Numerical simulation of the Tayler instability in liquid metals. *J. Power Sources* **15**, 043034 (2013)
- Weber, N., Galindo, V., Stefani, F., Weier, T.: Current-driven flow instabilities in large-scale liquid metal batteries, and how to tame them. *J. Power Sources* **265**, 166–173 (2014)
- Weber, N., Galindo, V., Stefani, F., Weier, T.: The Tayler instability at low magnetic Prandtl numbers: between chiral symmetry breaking and helicity oscillations. *New J. Phys.* **17**, 113013 (2015)
- Wicht J.: Flow instabilities in the wide-gap spherical Couette system. *J. Fluid Mech.* **738**, 184–221 (2014)
- Wicht J., Tilgner, A.: Theory and modeling of planetary dynamos. *Space Sci. Rev.* **152**, 501–542 (2010)
- Zahn, J.P.: In: Goupil, M.-J., Zahn, J.-P. (eds.) *Rotation and Mixing in Stellar Interiors. Lecture Notes of Physics*, vol. 336, p. 141. Springer, New York (1990)
- Zimmermann, D.S., Triana, S.A., Nataf, H.-C., Lathrop, D.P.: A turbulent, high magnetic Reynolds number experimental model of Earth's core. *J. Geophys. Res. - Sol. Earth* **119**, 4538–4557 (2010)

Chapter 6

Modeling Magnetospheric Fields in the Jupiter System

Joachim Saur, Emmanuel Chané, and Oliver Hartkorn

Abstract The various processes which generate magnetic fields within the Jupiter system are exemplary for a large class of similar processes occurring at other planets in the solar system, but also around extrasolar planets. Jupiter's large internal dynamo magnetic field generates a gigantic magnetosphere, which in contrast to Earth's magnetosphere is strongly rotational driven and possesses large plasma sources located deeply within the magnetosphere. The combination of the latter two effects is the primary reason for Jupiter's main auroral ovals. Jupiter's moon Ganymede is the only known moon with an intrinsic dynamo magnetic field, which generates a mini-magnetosphere located within Jupiter's larger magnetosphere including two auroral ovals. Ganymede's mini-magnetosphere is qualitatively different compared to the one from Jupiter. It possesses no bow shock but develops pronounced Alfvén wings similar to most of the extrasolar planets which orbit their host stars within 0.1 AU. New numerical models of Jupiter's and Ganymede's magnetospheres presented here provide quantitative insight into these magnetospheres and the processes which maintain them. Jupiter's magnetospheric field is time-variable on various scales. At the locations of Jupiter's moons time-periodic magnetic fields induce secondary magnetic fields in electrically conductive layers such as subsurface oceans. In the case of Ganymede, these secondary magnetic fields influence the oscillation of the location of its auroral ovals. Based on dedicated Hubble Space Telescope observations, an analysis of the amplitudes of the auroral oscillations provides evidence that Ganymede harbors a subsurface ocean. Callisto in contrast does not possess a mini-magnetosphere, but still shows a perturbed magnetic field environment generated by induction within an electrically conductive layer and due to the plasma interactions with its atmosphere. Callisto's ionosphere and atmospheric UV emission is different compared to the other Galilean satellites

J. Saur (✉) • O. Hartkorn

Institute of Geophysics and Meteorology, University of Cologne, Albertus Magnus Platz,
50937 Cologne, Germany

e-mail: saur@geo.uni-koeln.de; hartkorn@geo.uni-koeln.de

E. Chané

Centre for Mathematical Plasma Astrophysics, KU Leuven, Celestijnenlaan 200B, 3001 Leuven,
Belgium

e-mail: emmanuel.chane@kuleuven.be

as it has primarily been generated by solar photons compared to magnetospheric electrons. At Callisto a fluid-kinetic model of the ionospheric electron distribution provides constraints on Callisto's oxygen atmosphere.

6.1 Introduction

The plasma interactions in and around Jupiter's magnetosphere and around Jupiter's moons are so rich in various phenomena that a huge class of interactions occurring at other planetary bodies in the solar system and at extrasolar planets are represented by the processes in the Jupiter system. In this chapter, we will present results of new models of the interaction of Jupiter's magnetosphere with the solar wind and interactions at the Galilean moons with particular focus on Ganymede and Callisto.

Jupiter is the largest planet with the largest magnetic moment in the solar system. Its interaction with the solar wind generates a planetary magnetosphere, which would appear to an observer on Earth larger compared to how the sun appears to us in the sky if Jupiter's magnetosphere could be seen with the naked eye. The four large Galilean moons, Io, Europa, Ganymede, and Callisto are all located within Jupiter's gigantic magnetosphere, and are subject to the interactions generated by Jupiter's magnetospheric plasma. The interaction at these moons differs due to the different properties of the moons. For example, Ganymede possesses an internal dynamo magnetic field which leads to its own mini-magnetosphere within Jupiter's magnetosphere. The other moons in contrast only possess weak internal magnetic fields generated by electromagnetic induction in electrically conductive layers.

In the next Sect. 6.2 we categorize the plasma interactions in Jupiter's magnetosphere based on various parameters. With this background we then describe the interaction of the solar wind with Jupiter in order to better understand Jupiter's magnetosphere (see Sect. 6.3). In the subsequent Sect. 6.4 we investigate time-variable effects in Jupiter's magnetosphere, which can be subdivided into periodic and non-periodic variabilities. The associated time-variable magnetic fields induce secondary magnetic fields in electrically conductive layers within the moons. Measurements of these induced fields are diagnostic of internal layers, such as saline subsurface oceans. The plasma of Jupiter's magnetosphere interacts with the atmospheres and ionospheres and the interior of the moons. Properties of this interaction, the formation of the ionospheres and the generation of related magnetic fields will be discussed for Ganymede and Callisto in Sects. 6.5 and 6.7. A novel technique to search for induced magnetic fields from a subsurface ocean within Ganymede based on Hubble Space Telescope observations of its auroral ovals is described in Sect. 6.6.

6.2 Characterization and Description of the Interaction

The plasma interactions of flows past planetary bodies can be characterized into different classes, which we discuss in the next subsection. Afterwards we provide an overview of the magnetohydrodynamic (MHD) approach to describe these interactions.

6.2.1 Overview of the Interaction

The interaction of a planetary body with its surrounding plasma is controlled by two factors: (1) the properties of the plasma flowing past the planetary object (discussed in Sect. 6.2.1.1) and (2) the properties of the planetary body itself (discussed in Sect. 6.2.1.2). Other overviews of the plasma interaction at Jupiter and its moons can be found, e.g., in Neubauer (1998), Kivelson et al. (2004) or Krupp et al. (2004).

6.2.1.1 Mach Numbers and Nature of Interaction

A key property which controls the interaction is the ratio of the relative bulk flow velocity v_0 between the plasma and the planetary object compared to the group velocities of the three magnetohydrodynamic waves. These ratios are called the fast Mach number M_f , the Alfvén Mach number M_A , and the slow mode Mach number M_s and refer to the ratios of the flow velocity to the fast magneto-sonic mode, the Alfvén mode, and the slow magneto-sonic mode, respectively (e.g., Baumjohann and Treumann 1996). If the fast mode is larger than 1, a bow shock forms ahead of the object for nearly all object classes. Exceptions are inert moons, i.e., without atmosphere and intrinsic magnetic fields. For $M_f < 1$, the bow shock disappears which is always the case if $M_A < 1$, i.e., if the flow is sub-Alfvénic.

The interaction of all planets in the solar system with the solar wind is such that under average conditions the solar wind flow is super-fast, i.e., $M_f > 1$ and all planets are surrounded by a bow shock. Only exceptionally, i.e., approximately once every 2 years, the plasma density in the solar wind is so low that the resultant Alfvén velocity $v_A = B / \sqrt{\mu_0 \rho}$ is faster than the solar wind velocity with the mass density ρ and the magnetic permeability of free space μ_0 . In this case, the Earth loses its bow shock (Chané et al. 2012, 2015). This transition has however never been observed for Jupiter. In the case of Jupiter's moons, which are embedded within Jupiter's magnetosphere, the relative flow velocity is smaller than the Alfvén velocity and thus no bow shock forms, but so-called Alfvén wings develop (Neubauer 1980; Goertz 1980; Southwood et al. 1980). Alfvén wings are standing Alfvén waves in the restframe of the moons. The Alfvén waves are generated because the obstacle slows the flow of the magnetized plasma in its vicinity and generates stresses in the magnetic field. The Alfvén wings can be described as “tubes” in direction parallel

and anti-parallel to the magnetic field but with additional tilts by an angle $\Theta_A \approx \tan^{-1} M_A$ with respect to the magnetic field (Neubauer 1980).

Extrasolar planets are observed to orbit their host stars at a wide range of radial distances from ≈ 0.01 to 1000 AU. Because the stellar plasma properties are expected to strongly evolve as a function of distance similar to the solar wind properties of the sun (e.g., Parker 1958; Preusse et al. 2006; Lanza 2008), the plasma conditions around the observed extrasolar planets are expected to vary strongly. In Fig. 6.1, we show the expected Alfvén Mach number M_A near the 850 extrasolar planets known until 2013 (from Saur et al. 2013). The Mach number is calculated based on measured and estimated properties of the host stars and by applying the Parker (1958) model for the radial evolution of the stellar winds. Figure 6.1 shows that extrasolar planets at orbital distances approximately less than 0.1 AU are typically subject to sub-Alfvénic conditions. At these bodies no bow shock but Alfvén wings form. In case such an extrasolar planet possesses a dynamo magnetic fields as expected (Christensen et al. 2009), then the solar system analogue of these extrasolar planet is Ganymede. In case they do not possess a dynamo field, their interaction is qualitatively similar to Io, Europa, and Callisto. This comparison only relates to the sub-Alfvénic character of the interaction and the principal nature of the obstacle. The atmospheres of the close-in exoplanets however can be significantly different compared to those of the Galilean satellites. The interaction with these atmospheres and the planetary magnetic field is expected to generate plasma and magnetic field perturbations qualitatively similar to the moons of Jupiter. If the exoplanets possess electrically conductive layers, any time-variable external

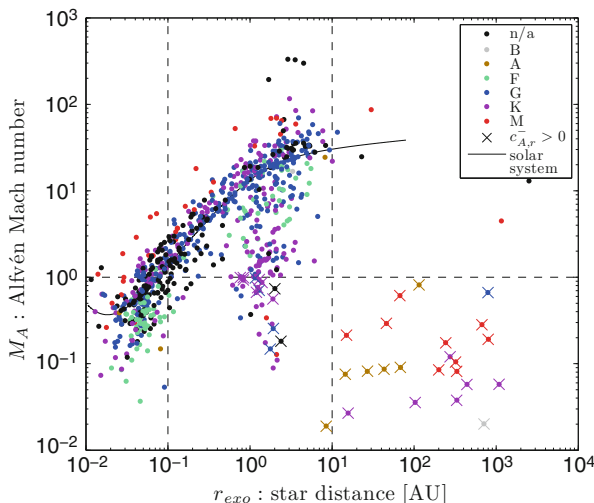


Fig. 6.1 Estimated Alfvén Mach numbers M_A near all 850 extrasolar planets known until 2013. For all extrasolar planets with $M_A < 1$ no bow shock forms, which is the case for most of the planets located within 0.1 AU of their host star (from Saur et al. 2013)

magnetic field will additionally induce secondary magnetic fields similar to the mechanisms at the Galilean satellites. Extrasolar planets at stellar separation larger than approximately 0.1 AU are on average subject to super-Alfvénic conditions ($M_A > 1$) and thus are expected to possess bow shocks if additionally $M_f > 1$ similar to Jupiter. Thus the interactions in the Jupiter system are textbook cases for the interactions at extrasolar planets with the benefit that a huge set of in-situ and remote-sensing observations are available. Thus an improvement of our understanding of the plasma and magnetic field environments in the Jupiter system is helpful as this understanding is also relevant for extrasolar planets.

6.2.1.2 The Planetary Body: Nature of the Obstacle

The nature of the planetary body, i.e., the obstacle to the flow, shapes the plasma and magnetic field environment in particular very close to the planetary body. The body can be a mechanical obstacle, e.g., due to collisions of the neutral particles in the atmosphere with the plasma or if the body possesses a solid surface. The body can also be an electromagnetic obstacle, e.g., if it possesses an internal magnetic field or if it is electrically conductive. The Galilean satellites are a mix of both mechanical and electromagnetic obstacles. They all possess very dilute atmospheres and solid, plasma absorbing surfaces. Among the Galilean satellites, Ganymede is the strongest electromagnetic obstacle because it possesses an internal dynamo magnetic field, which generates a mini-magnetosphere within Jupiter's large magnetosphere (Kivelson et al. 1996). But electrically conductive layers within all of the moons, e.g. saline oceans, metallic cores or a possible magma ocean, generate induced magnetic fields, which influence the external space and plasma environment around all of these moons (e.g., Khurana et al. 1998; Neubauer 1998; Khurana et al. 2011; Seufert et al. 2011).

6.2.2 MHD Model

The most common approach to describe the interaction of a planetary body within its surrounding plasma is the MHD approach. It describes the plasma as an electrically conductive fluid and is applicable to describe the overall properties of the interaction if typical length scales of the interaction are larger than the ion gyro radius and typical time scales are larger than the ion gyro period.

The MHD approach applies to describe the temporal and spatial evolution of the mass density ρ_m the continuity equation, for the plasma bulk velocity \mathbf{v} the velocity equation, for the magnetic field \mathbf{B} the induction equation, and an equation for the

internal energy ϵ , respectively,

$$\partial_t \rho_m + \nabla \cdot (\rho_m \mathbf{v}) = (P - L)m_i , \quad (6.1)$$

$$\rho_m \partial_t \mathbf{v} + \rho_m \mathbf{v} \cdot \nabla \mathbf{v} = -\nabla p + \left(\frac{1}{\mu_0} \nabla \times \mathbf{B} \right) \times \mathbf{B} - (\rho_m v_{in} + Pm_i) \mathbf{v} , \quad (6.2)$$

$$\partial_t \mathbf{B} = \nabla \times (\mathbf{v} \times \mathbf{B}) + \eta \Delta \mathbf{B} , \quad (6.3)$$

$$\partial_t \epsilon + \nabla \cdot (\epsilon \mathbf{v}) = -p \nabla \cdot \mathbf{v} + \frac{1}{2} \rho_m \mathbf{v}^2 \left(\frac{P}{n} + v_{in} \right) - \epsilon \left(\frac{L}{n} + v_{in} \right) . \quad (6.4)$$

The continuity equation (6.1) can include sources P due to ionization of neutral particles with mass m_i and losses L due to recombination. The velocity equation (6.2) includes in case of a mechanical obstacle the collisions and the mass loading in an atmosphere of the planetary body with v_{in} the collision frequency for momentum transfer between the ions and the neutrals through elastic collisions and charge exchange. Here we assumed that the velocity of the atmosphere is at rest. The evolution of the magnetic field is described by the induction equation (6.3), which can include a resistive term characterized by the magnetic diffusivity η . The evolution of the internal energy density ϵ , which is related to the plasma thermal pressure p through $\epsilon = 3/2 p$ is described through (6.4). The total thermal pressure p includes the effects of the electron temperature T_e and the ion temperature T_i by $p = nk_B(T_e + T_i)$ with the Boltzmann constant k_B , and the plasma number density n . The MHD approach does however not allow to constrain the T_e and T_i separately without further assumptions. In (6.4), next to the work done by the pressure, the collisions of the plasma with neutrals as well as plasma production and recombination are included.

In order to describe the interaction as a well-posed problem, initial and boundary conditions need to be specified. For the initial conditions, the unperturbed plasma or approximations to the final solutions are generally used. The outer boundary conditions are chosen so that on the upstream side of the obstacle inflowing conditions are set. They characterize the properties of the plasma flow upstream of the obstacle. Downstream of the obstacle outflowing boundary conditions are applied (e.g., Chané et al. 2013; Duling et al. 2014). The inner boundary for the plasma is located at the surface of the planetary body if the plasma reaches all the way to the surface (Duling et al. 2014). For a planet with a very dense atmosphere such as Jupiter, the inner boundary is located below the ionosphere (Chané et al. 2013). In case of the moons, the plasma is absorbed at the surfaces of the solid bodies, which are additionally assumed to be no source of plasma. These conditions imply that the radial component of the plasma flow v_r can only be negative or zero, which also sets the conditions for the plasma, momentum, and energy flow in Eqs. (6.1), (6.2), and (6.4) (Duling et al. 2014). In case of Jupiter the inner boundary conditions for the plasma is such that $v_r = 0$ (Chané et al. 2013). The boundary condition for the magnetic field is given by the electrically non-conductive nature of the solid surface of the moons and the neutral atmosphere below Jupiter's

ionosphere. This insulating nature implies that the radial component of the electric current at the boundary needs to vanish, i.e., $j_r = 0$. The latter condition has non-local effects on the magnetic field and can be implemented by decomposing the magnetic field at the surface into poloidal and toroidal fields, which are expanded into spherical harmonics. Duling et al. (2014) showed that for the resulting complex poloidal and toroidal coefficients p_{lm}^* and t_{lm}^* of the spherical harmonics Y_{lm}^* of degree l and order m , respectively, the following two equations need to be fulfilled

$$t_{lm}^*(R_0, t) = 0, \quad (6.5)$$

$$R_0 \frac{\partial p_{lm}^*(r, t)}{\partial r} \Big|_{r=R_0} - (l+1)p_{lm}^*(R_0, t) = -\frac{2l+1}{l} G_{lm}^*(t). \quad (6.6)$$

These equations need to be fulfilled at the inner boundary at every time step and thus set the magnetic field boundary conditions at the surface located at R_0 . This description of the inner boundary conditions for the magnetic field also allows that the planetary body possesses internal magnetic fields whose origin lie below the surface. They can be internal dynamo fields as is the case for Jupiter and Ganymede, but they can also be time-variable induction magnetic fields generated in saline electrically conductive subsurface oceans. The internal fields are represented in (6.6) through their complex Gauss coefficients $G_{lm}^*(t)$. In case of Jupiter and its very strong magnetic field, the inner boundary conditions can be approximated by setting the azimuthal and the longitudinal component of the magnetic field to the internal Jovian magnetic field (Chané et al. 2013).

The MHD approach is overall a very powerful approach to describe the plasma dynamics in the Jupiter system. Naturally, it does not capture all aspects of the plasma interaction, e.g., if electron scale physics is relevant and/or gyro radii and gyro periods need to be resolved. For example, reconnection at the magnetopause of Jupiter and Ganymede is a non-ideal MHD effect which is best described with models which resolve ion and electron kinetics, e.g., with full particle-in-cell models. Finite gyro radii effects can play a role in situations where non-thermal, high energy ions are involved or where ions with large velocities within a small background magnetic field are picked-up. In case the latter effects are important, appropriate models are hybrid models or particle-in-cell models. Even though MHD models cannot resolve ion and electron kinetics effects, one of their advantages in numerical simulations is that they generally enable better spatial resolutions compared to kinetic models in case of similar computational resources. This advantage is particularly helpful if small atmospheric scale heights need to be resolved.

6.3 Jupiter's Magnetosphere

Jupiter's magnetosphere is qualitatively different compared to the magnetosphere of the Earth. The magnetosphere of Jupiter is rotationally dominated throughout a large part of the magnetosphere and the moons of Jupiter are huge internal mass sources (e.g., Vasyliūnas 1983; Bagenal and Delamere 2011). Io provides approximately 10^3 kg s^{-1} mostly in form of SO₂ and Europa approximately 50 kg s^{-1} in form of O₂ to the magnetosphere (e.g., Broadfoot et al. 1979; Saur et al. 1998, 2003; Mauk et al. 2003). This mass is subsequently being ionized and picked up by the motional electric field of the fast rotating magnetosphere. Jupiter's sideric rotation period is $\sim 9.9 \text{ h}$. The plasma thus experiences large centrifugal forces responsible for radial transport of the plasma. Due to conservations of angular momentum the magnetospheric plasma while being transported radially outward is not rigidly corotating anymore. This sets up magnetic stresses and electric current systems which couple the magnetosphere to Jupiter's ionosphere. Through this coupling angular momentum is being transported from Jupiter's ionosphere into Jupiter's magnetosphere to bring the magnetosphere closer to full corotation. Jupiter's magnetosphere and its internal coupling has been described theoretically and numerically by a series of authors (e.g., Hill 1979; Vasyliūnas 1983; Hill 2001; Cowley and Bunce 2001; Southwood and Kivelson 2001; Ogino et al. 1998; Walker and Ogino 2003; Moriguchi et al. 2008; Ray et al. 2010).

Because of the immense importance of Jupiter's magnetosphere-ionosphere (MI) coupling, Chané et al. (2013) developed a new MHD model of Jupiter's magnetosphere. This model explicitly includes the ionosphere of Jupiter within the model domain. In Jupiter's ionosphere ion-neutral collisions transfer angular momentum from the neutrals onto the plasma. The resultant flow generates magnetic stresses between the ionosphere and magnetosphere, which accelerate the magnetosphere in the direction of Jupiter's rotation, but decelerate Jupiter's ionosphere in return. In the model of Chané et al. (2013) the MI-coupling is explicitly included and the magnetic field boundary conditions can be physically correctly set below the ionosphere (see Sect. 6.2.2). The downside of the approach is that for numerical reasons, the radial extension of the ionosphere is strongly exaggerated by 4 Jovian radii (R_J) and the surface of Jupiter has been set to be at $4.5 R_J$. Despite the latter assumption, the Chané et al. (2013) model however still uses the closest inner boundary of all published MHD models of Jupiter's magnetosphere. The model includes the mass loading in the Io plasma torus explicitly. It thus explicitly includes two of the most important features of Jupiter's magnetosphere: The coupling to the ionosphere and the mass loading in a fast rotating magnetosphere.

The overall density and magnetic field structure of the modelled magnetosphere is shown in Fig. 6.2. The bow shock is located at $73 R_J$ and the magnetopause at $69 R_J$ in agreement with in-situ measurements (Joy et al. 2002). The magnetosphere is compressed on the day side and strongly elongated on the night side. Figure 6.2 also shows an X-point on the night side where a plasmoid of plasma is being released as part of the mass loss processes in the tail of the magnetosphere. The figure also

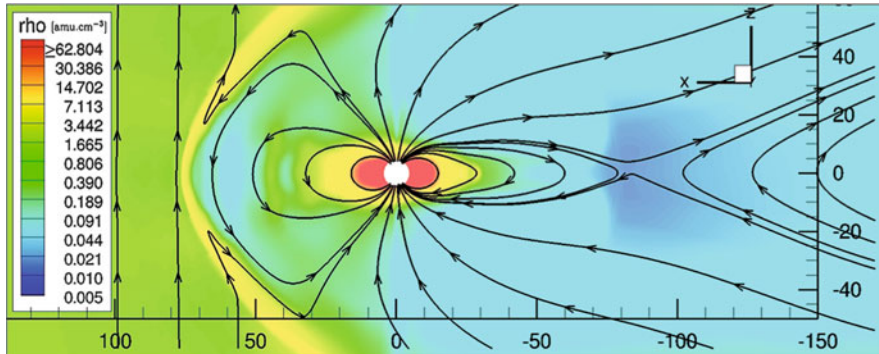


Fig. 6.2 Density contours in the noon-midnight meridian of Jupiter’s magnetosphere. The solar wind is coming from the left. The magnetic field lines are shown in *black* (from Chané et al. 2013)

shows that the plasma is concentrated in the equatorial regions of the magnetosphere due to the strong centrifugal forces. The radial density profile of the Chané et al. (2013) model agrees very well with measured density profiles taken by the Galileo spacecraft (Frank et al. 2002; Bagenal and Delamere 2011).

In Fig. 6.3, the electric current system which represents the angular momentum transfer between Jupiter’s ionosphere and magnetosphere is displayed. The electric current loop connects Jupiter’s ionosphere through field aligned currents directed away from Jupiter and which are fed into the equatorial plasma sheet of Jupiter’s magnetosphere at radial distances of 20 to 30 R_J . In this plasma sheet the currents are directed mostly radially outward and the related $\mathbf{j} \times \mathbf{B}$ forces spin up the magnetosphere. The current closure back to the ionosphere occurs at large radial distances (not clearly visible at low latitudes in Fig. 6.3) and enter the ionosphere in the polar region. The $\mathbf{j} \times \mathbf{B}$ forces slow the plasma in the ionosphere and are in balance with the forces exerted by the ion-neutral collisions, which accelerate the ionosphere.

The modeled azimuthal and radial velocities in Chané et al. (2013) are in good agreement with observations by the Galileo and Voyager spacecraft and the theoretical predictions by Hill (1979). In Fig. 6.4 the modeled azimuthal velocities as a function of radial distance are shown for various mass loading rates in comparison to Voyager measurements. The corotation breakdown (as defined by Hill (1979), 75% of rigid corotation) in the plane of Fig. 6.3 occurs at a radial distance of $32 R_J$, but the plasma starts to subcorotate at approximately $20 R_J$. These results are consistent with the locations of the field-aligned currents and match the theoretical predictions obtained for the same ionospheric conductances and total radial mass transport rates by Hill (1979, 2001).

On field lines with large parallel electric currents pointing away from the planet and on locations along these field lines where the charge carrier density is small, electrons need to be accelerated to large energies to maintain the electric current

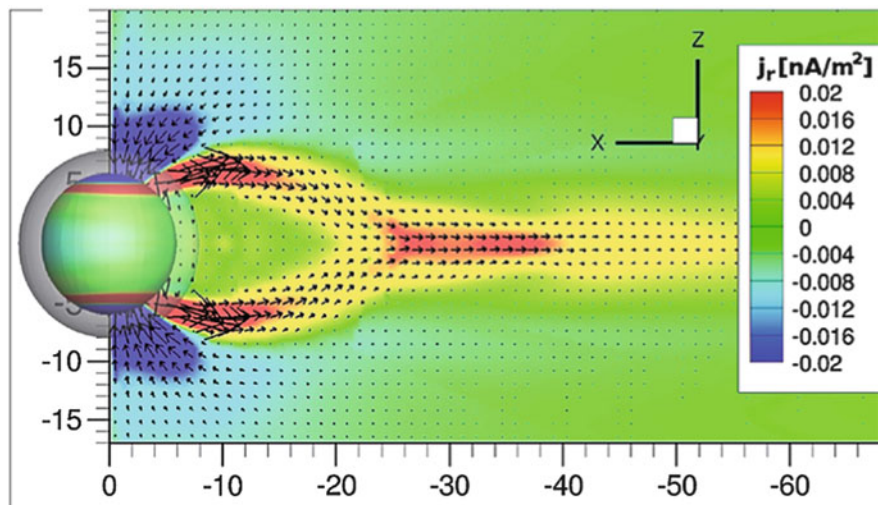


Fig. 6.3 Corotation enforcing current system on the night side of Jupiter in the noon-midnight meridian. The radial current is shown with color contours, and the direction of the current in the same plane is represented by the *black arrows*. The radial current in the ionospheric region is displayed on a sphere at $6 R_J$, and a transparent sphere at $8 R_J$ shows the extent of the ionospheric region. Note that the corotation breakdown of rigid corotation in this plane occurs at $32 R_J$ (from Chané et al. 2013)

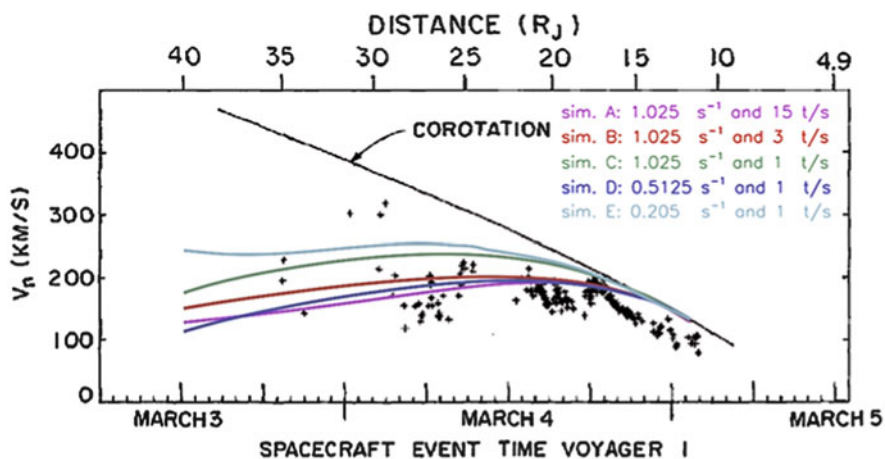


Fig. 6.4 Azimuthal velocity as a function of radial distance: Comparison between Voyager I measurements (*black plus signs*) and computational results (*color lines*). The model output values are over plotted on top of Figure 6.24 from Khurana et al. (2004), which was adapted from McNutt et al. (1981). The model values are shown for different Io torus mass loading rates and ionospheric ion-neutral collision frequencies. The *black line* represents rigid corotation. For the computations, the values given are for the equatorial plane and were averaged over a rotation period and over all local times (from Chané et al. 2013)

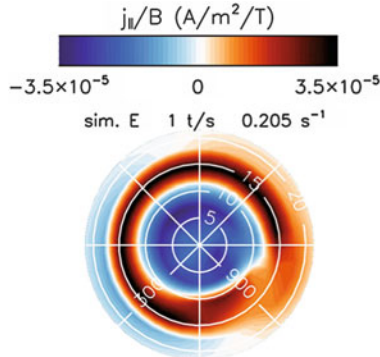


Fig. 6.5 Color contours show j_{\parallel}/B in Jupiter's northern hemisphere at $1 R_J$. The values of the current were projected from the ionosphere to a sphere at $1 R_J$ by following the dipole magnetic field lines. The value of j_{\parallel}/B is averaged over a rotation period. The colatitude and the local time are plotted in *white* on the figures; the dayside is located on the right (from Chané et al. 2013)

loop (Knight 1973; Hill 2001; Cowley and Bunce 2001). The resultant energetic electrons precipitate into Jupiter's ionosphere and excite Jupiter's main auroral oval, which has been extensively observed, e.g., with the Hubble Space Telescope (HST) (e.g., Clarke et al. 2005). Therefore the location in Jupiter's atmosphere, where field lines with large anti-planetward electric current densities map to, can be associated with auroral emission. In Fig. 6.5 we show the electric current density from the Chané et al. (2013) model mapped along dipole field lines into Jupiter's atmosphere. The images show that the current system matches to colatitudes of approximately 15° , which is in good agreement with observations (e.g., Clarke et al. 2005). Figure 6.5 also shows that the electric current is azimuthally asymmetric as expected from a magnetosphere with strong local-time asymmetries. In particular, between 8:00 and 11:00 LT the anti-planetward electric current density has a minimum, which is consistent with a discontinuity in the main oval observed by Radioti et al. (2008) within HST observations. The discontinuity in the electric current in the model of Chané et al. (2013) is caused by an asymmetry in the pressure distribution due to the interaction between the rotating plasma and the magnetopause.

6.4 Time-Variable Magnetosphere

While we discussed in the previous section mostly steady state components of Jupiter's magnetosphere, we address here magnetospheric time-variability caused by the solar wind, by variations of the internal sources, by the rotation of Jupiter, and by dynamical non-linear processes in the magnetosphere.

The internal plasma sources of Jupiter's magnetosphere, i.e., the mass loading at the moons might be time-variable which is however observationally not established

very well. The model of Chané et al. (2013) shows that if the mass loading rate of Io changes from 1×10^3 to $3 \times 10^3 \text{ kg s}^{-1}$, the azimuthal velocity profile changes and the breakdown of corotation occurs further inside (see Fig. 6.4). The change in the mass loading also implies changes in the size of the magnetosphere, the structure of the magnetic field, and in the field aligned auroral current systems. For enhanced mass-loading rates, Chané et al. (2013) find that the auroral becomes more symmetric, while the brightness barely changes.

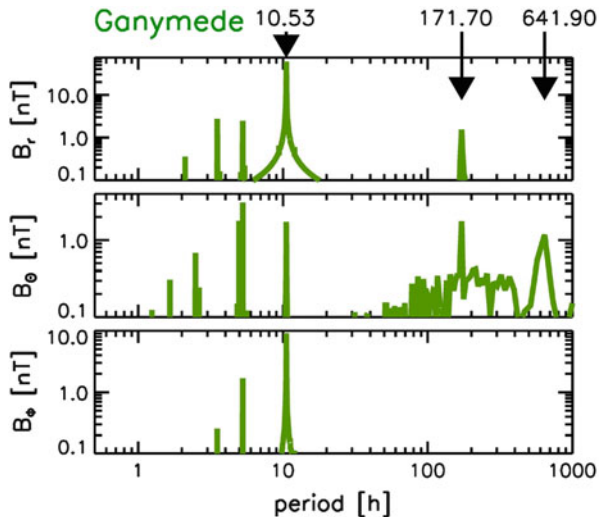
Changing solar wind conditions impacts Jupiter's magnetosphere as well. An increase in solar wind ram pressure decreases the size of the magnetosphere on the subsolar direction and stretches it towards the night side. An important question is how the auroral brightness responds to an increased ram pressure. Earlier theoretical work by Cowley and Bunce (2001), Southwood and Kivelson (2001), and Cowley and Bunce (2003) suggested that the aurora dims in this case because the decreased size of the magnetosphere moves the magnetospheric plasma somewhat radially inward, leading to increased angular velocities (since the angular momentum is conserved). This is expected to reduce the corotational enforcing electric currents and thus to lead to a reduced auroral brightness. The simulations of Chané et al. (2013) predict that the overall response to increased solar wind ram pressure strongly depends on local time, but leads in general to an overall increased auroral brightness (Chané et al. 2017). The primary reason is that the enhanced solar wind ram pressure increases the magnetic stresses in the magnetosphere leading to higher field-aligned electric currents. For deriving these results, the three-dimensional nature of the magnetosphere needs to be considered. Chané et al. (2017) find that only for a short period of time, during the transition phase from weak to strong solar wind ram pressure the aurora locally dims in the noon region.

Another cause of time-variability are dynamical processes in the magnetosphere. Among these processes are intermittent reconnection on the night side and the release of plasmoids on time scales on the order of 10 h (Bagenal 2007; Chané et al. 2013; Vogt et al. 2014; Chané et al. 2017). The radial transport within the magnetosphere occurs through flux tube interchange (e.g., Kivelson et al. 1997). The resultant perturbations of the magnetosphere are stochastic in nature. These perturbations in turn interact with each other generating a turbulent cascade of time-dependent magnetic field and velocity fluctuations (Saur et al. 2002).

Another class of time-variability is induced in Jupiter's magnetosphere due to the approximately 10° tilt of Jupiter's magnetic moment with respect to its spin axis. This tilt makes all properties of Jupiter's magnetosphere time-variable with a period of the sideric rotation period of Jupiter (9.9 h) when observed in an inertial rest frame. This time-variability is important for the magnetosphere itself, but it also leads to time-variable magnetic fields at the locations of the moons, which can be used to probe their interior structure (e.g., Khurana et al. 1998; Neubauer 1998; Kivelson et al. 2000; Zimmer et al. 2000).

The time-variability of the magnetic field near the Galilean moons has been explored extensively by Seufert et al. (2011) through considerations of a range of possibly frequencies. The magnetic field model of Seufert et al. (2011) includes (a) the dynamo magnetic field of Jupiter represented by an expansion in spherical

Fig. 6.6 Amplitudes of the time-variable radial B_r , azimuthal B_ϕ , and latitudinal B_Θ magnetic field components of Jupiter's magnetosphere at the location of Ganymede. The period 10.53 h is the synodic rotation period of Jupiter as seen from Ganymede, 171.7 h is the orbital period of Ganymede, and 641.9 h is solar rotation period (from Seufert et al. 2011)



harmonics, (b) the magnetic fields of the current sheet, and (c) fields due to the magnetopause boundary currents. With this magnetic field model, field components at the location of the moons are calculated and subsequently Fourier-transformed to obtain the time-variable magnetic field amplitudes as a function of their period as shown in Fig. 6.6. The figure shows three sources of time-variability at Ganymede, i.e., three sets of periods: (1) the rotation period of Jupiter and higher harmonics thereof due to non-dipole components of the interior field and due to non-sinusoidal components of the current sheet field. The synodic rotation period of Jupiter seen in the restframe of the satellites generates the strongest amplitudes of all periods with the maximum in the B_r component of ~ 80 nT (Seufert et al. 2011). The higher order harmonics are already significantly smaller on the order of a few nT or less. (2) The time-periodic contribution due to the orbital period of Ganymede is fairly small on the order of 1–2 nT due to the small inclination $i = 0.17^\circ$ and small eccentricity $e = 0.0011$ of Ganymede. (3) The solar rotation period of the sun is propagated out through the solar wind and can generate time-variable solar wind ram pressure, which generates time-variable magnetopause currents also called Chapman-Ferraro currents. The related currents cause amplitudes in the latitudinal B_Θ components of less than 1 nT. We will see in Sect. 6.5 that these various time-dependent fields generate induced magnetic fields in the interior of Ganymede. Observations of these induced magnetic field with the knowledge of the time-variable inducing fields from Fig. 6.6 or previous studies, e.g., by Kivelson et al. (2002) can be used to probe the interior of Ganymede and the other moons. Seufert et al. (2011) calculate the amplitudes and the phases of the induced magnetic fields for the three inducing frequencies and for various models of the electrical conductivity structure within Ganymede, e.g., with a poorly conductive surface, a conductive saline subsurface water ocean and very highly conductive metallic core.

6.5 Ganymede's Magnetosphere

Ganymede is the largest moon in the solar system and comparable in size to Mercury. It is also the only known moon with an intrinsic dynamo magnetic field. Thus it possesses a mini-magnetosphere within Jupiter's gigantic magnetosphere as studied by a number of authors, e.g., Kivelson et al. (1998, 2002), Kopp and Ip (2002), Ip and Kopp (2002), Paty and Winglee (2004, 2006), and Paty et al. (2008), Jia et al. (2008, 2009, 2010).

With the new MHD model developed for Ganymede by Duling et al. (2014) and introduced in Sect. 6.2.2, we model Ganymede's plasma and magnetic field environment as displayed in Fig. 6.7. The MHD model includes Ganymede's internal dynamo magnetic field after Kivelson et al. (2002) and induction in a subsurface ocean through the non-conducting boundary conditions given in Eqs. (6.5) and

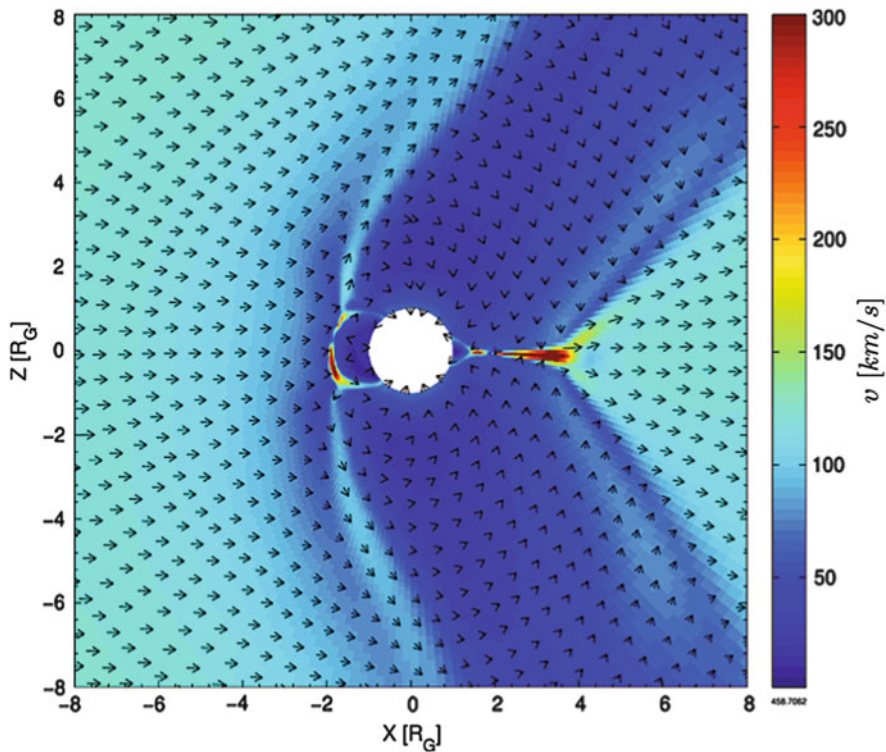


Fig. 6.7 Plasma velocity \mathbf{v} around Ganymede in a plane perpendicular to the direction Ganymede-Jupiter, i.e., the plane given by the unperturbed plasma flow and the north-south direction (for the conditions of Galileo spacecraft G8 flyby). The length of an arrow in this figure represents the magnitude of the vector components within the displayed plane. The total magnitude of the vector is displayed color coded. In this figure the color bar is capped while maximum values of $\sim 460 \text{ km s}^{-1}$ are reached in the dark red regions (from Duling et al. 2014)

(6.6). The model uses appropriate outer boundary and initial conditions given by the Galileo spacecraft measurements during each of its flybys at Ganymede. The model also includes a thin atmosphere, in which ionization with a constant ionization frequency generates an ionosphere as a source term in Eq. (6.1). Elastic collisions, charge exchange, and ionization slow the flow in the ionosphere, which is implemented in the source terms in the velocity equation (6.2). In the induction equation (6.3), we include the resistivity of the ionosphere and anomalous resistivity due to reconnection similar to Jia et al. (2010).

An appropriate description of the magnetic boundary condition at the surface of Ganymede (see Sect. 6.2.2) is crucial to correctly describe Ganymede's magnetic field environment. Commonly applied incorrect boundary conditions are to set the magnetic field at the surface of Ganymede to fixed values given by the internal magnetic field. This approach forces the plasma magnetic fields to be zero and allows electric current to enter through the electrically non-conducting surface of Ganymede. In Fig. 6.8, we show the magnetic field perturbations at the surface of Ganymede, which would be neglected if the magnetic field at surface is set to the values of the dynamo field. The plasma magnetic field assumes values up to ~ 120 nT. These values are larger than the time-variable components and the induction effects of an ocean and are about 20% of Ganymede's dynamo magnetic field. Thus applying incorrect boundary conditions significantly distorts the magnetic field environment around Ganymede.

The relative velocity of Jupiter's magnetospheric plasma with respect to Ganymede is sub-Alfvénic (e.g., Neubauer 1998) and thus no bow shock forms. Ganymede's internal magnetic field generates a mini-magnetosphere with a region of closed magnetic field lines as can be seen as the green shaded region in the top

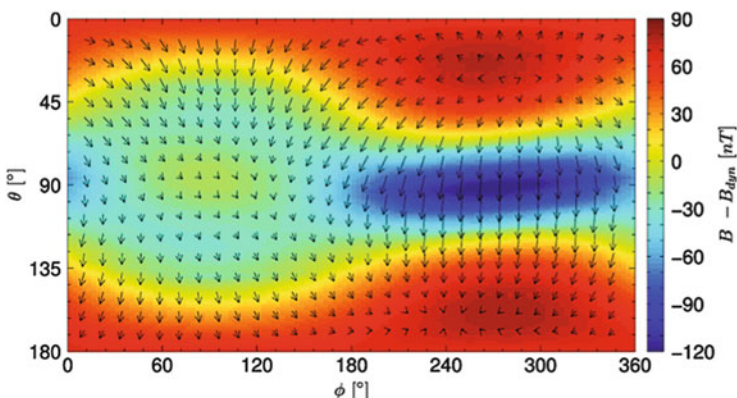


Fig. 6.8 Magnetic field components caused by the plasma interactions at Ganymede's surface. Color coded is the difference of the magnitude of the simulated total magnetic field and the magnitude of Ganymede's dynamo-generated magnetic field that is given by the dipole Gauss coefficients in Kivelson et al. (2002). The arrows show the tangential components of the plasma magnetic field (from Duling et al. 2014)

panel of Fig. 6.9. The closed field line region is shifted towards higher latitudes on the upstream side and is shifted towards the equator on the downstream side due to the magnetic stresses acting on Ganymede (Neubauer 1998). This effect is also well visible in Fig. 6.7. The same figure additionally shows that the plasma flow within the closed field line region is reversed, i.e., in the upstream direction compared to the unperturbed magnetospheric flow.

Due to the sub-Alfvénic nature of the incoming flow Alfvén wings form, which are displayed as blue region in the top panel of Fig. 6.9. The Alfvén wings are also visible in Fig. 6.7 as the large structures north and south of Ganymede where the plasma flow is strongly reduced. The width of the Alfvén wings is significantly larger compared to Ganymede and the width of the closed field region. This is due to the orientation of the internal magnetic field and the external field of Jupiter's magnetosphere. The width of the wings at the presence of an internal magnetic field shown in Fig. 6.9 is in agreement with quantitative expressions for the width derived in Neubauer (1998) and Saur et al. (2013).

In the bottom panel of Fig. 6.9 we quantitatively compare the MHD model results of Duling et al. (2014) shown in green with magnetic field measurements by the Galileo spacecraft taken during the G 29 flyby shown in red. This flyby crossed the northern Alfvén wings and is displayed as a yellow arrow in the top panel of Fig. 6.9. The MHD model fits the amplitude and locations of the wing crossing well. It also quantitatively reproduces the magnetic field measurements of all the other Ganymede flyby by the Galileo spacecraft (e.g., Duling et al. 2014).

6.6 Ganymede's Ocean

The time-periodic magnetic fields in Jupiter's magnetosphere as discussed in Sect. 6.4 can be used to explore electrically conductive layers within the moons of Jupiter (e.g., Khurana et al. 1998; Neubauer 1998; Zimmer et al. 2000). These fields establish one of the few currently available methods to search for saline and thus electrically conductive subsurface oceans. The method is based on the fact that water in its solid form possesses an electrically conductivity at least 4 orders of magnitude smaller compared to liquid water with salinities discussed in the context of the Galilean satellites (e.g., Seufert et al. 2011). The magnetic field measurements by the Galileo spacecraft near Ganymede have been searched for signs of induction signals from an ocean by Kivelson et al. (2002). It was found that the magnetic field measurements from multiple flybys are consistent with an ocean, however the measurements can be fitted quantitatively equally well by unknown quadrupole moments of Ganymede's dynamo magnetic field (Kivelson et al. 2002). Unfortunately, it is impossible to overcome this uncertainty, i.e., to separate spatial and temporal variability with subsequent flybys along different trajectories.

As discussed in Sect. 6.4 and visible in Fig. 6.6, the time-variable magnetic field component of Jupiter's magnetosphere with the largest amplitude is the B_r

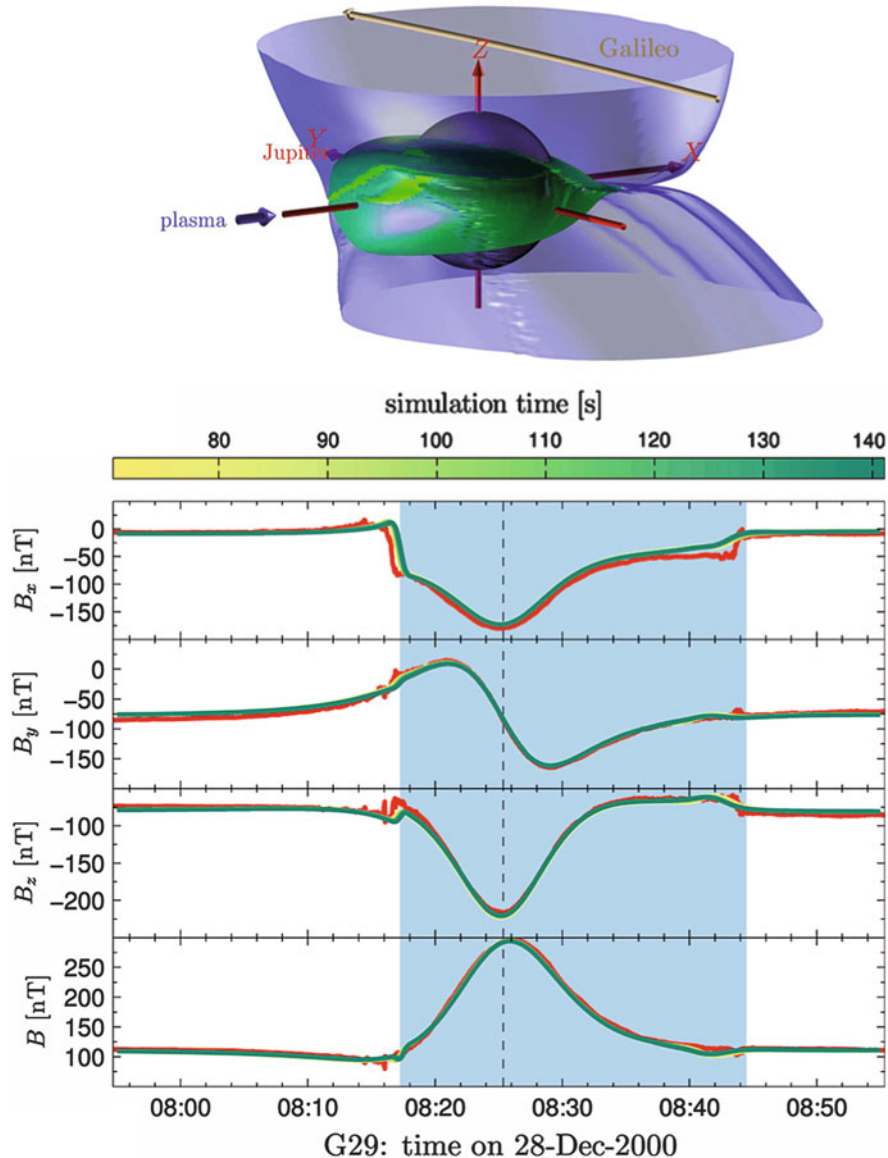


Fig. 6.9 Modeled structure of Ganymede's magnetosphere in *top panel* with closed field line region in *green* and open field line region in *blue*. Magnetic field measurements in *red* and model results in *yellow-green lines* are shown in *bottom*. Both panels are for the G 29 flyby (from Duling et al. 2014)

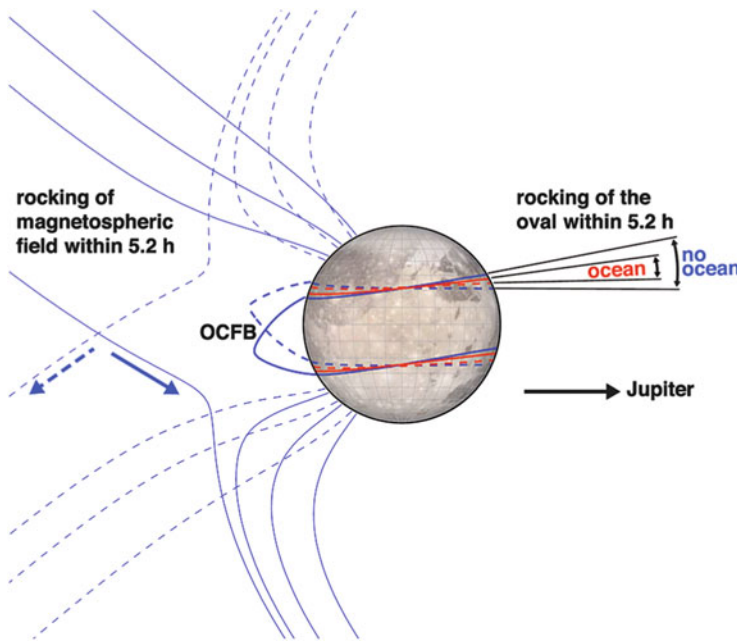


Fig. 6.10 Sketch of magnetic field lines and locations of auroral ovals when Ganymede is above (dashed lines) and below the current sheet (solid lines), respectively. The ovals are located where the open-closed field line boundary (OCFB) intersects Ganymede's surface. Induction in an ocean partly compensates Jupiter's time-variable field and thus reduces the oscillation of the ovals (red: with ocean; blue: without ocean) (from Saur et al. 2015)

component with values of ~ 80 nT. In Fig. 6.10 we show a sketch of the magnetic field environment around Ganymede for maximum positive B_r , i.e., pointing away from Jupiter (dashed lines) and for maximum negative B_r , i.e., pointing towards Jupiter (solid blue lines). The time-variable exterior component also modifies the open-closed field line boundary (OCFL) region of Ganymede's magnetosphere as displayed in Fig. 6.10 as well.

Ganymede also possesses two auroral ovals (Hall et al. 1998; Feldman et al. 2000; McGrath et al. 2013) similar to all known planetary bodies with an intrinsic dynamo magnetic field and an atmosphere. An example of two auroral images taken with the Hubble Space Telescope (HST) is shown in Fig. 6.11. The two auroral ovals are located near the region where the open-closed field line region intersects with Ganymede's atmosphere as shown as red and blue lines on the surface of Ganymede in Fig. 6.10. Because the time-variable external magnetic field modifies the open-closed field line boundary, the location of the auroral ovals are time-variable as well and oscillate in the way depicted by the solid and dashed blue lines on the disk of Ganymede shown in Fig. 6.10. The dashed/solid lines represent the location of the auroral ovals when Ganymede is above/below the plasma sheet of Jupiter's magnetosphere, respectively. When a saline and thus electrically conductive ocean

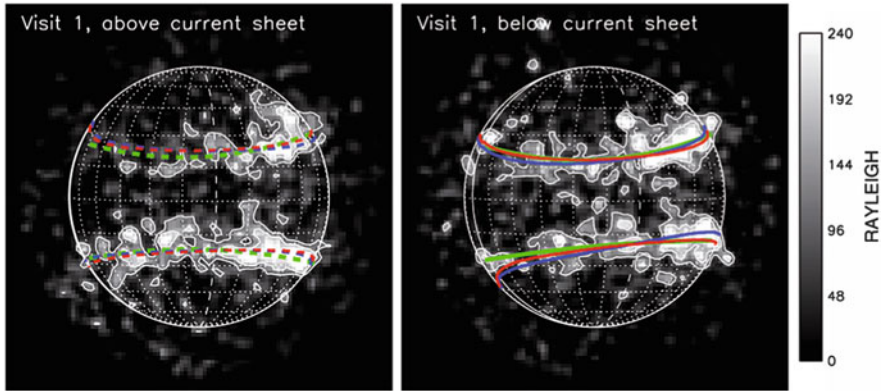


Fig. 6.11 Observed auroral brightness in Rayleigh of OI 1356 Å emission when Ganymede is (left) above and (right) below the current sheet. Contours are for 110 and 170 Rayleigh. North is up and Jupiter to the right. Green lines display fits to the observation, red and blue lines display model locations with and without ocean, respectively (from Saur et al. 2015)

is present, the time-variable external field will induce secondary magnetic fields which will reduce the primary time-variable external magnetic field. The existence of an ocean will thus also reduce the amplitude of the oscillation of the locations of the auroral ovals. The reduced oscillation amplitudes are shown in Fig. 6.10, where the solid and dashed red lines indicate the locations of the auroral ovals when an ocean is present in contrast to the blue lines when no ocean is present.

With dedicated HST observations obtained in November 2010 and October 2011, Saur et al. (2015) measured the locations of the ovals when Ganymede is maximum above and maximum below the current sheet in the search for a subsurface ocean. Figure 6.11 shows the HST observations from November 2010. Figure 6.11 also displays averaged locations of the ovals in green obtained from a polynomial fit to the observed ovals. The blue and the red lines in this figure show the expected locations of the ovals when an ocean and no ocean are present. The expected locations are calculated with the new MHD model of Ganymede by Duling et al. (2014) described in Sect. 6.5. Only from visual inspections of Fig. 6.11, it is nearly impossible to distinguish if the MHD runs with or without ocean fit better to the observations. We note that for this purpose the absolute locations of the ovals are not the important quantities, but the changes of the locations, i.e., the oscillation amplitudes (see Fig. 6.10) between the locations when Ganymede is above and below the current sheet. Therefore Saur et al. (2015) calculated these differences and associated them to an average oscillation angle, also called rocking angle α . The average rocking angle of the northern and southern ovals from the HST observations in 2010 and 2011 combined was found to be $\alpha = 2.0^\circ$.

The observed locations of Ganymede's auroral ovals in the HST data are unfortunately patchy (see, e.g., Fig. 6.11). This patchiness is due to intermittent reconnection near Ganymede's magnetopause and due to the finite signal to noise

ratio of the counts on the individual detector pixels (Saur et al. 2015). In order to assess the error when comparing model oscillation amplitudes α with and without ocean to the observations, Saur et al. (2015) introduced a Monte-Carlo test. In the Monte-Carlo test synthetic observations with and without ocean are generated based on the MHD model of Duling et al. (2014). Therefore patchiness produced with a random generator based on the physics of the intermittent reconnection and based on the finite signal to noise of the observations were added to the modeled locations of the ovals. The resultant synthetic images appear visually very similar to the actually observed ovals (see Figure 7 in Saur et al. (2015)). Subsequently 1024 synthetic HST campaigns were generated with individually different patchy ovals. These synthetic images were then analyzed in an identical ways compared to the real data. In Fig. 6.12, the resultant distribution of the rocking angles is shown with and without ocean (red and blue distribution, respectively). It can be seen that both distribution functions barely overlap, which implies that the ocean and the non-ocean hypotheses can be well separated with this approach. The expectation value is $2.2^\circ \pm 1.3^\circ$ for the ocean model and $5.8^\circ \pm 1.3^\circ$ for the model without ocean. The uncertainties are calculated based on the one-sigma area around the expectations values in Fig. 6.12. The observed rocking angle $\alpha = 2.0^\circ$ is thus consistent with the

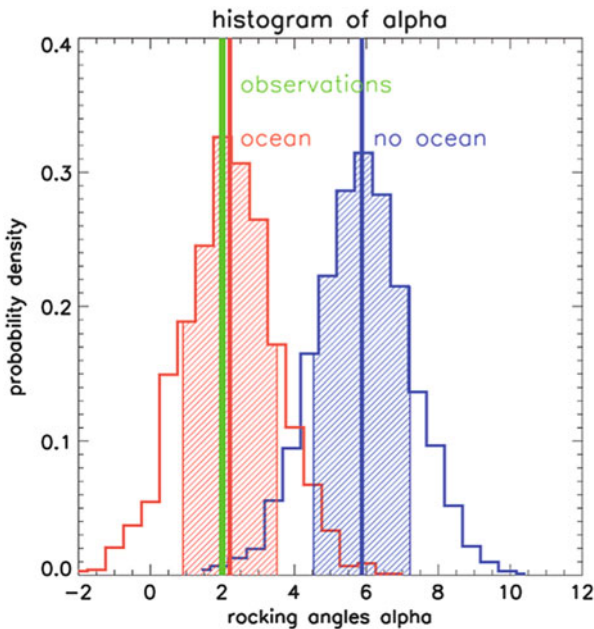
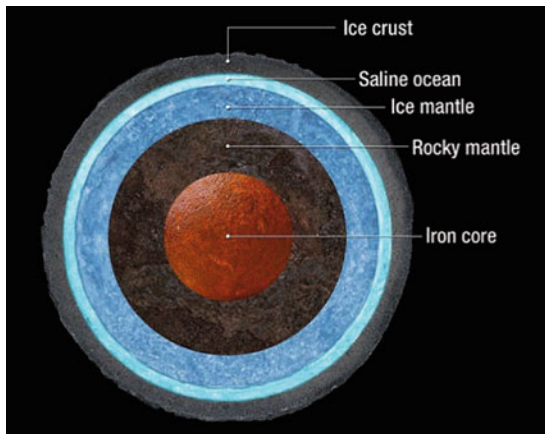


Fig. 6.12 Distribution function of modeled rocking angles α from a Monte-Carlo test with and without ocean, respectively. The test includes the effects of stochastic patchiness on the measurements. The *vertical green line* indicates rocking angle derived from observations. The *vertical red and blue lines* indicate expectation values of α , and the *shaded area* displays the 1 sigma area around the expectation values (from Saur et al. 2015)

Fig. 6.13 Sketch of the internal structure of Ganymede (Image credit NASA/STScI)



existence of a subsurface ocean and inconsistent with no ocean present below the surface of Ganymede.

With this new approach the non-uniqueness of the interpretation of the Galileo magnetometer measurements by Kivelson et al. (2002) could be overcome. The key advantage of the new HST technique by Saur et al. (2015) is to search for an ocean with time-resolved two-dimensional observations of the auroral ovals, i.e. to apply time-dependent “quasi two-dimensional images” of Ganymede’s magnetic field environment.

The resultant internal structure of Ganymede is shown in Fig. 6.13. The layer of liquid water is embedded within two layers of water in the solid phase. This structure is consistent with theoretical models by Sohl et al. (2002), Hussmann et al. (2006), Rambaux et al. (2011) and Vance et al. (2014). Based on the calculations in Saur et al. (2015), the ocean needs to have a minimum electrical conductivity of 0.09 S/m when assuming it to be located between 150 and 250 km depth. This conductivity corresponds to a minimum salt concentration of 0.9 g of MgSO₄ per kilogram ocean water. The measurement also requires that the top of the ocean cannot be deeper than 330 km when measured from the surface.

6.7 Callisto

Callisto is in size and average mass density similar to Ganymede, but structurally only a partially differentiated body (e.g., Showman and Malhotra 1999). Callisto also does not possess an intrinsic dynamo magnetic field in contrast to Ganymede. However, it encompasses similar to the other Galilean satellites a thin atmosphere and an ionosphere (Carlson 1999; Kliore et al. 2002; Cunningham et al. 2015). The time-variable components of Jupiter’s magnetospheric field induce electric currents within electrically conductive layers, such as a subsurface ocean, creating

an induced dipole magnetic field based on studies by Neubauer (1998) and Zimmer et al. (2000). Callisto's atmosphere and ionosphere interact with the plasma of Jupiter's magnetosphere, which generates additional magnetic field perturbations. In the following two subsections the formation of Callisto's ionosphere and the plasma interaction will be discussed.

6.7.1 Callisto's Ionosphere

The first component of Callisto's atmosphere to be observed was CO₂ with a column density of $0.8 \times 10^{19} \text{ m}^{-2}$ (Carlson 1999). The large ionospheric densities up to $4 \times 10^{10} \text{ m}^{-3}$ inferred by Kliore et al. (2002) imply that an additional atmospheric component is present, which was suggested to be O₂. Hubble Space Telescope observations with the STIS camera however only led to upper limits for O₂ (Strobel et al. 2002). But subsequent observations presented by Cunningham et al. (2015) with the more sensitive HST/COS camera revealed OI 135.6 and 130.4 nm emission with a brightness of 1–5 Rayleigh. The authors derived from these observations an O₂ column density of $4 \times 10^{19} \text{ m}^{-2}$.

A main difference of the ionosphere and the atmospheric UV emission of Callisto compared to those of the other Galilean satellites is that the plasma density of Jupiter's magnetosphere at Callisto is so dilute that electron impact is not the primary source of ionization and UV excitation anymore. Callisto's ionosphere and UV emission is in contrast primarily driven by solar photons (Cunningham et al. 2015). In order to better understand Callisto's atmosphere and ionosphere, Hartkorn et al. (2017) developed a new model to simultaneously explain the observed ionospheric electron column densities and the atmospheric UV emissions. This model solves for the electron distribution functions at every location in Callisto's atmosphere for a prescribed atmosphere which includes O₂, CO₂, and H₂O. It takes into account as the primary source of electrons the solar UV fluxes which are highly time-variable as displayed in Fig. 6.14. The model solves the Boltzmann equation for the supra-thermal electron population and considers a large set of inelastic collisions between the atmospheric species, which modifies the electron energies. As a loss for electrons recombination is included, which is energy dependent and more effective for lower electron energies. The model neglects spatial transport of the electrons, which is a good assumption for altitudes smaller than 180 km for the thermal electrons and smaller than 45 km for supra-thermal electrons (Hartkorn et al. 2017). For the low temperature electrons, i.e., energies approximately less than 0.5 eV, the electron distribution function is Maxwellian due to the importance of electron-electron collisions at these energy ranges. Therefore the model of Hartkorn et al. (2017) describes the electrons in this energy range, referred to as thermal electron range, with a fluid description for the electron particle densities and energy densities.

A resultant electron distribution function from the model of Hartkorn et al. (2017) is shown in Fig. 6.15. It demonstrates the highly non-Maxwellian nature of the

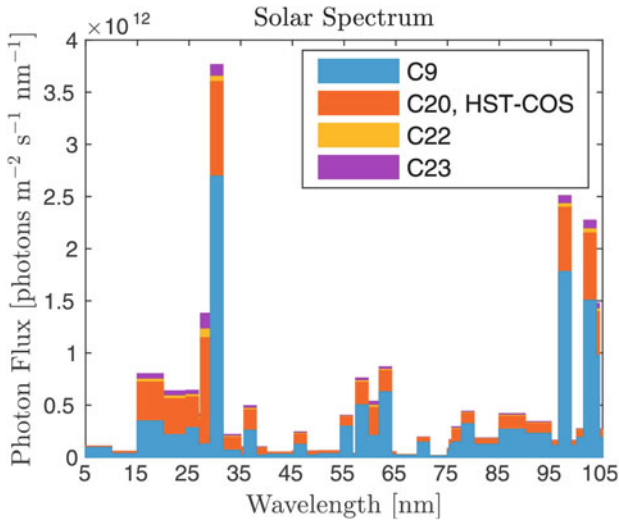


Fig. 6.14 Variability of the solar photon fluxes at Callisto's solar distance for the times of the Callisto C-9, C-20, C-22, C-23 flybys and the HST/COS observation. The fluxes are plotted overlapping. The largest fluxes occurred during C-23 while the smallest fluxes occurred during C-9. The according dates are: C-9: 1997/06/25, C-20: 1999/05/05, C-22: 1999/08/14, C-23: 1999/09/16, HST/COS: 2011/11/17 (from Hartkorn et al. 2017)

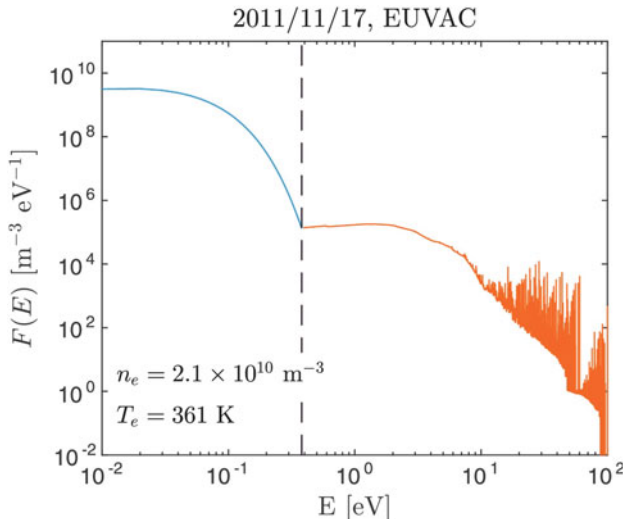


Fig. 6.15 Calculated electron energy distribution function of a volume element in Callisto's ionosphere. The prescribed neutral densities are $1.0 \times 10^{15} \text{ m}^{-3}$ for O₂ and $0.33 \times 10^{15} \text{ m}^{-3}$ for CO₂. Resulting electron density and temperature are $2.1 \times 10^{10} \text{ m}^{-3}$ and $T_e = 361 \text{ K}$. The *dashed black line* marks the transition from the kinetic to the fluid range, which is located for this volume element at 0.38 eV (from Hartkorn et al. 2017)

distribution function for energies larger than 0.5 eV. This distribution function at these energies can only be calculated with a kinetic model. It shows the imprints of the solar input spectrum and the large class of possible collisional processes with the atmospheric neutrals. At lower temperature the distribution function turns Maxwellian due to the electron–electron collisions.

For a joint interpretation of the observed UV emission and the ionospheric electron densities a kinetic description of the electrons is necessary. The high energy tail of this distribution function excites the UV emission emitted from Callisto's atmosphere. With a plain Maxwellian distribution with the temperature of the thermal population barely any UV radiation would be emitted.

With the combined kinetic and fluid model, Hartkorn et al. (2017) calculate electron densities in Callisto's ionosphere. Several examples of the resultant electron density structure are displayed in Fig. 6.16. The figure also shows line of sight paths of the Galileo spacecraft radio science signals through which ionospheric electron densities were derived by Kliore et al. (2002). The radio science observations were

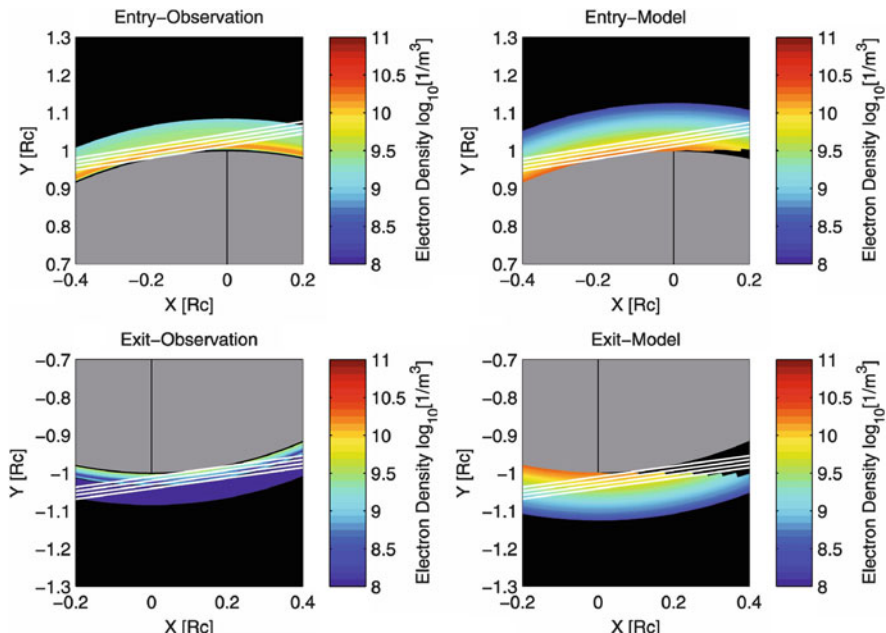


Fig. 6.16 Electron densities of the terminator regions in the equatorial plane according to the C-22 entry and exit electron density altitude profiles of Kliore et al. (2002) (left panels) and according to an exemplary model ionosphere with configurations of C-22 (right panels). For the shown model results (right panels), the prescribed atmosphere is spherically symmetric with an O_2 column density of $3.0 \times 10^{19} \text{ m}^{-2}$. White lines correspond to radio occultation LOS during entry (upper row) and exit (lower row) of flyby C-22. In this Cartesian coordinate system, the Sun is in the $-x$ direction and the y -axis is in the equatorial plane. Length scales are given in units of Callisto's radius $R_C = 2410 \text{ km}$ (from Hartkorn et al. 2017)

all taken around the terminator region and thus provide constraints on Callisto's ionosphere only in this region. Because the radio science technique constrains the integral electron density along a line of sight only, this effect has to be considered when comparing model results with observations.

With the kinetic-fluid model of Hartkorn et al. (2017) the HST observations of Cunningham et al. (2015) and the electron density measurement of Kliore et al. (2002) can be jointly explained within a certain range of O₂ densities in Callisto's atmosphere. Based on this comparison, Callisto's atmosphere has a mean O₂ column density of $2.1 \pm 1.1 \times 10^{19} \text{ m}^{-2}$ and the atmosphere possesses a day night asymmetry. The terminator O₂ column density has values of $\sim 0.4 \times 10^{19} \text{ m}^{-2}$ and associated subsolar O₂ column densities are in the range of $2.4\text{--}9.8 \times 10^{19} \text{ m}^{-2}$. The calculations by Hartkorn et al. (2017) also show that the electron density is very sensitive to the relative abundance of H₂O in Callisto's atmosphere due to the thermal electron cooling by rotational state excitation of H₂O. For the efficiency of Callisto's atmospheric UV emission it is found that on average one photon is emitted at OI 135.6 nm per every 170 electron ion pairs generated and per every 60 electron ion pairs produced by secondary electron impact ionization.

6.7.2 *Callisto's Plasma Interaction*

Callisto with its atmosphere and ionosphere is an obstacle to the dilute plasma of Jupiter's magnetosphere streaming past the moon. This interaction is characterized by a magnetospheric space plasma environment which is more variable compared to the other Galilean satellites. The magnetospheric field $B_0 = 4\text{--}42 \text{ nT}$, the relative velocity $v_0 = 122\text{--}272 \text{ km/s}$, the ion density $n_0 = 0.01\text{--}0.5 \times 10^6 \text{ m}^{-3}$, the Alfvén Mach numbers $M_A = 0.02\text{--}1.85$, and the ion gyro radius $r_g = 34\text{--}530 \text{ km}$ are highly variable due to the varying position of Callisto with respect to Jupiter's magnetospheric plasma sheet and due to stochastic effects within the magnetosphere (Kivelson et al. 2004; Seufert 2012).

Seufert (2012) constructed an MHD model of Callisto's interaction with Jupiter's magnetosphere similar to the model for Ganymede described in Sect. 6.5. The model includes the formation of an ionosphere through photoionization and electron impact ionization within a pure CO₂ atmosphere and alternatively within an atmosphere composed of CO₂ and O₂. The model also includes as internal magnetic fields the induced fields from a subsurface ocean within Callisto (see Sect. 6.4). The resultant magnetic fields from the MHD model of Seufert (2012) in comparison with measurements made by the Galileo spacecraft during the C21 flyby are displayed in Fig. 6.17. The C-21 flyby was a flyby through the wake of Callisto with a closest approach of about 1000 km. In Fig. 6.17, the observed fields are shown in black and the induced magnetic field combined with the background field are shown in red. The magnetic field including the plasma interaction with a CO₂ atmosphere only is shown as green dashed line and the field from the plasma interaction with a combination of CO₂ and O₂ is shown as solid green line. The

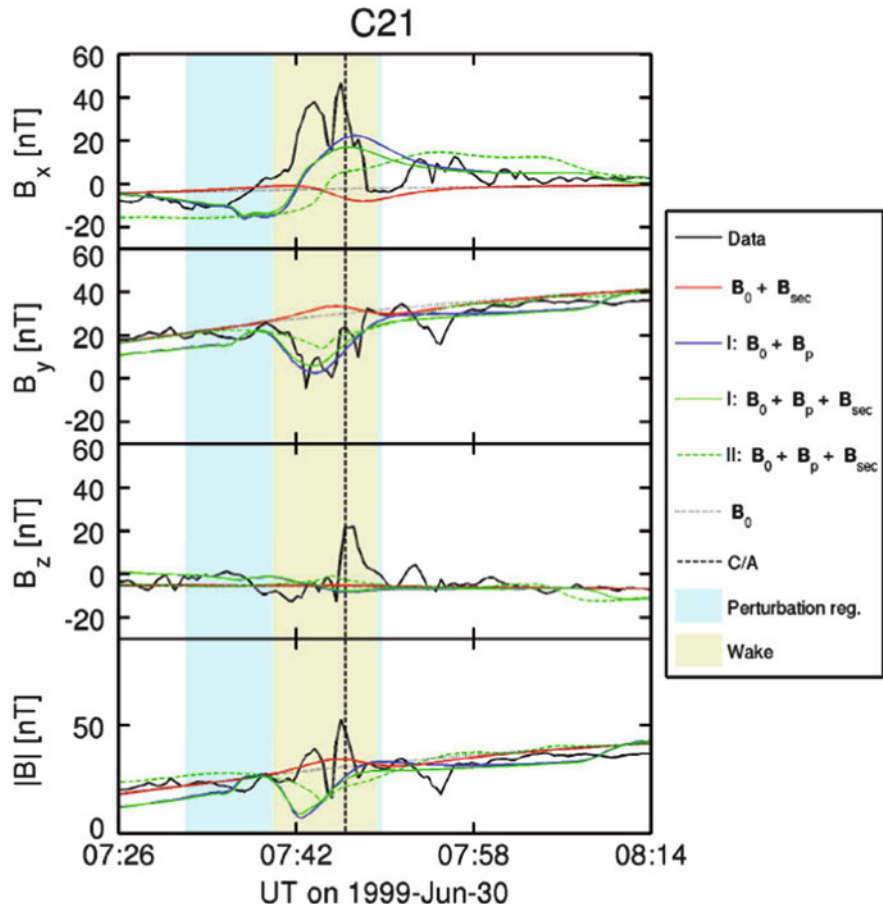


Fig. 6.17 Magnetic field measurements along the C-21 fly trajectory of the Galileo spacecraft (black solid lines) in comparison with modeled magnetic fields in nT. The superposition of the background magnetic field (black dotted lines) and the induced fields is shown in red. The blue solid lines depict a superposition of the background field and the modeled plasma interaction fields for a model (case I) using the measured plasma data with a velocity artificially decreased by a factor of five. The green solid lines represent a superposition of the plasma interaction and the induced fields for the case I as well. The green dashed lines give a similar superposition for the default model in Seufert (2012), i.e., using a corotational plasma velocity of 192 km/s (case II). Blue and ochre areas indicate the locations where the perturbation region and the geometrical wake for case I are crossed by the spacecraft trajectory. The vertical dashed line indicates the time of the closest approach (from Seufert 2012)

results demonstrate that both induction in a conductive ocean and the plasma interaction produce significant magnetic field perturbations. Similar conclusions have been reached by subsequent modeling of Liuzzo et al. (2015, 2016). Therefore an appropriate modeling of the plasma interaction and the induction effects is

necessary in the interpretation of the plasma and field measurements obtained by the Galileo spacecraft.

6.8 Summary

In this chapter, we discussed similarities and differences between the largest and one of the smallest magnetosphere in the solar systems, i.e., those of Jupiter and Ganymede. We introduced two new models for the description of their magnetic field and plasma environments. These models cover two classes of the plasma interaction between a magnetized body with its surrounding space plasma, i.e., sub-Alfvénic and super-fast interactions, which have counterparts at extrasolar planets. We also showed how HST observations in conjunction with MHD modeling of Ganymede's auroral ovals can be used to search for a subsurface ocean within Ganymede. We additionally investigated the non-Maxwellian nature of the electron distribution function in Callisto's ionosphere to constrain its atmosphere based on HST and Galileo spacecraft measurements.

References

- Bagal, F.: The magnetosphere of Jupiter: coupling the equator to the poles. *J. Atmos. Sol. Terr. Phys.* **69**, 387–402 (2007). [doi:10.1016/j.jastp.2006.08.012](https://doi.org/10.1016/j.jastp.2006.08.012)
- Bagal, F., Delamere, P.A.: Flow of mass and energy in the magnetospheres of Jupiter and Saturn. *J. Geophys. Res. Space Phys.* **116**, A05209 (2011). [doi:10.1029/2010JA016294](https://doi.org/10.1029/2010JA016294)
- Baumjohann, W., Treumann, R.A.: Basic Space Plasma Physics. Imperial College Press, London (1996)
- Broadfoot, A.L., et al.: Extreme ultraviolet observations from Voyager 1 encounter with Jupiter. *Science* **204**, 979–982 (1979)
- Carlson, R.: A tenuous carbon dioxide atmosphere on Jupiter's moon Callisto. *Science* **283**, 820–821 (1999)
- Chané, E., Saur, J., Neubauer, F.M., Raeder, J., Poedts, S.: Observational evidence of Alfvén wings at the Earth. *J. Geophys. Res. Space Phys.* **117**(A16), A09217 (2012). [doi:10.1029/2012JA017628](https://doi.org/10.1029/2012JA017628)
- Chané, E., Saur, J., Poedts, S.: Modeling Jupiter's magnetosphere: influence of the internal sources. *J. Geophys. Res. Space Phys.* **118**, 2157–2172 (2013). [doi:10.1002/jgra.50258](https://doi.org/10.1002/jgra.50258)
- Chané, E., Raeder, J., Saur, J., Neubauer, F.M., Maynard, K.M., Poedts, S.: Simulations of the Earth's magnetosphere embedded in sub-Alfvénic solar wind on 24 and 25 May 2002. *J. Geophys. Res. Space Phys.* **120**, 8517–8528 (2015). [doi:10.1002/2015JA021515](https://doi.org/10.1002/2015JA021515)
- Chané, E., Saur, J., Poedts, S., Keppens, R.: How is the Jovian main auroral emission affected by the solar wind? *J. Geophys. Res. Space Phys.* **122**, 1960–1978 (2017). [doi:10.1002/2016JA023318](https://doi.org/10.1002/2016JA023318)
- Christensen, U.R., Holzwarth, V., Reiners, A.: Energy flux determines magnetic field strength of planets and stars. *Nature* **457**, 167–169 (2009). [doi:10.1038/nature07626](https://doi.org/10.1038/nature07626)
- Clarke, J.T., Gérard, J.C., Grodent, D., Wannawichian, S., Gustin, J., Connerney, J., Crary, F., Dougherty, M., Kurth, W., Cowley, S., Bunce, E., Hill, T., Kim, J.: Morphological differences between Saturn's ultraviolet aurorae and those of Earth and Jupiter. *Nature* **433**, 717–719 (2005)

- Cowley, S.W.H., Bunce, E.J.: Origin of the main auroral oval in Jupiter's coupled magnetosphere-ionosphere system. *Planet. Space Sci.* **49**, 1067–1088 (2001)
- Cowley, S.W.H., Bunce, E.J.: Modulation of Jupiter's main auroral oval emissions by solar wind induced expansions and compressions of the magnetosphere. *Plant. Space Sci.* **51**, 57–79 (2003). doi:[10.1016/S0032-0633\(02\)00118-6](https://doi.org/10.1016/S0032-0633(02)00118-6)
- Cunningham, N.J., Spencer, J.R., Feldman, P.D., Strobel, D.F., France, K., Osterman, S.N.: Detection of Callisto's oxygen atmosphere with the Hubble Space Telescope. *Icarus* **254**, 178–189 (2015). doi:[10.1016/j.icarus.2015.03.021](https://doi.org/10.1016/j.icarus.2015.03.021)
- Duling, S., Saur, J., Wicht, J.: Consistent boundary conditions at nonconducting surfaces of planetary bodies: applications in a new Ganymede MHD model. *J. Geophys. Res. Space Phys.* **119**, 4412–4440 (2014). doi:[10.1002/2013JA019554](https://doi.org/10.1002/2013JA019554)
- Feldman, P.D., Most, H.W., Rutherford, K., Strobel, D.F., Wolven, B.C., McGrath, M.A., Roesler, F.L., Woodward, R.C., Oliversen, R.J., Ballester, G.E.: Lyman-alpha imaging of the SO₂ distribution on Io. *Geophys. Res. Lett.* **27**, 1787–1790 (2000)
- Frank, L.A., Paterson, W.R., Khurana, K.K.: Observations of thermal plasmas in Jupiter's magnetotail. *J. Geophys. Res.* **107**(A1), 101029 (2002)
- Goertz, C.K.: Io's interaction with the plasma torus. *J. Geophys. Res.* **85**(A6), 2949–2956 (1980)
- Hall, D.T., Feldman, P.D., McGrath, M.A., Strobel, D.F.: The far-ultraviolet oxygen airglow of Europa and Ganymede. *Astrophys. J.* **499**(5), 475 (1998)
- Hartkorn, O., Saur, J., Strobel, D.F.: Structure and density of Callisto's atmosphere from a fluid-kinetic model of its ionosphere: comparison with Hubble Space Telescope and Galileo observations. *J. Geophys. Res. Planets* **282**, 237–259 (2017). doi:[10.1016/j.icarus.2016.09.020](https://doi.org/10.1016/j.icarus.2016.09.020)
- Hill, T.W.: Inertial limit on corotation. *J. Geophys. Res.* **84**(A11), 6554–6558 (1979)
- Hill, T.W.: The Jovian auroral oval. *J. Geophys. Res.* **106**(A5), 8101–8107 (2001)
- Hussmann, H., Sohl, F., Spohn, T.: Subsurface oceans and deep interiors of medium-sized outer planet satellites and large trans-neptunian objects. *Icarus* **185**, 258–273 (2006)
- Ip, W., Kopp, A.: Resistive MHD simulations of Ganymede's magnetosphere: 2. Birkeland currents and particle energetics. *J. Geophys. Res.* **107**, CiteID 1491 (2002)
- Jia, X., Walker, R., Kivelson, M., Khurana, K., Linker, J.: Three-dimensional MHD simulations of Ganymede's magnetosphere. *J. Geophys. Res.* **113**, A06212 (2008)
- Jia, X., Walker, R., Kivelson, M., Khurana, K., Linker, J.: Properties of Ganymede's magnetosphere inferred from improved three-dimensional MHD simulations. *J. Geophys. Res.* **114**, A09209 (2009). doi:[10.1029/2009JA014375](https://doi.org/10.1029/2009JA014375)
- Jia, X., Walker, R.J., Kivelson, M.G., Khurana, K.K., Linker, J.A.: Dynamics of Ganymede's magnetopause: intermittent reconnection under steady external conditions. *J. Geophys. Res. Space Phys.* **115**, A12202 (2010). doi:[10.1029/2010JA015771](https://doi.org/10.1029/2010JA015771)
- Joy, S.P., Kivelson, M.G., Walker, R.J., Khurana, K.K., Russell, C.T., Ogino, T.: Probabilistic models of the Jovian magnetopause and bow shock locations. *J. Geophys. Res. Space Phys.* **107**, 1309 (2002). doi:[10.1029/2001JA009146](https://doi.org/10.1029/2001JA009146)
- Khurana, K.K., Kivelson, M.G., Stevenson, D.J., Schubert, G., Russell, C.T., Walker, R.J., Polanskey, C.: Induced magnetic fields as evidence for subsurface oceans in Europa and Callisto. *Nature* **395**, 777–780 (1998)
- Khurana, K.K., et al.: The configuration of Jupiter's magnetosphere. In: Bagenal, F. (ed.) *Jupiter*, chap. 24, pp. 593–616. Cambridge University Press, Cambridge (2004)
- Khurana, K.K., Jia, X., Kivelson, M.G., Nimmo, F., Schubert, G., Russell, C.T.: Evidence of a global magma ocean in Io's interior. *Science* **332**, 1186 (2011). doi:[10.1126/science.1201425](https://doi.org/10.1126/science.1201425)
- Kivelson, M.G., Khurana, K.K., Russell, C.T., Walker, R.J., Warnecke, J., Coroniti, F.V., Polanskey, C., Southwood, D.J., Schubert, G.: Discovery of Ganymede's magnetic field by the Galileo spacecraft. *Nature* **384**, 537–541 (1996)
- Kivelson, M.G., Khurana, K.K., Joy, S., Russell, C.T., Southwood, D.J., Walker, R.J., Polanskey, C.: Europa's magnetic signature: report from Galileo's first pass on 19 December 1996. *Science* **276**, 1239–1241 (1997)

- Kivelson, M.G., Warnecke, J., Bennett, L., Joy, S., Khurana, K.K., Linker, J.A., Russell, C.T., Walker, R.J., Polanskey, C.: Ganymede's magnetosphere: magnetometer overview. *J. Geophys. Res.* **103**, 19963–19972 (1998). doi:[10.1029/98JE00227](https://doi.org/10.1029/98JE00227)
- Kivelson, M.G., Khurana, K.K., Russell, C.T., Volwerk, M., Walker, J., Zimmer, C.: Galileo magnetometer measurements: a stronger case for a subsurface ocean at Europa. *Science* **289**(5483), 1340–1343 (2000)
- Kivelson, M.G., Khurana, K.K., Volwerk, M.: The permanent and inductive magnetic moments of Ganymede. *Icarus* **157**, 507–522 (2002)
- Kivelson, M.G., Bagenal, F., Neubauer, F.M., Kurth, W., Paranicas, C., Saur, J.: Magnetospheric interactions with satellites. In: Bagenal, F. (ed.) *Jupiter*, chap. 21, pp. 513–536. Cambridge University Press, Cambridge (2004)
- Kliore, A.J., Anabtawi, A., Herrea, R., Asmar, S., Nagy, A., Hinson, D.P., Flasar, F.M.: The ionosphere of Callisto from Galileo radio occultation observations. *J. Geophys. Res.* **107**, 1407 (2002). doi:[10.1029/2002JA009365](https://doi.org/10.1029/2002JA009365)
- Knight, S.: Parallel electric fields. *Planet. Space Sci.* **21**, 741 (1973)
- Kopp, A., Ip, W.: Resistive MHD simulations of Ganymede's magnetosphere: 1. Time variabilities of the magnetic field topology. *J. Geophys. Res.* **107**, SMP 41.1, CiteID 1490 (2002)
- Krupp, N., et al.: Dynamics of the Jovian Magnetosphere. In: Bagenal, F. (ed.) *Jupiter*, chap. 25, pp. 617–638. Cambridge University Press, Cambridge (2004)
- Lanza, A.F.: Hot Jupiters and stellar magnetic activity. *Astron. Astrophys.* **487**, 1163–1170 (2008). doi:[10.1051/0004-6361:200809753](https://doi.org/10.1051/0004-6361:200809753), 0805.3010
- Liuzzo, L., Feyerabend, M., Simon, S., Motschmann, U.: The impact of Callisto's atmosphere on its plasma interaction with the Jovian magnetosphere. *J. Geophys. Res. Space Phys.* **120**, 9401–9427 (2015). doi:[10.1002/2015JA021792](https://doi.org/10.1002/2015JA021792)
- Liuzzo, L., Simon, S., Feyerabend, M., Motschmann, U.: Disentangling plasma interaction and induction signatures at Callisto: the Galileo C10 flyby. *J. Geophys. Res. Space Phys.* **121**, 8677–8694 (2016). doi:[10.1002/2016JA023236](https://doi.org/10.1002/2016JA023236)
- Mauk, B., Mitchell, D., Krimigis, S., Roelof, E., Paranicas, C.: Energetic neutral atoms from a trans-Europa gas torus at Jupiter. *Nature* **412**(6926), 920–922 (2003)
- McGrath, M.A., Jia, X., Rutherford, K.D., Feldman, P.D., Strobel, D.F., Saur, J.: Aurora on Ganymede. *J. Geophys. Res.* **118**, 2043–2054 (2013). doi:[10.1002/jgra.50122](https://doi.org/10.1002/jgra.50122)
- McNutt, R., Belcher, J., Bridge, H.: Positive ion observations in the middle magnetosphere of Jupiter. *J. Geophys. Res.* **86**, 8319–8342 (1981)
- Moriguchi, T., Nakamizo, A., Tanaka, T., Obara, T., Shimazu, H.: Current systems in the Jovian magnetosphere. *J. Geophys. Res. Space Phys.* **113**, A05204 (2008). doi:[10.1029/2007JA012751](https://doi.org/10.1029/2007JA012751)
- Neubauer, F.M.: Nonlinear standing Alfvén wave current system at Io: theory. *J. Geophys. Res.* **85**(A3), 1171–1178 (1980)
- Neubauer, F.M.: The sub-Alfvénic interaction of the Galilean satellites with the Jovian magnetosphere. *J. Geophys. Res.* **103**(E9), 19843–19866 (1998)
- Ogino, T., Walker, R.J., Kivelson, M.G.: A global magnetohydrodynamic simulation of the Jovian magnetosphere. *J. Geophys. Res.* **103**, 225 (1998). doi:[10.1029/97JA02247](https://doi.org/10.1029/97JA02247)
- Parker, E.N.: Dynamics of the interplanetary gas and magnetic fields. *Astrophys. J.* **128**, 664 (1958). doi:[10.1086/146579](https://doi.org/10.1086/146579)
- Paty, C., Winglee, R.: Multi-fluid simulations of Ganymede's magnetosphere. *Geophys. Res. Lett.* **31**, L24806 (2004)
- Paty, C., Winglee, R.: The role of ion cyclotron motion at Ganymede: magnetic morphology and magnetospheric dynamics. *Geophys. Res. Lett.* **33**, L10106 (2006)
- Paty, C., Paterson, W., Winglee, R.: Ion energization in Ganymede's magnetosphere: using multifluid simulations to interpret ion energy spectrograms. *J. Geophys. Res.* **113**, A06211 (2008). doi:[10.1029/2007JA012848](https://doi.org/10.1029/2007JA012848)
- Preusse, S., Kopp, A., Büchner, J., Motschmann, U.: A magnetic communication scenario for hot Jupiters. *Astron. Astrophys.* **460**, 317–322 (2006). doi:[10.1051/0004-6361:20065353](https://doi.org/10.1051/0004-6361:20065353)

- Radioti, A., GéRard, J.C., Grodent, D., Bonfond, B., Krupp, N., Woch, J.: Discontinuity in Jupiter's main auroral oval. *J. Geophys. Res. Space Phys.* **113**, A01215 (2008). doi:[10.1029/2007JA012610](https://doi.org/10.1029/2007JA012610)
- Rambaux, N., van Hoolst, T., Karatekin, Ö.: Librational response of Europa, Ganymede, and Callisto with an ocean for a non-Keplerian orbit. *Astron. Astrophys.* **527**, A118 (2011). doi:[10.1051/0004-6361/201015304](https://doi.org/10.1051/0004-6361/201015304)
- Ray, L.C., Ergun, R.E., Delamere, P.A., Bagenal, F.: Magnetosphere-ionosphere coupling at Jupiter: effect of field-aligned potentials on angular momentum transport. *J. Geophys. Res. Space Phys.* **115**, A09211 (2010). doi:[10.1029/2010JA015423](https://doi.org/10.1029/2010JA015423)
- Saur, J., Strobel, D.F., Neubauer, F.M.: Interaction of the Jovian magnetosphere with Europa: constraints on the neutral atmosphere. *J. Geophys. Res.* **103**(E9), 19947–19962 (1998)
- Saur, J., Politano, H., Pouquet, A., Matthaeus, W.: Evidence for weak MHD turbulence in the middle magnetosphere of Jupiter. *Astron. Astrophys.* **386**(2), 699 (2002)
- Saur, J., Strobel, D., Neubauer, F., Summers, M.: The ion mass loading rate at Io. *Icarus* **163**, 456–468 (2003)
- Saur, J., Grambusch, T., Duling, S., Neubauer, F.M., Simon, S.: Magnetic energy fluxes in sub-Alfvénic planet-star and moon-planet interactions. *Astron. Astrophys.* **552**, A119 (2013). doi:[10.1051/0004-6361/201118179](https://doi.org/10.1051/0004-6361/201118179)
- Saur, J., Duling, S., Roth, L., Jia, X., Strobel, D.F., Feldman, P.D., Christensen, U.R., Rutherford, K.D., McGrath, M.A., Musacchio, F., Wennmacher, A., Neubauer, F.M., Simon, S., Hartkorn, O.: The search for a subsurface ocean in Ganymede with Hubble Space Telescope observations of its auroral ovals. *J. Geophys. Res. Space Phys.* **120**, 1715–1737 (2015). doi:[10.1002/2014JA020778](https://doi.org/10.1002/2014JA020778)
- Seufert, M.: Callisto: induction signals, atmosphere and plasma interaction. Dissertation, Institut für Geophysik und Meteorologie der Universität zu Köln (2012)
- Seufert, M., Saur, J., Neubauer, F.M.: Multi-frequency electromagnetic sounding of the Galilean moons. *Icarus* **214**, 477–494 (2011). doi:[10.1016/j.icarus.2011.03.017](https://doi.org/10.1016/j.icarus.2011.03.017)
- Showman, A.P., Malhotra, R.: The Galilean satellites. *Science* **296**, 77–84 (1999)
- Sohl, F., Spohn, T., Breuer, D., Nagel, K.: Implications from Galileo observations on the interior structure and chemistry of the Galilean satellites. *Icarus* **157**, 104–119 (2002)
- Southwood, D.J., Kivelson, M.G.: A new perspective concerning the influence of the solar wind on the Jovian magnetosphere. *J. Geophys. Res.* **106**, 6123–6130 (2001). doi:[10.1029/2000JA000236](https://doi.org/10.1029/2000JA000236)
- Southwood, D.J., Kivelson, M.G., Walker, R.J., Slavin, J.A.: Io and its plasma environment. *J. Geophys. Res.* **85**(A11), 5959–5968 (1980)
- Strobel, D.F., Saur, J., Feldman, P.D., McGrath, M.A.: Hubble Space Telescope Space Telescope Imaging Spectrograph search for an atmosphere on Callisto: a Jovian unipolar inductor. *Astrophys. J. Lett.* **581**, L51–L54 (2002)
- Vance, S., Bouffard, M., Choukroun, M., Sotin, C.: Ganymede's internal structure including thermodynamics of magnesium sulfate oceans in contact with ice. *Planet. Space Sci.* **96**, 62–70 (2014). doi:[10.1016/j.pss.2014.03.011](https://doi.org/10.1016/j.pss.2014.03.011)
- Vasyliunas, V.M.: Plasma distribution and flow. In: Dessler, A.J. (ed.) *Physics of the Jovian Magnetosphere*, chap. 11, pp. 395–453. Cambridge University Press, Cambridge (1983)
- Vogt, M.F., Jackman, C.M., Slavin, J.A., Bunce, E.J., Cowley, S.W.H., Kivelson, M.G., Khurana, K.K.: Structure and statistical properties of plasmoids in Jupiter's magnetotail. *J. Geophys. Res. Space Phys.* **119**, 821–843 (2014). doi:[10.1002/2013JA019393](https://doi.org/10.1002/2013JA019393)
- Walker, R.J., Ogino, T.: A simulation study of currents in the Jovian magnetosphere. *Planet. Space Sci.* **51**, 295–307 (2003). doi:[10.1016/S0032-0633\(03\)00018-7](https://doi.org/10.1016/S0032-0633(03)00018-7)
- Zimmer, C., Khurana, K., Kivelson, M.: Subsurface oceans on Europa and Callisto: constraints from Galileo magnetometer observations. *Icarus* **147**, 329–347 (2000)

Chapter 7

Empirical Modeling of Planetary Magnetospheres in Response to Solar Wind Dynamics Using EOF Analysis and Multivariate Linear Regression

Maosheng He and Joachim Vogt

Abstract A popular approach for empirical modeling is through representing a phenomenon as a linear combination of a set of predefined basis functions, such as polynomial and harmonic functions. In comparison with predefined basis functions, the empirical orthogonal basis functions (EOFs) are constructed from the dataset according to the variance distribution, and typically summarize the data into representative features. This chapter reviews comparatively three applications of EOF analysis associated with multivariate linear regression in empirical modeling, namely in the models of the Earth's ionospheric F_2 -layer peak, the field-aligned currents at Earth, and the induced magnetic field near Venus (He et al. Geophys. Res. Lett., 38(14): L14101, 2011; He et al. Geophys. Res. Lett., 39, 2012; He et al. 2017; He et al. J. Geophys. Res., 121(4), 3362–3380, 2016). We illustrate the physical meaning represented by the most important EOFs, detail the model constructions and methodology, and highlight the revealed main scientific results.

7.1 Introduction

The interaction between the solar wind and a planet shapes a region in space called magnetosphere. The associated planetary magnetic field shields planetary body against solar wind particles. The magnetosphere is a highly structured bullet-shaped

M. He (✉)

Department of Physics and Earth Sciences, Jacobs University Bremen, Bremen, Germany

Department of Radar Soundings, Leibniz-Institute of Atmospheric Physics, Rostock University, Kühlungsborn, Germany

e-mail: m.he@jacobs-university.de

J. Vogt

Department of Physics and Earth Sciences, Jacobs University Bremen, Bremen, Germany

e-mail: j.vogt@jacobs-university.de

region. The structure differs from planet to planet, typically comprising regions characterized by distinctive properties (e.g., magnetosheath, tail lobes, and cusp), separated by plasma boundaries (e.g., bow shock, magnetopause, and ionopause), and harboring various current systems (e.g., field-aligned currents and various tail current systems).

Solar system magnetospheres vary significantly in size and structure. The dimension and structure are mainly determined by the planetary internal magnetic field strength and orientation. Unmagnetized planets, like Venus and Mars, possess only small magnetospheres, because their magnetic fields are induced by the interaction between the ionosphere and the solar wind. Global internal magnetic fields give rise to magnetospheres that are classified as “intrinsic.”

In addition to the planetary magnetic field, another factor influencing the magnetosphere is the state of the upstream solar wind. Two common methods used to quantify these influences are numerical simulations of the first-principle equations and data-based empirical modeling. Over past decades, accumulated spacecraft data facilitated the construction of numerous empirical models for magnetospheric phenomena, such as for bow shock and magnetopause, for electric currents and magnetic field distributions, at Earth and other planets (e.g., Alken and Maus 2007; Chao et al. 2002; Martinecz et al. 2008; Masters et al. 2008a, b; Maus et al. 2006; Shue et al. 1998; Olsen 1996; Tsyganenko 2013a, b; Tsyganenko et al. 2015; Zhong et al. 2015).

A general approach for empirical modeling parameterizes an observation \mathbf{m} through parametric equations of the form $\mathbf{m} = \mathbf{G}_\alpha(\mathbf{s}|\mathbf{p})$. Here the response variable \mathbf{m} represents a magnetospheric property; α is the set of model coefficients to be determined; \mathbf{s} is the set of independent spatial or spatial/temporal variables; and the predictor variables are typically solar wind variables and other geospace indices. The magnetopause model by Shue et al. (1998) provides an example involving a nonlinear parametric equation, in which α comprises seven scales, \mathbf{m} is the observed location of the magnetopause, and \mathbf{p} corresponds to the solar wind variables. A popular and mathematically convenient choice for the parametric equation is a linear formulation of the form, $\mathbf{m} = \sum \alpha_i(\mathbf{p}) \mathbf{E}_i(\mathbf{s})$. Here $\mathbf{E}_i(\mathbf{s})$ are usually predefined basis functions such as polynomial functions in Taylor series, triangular functions in Fourier series, and spherical harmonic basis functions (SHBFs). An example here is the implementation of SHBFs in the model of field-aligned currents (FACs) by Papitashvili et al. (2002), in which \mathbf{m} refers to magnetic field observations that give rise to FACs, \mathbf{p} comprises the interplanetary magnetic field (IMF) and season, \mathbf{s} refers to magnetic local time and latitude (*MLT* and *MLat*), and the coefficients $\alpha_i(\mathbf{p})$ were determined through data binning.

An alternative to predefined basis functions is the set of data-derived $\mathbf{E}_i(\mathbf{s})$ called empirical orthogonal functions (EOFs) that do not require any prior knowledge about the underlying physical process. Typically, the most important EOFs can still be associated with the main physical processes can be confirmed through correlation analysis. EOFs are constructed typically through computing the eigenvectors of the covariance matrix of the dataset. Consequently, EOFs summarize the data on a multivariate phenomenon into its dominant, representative features. This helps in

focusing attention on the key features of the data. To illustrate characters of EOFs, we here briefly introduce the physical meaning of EOFs in three applications, namely an empirical model for ionospheric F_2 -layer peak density $NmF2$ and its height $hmF2$ (referred to F2COSMIC, only $hmF2$ is detailed as an example in this chapter), a high-resolution model of field-aligned currents through empirical orthogonal function analysis (MFACE), and an empirical model for the magnetic field configuration near Venus (EMVIM).

In F2COSMIC, the first and second most important EOFs, $\mathbf{E}_1(\mathbf{s})$ and $\mathbf{E}_2(\mathbf{s})$, are shown in Fig. 7.1b, c. The corresponding coefficients $\alpha_1(\mathbf{p})$ and $\alpha_2(\mathbf{p})$ were determined through data binning and spherical harmonic and linear regressions, shown in Fig. 7.1e, f. Here, \mathbf{s} refers to geomagnetic local time (MLT) and latitude ($MLat$), and \mathbf{p} refers to geomagnetic longitude($MLon$) and day of year (DoY). The maps of $\alpha_1(\mathbf{p})$ and $\alpha_2(\mathbf{p})$ indicate that the first two EOFs represent seasonal and longitudinal variation respectively. The seasonal variation, according to $\mathbf{E}_1(\mathbf{s})$, is interhemispherically antisymmetrical, whereas the longitudinal variation is less regular in the MLT - $MLat$ space.

In MFACE (He et al. 2012, Figures 3 and 4), the first EOF $\mathbf{E}_1(\mathbf{s})$ represents mainly the extension and intensity of the large-scale double ring R1&R2 currents pattern, and the second EOF $\mathbf{E}_2(\mathbf{s})$ represents mainly the cusp current (He et al.

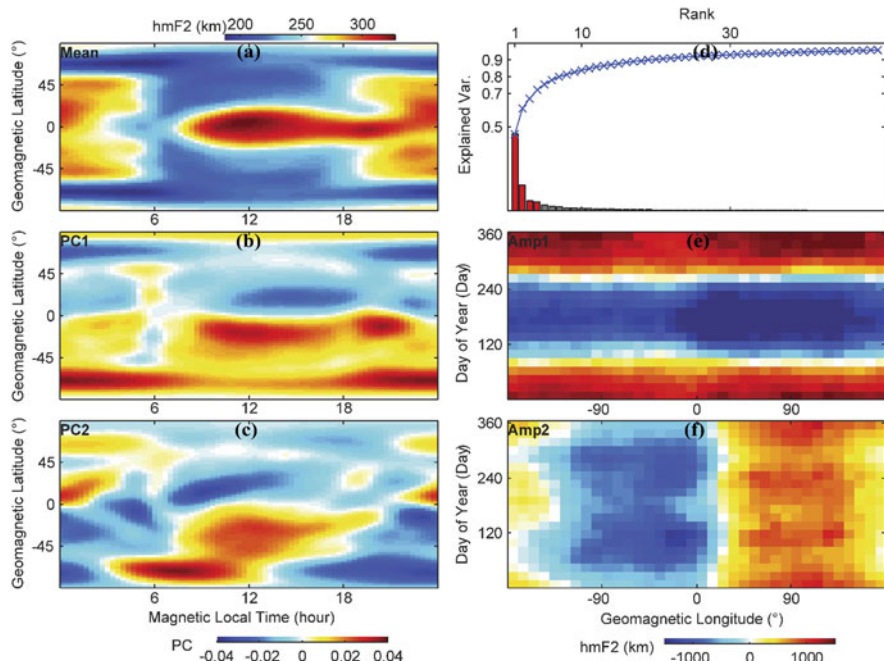


Fig. 7.1 (a) The average $hmF2$ as function of MLT and $MLat$, (b, c) the first and second most important EOFs of $hmF2$ in F2COSMIC, (d) Pareto chart illustrating the cumulative percentage of the explained variance, (e, f) the scores for EOFs shown in (b, c)

2012, 2014). The coefficients $\alpha_1(\mathbf{p})$ and $\alpha_2(\mathbf{p})$ were determined by means of a linear regression analysis. Here, \mathbf{s} refers to *MLat*, and \mathbf{p} comprises solar wind variables, *MLT*, *DoY*, the SuperMAG *SMU* and *SML* indices, and F10.7 index. (1) The regression analysis revealed that the variation of the first EOF (hence R1&R2 currents) is mainly determined by the IMF *Bz* component (*IMFz*), (2) the second EOF (hence the cusp current) is mainly determined by IMF *By* (*IMFy*) (He et al. 2012), and (3) the ionospheric conductivity is more influential for the cusp current than for the R1/R2 currents (He et al. 2014).

In EMVIM (He et al. 2016, Figures 8, 12, 15, and 17), the configuration of EOFs and the regression analysis suggest that the first EOF $\mathbf{E}_1(\mathbf{s})$ represents the draping configuration of IMF *Bz*, the second EOF $\mathbf{E}_2(\mathbf{s})$ represents the piling up and draping configuration of IMF *By* and inside harbors a sheet-like tail current, and the fourth EOF $\mathbf{E}_4(\mathbf{s})$ represents a double sheet structure (He et al. 2016, Figure 15). The coefficients $\alpha_1(\mathbf{p})$ and $\alpha_2(\mathbf{p})$ were determined by means of a linear regression analysis. Here \mathbf{s} is defined on a grid over Venus north pole, and \mathbf{p} summarizes the solar wind magnetic field and F10.7 index. $\alpha_2(\mathbf{p})$ allows quantifying the current density represented by $\mathbf{E}_2(\mathbf{s})$.

In this chapter, Sect. 7.2 reviews comparatively technical details of the three models mentioned above, and Sect. 7.3 highlights the main results revealed by these models.

7.2 Analysis Methodology

The construction of each of the three models is summarized in the flow charts shown in Figs. 7.2 and 7.3 in this chapter, and the Figure 4 of He et al. (2016), respectively. Each construction entails the preparation of response variables \mathbf{m} and predictor variables \mathbf{p} , and the calculation of the EOFs $\mathbf{E}_i(\mathbf{s})$ through EOF analysis and the coefficients $\alpha_i(\mathbf{p})$ through regression analysis and/or data binning. This section explains the technical details following the process flow diagrams. Readers are also referred to the corresponding papers for details of the construction.

7.2.1 Predictor Variables

In the case of Earth, there are solar wind monitors stationed at the Lagrange point L1 to provide continuously the solar wind variables. The variables are available through the NASA OMNI service. For Venus, the single satellite mission Venus Express (VEX) was not accompanied by an independent spacecraft monitoring the solar wind condition for the period of a magnetosphere transit. We estimate IMF as the actual observation of VEX's nearest solar wind encounter (He et al. 2016, 2017). The evaluation, confidence, and predicting efficiency of the estimation

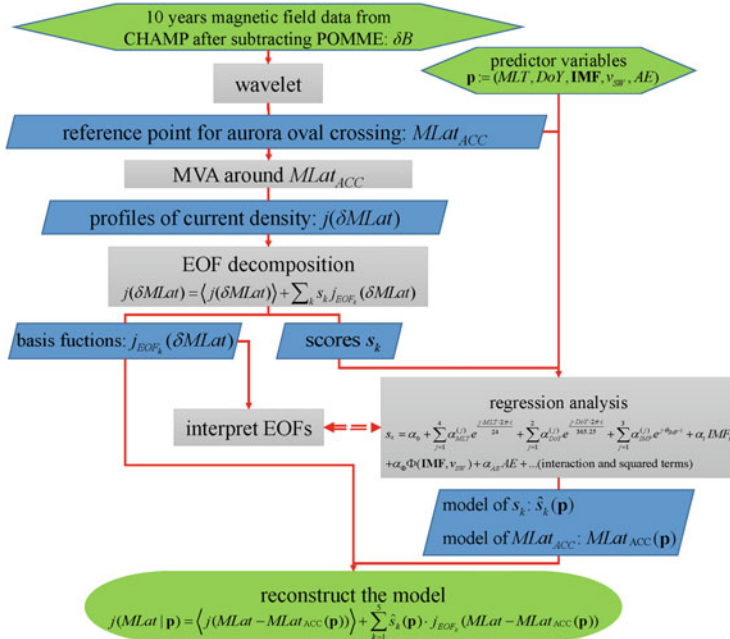


Fig. 7.2 Process flow diagram summarizing the processes of the construction of MFACE (for details also cf. He et al. 2012, 2014)

approach were carried recently by He et al. (2017) through a correlation analysis, a bootstrapping study, and an optimization based on a covariance distribution.

7.2.2 Response Variables

The response variables in the models involved in this chapter are the ionospheric F_2 -layer peak density ($NmF2$) and its height ($hmF2$) in F2COSMIC derived from COSMIC (Constellation Observing System for Meteorology, Ionosphere, and Climate) radio occultation (RO) observation, FAC density j in MFACE derived from magnetic field data of CHAMP (CHAllenging Minisatellite Payload), and the induced magnetic field \mathbf{B} in EMVIM derived from magnetic field data of VEX, respectively.

COSMIC comprises six satellites distributed in six polar low Earth orbits evenly separated 60° from each other. F2COSMIC made use of the first three million profiles. A cubic spline regression was implemented on each profile for determining $NmF2$ and $hmF2$. Further, $NmF2$ and $hmF2$ were modeled individually. Scattered distributed data were fitted onto a four-dimensional matrix ($MLT, MLat, DoY, MLon$) and normalized to $F10.7 = 75\text{sfu}$, through data binning and spherical harmonic combined with linear regression (for details cf. He et al. 2011).

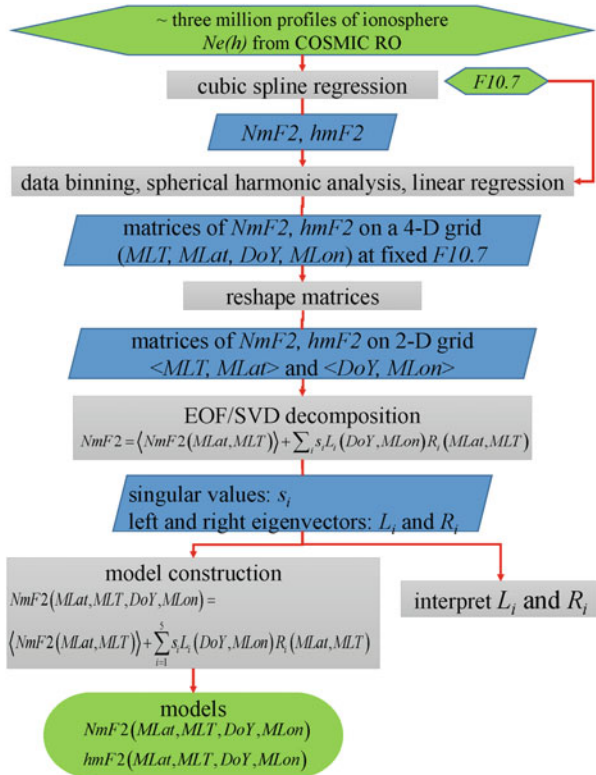


Fig. 7.3 Process flow diagram summarizing the processes constructing the F2COSMIC (for details also cf. He et al. 2011)

CHAMP orbited at 300–440 km altitude with a precession period of 260 days. All 10 years of about 53,000 orbits of 1 s-averaged magnetic vector data were used for constructing MFACE. The main field and large-scale magnetospheric field were firstly subtracted from the dataset according to the model POMME-6 (Maus et al. 2006), yielding magnetic perturbation vectors δB . Wavelet analysis was used to identify a reference point, called Auroral Current Center (ACC), for each quarter orbit between 0° and maximum magnetic latitude. In a 20° -MLat-width interval centered at ACC, δB was picked up for minimum variance analysis (MVA). MVA was conducted in the plane perpendicular to the ambient field, in the Orbit-Geomagnetic (OGM) coordinate system defined by He et al. (2012) according to the ambient magnetic field direction and the orbital plane. Under the stationary sheet-like FACs assumption, the current density j_z was estimated as a function of magnetic latitude $MLat$ according to Ampere's law, and mapped onto 110 km altitude. A low-pass filter was implemented on $j_z(MLat)$ to reduce small-scale fluctuations. The cutoff frequency was selected equivalent to 220 km wavelength or 55 km spatial resolution (Fig. 7.4).

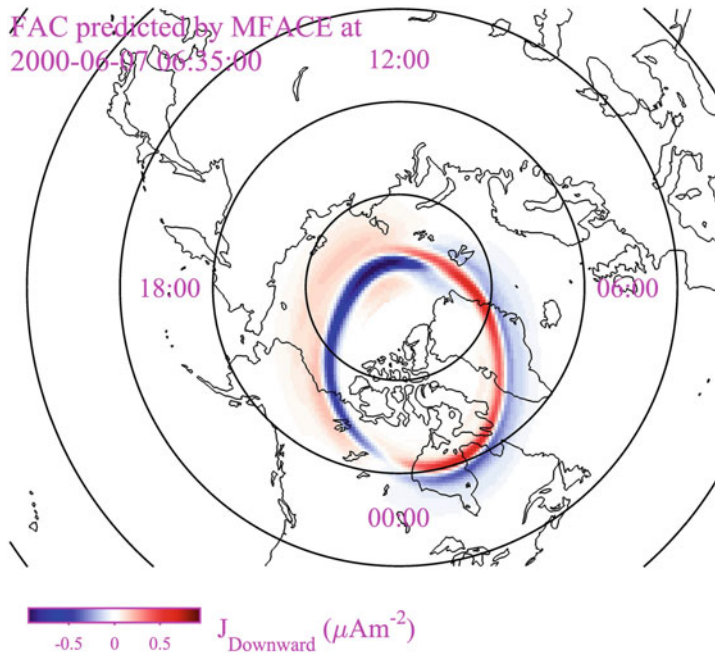


Fig. 7.4 FAC distribution at 06:35 UT on 7 July 2000 over the northern and southern pole according to MFACE

VEX operated in a highly elliptical polar orbit with perigee below 400 km over the north pole of Venus. All 2314 orbits of 4 s-averaged VEX magnetic field vector data were used for constructing EMVIM. The orbit crossed the low-altitude magnetosphere only over the northern polar cap, covering the full local times. According to the orientation of orbital angular momentum, the measurements were cataloged into two orbital sectors, in the noon-midnight and dawn-dusk direction. The EOF analysis and regression were performed in the two sectors separately. The magnetic field time series were averaged on a grid of orbital phase Φ_{grid} , resulting in $\mathbf{B}(\Phi_{grid})$. Φ is the latitude in the noon or dawn sector, and the colatitude plus 90° in the midnight or dusk sector, and the grid $\Phi_{grid} = 65, 66 \dots, 88, 92, 93 \dots, 115$. Then, for every VEX polar cap crossing, the $\mathbf{B}(\Phi)$ profile was represented by 144 scalars (3 components by 48 grids).

7.2.3 EOF Analysis

Through arranging the majority of variance onto few basis functions, EOF analysis provides a compact representation of the data and offers a genetic efficient and effective approximation for data analysis and interpretation. This section explains

the EOF analysis and the implementation on the response variables as described in Sect. 7.2.2.

7.2.3.1 Principles of EOF Analysis

EOF analysis is equivalent to minimum variance analysis (MVA) but possibly in high dimensional space. Mathematically, a set of n vectors, $(\mathbf{v}_1, \mathbf{v}_2, \dots, \mathbf{v}_n)$ has the EOF representation:

$$\mathbf{v}_j = \langle \mathbf{v}_i \rangle + \sum_i s_{ij} \hat{\mathbf{e}}_{EOFi} \quad (7.1)$$

Here, $\langle \mathbf{v}_i \rangle = \frac{1}{n} \sum_i^n \mathbf{v}_i$ is the expected value of \mathbf{v}_i , and $\hat{\mathbf{e}}_{EOFi}$ are EOFs, also termed principal components (PCs), and the expansion coefficients s_{ij} are EOF scores, also termed in several other contexts as EOF time series, PC amplitudes, PC scores, or PC time series. $\hat{\mathbf{e}}_{EOFi}$ corresponds to the $\mathbf{E}_i(\mathbf{s})$ introduced in Sect. 7.1. The first EOF $\hat{\mathbf{e}}_{EOF1}$ satisfies,

$$\hat{\mathbf{e}}_{EOF1} = \arg \max_{\|\hat{\mathbf{x}}\|=1} \hat{\mathbf{x}}^t \mathbf{M} \hat{\mathbf{x}} \quad (7.2)$$

Here the covariance matrix is $\mathbf{M} = \mathbf{V}_c \mathbf{V}_c^t$. $\mathbf{V}_c = (\mathbf{v}_1 - \langle \mathbf{v}_i \rangle, \mathbf{v}_2 - \langle \mathbf{v}_i \rangle, \dots, \mathbf{v}_n - \langle \mathbf{v}_i \rangle)$ is the centered matrix. Starting with $j = 2$, the j th EOF $\hat{\mathbf{e}}_{EOFj}$ satisfies,

$$\hat{\mathbf{e}}_{EOFj} = \arg \max_{\|\hat{\mathbf{x}}\|=1} (\hat{\mathbf{x}}^t \mathbf{M}_j \hat{\mathbf{x}}) \quad (7.3)$$

Here, \mathbf{M}_j is the residual covariance matrix of \mathbf{M} after projection onto the space perpendicular to $\hat{\mathbf{e}}_{EOFi}$ for all $i < j$, namely,

$$\mathbf{M}_j = \mathbf{M} - \sum_{i=1}^{j-1} \hat{\mathbf{e}}_{EOFi}^t \mathbf{M} \hat{\mathbf{e}}_{EOFi} \hat{\mathbf{e}}_{EOFi}^t \hat{\mathbf{e}}_{EOFi} \quad (7.4)$$

$\|\mathbf{M}_j\|$ usually decreases dramatically with increasing j . $\mathbf{M} - \mathbf{M}_j$ is a low-rank approximation of \mathbf{M} .

7.2.3.2 EOF in F2COSMIC

Section 7.2.2 prepared a four-dimensional matrix of *NmF2* and *hmF2* referring to four variables (*MLAT*, *MLT*, *DoY*, *MLON*). In principle, the four-dimensional matrix allows predicting the *NmF2* and *hmF2* for a given set of predictor variables through an interpolation, which works as an empirical model. EOF analysis was used for compressing the model and extracting the dominant features. The four

referring variables were separated into two groups (*DoY*, *MLon*) and (*MLat*, *MLT*), and accordingly, the four-dimensional matrix was organized into a two-dimensional. The reorganized matrix was decomposed through EOF analysis.

$$\begin{aligned} hmF2(MLT, MLat, DoY, Mlon) &= \langle hmF2(MLT, MLat) \rangle \\ &+ \sum_i \sigma_i L_i(DoY, Mlon) R_i(MLat, MLT) \end{aligned} \quad (7.5)$$

Here, $\sigma_i L_i$ corresponds to the EOF scores s_{ij} in Eq. (7.2) but in the formation of column vectors, and R_i is the EOF $\hat{\mathbf{e}}_{EOF_i}$. L_i and R_i are also called left and right eigenvectors of the two-dimensional matrix, satisfying $L_i L_i^t = \mathbf{I}$ and $R_i^t R_i = \mathbf{I}$. $\langle hmF2(MLT, MLat) \rangle$ is shown in Fig. 7.1a, representing the average *hmF2* as a function of *MLT* and *MLat*. Figure 7.1a is characterized mainly by a day-night variation at midlatitude, illustrating that the *F2* peak is higher during nighttime than daytime due to the diurnal variation of the meridional component of neutral wind. The maximum *hmF2* at noon over equator results from the upward electric drift. The Pareto chart shown in Fig. 7.1d displays $\sum_i^k \sigma_i^2 / \sum_i \sigma_i^2$, illustrating that the first four EOFs capture more than 70% of the total variance.

7.2.3.3 EOF in MFACE

In Sect. 7.2.2, a profile $j(MLat)$ was identified for each aurora oval crossing around the reference point ACC. The profiles were interpolated to a latitude grid *MLatgrid* for a superposed epoch analysis referring to the point ACC and for an EOF decomposition:

$$j(\Delta MLat_{grid}) = \langle j(\Delta MLat_{grid}) \rangle + \sum_i s_i \cdot EOF_i(\Delta MLat_{grid}) \quad (7.6)$$

Here, $\Delta MLat_{grid}$ is the relative distance to ACC in a unit of latitude degree, $\langle j(\Delta MLat_{grid}) \rangle$ is the average of all profiles resulting from the superposed epoch analysis, and s_i is the score for the basis function EOF_i . We truncated Eq. (7.6) at $i = 5$, and both $MLat_{ACC}$ and s_1, s_2, s_3, s_4 , and s_5 are used as the response variables in the regression in Sect. 7.2.4.1 (Figs. 7.5 and 7.6).

7.2.3.4 EOF in EMVIM

In Sect. 7.2.2, VEX magnetic field observation was represented by 144 scalars for each polar cap crossing. In principle, one could take the 144 scalars as response variables for a regression, which involves 144 individual regressions and hence is expensive in interpreting the regression results. Alternatively, a canonical correlation analysis (CCA) also works for the modeling purpose. CCA is mathematically elegant and could maximize the predicting efficiency r^2 , but it is difficult to reveal

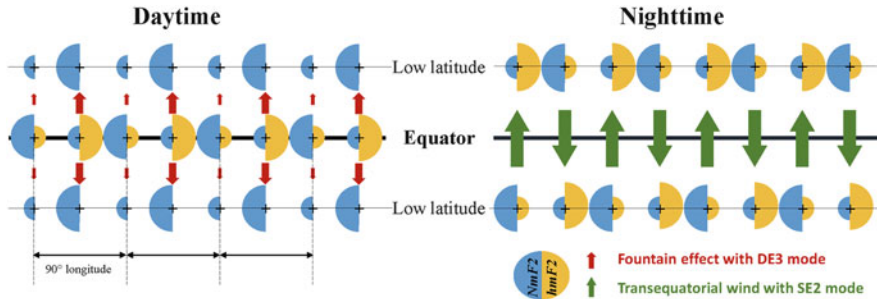


Fig. 7.5 Schematic diagram summarizing the in-phase/anti-phase relationships of the ionospheric wave-4 structures between (*top*) the northern and (*bottom*) southern hemispheres, between over the equator and at low-latitude, and between in (*blue*) $NmF2$ and (*orange*) $hmF2$, according to the empirical model constructed from COSMIC RO observation (He et al. 2011). The filled semicircles represent horizontal zonal wave-4 pattern, and their sizes represent the phase: the larger ones represent the wave-4 maximum, and the smaller ones represent the minimum. During daytime in the left panel, the *red arrows* represent the plasma transport due to the fountain effect, and the size of arrows illustrates the strength of the fountain effect. The fountain pumps plasma upwards over the equator, raises the $F2$ -layer peak there, drains the plasma over the equator, and transports them to low latitude along the magnetic field. In the longitude sector where the fountain effect maximizes, develops a zonal minimum in $NmF2$ and a maximum in $hmF2$ over the equator associated with a maximum in $NmF2$ at low latitude. During nighttime in the right panel, the *green arrows* indicate the transequatorial wind. The wind transports plasma along the geomagnetic field lines from the upwind hemisphere to the downwind, decreasing the plasma density on the upwind side and increasing on the downwind side. Meanwhile, the transport has a vertical component, upward in the upwind hemisphere and downward in the downwind hemisphere, raising the $F2$ -layer peak on the upwind side and depressing the peak on the downwind side

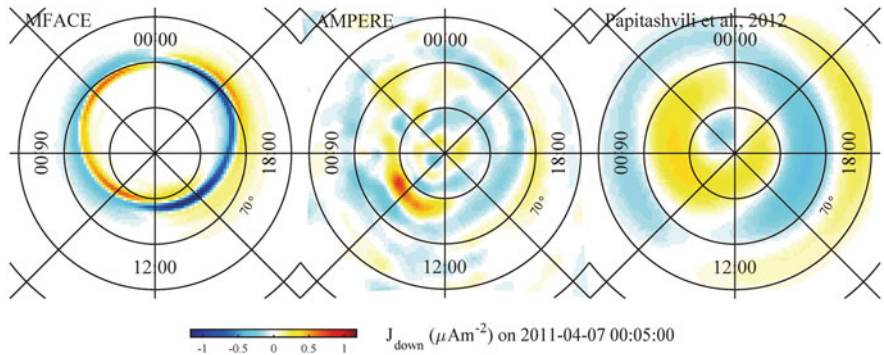


Fig. 7.6 FAC distribution at 00:05 on 7 April 2011 in the geomagnetic coordinate system according to (*left*) MFACE, (*middle*) AMPERE, and (*right*) the model by Papitashvili et al. (2002)

and interpret individually the potential relationship between predictor and response variables. On the other hand, EOFs are designed for extracting dominant coherent variations which are typically proxying physical phenomena separately. Through exploring the potential correlation between EOF scores and predictor variables,

regression analysis could reveal causality between the predictor variables and the physical phenomena represented by the corresponding EOF. EOF analysis was performed on the extracted $\mathbf{B}(\Phi_{grid})$ profiles according to,

$$\mathbf{B}(\Phi_{grid}) = \langle \mathbf{B}(\Phi_{grid}) \rangle + \sum_i^{144} S_i \mathbf{B}_{EOFi}(\Phi_{grid}) \quad (7.7)$$

Here, S_i is the score for i th EOF basis $\mathbf{B}_{EOFi}(\Phi_{grid})$ arranged in descending order by the variance it accounts for. The first four EOFs are displayed in Figures 8 and 15 of He et al. (2016), which contribute to the most variance as illustrated in Figure 7 of He et al. (2016). We truncate Eq. (7.7) at $i = 3$ which allows a low-rank approximation and captures more than 70% of the total variance. S_1 , S_2 , and S_3 are selected as the response variables for the regression in Sect. 7.2.4.2.

7.2.4 Regression Analysis and Model Reconstruction

Previous sections introduce the preparation of predictor and response variables. This section explains the reconstruction of the models. In constructing F2COSMIC, Eq. (7.5) was truncated at $i = k$ where k is the minimum value satisfying $\sum_i^k \sigma_i^2 / \sum_i \sigma_i^2 \geq 90\%$ for a low-rank approximation. For a given input (MLT_0 , $MLat_0$, DoY_0 , $MLon_0$), interpolations referring to L_i and R_i yield L_0 and R_0 values at the input, further allowing a prediction of $NmF20 = \sum_{i=1}^k \sigma_i L_0 R_0$. In constructing MFACE and EMVIM, each EOF score is utilized as a response variable for a regression to establish the relationship with the predictor variables.

7.2.4.1 Regression in MFACE

In Sect. 7.2.3.3, each FAC density profile $j(MLat)$ is represented by six scalars $MLat_{ACC}$, s_1, s_2, s_3, s_4 , and s_5 . These scalars were used as response variables for regressions according to,

$$\begin{aligned} s_k(\mathbf{p}) = & \alpha_0 + \sum_{j=1}^4 \alpha_{MLT}^{(j)} \exp\left(\frac{j \cdot MLT \cdot 2\pi i}{24\text{hours}}\right) + \sum_{j=1}^2 \alpha_{DoY}^{(j)} \exp\left(\frac{j \cdot DoY \cdot 2\pi i}{365.25\text{days}}\right) \\ & + \sum_{j=1}^3 \alpha_{IMF}^{(j)} \exp(j \cdot \theta_{IMF} \cdot i) + \alpha_t IMF_t + \alpha_\Phi \Phi(\mathbf{IMF}, v_{SW}) \\ & + \alpha_{AE} AE \dots \text{(interaction and squared terms)} \end{aligned} \quad (7.8)$$

Here, $\mathbf{p} := (MLT, DoY, \mathbf{IMF}, v_{SW}, AE)$ comprises predictor variables, Φ is the empirical polar cap potential (Boyle et al. 1997), MLT is the magnetic local time, DoY represents the seasonal variation, θ_{IMF} is IMF clock angle, IMF_t is the IMF cross-flow component, B is the IMF magnitude, v_{SW} is the solar wind speed, and

AE index represents the geomagnetic activity levels. All variables are referring to the moment when CHAMP crosses the reference point ACC. α s are coefficients to be determined. Regression yields models of $\widehat{MLat}_{ACC}(\mathbf{p})$ and $\hat{s}_k(\mathbf{p})$, in which $\mathbf{p} := (MLT, DoY, \theta_{IMF}, B_t, B, v_{SW}, AE)$. The regression allows reconstructing MFACE as,

$$\begin{aligned} j(MLat|\mathbf{p}) &= \left\langle j \left(MLat - \widehat{MLat}_{ACC}(\mathbf{p}) \right) \right\rangle \\ &+ \sum_{i=1}^5 \hat{s}_i(\mathbf{p}) \cdot j_{EOFi} \left(MLat - \widehat{MLat}_{ACC}(\mathbf{p}) \right) \end{aligned} \quad (7.9)$$

As an example, Fig. 7.4 presents the distribution of FAC at 06:35 on 7 July 2000, estimated according to MFACE. The pattern comprises clearly the R1&R2 currents and cusp currents. The meridional resolution is about 55 km or 0.5° in latitude determined by the low pass filtering implemented in Sect. 7.2.2, and the zonal resolution is about 1.5 h. determined by the highest order of the *MLT* harmonic term in Eq. (7.8).

The approach of MFACE was developed further in separate local time sectors (He et al. 2014). An empirical solar illumination-induced ionospheric conductivity, and SuperMAG *SMU* and *SML* indices were added to the list of the predictor variable.

7.2.4.2 Regression in EMVIM

EMVIM is constructed in two separate sectors, the noon-midnight sector and the dawn-dusk sector, predicting the magnetic field on two surfaces intersected over the Venusian terminator: a thin band extending from 65° to 115° without an extension in altitude and the other extending from 220 km to 440 km at 90° SZA, respectively. In each sector, the model construction entails four steps: EOF decomposition, regression analysis, reconstruction of the model, and map the model from northern polar cap cylindrically along the Sun-Venus axis. Section 7.2.3.4 explains the EOF decomposition. This section introduces the other steps for the modeling. For details of the whole process, readers are referred to the flow diagram in Figure 4 by He et al. (2016). Regressions analysis is implemented between the response variables S_1 , S_2 , and S_3 detailed in Sect. 7.2.3 and predictor variables of IMF components described in Sect. 7.2.1:

$$\begin{aligned} \hat{S}_i(\mathbf{IMF}, F10.7) &= \beta_0 + \beta_{IMFx} IMF_x + \beta_{IMFy} IMF_y + \beta_{IMFz} IMF_z \\ &+ \beta_{F10.7} \hat{F}10.7 + \dots \text{(quadratic interaction and squared terms)} \end{aligned} \quad (7.10)$$

Here $\hat{F}10.7$ proxies the solar activity level, which is the 81-days averaged solar radio flux of 10.7 cm in solar flux units (sfu) measured at Earth. Quadratic interactions and squared terms are introduced to try to take the nonlinear variation into account. For short, we define $\mathbf{p} := (\mathbf{IMF}, F10.7)$. The EOF score function $\hat{S}_i(\mathbf{p})$

resulted from the regression allows reconstructing the magnetic pattern on Φ_{grid} according to:

$$\mathbf{B}(\Phi_{grid}|\mathbf{p}) = \langle \mathbf{B}(\Phi_{grid}) \rangle + \sum_i^3 \hat{\mathbf{S}}_{ii}(\mathbf{p}) \cdot \mathbf{B}_{EOFi}(\Phi_{grid}) \quad (7.11)$$

The most important three EOFs explain 29% of the total variance.

The resultant model $\mathbf{B}(\Phi_{grid}|\mathbf{p})$ covers only a piece of curve representing dawn-dusk crossing ($SZA = 0$) over the northern pole. Venus is an unmagnetized body, the dependence of topology of the Venusian magnetosphere on IMF is cylindrically symmetrical with respect to the Sun-Venus axis, and its polarity is typically determined by the orientation of cross flow IMF component. Under the assumption of cylindrically symmetrical geometry, we can extend the model $\mathbf{B}(\Phi_{grid}|\mathbf{p})$ from the curves over the pole to the whole terminator, as illustrated in Figures 1 and 2 by He et al. (2016).

7.2.4.3 Regularization

The standard linear regression model $\mathbf{y} = \mathbf{X}\beta + \mathbf{e}$ has least square solution $\hat{\beta}_{LS} = (\mathbf{X}^T\mathbf{X})^{-1}\mathbf{X}^T\mathbf{y}$. The uncertainty of $\hat{\beta}_{LS}$, denoted as Δ_{LS} , is propagated from the experimental errors δ_y in \mathbf{y} : $\Delta_{LS} = (\mathbf{X}^T\mathbf{X})^{-1}\delta_y$. Assume δ_y is a mutual uncorrelated Gaussian random variable: $\delta_y \sim N(0, \sigma_y^2)$ and $\langle \delta_y^T \delta_y \rangle = \sigma_y^2$. When predictor variables are mutually correlated, $\mathbf{X}^T\mathbf{X}$ is ill-conditioned, which inflates the uncertainty Δ_{LS} . For handling the potential multicollinearity, we implement ridge regression (also known as Tikhonov L2-norm regularization) (He et al. 2014, 2016).

The ridge regression allows a small bias in the least square solution through a damping parameter λ : $\hat{\beta}_{ridge} = (\mathbf{X}^T\mathbf{X} + \lambda\mathbf{I})^{-1}\mathbf{X}^T\mathbf{y}$. Often, a small bias results in significant reduction in the uncertainty $\Delta_{ridge} = (\mathbf{X}^T\mathbf{X} + \lambda\mathbf{I})^{-1}\mathbf{X}^T\mathbf{X}(\mathbf{X}^T\mathbf{X} + \lambda\mathbf{I})^{-1}\delta_y$. $|\Delta_{ridge}|$ is a monotonically decreasing function of λ , such that as $\lambda = 0$, $\Delta_{ridge} = \Delta_{LS}$, and as $\lambda \rightarrow \infty$, $\Delta_{ridge} \rightarrow 0$. λ is determined by the method of generalized cross-validation.

7.3 Scientific Results

In the previous section, we introduced the construction of the models. This section illustrates how the models facilitated the data analysis, and highlights the main revealed scientific results (Fig. 7.7).

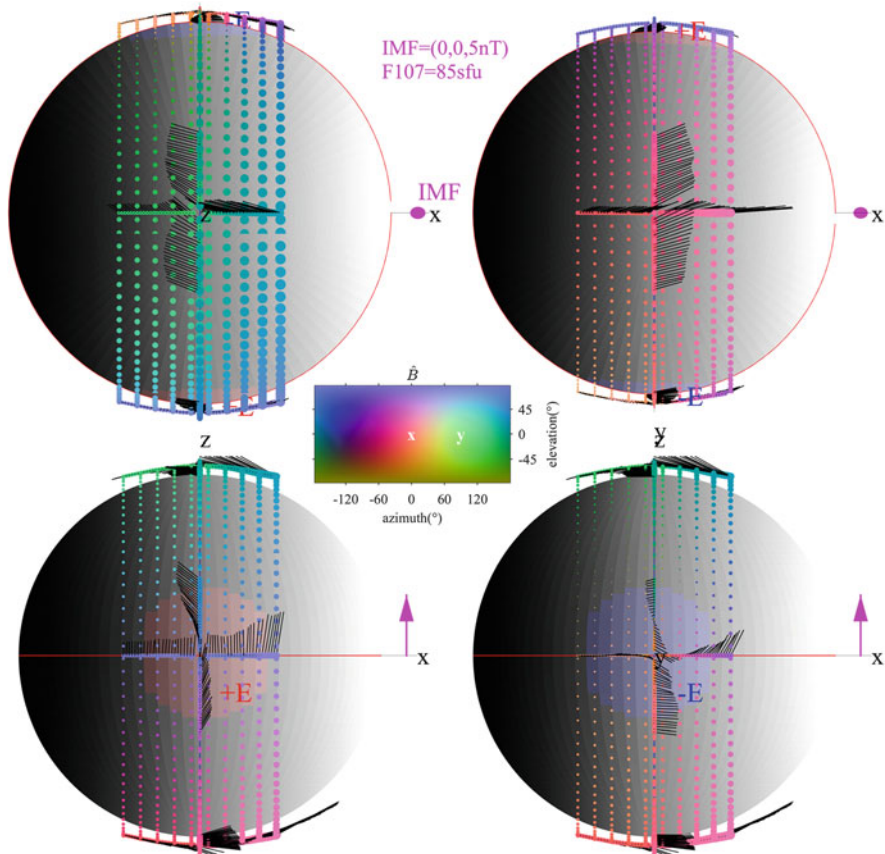


Fig. 7.7 Magnetic field configuration around Venus as predicted by EMVIM, at $\text{IMF} = (0, 0, 5)\text{nT}$ and $F10.7 = 85\text{sfu}$. The four panels show the same result but from different perspectives, namely, viewing from the $\pm\text{IMF}$ and $\pm E$ directions. In each panel, the illumination represents the solar zenith angle, the blue and red shadows show the polar caps of the $\pm E$ hemisphere, and the color and dimension of the points specify the orientation and magnitude of the magnetic field. Selected set of points is also shown as feather plot. The color map in the center is constructed by adding the additive primaries of red, green, and blue together, defining the magnetic field direction: the red, green, and blue channels measure the B_x , B_y , and B_z components, respectively. For example, in the map the white “x” presents the direction towards the $+x$ axis, and “y” points towards the $+y$ axis

7.3.1 Results of F2COSMIC

F2COSMIC revealed a comprehensive in-phase/anti-phase relationship of the ionospheric wave-4 structure, between the northern and southern hemispheres, between the equator and low-latitude, and between $NmF2$ and $hmF2$ (He et al. 2011). As summarized in Fig. 7.5, anti-phase wave-4 structures were found between daytime

$NmF2$ over the equator and that at low latitude, between daytime $NmF2$ and $hmF2$ over the equator, between nighttime $NmF2$ and $hmF2$ at low latitude, and between nighttime $hmF2$ in the Northern hemisphere and that in the Southern hemisphere; whereas in-phase *wave-4* structures were observed in between daytime $NmF2$ in the Northern hemisphere and that in the Southern hemisphere, between daytime $hmF2$ over equator and that at low latitude, between daytime $NmF2$ and $hmF2$ at low latitude. These results suggest that the well-accepted DE3 tidal modulation on the *E*-region dynamo only dominates the daytime ionospheric *wave-4* structure, whereas the SE2 transequatorial tidal wind accounts for the nighttime wave-4 structure.

7.3.2 Results of MFACE

MFACE captures almost all known features of FAC climatology, including the realistic current intensity, seasonal variation, latitudinal extension, *MLT* distribution, the NBZ structure, the evolution during substorm, dependence on solar wind variables, on conductivity, and on the corresponding interaction terms (for details cf., He et al. 2012, 2014). Figure 7.6 displays a comparison between MFACE, AMPERE, and the model constructed by Papitashvili et al. (2002). Both AMPERE and the *Papitashvili* models are based on the spherical harmonic basis functions. The AMPERE latitudinal distribution is largely consistent with MFACE, but AMPERE shows more longitudinal structure due to the limited data coverage. The *Papitashvili* model presents the basic double ring topology but is weak and broadly extending in latitude due to the large smearing effect of the approach. In the MFACE distribution, the topology, latitudinal extension, maximum current density, and local time variation are consistent with those observed in single auroral oval crossing events and the classic FAC pattern (Iijima and Potemra 1976, 1978).

The determination coefficient r^2 quantifies the model quality and allows estimating the time FACs take in response to solar wind changes. Correlation analysis suggests that FACs respond to solar wind changes in both the latitude location and current intensity, but not synchronously, 20 min and 35–40 min, respectively (He et al. 2012). With regard to the local time difference, FAC density responds to solar wind change more rapidly on the dayside than the nightside, around 15–25 min vs. 35–95 min (He et al. 2014). The values of r^2 for both FAC density and latitude are greater on the dayside than on the nightside, revealing that the predictability is higher on the dayside. The day-night differences can be attributed to the two modes of solar wind-magnetosphere interaction, namely, the direct driven processes responsible for the dynamics on the dayside and the loading/unloading processes acting on the nightside.

7.3.3 Results of EMVIM

EMVIM provides an empirical description of the induced magnetic field around Venus in terms of **IMF** and solar activity level. As an example, Fig. 7.7 illustrates the induced magnetic field under $\text{IMF} = (0\ 0\ 5)\text{nT}$ and $F10.7 = 85\text{sfu}$ according to EMVIM. The color of the points represents the orientation referring to the color map in the center, and the radius of the points represents the magnitude of the magnetic field. Feather plots show selected sets of magnetic field vectors. The color map is constructed by adding the additive primaries of red, green, and blue together, defining the magnetic field direction: the red, green, and blue channels measure the B_x , B_y , and B_z components, respectively. The upstream z-component-dominated IMF drapes antisymmetrical into components antiparallel to the x-axis in the +z hemisphere and parallel to the x-axis in the -z hemisphere. At the flanks, the magnetic field is neither symmetric nor antisymmetric between the +y and -y hemispheres. Further analysis indicated that the cross-tail current density decreases with increasing solar activity level. The double sheet structure corresponds to the “poloidal dipole structure” (Dubinin et al. 2013), which was suggested to be induced by IMF B_x . However, this suggestion is not supported by our analysis, because the score of the EOF representing the structure is not significantly dependent on IMF B_x .

7.4 Summary

This chapter reviews a novel empirical modeling approach. The approach synthesizes the EOF analysis and multivariable regression analysis flexibly. Different from predefined basis functions and parametric equations, EOFs are data-customized and do not require prior information. The approach can be tailored to different datasets. Applications on COSMIC RO observation and CHAMP and VEX magnetic field datasets provide quantitative descriptions for the ionospheric F2-layer peak, the field-aligned currents at Earth, and the induced magnetic field near Venus. A component of this approach was used recently for modeling Mercury’s magnetospheric cusp from MESSENGER (MErcury Surface, Space ENvironment, GEochemistry, and Ranging) magnetic field data as summarized in the flow diagram in Fig. 7.8 (also cf. He et al. 2017). The results illustrated that all IMF components and the Mercury orbital phase affect the horizontal location and extension of Mercury’s cusp significantly.

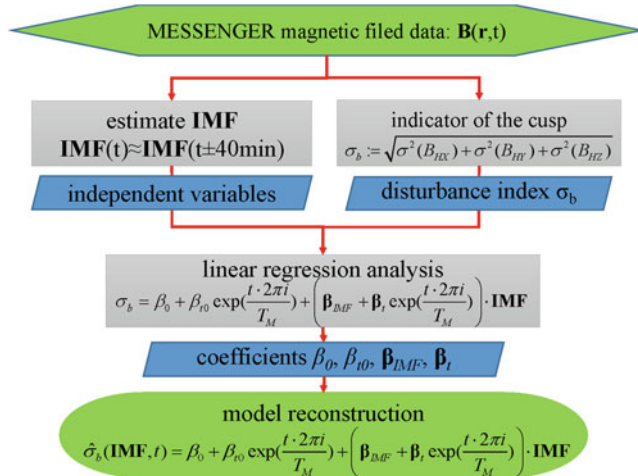


Fig. 7.8 Process flow diagram summarizing the processes constructing the model of Mercury's magnetospheric cusp from MESSENGER magnetic field data (for details cf. He et al. 2017)

Acknowledgments The authors acknowledge the online services provided by NASA's Planetary Data System (MESSENGER data), ESA's Planetary Science Archive (VEX data), GFZ Potsdam (CHAMP data), NGDC (POMME-6.2 coefficients), John Hopkins University APL (AACGM coefficients), and NASA OMNI (IMF/SW and other geophysical parameters). The corresponding codes are available on Source Forge or File change of MATLAB Central. This work was supported by the Deutsche Forschungsgemeinschaft through grants DFG HE6915/1-1 and VO 855/3-1.

References

- Alken, P., Maus, S.: Spatio-temporal characterization of the equatorial electrojet from CHAMP, Ørsted, and SAC-C satellite magnetic measurements. *J. Geophys. Res.* **112**(A9), A09305 (2007). <https://doi.org/10.1029/2007ja012524>
- Boyle, C.B., Reiff, P.H., Hairston, M.R.: Empirical polar cap potentials. *J. Geophys. Res.* **102**(A1), 111–125 (1997)
- Chao, J.K., Wu, D.J., Lin, C.H., Yang, Y.H., Wang, X.Y., Kessel, M., Chen, S.H., Lepping, R.P.: Models for the size and shape of the earth's magnetopause and bow shock. *COSPAR Colloq. Ser.* **12**, 127–135, L. Ling-Hsiao (Eds.), Pergamon (2002). [https://doi.org/10.1016/S0964-2749\(02\)80212-8](https://doi.org/10.1016/S0964-2749(02)80212-8)
- Dubinin, E., Fraenz, M., Woch, J., Zhang, T.L., Wei, Y., Fedorov, A., Barabash, S., Lundin, R.: Toroidal and poloidal magnetic fields at Venus. *Venus express observations. Planet. Space Sci.* **87**, 19–29 (2013). <https://doi.org/10.1016/j.pss.2012.12.003>
- He, M., Liu, L., Wan, W., Wei, Y.: Strong evidence for couplings between the ionospheric wave-4 structure and atmospheric tides. *Geophys. Res. Lett.* **38**(14), L14101 (2011). <https://doi.org/10.1029/2011GL047855>
- He, M., Vogt, J., Luhr, H., Sorbalo, E., Blagau, A., Le, G., Lu, G.: A high-resolution model of field-aligned currents through empirical orthogonal functions analysis (MFACE). *Geophys. Res. Lett.*, 39 (2012). doi: <https://doi.org/10.1029/2012gl053168>

- He, M., Vogt, J., Luhr, H., Sorbalo, E.: Local time resolved dynamics of field-aligned currents and their response to solar wind variability. *J. Geophys. Res.* **119**(7), 5305–5315 (2014). <https://doi.org/10.1002/2014JA019776>
- He, M., Vogt, J., Zhang, T., Rong, Z.: EMVIM: an empirical model for the magnetic field configuration near venus. *J. Geophys. Res.* **121**(4), 3362–3380 (2016). <https://doi.org/10.1002/2015JA022049>
- He, M., Vogt, J., Heyner, D., Zhong, J.: Solar wind controls on Mercury's magnetospheric cusp, *J. Geophys. Res. Space Physics*, **122**, 6150–6164 (2017). <https://doi:10.1002/2016JA023687>
- Iijima, T., Potemra, T.A.: Field-aligned currents in the dayside cusp observed by triad. *J. Geophys. Res.* **81**(34), 5971–5979 (1976). <https://doi.org/10.1029/JA081i034p05971>
- Iijima, T., Potemra, T.A.: Large-scale characteristics of field-aligned currents associated with substorms. *J. Geophys. Res.* **83**(A2), 599–615 (1978). <https://doi.org/10.1029/JA083iA02p00599>
- Martinez, C., et al.: Location of the bow shock and ion composition boundaries at Venus—initial determinations from venus express ASPERA-4. *Planet. Space Sci.* **56**(6), 780–784 (2008). <https://doi.org/10.1016/j.pss.2007.07.007>
- Masters, A., Achilleos, N., Dougherty, M.K., Slavin, J.A., Hospodarsky, G.B., Arridge, C.S., Coates, A.J.: An empirical model of Saturn's bow shock: cassini observations of shock location and shape. *J. Geophys. Res.* **113**(A10), A10210 (2008a). <https://doi.org/10.1029/2008ja013276>
- Masters, A., Achilleos, N., Dougherty, M.K., Slavin, J.A., Hospodarsky, G.B., Arridge, C.S., Coates, A.J.: An empirical model of Saturn's bow shock: cassini observations of shock location and shape. *J. Geophys. Res.* **113**(A10), (2008b). <https://doi.org/10.1029/2008ja013276>
- Maus, S., Rother, M., Stolle, C., Mai, W., Choi, S., Lühr, H., Cooke, D., Roth, C.: Third generation of the Potsdam Magnetic Model of the Earth (POMME). *Geochem. Geophys. Geosyst.* **7**(7), Q07008 (2006)
- Olsen, N.: A new tool for determining ionospheric currents from magnetic satellite data. *Geophys. Res. Lett.* **23**(24), 3635–3638 (1996). <https://doi.org/10.1029/96gl02896>
- Papitashvili, V.O., Christiansen, F., Neubert, T.: A new model of field-aligned currents derived from high-precision satellite magnetic field data. *Geophys. Res. Lett.*, **29**(14), 1683 (2002). <https://doi:10.1029/2001gl014207>
- Shue, J.H., et al.: Magnetopause location under extreme solar wind conditions. *J. Geophys. Res.* **103**(A8), 17691–17700 (1998). <https://doi.org/10.1029/98JA01103>
- Tsyganenko, N.A.: Data-based modelling of the Earth's dynamic magnetosphere: a review. *Ann. Geophys.* **31**(10), 1745–1772 (2013a). <https://doi.org/10.5194/angeo-31-1745-2013>
- Tsyganenko, N.A.: Empirical magnetic field models for the space weather program. *Space Weather.* 273–280 (2013b). <https://doi.org/10.1029/GM125p0273>. American Geophysical Union
- Tsyganenko, N. A., Andreeva, V.A., Gordeev, E. I.: Internally and externally induced deformations of the magnetospheric equatorial current as inferred from spacecraft data. *Ann. Geophys.*, 33(1) (2015). doi:<https://doi.org/10.5194/angeo-33-1-2015>
- Zhong, J., et al.: Mercury's three-dimensional asymmetric magnetopause. *J. Geophys. Res.* **120**(9), 7658–7671 (2015). <https://doi.org/10.1002/2015JA021425>

Chapter 8

Kinetic Simulations of Electron Acceleration at Mercury

Jörg Büchner, Patrick Kilian, Patricio A. Muñoz, Felix Spanier,
Fabien Widmer, Xiaowei Zhou, and Neeraj Jain

Abstract In preparation of the ESA-JAXA mission Bepi Colombo we reconsidered the electron acceleration near Mercury. We first reviewed the existing observations starting from NASA's Mariner-10 (1974–1975). Some of them later were shown to be inaccurate. Recently NASA's Messenger mission newly observed energetic electrons including bursts of energies up to 100–200 keV. This by far exceeds the electron energies in the upstream solar wind. The acceleration mechanisms are, however, still not well understood. We derive models of electron acceleration near Mercury by passing strong interplanetary shocks, by reconnection at the magnetopause and in the Hermean magnetotail. We obtained the resulting electron energies and spectra in the near-Mercury MHD- and kinetic plasma turbulence as well as due to electric field structures by means of test particle calculations and also by fully self-consistent kinetic two- and three-dimensional PIC-code simulations whose results and, therefore, the acceleration mechanisms should be verified by the coming ESA-JAXA Bepi-Colombo mission to Mercury.

J. Büchner (✉) • P.A. Muñoz • N. Jain

Max Planck Institute for Solar System Research, 37077 Göttingen, Germany
e-mail: buechner@mps.mpg.de

P. Kilian

Max Planck Institute for Solar System Research, 37077 Göttingen, Germany
Centre for Space Research, North-West University, Potchefstroom, South Africa

F. Spanier

Centre for Space Research, North-West University, Potchefstroom, South Africa

F. Widmer

Max Planck Institute for Solar System Research, 37077 Göttingen, Germany

Institut de Recherche sur la Fusion Magnétique, Cadarache, F-13108 Saint-Paul-lez-Durance, France

X. Zhou

Purple Mountain Observatory of the Chinese Academy of Sciences, Nanjing, People's Republic of China

8.1 Introduction

In contrast to other small planets or moons, Mercury possesses an intrinsic magnetic field. In the absence of an ionosphere this magnetic field directly interacts with the (shocked) solar wind, the Hermean magnetosheath plasma. Typical phenomena of the Mercury's magnetized environment like aurorae, radiation belts, and magnetospheric substorms go along with particle acceleration. The first in situ measurements at Mercury were carried out in 1974–1975 by Mariner 10. They seemed to have discovered electrons with energies of up to 300 keV and protons with energies up to 550 keV near the Hermean magnetotail (Simpson et al. 1974). Later re-interpretations of the experimental data led, however, to the conclusion that the particle energies were over-estimated. They discredited the earlier claims and attributed the seemingly high energies to high fluxes of electrons with energies of 35–100 keV causing pileup in the instrument electronics (Armstrong et al. 1975). The necessity to reinterpret the early claims of high energy electron fluxes was confirmed by the MErcury Surface, Space ENvironment, GEochemistry and Ranging (MESSENGER) mission starting 2011. MESSENGER regularly observed electron energies up to 100–200 keV during short duration episodes which take place several times per day primarily in the magnetotail, but did not find energetic ions (Ho et al. 2011, 2012; Lawrence et al. 2015; Baker et al. 2016). In 1974–1980 the two Helios spacecraft were probing the solar wind also at Mercury distances from the Sun. In 1979, as Kirsch and Richter reported, Helios detected energetic ions with energies above 80 keV and electrons with energies above 60 keV propagating sunward and coming from the direction of Mercury, while the solar wind particle energies were typically more like 1.5–10 keV. Note that the energetic particle fluxes were observed with a significance of 2–5 times above the statistical error (Kirsch and Richter 1985). These results independently confirmed that charged particles are accelerated in the Hermean environment. Zelenyi et al. reviewed in 2007 the state of understanding the particle acceleration in the Hermean magnetosphere before the MESSENGER mission was launched (Zelenyi et al. 2007). They considered inductive electric fields, centrifugal impulse forces, stochastic acceleration in turbulent magnetic fields, wave–particle interactions, and shock acceleration comparing them to the situation at the Earth. They conjectured that while electrons can be accelerated to high energies in the very dynamic and compact Hermean magnetosphere, the ions are non-adiabatic at those spatial scales and that they, therefore, cannot be accelerated to energies above 100 keV (Zelenyi et al. 2007).

Recently the MESSENGER mission is continuously adding more and more detailed observations. They help to understand the Hermean particle acceleration processes better, in particular they help to distinguish them from processes external to Mercury's magnetosphere. Since the presence of MeV electrons during impulsive solar energetic particle (SEP) events has been known for years, the MESSENGER was designed to survive SEP radiation without permanent damage. During SEP events the inner heliosphere is bathed in relativistic MeV electrons which, through magnetopause reconnection, can enter the Hermean magnetosphere. These energetic

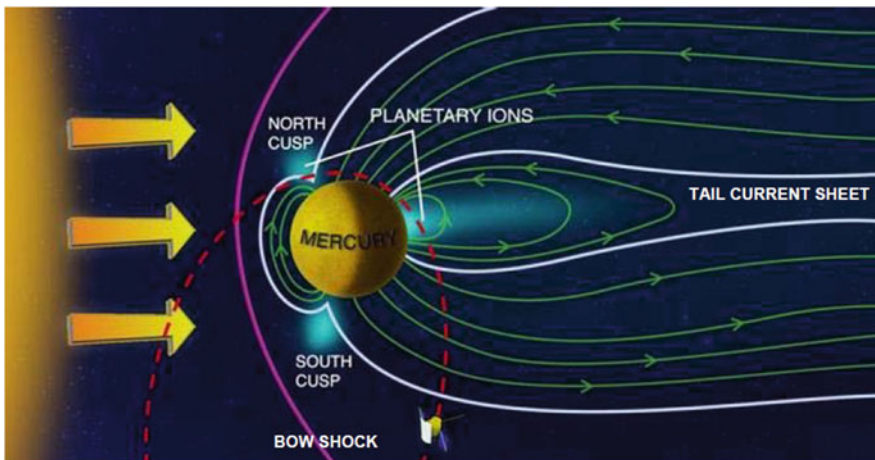


Fig. 8.1 Mercury's boundaries, an artist's impression. *White lines:* magnetopause and tail boundary. Image Credit: Science/AAAS

electrons will fill nearly instantaneously regions magnetically open to the solar wind and precipitate to the Hermean surface (Gershman et al. 2015). Since these energetic particles are not accelerated at Mercury and commonly occur throughout the Solar System we will not discuss them any further here.

The questions to be addressed here are, therefore: what are the specific conditions for the particle acceleration at Mercury? And: what are the preferred mechanisms and sites of acceleration to high energies? In the following we shortly review the potential sites of acceleration (cf. also Fig. 8.1).

Boundary layers are formed as interfaces in the interaction of the planetary plasma with the solar wind and inside the magnetosphere. Based on the experience of observations at the Earth and other planets, boundaries are important sites of fundamental energy conversion including particle acceleration. Mercury has a small own magnetic field which consists of dipolar, quadrupolar and higher order multipolar components. Since the intrinsic magnetic field of Mercury is small, the Hermean magnetosphere is small as well. Its size determines the effective cross section of the planet as an obstacle in the solar wind flow. In the latter a bow shock wave forms which compresses the solar wind into the magnetosheath and deflects it around Mercury. More boundaries are located downstream of the bow shock like the magnetopause, the boundary and the central current sheet of the Hermean magnetotail. All these boundaries can be major particle acceleration sites. Mariner-10, Helios, and MESSENGER observations already revealed a number of parameters and properties characterizing the Hermean boundaries. For their locations, see Fig. 8.1.

The Hermean bow shock is a fast magnetosonic shock that stands in the solar wind diverting it around the planetary magnetospheric cavity (Spreiter et al. 1966). The bow shock wave is dynamic, permanently reforming, changing its shape. It

moves closer or farther away from the planet responding to variations in the solar wind. Important parameters determining its properties are the magnetosonic Mach number, the plasma beta and, to a lesser extent, the IMF (Interplanetary Magnetic Field) direction (Slavin and Holzer 1981). Re-analyzing the solar wind properties at heliocentric distances around Mercury's perihelion (0.31–0.35 AU) using Helios data Slavin et al. obtained typical magnetosonic and Alfvénic Mach-numbers of about $3 \lesssim M_s \lesssim 6$ and $2 \lesssim M_A \lesssim 5$, respectively (Slavin and Holzer 1981; Sarantos and Slavin 2009).

The average Mach numbers of the Hermean bow shock are, therefore, smaller than those of the Earth's bow shock ($M_s \sim M_A \sim 7 \dots 9$) and smaller than those of the outer planets of the Solar System. This is true also for coronal mass ejections (CMEs) hitting Mercury. Recent models based on spacecraft data predict that the Mach numbers of CMEs increase with the distance from the Sun as $M_A(r) \sim r^{0.24}$ (Sarantos and Slavin 2009; Liu et al. 2005). The Helios spacecraft measured even Mach numbers as low as 1 during the interaction of CMEs with Mercury, providing conditions for the formation of Alfvén wings (Sarantos and Slavin 2009). Some models of solar flare driven CMEs predicted, however, that the Mach-numbers at the front of interplanetary shocks can become as large as $M_s \sim 40$ at the Mercury orbit distance from the Sun (Smart and Shea 1985). This motivated studies of electron acceleration for high Mach-number shocks (Hoshino and Shimada 2002; Amano and Hoshino 2007).

The typical interplanetary (solar wind) conditions at Mercury are, however, solar wind velocities between 300 and 600 km/s, electron temperatures of about 20000 K or 1.7 eV, a strength of the, practically radial, magnetic field of about 30–50 nT, densities of the order of 70 cm^{-3} and a plasma-beta in the range of $0.4 \lesssim \beta \lesssim 2$. Those values were originally measured already by the Helios spacecraft in the 1970s (Slavin and Holzer 1981; Burlaga 2001; Sarantos et al. 2007; Sarantos and Slavin 2009). The solar wind parameters at Mercury could not be measured directly by the more recent MESSENGER mission due to the obstruction of the spacecraft shade (the sunshade blocked nearly all of the solar wind, see above). Hence they were usually inferred from an extrapolation using some partial measurements combined with the use of some solar wind models (Le et al. 2013; Gershman et al. 2012; Baker et al. 2013; Gershman et al. 2013).

Winslow et al. 2013, e.g., estimated shock parameters using ENLIL models. They obtained a very small typical standoff distance of the Hermean bow shock of $R_{ss} \sim 1.45 R_\oplus$ (where R_\oplus is the Mercury radius—2440 km). Hence, the Hermean bow shock is much smaller than that of the Earth. The bow shock shape found by a best fit for a typical Alfvén Mach-number of $M_A = 6.6$ is a hyperboloid with a standoff distance $R_{ss} = 1.96 R_\oplus$ and an eccentricity of 1.02. For M_A in the range of 4.12–11.8 the bow shock standoff distance R_{ss} would vary from 2.29 to $1.89 R_\oplus$. As the Earth's bow shock that of Mercury is also permanently reformed. Recently a bow shock crossing by the MESSENGER spacecraft was reported during which the upstream interplanetary magnetic field (IMF) was nearly radial and steady over a time period longer than the spacecraft transit time (Sundberg et al. 2013).

The observations clearly revealed an extremely periodic self-reformation. Over 25-min of observations, a 10-s shock reformation period of the bow shock was established which could also be seen in the magnetosheath, in the upstream solar wind and also within the magnetosphere (in form of magnetic compressions). These observations showed that the bow shock is a direct source of energy input into the Hermean magnetosphere. The extreme periodicity of the event can be attributed to the small spatial scales at Mercury, which leads to a collective behavior of the bow shock rather than to a patchwork of pulsations and reformations usually observed at the bow shock upstream of the Earth. The very small and limited foreshock region upstream of Mercury's weak bow shock has been analyzed by Le et al. in 2013 (Le et al. 2013). Since most of the time the Hermean bow shock was found to be weak, according to theoretical investigations, not much particle acceleration can be expected (Balogh and Treumann 2013; Burgess and Scholer 2015).

Interplanetary shocks with higher Mach numbers could, however, essentially accelerate particles. We will discuss in Sect. 8.2 the consequences of a $M_A = 40$ interplanetary shock.

The Hermean magnetopause is a current layer separating the magnetosheath (shocked solar wind) plasma (and IMF) from the (magnetospheric) plasma dominated by the planetary magnetic field. As already evidenced by Mariner 10 MESSENGER confirmed that the Hermean magnetosheath, i.e. the plasma layer inside the bow shock, is very thin. Hermean magnetopause current sheets were clearly identified next to the quasi-perpendicular portion of the bow shock while they so far could hardly be recognized next to the quasi-parallel part of the bow shock. The latter is, perhaps, due to a strong interaction. Quasi-perpendicular shocks and the magnetospheric boundary mediate magnetosheath flows. Three-dimensional global hybrid simulations of magnetopause location and shape carried out for different IMF orientations appeared to be in accordance with MESSENGER observations. This proved that magnetopause location and shape are controlled by the pressure exerted on the magnetopause by the magnetosheath (shocked solar wind) plasma. Hence they are indeed determined by the solar wind ram pressure balanced by the planetary magnetic field as already pointed out by Spreiter et al. in 1966 (Spreiter et al. 1966). The average shape and location of Mercury's magnetopause and bow shock were established by orbital observations using the MESSENGER magnetometer. Fits of empirical models of the midpoints of the boundary crossings and probability density maps of the Hermean magnetopause and bow shock positions for the magnetopause revealed a subsolar standoff distance $R_{ss} \sim 1.45 R_\oplus$ for a mean solar wind ram pressure $P_{\text{ram}} = 14.3 \text{ nPa}$. While the boundaries move when P_{ram} and M_A vary, their shapes remain unchanged. The magnetopause R_{ss} varies, e.g., from 1.55 to $1.35 R_\oplus$ for a P_{ram} in the range 8.8–21.6 nPa (Winslow et al. 2013). The usually small Alfvén-Mach-numbers at Mercury result in a sub-Alfvénic magnetosheath and thick plasma depletion layers adjacent to the magnetopause (Gershman et al. 2013).

Magnetic reconnection transfers the solar wind energy via the magnetosheath through the Hermean magnetopause. It determines the degree of connectivity

between IMF and the planetary magnetic field. The magnetopause reconnection rate is usually high (Slavin and Holzer 1979; Slavin et al. 2009). As a result the magnetopause current sheet might be a site of efficient particle acceleration by magnetic reconnection.

During MESSENGER's second flyby of Mercury, during steady southward directed IMF conditions, a strong magnetic field was observed to thread through the magnetopause at a reconnection rate which was ~ 10 times larger than that typically observed at the Earth! Also, a large flux transfer event was observed in the magnetosheath downstream of the magnetopause as well as plasmoids and multiple traveling compression regions in Mercury's magnetotail—all caused by magnetic reconnection. These observations indicate that the Hermean magnetosphere is very responsive to the IMF direction and that reconnection is even more dominant at Mercury than near the Earth and other magnetized planets (Slavin et al. 2009; Sun et al. 2016). At Mercury, reconnection is especially significant due to extreme conditions for CMEs encounters and high-speed solar wind streams. This was confirmed by measured reconnection rates as high as 0.2 for very low plasma- β conditions and magnetic shear angles as small as 27° (Slavin et al. 2014), which reveals strong guide-field fast reconnection (Muñoz et al. 2015).

Using high-resolution (150 ms) MESSENGER-spacecraft measurements of energetic electrons over Mercury's dayside polar cap boundary, Gershman et al. (2016) inferred small-scale changes in magnetic topology and reconnection rates. They provided first direct measurements of the open magnetic topology and flux transfer events at Mercury, reconnected structures thought to account for a significant portion of the open magnetic flux transport throughout the Hermean magnetosphere. Intermittent bursts of $\sim 0.3\text{--}3$ mV/m reconnection electric fields separated by $\sim 5\text{--}10$ s resulted in average and peak normalized dayside reconnection rates of 0.02–0.2, respectively (Gershman et al. 2016). These observations indicate that the thickness of the Hermean-magnetopause current sheet is determined by the ions while the strength and time dependence of the electric field is related to the rate of reconnection between the solar wind and the planetary magnetic field. Since reconnection through the Hermean magnetopause takes place at the smallest (ion-) kinetic scales, it has to be treated kinetically. As in all collisionless plasmas, reconnection at Mercury needs a balance of the electric fields, e.g., by anomalous dissipation (Büchner 2007), by a non-gyrotropy of the electrons (finite off-diagonal elements of the electron pressure tensor) (Dungey 1989) or by electron inertia (Speiser 1970). For their determination one has to understand the kinetic physics of the Hermean plasma. Since the particle acceleration by reconnection has to take into account the shear angle between the shocked solar wind IMF in the magnetosheath and the Hermean magnetic field, a finite guide field perpendicular to the reconnecting field components has to be taken into account. In Sect. 8.3 we address the particle acceleration by reconnection including a finite guide magnetic field by fully kinetic simulations.

The **near-Mercury Hermean magnetotail** can accumulate free magnetic energy which can energize charged particles. Using MESSENGER observations and masking quantifiable effects of the interplanetary magnetic field causing a

large dynamic variability of the Hermean magnetotail, Winslow et al. (2013) found that the boundary of the magnetotail is nearly cylindrical, with a radius of $\sim 2.7R_\oplus$ at a distance of $3R_\oplus$ downstream of the planet. For comparison, the Earth's magnetotail flaring continues until a downstream distance of $\sim 10R_{ss}$. In the near-Mercury portion of the tail, perhaps, betatron acceleration during tail dipolarization events prevails. Delcourt et al. examined in 2005 the nonlinear dynamics of electrons during the expansion phase of substorms at Mercury by test particle calculations (Delcourt et al. 2005). The substorm-induced Hermean magnetic field dipolarization was obtained by appropriately rescaling a (Tsyganenko-) model of the Earth's magnetosphere. Their simulations demonstrated that electrons may significantly be energized at time scales as short as several seconds. Similar to the ions in the near-Earth's magnetosphere, low-energy (up to several tens of eV) electrons may not conserve the second adiabatic invariant during dipolarization. This creates clusters of bouncing particles in the near-Mercury part of the magnetotail. Due to the fast stretching of the magnetic field, high-energy electrons (several keVs and above) do not gyrate any more but experience meandering on Speiser-type orbits across the tail midplane. This way the dipolarization of the Hermean tail magnetic field may be responsible for significant, though transient (lasting only a few seconds) events of energetic (dozens of keV) electron precipitation onto Mercury's surface. These injections do not exhibit, however, the short-period temporal modulations observed by Mariner-10 which must be due to other acceleration processes rather than a simple convection surge.

Magnetotail flux-rope reconnection can accelerate particles along the whole Hermean tail (Slavin et al. 2009). The first three MESSENGER flybys of Mercury, e.g., (M1–M3) traversed the magnetotail, e.g., between 1.25 and $3.25R_\oplus$ downstream of the planet. MESSENGERS M1, M2, and M3 tail encounters took place under northward, southward, and variable-polarity interplanetary magnetic field (IMF) conditions, respectively. The magnetic field strength (B) in the Hermean magnetotail decreases following a power law $B \sim |X|^{-\gamma}$ with the antisunward distance $|X|$ and with γ between ~ 5.4 for northward and ~ 1.6 for southward IMF. Clear signatures of tail reconnection were found, e.g., in the M2 and M3 magnetic field data. Plasmoids were observed during M2 and M3 with typical durations of ~ 3 s, suggesting plasmoid sizes of the order of ~ 1500 km. Overall, the response of Mercury's magnetotail to the steady southward IMF during M2 appeared very similar to steady magnetospheric convection at Earth, which is believed to be driven by quasi-continuous reconnection. Contrary, the M3 measurements are dominated by tail loading and unloading. This resembles the large-scale tail magnetic field reconfigurations observed during magnetospheric substorms at Earth and caused by unsteady magnetic reconnection (Slavin et al. 2012). Another observation in favor of the magnetotail being a site of particle acceleration by reconnection are flux ropes. A search for them in the Hermean magnetotail was carried out using MESSENGER magnetometer and Fast Imaging Plasma Spectrometer (FITS) observations during seven “hot seasons” when the periapsis of the spacecraft orbit was on Mercury's dayside. DiBraccio et al. in 2015 and Sun et al. in

2016 published an analysis of 49 flux ropes observed between 1.7 and $2.8 R_{\odot}$ down the tail from the center of the planet. Using a minimum variance analysis they looked for events when the spacecraft passed near the central axis of the structure. An average Alfvén speed of 465 km s^{-1} was measured in the plasma sheet surrounding these flux ropes. Under the assumption that the flux ropes moved at the local Alfvén speed, the mean duration of $0.74 \pm 0.15 \text{ s}$ implies a typical flux rope diameter of $\sim 345 \text{ km}$ (or $\sim 0.14 R_{\odot}$). This is comparable to a proton gyroradius in the plasma sheet of $\sim 380 \text{ km}$. Mean radius and core magnetic field determined in this manner were $\sim 450 \text{ km}$ (or $\sim 0.18 R_{\odot}$) and $B \sim 40 \text{ nT}$, respectively. A superposed epoch analysis of the magnetic field during these events shows variations similar to those observed in the Earth magnetotail, including a filling of the post-plasmoid plasma sheet by disconnected magnetic flux. The timescales of the events in the Hermean magnetotail are, however, 40 times shorter. The results of this flux-rope survey indicate that intense magnetic reconnection occurs frequently in the cross-tail current sheet of the small but extremely dynamic Hermean magnetotail (DiBraccio et al. 2015; Sun et al. 2016) compared to the flux ropes formed in the Earth’s magnetotail (Büchner et al. 1991). As it is well known for the Earth’s magnetotail (Büchner and Zelenyi 1990), but also for the trailing current sheets of coronal mass ejections (Zhou et al. 2015, 2016), tail-like current sheet can easily accelerate ions and electrons (Büchner and Kuska 1998; Muñoz and Büchner 2016). The discovery of high-intensity electron bursts with energies of up to 200 keV during Hermean nightside encounters by Mariner 10 and later confirmed by MESSENGER, already provided some evidence for very strong particle acceleration during explosive magnetic field reconnection in Mercury’s magnetotail (Eraker and Simpson 1986). Such strong energetic particle bursts at Mercury have been a source of curiosity and controversy because prior to MESSENGER, instrumental effects prevented an unambiguous determination of species, flux, and energy spectrum. MESSENGER data taken by the Energetic Particle Spectrometer (EPS) have now shown that these energetic particle bursts are entirely composed of electrons. Not only by using the EPS measurements MESSENGER has provided a wealth of new unique information about energetic particles at Mercury. Energetic electrons are recorded by MESSENGER also by the X-Ray Spectrometer XRS as well as by the Gamma-Ray and Neutron Spectrometer GRNS. The combined data sets cover electron energies ranging from a few keV up to several 100 keV with a relatively good spatial and temporal resolution for many events. Energetic electron bursts measured by GRNS were placed in the context of possible solar wind and magnetospheric forcing. High temporal resolution measurements (10 ms) during the period March 2013 through October 2014 strongly supports energetic electrons acceleration by dipolarization events in the near-tail region of Mercury’s magnetosphere subsequently “injected” onto closed magnetic field lines on the nightside of the planet. The electrons populate the plasma sheet and drift rapidly eastward toward the dawn and prenoon sectors, at times executing multiple complete drifts around the planet to form “quasi-trapped” populations (Baker et al. 2016). EPS made directional measurements of these

electrons from \sim 30 to 300 keV at 3 s resolution. The energy of these electrons sometimes exceeded 200 keV and their energy distributions usually exhibited a cutoff near 100 keV. The Gamma Ray Spectrometer GRS measured energetic electrons at a very high time resolution (10 ms) and with a higher-energy threshold (>50 keV) compared to EPS. MESSENGER/GRS observations near the plasma sheet of the Hermean magnetotail now being extensively analyzed provide, e.g. details about strong electron acceleration. Dewey et al. 2016, e.g., just published new results about strong electron acceleration to \sim 100–200 keV at dipolarization fronts (betatron acceleration) but also within flux ropes in the cross-tail current sheet and during encounters with separatrix layers in the tail of flux ropes (Fermi-acceleration) and by tail loading/unloading (non-stationary X-line-) acceleration.

In order to understand these observations as well as in preparation of the ESA-JAXA mission BEPI COLOMBO to be launched in 2018 and to arrive at Mercury in 2024 (Benkhoff et al. 2010), we carried out plasma simulations to verify possible bow shock and magnetotail acceleration processes in the Hermean environment. In particular we are looking for the possibility of particle acceleration by strong bow shock waves as well as by magnetic reconnection at the Hermean magnetopause and in its magnetotail. In the following we summarize our results obtained in the framework of the DFG Schwerpunktprogramm “Planetmag.” In Sect. 8.2 the first simulation results of strong Hermean bow shock waves are presented, in Sect. 8.3 the results of evaluating electron acceleration by finite guide-field reconnection in the Hermean magnetopause and in Sect. 8.4 acceleration processes in Hermean magnetotail flux ropes. Our results are summarized and discussed in Sect. 8.5.

8.2 High Mach-Number Interplanetary Shocks at the Mercury Distance from the Sun

The typical solar wind conditions reveal a weak Hermean bow shock with small Alfvén Mach-numbers (M_A) (Sarantos and Slavin 2009), so electrons cannot be efficiently accelerated there. On the other hand, interplanetary shocks can be strong at the Mercury distance from the Sun causing the acceleration of electrons which subsequently can reach the Hermean environment. As an example we explored the particle acceleration at an interplanetary shock with a $M_A \approx 40$ (Smart and Shea 1985; Hoshino and Shimada 2002; Amano and Hoshino 2007). These would be strong interplanetary shocks, but shocks with Mach numbers as high as 100 have been detected in the solar system. The Cassini spacecraft measured strong quasi-parallel (Masters et al. 2013) and quasi-perpendicular (Sulaiman et al. 2015) shocks near Saturn as well as energetic electrons.

We focus here on the microphysics of strong quasi-perpendicular shocks down to electron scales to understand under which circumstances strong interplanetary shocks could accelerate electrons to high energies.

In particular we addressed the following questions:

- How do such strong interplanetary shocks self-consistently form at the kinetic level?
- What is the structure of such strong interplanetary shocks at electron scales?
- Under which conditions can such strong interplanetary shocks efficiently accelerate electrons?

The acceleration of particles to supra-thermal energies in self-reforming strong shocks has to be described by a plasma-kinetic approach. While pure fluid-like MHD simulations may approximate the large scale shock structure they completely ignore kinetic effects. On the other hand, in-situ measurements in the Hermean plasma environment gave evidence, e.g., of finite Larmor radius effects and kinetic turbulence (Uritsky et al. 2011). Hybrid simulations, where protons are treated as particles and electrons as fluid, can reproduce kinetic effects beyond the ion gyrofrequency, but they are still not capable to cover electron kinetic effects. This narrows the choice down to fully kinetic methods like Particle-in-Cell (PIC) (Hockney and Eastwood 1988) and Vlasov-code (Elkina and Büchner 2006) simulations. Explicit kinetic simulations usually require the resolution of small plasma scales down to the Debye length. Due to the large ion-to-electron mass ratio this would require to bridge large parameter ratios between smallest and largest scales. Even on the most advanced Supercomputers this problem can be dealt with only by assuming artificially smaller mass ratios and higher temperatures, solving the kinetic equations using a PIC-code, ACRONYM like (e.g., Kilian et al. 2011). A two-dimensional spatial Cartesian grid is used (2D3V) with periodic boundary conditions in the spatial directions. In the code, the electric and magnetic field information is stored according to a standard Yee scheme (Yee 1966) while the current density is calculated following the Esirkepov scheme (Esirkepov 2001). Current and charge density are deposited on the grid via a triangular shaped cloud (TSC) form factor providing a good balance of computational speed and numerical accuracy (Kilian et al. 2013; Muñoz et al. 2014). Maxwell's equations are solved by ACRONYM code using an explicit second-order leap-frog scheme. The field is interpolated to the macro-particle positions using the same TSC form factor. The relativistic equations of motion are solved by an implicit method (Vay 2008). It was proven that a standard Boris push (Boris 1970) would suffice as well. In the framework of our Mercury's electron acceleration project we separately considered two aspects of shock acceleration:

1. A kinetic simulation of the very shock formation by letting plasma stream fastly into a box with a reflecting wall on the other side. After the plasma is reflected from the wall a shock front is formed moving upstream.
2. Single-wave simulations to test the interaction of the electrons with the self-generated turbulence as a prerequisite for shock acceleration.

Note that such simulations are performed in the downstream rest-frame of the shock, not in the frame moving with the shock front. For the simulation of the shock formation we used a rectangular box sized $L_x \times L_y \times L_z$ as depicted by the first panel

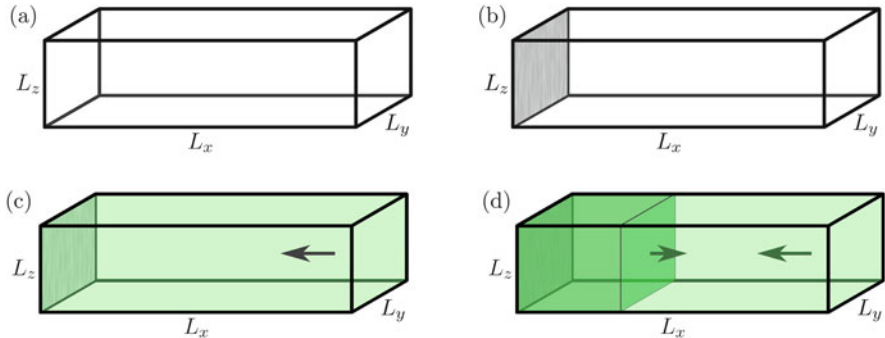


Fig. 8.2 Numerical setup that leads to a self-consistent shock. (a) Desired result: upstream and Downstream divided by a shock front. (b) Important tool: a conducting wall, that reflects particles. (c) Initial conditions: plasma streaming against the wall. (d) Result: a shock front moving upstream

(a) in Fig. 8.2. The right-hand side box-boundary is open, the opposite boundary is a conducting/reflecting wall (see panel (b) of Fig. 8.2). The other four boundary conditions are periodic. The conducting wall reflects particles as well as waves. Initially the whole box is filled with a plasma streaming with the desired drift against the conducting wall (see panel (c) of Fig. 8.2). After hitting the wall the plasma is reflected and streams into the incoming upstream plasma (see panel (c) of Fig. 8.2). This is equivalent to the encounter of two colliding plasma populations which causes plasma instabilities. Due to the interaction with the resulting turbulence the plasma flow is decelerated. After some time this will result in a situation illustrated by panel (d) of Fig. 8.2: near the reflecting (left) wall a dense, hot downstream plasma resides which is separated from the dilute, still cold upstream plasma by a shock front.

The second simulations setup is used to study the wave–particle interaction of electrons and (possibly dispersive) plasma waves in order to understand their contribution to electron acceleration. Its initial conditions involve a warm background plasma in a periodic box. In this plasma a single, low-frequency wave is excited by choosing conditions for the electromagnetic fields and particle velocities for specific wave numbers k_{\parallel} . The wave frequency ω is chosen according to a solution of the dispersion relation. For circularly polarized waves the different components of the electric and magnetic field can easily be found solving textbook dispersion relations (Stix 1992). To this wave, background energetic electrons are added and their interaction with the wave is traced.

8.2.1 Interplanetary High-mach Number Shock Formation

Since a direct simulation of a shocked plasma with these parameters would be technically impossible (see above) we used parameters as they are given in Table 8.2. The compromises in order to keep the computation time in an acceptable range are mainly higher plasma velocities and an artificial mass ratio of protons to

Table 8.1 High-Mach-number interplanetary shock wave parameters

| | | |
|-------------------------------|------------------------|-------------------------|
| Plasma beta | β | 1.00 |
| Solar wind velocity | u | 5.0×10^8 cm/s |
| Alfvén velocity | v_A | 1.0×10^7 cm/s |
| Speed of sound | v_S | 1.4×10^6 cm/s |
| Alfvénic Mach number | M_A | 39.4 |
| Upstream electron temperature | T_e | 2.2×10^4 K |
| Magnetic field strength | $ B $ | 4×10^{-4} G |
| Plasma frequency | ω_{pe} | 4.7×10^5 rad/s |
| Magnetization | ω_{pe}/Ω_e | 66 |

Table 8.2 Simulation parameters

| | | |
|---|------------------------|------------------------------|
| Plasma beta | β | 1 |
| Solar wind velocity | u | 3×10^9 cm/s |
| Alfvén velocity | v_A | 9.1×10^7 cm/s |
| Speed of sound | v_S | 8.36×10^7 cm/s |
| Alfvénic Mach number | M_A | 39 |
| Upstream electron temperature | T_e | 1.18×10^6 K |
| Magnetic field strength | $ B $ | 2.313×10^{-4} G |
| Plasma frequency | ω_{pe} | 2.03×10^5 Hz |
| Magnetization | ω_{pe}/Ω_e | 50 |
| Upstream electron thermal velocity | $v_{th,u}$ | 4.24×10^8 cm/s |
| Upstream density | n_e | $26/\text{cm}^3$ |
| Angle between shock normal and magnetic field | Θ | 81° |
| Cell size | Δx | 736.86 cm |
| Ion inertial length | c/ω_{pe} | 9.65×10^5 cm |
| Time step | Δt | $1.419\,07 \times 10^{-8}$ s |
| Mass ratio | M_p/m_e | 42.85 |
| Box size | L | 3.68×10^8 cm |
| Cell number | N_x | 500,000 |
| Particles per cell | ppc | 16 |
| Simulation time steps | | 2.72×10^7 |

electrons $M_p/m_e \cong 43$. This allows to take into account the reaction of the ions over many electron time scales which for real mass-ratios would leave the ions practically almost immobile during affordable simulation times. The velocities, on the other hand, are changed since the speed of light has to be resolved by an explicit PIC code. Note that while the absolute velocities and frequencies are different in the PIC-code simulations, their ordering is unchanged—for comparison see Table 8.1 for typical parameters of Mach number 40 interplanetary shock waves and Table 8.2 for the parameters used in the simulations.

We have run a number of shock simulations for the parameters given by Table 8.2 in a 1D simulation box extending in the x direction. Note that the simulated shock

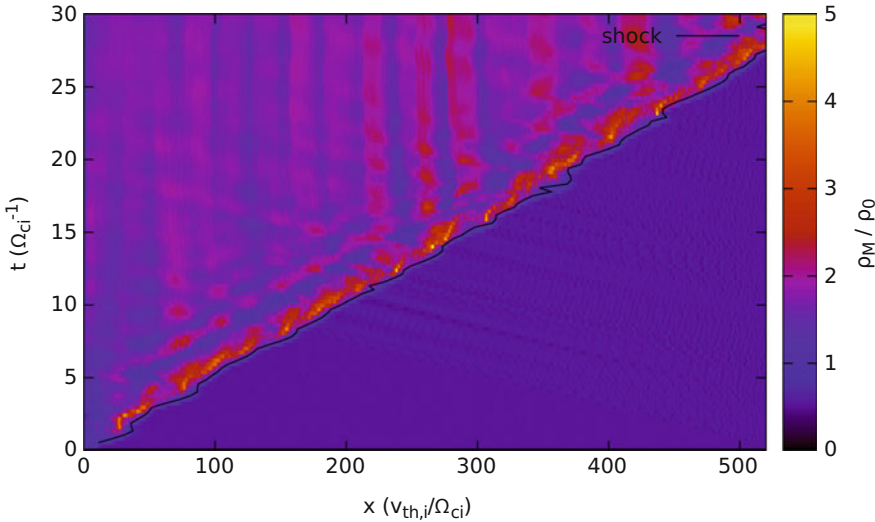


Fig. 8.3 Simulated mass density structure and evolution of the shock. The *horizontal axis* corresponds to the x direction of shock formation and the *vertical axis* is the time line

is quasi-perpendicular, the angle between the shock normal (the x -direction) and the magnetic field direction (practically the y -direction) is close to 90° , whose front propagates nearly perpendicular to the upstream magnetic field. We found that the shock is dominated by the ions, they fulfill the MHD jump conditions to an acceptable degree. Figure 8.3 shows the temporal evolution of the mass density obtained by the simulation. The shock front propagation along the x -direction is clearly visible. As one can see in the figure, the shock wave is not characterized by a constant density jump but undergoes permanent reformations with a period of about $5\text{--}10 \Omega_i^{-1}$. A periodic shock reformation was, indeed, observed at Mercury (Sundberg et al. 2013).

The initial electron- and proton distributions were drifting isotropic Maxwellians. The expectation is that downstream of the shock (to the left in Fig. 8.3) particles are heated and accelerated.

Figure 8.4 depicts at $t = 13.5 \Omega_i^{-1}$ the resulting downstream proton distribution for all three spatial directions. The quasi-perpendicular to the magnetic field velocity components v_x and v_z show that downstream protons are heated by a factor of 10–12 with respect to the upstream proton distribution which stay very close to their initial distribution. The downstream proton distribution in the direction quasi-parallel to the magnetic field (v_y) clearly deviates from the initial Maxwellian distribution. It can be considered as a superposition of a non-drifting cold thermal distribution and a hot population drifting at a speed of about $40 v_{th,i}$ in the positive v_y direction. Note that, since the simulation has been undertaken to understand the electron acceleration at the shock, the run time is too short to obtain the final steady state proton spectra.

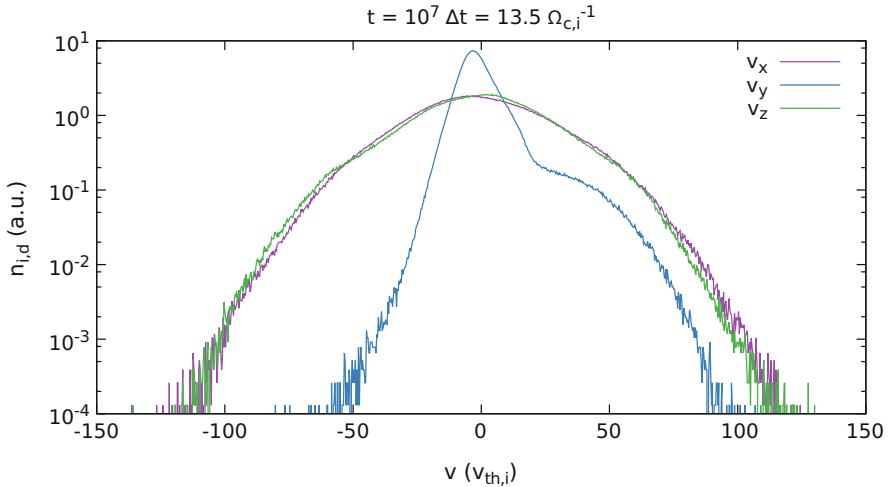


Fig. 8.4 Resulting proton velocity space distributions in all spatial directions after $t = 13.5 \Omega_i^{-1}$

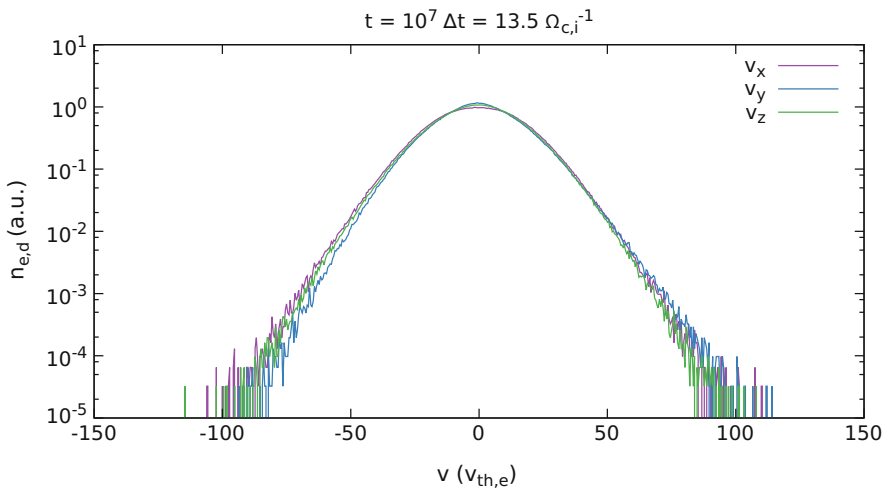


Fig. 8.5 Same as Fig. 8.4, but for the electrons

Figure 8.5 shows the electron distributions formed after $t = 13.5 \Omega_i^{-1}$. The distribution functions indicate a very strong electron heating but only a weak unidirectional electron acceleration. The degree of heating with respect to the initial temperature is very similar to those of the protons. The thermalization of the directional kinetic energy of the fast upstream plasma operates very efficiently decelerating the plasma to sub-Alfvénic and sub-sonic velocities downstream of a strong interplanetary shock. Figure 8.6 depicts the v_x -component of the electron velocity space distribution. It shows that the electrons are strongly heated in the whole downstream region after passing a very small kinetically formed collisionless shock front.

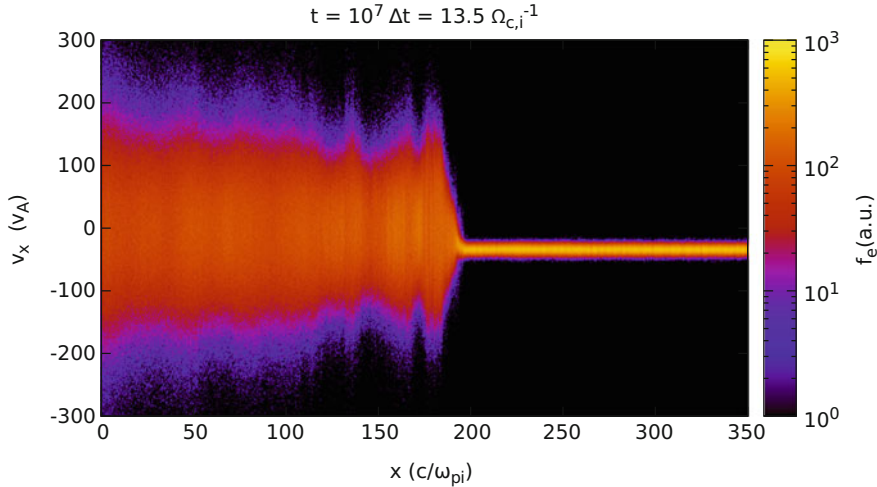


Fig. 8.6 Electron velocity space distribution upstream ($x > 200c/\omega_{pi}$) and downstream ($x < 200c/\omega_{pi}$) of the simulated strong ($M_A = 40$) shock

We found, therefore, a strong kinetic electron heating which fulfill the Rankine-Hugoniot conditions while no efficient directional electron acceleration takes place. We verified whether this is due to an insufficient resolution of resonant processes. In fact, due to the limited simulation box size the number of modes is quantized. Since the shock is quasi-perpendicular, the modes propagating obliquely to the magnetic field might not be resolved due to the minimum wave-number k required for excitation of waves which might accelerate particles through resonant instabilities and wave-particle interactions. On the other hand, there is the well-known problem of the necessity to pre-accelerate electrons to efficiently accelerate them at shocks, the so-called injection problem of shock acceleration (Treumann 2009). The latter is fundamental for Fermi-type acceleration. Since we could not make any safe assumption about the injection, we did not obtain electron acceleration even by a very strong interplanetary shock wave. Meanwhile protons were accelerated (although not very efficiently during the limited simulation time) by the strong shock which proves that our PIC simulation model is in principle suitable to describe particle acceleration at strong shocks but has to be extended to consider appropriate pre-accelerated seed electrons.

8.2.2 *Role of the Resonant Electron-Wave Interaction*

Electrons resonate in the vicinity of the shock with other dispersive waves rather than the protons. We investigated the resonant wave-electron interaction by another PIC-code simulation (Schreiner and Spanier 2014; Schreiner et al. 2017). For this sake we added dispersive ion-cyclotron L or whistler mode R-Alfvén waves and non-thermal electrons to the thermal plasma in the simulation box. The resulting

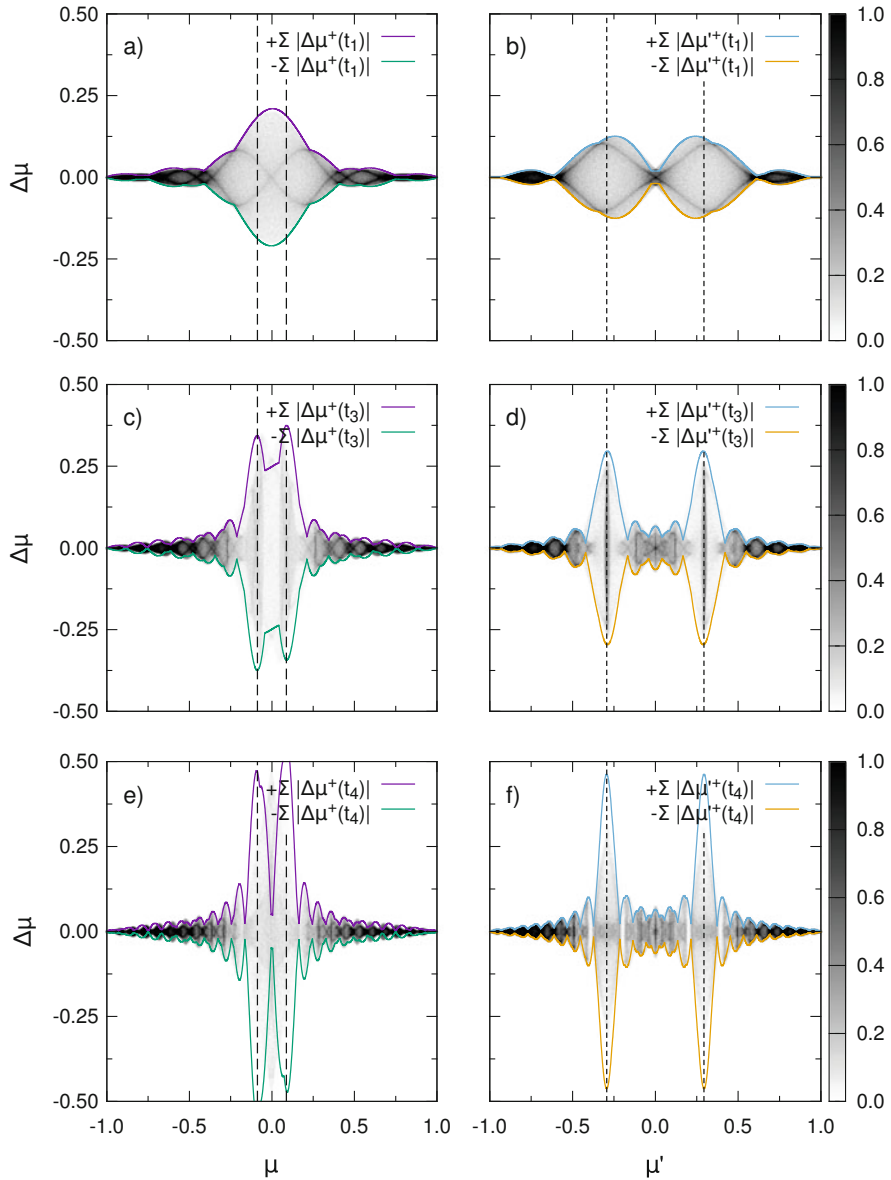


Fig. 8.7 Change of the magnetic moment depends on the initial moment. The gray shaded areas depict the simulation results, while the colored curves are the theoretically predicted values. Left panels (a, c, and e) are for a L wave, while the right panels (b, d, and f) are for an R wave. The different panels' rows indicate different times in the simulation: (a and b) $t\Omega_{ce} = 7.0$, (c and d) $t\Omega_{ce} = 17.5$, (e and f) $t\Omega_{ce} = 28.0$. See references cited in the text for further details

change of the electron pitch-angles of the particle momentum with respect to the magnetic field, given by the change of their magnetic moment μ , is plotted in Fig. 8.7. The figure compares the simulated change of the magnetic moment with the predictions of the wave–electron interaction theory.

As one can see in Fig. 8.7 the theory of the resonant interactions predicts well the obtained scattering which validates the correctness of the description of the resonant electron–wave interactions by the shock simulations. This work must be continued until the electron acceleration by strong interplanetary shocks is understood.

8.3 Magnetopause Electron Acceleration by Finite Guide-Field Reconnection

In order to understand the electron acceleration near X-lines of reconnection through the Hermean magnetopause and in its tail current sheet, we adapted the ACRONYM code to the problem of magnetic reconnection through ion-scale current sheets (Muñoz et al. 2014) including finite guide fields (Muñoz and Büchner 2016; Muñoz et al. 2015), a more common configuration than antiparallel magnetic fields. Strong guide-field reconnection events have indeed been measured when CMEs hit Mercury (Slavin et al. 2014). Via fast connectivity changes of magnetic fluxes, reconnection converts magnetic energy into plasma heating and bulk flow energy, but also into non-thermal particle acceleration (Büchner 2007). As in the case of collisionless shocks (see Sect. 8.2), magnetic reconnection in the collisionless plasma of the Hermean environment is closely related to kinetic scale turbulence (see, e.g., (Treumann 2009) and the references therein). In this section, we focus on acceleration mechanisms taking place in a single magnetic guide field reconnection, mainly due to the reconnection electric field in the Hermean magnetopause and, maybe, depending on the solar wind and IMF conditions, in its magnetotail. Acceleration in multiple X-line configurations and magnetic islands (plasmoids, flux ropes) will be considered in Sect. 8.4.

Note that electron acceleration by reconnection due to the reconnection electric field at X-lines was not found to be efficient when small simulations boxes were used (Zenitani and Hoshino 2001; Melzani et al. 2014). But electrons can also be accelerated by magnetic field curvature and gradient drift effects (Zhou et al. 2015) or due to the pile up of magnetic flux when the reconnection outflows collide with pre-existing current sheets (Hoshino et al. 2001). Electrons can also be accelerated by “surfing” along the polarization/ambipolar electric fields of driven reconnection (Hoshino 2005). In guide field reconnection those mechanisms disappear. Some evidence of electron acceleration in guide field reconnection with $b_g \lesssim 1$ (here $b_g = B_g/B_{\infty y}$ is the guide field B_g normalized to the reconnecting magnetic field strength $B_{\infty y}$) in 2D Harris current sheets was found by Pritchett (2006) and Wan et al. (2008), attributed to secondary acceleration in either the low-density separatrix by parallel electric fields, or to the bipolar electric field generated in the outflow regions just outside of the main X-line. Magnetic field generation due to kinetic instabilities such as streaming and Weibel instabilities can also accelerate

particles as seen especially in simulations with large mass ratios (Lloyd-Ronning and Fryer 2016). All these mechanisms can contribute, in principle, to the electron acceleration at Mercury.

In order to explore to what energies particles can be accelerated by Hermean collisionless magnetopause reconnection, we carried out ACRONYM-PIC code simulations of force-free current sheets in 2D and 3D. We initialized the force-free current sheets by electron-shear-flow currents causing a magnetic field $\mathbf{B}(x) = B_y(x)\hat{y} + B_z(x)\hat{z}$ given by:

$$B_y = B_{\infty y} \left[\tanh\left(\frac{x - L_x/4}{L}\right) - \tanh\left(\frac{x - 3L_x/4}{L}\right) - 1 \right], \quad (8.1)$$

$$B_z = B_{\infty y} \left[b_g^2 + \cosh^{-2}\left(\frac{x - L_x/4}{L}\right) + \cosh^{-2}\left(\frac{x - 3L_x/4}{L}\right) \right]^{1/2}. \quad (8.2)$$

where L is the halfwidth of the current sheet and b_g is the relative guide field strength. We use a small long wavelength perturbation to quickly saturate the tearing instability. We simulate double current sheets in order to use periodic boundary conditions in both directions of the reconnection plane.

The most important parameters of our fully kinetic simulation of acceleration, similar to the shock simulations in Sect. 8.2, are chosen to reduce computational efforts while capturing the main physics of the electron acceleration at the Hermean magnetopause. The main simplification necessary in PIC-code simulations is an initially much higher than the realistic electron temperature and a reduced mass ratio. Let us illustrate our results first by a case of a guide field $b_g = 5$ in 2D and then for $b_g = 3$ for the 3D case. The total initial magnetic field has constant magnitude $B_T = B_{\infty y} \sqrt{1 + b_g^2}$, and the density for both ions (“i”) and electrons (“e”) is constant $n_0 = n_i = n_e$. In the 2D cases the mass ratio is $m_i/m_e = 25$, while in the 3D cases it is $m_i/m_e = 100$. The CS halfwidth is $L = 0.2d_i$ in the 2D case and $L = 0.25d_i$ in the 3D case. The plasma $\beta_e = \beta_i$ was 0.01 in the 2D case and 0.08 in the 3D case. These parameters give an electron thermal speed of $v_{th,e}/c = \sqrt{k_B T_e/m}/c = 0.125$ and 0.1 in the 2D and 3D case, respectively. The simulation box size is $L_x \times L_y = (12.56 d_i \times 12.56 d_i)$ for the 2D case and $L_x \times L_y \times L_z = (4 d_i \times 8 d_i \times 16 d_i)$ for the 3D case. We spanned a numerical mesh of 1024×1024 grid points in the 2D case and $256 \times 512 \times 1024$ in the 3D simulations. One thousand and twenty four particle per cell and per specie were used in the 2D case, and 25 in the 3D case.

Note that several numerical considerations have to be kept in mind when simulating acceleration. A sufficiently large number of particles (especially in 2D) are needed to avoid a slowing of energetic particles and their thermalization. Those effects are known to happen in simulations with too small numbers of particles or too small order of the particles shape function which would enhance numerical collisions (Kato 2013; May et al. 2014).

Figure 8.8 shows the electron spectra resulting from 2D and 3D reconnection acceleration. The spectra were obtained near the reconnection X-point. In this sim-

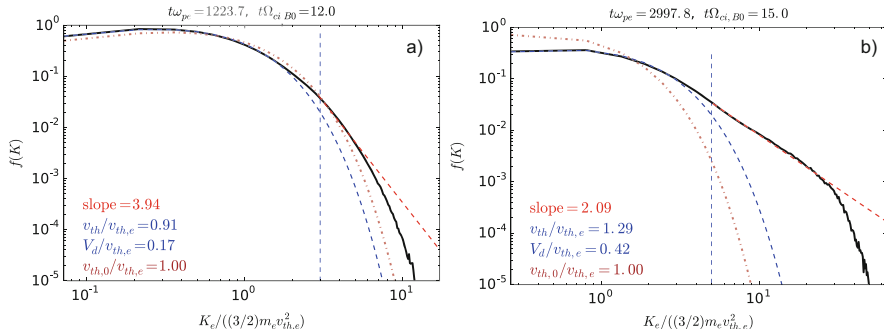


Fig. 8.8 Electron spectra for magnetic reconnection. (a) 2D and (b) 3D cases. The particles were selected in a region near the X-line for the indicated times at the end of the simulation run. The *brown dotted line* represents the initial Maxwellian energy distribution. The *blue dashed line* represents a Maxwellian fit to the thermal part of the spectrum, while the *red dashed line* is a power-law fit of the non-thermal part of the spectrum with spectral indices of (a) -3.94 , (b) -2.09

ulation, the size of the simulation domain in the reconnection plane is chosen small enough so that the system cannot develop multiple magnetic islands that would accelerate electrons via a first-order Fermi process in the contracting magnetic islands (as discussed in Sect. 8.4). The spectrum of electrons accelerated by 2D reconnection with $b_g = 5$ is depicted in Fig. 8.8a. The figure shows that 2D guide-field magnetic reconnection does not accelerate a sufficient amount of electrons to form a distinct power law spectrum in the supra-thermal energy range. Instead, a large number of electrons are heated. The corresponding Maxwellian fitting is also shown in Fig. 8.8a (blue dashed line). The non-Maxwellian tail remains small since acceleration takes place mainly near the X-line due to the strong reconnection electric field component E_{\parallel} aligned with the guide field. The maximum values of E_{\parallel} are reached at and near the X-lines as one can see in Fig. 8.9, left upper panel (2D case).

Electrons from the inflow region (solar wind or magnetosheath) are accelerated while they pass through this region. This can take place only once before they are ejected from the magnetopause, since no significant electron reflection or trapping takes place near the X-point neither in the magnetic nor in the electric fields of reconnection in our simulations. In other words, the acceleration potential calculated according to (Egedal et al. 2012, 2013) is too small to let the electrons pass the acceleration region a second time. We did not find enough evidence of secondary acceleration mechanisms close to the X-line (Hoshino et al. 2001; Pritchett 2006; Wan et al. 2008; Lloyd-Ronning and Fryer 2016). This kind of acceleration, therefore, seem not to be significant in the case of strong guide field reconnection typical for the Hermean magnetopause in case of small shear angles between the solar wind magnetic field (IMF) and the magnetosheath field. In larger regions, the number of high energy electrons can slightly increase due to a more elongated X-line along which the particles can spend longer times. This is, however, not possible at Mercury due to the limited Hermean magnetopause size.

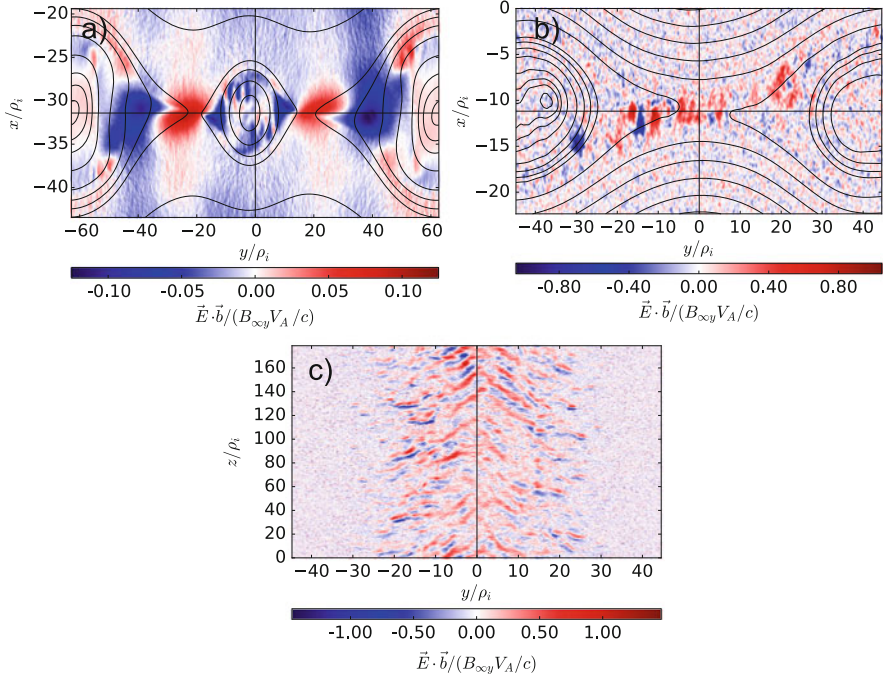


Fig. 8.9 Parallel electric field in (a) 2D case (b) 3D case, reconnection plane, (c) 3D case, out-of-reconnection plane

Mercury's magnetosphere is, however, very dynamic and the guide field strength in its magnetopause can vary. In order to assess the influence of the guide field on the acceleration, we carried out also 2D Harris current sheet simulations (Harris 1962), which allow vanishing guide field strengths, the limit of antiparallel reconnection. Different from the force free equilibrium, the Harris equilibrium must be sustained by a thermal pressure gradient, i.e. a density profile with a constant current carrying drift speed of electrons and ions. On the other hand, the out-of-plane magnetic field B_g is constant in space and time and does not affect the Harris equilibrium, different from the spatially varying B_g for the force free equilibrium. We added a constant background density of 20% of the maximum density of the current sheet. The parameters are similar to the previously mentioned, with the exception that we use a mass ratio of $m_i/m_e = 100$ and a current sheet halfwidth of $L = 0.5d_i$. Our results are shown in Fig. 8.10. The stronger the guide field is, the more energetic the electrons become as a result of spending more time near the X-line, in agreement with previous findings (Ricci et al. 2003; Fu et al. 2006; Pritchett 2006; Wan et al. 2008). Nevertheless, we also observed another phenomenon: there is a range of guide fields close to $b_g \sim 1$ (Fig. 8.10b) where the electron spectra near the X-line develops a power law section $f(K) = K^{-\alpha}$ with spectral index $\alpha = -3.5$, where $K = m_e c^2 (\gamma - 1)$ is the electron (kinetic) energy and γ is the relativistic Lorentz factor. At higher energies, the spectrum continues and another energetic,

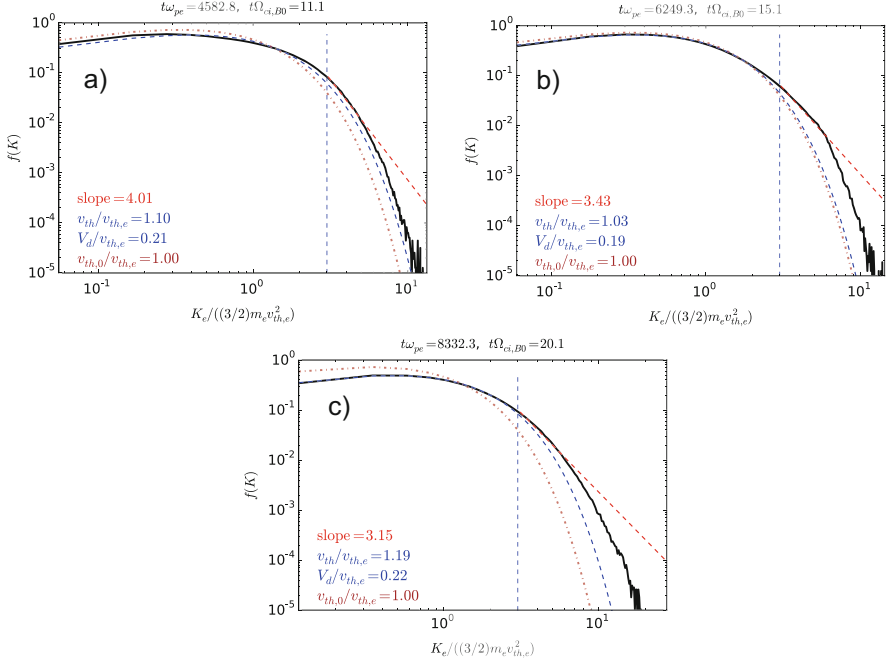


Fig. 8.10 Electron spectra for magnetic reconnection for 2D Harris CS and different guide fields. (a) $b_g = 0.2$, (b) $b_g = 1$, (c) $b_g = 5$. The particles were selected in a region near the X-line, for a time shortly after the maximum of the reconnection rate (later for stronger guide fields)

but thermally heated, electron population arises. This indicates that those particles are accelerated by a different mechanism, which is still unclear. For stronger guide fields such as $b_g = 5$ (Fig. 8.10c), the electrons are accelerated to higher energies compared to $b_g = 1$, but no section in their energy distribution can be represented by a power law, which would indicate efficient acceleration (Ho et al. 2011, 2012; Lawrence et al. 2015).

A very hard spectrum is, however, obtained when considering reconnection in a 3D geometry. Note that this case is more realistic for applications because it allows instabilities developing in the guide field direction. Figure 8.8b shows the resulting electron spectra near the X-line. The spectra can be approximated, in the indicated section of energies, as a power law with spectral index $\alpha = -2$. Beyond the power-law part of the spectrum, even higher electron energies are obtained with an exponential cutoff. Away from the X-line, toward the separatrices, the power-law electron energy spectra is softer and turn, finally, into a heated Maxwellian (not shown here). The thermalization is due to the interaction of the electrons with their self-generated turbulence at the separatrices (plots not shown here). Power-law spectra can be obtained more easily in fully 3D considerations allowing the generation of turbulence expected in the Hermean magnetopause. Figure 8.9b, c show that the parallel electric field $E_{||}$ is patchy in space and alternating quickly in time (not shown here). This component of the electric field, capable to energize

electrons, is distributed along filamentary structures in the current direction. As it was pointed out earlier, one reason of the more efficient acceleration in 3D guide-field magnetic reconnection can be a Fermi acceleration mechanism due to contracting magnetic islands (Dahlin et al. 2015). The stochastic nature of the magnetic field lines (the filamentary structures in the out-of-plane direction) implies that the electrons can gain energy in a larger volume than in 2D, where they are confined. In our case, since our simulation box is smaller along the reconnected magnetic field direction, this mechanism cannot operate. We found that the more efficient particle acceleration in 3D is due to purely kinetic instabilities and turbulence propagating in the current-direction from the X-point. The self-generated turbulence fed from the relative electron-ion stream and shear flows, which can accelerate electrons and generate power-law tails. Indeed, the relative fluid electron-ion drift speed increases beyond the threshold of Buneman-like instabilities, the electron thermal speed. The electron drift speed keeps increasing beyond this threshold afterwards, as a result of the current sheet thinning (plots not shown here). Since the Alfvén speed is half of the electron thermal speed, the electron drift speed is highly supersonic and super-Alfvénic. These conditions are even favorable for shock waves after the saturation of reconnection. Note that in addition to streaming instabilities and shear flows, also strong density gradients, temperatures anisotropies and high temperature ratios T_e/T_i provide additional sources of free energy for the instabilities contributing to the turbulent spectrum (plots not shown here).

Such turbulence is seen by in-situ measurements in magnetic reconnection regions in Mercury (Uritsky et al. 2011; Boardsen et al. 2012). Streaming instabilities produce a broadband spectrum of magnetic and electric field fluctuations (plots not shown here). This turbulence is not confined to frequencies of the order of the lower-hybrid frequency as seen in 2D simulations of magnetic reconnection, but it also reaches up to electron frequencies. This suggests that these waves have the right frequencies that might accelerate the electrons stochastically through turbulent magnetic fields via second-order Fermi acceleration (diffusive acceleration), (Spitkovsky 2008). This hypothesis is supported by the additional evidence that even though the separatrix regions are turbulent, the spectra are restricted to lower frequencies than near an X-line. Therefore, electrons are thermally heated (mostly pitch-angle scattered) but not efficiently accelerated, as evidenced by the lack of a clear power-law tail.

8.4 Particle Acceleration in Hermean Magnetotail Flux Ropes

Particle acceleration in current sheets developing multiple magnetic islands have been investigated by a number of previous studies using fully kinetic PIC simulations (see, e.g., Drake et al. 2006, 2010; Oka et al. 2010; Hoshino and Lyubarsky 2012; Dahlin et al. 2014, 2015; Guo et al. 2015). Such investigations usually

start with thin (at ion kinetic scales) and long current sheets, which develop multiple islands via tearing instability, starting from the initial thermal noise. The basic acceleration mechanism is the first-order Fermi-type acceleration in the reconnection-plane due to the curvature drifts in contracting magnetic islands, as well as parallel electric field acceleration around reconnection sites, etc. The Fermi acceleration involves the interaction between multiple flux ropes which might merge (coalescence), causing a mirror force acting on the particles. This can happen in long chains of plasmoids/flux ropes or between neighboring plasmoids/flux ropes in the Hermean magnetotail. Long current sheets can also produce a more efficient acceleration because particles can subsequently become accelerated at a number of reconnection sites (Melzani et al. 2014).

8.4.1 Test Particle Acceleration in a Plasmoid-Unstable Hermean Magnetotail Current Sheets

We first applied an MHD model of plasmoid-unstable Hermean tail current sheets with an ad-hoc resistivity providing dissipation for magnetic reconnection. Spontaneous current-layer fragmentation causes cascading reconnection transferring energy from large down to the smallest scales (Bárta et al. 2011). This model, originally developed for the trailing current sheet of CMEs at the Sun, in principle, can apply also to the conditions of the Mercury's magnetotail. Fast magnetic reconnection in tail-like current sheets can be obtained by a plasmoid-instability (Loureiro et al. 2007; Loureiro 2013). Such instability is efficient in large-Lundquist-number plasmas with Lundquist numbers $S = LV_A/\eta$, the magnetic Reynolds number for the Alfvén velocity V_A and an ad-hoc resistivity η . The critical Lundquist number S_{crit} for the excitation of the plasmoid instability is about 10^4 (Loureiro 2013; Bhattacharjee et al. 2009). A plasmoid instability in the Hermean magnetotail might explain fast reconnection and efficient particle acceleration. Daughton et al. 2009 e.g., expressed the global magnetic reconnection rate of plasmoid reconnection in terms of the number of small scale plasmoids N_p . These small plasmoids are described by their length $L_p \sim L/N_p$ and width $\delta_p \sim \delta/\sqrt{N_p}$ for the macroscopic diffusion region length L and width δ of the current sheet. The slow Sweet-Parker reconnection, given as a proxy by L/δ , is enhanced by a factor of $\sqrt{N_p}$.

In order to numerically simulate plasmoid-unstable current sheets, we solved the resistive MHD equations using the GOEMHD3 code (Skála et al. 2015). The simulations are initialized by the same equilibria used in Sect. 8.3: a force-free (double) current sheet with a finite guide field of $b_g = 2$. The ad-hoc resistivity is chosen to be $\eta = 10^{-1}\eta_0$, where $\eta_0 = \mu_0 LV_A = 7.8 \cdot 10^2 \Omega \text{ m}$. The simulation box is $L_x \times L_y \times L_z = 0.4 \times 80 \times 320 L^3$ resolved by $4 \times 3200 \times 12800$ grid points, where L is the current sheet halfwidth. We use the mean field macroscopic MHD fields averaged by using a Gaussian spatial filter with an appropriate small enough width,

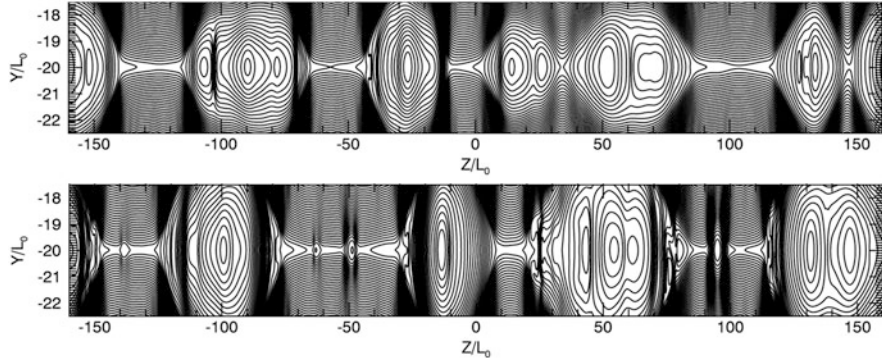


Fig. 8.11 Magnetic field structure of plasmoid reconnection at $t = 100\tau_A$ (top) and $t = 200\tau_A$ (bottom)

neglecting the small scale turbulent fluctuations (Widmer et al. 2016). Figure 8.11 shows snapshots of the magnetic field lines near the current sheet center, at two typical times during the fully developed stage of the plasmoid instability.

We first study the particle acceleration in Hermean magnetotail plasmoid reconnection by means of test particle calculations (Zhou et al. 2015, 2016). For this sake we trace electrons in the framework of the relativistic guiding center approximation (Northrop 1963). Note that the guiding center approximation is valid only for strongly magnetized electrons, such as their magnetic moment (the first adiabatic invariant) is conserved. This condition is fulfilled for current sheets with a finite guide magnetic field. Previous studies using test particle calculations in MHD fields were carried out for single X-lines. They focused on the parallel component of the electric field, finding power-law electron distributions (especially at the separatrices) and beam-like structures in the outflow region of reconnection (Zharkova and Gordovskyy 2005; Wood and Neukirch 2005; Gordovskyy et al. 2010). Acceleration by the convective electric field near a magnetic null point was also investigated (Guo et al. 2010). Recently it was pointed out that multiple reconnection sites (X-lines) might have an important effect on the overall electron acceleration (Li and Lin 2012; Zhou et al. 2015, 2016) but with parameters which are not suitable for the Mercury's magnetotail. Though test particle calculations applied to Mercury's magnetosphere were carried out, they did not consider reconnection in the magnetotail (Delcourt et al. 2005). We, therefore, for the Mercury case, first traced $\sim 1.2 \cdot 10^5$ test electrons being accelerated in the flux ropes as long as they remain inside the current sheet. Initially, the electrons are randomly distributed along the current sheet midplane. The initial electron energy is randomly chosen in the range 10 eV–10 keV according to a Maxwellian thermal distribution with an energy of 60 eV. The initial pitch angles are similarly random. Later, the electrons move under the influence of time-dependent electromagnetic fields given by the MHD simulation. Note that even though the MHD equations solved by the GOEMHD3 code are scale-invariant, the equations to be solved by the test particle method are not. We match the Hermean

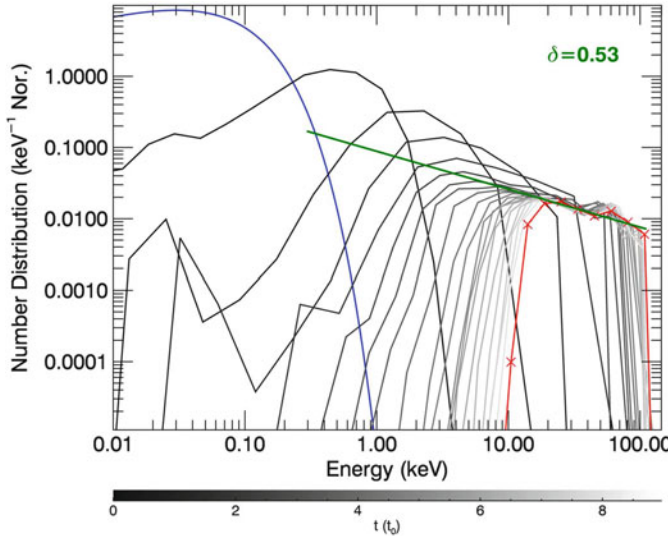


Fig. 8.12 Electron spectra evolving with time from $t = 0$ (blue line) with decreasing gray scale intensity to the final one, highlighted by a red line. The green straight line is a power law fitting with spectral index -0.53

magnetotail conditions by choosing a normalization of $L = 25$ km for the length (and current sheet halfwidth), $B = 7.5 \cdot 10^{-4} G$ for the magnetic field strength, an Alfvén speed of $v_A = 25$ km/s, i.e. a typical Alfvén transit time $\tau_A = L/V_A = 1$ s. The total acceleration time of the original MHD simulations is rescaled to 9 s, the typical period of bursty reconnection events in the Hermean magnetotail (Zelenyi et al. 2007).

Figure 8.12 summarizes the results of our calculation, showing the evolution of the (test) electrons energy spectra. The spectra are ordered in time by a gray scale from dark (t_0 or $t = 0$) to bright ($t = 9$ s). The blue line corresponds to t_0 , the initial Maxwellian distribution. The electrons are accelerated with time as evidenced by the shift of the maximum of the distribution towards larger energies. For later times (towards the brighter end of the gray scale scheme), and in particular for the last timestep calculated $t = 9$ s (red line), the electron distribution increasingly develops a power law part with a spectral index of -0.53 (for 20–100 keV, see the green fitting line in the figure). This indicates an efficient electron acceleration. A comparison with the corresponding PIC results shown before in Figs. 8.8 and 8.10 displays a similarity with the spectrum of energetic electrons accelerated by 3D kinetic reconnection (cf. Fig. 8.8b). The difference is that in PIC simulations, the main part of the electron distribution is still thermally distributed according to the initial Maxwellian. This is because all particles contribute to the spectrum in case of self-consistent simulations. Note also that due to technical restrictions, the self-consistent simulations discussed in Sect. 8.3 already started with an electron temperature as high as 7 keV, which is much higher than that of the real Hermean

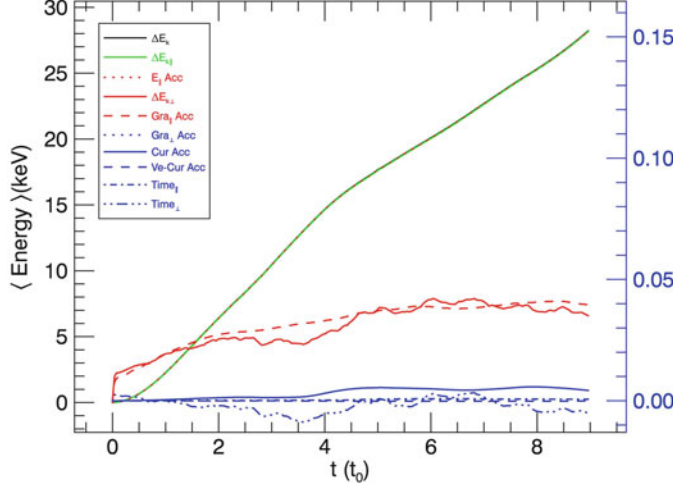


Fig. 8.13 Average energy evolution of the test electrons in the MHD fields and their corresponding contributions from the guiding center approximation. The *left* y axis is for the total energy gain, the parallel energy gain and the acceleration due to the parallel electric field, while the *right* y axis is for the remaining terms contributing to the electron acceleration due to gradients and curvature of the magnetic field

electron temperature, while test particle calculations are carried out for realistic initial temperatures. Both PIC-code simulations and test particle calculations in MHD field of flux ropes reveal power law energetic electron distributions, but their acceleration efficiency is very different.

The test particle method has an advantage that it allows to easily analyze the contributions of different particle acceleration mechanisms. Figure 8.13, e.g., shows the evolution of the average energy of all the test electrons that do not escape from the current sheet before the final simulation time. The energy contributions are decomposed according to the different terms in the guide-center approximation. The rate of change of the parallel component of the kinetic energy of a single electron can be written as (Northrop 1963):

$$\begin{aligned} \frac{1}{2} \frac{d(\gamma v_{\parallel})^2}{dt} = & \frac{q}{m} (\gamma v_{\parallel}) \mathbf{E} \cdot \mathbf{b} - \mu v_{\parallel} [\mathbf{b} \cdot \nabla B] \\ & + (\gamma v_{\parallel})^2 \mathbf{u}_E \cdot [(\mathbf{b} \cdot \nabla) \mathbf{b}] + \gamma^2 v_{\parallel} \mathbf{u}_E \cdot [(\mathbf{u}_E \cdot \nabla) \mathbf{b}] \\ & + \gamma^2 v_{\parallel} \mathbf{u}_E \cdot \frac{\partial \mathbf{b}}{\partial t}. \end{aligned} \quad (8.3)$$

while the perpendicular component is:

$$\frac{1}{2} \frac{d(\gamma v_{\perp})^2}{dt} = \mu \frac{\partial B}{\partial t} + \mu v_{\parallel} [\mathbf{b} \cdot \nabla B] + \mu \mathbf{u}_E \cdot \nabla B. \quad (8.4)$$

Here, v_{\parallel}/v_{\perp} are the parallel/perpendicular components of the electron velocity, μ is the magnetic moment, u_E is the $\mathbf{E} \times \mathbf{B}$ drift and the other symbols are standard. In Fig. 8.13, the following abbreviations represent the contribution of each one of those terms:

- $E_{\parallel} \text{ Acc} = \frac{q}{m}(\gamma v_{\parallel})\mathbf{E} \cdot \mathbf{b}$ (red dotted line). Parallel electric field acceleration.
- $\text{Gra}_{\parallel} \text{ Acc} = -\mu v_{\parallel}[\mathbf{b} \cdot \nabla B]$ (red dashed line). It cancels out when adding the parallel and perpendicular components.
- $\text{Cur Acc} = (\gamma v_{\parallel})^2 \mathbf{u}_E \cdot [(\mathbf{b} \cdot \nabla) \mathbf{b}]$ (blue continuous line). (Curvature) Fermi acceleration.
- $V_e\text{-Cur Acc} = \gamma^2 v_{\parallel} \mathbf{u}_E \cdot [(\mathbf{u}_E \cdot \nabla) \mathbf{b}]$ (blue dashed line). (Curvature) Fermi acceleration.
- $\text{Time}_{\parallel} = \gamma^2 v_{\parallel} \mathbf{u}_E \cdot \frac{\partial \mathbf{b}}{\partial t}$ (blue dashed dotted line). Magnetic gradient acceleration.
- $\text{Time}_{\perp} = \mu \frac{\partial B}{\partial t}$ (blue dashed dotted line). Magnetic gradient acceleration.
- $\text{Gra}_{\perp} \text{ Acc} = \mu \mathbf{u}_E \cdot \nabla B$ (blue dotted line). Magnetic gradient acceleration.
- $\Delta E_{k,\parallel} = E_{\parallel} \text{ Acc} + \text{Gra}_{\parallel} \text{ Acc} + \text{Cur Acc} + V_e\text{-Cur Acc} + \text{Time}_{\parallel}$ (green continuous line). Parallel energy gain.
- $\Delta E_{k,\perp} = \text{Time}_{\perp} + \text{Gra}_{\perp} \text{ Acc}$ (red continuous line). Perpendicular energy gain.
- $\Delta E_k = \Delta E_{k,\parallel} + \Delta E_{k,\perp}$ (black continuous line). Total energy gain.

Figure 8.13 shows that the main electron energy gain is due to the parallel electric field. It is mainly contributed by the resistive MHD electric field $\mathbf{E}_{\text{res}} \sim \eta \mathbf{J}$. The acceleration due to magnetic curvature is small. It varies weakly in the course of reconnection by the interaction of the flux ropes/plasmoids. The magnetic gradients ∇B even reduce the energy of the electrons. This agrees with the results obtained by fully kinetic PIC-code simulations (Dahlin et al. 2014). Hence, the test particle calculation has shown that at (large) MHD scales, Fermi acceleration in plasmoids will not significantly contribute to the electron acceleration if compared to that obtained in parallel reconnection electric fields. At the same time at smaller scales, described by fully kinetic PIC-code simulations, Fermi acceleration usually dominates the parallel acceleration since the relevant curvature radii are much smaller than those in the large scale MHD structures (Dahlin et al. 2014). Note also that due to the relatively small cross-size of the Hermean magnetotail, it will accelerate less efficiently if compared, e.g., to the solar corona (Zhou et al. 2015, 2016).

Still, the maximum electron energy (normalized value 10^{-5}) which we obtained by test particle calculations for a chain of magnetic flux ropes exceeded the initial one more than 100 times compared to the results that we obtained by 3D fully kinetic simulations of single X-line magnetopause reconnection (they revealed an increase by a factor of only 5). The high efficiency of acceleration obtained by the test particle approach is achieved, however, by neglecting any feedback of plasma instabilities, which will dissipate part of the streaming energy of the accelerated electrons slowing them down. While test particle calculations revealed a highly efficient electron acceleration in Hermean magnetotail flux ropes, one should

take into account possible kinetic self-limitation processes to obtain more realistic energies and spectra. For this sake we carried out self-consistent simulations in the framework of a fully kinetic approach which are presented in the following Sect. 8.4.2.

8.4.2 *Kinetic Physics of Electron Acceleration in Magnetotail Flux Ropes*

As shown in Sect. 8.4.1 by test particle calculations, electrons could be accelerated in Hermean magnetotail flux ropes even during short periods of time to energies as high as 100 keV. These results should be verified, however, by self-consistent kinetic investigations in order to take into account possible feedback of the accelerated electrons via, e.g., the kinetic scale plasma turbulence generated by themselves. Since the underlying interactions are highly non-linear, such investigations require numerical simulations of the plasma-kinetic effects. As discussed in Sects. 8.2 and 8.3, even for the largest available computers self-consistent kinetic simulations investigations require a modification of the plasma parameters by an appropriate reduction of the ion-to-electron mass ratio and the initial plasma temperatures in order to reduce the computational costs. For the simulations, we initialized a Harris current sheet extended along the reconnected (asymptotic) magnetic field in a simulation domain size of $L_x \times L_y = (31 d_i \times 402 d_i)$, allowing the generation and interaction of multiple magnetic islands in a process similar but physically not the same as an MHD plasmoid instability (described in Sect. 8.4.1). For 2D simulations we spanned a numerical mesh resulting in 1250×16000 grid points. Other physical and numerical parameters are similar to the 2D Harris current sheet simulations of Sect. 8.3. The main difference is that the only perturbation of the current sheet equilibrium is the PIC-code shot noise, i.e. no preference is given to any particular mode or plasmoid/magnetic island size.

The resulting islands structure is illustrated in Fig. 8.14 showing the density of the out-of-plane current J_z in the sheet (a) for antiparallel magnetic fields (i.e. $b_g = 0$) and b) for a finite initial guide field ($b_g = 1$). After the reconnection is saturated ($t\Omega_{ci,B_o} = 48.4$ for $b_g = 0$ and $t\Omega_{ci,B_o} = 56.4$ for $b_g = 1$), a number of magnetic islands/plasmoids/flux ropes (in the finite guide field case $b_g = 1$) is formed which grow until their boundaries fill the whole current sheet domain. Note that antiparallel reconnection causes symmetric plasmoids (panel (a) of Fig. 8.14) with the same (positive) current flow direction throughout the plasmoid cross section, while finite guide field reconnection causes asymmetric flux ropes with negative values of J_z in their “cores” (O-line regions), cf. Fig. 8.14 panel (b). Note also that the extreme (maximum and minimum) current densities J_z in the finite guide field case exceed those of the antiparallel reconnection plasmoids. This is due to the enhanced current sheet thinning due to the smaller kinetic scales forced by the guide magnetic field.

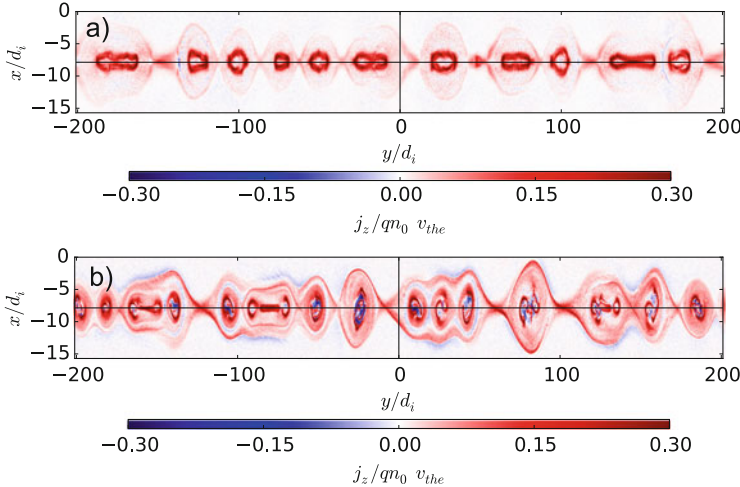


Fig. 8.14 Contours of the out-of-plane current density j_z for fully kinetic PIC simulations of Harris sheets with long domains. (a) $b_g = 0$, (b) $b_g = 1$

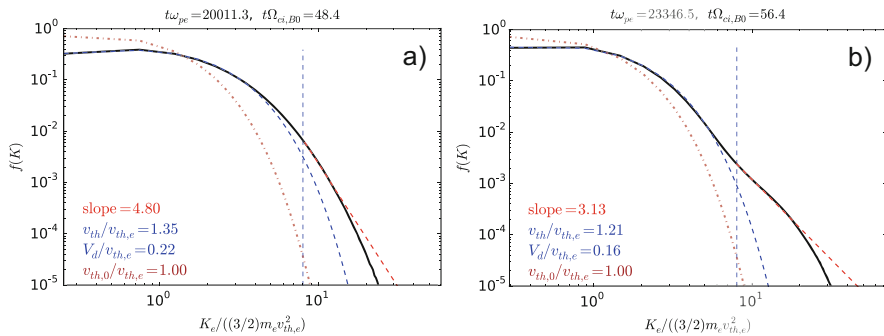


Fig. 8.15 Electron spectra for fully kinetic PIC simulations of Harris sheets with long domains. (a) $b_g = 0$, (b) $b_g = 1$. Same times as Fig. 8.14

Figure 8.15b shows the resulting spectra of energetic electrons. While they stay Maxwellian in the antiparallel magnetic field case ($b_g = 0$), induced plasmoids in the flux ropes formed by finite guide field reconnection ($b_g = 1$) form a section in their spectrum with a power law with a spectral index of -3.1 . Note that the spectra is calculated in an area containing several X-lines and magnetic islands/flux ropes. Efficient acceleration is, therefore, possible by flux ropes formed by finite-guide-field magnetic reconnection. This is an enhanced effect compared to the already obtained for single X-line reconnection and the same guide field $b_g = 1$ (cf. Fig. 8.10b), where the power law section in the electron energy spectra covers a very small range of energies.

Note also that the energetic electron spectra behaves similarly to those obtained by test particle calculations (cf. Fig. 8.12), even though the scales of the system are much larger in the elongated Hermean magnetotail. On the other hand, electron acceleration by 2D reconnection is less efficient than in the 3D force free current sheet in Fig. 8.9b, where the power law spectrum starts at lower energies than in 2D. Therefore, in the realistic 3D Hermean magnetotail with many reconnecting flux ropes, one can expect most efficient electron acceleration.

In order to explore in detail the mechanisms of electron acceleration, and to check how different are from the test particle method in MHD fields (see Fig. 8.13) we depict in Fig. 8.16 the contributions of the different terms to the rate of change of the electron kinetic energy in the guiding center approximation for the case of flux rope reconnection (case of finite guide field $b_g = 1$). This is obtained first by adding up Eqs. (8.3) and (8.4) (for single electron energies), multiplying them by m_e/γ and finally integrating the result for each volume element, yielding the rate of change of the electron kinetic energy density U (Dahlin et al. 2014):

$$\frac{dU}{dt} = E_{\parallel} J_{\parallel} + \frac{p_{e,\perp}}{B} \left(\frac{\partial B}{\partial t} + \mathbf{u}_E \cdot \nabla B \right) + \left(p_{e,\parallel} + m_e n u_{\parallel}^2 \right) \mathbf{u}_E \cdot \boldsymbol{\kappa}, \quad (8.5)$$

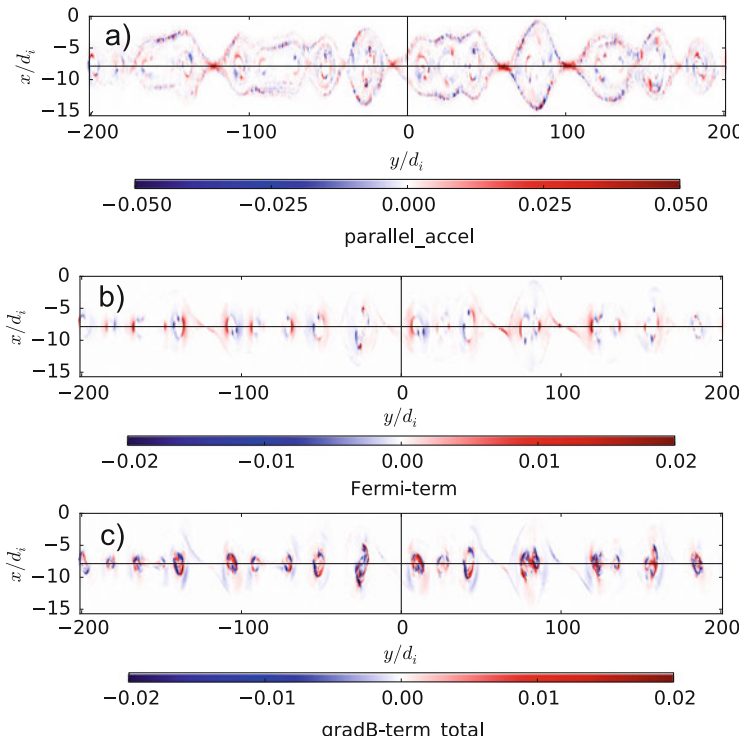


Fig. 8.16 Evolution of the contribution to the electron acceleration according to Eq. (8.5) for a Harris-type current sheet with a guide field $b_g = 1$. **(a)** Parallel acceleration, first term. **(b)** Curvature related Fermi-type acceleration, third term. **(c)** ∇B acceleration, second term

where \mathbf{u}_E is the $\mathbf{E} \times \mathbf{B}$ drift speed, p_{\parallel}/p_{\perp} are the parallel/perpendicular electron pressures, u_{\parallel} the parallel electron bulk flow velocity. $\kappa = (\mathbf{B}/B) \cdot \nabla(\mathbf{B}/B)$ is the curvature of the magnetic field. The other symbols are standard. The first term in Eq. (8.5) describes the acceleration by the magnetic-field-parallel electric fields. The second is the gradient of magnetic fields term, due to the conservation of the adiabatic invariant magnetic moment. The third term is, finally, the acceleration due to the curvature of magnetic field lines, the first-order Fermi-type acceleration.

Thus, Fig. 8.16a shows that as test particles in MHD fields, in the self-consistent kinetic reconnection simulations electrons are accelerated mainly by parallel reconnection electric fields. The self-consistent kinetic approach reveals, however, that the parallel electric fields are very localized near the X-lines of reconnection. Hence, they cannot accelerate the electrons residing, e.g., in the flux ropes of guide field reconnection which form the power law part of the test particle spectrum. The first-order Fermi acceleration term related to the curvature of the magnetic field is smaller by a factor of 3 compared to the parallel electric field contribution. It acts, however, throughout the whole cross section of the flux ropes. The $\nabla\mathbf{B}$ related acceleration (second term in Eq. (8.5)) is relevant mainly inside the flux ropes where it becomes comparable with the acceleration by parallel electric fields (Drake et al. 2006, 2010; Dahlin et al. 2014). Fermi-type acceleration seems to be the most important in flux ropes. Indeed, we could confirm that most of the accelerated particles are located in regions where the Fermi acceleration term dominates (results not shown here) contributing to a large extent to the overall acceleration at the level of the acceleration in the parallel electric field. A full proof of this hypothesis requires a detailed analysis of the electron trajectories in the fields obtained by the PIC code simulations.

8.5 Summary, Conclusions, and Outlook

8.5.1 Particle Acceleration at Strong Interplanetary Shock Waves at the Mercury Distance from the Sun

Plasma and magnetic field observations in the Mercury environment, the streaming solar wind and magnetic field jumps indicate that the bow shock of Mercury is typically weak so that no strong particle acceleration by the bow shock wave can be expected. The key parameter controlling the shock dynamics is the Mach number of the flows against the background medium. For quiet conditions, the solar wind speed at the Mercury orbit is almost the same as at the Earth while the interplanetary magnetic field (IMF) is about five times larger and the solar wind density is almost an order of magnitude higher than at 1 AU. The solar wind Mach number causing the Hermean bow shock is, therefore, smaller than that at 1 AU. During extreme flow conditions it could be even less than unity. Unlike the Hermean bow shock interplanetary shocks can pass the Mercury orbit after flare and CME eruptions at the Sun

at very high Mach numbers. Observational and modeling studies have shown that the Alfvénic Mach numbers of the strongest interplanetary shocks can reach several dozens (Smart and Shea 1985; Cliver et al. 1990). Observation of energetic particles from high Mach number interplanetary shocks at the Mercury orbit could provide an important clue to bridge the gap of our incomplete understanding of the super-high Mach number astrophysical shocks and those seen in the heliosphere. Thus questions of shock physics at the edges of the in situ observable Mach number range might be answered by the upcoming BEPI COLOMBO observations: What are the physical processes leading to particle acceleration at high Mach number shocks? Observations around 0.3 AU compared to observations at the Earth orbit may give us an important clue to energetic electron acceleration by shock waves. Mercury orbit observations provide a good chance to observe the consequences of high Mach number interplanetary shock wave acceleration in the solar system. A comparison of simulation results and observations will make a great impact on shock physics. Here we concentrated on high Mach-number ($M_A \sim 40$), mildly relativistic interplanetary shocks using the Particle-in-Cell code ACRONYM to analyze the formation of thin collisionless quasi-perpendicular shocks for parameters modified for numerical feasibility in plasma temperature and electron-to-ion mass ratio, but keeping the same ordering of the effective parameters. We validated our approach by simulating the resonant scattering of the electrons in their interaction with dispersive waves. Our simulations correctly described the formation of the high Mach-number shocks self-consistently fulfilling the jump conditions. We found that while a non-thermal proton distribution is formed superposing two populations, no essential electron acceleration takes place out of an initial thermal electron distribution. Instead collisionless kinetic thermalization processes relax any higher-energy tails of the electron distributions suppressing the production of energetic electrons. Even varying the parameters the streaming instabilities are not efficiently accelerating electrons. Hence we found that high Mach-number interplanetary shocks will heat the electron gas but do not significantly directionally accelerate them to high energies. This is similar as the results obtained for weak quasi-perpendicular shocks with small Mach-numbers ($M_A < 10$, see, e.g. (Balogh and Treumann 2013; Burgess and Scholer 2015) and the references therein). But it seems to contradict heuristic predictions of electron acceleration which was conjectured for higher Mach-number shocks based on the argument of an increasing saturation level of streaming instabilities (Papadopoulos 1988; Matsukiyo 2010). Indeed, simulations of weakly magnetized shocks with $\omega_{pe} = 20\Omega_{ce}$ found for high Mach-number shocks ($M_A = 32$) enhanced electrostatic waves that are excited by Buneman-type streaming instabilities due to the interaction of reflected ions and incident electrons (Shimada and Hoshino 2000; Hoshino and Shimada 2002). As a result a non-thermal electron population could be created by “electron shock surfing” or “surfatron acceleration” in analogy to a mechanism earlier suggested for ion shock acceleration (McClements et al. 2001). The reason for missing electron acceleration in our simulations of the Hermean bow shock was the lack of pre-accelerated seed electrons. Since surfatron conditions cannot be fulfilled the open question is what could accelerate the seed electrons? In turbulent collisionless shocks current sheets

might form and reconnection through them may take place (Zank et al. 2015). This could efficiently pre-accelerate electrons by converting the bulk flow energy of the Solar wind to magnetic energy by a Weibel instability and then converting the magnetic into particle energy by localized turbulent reconnection (Matsumoto et al. 2015). This acceleration mechanism involves small scale magnetic reconnection and the interaction between multiple magnetic islands or flux ropes which we analyzed separately in application to Mercury's magnetopause and the Hermean magnetotail (see below).

8.5.2 Electron Acceleration by Hermean Magnetopause Reconnection

The limited size Hermean magnetosphere is open to the shocked solar wind plasma of the magnetosheath by reconnection across the magnetopause. Reconnection causes particle acceleration. In order to investigate the electron acceleration at the Hermean magnetopause we carried out self-consistent kinetic (PIC-code) simulations for the finite guide-field- and plasma parameter conditions at the Hermean outer magnetospheric boundary. We found that three-dimensional magnetopause reconnection can indeed provide efficient electron acceleration. Three-dimensional guide-field reconnection develops plasma turbulence as it is observed at Mercury. Since in the usually considered (for simplicity) limiting case of two-dimensional guide-field reconnection at a single X-line no significant turbulence develops, we investigated the influence of the turbulence by means of 3D simulations. We found that, starting with a guide field strength $b_g \sim 1$, the electron spectra follow a power law at high energies while in smaller guide-fields ($b_g < 1$) the electrons are not efficiently accelerated by reconnection. In case of very strong guide fields ($b_g > 1$), however, very high electron energies can be reached since now the particles spend longer times in the reconnection electric field. The power-law electron distribution obtained in our simulations agree with observations at the Hermean magnetopause. In fact, MESSENGER has measured energetic electron distributions with power-law indices between 1.5 and 4 (Ho et al. 2011, 2012; Lawrence et al. 2015) while our results for 3D guide-field reconnection revealed power-law spectra with a spectral index of the order of two. The power-law spectrum is mostly due to the reconnection electric field, and to a smaller degree due to the broadband electromagnetic field turbulence self-generated by 3D guide-field reconnection.

8.5.3 Acceleration by Flux Ropes in the Magnetotail

In contrast to the curved at small scales magnetopause current sheet, the current sheet in the Hermean magnetotail is extended. It allows the formation and

interaction of flux ropes which might enhance the electron acceleration beyond the limits of single X-line reconnection as at the magnetopause. In order to estimate the electron energies and energy spectra due to flux ropes in the Hermean magnetotail, we have carried out test particle calculations as well as self-consistent fully kinetic PIC-code simulations. We carried out test particle calculations using a guiding center approximation and utilizing the MHD fields obtained by a simulation of extended current sheets prone to a plasmoid instability forming multiple reconnection sites. The test particle calculations have shown that for the conditions of the Hermean magnetotail electrons could be efficiently accelerated to energies of the order of 100 keV. The energetic electron distribution was found to develop a flat power-law with a spectral index of the order of one half. The acceleration took place mainly in the parallel electric fields of the multiple X-lines. Fermi-type acceleration between regions of a strongly curved magnetic field was not found to be significant (Zhou et al. 2015, 2016).

In order to verify these test particle findings we also carried out fully kinetic self-consistent PIC-code simulations of long unstable Hermean magnetotail-like current sheets prone to form multiple flux ropes. Note that the kinetic flux-rope instability mechanism is different from that of the almost-ideal MHD plasmoid instability which we investigated by MHD simulations and test particle calculations. We have shown that for the kinetically unstable Hermean tail current sheet, the acceleration of electrons is still highly efficient. While the test particle calculations revealed the parallel electric fields near reconnection X-lines as the main electron accelerators, the self-consistent PIC simulations have shown that the Fermi-type acceleration due to the magnetic field curvature is more important at smaller scales but throughout whole flux ropes. While 2D flux rope simulations revealed only a small number of accelerated electrons, higher numbers are obtained by 3D single X-line guide-field reconnection (cf. Sect. 8.3). We conclude that fully 3D considerations of magnetotail flux rope configurations are required to fully understand the electron acceleration in the Hermean magnetotail.

8.5.4 Outlook

Simulation of even strong, high Mach-number, interplanetary shock waves have shown that they only, at their rare events, might be able to accelerate electrons to the energies observed in the environment of the Mercury but only, if pre-acceleration of seed electrons takes place.

On the other hand, we established essentially 3D magnetic reconnection as the most efficient electron acceleration mechanism at Mercury. We could show that single 3D reconnection through the magnetopause could accelerate electrons to high energies if the guide-field strength is large enough. The resulting power law spectrum is in the range of those observed at Mercury. Even higher electron energies can be expected from 3D reconnection between flux ropes in the Hermean magnetotail. Our test particle calculations in the fields of a flux rope unstable current

sheet supports this idea as well as our preliminary locally 3D self-consistent kinetic simulations. Required now are large-scale 3D self-consistent kinetic simulations of multiple-flux-rope reconnection. Although 3D simulations of sufficiently long current sheets with realistic parameters are not computationally feasible right now, yet, they should be carried out as soon as a new generation of supercomputers becomes available, hopefully close to the data phase of the ESA-JAXA mission BEPI COLOMBO to Mercury.

Acknowledgements This work was possible only due to the support by the German Science Foundation “Schwerpunktprogramm Planetmag.” Jörg Büchner, Neeraj Jain, Patricio A. Muñoz also acknowledge their support by the Max-Planck-Princeton Center for Plasma Physics, Fabien Widmer and Neeraj Jain also their support by the German Science Foundation CRC 963 and Xiaowei Zhou the support by the Max-Planck-Society for a post-doc stipend.

References

- Amano, T., Hoshino, M.: Electron injection at high Mach number quasiperpendicular shocks: surfing and drift acceleration. *Astrophys. J.* **661**(1), 190–202 (2007)
- Armstrong, T.P., Krimigis, S.M., Lanzerotti, L.J.: A reinterpretation of the reported energetic particle fluxes in the vicinity of Mercury. *J. Geophys. Res.* **80**(28), 4015–4017 (1975)
- Baker, D.N., Poh, G., Odstrcil, D., Arge, C.N., Benna, M., Johnson, C.L., Korth, H., Gershman, D.J., Ho, G.C., McClintock, W.E., Cassidy, T.A., Merkel, A., Raines, J.M., Schriver, D., Slavin, J.A., Solomon, S.C., Trávníček, P.M., Winslow, R.M., Zurbuchen, T.H.: Solar wind forcing at Mercury: WSA-ENLIL model results. *J. Geophys. Res. Space Phys.* **118**(1), 45–57 (2013)
- Baker, D.N., Dewey, R.M., Lawrence, D.J., Goldsten, J.O., Peplowski, P.N., Korth, H., Slavin, J.A., Krimigis, S.M., Anderson, B.J., Ho, G.C., L, R.: McNutt, Raines, J.M., Schriver, D., Solomon, S.C.: Intense energetic electron flux enhancements in Mercury’s magnetosphere: an integrated view with high-resolution observations from MESSENGER. *J. Geophys. Res. Space Phys.* **121**(3), 2171–2184 (2016)
- Balogh, A., Treumann, R.A.: Physics of Collisionless Shocks: Space Plasma Shock Waves. ISSI Scientific Report Series, vol. 12. Springer Science+Business Media, New York (2013)
- Bárta, M., Büchner, J., Karlický, M. Skála, J.: Spontaneous current-layer fragmentation and cascading reconnection in solar flares. I. Model and analysis. *Astrophys. J.* **737**, 24 (2011)
- Benkhoff, J., van Casteren, J., Hayakawa, H., Fujimoto, M., Laakso, H., Novara, M., Ferri, P., Middleton, H.R., Ziethe, R.: BepiColombo-comprehensive exploration of mercury: mission overview and science goals. *Planet. Space Sci.* **58**(1–2), 2–20 (2010)
- Bhattacharjee, A., Huang, Y.-M., Yang, H., Rogers, B.: Fast reconnection in high-lundquist-number plasmas due to the plasmoid instability. *Phys. Plasmas* **16**(11), 112102 (2009)
- Boardsen, S.A., Slavin, J.A., Anderson, B.J., Korth, H., Schriver, D., Solomon, S.C.: Survey of coherent 1 Hz waves in Mercury’s inner magnetosphere from MESSENGER observations. *J. Geophys. Res. Space Phys.* **117**(A12), A00M05 (2012)
- Boris, J.P.: Relativistic plasma simulation—optimization of a hybrid code. In: Boris, J., Shanny, R. (eds.) Proceedings of the Fourth Conference on the Numerical Simulation of Plasmas, Washington DC, pp. 3–67. Naval Research Laboratory, Washington, DC (1970)
- Büchner, J.: Astrophysical reconnection and collisionless dissipation. *Plasma Phys. Controlled Fusion* **49**, B325–B339 (2007)
- Büchner, J., Kuska, J.-P.: Consequences of strong ion acceleration in current sheets and due to reconnection. *Adv. Space Res.* **21**(4), 567–572 (1998)

- Büchner, J., Zelenyi, L.M.: The separatrix tentacle effect of ion acceleration to the plasma sheet boundary. *Geophys. Res. Lett.* **17**(2), 127–130 (1990)
- Büchner, J., Kuznetsova, M., Zelenyi, L.M.: Sheared field tearing mode instability and creation of flux ropes in the Earth magnetotail. *Geophys. Res. Lett.* **18**(3), 385–388 (1991)
- Burgess, D., Scholer, M.: Collisionless Shocks in Space Plasmas: Structure and Accelerated Particles. Cambridge University Press, Cambridge (2015)
- Burlaga, L.F.: Magnetic fields and plasmas in the inner heliosphere: Helios results. *Planet. Space Sci.* **49**(14–15), 1619–1627 (2001)
- Cliver, E.W., Feynman, J., Garrett, H.B.: An estimate of the maximum speed of the solar wind, 1938–1989. *J. Geophys. Res.* **95**, 17103–17112 (1990)
- Dahlin, J.T., Drake, J.F., Swisdak, M.: The mechanisms of electron heating and acceleration during magnetic reconnection. *Phys. Plasmas* **21**(9), 092304 (2014)
- Dahlin, J.T., Drake, J.F., Swisdak, M.: Electron acceleration in three-dimensional magnetic reconnection with a guide field. *Phys. Plasmas* **22**(10), 100704 (2015)
- Daughton, W., Roytershteyn, V., Albright, B.J., Karimabadi, H., Yin, L., Bowers, K.J.: Transition from collisional to kinetic regimes in large-scale reconnection layers. *Phys. Rev. Lett.* **103**(6), 065004 (2009)
- Delcourt, D.C., Seki, K., Terada, N., Miyoshi, Y.: Electron dynamics during substorm dipolarization in Mercury's magnetosphere. *Ann. Geophys.* **23**, 3389–3398 (2005)
- Dewey, R., Slavin, J.A., Baker, D., Raines, J., Lawrence, D.: MESSENGER observations of energetic electron acceleration in Mercury's magnetotail. In: AAS/Division for Planetary Sciences Meeting Abstracts, vol. 48, p. 117.02 (2016)
- DiBraccio, G.A., Slavin, J.A., Imber, S.M., Gershman, D.J., Raines, J.M., Jackman, C.M., Boardsen, S.A., Anderson, B.J., Korth, H., Zurbuchen, T.H., McNutt, R.L., Solomon, S.C.: MESSENGER observations of flux ropes in Mercury's magnetotail. *Planet. Space Sci.* **115**, 77–89 (2015)
- Drake, J.F., Swisdak, M., Che, H., Shay, M.A.: Electron acceleration from contracting magnetic islands during reconnection. *Nature* **443**(7111), 553–556 (2006)
- Drake, J.F., Opher, M., Swisdak, M., Chamoun, J.N.: A magnetic reconnection mechanism for the generation of anomalous cosmic rays. *Astrophys. J.* **709**(2), 963–974 (2010)
- Dungey, J.W.: Noise-free neutral sheets. In: Guyenne, T.D. (ed.) Reconnection in Space Plasma. ESA Special Publication, vol. 285, pp. 15–19. European Space Agency, Paris (1989)
- Egedal, J., Daughton, W., Le, A.: Large-scale electron acceleration by parallel electric fields during magnetic reconnection. *Nat. Phys.* **8**(4), 321–324 (2012)
- Egedal, J., Le, A., Daughton, W.: A review of pressure anisotropy caused by electron trapping in collisionless plasma, and its implications for magnetic reconnection. *Phys. Plasmas* **20**(6), 061201 (2013)
- Elkina, N., Büchner, J.: A new conservative unsplit method for the solution of the Vlasov equation. *J. Comput. Phys.* **213**(2), 862–875 (2006)
- Eraker, J.H., Simpson, J.A.: Acceleration of charged particles in Mercury's magnetosphere. *J. Geophys. Res.* **91**, 9973–9993 (1986)
- Espirkevop, T.Z.: Exact charge conservation scheme for particle-in-cell simulation with an arbitrary form-factor. *Comput. Phys. Commun.* **135**(2), 144–153 (2001)
- Fu, X.R., Lu, Q.M., Wang, S.: The process of electron acceleration during collisionless magnetic reconnection. *Phys. Plasmas* **13**(1), 012309 (2006)
- Gershman, D.J., Zurbuchen, T.H., Fisk, L.A., Gilbert, J.A., Raines, J.M., Anderson, B.J., Smith, C.W., Korth, H., Solomon, S.C.: Solar wind alpha particles and heavy ions in the inner heliosphere observed with MESSENGER. *J. Geophys. Res. Space Phys.* **117**(A12), A00M02 (2012)
- Gershman, D.J., Slavin, J.A., Raines, J.M., Zurbuchen, T.H., Anderson, B.J., Korth, H., Baker, D.N., Solomon, S.C.: Magnetic flux pileup and plasma depletion in Mercury's subsolar magnetosheath. *J. Geophys. Res. Space Phys.* **118**(11), 7181–7199 (2013)

- Gershman, D.J., Raines, M.J., Slavin, J.A., Zurbuchen, T.H., Anderson, B.J., Korth, H., Ho, G.C., Boardsen, S.A., Cassidy, T.A., Walsh, B.M., Solomon, S.C.: MESSENGER observations of solar energetic electrons within Mercury's magnetosphere. *J. Geophys. Res. Space Phys.* **120**, 8559–8571 (2015)
- Gershman, D.J., Dorelli, J.C., DiBraccio, G.A., Raines, J.M., Slavin, J.A., Poh, G., Zurbuchen, T.H.: Ion-scale structure in Mercury's magnetopause reconnection diffusion region. *Geophys. Res. Lett.* **43**, 5935–5942 (2016)
- Gordovskyy, M., Browning, P.K., Vekstein, G.E.: Particle acceleration in a transient magnetic reconnection event. *Astron. Astrophys.* **519**, A21 (2010)
- Guo, J.-N., Büchner, J., Otto, A., Santos, J., Marsch, E., Gan, W.-Q.: Is the 3-D magnetic null point with a convective electric field an efficient particle accelerator? *Astron. Astrophys.* **513**, A73 (2010)
- Guo, F., Liu, Y.-H., Daughton, W., Li, H.: Particle acceleration and plasma dynamics during magnetic reconnection in the magnetically dominated regime. *Astrophys. J.* **806**(2), 167 (2015)
- Harris, E.G.: On a plasma sheath separating regions of oppositely directed magnetic field. *Nuovo Cim.* **23**(1), 115–121 (1962)
- Ho, G.C., Krimigis, S., Gold, R., Baker, D., Slavin, J.A., Anderson, B.J., Korth, H., Starr, R.D., Lawrence, D.J., McNutt, R.L., Solomon, S.C.: MESSENGER observations of transient bursts of energetic electrons in mercury's magnetosphere. *Science* **333**(6051), 1865–1868 (2011)
- Ho, G.C., Krimigis, S.M., Gold, R.E., Baker, D.N., Anderson, B.J., Korth, H., Slavin, J.A., McNutt, R.L., Winslow, R.M., Solomon, S.C.: Spatial distribution and spectral characteristics of energetic electrons in Mercury's magnetosphere. *J. Geophys. Res. Space Phys.* **117**(A12), A00M04 (2012)
- Hockney, R.W., Eastwood, J.W.: Computer Simulation Using Particles. Hilger, Bristol (1988)
- Hoshino, M.: Electron surfing acceleration in magnetic reconnection. *J. Geophys. Res. Space Phys.* **110**(A10), 1–8 (2005)
- Hoshino, M., Lyubarsky, Y.: Relativistic reconnection and particle acceleration. *Space Sci. Rev.* **173**(1–4), 521–533 (2012)
- Hoshino, M., Shimada, N.: Nonthermal electrons at high mach number shocks: electron shock surfing acceleration. *Astrophys. J.* **572**(2), 880–887 (2002)
- Hoshino, M., Mukai, T., Terasawa, T., Shinohara, I.: Suprathermal electron acceleration in magnetic reconnection. *J. Geophys. Res. Space Phys.* **106**(A11), 25979–25997 (2001)
- Kato, T.N.: Energy loss of high-energy particles in particle-in-cell simulation (2013). arXiv preprint 1312.5507
- Kilian, P., Burkart, T., Spanier, F.: The influence of the mass ratio on particle acceleration by the filamentation instability. In: Nagel, W.E., Kröner, D.B., Resch, M.M. (eds.) High Performance Computing in Science and Engineering '11, pp. 5–13. Springer, Berlin, Heidelberg (2012)
- Kilian, P., Ganse, U., Spanier, F.: Different choices of the form factor in particle-in-cell simulations. In: Pogorelov, N.V., Audit, E., Zank, G.P. (eds.) Numerical Modeling of Space Plasma Flows (ASTRONUM2012). Astronomical Society of the Pacific Conference Series, vol. 474 p. 208 (2013)
- Kirsch, E., Richter, A.K.: Possible detection of low energy ions and electrons from planet Mercury by the HELIOS spacecraft. *Ann. Geophys.* **3**, 13–18 (1985)
- Lawrence, D.J., Anderson, B.J., Baker, D.N., Feldman, W.C., Ho, G.C., Korth, H., McNutt, R.L., Peplowski, P.N., Solomon, S.C., Starr, R.D., Vandegriff, J.D., Winslow, R.M.: Comprehensive survey of energetic electron events in Mercury's magnetosphere with data from the MESSENGER Gamma-Ray and Neutron Spectrometer. *J. Geophys. Res. Space Phys.* **120**(4), 2851–2876 (2015)
- Le, G., Chi, P., Blanco-Cano, X., Boardsen, S., Slavin, J.A., Anderson, B.J., Korth, H.: Upstream ultra-low frequency waves in Mercury's foreshock region: MESSENGER magnetic field observations. *J. Geophys. Res. Space Phys.* **118**(6), 2809–2823 (2013)
- Li, Y., Lin, J.: Acceleration of electrons and protons in reconnecting current sheets including single or multiple X-points. *Sol. Phys.* **279**(1), 91–113 (2012)

- Liu, Y., Richardson, J., Belcher, J.: A statistical study of the properties of interplanetary coronal mass ejections from 0.3 to 5.4AU. *Planet. Space Sci.* **53**(1–3), 3–17 (2005)
- Lloyd-Ronning, N.M., Fryer, C.L.: Particle acceleration in relativistic electron-ion outflows (2016). arXiv preprint 1603.01490
- Loureiro, N., Schekochihin, A.A., Cowley, S.C.: Instability of current sheets and formation of plasmoid chains. *Phys. Plasmas* **14**, 100703 (2007)
- Loureiro, N.F., Schekochihin, A.A., Uzdensky, D.A.: Plasmoid and Kelvin-Helmholtz instabilities in Sweet-Parker current sheets. *Phys. Rev. E* **87**(1), 013102 (2013)
- Masters, A., Stawarz, L., Fujimoto, M., Schwartz, S.J., Sergis, N., Thomsen, M.F., Retinò, A., Hasegawa, H., Zieger, B., Lewis, G.R., Coates, A.J., Canu, P., Dougherty, M.K.: Electron acceleration to relativistic energies at a strong quasi-parallel shock wave. *Nat. Phys.* **9**(3), 164–167 (2013)
- Matsukiyo, S.: Mach number dependence of electron heating in high Mach number quasiperpendicular shocks. *Phys. Plasmas* **17**(4), 042901 (2010)
- Matsumoto, Y., Amano, T., Kato, T.N., Hoshino, M.: Stochastic electron acceleration during spontaneous turbulent reconnection in a strong shock wave. *Science* **347**(6225), 974–978 (2015)
- May, J., Tonge, J., Ellis, I., Mori, W.B., Fiuza, F., Fonseca, R.A., Silva, L.O., Ren, C.: Enhanced stopping of macro-particles in particle-in-cell simulations. *Phys. Plasmas* **21**(5), 052703 (2014)
- McClements, K.G., Dieckmann, M.E., Ynnerman, A., Chapman, S.C., Dendy, R.O.: Surfatron and stochastic acceleration of electrons at supernova remnant shocks. *Phys. Rev. Lett.* **87**(25), 255002 (2001)
- Melzani, M., Walder, R., Folini, D., Winisdoer, C., Favre, J.M.: The energetics of relativistic magnetic reconnection: ion-electron repartition and particle distribution hardness. *Astron. Astrophys.* **570**, A112 (2014)
- Muñoz, P.A., Büchner, J.: Non-Maxwellian electron distribution functions due to self-generated turbulence in collisionless guide-field reconnection. *Phys. Plasmas* **23**(10), 102103 (2016)
- Muñoz, P.A., Kilian, P., Büchner, J.: Instabilities of collisionless current sheets revisited: the role of anisotropic heating. *Phys. Plasmas* **21**(11), 112106 (2014)
- Muñoz, P.A., Told, D., Kilian, P., Büchner, J., Jenko, F.: Gyrokinetic and kinetic particle-in-cell simulations of guide-field reconnection. I. Macroscopic effects of the electron flows. *Phys. Plasmas* **22**(8), 082110 (2015)
- Northrop, T.G.: The Adiabatic Motion of Charged Particles. Interscience, New York (1963)
- Oka, M., Phan, T.-D., Krucker, S., Fujimoto, M., Shinohara, I.: Electron acceleration by multi-island coalescence. *Astrophys. J.* **714**(1), 915–926 (2010)
- Papadopoulos, K.: Electron heating in superhigh mach number shocks. *Astrophys. Space Sci.* **144**(1–2), 535–547 (1988)
- Pritchett, P.L.: Relativistic electron production during guide field magnetic reconnection. *J. Geophys. Res.* **111**(April), A10212 (2006)
- Ricci, P., Lapenta, G., Brackbill, J.U.: Electron acceleration and heating in collisionless magnetic reconnection. *Phys. Plasmas* **10**(9), 3554 (2003)
- Sarantos, M., Slavin, J.A.: On the possible formation of Alfvén wings at Mercury during encounters with coronal mass ejections. *Geophys. Res. Lett.* **36**(4), L04107 (2009)
- Sarantos, M., Killen, R.M., Kim, D.: Predicting the long-term solar wind ion-sputtering source at Mercury. *Planet. Space Sci.* **55**(11), 1584–1595 (2007)
- Schreiner, C., Spanier, F.: Wave-particle-interaction in kinetic plasmas. *Comput. Phys. Commun.* **185**(7), 1981–1986 (2014)
- Schreiner, C., Kilian, P., Spanier, F.: Particle scattering off of right-handed dispersive waves. *Astrophys. J.* **834**(2), 161 (2017)
- Shimada, N., Hoshino, M.: Strong electron acceleration at high Mach number shock waves: simulation study of electron dynamics. *Astrophys. J.* **543**(1), L67–L71 (2000)
- Simpson, J.A., Eraker, J.H., Lampert, J.E., Walpole, P.H.: Electrons and protons accelerated in mercury's magnetic field. *Science* **185**(4146), 160–166 (1974)

- Skála, J., Baruffa, F., Büchner, J., Rampp, M.: The 3D MHD code GOEMHD3 for astrophysical plasmas with large Reynolds numbers. Code description, verification, and computational performance. *Astron. Astrophys.* **580**, A48 (2015)
- Slavin, J.A., Holzer, R.E.: The effect of erosion on the solar wind stand-off distance at Mercury. *J. Geophys. Res.* **84**, 2076–2082 (1979)
- Slavin, J.A., Holzer, R.E.: Solar wind flow about the terrestrial planets. I - Modeling bow shock position and shape. *J. Geophys. Res.* **86**, 11401–11418 (1981)
- Slavin, J.A., Acuña, M.H., Anderson, B.J., Baker, D.N., Benna, M., Boardsen, S.A., Gloeckler, G., Gold, R.E., Ho, G.C., Korth, H., Krimigis, S.M., McNutt, R.L., Raines, J.M., Sarantos, M., Schriver, D., Solomon, S.C., Trávníček, P., Zurbuchen, T.H.: MESSENGER observations of magnetic reconnection in mercury's magnetosphere. *Science* **324**, 606 (2009)
- Slavin, J.A., Anderson, B.J., Baker, D.N., Benna, M., Boardsen, S.A., Gold, R.E., Ho, G.C., Imber, S.M., Korth, H., Krimigis, S.M., McNutt, R.L., Raines, J.M., Sarantos, M., Schriver, D., Solomon, S.C., Trávníček, P., Zurbuchen, T.H.: MESSENGER and Mariner 10 flyby observations of magnetotail structure and dynamics at Mercury. *J. Geophys. Res. Space Phys.* **117**(A1), A01215 (2012)
- Slavin, J.A., DiBraccio, G.A., Gershman, D.J., Imber, S.M., Poh, G.K., Raines, J.M., Zurbuchen, T.H., Jia, X., Baker, D.N., Glassmeier, K.-H., Livi, S.A., Boardsen, S.A., Cassidy, T.A., Sarantos, M., Sundberg, T., Masters, A., Johnson, C.L., Winslow, R.M., Anderson, B.J., Korth, H., McNutt, R.L., Solomon, S.C.: MESSENGER observations of Mercury's dayside magnetosphere under extreme solar wind conditions. *J. Geophys. Res. Space Phys.* **119**(10), 8087–8116 (2014)
- Smart, D.F., Shea, M.A.: A simplified model for timing the arrival of solar flare-initiated shocks. *J. Geophys. Res. Space Phys.* **90**(A1), 183–190 (1985)
- Speiser, T.W.: Conductivity without collisions or noise. *Planet. Space Sci.* **18**, 613–622 (1970)
- Spitkovsky, A.: Particle acceleration in relativistic collisionless shocks: Fermi process at last? *Astrophys. J.* **682**(1), L5–L8 (2008)
- Spreiter, J.R., Summers, A.L., Alksne, A.Y.: Hydromagnetic flow around the magnetosphere. *Planet. Space Sci.* **14**, 223 (1966)
- Stix, T.H.: Waves in Plasma. Springer, New York (1992)
- Sulaiman, A.H., Masters, A., Dougherty, M.K., Burgess, D., Fujimoto, M., Hospodarsky, G.B.: Quasiperpendicular high Mach number shocks. *Phys. Rev. Lett.* **115**(12), 125001 (2015)
- Sun, W.J., Fu, S.Y., Slavin, J.A., Raines, J.M., Zong, Q.G., Poh, G.K., Zurbuchen, T.H.: Spatial distribution of Mercury's flux ropes and reconnection fronts: MESSENGER observations. *J. Geophys. Res. Space Phys.* **121** (2016). doi:10.1002/2016JA022787
- Sundberg, T., Boardsen, S.A., Slavin, J.A., Uritsky, V.M., Anderson, B.J., Korth, H., Gershman, D.J., Raines, J.M., Zurbuchen, T.H., Solomon, S.C.: Cyclic reformation of a quasi-parallel bow shock at Mercury: MESSENGER observations. *J. Geophys. Res. Space Phys.* **118**(10), 6457–6464 (2013)
- Treumann, R.A.: Fundamentals of collisionless shocks for astrophysical application, 1. Non-relativistic shocks. *Astron. Astrophys. Rev.* **17**(4), 409–535 (2009)
- Uritsky, V.M., Slavin, J.A., Khazanov, G.V., Donovan, E.F., Boardsen, S.A., Anderson, B.J., Korth, H.: Kinetic-scale magnetic turbulence and finite Larmor radius effects at Mercury. *J. Geophys. Res. Space Phys.* **116**(A9), A09236 (2011)
- Vay, J.L.: Simulation of beams or plasmas crossing at relativistic velocity. *Phys. Plasmas* **15**, 056701 (2008)
- Yee, K.: Numerical Solution of Initial Boundary Value Problems Involving Maxwell's Equations in Isotropic Media. IEEE Trans. Antennas Propag. **14**(3), 302–307 (1966)
- Wan, W., Lapenta, G., Delzanno, G.L., Egedal, J.: Electron acceleration during guide field magnetic reconnection. *Phys. Plasmas* **15**(3), 032903 (2008)
- Widmer, F., Büchner, J., Yokoi, N.: Characterizing plasmoid reconnection by turbulence dynamics. *Phys. Plasmas* **23**(9), 092304 (2016)

- Winslow, R.M., Anderson, B.J., Johnson, C.L., Slavin, J.A., Korth, H., M.E., Purucker, Baker, D.N., Solomon, S.C.: Mercury's magnetopause and bow shock from MESSENGER Magnetometer observations. *J. Geophys. Res. Space Phys.* **118**(5), 2213–2227 (2013)
- Wood, P., Neukirch, T.: Electron acceleration in reconnecting current sheets. *Sol. Phys.* **226**(1), 73–95 (2005)
- Zank, G.P., Hunana, P., Mostafavi, P., Roux, J.A.L., Li, G., Webb, G.M., Khabarova, O., Cummings, A., Stone, E., Decker, R.: Diffusive shock acceleration and reconnection acceleration processes. *Astrophys. J.* **814**(2), 137 (2015)
- Zelenyi, L., Oka, M., Malova, H., Fujimoto, M., Delcourt, D., Baumjohann, W.: Particle acceleration in mercury's magnetosphere. *Space Sci. Rev.* **132**, 593–609 (2007)
- Zenitani, S., Hoshino, M.: The generation of nonthermal particles in the relativistic magnetic reconnection of pair plasmas. *Astrophys. J.* **562**(1), L63–L66 (2001)
- Zharkova, V.V., Gordovskyy, M.: Energy spectra of particles accelerated in a reconnecting current sheet with the guiding magnetic field. *Mon. Not. R. Astron. Soc.* **356**(3), 1107–1116 (2005)
- Zhou, X., Büchner, J., Bárta, M., Gan, W., Liu, S.: Electron acceleration by cascading reconnection in the solar corona. I. Magnetic gradient and curvature drift effects. *Astrophys. J.* **815** 6 (2015)
- Zhou, X., Büchner, J., Bárta, M., Gan, W., Liu, S.: Electron acceleration by cascading reconnection in the solar corona. II. Resistive electric field effects. *Astrophys. J.* **827**, 94 (2016)

Chapter 9

Physical Processes in the Dusty Plasma of the Enceladus Plume

Victoria Yaroshenko, Patrick Meier, Hermann Lühr, and Uwe Motschmann

Abstract This chapter presents a short overview of physical processes in a specific plasma region (a so-called plume) found by the Cassini orbiter in the vicinity of the icy moon Enceladus. In particular, we summarize highlights of scientific results which have been performed by German research groups in GFZ German Research Centre for Geosciences, Potsdam and Technical University of Braunschweig as part of the Special Priority Program “PlanetMag” of the Deutsche Forschungsgemeinschaft between 2013 and 2016. The highlights cover mostly those theoretical and numerical studies in which measurements of different Cassini instruments could be compared with theory or where the phenomenon has a diagnostic application. Dust charging, role of dust size distributions, and dust charge fluctuations are discussed. The findings are used for interpretations of the Cassini Plasma Spectrometer data and improve constraints on the dust characteristics. Then the main forces and dust dynamics are discussed in conditions relevant for the near-Enceladus environment. It is also examined how the charged dust can affect the plasma shielding length which is of importance for the reliable Cassini Langmuir probe measurements. Considering the dust grains as heavy negative ion species, the electric conductivity tensor is modified, whose elements are the key quantities for understanding the magnetic field perturbations registered by the Cassini Magnetometer during Enceladus flybys.

V. Yaroshenko (✉)

German Research Center for Geosciences, Telegrafenberg, 14473 Potsdam, Germany

e-mail: yarosh@gfz-potsdam.de

P. Meier

Institute of Theoretical Physics and Institute for Geophysics and Extraterrestrial Physics, TU Braunschweig, Braunschweig, Germany

e-mail: patrick.meier@tu-braunschweig.de

H. Lühr

Deutsches GeoForschungsZentrum GFZ, 14473 Potsdam, Germany

e-mail: hluehr@gfz-potsdam.de

U. Motschmann

Institute of Theoretical Physics, TU Braunschweig, Braunschweig, Germany

e-mail: u.motschmann@tu-braunschweig.de

9.1 Introduction

Dusty plasmas are gas plasmas consisting of electrons, ions, and neutral atoms (molecules) that additionally contain fine solid particles loosely referred as “dust.” This state of matter is ubiquitous in space, e.g., in the interplanetary medium, in interstellar clouds, in comet tails, and in the ring systems of the giant planets as well as in mesospheric noctilucent clouds (Goertz 1989). Recently the Cassini orbiter found such a medium in the direct vicinity of the icy moon Enceladus orbiting Saturn at a planet-centered distance of about $4 R_S$ (Saturn radius $R_S \simeq 60,268$ km). It turns out that this geologically active small moon (radius $R_E \simeq 250$ km) feeds the most extended, Saturn’s E ring by dust particles (Kempf et al. 2010) and creates a specific multispecies plasma environment (Tokar et al. 2009).

The Enceladus geological activity is concentrated at its south pole region, along the four “tiger stripe” fractures, which radiate heat at temperatures up to at least 167 K and are the source of multiple jets producing in total ~ 200 kg/s mainly water vapor (Spencer et al. 2006). The escaping gas interacts with Saturn’s corotating plasma flow and changes locally the plasma parameters. The vapor jets also contain copious amounts of ice grains with sizes ranging from a few nanometers to a few micrometers. The micron-sized dust was detected by the Cassini Cosmic Dust Analyzer (CDA) (Spahn et al. 2006) and is visible in the forward scattering sunlight images of the moon’s plume (Porco et al. 2006). More numerous smallest, nanometer-sized, grains have been registered directly in the plume region by the Cassini Plasma Spectrometer (CAPS) (Jones et al. 2009; Hill et al. 2012).

The grains emanating from the moon’s interior become electrically charged by collection of magnetospheric plasma electrons and ions, as well as by photo-emission and secondary electron emission. In the near-Enceladus environment the collection processes dominate, and the grains attain mainly negative charges (Yaroshenko et al. 2014). The presence of a small fraction of high-energy electrons (≥ 100 eV), however, might significantly increase the role of the secondary electron emission in the charging of nanoparticles (Dzhanoev et al. 2015) and even provide a small positive charge on some grains. During a few plume encounters CAPS detected both negatively and positively charged nanoparticles with a strong domination of the negatively charged dust. The negatively charged grain population in the central part of the plume is characterized by mass-to-charge ratios around $m_d/q_d \sim 10^4$ amu/e and cumulative dust number density up to $n_d \sim 10^9$ m⁻³ which appear to be close to the local plasma density (Hill et al. 2012).

Such charged nanograins together with usual microparticles (electrons, ions, and neutrals) generate a specific plasma region which extends more than ~ 1000 km in space and is associated with the name “plume.” Physically, this region represents a low-temperature weakly ionized dusty plasma (Yaroshenko and Lühr 2015). As will be discussed later, the name of a dusty plasma is used, as now the fine dust is an essential ingredient of the total plasma mixture. It turns out that Enceladus’ plume environment provides perhaps the most promising example of dusty plasmas in the outer solar system and the active moon’s jets allow the unique opportunity for direct

sampling of that zone. The Enceladus plume became a prime target for Cassini's continued exploration of Saturn's system and will be probably a tempting target for future missions.

In many ways, the plume plasma can be considered as a conventional plasma with additional negatively charged plasma species. However, dust particles are unusual charge carriers. They are many orders of magnitude heavier than the other plasma components and they can have orders of magnitude higher charges. Moreover, there are some essential features that prevent analogies with standard plasma components to be fully exploited since the grain charges are determined by the plasma potential and can fluctuate, and dust comes in all sizes in an almost continuous range from macromolecules to rock fragments. The difficult task to describe such a variety of dust sizes, masses, and charges by any form of tractable distribution has so far deterred the preliminary efforts. Naturally, most efforts have gone in modeling the dust grains as if they were an additional, heavy ion species. Even within these limitations, however, the study of the plume dusty plasma will lead to many interesting and new results.

This chapter surveys some general properties of the Enceladus plume dusty plasma. As examples mostly such situations are selected, where the theories could explain some Cassini measurements. Many of these phenomena are relevant for the determination of fundamental properties of the moon's environment such as the grain potential/charge and dust sizes, plasma shielding effect, or plasma conductivity.

9.2 Plasma Parameters and Dust Characteristics of the Plume

The Cassini spacecraft has made more than 20 targeted Enceladus flybys. Some of these north-to-south encounters passed very close to the plume axis which is aligned with the south polar direction of the moon (Fig. 9.1). We will mainly focus on the well-studied flybys E3 (12 March 2008) and E5 (9 October 2008) whose trajectories are displayed in Fig. 9.1 in the Enceladus Interaction System (ENIS). The coordinate system ENIS is defined in the caption of Fig. 9.1. During the E3 and E5 encounters most instruments were favorably oriented to study the plasma composition and dust characteristics. Figure 9.2 shows the data obtained by various Cassini instruments for a 3-min interval surrounding the E5-encounter with the Enceladus plume: the Ion and Neutral Mass Spectrometer (INMS) provided variations of the water vapor density, n_n (Teolis et al. 2010), RPWS-LP (Radio Plasma Wave Science instrument, Langmuir Probe) the ion density, n_i (Morooka et al. 2011), and CAPS - variations of the nanograin number densities, n_d (Hill et al. 2012). As seen, the neutral density covers the range $n_n \sim 10^{11} - 10^{14} \text{ m}^{-3}$, while the plasma density, which can be associated with the ion population $n_i \simeq n_0$, ranges between 10^8 m^{-3} and $3 \times 10^{10} \text{ m}^{-3}$ according to the RPWS-LP data. On the other

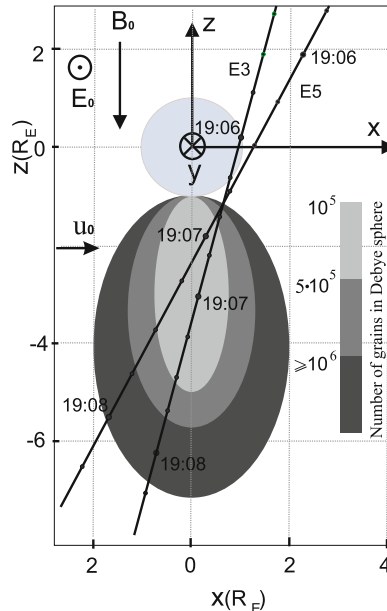


Fig. 9.1 Schematic representation of the Enceladus plume and Cassini trajectories during the E3 (12 March) and E5 (9 October) encounters in the Enceladus Interaction System (ENIS), whose origin coincides with the center of the moon. The (+x) axis is aligned with the direction of ideal corotation, the (+z) axis is anti-parallel to the ambient magnetosospheric field \mathbf{B}_0 , while the (+y) axis completes the right-handed coordinate system and points towards Saturn, being anti-parallel to the convective electric field in the unperturbed magnetosospheric flow upstream of Enceladus \mathbf{E}_0 . The undisturbed corotating ion flow approaches the plume from the left in the diagram (flow vectors labeled u_0). Variations of the plasma parameter for dust species $N = 4\pi n_d \lambda_{Dd}^3 / 3$ are displayed as the contour plot qualitatively consistent with the CAPS measurements of the nanograin density during the E3 and E5 flybys (Hill et al. 2012)

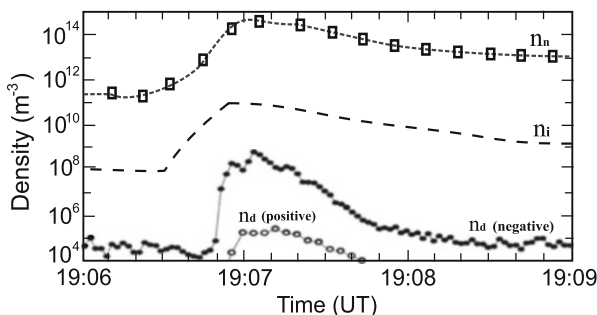


Fig. 9.2 Data of the Cassini instruments during the close plume encounter E5 on Oct. 9, 2008: INMS water vapor density, n_n (Teolis et al. 2010); RPWS-LP ion (plasma) density, n_i (Morooka et al. 2011) and CAPS cumulative nanograin number densities, n_d (negatively and positively charged) (Hill et al. 2012)

hand, recent studies of the RPWS data inferred from Langmuir oscillations excited by dust impacts indicate a rather weak increase of the electron density $n_e \sim 10^6 \text{ m}^{-3}$ in the middle of the plume (Ye et al. 2014). Based on these measurements, we adopt the value $n_i \sim n_e + n_d \sim 10^9 \text{ m}^{-3}$ as the maximum ion density. Note that such numbers are in good agreement with n_i inferred from the measurements of the Cassini Magnetometer (MAG) (Kriegel et al. 2014). In any case, the plume plasma is weakly ionized with a low ionization fraction $n_i/n_n \sim 10^{-5} - 10^{-3}$. Water group products were found to be the primary constituents of the plume (Tokar et al. 2009). We consider their cumulative effect ($O^+; OH^+; H_2O^+; H_3O^+; H_2O$; etc.), introducing the average ion/neutral mass $m_i \simeq m_n \simeq 18 \text{ amu}$. The jets of cold water-vapor (the gas temperature is $T_n \sim 200 \text{ K}$, Halevy and Stewart 2008) interacts directly with Saturn's corotating plasma (its unperturbed velocity in the Enceladus frame of reference is $u_0 \sim 2 \times 10^4 \text{ m/s}$), loading the magnetosphere with fresh cold ions and decelerating the plasma flow almost to its stagnation (Tokar et al. 2006). For the plasma velocity directly in the plume we take $u_0 \geq 10^3 \text{ m/s}$ which is consistent with the RPWS-LP measurements (Morooka et al. 2011) and plume modeling (Fleshman et al. 2010). For the plume ions we assume the temperature $T_i \sim 10^4 - 3 \times 10^4 \text{ K}$ close to the electron temperature $T_e \sim 10^4 \text{ K}$ measured by the RPWS-LP (Morooka et al. 2011).

The dust characteristics namely grain sizes and size distribution are difficult to quantify observationally. The Cassini dust analyzer (CDA) reliably detects large micron-sized particles ($a \geq 0.9 \mu\text{m}$) (Kempf et al. 2008). The CAPS instrument can measure the charge-to-mass ratio of essentially smaller grains. Assuming a charging state, the CAPS data can be transformed into the dust sizes (Jones et al. 2009). The CAPS detected particles with mass-to-charge ratios $m_d/q_d \sim 10^4 \text{ amu/e}$ were interpreted as nanometer-sized ($\sim 1 \text{ nm}$) water-ice grains carrying very small charges $q_d \sim 1e$ (Hill et al. 2012). According to the CDA, RPWS and CAPS data, a grain size distribution with power law decay $dn_d \propto a^{-\mu} da$, (a being the particle size) is the most probable one in the near-Enceladus environment. The power law index μ matching measurements of the various Cassini instruments yields $\mu \sim 4$ (Dong et al. 2015), providing that smallest grains are significantly more numerous than larger ones. Hill et al. (2012) reported variations of the cumulative number density in the range $n_d \sim (10^4 - 10^9) \text{ m}^{-3}$ during E3 and E5 flybys (see also Fig. 9.2). Since the dust and plasma characteristics essentially vary with radial and azimuthal distance from Enceladus, we will in most cases use a ratio of the dust-to-ion density, n_d/n_i , as a variable. Such an approach seems to be adequate for the initial study of the plume electrodynamics. Finally, note that the dust particles being ejected together with neutral gas are also assumed to be cold with a temperature $T_d \sim T_n \sim 200 \text{ K}$. Table 9.1 summarizes the relevant plasma and dust characteristics of the Enceladus plume which will be used for numerical estimates.

Table 9.1 Main plasma/dust parameters of the Enceladus plume

| Parameter | Symbol | Value |
|----------------------------------|----------------|---|
| Plasma number density | n_0 | $\leq(10^8\text{--}10^9)\text{ m}^{-3}$ |
| Neutral gas density | n_n | $(10^{11}\text{--}10^{14})\text{ m}^{-3}$ |
| Nanograin number density | n_d | $(10^4\text{--}10^9)\text{ m}^{-3}$ |
| Dust mass-to-charge ratio | m_d/q_d | $10^4 \text{ amu}/e$ |
| Ion flow velocity | u_0 | $\geq 10^3 \text{ m/s}$ |
| Electron temperature | T_e | $10^4 - 2 \times 10^4 \text{ K}$ |
| Ion temperature | T_i | $(10^4 - 3 \times 10^4) \text{ K}$ |
| Neutral gas/dust gas temperature | $T_n \sim T_d$ | 200 K |
| Local magnetic field | \mathbf{B}_0 | $(0,0,-325) \text{ nT}$ |

9.3 Charging Model

The basic process associated with dust in plasma is the grain charging. In Saturn's magnetosphere, including the Enceladus proximity, this issue has been extensively studied both theoretically and numerically (Horányi 1996; Horányi et al. 2004; Hsu et al. 2013; Graps et al. 2008; Kempf et al. 2006). Incorporating the parameters relevant for the near-Enceladus plasma, a predominant mechanism of dust charging is found to be a collection of plasma electrons and ions. Hence, a balance of thermal fluxes between electrons and ions, $J_e = J_i$, determines the grain equilibrium negative charge as a first rate approximation (Yaroshenko et al. 2014). In Maxwellian plasma the electron and ion fluxes are given by the orbital-motion-limited (OML) approximation (Horányi 1996)

$$J_e = \sqrt{8\pi}a^2n_ev_{Te} \exp(-z), \quad (9.1)$$

and

$$J_i = \sqrt{8\pi}a^2n_iv_{Ti}(1+z\tau). \quad (9.2)$$

Here z denotes the normalized grain floating potential φ in units of $\kappa T_e/e$ ($z = -e\varphi/\kappa T_e$), τ stands for the temperature ratio T_e/T_i , $n_{e(i)}$ is the electron (ion) number densities, and $v_{Te(i)} = \sqrt{\kappa T_{e(i)}/m_{e(i)}}$ refers to the thermal electron (ion) velocity with κ being the Boltzmann constant.

In the plume region average interparticle distances can be smaller than the plasma Debye length, and a net negative dust charge density $\rho_d = 4\pi\varepsilon_0 \int_{a_{\min}}^{a_{\max}} \varphi adn_d$ (Yaroshenko et al. 2014) can contribute to the plasma quasineutrality reducing the number of free electrons through $n_e/n_i = 1 - \rho_d/(en_i)$. Apparently, a growth of the cumulative dust density $n_d = \int_{a_{\min}}^{a_{\max}} dn_d$ (with $dnd = dn_d(a)$ being the differential dust distribution) reduces the electron charging current (9.1) and eventually leads to lower values of the surface potential z . A typical example is shown in Fig. 9.3, where

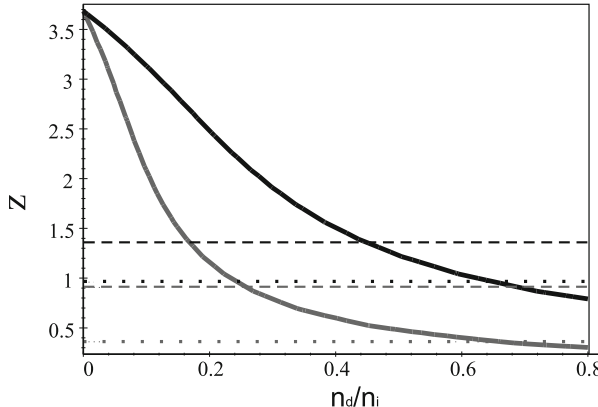


Fig. 9.3 Decrease in equilibrium grain potential, $z = -e\varphi/\kappa T_e$ with a dust/plasma density ratio, n_d/n_i , for the power law dust-size distribution ($\mu = 4$): upper (black) curve for $a_{\min} = 1.5 \text{ nm}$, $T_e = T_i = 10^4 \text{ K}$; lower (gray) curve for $a_{\min} = 2 \text{ nm}$, $T_e = T_i = 2 \times 10^4 \text{ K}$. The horizontal lines indicate the cutoff potentials imposed by the field emission (dashed) and the condition $Z_d = 1$ (dotted) (adapted from Yaroshenko and Lühr (2015))

we depict the variations of the normalized potential z versus the dust fraction, n_d/n_i . The curves are calculated for the power law size distribution with $\mu = 4$ at several values of the particle minimum size a_{\min} and plasma temperatures relevant for the plume region. Both plots are not very sensitive to the changes in plasma conditions and display a significant reduction of the grain potential with the density ratio n_d/n_i . There are two physical conditions which restrict the potential value from below and above for a given grain size. The dotted lines in Fig. 9.3 indicate the lower cutoff for z corresponding to the singly charged ($Z_d = q_d/e = 1$) grains with size a_{\min} . Another cutoff occurs due to the electron field emission effect. Due to the small size of the grains, even a moderate dust charge induces a large electric field on its surface, which may be strong enough for causing an electron field emission. For spherical ice grains the critical field $\sim 10^9 \text{ V/m}$ sets up the attainable grain charge $Z_d \leq 0.63a^2$, where the dust radius a is in nm (Mendis and Axford 1974). The latter gives the highest possible surface potential z at a grain with size a_{\min} shown by dashed lines in Fig. 9.3. As seen, the nanograins with given a_{\min} reach their equilibrium potentials/charges only in significantly dense dust regions when the plasma density ratio satisfies a certain condition, e.g., for $a_{\min} = 1.5 \text{ nm}$ $n_d/n_i \sim 0.5 - 0.7$ and for $a_{\min} = 2 \text{ nm}$ $n_d/n_i \sim 0.25 - 0.65$, respectively.

9.4 Stochastic Dust Charge Fluctuations

Contrary to the plasma particles, the grain charges are not fixed but can fluctuate. There are two reasons for fluctuating dust charges. First, the charging of the particles depends on local plasma characteristics, and thus their temporal or spatial

perturbations will ultimately affect equilibrium charges. The second reason is the discrete nature of charge carriers. Electrons and ions absorbed or emitted by the grain surface randomly provide stochastically fluctuating dust charges. These random fluctuations exist always even in a steady-state uniform plasma, but their studies have mainly been limited to the approximation of an isolated grain. Several papers (Matsoukas and Russell 1995; Matsoukas et al. 1996) discussed an analytical model of stochastic charge fluctuations on a single grain, while some emission processes have been included by Khrapak et al. (1999). According to a numerical simulation by Cui and Goree (1994), the root mean square (rms) of the dust charge fluctuations $\sigma_Z = \eta\sqrt{Z_d}$ has a coefficient $\eta \simeq 0.5$ for a wide range of plasma and grain parameters in the case ($Z_d \gg 1$) (here Z_d means an equilibrium dust charge number). Thus, the charge fluctuations are small for individual micrometer-sized ($Z_d \simeq 10^3$) and larger grains, since the rms is orders of magnitude lower than the mean charge number ($\sigma_Z \ll Z_d$). Hence, their charges on average are mainly specified by the floating potential φ , i.e., the dust potential with respect to the local plasma potential. Recently, a description of random dust charge fluctuations for grain ensembles has been given by Yaroshenko and Lühr (2014). It is pointed out that all statistic characteristics obtained in the limit of a dust-loaded plasma are significantly modified compared to earlier works. At high grain densities, the difference can be quite appreciable: η -values become significantly lower than $\eta = 0.5$ as shown in Fig. 9.4 thus reducing the range of charge fluctuations even more. In contrast to the large grains, however, such dust charge fluctuations become significant for nanograins ($Z_d < 10$), because even in the dense limit the rms is on the same order of magnitude ($\sigma_Z \sim 1$). Applying the analytical theory of random charge fluctuations by Yaroshenko and Lühr (2014) to the plume conditions shows that a majority of the grains in the dust-loaded Enceladus plume acquire fluctuating negative charges obeying the Gaussian probability distribution. The distributions become narrower with growth of the dust density. Moreover, the approach indicates

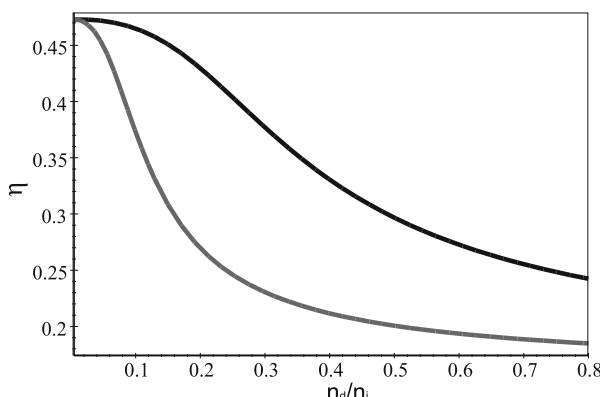


Fig. 9.4 Normalized amplitude of the random dust charge fluctuations $\eta = \sigma_Z/\sqrt{Z_d}$ versus relative grain density n_d/n_i for the plasma and dust parameters as in Fig 9.3

that there might appear a minority of positively charged particles. The probability of the coexistence of two oppositely charged dust species is mainly determined by the ratio of the dust/plasma number densities. These findings suggest two qualitative conclusions that allow a direct comparison with Cassini observations: (1) the higher relative density of negatively charged dust (ratio n_d/n_0), the more probable and thus more numerous seem to be the positively charged grains; (2) the maxima of number densities of negatively and positively charged dust have to coincide locally. Close inspection of the CAPS data for the available plume encounters at which the negative/positive nanograins have been registered (Hill et al. 2012; Dong et al. 2015) indicates that both predictions are fully consistent with the measured grain density profiles. Although these findings qualitatively match the available Cassini data, the continuous model of charge fluctuation restrictions do not allow us to give quantitative estimates of the ratio between positive and negative dust particles. Even though, we consider the obtained results as an indication of the importance of random dust charge fluctuations for the physics of the near-Enceladus plasma and for interpretations of the Cassini measurements.

Recently self-consistent numerical studies have been carried out, where the stochastic charging of the grains and their feedback to the plasma environment of the plume were considered (Meier et al. 2014, 2015). A comparison between continuous and discrete charging of an initially uncharged nanograin is shown in Fig. 9.5. After the switch-on-phase the grain charge remains at the equilibrium value determined by the potential φ for continuous charging, while fluctuations around the equilibrium charge permanently occur for discrete charging providing a certain

| t/Δt | Z _p (Discrete) | Z _p (Continuous) |
|-------|---------------------------|-----------------------------|
| 0 | 0 | 0 |
| 1000 | 5 | ~5.5 |
| 2000 | 7 | ~6.5 |
| 3000 | 5 | ~6.5 |
| 4000 | 7 | ~6.5 |
| 5000 | 8 | ~6.5 |
| 6000 | 9 | ~6.5 |
| 7000 | 8 | ~6.5 |
| 8000 | 10 | ~6.5 |
| 9000 | 8 | ~6.5 |
| 10000 | 8 | ~6.5 |
| 12000 | 6 | ~6.5 |
| 14000 | 7 | ~6.5 |
| 15000 | 5 | ~6.5 |
| 16000 | 7 | ~6.5 |
| 17000 | 8 | ~6.5 |
| 18000 | 7 | ~6.5 |
| 19000 | 6 | ~6.5 |
| 20000 | 8 | ~6.5 |

Fig. 9.5 Charge development of an initial uncharged 2 nm grain for continuous (dashed curve, via Eqs. (9.1) and (9.2)) and discrete grain charging (stepped curve, via corresponding charge probabilities). The dotted line indicates the equilibrium grain charge number (adapted from Meier et al. (2015))

$\sigma_Z \neq 0$. Interestingly enough a full numerical modeling of the discrete nanograin charging qualitatively leads to results similar to those obtained in the continuous charging model (Yaroshenko and Lühr 2014).

Addressing a problem of the grain ensembles, Meier et al. (2015) have applied a numerical formalism to describe the dust charge fluctuations. The discrete nature of the charge is taken into account for small charge states, which yields the transition probabilities $p_{e,Z}$ and $p_{i,Z}$ describing the probability that an electron or ion is collected by a dust grain with a charge number Z during a certain time interval Δt . The quantities $p_{e,Z}$ and $p_{i,Z}$ are determined from the OML thermal electron (9.1) and ion fluxes (9.2). Under stationary conditions, assuming that a collision of an ion or electron with the grain changes the charge state by a discrete step, we get the balance equation $p_{i,Z}n_Z = p_{e,Z+1}n_{Z+1}$ with n_Z being the number density of grains in charge state Z . For arbitrary Z , there is an infinite set of balance equations, which can be rewritten in the form of an eigenvalue problem according to the underlying Markov chain (see for details Meerschaert (2013)). Thus the equilibrium grain charge distribution for multiply charged grains can be derived from the eigenvalue problem of the corresponding stochastic matrix to the eigenvalue 1 (Meier et al. 2015). This stochastic equilibrium means that the grain charge fluctuations of different dust particles cancel each other out in the time interval Δt . The equilibrium dust charge distribution is presented by the components of the eigenvector, independent of the initial distribution of the ensemble and also obeys the Gaussian distribution. Such an approach allows to calculate the ratio of negatively to positively charged grains which approaches 1:1 in the limit $n_d/n_i \rightarrow \infty$ (Fig. 9.6). Though the

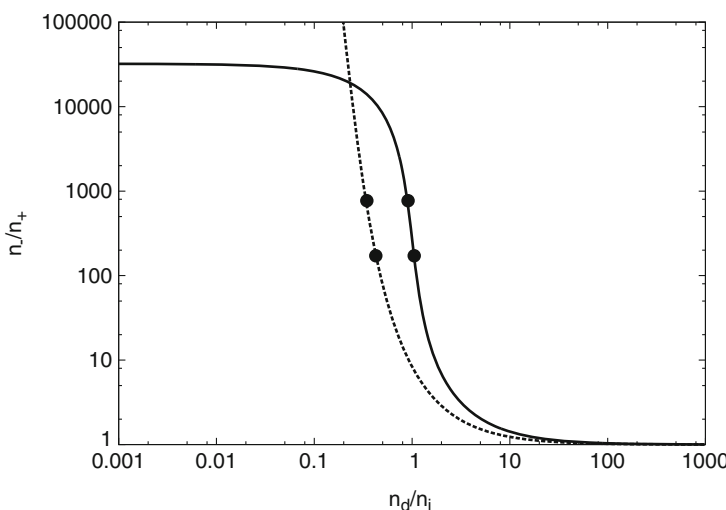


Fig. 9.6 Ratio of negatively to positively charged nanograins (n_-/n_+) as function of the dust-ion-ratio (n_d/n_i) resulting from the stochastic equilibrium model for $T_e = T_i \sim 10^4$ K. The ratio range in Enceladus plume resulting from CAPS data (Hill et al. 2012) is indicated by the dots. The right (solid) curve corresponds to the model with charge restriction by field emission, while the left (dashed) curve is yielded without any restriction

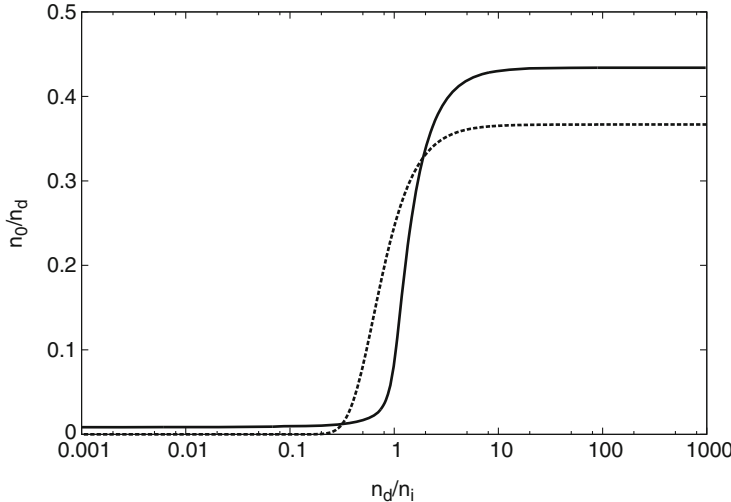


Fig. 9.7 Fraction of uncharged grains (n_0/n_d) as function of the dust-ion-ratio (n_d/n_i) resulting from the stochastic equilibrium model analogous to Fig. 9.6

mean grain charge approaches 0, there are *non-negligible* fractions of negatively as well as positively charged particles. Moreover, the stochastic equilibrium model allows estimations for the fraction of uncharged grains (Fig. 9.7) that cannot be detected by Cassini in Enceladus' plume. The stochastic charging model turns out to be largely applicable to Enceladus' plume despite of the inhomogeneous plasma characteristics and finite dust charge time as shown by means of simulations (Meier et al. 2015). Furthermore, the coexistence of oppositely charged dust species is clearly expected in the plume even without the charge restriction by field emission (Mendis and Axford 1974), while the fraction of uncharged grains is negligible within wide parts of the plume.

Finally, note that the dust charge fluctuations might be of importance for the plume diagnostics. In particular, an inclusion of the fluctuating charges in the interpretation of the CAPS measurements modifies the range of plasma and grain parameters consistent with the measured limit $m_d/q_d \sim 10^4$ amu/e as discussed (Yaroshenko and Lühr 2015). In particular, the predicted range of dust sizes satisfying the CAPS facilities is expected to be a (1.5–3.5) nm.

9.5 Plume Grains as Heavy Plasma Species and Their Effect on Plasma Screening

In Saturn's magnetosphere a competition between the gravitational, F_{GS} , and electromagnetic, F_L , forces mainly determines the dust dynamics. Large dust particles will follow gravitationally bound Keplerian orbits, without being distracted

from them by the electromagnetic force (case $F_L \ll F_{GS}$). Very small grains, on the other hand, will be trapped by the planetary magnetic field much like electrons and ions, and almost rigidly corotate with the planet ($F_L \gg F_{GS}$). The limiting dust size providing $F_{GS}/F_L \sim 1$ depends mostly on the orbital distance, dust grain potential, and material density. Considering the plume dust with $m_d/q_d \sim 10^4$ amu/e, we compare the gravitational force due to the attraction of the planet, $F_{GS} \simeq \mu_S m_d/r^2$ to the Lorentz force, $\mathbf{F}_L \simeq eZ_d [(\mathbf{V}_p - \mathbf{V}_d) \times \mathbf{B}_0]$. Here $\mu_S = 3.7931 \cdot 10^{16} \text{ m}^3 \text{ s}^{-2}$, $r \simeq 4R_S$ the orbital distance and \mathbf{B}_0 , \mathbf{V}_d and \mathbf{V}_p denote the planetary magnetic field and also dust and plasma velocity vectors at the location of Enceladus, respectively. For the given parameters and relative velocities $|\mathbf{V}_p - \mathbf{V}_d| = u_0 \geq 10^3 \text{ m/s}$ (Morooka et al. 2011; Tokar et al. 2006; Fleshman et al. 2010) the Lorentz force dominates gravitational attraction to the planet. Furthermore, for nano-sized grains gravity of Enceladus is negligible already at distances $\geq 10^5 \text{ m}$ from the moon surface. Such a domination of the electromagnetic forces in the dust dynamics makes the plume nanograins very similar to negative ions and gives a prerequisite to consider them like a new heavy plasma species (with charge-to-mass ratios much smaller than that for the water group ions).

The standard criteria for a plasma component requires a large number of grains in the dust Debye sphere, viz. $N = 4\pi n_d \lambda_{Dd}^3/3 \gg 1$. Here λ_{Dd} stands for the dust Debye length $\lambda_{Dd} = \sqrt{\varepsilon_0 \kappa T_d / (Z_d^2 e^2 n_d)}$. To check the validity of the plasma criteria for the dust population in the plume, we have calculated the values of N using the CAPS measurements of the cumulative grain population along the spacecraft trajectories E3 and E5 reported by Hill et al. (2012). In Fig. 9.1 we include estimates of N as a contour plot quantitatively consistent with the CAPS measurements of the negatively charged grain density. As seen, the N -values are typically in the range $N \sim 10^5$ – 10^6 , and thereby the plasma approximation is fully appropriate for the tiny nanograins as now the dust is an essential ingredient of the total plasma mixture. Hence collective effects associated with the charged grains become important.

Since the plume grains can be considered as a plasma species, the plasma shielding length λ_D has to incorporate contributions of all constituents. For a steep power law dust size distribution the net dust charge density is mainly defined by the smallest nano-sized grains (Yaroshenko et al. 2014). As a first approximation, we thus reduce the problem of the dust-size distribution to the monodisperse case, introducing a single grain species $a = a_{\min}$. Below we will explore several different nanograin sizes ($a \sim 2$ – 3 nm) which can provide values close to the CAPS limit $m_d/q_d \sim 10^4$ amu/e (Yaroshenko and Lühr 2015).

In a thermal plasma or in the case of subthermal particle drifts, the shielding is isotropic and the effective screening length, λ_D , is generalized as

$$\lambda_D = \frac{1}{[\lambda_{Dd}^{-2} + \lambda_{Di}^{-2} + \lambda_{De}^{-2}]^{1/2}}, \quad (9.3)$$

where the species Debye length is given in a standard way by $\lambda_{D\alpha} = \sqrt{\varepsilon_0 \kappa T_\alpha / (e^2 n_\alpha)}$, $\alpha = e, i, d$. In situations with superthermal streaming species

the temperature T_α has to be replaced by the appropriate kinetic energy in the definition of the appropriate $\lambda_{D\alpha}$, changing the net effective screening length (9.4) in the flow direction (Piel and Melzer 2002).

In the Enceladus plume the ambient electrons can be considered as Maxwellian ($T_e \sim 10^4$ K), while the ions (the initial corotating flow along the x -axis in Fig. 9.1) are significantly slowed down and deflected with respect to the x -direction. Using estimates of the ion velocity $u_0 \sim 10^3$ m/s (Morooka et al. 2011; Tokar et al. 2006; Fleshman et al. 2010), the plausible condition for the velocity projections on the axes x, y, z is $u = u_0/v_{Ti} \leq 2$. The nanograins emanating from the moon drift mainly along the ($-z$) direction in the ENIS coordinate system (Fig. 9.1). Such a southward-directed dust velocity is expected to be close to the gas velocity associated with values $v_g \sim 660$ –2000 m/s (Kriegel et al. 2014). The grains acquire also smaller velocity components along x and y axes $\sim v_g \tan \theta \geq 200$ m/s, where the injection angle is typically in the range $\theta \leq 15$ –35° (Kriegel et al. 2014). Low dust temperature $T_d \sim 200$ K yields a very low thermal dust velocity $v_{Td} = \sqrt{\kappa T_d/m_d} \sim 1$ m/s leading to $v_{Td} \ll v_g \tan \theta$. Because of this, the dust kinetic energy significantly dominates over grain thermal energy, and the direct dust contribution into the effective shielding length (9.4) becomes negligible. As a result, the effective screening length in the plume dusty plasma formally includes only the contributions from electrons and ions through

$$\lambda_D \simeq \frac{1}{[\lambda_{Di}^{-2}(1+u^2)^{-1} + \lambda_{De}^{-2}]^{1/2}}. \quad (9.4)$$

The influence of the negatively charged dust is due to the depletion of the ambient electron population ($n_e = n_i - Z_d n_d$) which increases the electron Debye length λ_{De} . It turns out, however, that the plume nanograins being effectively excluded from the electrostatic shielding can alter the screening length by a factor of 2 or 3 even in the case $T_e = T_i$ (see Fig. 5 in Yaroshenko and Lühr (2015)).

Much more pronounced variations in shielding lengths can be associated with the Cassini orbiter traversing the near-Enceladus plasma. A combination of ion and dust flows (in the Cassini frame of reference) produces highly divergent anisotropic plasma-sheath configurations as has been revealed in the particle-in-cell (PIC) simulation of the plasma/spacecraft interactions in the plume (Yaroshenko et al. 2015, 2012). Figure 9.8 gives one example of such a potential distribution around a negatively charged spherical spacecraft in the conditions valid for the central part of the plume, where $n_d > n_e$ (see case B2 in Yaroshenko et al. (2015)). The arising potential structure engenders an ion accumulation and electron depopulation in the direct vicinity of the spacecraft and thus the probe mounted on the orbiter can mostly measure $n_e < n_i$. The Cassini RPWS-LP is attached to the orbiter by a 1.5 m deployable boom (Gurnett et al. 2014) and in Fig. 9.9 we show an angular distributions of the plasma imbalance, $(n_i - n_e)$ at possible LP positions (as a function of the orientation angle θ) resulting from the potential distribution of Fig. 9.8. As seen, the spatial plasma configuration reveals a significant domination

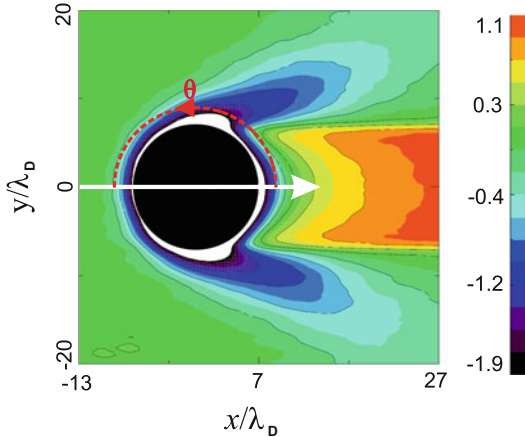


Fig. 9.8 Contour plot of the electrostatic potential around a spherical model of the Cassini orbiter resulting from PIC simulation in the dust-loaded plume plasma. The coordinate system (x, y) is associated with the moving orbiter, a relative plasma flow velocity (white arrow) indicates the positive x direction (for more details see Yaroshenko et al. (2015)). Calculations are made for $n_i = 10^9 \text{ m}^{-3}$, $n_d = 0.76 \times 10^9 \text{ m}^{-3}$, $T_e = T_i = 3 \times 10^4 \text{ K}$, plasma velocity 14.4 km/s, and $m_d/q_d \sim 10^3 \text{ amu}/e$. Possible positions of RPWS-LP are defined by the orientation angle θ counting from the downstream direction

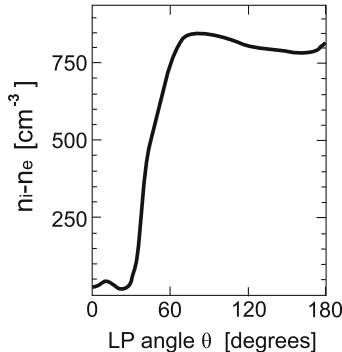


Fig. 9.9 Angular dependence of the plasma imbalance ($n_i - n_e$) at possible RPWS-LP positions due to the potential distribution around the Cassini orbiter shown in Fig. 9.8 (adapted from Yaroshenko et al. (2015)). The RPWS-LP orientation angle θ counts from the positive x axis in Fig. 9.8

of the ion population over the electrons at the upstream LP orientation ($\theta \sim 180^\circ$), while at the downstream orientation ($\theta \sim 0^\circ$) it leads to the condition $n_e \simeq n_i$ which contradicts the initial assumption of the presence of a dense dust component ($n_d > n_e$). Our results therefore indicate that the plasma distribution around the orbiter can directly impact the ambient plasma density measurements by the Cassini LP. Moreover, the investigation of other dust-plasma configurations in the near-

Enceladus environment shows that the electron depletion observed by the RPWS-LP cannot always be attributed to the electron attachment to the abundant dust particles, as has been discussed earlier (Morooka et al. 2011; Farrell et al. 2010; Wahlund et al. 2009; Yaroshenko et al. 2009) but might be a consequence of self-consistent charge separations in the electric field of the charged spacecraft.

9.6 Conductivity of Dusty Plasma

Electromagnetic coupling between the magnetospheric plasma and Enceladus' dust is not only restricted by the grain charging. Among the open questions is a problem how the charged dust disturbs Saturn's local magnetospheric structure. The magnetic field perturbations observed by the Cassini magnetometer near the moon could not really be explained on grounds of standard models of the moon-magnetosphere interactions (Dougherty et al. 2004). Simon et al. (2011) assumed that the key issue is the influence of charged dust on the plasma conductivity components which determine the Alfvén wing system generated by the interaction between the moon's plume and the corotating plasma. They suggested that immobile charged dust contributes in the quasineutrality condition. The ensuing depletion of free magnetospheric electrons decreases the value of the Hall conductivity term and once the charge density accumulated by the grains exceeds a certain critical value, the Hall conductivity becomes negative providing a reversal in the Hall current (reversed-Hall effect). This approach has been used to explain the observed field signature: the component of the magnetic field perturbations towards and away from Saturn became also reversed. One of the conclusions of this study, however, is that the considered submicron-sized grains mainly contribute to the Enceladus/plasma interaction by absorbing the ambient electrons while the contribution of dust dynamics to the magnetic field perturbations can safely be neglected. Since then several numerical studies have been carried out to interpret the magnetic field and plasma observations during the available Cassini encounters with the plume (see Kriegel et al. (2014, 2011) and references herein). The numerical approach by Kriegel et al. (2011) has included tiny, nano-sized grains in the modeling of the perturbed magnetic field. These studies, however, also supported the conclusion that the magnetic field distortions in the plume region are mainly associated with an accumulation of negative charge density on the grains and the consequent electron depletion. At the same time, as we have discussed, the plasma approximation seems to be fully appropriate for the tiny nanograins detected by CAPS ($m_d/q_d \sim 10^4$ amu/e) and hence collective effects associated with the charged grains are important. Therefore there is a need to advance the plasma conductivity description due to the incorporation of the grains as additional plasma component including dust charging and grain dynamics in a self-consistent way.

Revisiting the problem of the plasma conductivity in the fluid dynamic approach, we do not distinguish between the plasma electrons, ions, and dust particles but treat them in the standard way of the plasma electrodynamics. Neglecting any

contributions from the pressure gradient terms and external gravitational forces the momentum equations for various plasma species in a steady state reads as

$$v_{\alpha n} \mathbf{v}_\alpha = -\frac{q_\alpha}{m_\alpha} (\mathbf{E}_0 + [\mathbf{v}_\alpha \times \mathbf{B}_0]), \quad (9.5)$$

Here \mathbf{v}_α refers to the fluid velocities of the different plasma species ($\alpha = e, i, d$) having mass m_α and charge q_α . Regarding the particle charges, we put $q_e = -q_i = e$ for the plasma electrons and ions, while for the dust grains $q_d = eZ_d$, where Z_d , as earlier, satisfies the balance of the electron and ion currents flowing to or from the dust grain as given by Eqs. (9.1) and (9.2). Furthermore, the vectors \mathbf{E}_0 and \mathbf{B}_0 denoting the convective electric field and planetary magnetic field for simplicity are assumed to be constant within the plume ($\mathbf{E}_0 = -u_0 B_0 \hat{\mathbf{y}}$, $\mathbf{B}_0 = -B_0 \hat{\mathbf{z}}$ in the ENIS coordinates, values with “hats” denote unit vectors). Collisions with neutral molecules are described by collisional frequencies v_{en} , v_{in} and v_{dn} for the electrons, ions, and dust particles, respectively. Due to the deceleration of the corotating plasma flow ($u_0 \sim v_{Ti}$ and $u_0 \ll v_{Te}$), the collisional frequencies for the plasma electrons and ions can be approximated by $v_{\alpha n} \simeq n_n \sigma_{\alpha n} v_{T\alpha}$, where $\sigma_{\alpha n}$ is the appropriate collisional cross section. For the plasma energy ~ 1 eV, the momentum transfer cross section in the electron–water molecule collisions can be estimated as $\sigma_{en} \sim 6 \times 10^{-20} \text{ m}^2$ (Itikawa and Mason 2005), while the cross section in the ion–neutral collisions yields $\sigma_{in} \sim 3 \times 10^{-19} \text{ m}^2$ (Cassidy and Johnson 2010). Finally, for the momentum transfer frequency in dust–neutral collisions we can adopt the standard theory by Epstein (1924) yielding $v_{dn} = (8\sqrt{2\pi}/3)a^2 n_n m_n v_{Tn}/m_d$, where $v_{Tn} = \sqrt{\kappa T_n/m_n}$ is the thermal velocity of neutral molecules.

Solving (9.5) for the bulk speed \mathbf{v}_α of each component we calculate the net current density $\mathbf{j} = -\sum_\alpha q_\alpha n_\alpha \mathbf{v}_\alpha$. Ohm’s law is now a matrix equation $\mathbf{j} = \widehat{\sigma} \mathbf{E}_0$ with the conductivity tensor given by

$$\widehat{\sigma} = \begin{pmatrix} \sigma_P & \sigma_H & 0 \\ -\sigma_H & \sigma_P & 0 \\ 0 & 0 & \sigma_{\parallel} \end{pmatrix}. \quad (9.6)$$

The tensor components are defined by the Pedersen conductivity

$$\sigma_P = \sum_{(\alpha)} \frac{n_\alpha |q_\alpha|}{B_0} \left(\frac{\eta_\alpha}{1 + \eta_\alpha^2} \right), \quad (9.7)$$

the Hall conductivity

$$\sigma_H = \sum_{(\alpha)} \frac{n_\alpha q_\alpha}{B_0} \left(\frac{\eta_\alpha^2}{1 + \eta_\alpha^2} \right), \quad (9.8)$$

and by the parallel conductivity

$$\sigma_{\parallel} = \sum_{(\alpha)} \frac{n_{\alpha} |q_{\alpha}| \eta_{\alpha}}{B_0}. \quad (9.9)$$

Here we use the notations $\eta_{\alpha} = \omega_{B\alpha}/v_{\alpha n}$ with $\omega_{B\alpha} = |q_{\alpha}|B_0/m_{\alpha}$ being the gyrofrequency of each plasma species.

If the plasma contains no dust ($n_i = n_e$), all components of the conductivity tensor are positive. The conductivity treatment by Simon et al. (2011) predicts the negative Hall conductivity in the plume caused by a significant electron depletion associated with the presence of immobile ($\eta_d = 0$) negatively charged dust. To explore the contribution of grain dynamics to the full conductivity mechanism we first estimate η_{α} assuming a gas density $n_n \sim 10^{13}\text{--}10^{14} \text{ m}^{-3}$ typical for the central plume region, as inferred from the measurements of different Cassini instruments during the close moon encounters (Teolis et al. 2010; Waite et al. 2006; Hansen et al. 2008; Smith et al. 2014; Dong et al. 2011, see also Fig. 9.2). It follows immediately that for the cross section $\sigma_{en} \sim 6 \times 10^{-20} \text{ m}^2$ and $T_e \sim 10^4 \text{ K}$ the electron-neutral collision frequency will be clearly exceeded by the electron gyrofrequency ($\omega_{Be} \sim 5 \times 10^4 \text{ s}^{-1}$) leading to $\eta_e \geq 10^4$. In a similar way, for the adopted ion-neutral cross section $\sigma_{in} \sim 3 \times 10^{-19} \text{ m}^2$ and $T_i \sim T_e$ the ion term obeys $\eta_i \leq 100$. The quantity responsible for the grain dynamics η_d at typical ratio $m_d/q_d \sim 10^4 \text{ amu/e}$ gives $\eta_d \leq 10$. Hence one can use the ordering : $\eta_d < \eta_i \leq 100$ and reduce the general expressions for the tensor components to

$$\sigma_P \simeq \sigma_{P0} \left(1 + p \frac{\eta_i}{\eta_d} \right), \quad (9.10)$$

$$\sigma_H \simeq \sigma_{H0} \left(1 - p \frac{\eta_i^2}{\eta_d^2} \right), \quad (9.11)$$

$$\sigma_{\parallel} \simeq \sigma_{\parallel 0} \left((1-p) + \frac{\eta_i + p\eta_d}{\eta_e} \right), \quad (9.12)$$

where $\sigma_{P0} = en_i/(B_0\eta_i)$, $\sigma_{H0} = en_i/(B_0\eta_i^2)$ and $\sigma_{\parallel 0} = en_i\eta_e/B_0$ define the respective conductivity elements in the conventional electron-ion plasma. The terms proportional to the Havnes parameter $p = Z_d n_d/n_i$ in (9.10)–(9.12) are associated with the dust component. As can be seen in Fig. 9.10 the grain contribution increases the Pedersen conductivity. It is interesting enough that within the plume parameter space σ_P given by Eq. (9.10) becomes independent of the dust charge, but grows linearly with the dust fraction $\sigma_P \propto p/\eta_d \propto n_d/n_i$. At very high grain densities, when $n_d/n_i \rightarrow 1$, the normalized Pedersen component has an upper limit which can be approximated as $\sigma_{Pmax}/\sigma_{P0} \simeq 20\sqrt{T_n/T_i}a^2$, where a is measured in nm. Adapting this result for the relevant ion temperature $T_i \sim 10^4 \text{ K}$ and admissible particle sizes $a \geq 2 \text{ nm}$ will cause the limiting value σ_{Pmax} to be at least one order

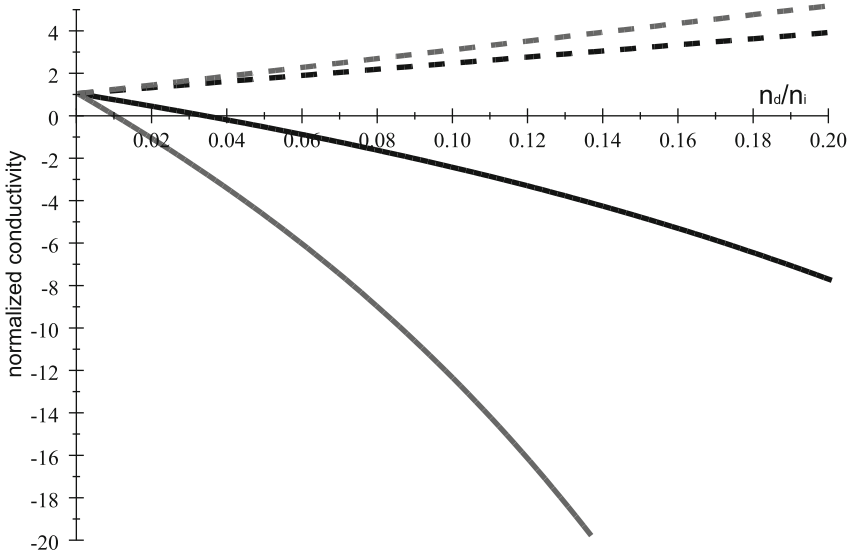


Fig. 9.10 Modifications of the normalized Pedersen conductivity, $\sigma_P/(en_i/B_0)$ (dashed), and Hall conductivity, $\sigma_H/(en_i/B_0)$ (solid), at small dust fractions $n_d/n_i \leq 0.2$ for $a = 2\text{ nm}$ (internal black curves), and $a = 3\text{ nm}$ (external, gray curves). In all cases $T_e = T_i = 10^4\text{ K}$ and particle charge number Z_d is derived from the balance of currents (9.1) and (9.2) assuming $n_e = n_i - Z_d n_d$

of magnitude higher than the usual plasma value σ_{P0} . Note that the increase of the Pedersen conductivity occurs solely because of the contribution of the dust current and this effect hence was sidestepped by Simon et al. (2011) assuming the grains to be immobile. Quite to the contrary, the parallel conductivity in the first order approximation is mainly determined by the electron depletion due to the presence of the dust species $\sigma_{\parallel} \propto (1-p)$. The value of σ_{\parallel} decreases with growth of n_d/n_i because more and more free electrons are accommodated on dust grains. In the extreme limit $p \rightarrow 1$, the reduced electron density would lead to a very small value of $\sigma_{\parallel}/\sigma_{\parallel 0} \simeq (\eta_i + \eta_d)/\eta_e \simeq \eta_i/\eta_e \ll 1$. It is important that both terms σ_p and σ_{\parallel} necessarily remain positive. Contrary to these elements, the Hall conductivity (9.11) can be either positive or negative depending on the contribution of the charged nanograins (Fig. 9.10). Indeed, the expression (9.11) introduces a critical dust fraction

$$(n_d/n_i)_{\text{cr}} = \frac{\eta_d^2}{Z_d \eta_i^2}, \quad (9.13)$$

so that for $n_d/n_i > (n_d/n_i)_{\text{cr}}$ σ_H becomes negative. The condition (9.13) ensures the reversed direction of the Hall current in the plume plasma and thus might be of importance for the interpretations of the Cassini MAG measurements in proximity to Enceladus (Kriegel et al. 2014; Simon et al. 2011). Since $\eta_d < \eta_i$ and

$Z_d \geq 1$, the threshold dust fraction $(n_d/n_i)_{\text{cr}}$ is relatively small. For the admissible parameters it yields $(n_d/n_i)_{\text{cr}} \simeq 10^{-2}$. Such dust fractions are quite realistic in the central plume regions: the MAG data constrained the plasma density to the range $n_i \sim 10^8\text{--}10^9 \text{ m}^{-3}$ (Kriegel et al. 2014), while the CAPS measurements give $n_d \sim 10^4\text{--}10^9 \text{ m}^{-3}$ (Table 9.1). In any case, even for singly charged grains ($Z_d = 1$) a plume dust population can easily provide the condition $n_d/n_i \geq 10^{-2}$ and thus the reversed Hall effect might be indeed associated with the plume plasma. Note that the model of immobile dust by Simon et al. (2011) predicts a few orders of magnitude lower threshold $(n_d/n_i)_{\text{cr}} \sim \eta_i^{-2} Z_d^{-1} \leq 10^{-4}$ in the considered gas density range, $n_n \sim 10^{13}\text{--}10^{14} \text{ m}^{-3}$.

Finally coming back to the Hall conductivity (9.11) a main conclusion is that within the plume σ_H (similar to σ_P) is primarily governed by the dust dynamics and already at small dust fraction like $n_d/n_i > 10^{-2}$ achieves significant negative values as shown in Fig. 9.10. At the extremely dense dust limit $n_d/n_i \rightarrow 1$, the Hall conductivity would be limited by a high negative value $\sigma_{H\max}/\sigma_{H0} \sim -500(T_n/T_i)a^4[\text{nm}]$. The latter leads to a ratio $|\sigma_{H\max}|/\sigma_{H0} \sim 10^2\text{--}10^3$ for typical grains sizes $a \sim 2\text{--}3 \text{ nm}$. As seen, the dust influence on the value of the Hall conductivity becomes even more crucial than on the Pedersen term. Recently, the treatment of the conductivity components (9.7)–(9.9) has been advanced to include an additional dissipative process associated with momentum exchange between the charged dust and ion plasma species which can be relevant for the near-Enceladus plasma (Yaroshenko and Lühr 2016). Note that the general results obtained in the frame of this approach support the above-mentioned conclusions.

Summing up, incorporation of the negatively charged dust in the plasma dynamics can significantly influence the conductivity tensor elements and hence determine value and direction of the electric current even at low dust densities. We expect that modifications of the Hall and Pedersen conductivity associated with localized increases in the plume dust density might significantly influence Enceladus' Alfvén wing structure (Simon et al. 2011), especially its large-scale properties, and thus be useful for understanding of magnetic field perturbations observed by the Cassini MAG in the Enceladus proximity.

9.7 Conclusions and Outlook

In this chapter we have reviewed the major results obtained by German research groups in GFZ German Research Centre for Geosciences, Potsdam and Technical University of Braunschweig as part of the Special Priority Program "Planetary Magnetic Fields" of the Deutsche Forschungsgemeinschaft between 2013 and 2016. Our findings refer to dust-magnetosphere interactions developing in the direct vicinity of Saturn's icy moon Enceladus which is the main source of dust for Saturn's extended E ring. Based on our theoretical treatments and numerical simulations we summarize:

1. Employing the parameter space, consistent with available Cassini data, dust charging has been studied in the near-Enceladus plasma with special focus on the region close to the moon's plume. The emphasis is on the role of dust size distribution and grain density, the electron temperature, fraction of the hot electrons, and multi-ion composition including the effect of newborn, nonthermalized ions. It is shown that a significant reduction of the electrical potential and the charging time in the dust-loaded regions occurs. This can explain the predominance of nanograins with small negative charges (on the order of a few electrons) in the dust reached plume as detected by the Cassini Plasma Spectrometer during close encounters with Enceladus. The theoretical findings might be of importance for reliable interpretations of the Cassini Langmuir probe measurements.
2. A description has been given of stochastic dust charge fluctuations in the light of Cassini data on the near-Enceladus plasma environment. Estimates of fluctuation time scales showed that this process can be of importance for the grains emanating from the icy moon. The analytical modeling predicts that in the dust-loaded Enceladus plasma a majority of the grains acquire fluctuating negative charges, but there might appear a minority of positively charged particles. Our findings appear to be supported by the available Cassini Plasma Spectrometer measurements of the charged grain distributions obtained during the plume flybys. The theoretical results impose new restrictions on the plume dust grains.
3. The Particle In Cell numerical simulations of the Cassini-plasma interactions in the near-Enceladus plasma have revealed a formation of a new kind of the plasma configuration with self-consistent charge separation of the plasma species in the electric field of SC. Such a structure can significantly affect the plasmas measurements of the Cassini instruments, especially when the instrument view directions cover either upstream or downstream directions. The results obtained for the plume flybys yield that the LP instrument could a priori register an apparent nonquasineutral plasma with a rather large deficit in electrons with respect to ion density.
4. Since the plasma conductivity is an important issue for understanding the magnetic field structure in the Enceladus proximity, the conductivity formalism has been revised to include the plume nanograins as a new plasma species. An incorporation of the dust dynamics affects both the Pedersen and Hall conductivity more efficiently than the electron depletion associated with the presence of the negatively charged dust as has been suggested earlier. The electron depletion remains a decisive factor only for the parallel conductivity. In the parameter regime relevant for the Enceladus plume one finds increase of the Pedersen and decrease of the parallel components, whereas for the Hall conductivity the charged dust changes both—its value and the sign. The associated reversed Hall effect depends significantly upon the local dust-to-plasma density ratio. An onset of the reversed Hall effect starts at the outer parts and prevails through the center of the Enceladus plume. The results obtained can significantly modify Enceladus' Alfvén wing structure and thus be useful

for interpretations of the magnetic field perturbations registered by the Cassini Magnetometer during the close Enceladus flybys.

To conclude, dust plays a crucial role in the near-Enceladus environment, in particular, in the moon's plume. The examples discussed in this chapter demonstrate the richness of new physical phenomena in the plume dusty plasma, which in many cases have no counterpart in common plasmas. Moreover, with all these particular features it seems that the plasma diagnostics in the direct vicinity of the moon might be significantly compromised by the presence of the dust constituent and great care is needed to determine the reliable plasma parameters. For future research this issue might be a key problem. Further area awaiting scrutiny are the role of charged dust in the formation of the plasma-driven and dust-driven currents in Saturn's inner magnetosphere and possible relation to the Saturn Kilometric Radiations, SKR.

References

- Cassidy, T.A., Johnson, R.E.: Icarus **209**, 696 (2010)
Cui, C., Goree, J.: IEEE Trans. Plasma Sci. **22**, 151 (1994)
Dong, Y., Hill, T.W., Teolis, B.D., Magee, B.A., Waite, J.H.: J. Geophys. Res. **116**, A10204 (2011)
Dong, Y., Hill, T.W., Ye, S.-Y.: J. Geophys. Res. Space Phys. **120**, 915 (2015)
Dougherty, M.K., et al.: Space Sci. Rev. **114**, 331 (2004)
Dzhanev, A.R., Spahn, F., Yaroshenko, V., Lühr, H., Schmidt, J.: Phys. Rev. B **92**, 125430 (2015)
Epstein, P.S.: Phys. Rev. **23**, 710–733 (1924)
Farrell, W.M., Kurth, W.S., Tokar, R.L., et al.: Geophys. Res. Lett. **37**, L20202 (2010)
Fleshman, B.L., Delamere, P.A., Bagenal, F.: Geophys. Res. Lett. **37**, L03202 (2010)
Goertz, C.K.: Rev. Geophys. **27**, 271 (1989)
Graps, A.L., et al.: Space Sci. Rev. **137**, 435 (2008)
Gurnett, D.A., et al.: Space Sci. Rev. **114**, 395 (2004)
Halevy, I., Stewart, S.T.: Geophys. Res. Lett. **35**, L12203 (2008)
Hansen, C.J., et al.: Nature **456**, 477 (2008)
Hill, T.W., et al.: J. Geophys. Res. **117**, A05209 (2012)
Horányi, M.: Annu. Rev. Astrophys. **34**, 383 (1996)
Horányi, M., Hartquist, T.W., Havnes, O., Mendis, D.A., Morfill, G.E.: Rev. Geophys. **42**, RG4002 (2004)
Hsu, H.-W., Horányi, M., Kempf, S.: Earth Planets Space **65**, 149 (2013)
Itikawa, Y., Mason, N.: J. Phys. Chem. Ref. Data **34**, 1 (2005)
Jones, G.H., et al.: Geophys. Res. Lett. **36**, L16204 (2009)
Kempf, S., et al.: Planet. Space Sci. **54**, 999 (2006)
Kempf, S., Beckmann, U., Moragas-Klostermeyer, G., et al.: Icarus **193**, 420 (2008)
Kempf, S., et al.: Icarus **206**, 446 (2010)
Khrapak, S.A., et al.: Phys. Rev. E, **59**, 6017 (1999)
Kriegel, H., Simon, S., Motschmann, U., Saur, J., Neubauer, F.M., Persoon, A.M., Dougherty, M.K., Gurnett, D.A.: J. Geophys. Res. **116**, A10223 (2011)
Kriegel, H., et al.: J. Geophys. Res. **119**, 2740 (2014)
Matsoukas, T., Russell, M.: J. Appl. Phys. **77**, 4285 (1995)
Matsoukas, T., Russell, M., Smith, M.: J. Vac. Sci. Technol. A**14**, 624 (1996)
Meerschaert, M.M.: In: Meerschaert, M.M. (ed.) Mathematical Modeling, p. 251. Academic, Boston (2013)
Meier, P., Kriegel, H., Motschmann, U., Schmidt, J., et al.: Planet. Space Sci. **104**, 216 (2014)

- Meier, P., Motschmann, U., Schmidt, J., et al.: *Planet. Space Sci.* **119**, 208 (2015)
- Mendis, D.A., Axford, W.I.: *Annu. Rev. Earth Planet. Sci.* **2**, 419 (1974)
- Morooka, M.W., et al.: *J. Geophys. Res.* **116**, A12221 (2011)
- Piel, A., Melzer, A.: *Plasma Phys. Controlled Fusion* **44**, R1 (2002)
- Porco, C.C., et al.: *Science* **311**, 1393 (2006)
- Simon, S., et al.: *J. Geophys. Res.* **116**, A04221 (2011)
- Smith, H.T., Johnson, R.E., Perry, M.E., et al.: *J. Geophys. Res.* **115**, A10252 (2014)
- Spahn, F., et al.: *Science* **311**, 1416 (2006)
- Spencer, J.R., Pearl, J.C., Segura, M., Flasar, F. M., Mamoutkine, A., Romani, P., Buratti, B.J., Hendrix, A.R., Spilker, L.J., Lopes, R.M.C.: *Science* **311**, 1401 (2006)
- Teolis, B.D., et al.: *J. Geophys. Res.* **115**, A09222 (2010)
- Tokar, R.L., et al.: *Science* **311**, 1409 (2006)
- Tokar, T.L., et al.: *Geophys. Res. Lett.* **36**, L13203 (2009)
- Wahlund, J.E., et al.: *Planet. Space Sci.* **57**, 1795 (2009)
- Waite, J.H. Jr., et al.: *Science* **311**, 1419 (2006)
- Yaroshenko, V.V., Lühr, H.: *J. Geophys. Res.* **119**, 6190 (2014)
- Yaroshenko, V.V., Lühr, H.: *Plasma Phys. Controlled Fusion* **58**, 014010 (2015)
- Yaroshenko, V., Lühr, H.: *Icarus* **278**, 79 (2016)
- Yaroshenko, V.V., et al.: *Planet. Space Sci.* **57**, 1807 (2009)
- Yaroshenko, V.V., Miloch, W.J., Thomas, H.M., Morfill, G.E.: *J. Geophys. Res. Lett.* **39**, L18108 (2012)
- Yaroshenko, V.V., Lühr, H., Miloch, W.J.: *J. Geophys. Res.* **119**, 221 (2014)
- Yaroshenko, V.V., Miloch, W.J., Lühr, H.: *Icarus* **257**, 1 (2015)
- Ye, S.-Y., et al.: *J. Geophys. Res.* **119**, 3373 (2014)

Chapter 10

Modeling of the Ionospheric Current System and Calculating Its Contribution to the Earth’s Magnetic Field

**Boris E. Prokhorov, Matthias Förster, Vincent Lesur,
Alexander A. Namgaladze, Matthias Holschneider, and Claudia Stolle**

Abstract The additional magnetic field produced by the ionospheric current system is a part of the Earth’s magnetic field. This current system is a highly variable part of a global electric circuit. The solar wind and interplanetary magnetic field (IMF) interaction with the Earth’s magnetosphere is the external driver for the global electric circuit in the ionosphere. The energy is transferred via the field-aligned currents (FACs) to the Earth’s ionosphere. The interactions between the neutral and charged particles in the ionosphere lead to the so-called thermospheric neutral wind dynamo which represents the second important driver for the global current system. Both processes are components of the magnetosphere–ionosphere–thermosphere (MIT) system, which depends on solar and geomagnetic conditions, and have significant seasonal and UT variations.

The modeling of the global dynamic Earth’s ionospheric current system is the first aim of this investigation. For our study, we use the Potsdam version of the Upper Atmosphere Model (UAM-P). The UAM is a first-principle, time-dependent, and fully self-consistent numerical global model. The model includes the thermosphere, ionosphere, plasmasphere, and inner magnetosphere as well as the electrodynamics of the coupled MIT system for the altitudinal range from 80 (60) km up to the 15 Earth radii. The UAM-P differs from the UAM by a new electric field block. For this study, the lower latitudinal and equatorial electrodynamics of the UAM-P model was improved.

B.E. Prokhorov (✉) • M. Förster • C. Stolle

GFZ German Research Centre for Geosciences, Helmholtz Centre Potsdam, Potsdam, Germany
e-mail: boris.prokhorov@gfz-potsdam.de; mfo@gfz-potsdam.de

V. Lesur

Institut de Physique du Globe de Paris, Sorbonne Paris Cité, Université Paris-Diderot, Paris, France

A.A. Namgaladze

Murmansk Arctic State University, Murmansk, Russia

M. Holschneider

Institute of Applied Mathematics, University of Potsdam, Potsdam, Germany

The calculation of the ionospheric current system's contribution to the Earth's magnetic field is the second aim of this study. We present the method, which allows computing the additional magnetic field inside and outside the current layer as generated by the space current density distribution using the Biot-Savart law. Additionally, we perform a comparison of the additional magnetic field calculation using 2D (equivalent currents) and 3D current distribution.

10.1 Introduction

The Earth ionosphere is a part of the coupled magnetosphere–ionosphere–thermosphere (MIT) system. This highly variable system is driven by the solar wind and interplanetary magnetic field (IMF) interaction with the Earth's magnetosphere. The field-aligned currents (FACs) are the energetic link between the magnetospheric current system and the ionosphere. The FACs play an important role at the high-latitude areas. The second important driver for the MIT system is the thermospheric neutral wind dynamo. The neutral wind dynamo results from the interactions between the neutral and charged particles in the ionosphere. The dynamo currents are dominating at lower and equatorial latitudes. The magnetospheric generator together with the thermospheric neutral wind dynamo is the component of the global MIT electric chain, which depends on season, UT time moment, as well as solar and geomagnetic conditions. As a result, the electric field as well as the ionospheric current system have significant spatial and temporal variations.

The first aim of this study is to define the ionospheric current system using the Potsdam version (UAM-P) of the global, first-principle, three-dimensional, time-dependent, numerical Upper Atmosphere Model (UAM). The UAM-P model is an improved version of the UAM model which describes the thermosphere, ionosphere, plasmasphere, and inner magnetosphere as well as the electrodynamics of the coupled MIT system for the altitudinal range from 80 (60) km up to 15 Earth radii. For the present investigation, the lower latitudinal and equatorial electrodynamics of the UAM model was improved.

The second aim of this research is the calculation of the additional magnetic field generated by the Earth's ionospheric current system. For this purpose, we use the ionospheric current distribution obtained with the UAM-P model. Together with it, we present the method which allows to calculate this additional magnetic field inside and outside the current layer as generated by the space current density distribution using the Biot-Savart law.

In this study, we mainly focus on the dayside of the middle, lower, and equatorial ionospheric current system. For the calculation of the additional magnetic field, we use those ionospheric currents, which flow perpendicular to the magnetic field in the altitude range from 80 up to 526 km. We take a much wider height range into account than the usually considered E-region dynamo with maximum current flows around 110–130 km altitude.

10.2 The Upper Atmosphere Model (UAM)

The model was created at the Kaliningrad Observatory which is now the West Department of the Institute of Terrestrial Magnetism, Ionosphere and Radiowave Propagation of the Russian Academy of Sciences (IZMIRAN) (Namgaladze et al. 1988, 1990, 1991, 1994). This model was known as the Global Self-consistent Model of the Thermosphere, Ionosphere, and Protonosphere (GSM TIP). The further development of the model was performed at the Polar Geophysical Institute and at the Murmansk State Technical University (Namgaladze et al. 1998; Förster et al. 1999; Namgaladze et al. 2000b,a; Volkov and Namgaladze 1996). As a result, the UAM model was obtained. The GSM TIP was the base for the UAM model. Since 1998, these two models were evolved independently from each other. Now, we continue developing the UAM model at the Helmholtz Centre Potsdam, GFZ German Research Centre for Geosciences, and the University of Potsdam (Förster et al. 2012; Namgaladze et al. 2013; Prokhorov et al. 2014; Prokhorov 2016).

In previous versions of the UAM, the vertical electric field inside the ionospheric current layer (80–175 km) was neglected ($E_r = 0$). This assumption allowed integrating the current system along the vertical direction within the ionospheric current layer. This is correct for the high latitudes where the magnetic field lines are more or less vertical. The situation is different for the lower latitudinal (significant inclination of the magnetic field line) and equatorial area (magnetic field parallel to the Earth's surface).

For this study, we use a new version of the model with an improved electric field block (UAM-P), which will be described in more detail in the subsequent sections. For this purpose, we extend the altitudinal range for the ionospheric current layer (80–526 km). Together with it, we neglect the parallel (to the magnetic field) electric field component along the magnetic field line ($E_q = 0$). This assumption allows integrating the current system along the magnetic field line instead of vertically.

10.2.1 *The Structure of the UAM-P Model*

In the Potsdam version of the UAM model (UAM-P) we use a new electric field block, while the other blocks such as the neutral atmosphere and lower ionosphere block, the ionospheric F2 region and protonospheric block, and the magnetospheric block are the same as in the UAM model.

The neutral atmosphere block calculates the three-dimensional distribution of the neutral atmosphere parameters, such as the neutral mass density, neutral gas temperature, thermospheric neutral wind velocity vector, and concentration of the main neutral gas components N₂, O₂, and O. These parameters are calculated using the system of the hydrodynamic equations (continuity, momentum, and energy balance) in a self-consistent way. The model equations of this part of the UAM-P

model are solved numerically in spherical geomagnetic coordinates for an altitudinal range from 80 to 526 km. The initial condition for the neutral atmosphere equations is obtained from global empirical models such as the MSISE-90 (Hedin et al. 1991; Hedin 1991) or its later modified version NRLMSISE-00 (Picone et al. 2002). These models are included into the UAM-P model as optional choices. Additionally, these empirical models can be used for one or more of the neutral atmosphere parameters. In other words, the UAM-P model can use both theoretical and empirical solutions for the neutral atmosphere parameters. For this study, we use the full theoretical solution.

The lower ionosphere section of the UAM-P model calculates the ionospheric parameters of the D, E, and F1 regions such as the concentration of the molecular ions NO^+ , O_2^+ and N_2^+ together with ion velocity vector for the altitudinal range from 80 up to 526 km. The ion and electron temperatures are computed for heights of 80 up to the 175 km. These parameters are calculated using the system of the continuity, momentum, and energy balance equations in a spherical geomagnetic coordinate system.

The ionospheric F2 region and protonosphere block describe the ionospheric parameters of the F2 region, plasmasphere, and inner magnetospheric cold plasma. Here, the distributions of the electrons, atomic oxygen, and hydrogen ion densities O^+ and H^+ together with the electron and ion temperatures and ion velocities $V(\text{O}^+)$ and $V(\text{H}^+)$ are calculated. These parameters are obtained from the system of hydrodynamic equations (continuity, momentum, and energy balance) in a self-consistent way. These equations are solved numerically using the geomagnetic dipole coordinate system. The altitude range is from 175 km up to 15 Earth radii of geocentric distance. The basic assumption of this block is that all charged components are fully magnetized above 175 km.

The charged particle distribution obtained from the IRI model (Bilitza 2001) is used as initial conditions for the lower ionosphere and ionospheric F2 region blocks of the UAM-P model.

The magnetospheric block describes the more energetic magnetospheric plasma using the system of continuity and momentum equations for $\sim 30 \text{ keV}$ ions. This block is based on several assumptions such as the following: the magnetospheric electrons are considered to be cold; their pressure is neglected in comparison with that of the magnetospheric ions; the Earth magnetic field has a pure dipole geometry; the geomagnetic field lines are closed at latitudes equatorward of the polar cap boundary (latitude equatorward of $\pm 75^\circ$); and the field lines are open inside the polar cap areas. This section is included into the UAM-P model as an option. We do not use it in our study.

The electric field block calculates the distribution of the electric potential at the lower boundary of the UAM-P model using the continuity equation for the charge flux (current). The basic assumptions for this section are the equipotentiality of the geomagnetic field lines above 80 km and a static magnetic field. These assumptions allow to reconstruct the global electric field from the known (at the lower boundary) electric potential distribution.

The equation systems of the UAM-P model are solved numerically for the nodes of the spatial grid using finite-difference methods. More information about the model equations, assumptions, input parameters, boundary conditions, and numerical schemes can be found in Brunelli and Namgaladze (1988), Namgaladze et al. (1988, 2013), and Prokhorov (2016).

10.2.2 The New Version of the Electric Field Calculation

As in previous versions of the UAM model, we suppose that the Earth magnetic field is static and has dipole geometry. The Earth's core magnetic field is larger by several orders of magnitude than the disturbances of the geomagnetic field and the additional magnetic field generated by currents in the ionosphere. In other words, non-dipole components of the geomagnetic field as well as variations of the magnetic field are neglected in the UAM-P model. Therefore, Maxwell's equation for the electric field $\nabla \times \mathbf{E} = -\frac{\partial \mathbf{B}}{\partial t}$ can be written as $\nabla \times \mathbf{E} = 0$. The electric field in the UAM-P model is a potential field.

Ohm's law for the ionospheric current density can be written in the following way:

$$\begin{aligned}\mathbf{j}_i &= \sigma_{\parallel} \mathbf{E}_{\parallel} + \sigma_P \mathbf{E}_{\perp} + \sigma_H [\mathbf{b} \times \mathbf{E}_{\parallel}] \\ \mathbf{E}_{\parallel} &= \mathbf{B}(\mathbf{B}, \mathbf{E})/B^2 \\ \mathbf{E}_{\perp} &= \mathbf{B} \times [\mathbf{E} \times \mathbf{B}]/B^2\end{aligned}$$

where \mathbf{j}_i represents the ionospheric current density and σ_H , σ_P , σ_{\parallel} are the Hall, Pedersen, and parallel to the magnetic field conductivities, correspondingly. These components can be written as

$$\begin{aligned}\sigma_H &= e^2 n_e [\Omega_e/m_e (\Omega_e^2 + v_{en}^2) - \Omega_i/m_i (\Omega_i^2 + v_{in}^2)] \\ \sigma_P &= e^2 n_e [v_{en}/m_e (\Omega_e^2 + v_{en}^2) + v_{in}/m_i (\Omega_i^2 + v_{in}^2)] \\ \sigma_{\parallel} &= e^2 n_e [1/m_e v_{en} + 1/m_i v_{in}]\end{aligned}$$

where m_i and m_e are ion and electron masses, respectively; Ω_i and Ω_e are ion and electron cyclotron frequencies; and v_{in} and v_{en} are ion-neutral and electron-neutral collision frequencies (Namgaladze et al. 2013).

The conductivity tensor for the Earth ionosphere can be represented for a dipole coordinate system (q, v, u) as shown below:

$$\sigma = \begin{pmatrix} \sigma_{\parallel} & 0 & 0 \\ 0 & \sigma_P & \sigma_H \\ 0 & -\sigma_H & \sigma_P \end{pmatrix} \quad (10.1)$$

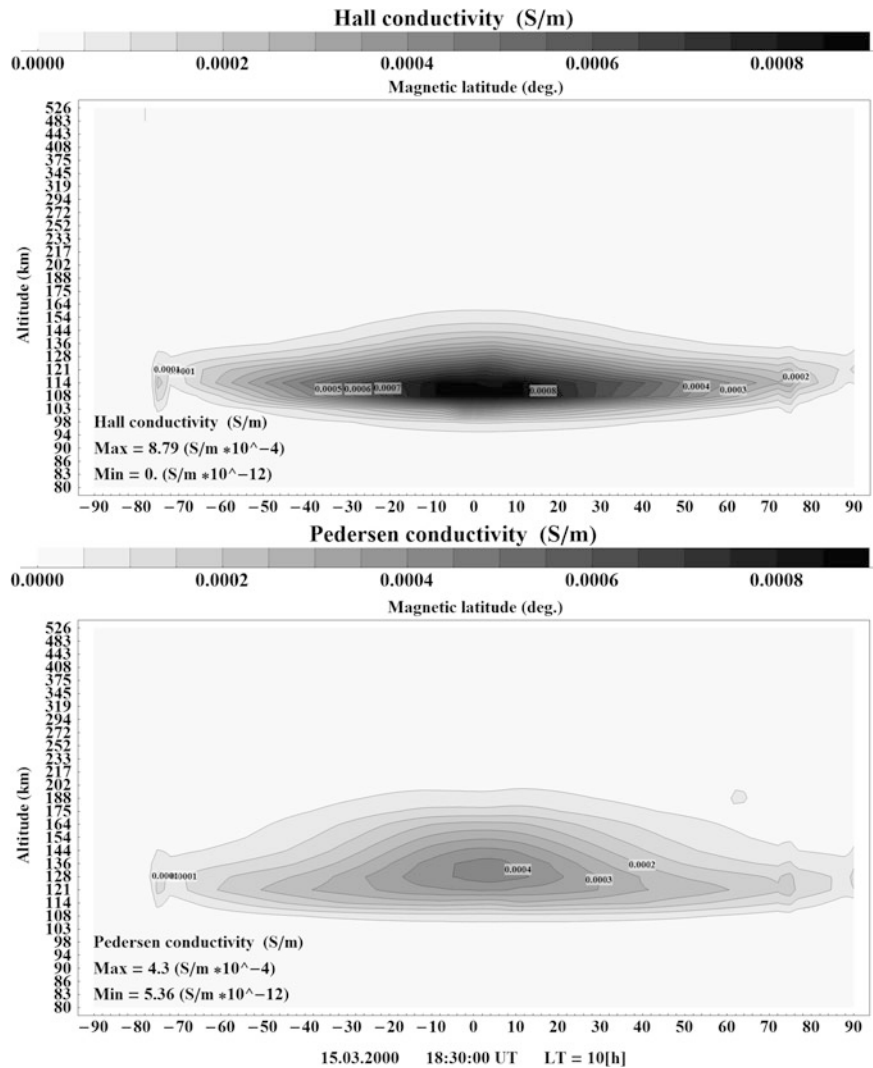


Fig. 10.1 An example of the Hall (upper panel) and Pedersen (bottom panel) conductivity distributions calculated with the UAM-P model. The time moment is 18:30 UT of March 15, 2000. The patterns show a vertical cut along 10 LT in the geomagnetic coordinate system. The contour spacing is 0.00005 S/m. The latitude of the subsolar point is 7.95°

The q -axis is oriented along the geomagnetic field in Formula (10.1). The u and v axes are perpendicular to the magnetic field. The u -axis lays in the magnetic meridional plane while the v -axis is orientated in zonal direction.

Figures 10.1 and 10.2 illustrate the vertical distribution (meridional cut along 10 LT) of the Hall, Pedersen, and parallel to the magnetic field conductivities. The

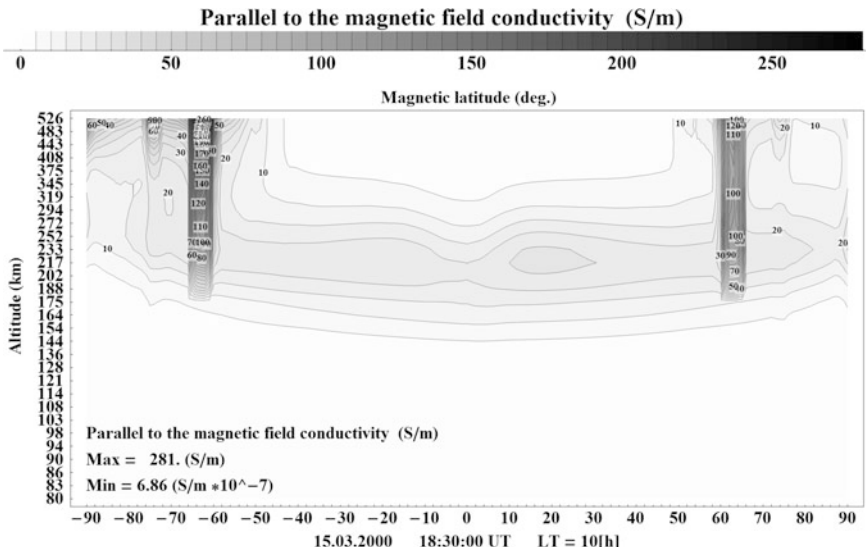


Fig. 10.2 The same as in Fig. 10.1, but for the conductivity distribution parallel to the magnetic field as calculated with the UAM-P model. The time moment is 18:30 UT of March 15, 2000. The patterns show a vertical cut along 10 LT in the geomagnetic coordinate system. The contour spacing is 5 S/m. The latitude of the subsolar point is 7.95°

Hall and Pedersen conductivities are significantly smaller (by several orders of magnitude) than the parallel to the magnetic field conductivity. Due to this feature, the component of the electric field parallel to the magnetic field can be neglected and thus the magnetic field lines can be described as electric equipotential lines.

The Hall conductivity has its maximum near the geomagnetic equator at an altitude of 114 km. The Pedersen conductivity is smaller than the Hall conductivity (approximately in twice) and maximizes also near the equator but at an altitude of 128 km. The equatorial maximum of the Pedersen conductivity is slightly shifted to the Northern Hemisphere. This is a result of the difference in solar EUV ionization fluxes between the hemispheres for the current time moment (18:30:00 UT). The subsolar point is shifted toward the Northern Hemisphere.

The ionospheric currents are driven by the external generators: the magnetospheric generator and the ionospheric generator (thermospheric wind dynamo). The current system satisfies the continuity equation:

$$\begin{aligned} \operatorname{div} \mathbf{j} &= \operatorname{div} (\mathbf{j}_i + \mathbf{j}_m) \\ &= \nabla \cdot [\sigma(-\nabla \phi + \mathbf{V} \times \mathbf{B}) + \mathbf{j}_m] = 0 \end{aligned} \quad (10.2)$$

In Eq. (10.2), σ is the tensor of ionospheric conductivity; \mathbf{j}_i and \mathbf{j}_m are the vectors of ionospheric and magnetospheric current densities, respectively. The ionospheric current density \mathbf{j}_i is the result of the dynamo action of thermospheric winds. The neutral wind dynamo currents are calculated inside the UAM-P model for the

altitudinal range 80–526 km. The magnetospheric current density \mathbf{j}_m is external to the UAM-P model. To define the magnetospheric current system we use optionally various empirical models such as those of Iijima and Potemra (1976) (IPM), Papitashvili and Rich (2002) (PM), or He et al. (2012) (MFACE). These models are incorporated into the UAM-P model. The IPM was used for this study.

The UAM-P model uses the ideal dipole coordinate system for the electric field calculation.

$$\begin{aligned} q &= (R_E/h)^2 \cos \Theta \\ u &= (R_E/h) \sin^2 \Theta \\ v &= \Lambda \\ h_q &= \frac{R_E}{\left(\frac{R_E}{R_E+h}\right)^3 \cdot \sqrt{1 + 3 \cos^2 \theta}} \\ h_u &= \frac{R_E}{\left(\frac{R_E}{R_E+h}\right)^2 \cdot \sin \theta \cdot \sqrt{1 + 3 \cos^2 \theta}} \\ h_v &= \frac{R_E \sin \theta}{\left(\frac{R_E}{R_E+h}\right)} \end{aligned}$$

where u is perpendicular to the vector of the geomagnetic field and variable in the geomagnetic meridional plane, q varies along field lines, and v is perpendicular to u and q . Θ and Λ are the geomagnetic colatitude and longitude, respectively; R_E is the radius of the Earth; and h_q , h_u , and h_v are the Lamé coefficients for the dipole coordinate system.

In the UAM-P model, we assume that the geomagnetic field lines are equipotential. The currents perpendicular to the magnetic field lines are assumed to flow only in the altitudinal range 80–526 km. They are neglected above 526 km, where only FACs are allowed.

Equation (10.2) can be rewritten for the dipole coordinate system in the following way:

$$\operatorname{div} \mathbf{j} = \frac{1}{h_q h_v h_u} \left(\frac{\partial(h_v h_u) j_q}{\partial q} + \frac{\partial(h_q h_u) j_v}{\partial v} + \frac{\partial(h_q h_v) j_u}{\partial u} \right) = 0 \quad (10.3)$$

Using Ohm's law ($\mathbf{j} = \sigma \mathbf{E}$), the ionospheric current components perpendicular to the magnetic field can be written as

$$j_v = \sigma_P E_v + \sigma_H E_u + \mathbf{B} \cdot (\sigma_P v_u - \sigma_H v_v) \quad (10.4)$$

$$j_u = \sigma_P E_u - \sigma_H E_v - \mathbf{B} \cdot (\sigma_H v_u + \sigma_P v_v) \quad (10.5)$$

where σ_H and σ_P are the Hall and Pedersen conductivities; E_v and E_u are the electric field components perpendicular to the magnetic field; v_v and v_u are the components

of the thermospheric wind perpendicular to the magnetic field, respectively; and B is the magnitude of the magnetic field.

The model electric field is a potential field; therefore it can be found as the negative gradient of the electric potential and can be written for the dipole coordinate system as

$$\mathbf{E} = -\frac{1}{h_v} \frac{\partial \phi}{\partial v} \cdot \mathbf{e}_v - \frac{1}{h_u} \frac{\partial \phi}{\partial u} \cdot \mathbf{e}_u \quad (10.6)$$

Equation (10.3) can be presented using Eqs. (10.4)–(10.6) in the following way:

$$\begin{aligned} & \frac{\partial}{\partial v} \left(\frac{h_q h_u}{h_v} \cdot \sigma_P \frac{\partial \phi}{\partial v} \right) + \frac{\partial h_q \sigma_H}{\partial v} \frac{\partial \phi}{\partial u} + \frac{\partial}{\partial u} \left(\frac{h_q h_v}{h_u} \cdot \sigma_P \frac{\partial \phi}{\partial u} \right) - \frac{\partial h_q \sigma_H}{\partial u} \frac{\partial \phi}{\partial v} \\ &= \frac{\partial}{\partial q} (h_v h_u j_q) + \frac{\partial}{\partial v} (h_q h_u (\sigma_P v_u - \sigma_H v_v)) - \frac{\partial}{\partial u} (h_q h_v (\sigma_H v_u + \sigma_P v_v)) \end{aligned} \quad (10.7)$$

The assumption of the equipotentiality of the geomagnetic field lines allows to neglect the electric field and integrate Eq. (10.7) along the magnetic field lines inside the current layer (80–526 km). This equation is integrated up to the upper boundary (526 km) for the field lines going outside of the current layer and up to the apex point (equatorial point) for others. Due to this assumption, the ionospheric current-carrying layer can be described as a 2D distribution. Equation 10.7 can be written for the dipole coordinate system in the following way:

$$\begin{aligned} & \frac{\partial}{\partial u} \left(\int_{q_1}^{q_2} \left(\frac{h_q h_v}{h_u} \cdot \sigma_P \frac{\partial \phi}{\partial u} \right) dq \right) + \int_{q_1}^{q_2} \frac{\partial h_q \sigma_H}{\partial v} \frac{\partial \phi}{\partial u} dq + \frac{\partial}{\partial v} \left(\int_{q_1}^{q_2} \left(\frac{h_q h_u}{h_v} \cdot \sigma_P \frac{\partial \phi}{\partial v} \right) dq \right) \\ & - \int_{q_1}^{q_2} \frac{\partial h_q \sigma_H}{\partial u} \frac{\partial \phi}{\partial v} dq = \epsilon + \psi \end{aligned}$$

or:

$$\frac{\partial}{\partial u} \left(\alpha \frac{\partial \phi}{\partial u} \right) + \gamma \frac{\partial \phi}{\partial u} + \frac{\partial}{\partial v} \left(\beta \frac{\partial \phi}{\partial v} \right) - \delta \frac{\partial \phi}{\partial v} = \epsilon + \psi \quad (10.8)$$

where

$$\alpha = \int_{q_1}^{q_2} \left(\frac{h_q h_v}{h_u} \cdot \sigma_P \right) dq$$

$$\gamma = \frac{\partial}{\partial v} \left(\int_{q_1}^{q_2} h_q \sigma_H dq \right)$$

$$\beta = \int_{q_1}^{q_2} \left(\frac{h_q h_u}{h_v} \cdot \sigma_P \right) dq$$

$$\delta = \frac{\partial}{\partial u} \left(\int_{q_1}^{q_2} h_q \sigma_H dq \right)$$

$$\epsilon = \begin{cases} +h_v h_u j_m, & \theta > \pi/2 \\ -h_v h_u j_m, & \theta < \pi/2 \end{cases}$$

$$\psi = \frac{\partial}{\partial v} \left(\int_{q_1}^{q_2} h_q h_u (\sigma_P v_u - \sigma_H v_v) dq \right)$$

$$-\frac{\partial}{\partial u} \left(\int_{q_1}^{q_2} h_q h_v (\sigma_H v_u + \sigma_P v_v) dq \right)$$

The coefficients ϵ and ψ represent the magnetospheric FACs and the field-aligned current generated by the thermospheric neutral winds, respectively.

The characteristic time for neutral wind variations is much larger compared to the modeling time steps. The relatively slow variation of the neutral wind allows to use the thermospheric wind distribution calculated in the preceding time step. The characteristic time of the neutral wind variation is $\sim 0.5\text{--}1$ h, while the modeling time steps are $\sim 3\text{--}30$ s. In other words, the neutral wind variation is negligibly small compared to the modeling time steps.

The description of a similar numerical scheme as used in the new UAM-P version can be found in Takeda and Maeda (1980), Yu et al. (2003), and Klimenko et al. (2006b).

Similar numerical schemes (with integration along geomagnetic field lines) as used in the new electric field block of the UAM-P model are well known for many years. They were applied in various models as, for example, in the thermosphere ionosphere general circulation model with coupled electrodynamics (TIE GCM) of Richmond et al. (1992), in the theoretical model for the ionospheric electric field at mid- and low latitudes (Yu et al. 2003), and in the GSM TIP (Klimenko et al. 2006b,a, 2007).

The electric field potential distribution from Eq. (10.8) defines the electric potential for each geomagnetic field line. Using the assumption of the equipotentiality of the geomagnetic field lines we obtain the global electric field potential distribution. The electric field can be then calculated using Eq. (10.6). The resulting electric field is used in the other blocks of the UAM-P model.

Figure 10.3 illustrates the electric field potential distribution at the lower boundary of the UAM-P model (80 km) for the specific time moment. The distribution was calculated for a moderate magnetic activity (AE index is 300 nT) with symmetrical FACs for the Southern and Northern Hemispheres. The minima and maxima of the

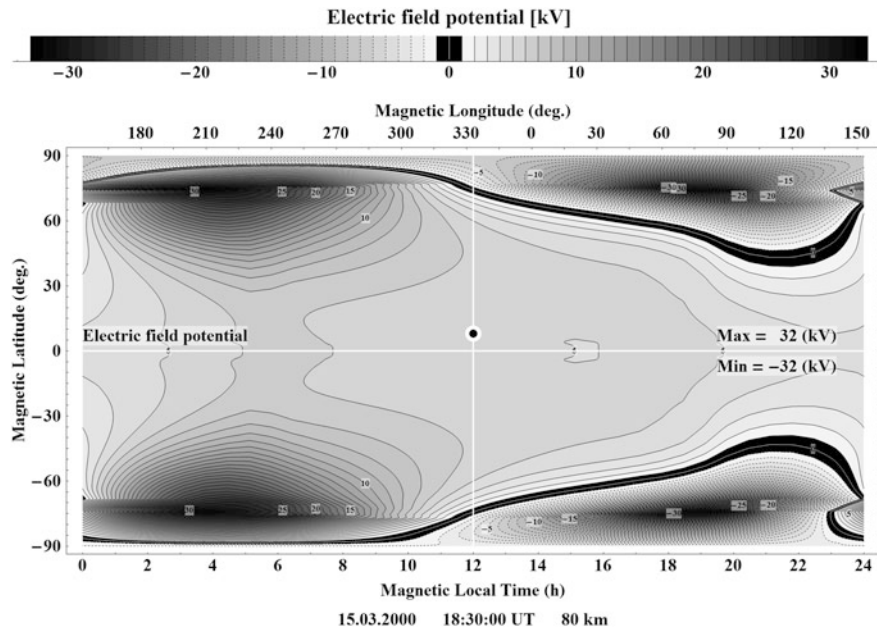


Fig. 10.3 An example of the electric field potential distributions calculated with the UAM-P model. The time moment is 18:30 UT of March 15, 2000. The pattern is presented in the geomagnetic coordinate system. The contour spacing is 1 kV. The position of the subsolar point is shown by the *black dot* at the 12 MLT meridian

electric potential in the polar regions are located in the evening and morning side, respectively. The electric field potential distribution is mirror symmetrical (with respect to the geomagnetic equator) for closed field lines, but has some differences inside the polar caps, where the field lines are open. An eastward electric field is clearly seen on the dayside near the geomagnetic equator. The equatorial electric field is smaller than the high-latitudinal electric field, but nevertheless it plays a significant role in the formation of the equatorial electrojet.

The three-dimensional ionospheric current system can be reconstructed using Eqs. (10.4) and (10.5), if the electric field, conductivity, and thermospheric neutral wind dynamo action are known.

The perpendicular to the magnetic field ionospheric currents is illustrated in Fig. 10.4. The ionospheric currents have their maxima in the altitudinal range 110–130 km, as clearly seen in this figure.

The vertical cut of the v -component (zonal component) of the ionospheric current density is shown at the bottom panel. The positive direction for this component is eastward. The pattern presents the equatorial and polar electrojets, which are positive for this local time (10 LT). Additionally, the negative (westward) currents are visible at middle latitudes with maximum values near 25° and -25° magnetic latitude. These negative currents together with the positive equatorial electrojet are

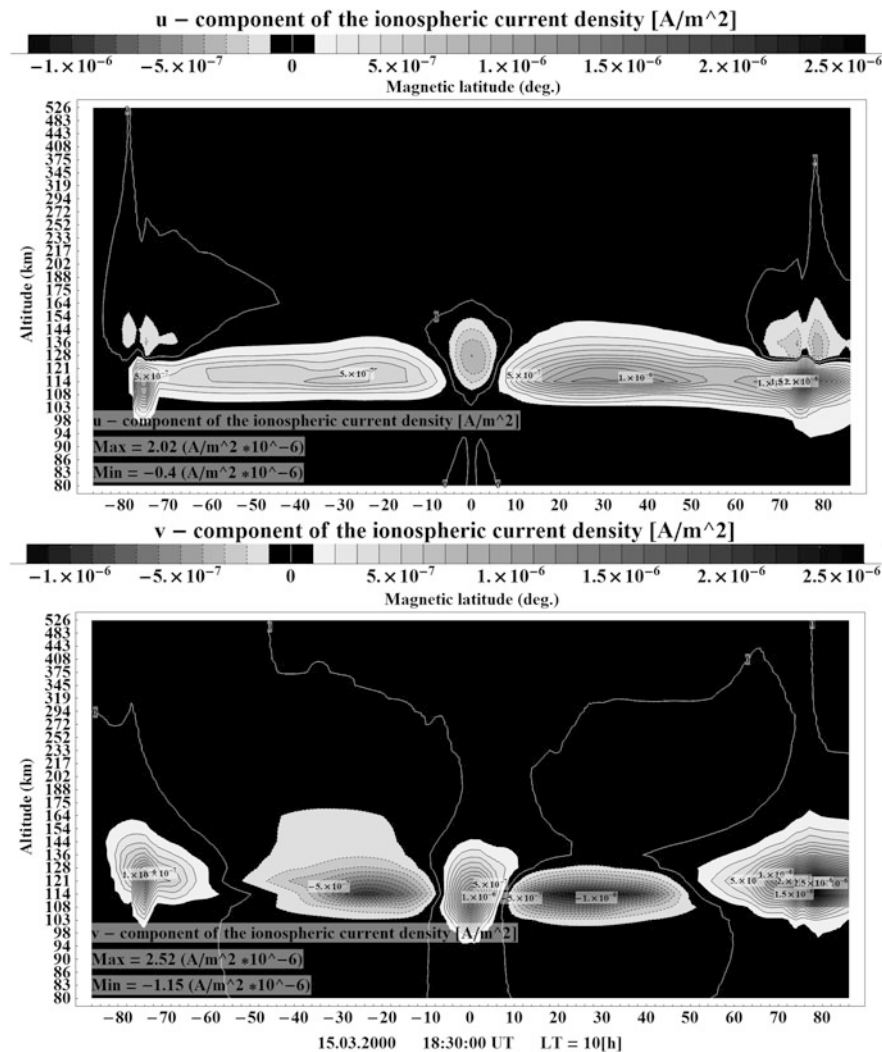


Fig. 10.4 Two components of the ionospheric current density calculated with the UAM-P model. The time moment is 18:30 UT of March 15, 2000. The patterns show a vertical cut along 10 LT in the polar geomagnetic coordinate system. The contour spacing is 10^{-7} A/m^2 . Black area is smaller than $\pm 10^{-7} \text{ A/m}^2$. The latitude of the subsolar point is 7.95°

parts of the so-called Sq current system. The currents are stronger in the Northern Hemisphere due to the higher conductivity.

The upper panel represents the vertical cut of the u -component of the ionospheric current density. This component is perpendicular to the vector of the geomagnetic field and located in the geomagnetic meridional plane. The positive direction for this component is equatorward (at high latitudes), inclined at midlatitudes, and

downward (at the equator). This example shows equatorward currents which are flowing in the Northern and Southern Hemispheres. These currents have maximum values near 30° and -30° magnetic latitude and they are also part of the Sq current system. As in the case of the zonal component, the u -component of the ionospheric current is larger in the Northern Hemisphere (for the time moment shown).

The negative upward current is clearly seen near the equator in Fig. 10.4 (upper panel). This current is the result of the vertical electric field. Such vertical electric field was not resolvable in previous versions of the model.

10.3 Ionospheric Contribution to the Earth's Magnetic Field

For this study we use currents flowing perpendicular to the magnetic field within an altitudinal range of 80–526 km. The currents along the geomagnetic field lines (FACs) should be included to obtain a complete system of the ionospheric currents, but this is the subject for further investigations. They have been shown to be of minor importance for magnetic variations on Earth's surface (Fukushima 1976), but might be important at satellite height.

10.3.1 Basic Physical Equations

The additional magnetic field generated in the ionosphere can be obtained by using the Biot-Savart law, if the current density distribution is known. The ionospheric current system can be represented as a composite of small- volume elements. For each component of the differential volume element it can be written as

$$d\mathbf{B} = \frac{\mu_0}{4\pi} \cdot \frac{I}{r^3} [\mathbf{dl}, \mathbf{r}] \quad (10.9)$$

where $d\mathbf{B}$ is the additional magnetic field generated by one component of the differential current volume element, $I = \mathbf{j} \cdot d\mathbf{s}$ ($d\mathbf{s}$ denotes the cross sections of the differential volume element and \mathbf{j} the corresponding normal components of the current density in that volume element) describes the component of the differential current element with $d\mathbf{l}$ as the directed bin size vector perpendicular to the cross sections, and \mathbf{r} , finally, is the distance vector between the center position of a differential volume element and the observation point. $\mu_0 = 4\pi 10^{-7} \text{ N/A}^2$ is magnetic constant.

The ionospheric current system has a horizontal distribution with maximum values in a relatively narrow area between 100 and 130 km as seen in Fig. 10.4. Therefore, the spherical geomagnetic coordinates (z, θ, λ) (where θ is the colatitude) are better suitable for the presentation of the ionospheric current system. The

currents can be rewritten for spherical coordinates in the following way:

$$j_z = -j_u \cdot \cos I$$

$$j_\theta = j_u \cdot \sin I$$

$$j_\lambda = j_v$$

where I is inclination of the magnetic field:

$$\cos I = \sin \theta / \sqrt{1 + 3 \cos^2 \theta}$$

$$\sin I = 2 \cdot \cos \theta / \sqrt{1 + 3 \cos^2 \theta}$$

Additionally, we assume that the current density vector in the small-volume elements does not change. This assumption allows to divide Eq.(10.9) into three parts and to rewrite them in the following way:

$$d\mathbf{B} = \frac{\mu_0}{4\pi} \cdot \frac{I_z[\mathbf{dl}_z, \mathbf{r}] + I_\theta[\mathbf{dl}_\theta, \mathbf{r}] + I_\lambda[\mathbf{dl}_\lambda, \mathbf{r}]}{r^3} \quad (10.10)$$

where $I_z = j_z \cdot ds_z$, $I_\theta = j_\theta \cdot ds_\theta$, and $I_\lambda = j_\lambda \cdot ds_\lambda$ (ds_z , ds_θ , and ds_λ are the cross sections of the respective differential volume elements) describe the components of the differential current element with \mathbf{dl}_z , \mathbf{dl}_θ , and \mathbf{dl}_λ as the directed bin size vectors perpendicular to the cross sections, and \mathbf{r} as the distance vector between the center position of a differential volume element and the observation point.

From physical point of view, this means that if the distance between the observation point and the center of the volume element (r) is significantly larger than the size of the volume element (dl) then the current volume can be replaced by an ideal current wire. This current wire should be oriented along the original current flow and located at the center of the current volume element. The length vector of this wire is \mathbf{dl} . The current magnitude is $I = \mathbf{j} \cdot \mathbf{ds}$, where j is the current density and ds is the cross section of the current volume element in the direction perpendicular to the current flow component.

The assumption that the size of the volume element is relatively small and the distance between the center of the volume element position and the observation point (r) is significantly larger than the current length (dl) allows to rewrite Eq.(10.10) in this way:

$$\Delta \mathbf{B}_i = \frac{\mu_0}{4\pi} \cdot \frac{I_z[\Delta \mathbf{l}_z, \mathbf{r}] + I_\theta[\Delta \mathbf{l}_\theta, \mathbf{r}] + I_\lambda[\Delta \mathbf{l}_\lambda, \mathbf{r}]}{r^3} \quad (10.11)$$

As a result the additional magnetic field generated by the ionospheric currents can be found as the superposition of the magnetic field generated by each volume element:

$$B = \sum \Delta \mathbf{B}_i$$

10.3.2 Numerical Scheme

The ionospheric current system can be divided into various composites of volume elements. At the same time, one ionospheric current system generates just one unique solution for the additional magnetic field. In other words, the result should not be dependent on the size of the current volume elements.

Our numerical scheme is based on Eq. (10.11), which can be used only if the distance between the center position of the current volume element and the observation point (r) is significantly larger than the bin size (Δl). The size of the volume element is defined by three components: Δl_z , Δl_θ , and Δl_λ . The maximum value of these components is used as bin size (Δl).

As a result, we get one most important parameter of the numerical scheme. This is the ratio between the size of the volume element (bin size Δl) and the distance to the observation point (r). From mathematical point of view, the ratio $r/\Delta l$ should be as large as possible. On the other hand, a large ratio of $r/\Delta l$ leads to an enhancement of the number of volume elements. The number increases as cube of the ratio $r/\Delta l$. Therefore, from practical point of view, the ratio $r/\Delta l$ should be as small as possible.

The optimal ratio $r/\Delta l$ was found in an empirical way. For this purpose, the magnetic field generated by the ionospheric current system was calculated using Eq. (10.11). Here, we use the ionospheric current system in the altitudinal range 80–175 km. The magnetic field was calculated at 350 km along one meridian (220° magnetic longitude) in the latitudinal range from 80°S to 80°N (latitudinal step is 0.5°). The ionospheric current system was represented as composites of volume elements with various bin sizes: here $\Delta\theta = \Delta\phi = \{5.0; 4.0; 3.0; 2.0; 1.8; 1.6; 1.5; 1.4; 1.2; 1.0; 0.9; 0.8; 0.7; 0.6; 0.5; 0.4; 0.3; 0.2\}$ [deg]. The vertical steps are the same for all variants. Here, we use the height levels of the numerical grid scheme. The maximum altitudinal step in the range 80–175 km is ~ 11 km ($\min(\Delta l_z) \approx 16.36$). The minimum distance between the center position of the current volume element and the observation point (r) is in this case 175 km.

Figure 10.5 illustrates that the obtained additional magnetic field significantly depends on the sizes of the volume elements. Therefore, larger sizes of the volume elements (with ratio $r/\Delta l < 2$) cannot be used for the calculation (panels a, b, and c). At the same time, the variants with small sizes of the volume elements (panel d, here with $\Delta\theta = \Delta\phi = 0.5$ or $r/\Delta l \approx 3.97; 0.3$ or $r/\Delta l \approx 5.30$; and 0.2 or $r/\Delta l \approx 7.95$) provide almost identical results. This fact allowed us to conclude that the minimal ratio $r/\Delta l$ should be larger than 3.18.

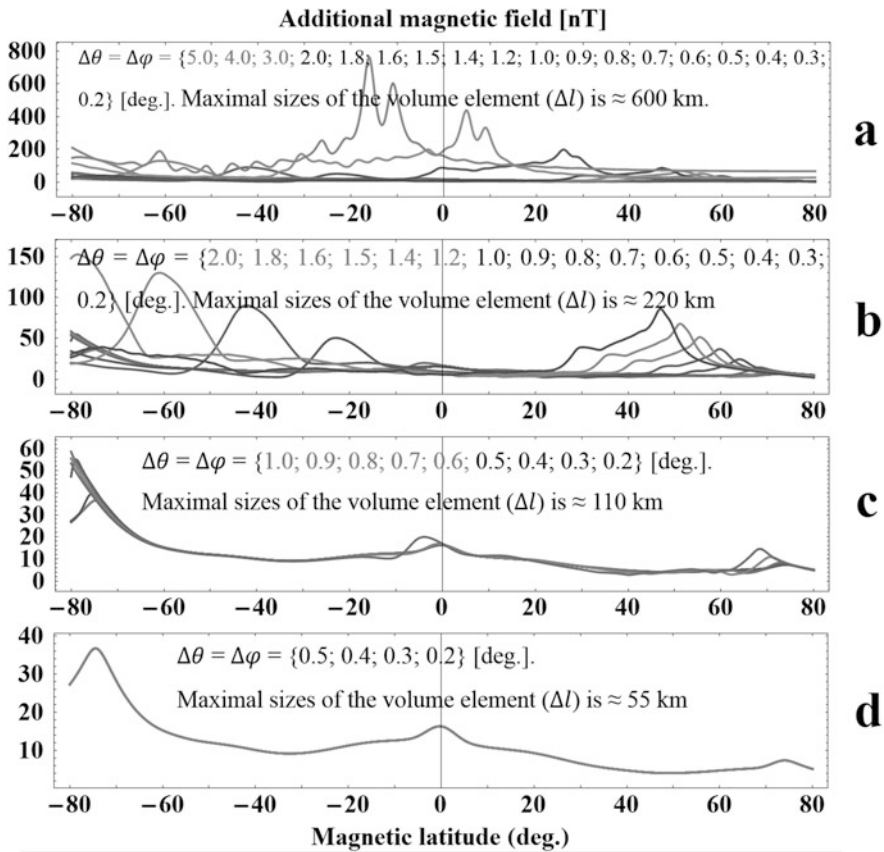
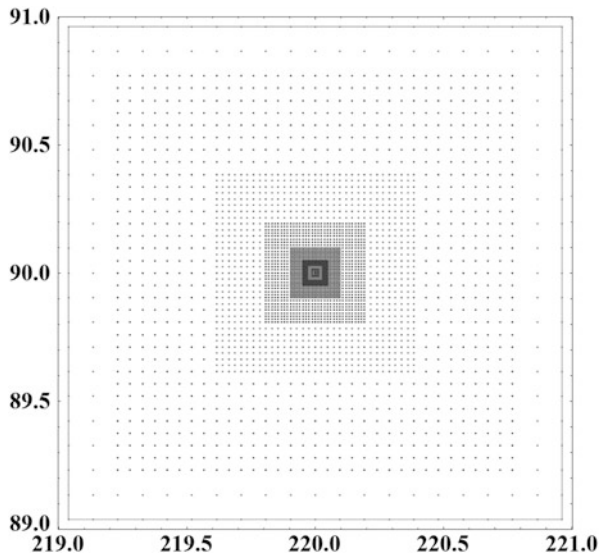


Fig. 10.5 The absolute value of the additional magnetic field generated by the ionospheric current system calculated at 350 km along one meridian (220° magnetic longitude). The magnetic field was calculated using different sizes

For all subsequent additional magnetic field calculations a ratio of $r/\Delta l > 7$ was used. We do this to exclude any dependence on the size of the volume elements.

The information about the minimal ratio $r/\Delta l$ can be used in a practical way. This knowledge allows us to use an irregular space grid instead of a grid with fixed sizes of the volume elements. The irregular grid significantly reduces the number of numerical grid points and keeps all primary information (the UAM-P model calculates currents using an irregular space grid). A smaller amount of grid points provides a higher performance of the calculations. At the same time, the irregular grid allows to reduce the numerical fluctuations, which are growing with an enhancement of the number of grid points. As a result we have a fast, high-resolution method with good numerical precision.

Fig. 10.6 An example of the part of the irregular space grid used for the additional magnetic field calculation at the observation point (220° magnetic longitude, 90° magnetic colatitude)



The irregular numerical grid contains several subregions with different spatial resolution. At the first subregion where the ratio is $r/\Delta l > 7$, we use the original space grid of the ionospheric current system. In the area where the ratio is $r/\Delta l < 7$, we increase the space resolution in two times. As a result we obtain the second inner resolution subregion. For the next grid subregion, we increase the space resolution in two times of the previous subregion grid for the area where the ratio is $r/\Delta l < 7$. We repeat this iterative process if there are points at the subregion grid, which do not fit to the condition (the ratio $r/\Delta l > 7$ if we are outside the current area of 80–526 km).

As a result, we obtain an irregular grid with different resolution subregions. The ratio $r/\Delta l > 7$ is assured for all points of this grid. The subregion with highest resolution is located near the observation point (the point, where we calculate the additional magnetic field generated by the ionospheric current system). Figure 10.6 shows the horizontal part of such an irregular spatial grid.

For the observation point located inside the current layer, we divide the space area into the inner and outer parts. The inner part is the relatively small volume element with its center at the observation point. The outer part is the whole other space. The magnetic field generated by ionospheric currents can be found as a superposition of the magnetic field contributions generated by the inner and outer parts. We use the method described above for the outer part. The additional magnetic field in the geometrical center is zero, with the assumption that the current density is constant or symmetrical with respect to the geometrical center. In our case, the length size of the inner volume element is less than 1 m. Therefore, we can assume that the current density is constant (does not change too much) inside the inner volume element. In other words, the magnetic field in the geometrical center of the inner volume

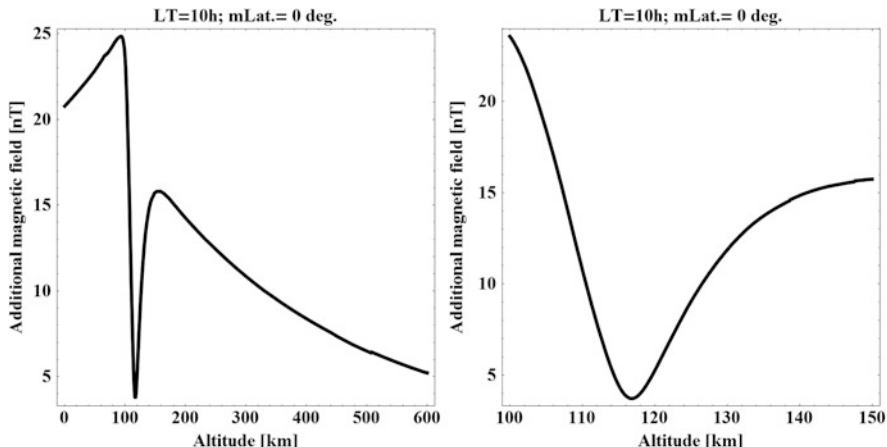


Fig. 10.7 An example of vertical profile of the additional magnetic field calculated for the observation points (10 MLT, 90° magnetic colatitude). The *left panel* represents the additional magnetic field calculated for the altitudinal range 0–600 km; the altitudinal step is 1 km. The *right panel* shows the additional magnetic field calculated for the altitudinal range 100–150 km with an altitudinal step of 0.1 km

element is generated only by the outer currents and the additional magnetic field generated by the inner part can be neglected.

The equatorial electrojet has a maximum value of $\sim 10^{-6} \text{ A/m}^2$ near 10 LT at 114 km. This is clearly seen in Fig. 10.4. On the other hand, the additional magnetic field generated by the ionospheric current system has a minimum value near this altitude. The northward magnetic field generated by the upper part (above 114 km) of the equatorial electrojet is compensated by the southward magnetic field generated by its bottom part (below 114 km). The meridional distribution of the zonal current component is almost symmetrical about the geomagnetic equator. The Northern part of the equatorial electrojet provides a downward magnetic field while the Southern part of the electrojet produces an upward magnetic field. Due to the symmetry, the upward and downward magnetic fields compensate each other. As a result, the additional magnetic field in the vicinity to the maximum of the equatorial electrojet has the minimum value. This is illustrated in Fig. 10.7.

10.3.3 Examples of the Additional Magnetic Field

The global distribution of the additional magnetic field generated by the ionospheric current system obtained with the UAM-P model was calculated using the Biot-Savart law. A few examples are presented below:

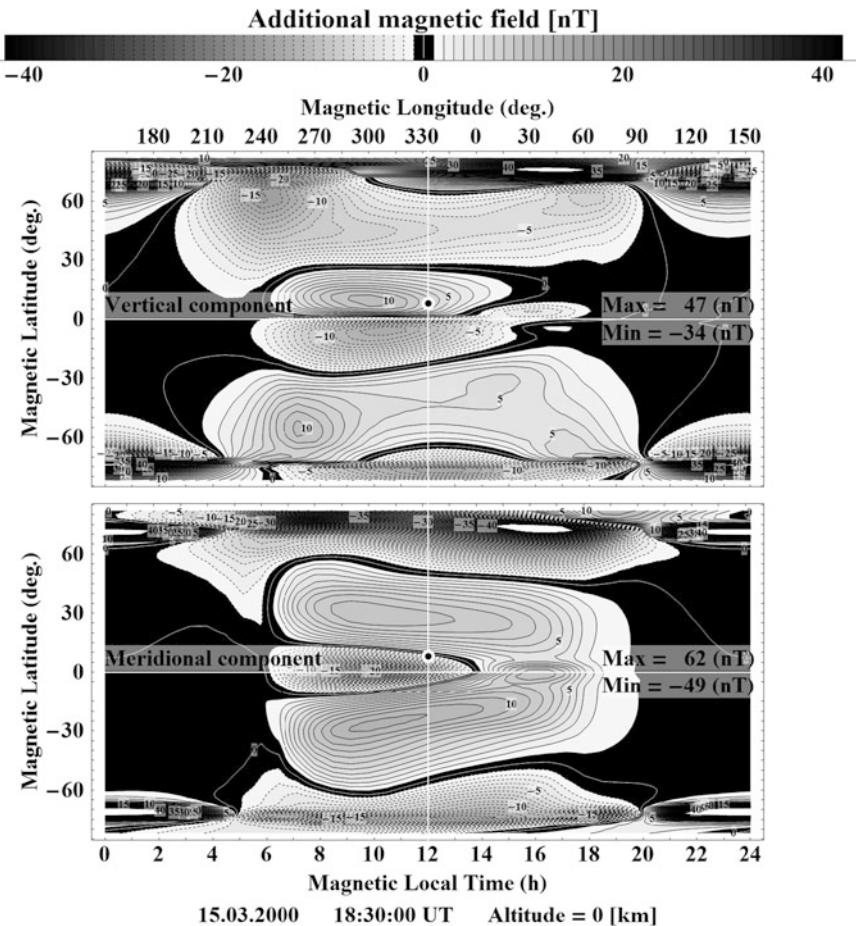


Fig. 10.8 Example of the horizontal distribution of the vertical and meridional components of the additional magnetic field. The contour spacing is 1 nT. Black area is smaller than ± 1 nT. Positive directions are upward and southward, respectively. The patterns are presented in the geomagnetic coordinate system. The position of the subsolar point is shown by the black dot

The horizontal distribution of the additional magnetic field at the ground level (0 km) is shown in Figs. 10.8 and 10.9. These figures illustrate the three components of the magnetic field: the vertical, meridional, and zonal in the geomagnetic coordinate system. Additionally, the bottom panel of Fig. 10.9 presents the absolute value of the additional magnetic field of ionospheric origin.

The effect related to the equatorial electrojet is clearly seen in the meridional component of the additional magnetic field. This component has its maximum value at the geomagnetic equator near the maximum of the electrojet. The vertical component of the additional magnetic field has two maxima at low latitudes. These maxima are partially related to the equatorial electrojet. A similar behavior of the

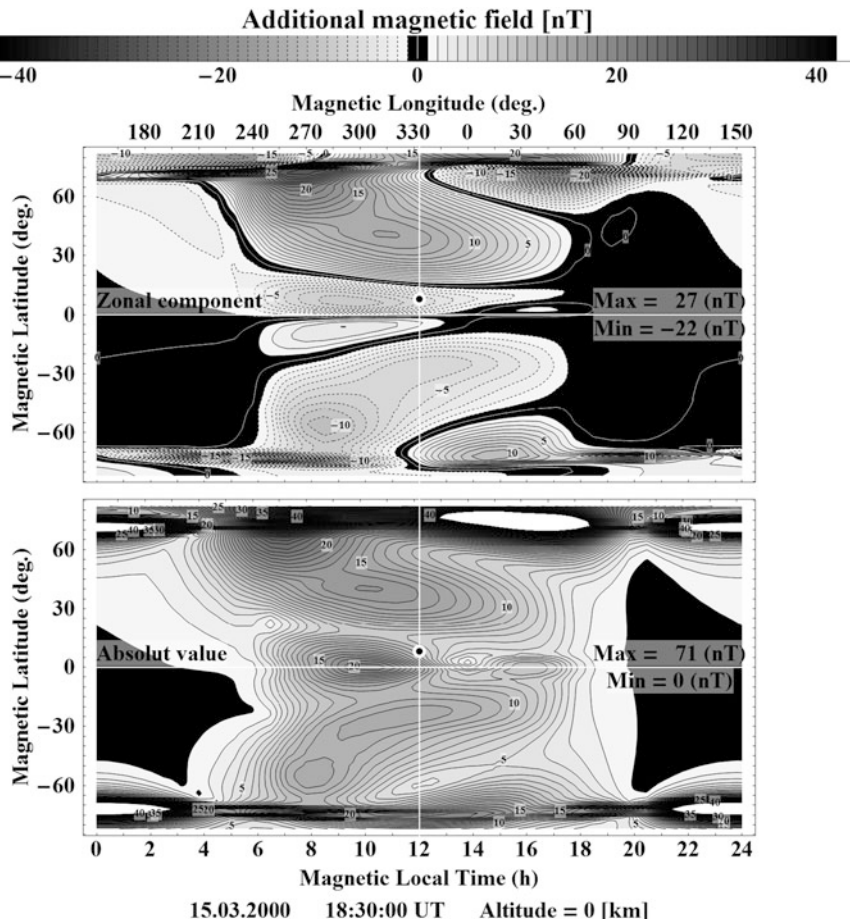


Fig. 10.9 Example of the horizontal distribution of the zonal component of the additional magnetic field (*upper panel*). The *bottom panel* shows the (total) magnitude of the additional magnetic field vector. The contour spacing is 1 nT. Black area is smaller than ± 1 nT. Positive direction is eastward for the *upper panel*. The patterns are presented in the geomagnetic coordinate system. The position of the subsolar point is shown by the black dot

meridional and vertical components of the additional magnetic field takes place in the vicinity to the focuses of the Sq-current system at the middle latitudes ($\pm 30^\circ$) and near the auroral electrojets in the Northern and Southern Hemispheres.

The various maxima of the absolute value of the additional magnetic field (lower panel of Fig. 10.9) are related to the equatorial electrojet at the equatorial area, the focuses of the Sq current system at middle latitudes, and the auroral electrojets at high latitudes.

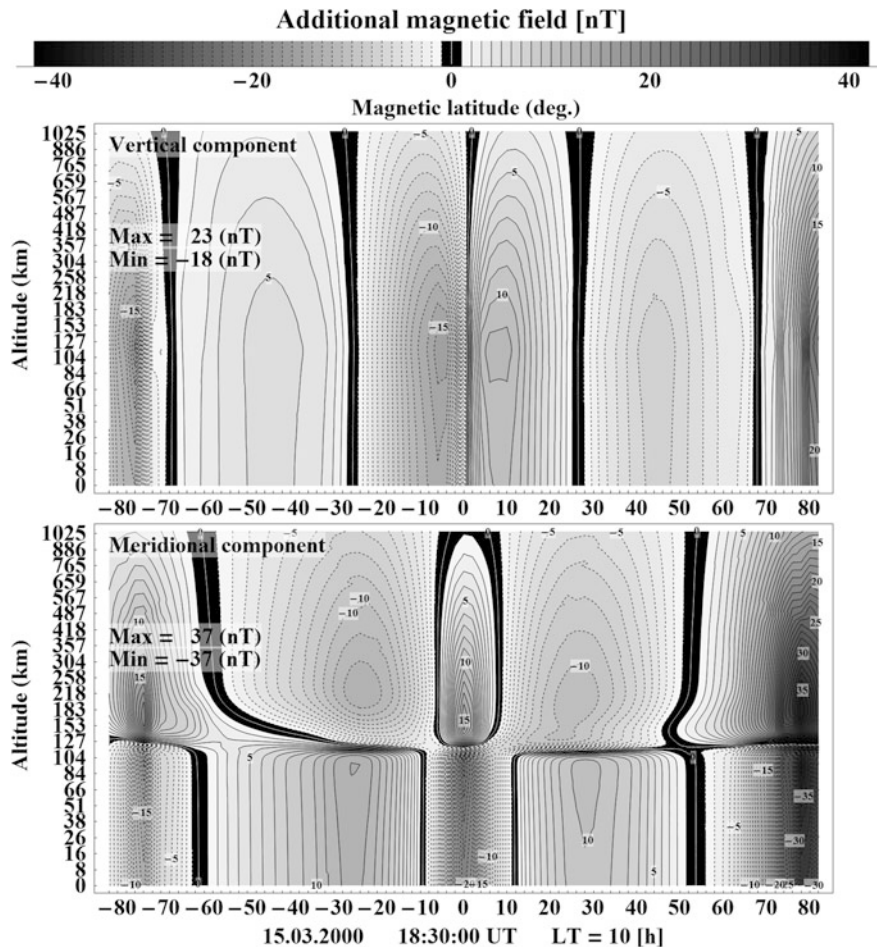


Fig. 10.10 Example of the vertical distribution of the vertical and meridional components of the additional magnetic field. The contour spacing is 1 nT. *Black area* is smaller than ± 1 nT. Positive directions are upward and southward, respectively. The patterns are presented in the geomagnetic coordinate system. The latitude of the subsolar point is 7.95°

Due to an UT effect of the magnetic reference frame, the conductivity in the Northern Hemisphere is better than in the Southern Hemisphere for the particular UT moment (the Northern magnetic pole is tilted toward the sun). Therefore, the current system is stronger in the Northern Hemisphere. As a result, the additional magnetic field in the Northern Hemisphere is larger than in the Southern Hemisphere. This is clearly visible in all components of the additional magnetic field in Figs. 10.8 and 10.9.

The vertical distribution of the additional magnetic field generated by the ionospheric current system is illustrated in Figs. 10.10 and 10.11. The vertical,

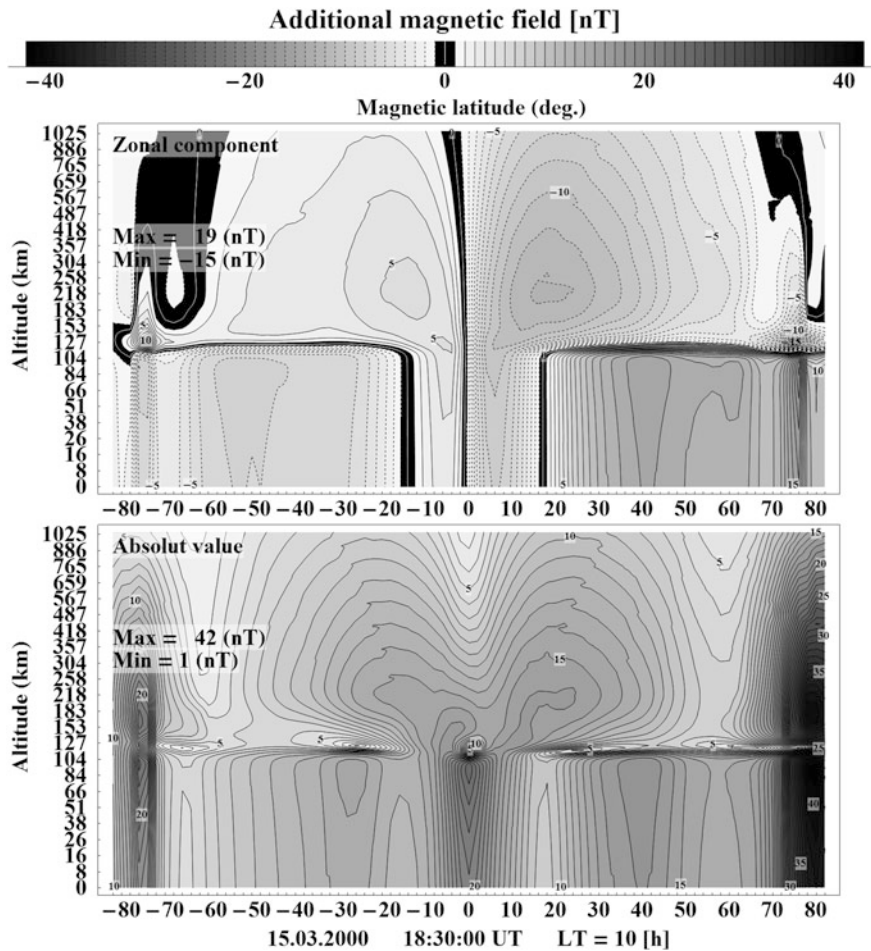


Fig. 10.11 Example of the zonal component of the additional magnetic field (*upper panel*). The *bottom panel* shows the (total) magnitude of the additional magnetic field vector. The contour spacing is 1 nT. Black area is smaller than ± 1 nT. Positive direction is eastward for the *upper panel*. The patterns are presented in the geomagnetic coordinate system. The latitude of the subsolar point is 7.95°

meridional, and zonal components of the additional magnetic field were calculated for the altitudinal range from 0 up to 1025 km. Additionally, the right bottom panel of the figure presents the absolute value of the additional magnetic field of ionospheric origin.

The meridional and zonal components of the additional magnetic field have their minima close to the height range of the maximum values of the ionospheric currents.

This effect is also seen in the vertical distribution of the absolute value of the additional magnetic field (bottom right panel). At the same time, the minimum is embedded into two maximum values of the additional magnetic field just adjacent to the area of the minimum additional magnetic field (see Fig. 10.7).

10.3.4 The Equivalent Current System

The ionospheric current system can be height integrated inside the current layer (80–526) with the assumption that the vertical currents are not significant and can be neglected. This assumption was used for previous UAM model versions for an altitudinal range of 80–175 km. As a result, we obtain a slightly different horizontal distribution of the integrated zonal and meridional component of the ionospheric current system, as shown in Fig. 10.12.

The equatorial and auroral electrojets are clearly seen in the integrated zonal component of the ionospheric current density in Fig. 10.12 as well as the midlatitudinal part of the Sq current system.

The integrated ionospheric current density (equivalent currents) can be used for the calculation of the additional magnetic field. For this purpose, these currents are assumed to be located at 110 km height level. The single layer significantly simplifies the calculation of the additional magnetic field, because we have only a two-dimensional distribution of the two current components (zonal and meridional), instead of the three-dimensional distribution of the full current vector with three components (vertical, zonal, and meridional). The computational effort for this approach is larger by an order of magnitude (memory and run time).

Figures 10.13 and 10.14 show that the additional magnetic field obtained using the equivalent current system reproduces the general structures related to the current distribution. The pattern is similar to the additional magnetic field calculated using the three-dimensional distribution of the currents perpendicular to the magnetic field lines presented in Figs. 10.8 and 10.9. The absolute value of the additional magnetic field has its maxima in the vicinity of the equatorial and auroral electrojets as well as near the focuses of the Sq current system.

The differences for the three components and the magnitude of the additional magnetic field vectors (obtained by using the 3D and equivalent current systems) are shown in Figs. 10.15 and 10.16. The differences amount to a range of –9; 13 nT. These differences are significant in comparison with the magnitude of the absolute values of the additional magnetic field generated by the ionospheric current system. For example, the magnitude variation of the absolute values of the additional magnetic field generated by the dayside Sq current system is 0–20 nT (see Figs. 10.8 and 10.9).

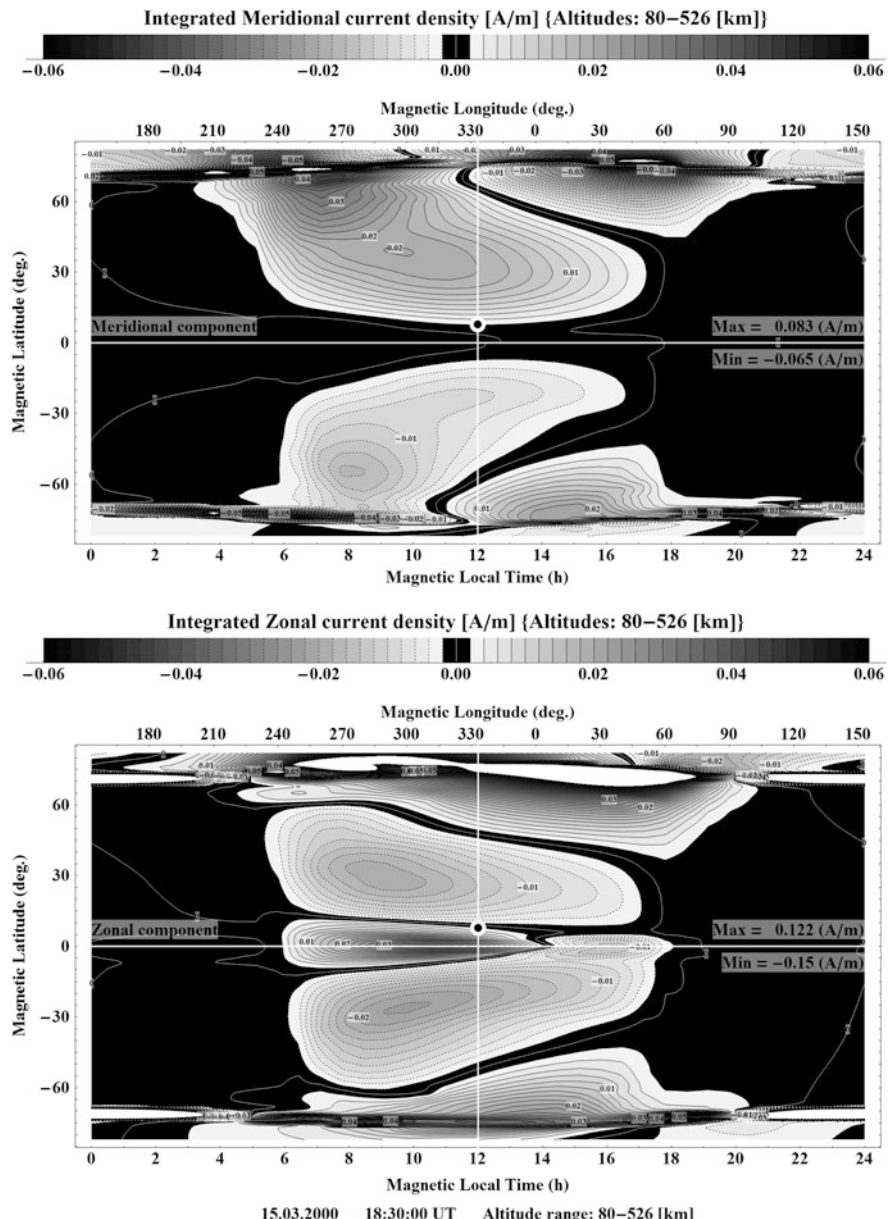


Fig. 10.12 Example of the integrated meridional and zonal components of the ionospheric current density. Positive directions are southward and eastward. The contour spacing is 0.002 A/m. Black area is smaller than ± 0.002 A/m. The patterns are presented in the geomagnetic coordinate system. The position of the subsolar point is shown by the black dot

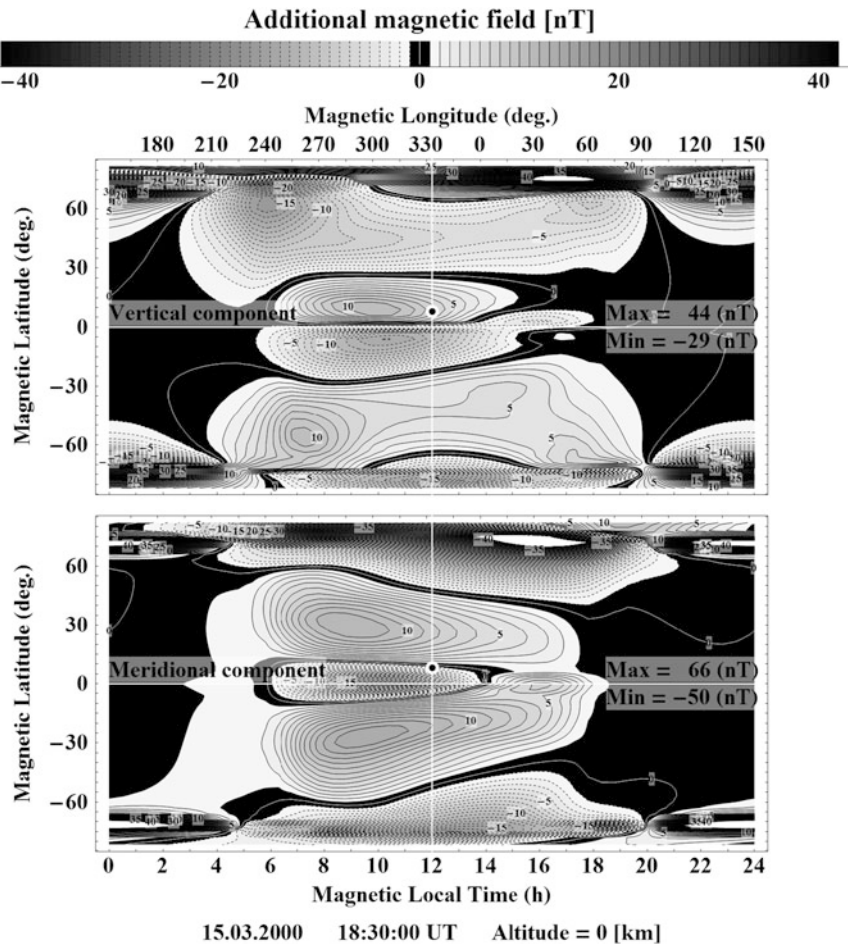


Fig. 10.13 Example of the horizontal distribution of the vertical and meridional and zonal components of the additional magnetic field generated by the equivalent current system located at 110 km. The contour spacing is 1 nT. Black area is smaller than ± 1 nT. Positive directions are upward and southward, respectively. The patterns are presented in the geomagnetic coordinate system. The position of the subsolar point is shown by the black dot

This large difference is due to the assumption of the equivalent currents, which was done during the altitudinal integration of the ionospheric current system. It neglects the vertical current component inside the current layer and its contribution to the additional magnetic field. As a result, the most significant difference is seen in the zonal and meridional components of the additional magnetic field, while for the vertical component the difference is not so significant (less than 0.5 nT) at lower and equatorial latitudes.

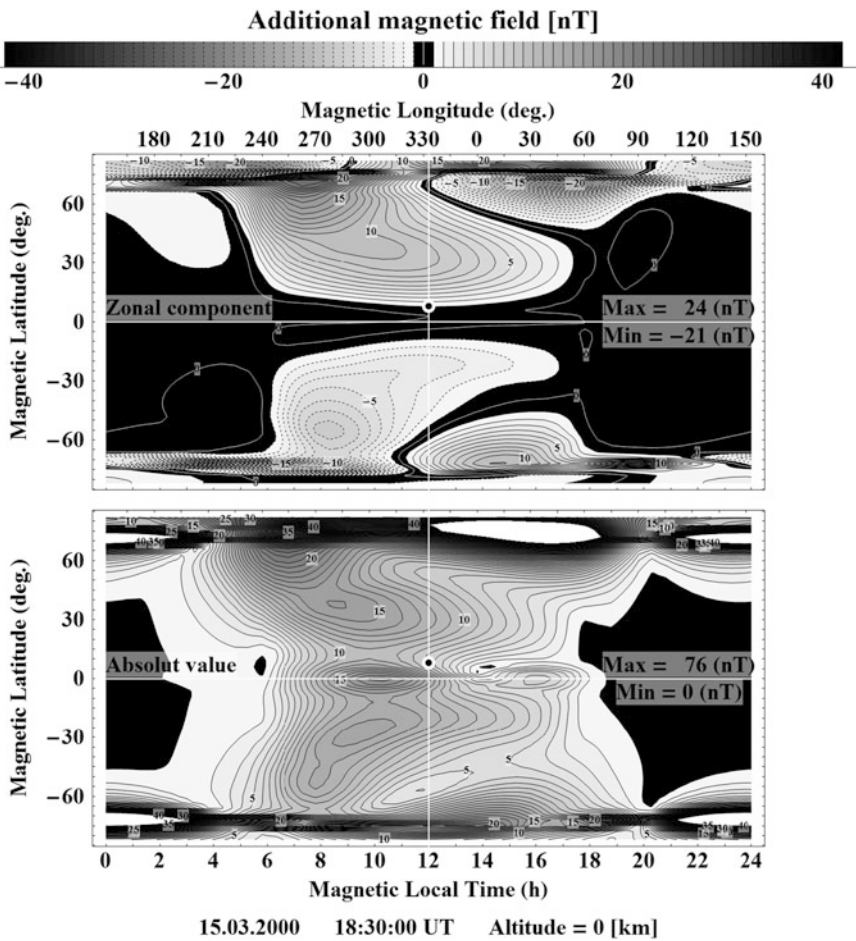


Fig. 10.14 Example of the horizontal distribution of the zonal component (*upper panel*) of the additional magnetic field generated by the equivalent current system located at 110 km. The *bottom panel* shows the (total) magnitude of the additional magnetic field vector. The contour spacing is 1 nT. *Black area* is smaller than ± 1 nT. Positive direction is eastward for the *upper panel*. The patterns are presented in the geomagnetic coordinate system. The position of the subsolar point is shown by the *black dot*

Additionally, the equivalent currents do not represent the altitudinal structure of the ionospheric current system. These aspects justify the use of the full three-dimensional current system for the calculation of the additional magnetic field contributions, although this requires larger computation resources.

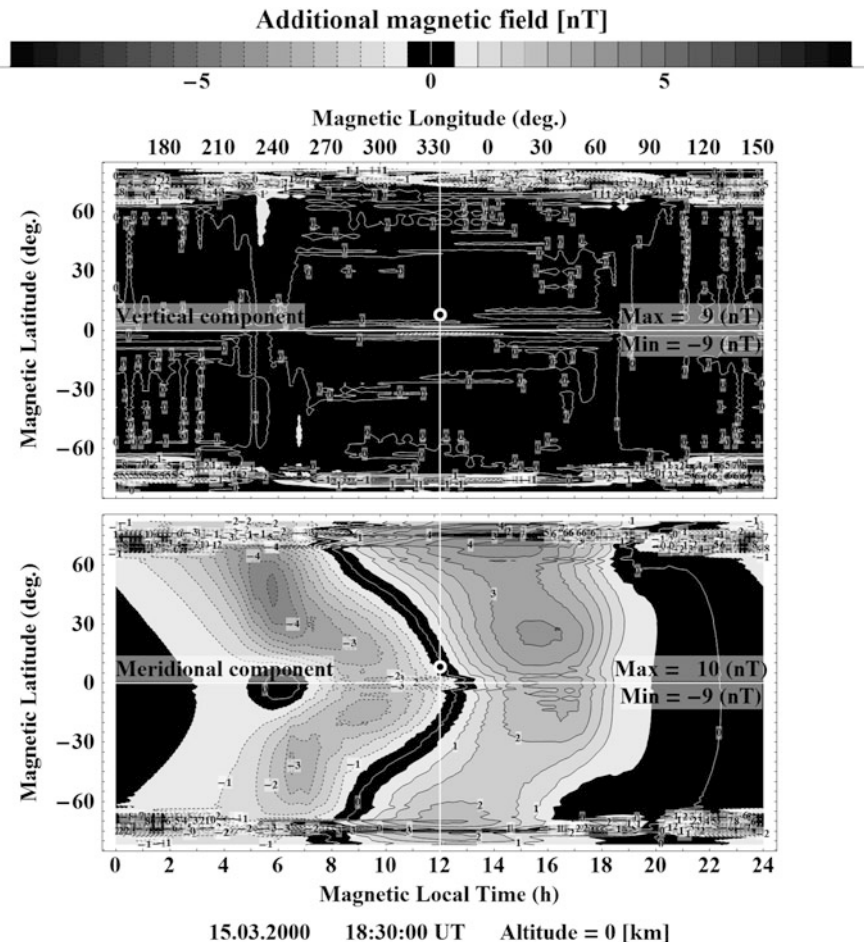


Fig. 10.15 The difference between the values of the vertical and meridional of the additional magnetic field generated by the three-dimensional current density distribution (80–526 km) and equivalent current system located at 110 km. The contour spacing is 0.5 nT. Black area is smaller than ± 0.5 nT. The patterns are presented in the geomagnetic coordinate system. The position of the subsolar point is shown by the black dot

10.4 Conclusions

The UAM-P model reproduces the general global structure of the ionospheric current system of the high-latitude, midlatitude, and near-equatorial areas. The equatorial and auroral electrojets as well as the foci of the Sq current system are clearly seen in Fig. 10.4.

The method described in this study allows calculating the additional magnetic field generated by the ionospheric current system both outside and inside the

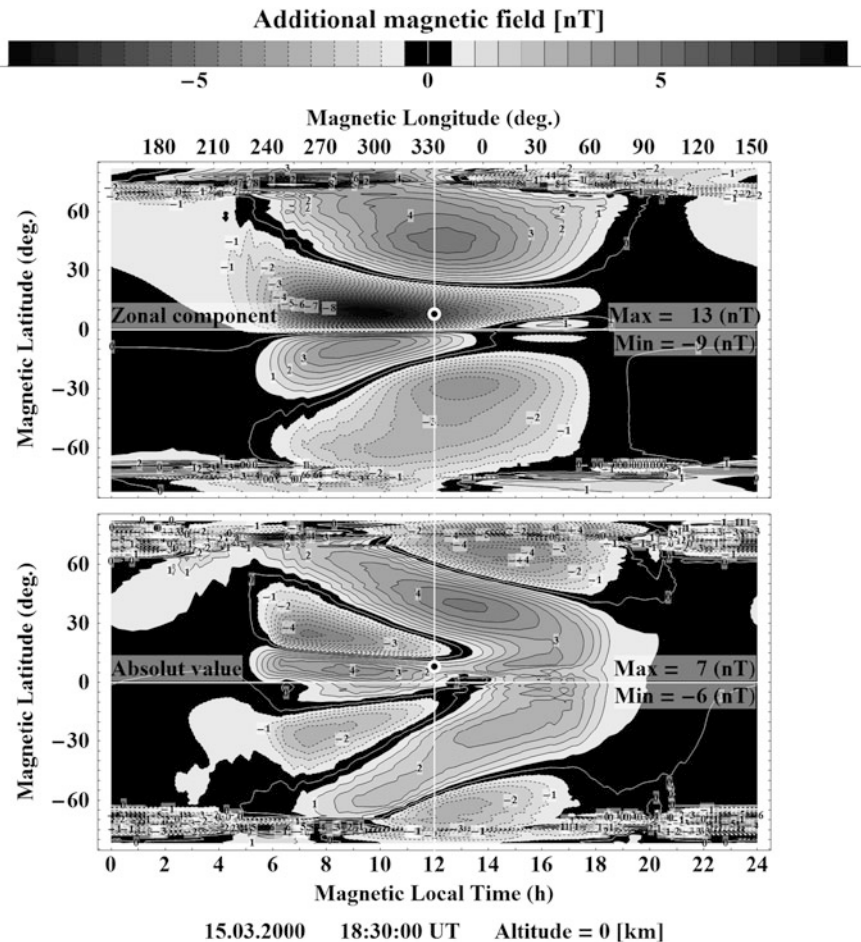


Fig. 10.16 The difference between the values of the zonal components of the additional magnetic field generated by the three-dimensional current density distribution (80–526 km) and equivalent current system located at 110 km. The *bottom panel* shows the difference between the values of the (total) magnitude of the additional magnetic field vectors. The contour spacing is 0.5 nT. *Black area* is smaller than ± 0.5 nT. The patterns are presented in the geomagnetic coordinate system. The position of the subsolar point is shown by the *black dot*

current layer. Additionally, this method takes into account the three-dimensional distribution of the current density with the full altitudinal structure and vertical current densities. As a result using this method together with all information about the ionospheric current density distribution, we obtain a robust solution for the additional magnetic field with high precision.

The method, however, which is based on the assumption of the equivalent currents, does not describe the vertical current structure as well as any information about the altitudinal distribution of the ionospheric current system. As a result, the

additional magnetic field calculated by this method has a poorer precision. These current methods cannot be used for the calculation of the additional magnetic field inside the current layer itself, i.e., in the vicinity of the their altitude (110 km). On the other hand, the equivalent current method allows to improve significantly the computation performance (in comparison with the method based on the three dimensional current system). Therefore, they can be recommended only as a fast (but relatively rough) solution for the additional magnetic field calculation.

The examples of the additional magnetic field were calculated using only the currents which are perpendicular to the geomagnetic field line and located in an altitudinal range from 80 up to 526 km. The FAC system was not included into the additional magnetic field calculation. These currents play a significant role mainly at high latitudes. The inclusion of the FAC system as well as the description of the high-latitude dynamics of the additional magnetic field as well as the comparison of the results with ground measurements and satellite data are topics for further investigations.

Acknowledgements This work was partially supported by Deutsche Forschungsgemeinschaft (DFG).

References

- Bilitza, D.: International reference ionosphere 2000. *Radio Sci.* **36**(2), 261–275 (2001)
- Brunelli, B.E., Namgaladze, A.A.: *Fizika Ionosfery*. Nauka, Moscow (1988). ISBN: 5-02-000716-1 (in Russian)
- Förster, M., Namgaladze, A.A., Yurik, R.Y.: Thermospheric composition changes deduced from geomagnetic storm modeling. *Geophys. Res. Lett.* **26**, 2625–2628 (1999)
- Förster, M., Prokhorov, B.E., Namgaladze, A.A., Holschneider, M.: Numerical modeling of solar wind influences on the dynamics of the high-latitude upper atmosphere. *Adv. Radio Sci.* **10**, 299–312 (2012)
- Fukushima, N.: Generalized theorem for no ground magnetic effect of vertical currents connected with Pedersen currents in the uniform-conductivity ionosphere. *Rep. Ionosph. Space Res. Jap.* **30**(1/2), 35–40 (1976)
- He, M., Vogt, J., Lühr, H., Sorbalo, E., Blagau, A., Le, G., Lu, G.: A high-resolution model of field-aligned currents through empirical orthogonal functions analysis (MFACE). *Geophys. Res. Lett.* **39**, L18105 (2012)
- Hedin, A.E.: Extension of the MSIS thermosphere model into the middle and lower atmosphere. *J. Geophys. Res.* **96**, 1159–1172 (1991)
- Hedin, A.E., Biondi, M.A., Burnsides, R.G., Hernandez, G., Johnson, R.M., Killeen, T.L., Mazaudier, C., Meriwether, J.W., Salah, J.E., Sica, R.J., Smith, R.W., Spencer, N.W., Wickwar, V.B., Virdi, T.S.: Revised global model of thermosphere winds using satellite and ground-based observations. *J. Geophys. Res.* **96**, 7657–7688 (1991)
- Iijima, T., Potemra, T.A.: The amplitude distribution of the field-aligned currents at northern high latitudes observed by TRIAD. *J. Geophys. Res.* **81**, 2165–2174 (1976)
- Klimenko, M.V., Klimenko, V.V., Bryukhanov, V.V.: Numerical simulation of the electric field and zonal current in the Earth's ionosphere: the dynamo field and equatorial electrojet. *Geomagn. Aeron.* (Engl. translation) **46**(4), 457–466 (2006)

- Klimenko, V.V., Klimenko, M.V., Bryukhanov, V.V.: Numerical modeling of the electric field and zonal current in the Earth's ionosphere - statement of the problem and test calculations (in Russian). *Matem. Mod.* **18**(3), 77–92 (2006)
- Klimenko, M.V., Klimenko, V.V., Bryukhanov, V.V.: Numerical modeling of the equatorial electrojet UT-variation on the basis of the model GSM TIP. *Adv. Radio Sci.* **5**, 385–392 (2007)
- Namgaladze, A.A., Korenkov, Yu.N., Klimenko, V.V., Karpov, I.V., Bessarab, F.S., Surotkin, V.A., Glushchenko, T.A., Naumova, N.M.: Global model of the thermosphere-ionosphere-protonosphere system. *Pure Appl. Geophys.* **127**(2/3), 219–254 (1988)
- Namgaladze, A.A., Korenkov, Yu.N., Klimenko, V.V., Karpov, I.V., Bessarab, F.S., Surotkin, V.A., Glushchenko, T.A., Naumova, N.M.: A global numerical model of the thermosphere, ionosphere, and protonosphere of the earth. *Geomagn. Aeron. (Engl. translation)* **30**(4), 515–521 (1990)
- Namgaladze, A.A., Korenkov, Yu.N., Klimenko, V.V., Karpov, I.V., Surotkin, V.A., Naumova, N.M.: Numerical modelling of the thermosphere-ionosphere-protonosphere system. *J. Atmos. Terr. Phys.* **53**, 1113–1124 (1991)
- Namgaladze, A.A., Korenkov, Yu.N., Klimenko, V.V., Karpov, I.V., Bessarab, F.S., Smertin, V.M., Surotkin, V.A.: Numerical modelling of the global coupling processes in the near-earth space environment. In: Baker, D.N., Papitashvili, V.O., Teague, M.J., (eds.) *Proceedings of the 1992 Symposium/5th COSPAR Colloquium*, vol. 5, pp. 807–811. Pergamon Press, Washington (1994)
- Namgaladze, A.A., Martynenko, O.V., Namgaladze, A.N.: Global model of the upper atmosphere with variable latitudinal integration step. *Int. J. Geomagn. Aeron.* **1**(1), 53–58 (1998)
- Namgaladze, A.A., Namgaladze, A.N., Yurik, R.Yu.: Global modeling of the quiet and disturbed upper atmosphere. *Phys. Chem. Earth Part C* **25**(5/6), 533–536 (2000)
- Namgaladze, A.A., Förster, M., Yurik, R.Y.: Analysis of the positive ionospheric response to a moderate geomagnetic storm using a global numerical model. *Ann. Geophys.* **18**, 461–477 (2000)
- Namgaladze, A.A., Förster, M., Prokhorov, B.E., Zolotov, O.V.: Electromagnetic drivers in the upper atmosphere: observations and modeling. *Physics of Earth and Space Environment*, pp. 165–219. Springer, Dordrecht (2013). ISBN: 978-94-007-2913-1 (Print) 978-94-007-2914-8 (online)
- Papitashvili, V.O., Rich, F.J.: High-latitude ionospheric convection models derived from defense meteorological satellite program ion drift observations and parameterized by the interplanetary magnetic field strength and direction. *J. Geophys. Res.* **107**(A8), SIA 17-1–SIA 17-13 (2002)
- Picone, J.M., Hedin, A.E., Drob, D.P., Aikin, A.C.: NRLMSISE-00 empirical model of the atmosphere: statistical comparisons and scientific issues. *J. Geophys. Res.* **107**(A12), 1468 (2002)
- Prokhorov, B.E.: High-latitude coupling processes between thermospheric circulation and solar wind driven magnetospheric currents and plasma convection. PhD thesis, Universität Potsdam, Mathematisch-Naturwissenschaftliche Fakultät, Potsdam, Germany (2016)
- Prokhorov, B.E., Förster, M., He, M., Namgaladze, A.A., Holschneider, M.: Using MFACE as input in the UAM to specify MIT dynamics. *J. Geophys. Res.* **119**(8), 6704–6714 (2014)
- Richmond, A.D., Ridley, E.C., Roble, R.G.: A thermosphere/ionosphere general circulation model with coupled electrodynamics. *Geophys. Res. Lett.* **19**(6), 601–604 (1992)
- Takeda, M., Maeda, H.: Three-dimensional structure of ionospheric currents, I. Currents caused by diurnal tidal winds. *J. Geophys. Res.* **85**(A12), 6895–6899 (1980)
- Volkov, M.A., Namgaladze, A.A.: Models of field-aligned currents needful to simulate the substorm variations of the electric field and other parameters observed by EISCAT. *Ann. Geophys.* **14**(12), 1356–1361 (1996)
- Yu, T., Wan, W., Liu, L.: A theoretical model for ionospheric electric fields at mid- and low-latitudes. *Sci. China Ser. G* **46**(1), 23–32 (2003)

Chapter 11

Climatology of Air Upwelling and Vertical Plasma Flow in the Terrestrial Cusp Region: Seasonal and IMF-Dependent Processes

Guram N. Kervalishvili and Hermann Lühr

Abstract At polar regions a continuous outflow occurs of terrestrial atmosphere into space. Thermodynamic forces are not strong enough to allow air parcels escaping the Earth's gravity field. But due to the partial ionization of the upper atmosphere by the sun's short-wavelength radiation electrodynamic forces can move the charged particles upward along open field lines. Already in the early space age it was recognized that considerable amounts of ionospheric ions populate the magnetosphere. In this chapter, the acceleration mechanisms of the upwelling ions at altitudes of source regions are investigated. For the first time the role of the neutral particles in the thermosphere is also included in the considerations. In our studies we make use of data from the satellites CHAMP (400 km), GRACE (500 km), and DMSP (830 km). Detailed studies are performed to analyze the conditions accompanying the upwelling of neutral and ionized particles. Here we consider average properties of field-aligned currents, thermospheric wind, and electron temperature. Also, the dependences on environmental conditions are tested. Hardly any dependence on seasons emerges either for air upwelling or for ion upflow. An important driver for the processes seems to be magnetic field reconnection between the terrestrial and interplanetary magnetic field (IMF) and with that the orientation of the IMF. Intense flows of precipitating electrons, which are caused by the merging process, play a central role for both kinds of upflow. But further drivers, different for the two species, are needed to facilitate the observed ion and neutral upwelling.

G.N. Kervalishvili (✉)

GFZ German Research Centre for Geosciences, Telegrafenberg, 14473 Potsdam, Germany
e-mail: gmk@gfz-potsdam.de

H. Lühr

Deutsches GeoForschungsZentrum GFZ, 14473 Potsdam, Germany
e-mail: bluehr@gfz-potsdam.de

11.1 Introduction

In the late 1960s, the existence of ionospheric plasma in the magnetosphere was discovered. For explaining that, an outflow of thermal plasma on open field lines was postulated. Axford (1968), and later Banks and Holzer (1968), coined the term “polar wind” for this phenomenon in analogy to the solar wind plasma flow. The spatial separation between the heavy O⁺ ion population and the lighter and hotter electrons is thought to set up a vertical electric field, which moves the ions upward (along the open field lines). This effect is supported further by the divergence of the geomagnetic field and the outward-directed magnetic mirror force. A review about the history of the polar wind theory is given by Lemaire et al. (2007).

As more observations became available, it was realized that the polar wind model was not sufficient. Further acceleration mechanisms had to be considered and also source regions other than the polar cap were identified. Important contributions come from the polar cusp ion fountain (CIF) and the auroral bulk upflow during magnetically active periods (e.g., Wahlgren et al. 1992). Now the more general term “ionospheric upwelling” has become more popular. Pollock et al. (1990) provided a rather comprehensive presentation of the upwelling ion characteristics, as observed by the DE-1 satellite. From their report it can be read that atomic oxygen ions, O⁺, exhibit the highest fluxes, up to $\Phi_0 = 10^{13} \text{ m}^{-2} \text{ s}^{-1}$ at 1000 km altitude. Fluxes of H⁺ are typically an order of magnitude lower. Third in line is He⁺.

Besides the “classical” acceleration mechanisms, other processes have been found to be much more efficient in lifting up the ions. One of them is the transverse heating of ionospheric ions. Due to the locally enhanced plasma pressure, energized ions are pushed into the direction of lower magnetic field strength (upward). The high efficiency of transverse heating by waves has been shown by Miyake et al. (1993). For the generation of these waves, intense small-scale field-aligned currents (FACs) and electric fields play an important role. Such filamentary structures occur preferably in the cusp/cleft region during magnetically disturbed periods. Based on the observations of DE-1, Yau et al. (1988) have integrated the outflow over the whole Northern Hemisphere. The obtained ion flow rates of both H⁺ and O⁺ increase with K_p surpassing rates of 10^{26} ions/s for moderate activity (10^{26} O⁺ ions correspond to 3 kg). Interestingly, they found no dependence of H⁺ outflow on the solar flux level (F10.7). However, later studies (e.g., Engwall et al. 2009; André et al. 2015) report about clear connection between F10.7 and H⁺ outflow. They primarily refer to the cold outflow (see below) from the polar cap. In any case, O⁺ shows a clear dependence on solar activity. It is known that the O⁺-dominated thermosphere expands significantly with the increase in solar flux. This was interpreted as an indication that enhanced F10.7 lifts more O⁺ ions into the height range where the transverse heating becomes increasingly efficient. In spite of active research on atmospheric escape over the past 40 years, several important questions still exist. In a comprehensive review Yau et al. (2007) summarize our present knowledge about polar wind and ion outflow.

In a more recent *Nature Geoscience* paper “Earth’s ionospheric outflow dominated by hidden cold plasma,” Engwall et al. (2009) reported about Cluster

observations that demonstrate the presence of large amounts of very-low-energy ionospheric particles in the magnetosphere, which could not be detected by previous spacecraft. This so far invisible population is dominating the bulk of lost ions, as confirmed recently by André and Cully (2012). Such low-energy ($<10\text{ eV}$) gas has to originate from deep in the thermosphere and must be transported upward without strong heating. In the environment of the collisionless magnetosphere there is no way to cool down the gas again. The previously favored acceleration mechanisms, such as transverse heating together with magnetic mirror force action (e.g., Miyake et al. 1993), do not seem to be appropriate for the cold outflow component.

Motivated by these controversial statements, we have investigated some phenomena that may be related to the root cause of atmospheric escape. Our work focused first on thermospheric upwelling events in the cusp region. Since the initial publication of this phenomenon (Lühr et al. 2004) many research groups have been fascinated by the localized air density peaks observed by the CHAMP satellite and tried to explain them by supporting measurements (e.g., Clemmons et al. 2008; Sadler et al. 2012) or by numerical model simulation (e.g., Demars and Schunk 2007; Crowley et al. 2010). Special processes need to be active during these events to raise parcels of air by several hundred kilometers. We believe that the root cause is the energy released by magnetopause reconnection, which is routed along geomagnetic field lines and enters the upper atmosphere in the cusp region. Carlson et al. (2012) have provided in a recent paper the basic principles why the ionospheric cusp is so responsive to energy input from reconnection on the dayside. Based on different kinds of observations, Lühr and Marker (2013) have tried to identify the chain of processes that leads to the substantial uplift of air and make the cusp to the prominent source region for atmospheric escape. A key issue seems to be a strong heating at altitudes well above the E region ($<200\text{ km}$). This inference could be confirmed by EISCAT measurements showing that a hot ion layer exists in regions where CHAMP observed collocated air density anomalies (Figs. 11.6 and 11.7 of Lühr and Marker 2013). Large fluxes of low-energy ($\sim 50\text{ eV}$) electron precipitation produced a conducting layer at altitudes well above the E-layer. Such beams of soft electrons occur predominantly in the cusp region. They are typically accompanied by intense bursts of small-scale field-aligned currents (FACs) (e.g., Watermann et al. 2009). These intense FACs fuel Joule heating in the elevated layer and heat the ambient gas to high temperatures. The importance of a combined action of FACs with soft electron precipitation for atmospheric upwelling has been confirmed by Deng et al. (2011) based on results obtained with the global ionosphere thermosphere model (GITM).

From hydrostatic considerations it is expected that hot air parcels move upward when the size of the heated region is much larger than the local scale-height. At 200 km altitude, the scale height is about 20 km ; therefore this condition is easily met. In connection with air upwelling in the cusp region vertical winds are expected during a disturbed period. Unfortunately, no such radial wind observations have been published so far. All these processes are able to transport neutral air and plasma up to exospheric heights.

Another feature of the cusp region is the locally elevated electron temperature (e.g., Prölss 2006). This effect is also attributed to the high fluxes of precipitating

electrons. The hot electron gas causes an enhancement of the plasma scale height and consequently pulls cold ionospheric ions by means of ambipolar acceleration up to high altitudes. The combination of all these effects makes the cusp a favorable region for low-energy ion outflow.

In this chapter we present satellite observations of the various quantities that are assumed to contribute to ionospheric upwelling. Based on statistical studies the average properties of mass density anomaly, field-aligned currents, electron temperature, and ion upflow are presented. In a next step we investigate the spatial and temporal relation of air density anomalies in the cusp region with thermospheric wind, FAC distribution, electron temperature maximum, and ion upflow peak by means of a superposed epoch analysis, separately for the different seasons. Finally we try to localize the source region of air upwelling and ion upflow with respect to the topology of FAC regions at auroral latitudes. As expected, this depends on the orientation of the interplanetary magnetic field. The obtained results are interpreted in the context of previous publications and finally conclusions are drawn.

11.2 Data Set and Observations

The data interpreted here are taken from the CHAllenging Minisatellite Payload (CHAMP) satellite, Gravity Recovery And Climate Experiment (GRACE) satellites, and Defense Meteorological Satellite Program (DMSP) measurements. The interplanetary magnetic field (IMF) data (at Earth's orbit) are available at the National Space Science Data Center (NSSDC) of NASA's Goddard Space Flight Center (GSFC). The observations investigated here were continuously sampled by the CHAMP, GRACE, and DMSP satellites in the Northern Hemisphere.

11.2.1 CHAMP Data

CHAMP, a German satellite mission, was launched on 15 July 2000 into a circular, near-polar orbit (87.2° inclination) at 460 km altitude (Reigber et al. 2002), which decayed to about 250 km over the 10-year mission lifetime (19 September 2010). CHAMP had an orbital period of about 94 min and needed a period of about 130 days to cover all local times.

CHAMP thermospheric mass density, ρ^{ch} , can be derived from the Space Triaxial Accelerometer for Research (STAR) measurements with time resolution of 10 s. This time sampling is equivalent to a spatial resolution of about 76 km. The thermospheric density can be derived from the basic equation of acceleration caused by air drag (Doornbos et al. 2010):

$$\rho^{\text{ch}} = \frac{2m}{C_d A_{\text{eff}}} \frac{\mathbf{a} \cdot \mathbf{v}}{v^2}, \quad (11.1)$$

where m is the satellite mass (about 500 kg), C_d is the drag coefficient (with different values for along-track and cross-track directions), A_{eff} is the effective cross-sectional area in ram direction, \mathbf{a} is the measured acceleration (deceleration), v is the total speed of CHAMP, and \mathbf{v} is the velocity unit vector in the ram direction.

CHAMP zonal wind, U_{zon} , can also be derived from the STAR data with time resolution of 10 s. If we approximate the total cross-track wind as a sum of the zonal wind and the co-rotational component and take into account that the acceleration and velocity are aligned, then U_{zon} can be expressed as follows (Liu et al. 2006):

$$U_{\text{zon}} = -\frac{a_y}{a_x} v_x - v_c, \quad (11.2)$$

where x is the satellite along-track component, y is the satellite cross-track component, a_y and a_x are the measured accelerations (decelerations), v_x is approximated by CHAMP's orbital velocity (7.6 km s^{-1}), and v_c is the co-rotation speed of the atmosphere, which can be calculated for each latitude from the Earth's rotation (Doornbos et al. 2010). Note that negative values represent westward and positive eastward zonal wind velocities.

CHAMP electron temperature, T_e , is derived from the planar Langmuir probe (PLP) measurements with a time resolution of 15 s (Rother et al. 2010). This time sampling is equivalent to the spatial resolution of about 115 km. The slope of the Langmuir probe current-voltage characteristic curve is used to obtain the electron temperature values.

CHAMP field-aligned current (FAC) density can be derived from fluxgate magnetometer (FGM) measurements with a time resolution of 1 s (Wang et al. 2005; Rother et al. 2007). This time sampling is equivalent to the spatial resolution of about 7.6 km. The standard approach for estimating FAC densities makes use of the Ampère-Maxwell law, which in case of single-satellite observations, where temporal variations are interpreted as spatial gradients, has the following form: (Lühr et al. 1996):

$$j_z = \frac{1}{\mu_0 v_x} \frac{\Delta B_y}{\Delta t}, \quad (11.3)$$

where μ_0 is the vacuum permeability, v_x is the velocity perpendicular to the current sheet, and B_y is the magnetic component parallel to the current sheet in the projected xy plane. In this study small-scale FAC (SSFAC) and large-scale FAC (LSFAC) will refer to FACs with time resolution of 1 s and 20 s, respectively.

11.2.2 GRACE Data

The twin GRACE A and B satellites (flying about 220 kilometers behind each other), a joint mission of NASA and DLR (German Aerospace Center), were launched on 17 March 2002 into a near-circular orbit (89.5° inclination) at an altitude around 500 km (Tapley et al. 2004). In this study we consider GRACE A satellite

measurements. GRACE has an orbital period of about 95 min and needs a period of about 160 days to cover all local times.

GRACE thermospheric mass density, ρ^{gr} , can be derived from the Super STAR accelerator measurements with time resolution of 10 s. This time sampling is equivalent to the spatial resolution of about 75 km. The thermospheric density determination method is the same as for CHAMP (Sect. 11.2.1). More information with a detailed description of algorithms can be found in Doornbos et al. (2010).

11.2.3 DMSP Data

The DMSP F13 and F15 satellites, a mission of the US Department of Defense, were launched on 24 March 1995 and on 12 December 1999, respectively, into a circular, sun-synchronous orbit (98° inclination) at an altitude around 850 km. DMSP F13 had an orbital period of about 102 min and fixed local time orientation 17:11–05:11 h (it exploded in orbit on 3 February 2015). DMSP F15 has an orbital period of about 102 min and fixed local time orientation 21:10–09:10 h.

DMSP F13 and F15 ion vertical flows, V_z^{F13} and V_z^{F15} , respectively, are derived from the ion drift meter (IDM) measurements (Rich and Hairston 1994). The IDM is a part of special sensor ion and electron scintillation monitor (SSIES) instrument package.

DMSP F13 and F15 plasma density data, N_i^{F13} and N_i^{F15} , respectively, come from the scintillation meter measurements. Both the ion vertical velocity and the plasma density are provided with time resolution of 4 s at the DMSP SSIES data distribution webpage by the Center for Space Sciences at the University of Texas at Dallas: <http://cindispace.utdallas.edu/DMSP/>. The 4 s time sampling is equivalent to a spatial resolution of about 30 km considering the DMSP orbital velocity of 7.45 km s^{-1} .

Along with the data measured by DMSP satellites, we also use a new variable, the vertical plasma flow. This new variable, $V_z N_i$, plasma density times ion vertical velocity, has the following dimension $10^6 \text{ m}^{-2} \text{ s}^{-1}$ taking into account that the values of V_z and N_i are m s^{-1} and 10^6 m^{-3} , respectively.

11.2.4 IMF Data

The high-resolution IMF data propagated from the measurement at the Lagrange point, L1, to the Earth's bow shock can be obtained from NASA/GSFC's OMNI online data set using the NSSDC OMNIWeb (King and Papitashvili 2005). To examine the dependence on the IMF total magnetic field, B_t , and B_x , B_y , and B_z components for any epoch of satellite observation, we use the 1 min resolution data downloaded from the OMNIWeb (http://omniweb.gsfc.nasa.gov/form/omni_min.html) for the period 2000–2010. The direction of all IMF components is described in geocentric solar magnetospheric (GSM) coordinates.

11.3 Data Selection and Processing Approach

To investigate the influence of seasonal variations the available data are subdivided into three Lloyd seasons of about 130 days each, which are defined as follows: local winter ($1\text{ January} \pm 65\text{ days}$), combined equinoxes ($1\text{ April} \pm 32\text{ days}$ and $1\text{ October} \pm 32\text{ days}$), and local summer ($1\text{ July} \pm 65\text{ days}$). A period of 130 days corresponds to the time needed by CHAMP to pass through all local times. Figure 11.1 shows as an example three Lloyd seasons for the year 2003 in the Northern Hemisphere. The local winter is centered at 1 January 2004 in order to avoid combination of largely separated parts from the beginning and the end of the same year with quite different geomagnetic and solar conditions.

11.3.1 Electron Temperature and Zonal Wind Velocity

The electron temperature, T_e , and zonal wind velocity, U_{zon} , data obtained from CHAMP satellite measurements are used as provided by data centers (see Kervalishvili and Lühr 2013, 2014).

11.3.2 Thermospheric Density

The relative density variations are an appropriate way to characterize the high-latitude thermospheric density anomalies measured by CHAMP (Rentz and Lühr 2008). This quantity is less dependent on solar EUV flux level and sampling heights (e.g., CHAMP's orbit decayed from 460 to 320 km during 8 years) and gives us the

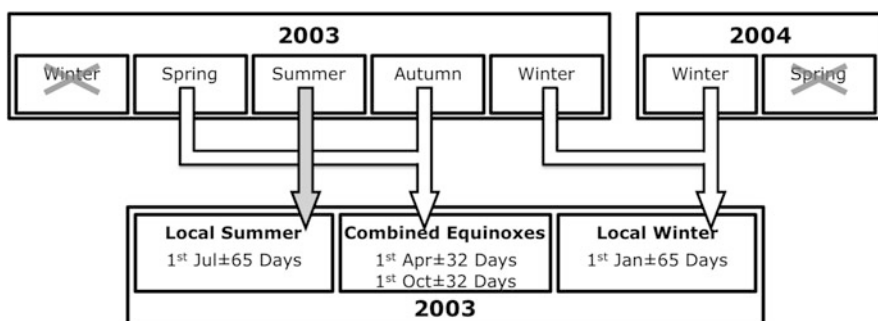


Fig. 11.1 Three Lloyd seasons of 130 days each as an example are shown for the year 2003 in the Northern Hemisphere: local winter ($1\text{ January} \pm 65\text{ days}$), combined equinoxes ($1\text{ April} \pm 32\text{ days}$ and $1\text{ October} \pm 32\text{ days}$), and local summer ($1\text{ July} \pm 65\text{ days}$). Modified after Fig. 2 from Kervalishvili and Lühr (2013)

possibility to compare CHAMP and GRACE measurements at different altitudes. Here, we use the definition of relative density enhancement, ρ_{rel} (this definition is applicable for both CHAMP and GRACE satellites), as defined by Kervalishvili and Lühr (2013):

$$\rho_{\text{rel}} = \frac{\rho}{\rho_{\text{background}}} = \frac{\rho}{\rho_{\text{msis}} + \rho_{\text{bias}}}, \quad (11.4)$$

where ρ is the density derived from CHAMP (GRACE) measurements according to Eq. (11.1) and the background density, $\rho_{\text{background}}$, is defined as a sum of two parts, ρ_{msis} and ρ_{bias} . Here ρ_{msis} is the NRLMSISE-00 (Naval Research Laboratory Mass Spectrometer and Incoherent Scatter) model density and ρ_{bias} is a linear bias function determined from the systematic differences between observed and model density for every CHAMP (GRACE) polar pass. More details about the bias function determination can be found in section 3.1 of Kervalishvili and Lühr (2013).

11.3.3 Field-Aligned Current

Small-scale and large-scale field-aligned currents are the dominant energy and momentum transfer mechanism from the magnetosphere to the high-latitude ionosphere-thermosphere region. It was shown by many authors that thermospheric density enhancements in the cusp region are accompanied by small-scale FACs (SSFACs) during geomagnetically quiet (e.g., Lühr et al. 2004) and active periods (e.g., Liu et al. 2010) and during both periods (Kervalishvili and Lühr 2013, 2014). The filamentary structure of the SSFACs with rapidly varying directions between negative and positive values does not allow to present their intensity or spatial pattern. Therefore, we use the root mean square (RMS) values of the SSFACs to express their intensity (Kervalishvili and Lühr 2013). The large-scale FACs (LSFACs) are used to represent the spatial pattern of FACs. LSFACs are derived from FAC data by using a low-pass filter with a 3 dB cutoff period of 40 s. This time sampling is equivalent to a spatial wavelength of about 300 km.

11.3.4 Vertical Ion Flow

The vertical plasma velocity data of DMSP satellites come with an IDM quality flag from 1 to 4, referring from good to undetermined, respectively. Here we used data only with highest quality flag 1. The vertical velocity, V_z^{F13} , and plasma density, N_i^{F13} and N_i^{F15} , data obtained from DMSP measurements are used as provided. However, as it was shown by Hartman and Heelis (2007) the vertical velocity values from the DMSP F15 satellite have a bias, which was estimated in the equatorial region. This uncertainty was varying between 70 and 140 m s⁻¹. Similar results were shown

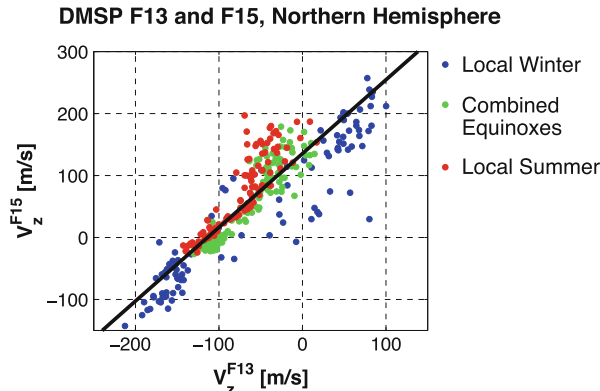


Fig. 11.2 Correlation analysis results between plasma velocity readings of two DMSP satellites, F13 and F15, in the northern high-latitude region. The *black line* denotes the regression relationship derived from data set, which includes all local seasons. Correlation coefficient is equal to 0.93

by Kervalishvili and Lühr (2013), but in the high-latitude region. To overcome this uncertainty in the northern cusp region Kervalishvili and Lühr (2013) have rescaled DMSP F15 velocity values with respect to DMSP F13 using a linear relationship:

$$V_z^{\text{F15}^{\text{new}}} = 0.84 V_z^{\text{F15}^{\text{old}}} - 113.7 \text{ [m s}^{-1}\text{].} \quad (11.5)$$

This is derived from a comparison of collocated measurements and confirmed by a correlation coefficient equal to 0.93. Figure 11.2 shows the overlapping median values of bin-averaged F13 and F15 satellite readings on which the analysis is based. More details about this procedure can be found in Kervalishvili and Lühr (2013). These rescaled $V_z^{\text{F15}^{\text{new}}}$ values will be used in our paper.

11.4 Statistical Properties of Observations

In this section, we present and interpret the spatial distribution and correlation analysis results to study the various relationships between the quantities discussed earlier in Sect. 11.2. Our results are presented in magnetic latitude (MLat) and magnetic local time (MLT) coordinates, which are based on the quasi-dipole coordinate system as described by Emmert et al. (2010).

The high-latitude spatial distributions are presented in MLat versus MLT coordinate frames as dial plots (Fig. 11.3). These dial plots are based on a binning procedure similar to the one used by Lühr et al. (2007) and Kervalishvili and Lühr (2013), which covers the high latitudes ($\text{MLat} > 49^\circ$) and all 24 h of MLT. The polar region is divided into N concentric rings, 2° wide in MLat and centered on the geomagnetic pole, where $N \geq 1$. The innermost ring, $N = 1$, is the closest

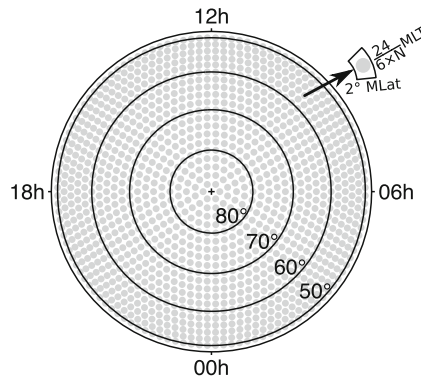


Fig. 11.3 Schematic illustration of the dial plot example. The high-latitude regions are divided into concentric rings 2° wide in MLat; rings are further subdivided into $6 \times N$ equal-area MLT sectors, where $N \geq 1$. $N = 1$ corresponds to the innermost (closest to the geomagnetic pole) concentric ring, where $89^\circ \geq \text{MLat} > 87^\circ$

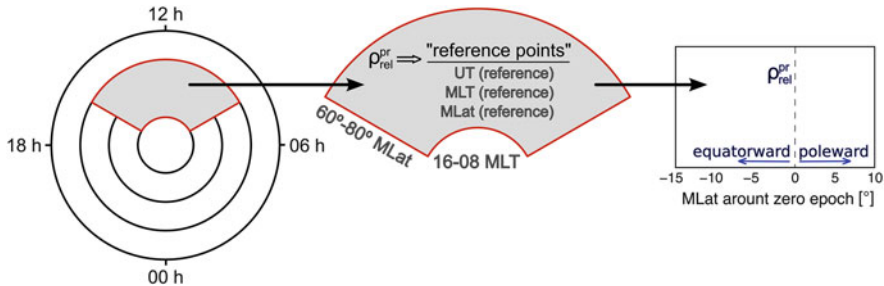


Fig. 11.4 Schematic illustration of the SEA method applied for example to the relative density enhancement, $\rho_{\text{rel}}^{\text{pr}}$, in the high-latitude region. The poleward (positive MLat) and equatorward (negative MLat) directions with respect to zero epoch are also shown

concentric ring to the geomagnetic pole reaching from 87° to 89° MLat. Each of these concentric rings are further subdivided into equal-area MLT sectors with an area of about 220×232 km. As we can see from Fig. 11.3, each N th ring consists of $6 \times N$ MLT sectors.

In order to investigate the internal relationship among the various presented quantities a superposed epoch analysis (SEA) is performed. SEA is centered on phenomena to be investigated (at so-called zero epoch). Afterwards these centered profiles are stacked together along some coordinate, e.g., MLT or MLat. Figure 11.4 shows the schematic illustration of the SEA method in the high-latitude region, where the relative density enhancement, $\rho_{\text{rel}}^{\text{pr}}$, distribution along MLat is used as an example. In the given example time and location of the relative density enhancement define the “reference time” (zero epoch) and “reference latitude” (zero epoch latitude) if the density anomaly falls into the window confined to 8:00–16:00 MLT and 60° – 80° MLat. In this example (right part of Fig. 11.4), the positive and negative

MLat define the poleward and equatorward directions, respectively, with respect to zero epoch. More details about the SEA method can be found in Kervalishvili and Lühr (2013).

11.4.1 Cusp Density Anomalies in CHAMP and GRACE Observations

Figure 11.5 shows the bin-averaged median values of relative density anomaly for CHAMP (Fig. 11.5a) and GRACE (Fig. 11.5b) satellites, $\rho_{\text{rel}}^{\text{ch}}$ and $\rho_{\text{rel}}^{\text{gr}}$, respectively. Data used here cover 5 years (March 2002–March 2007) of CHAMP and GRACE satellite observations. In order to improve visual clarity of comparison GRACE observations were plotted using the same maximum and minimum scale values as for CHAMP (the maximum value of $\rho_{\text{rel}}^{\text{gr}}$ is about 1.12). The distributions of the relative density enhancements are shown for the three Lloyd seasons: local winter, combined equinoxes, and local summer from left to right, respectively. First what we can observe from these figures is that the density anomalies are more pronounced at higher altitudes. Table 11.1 shows the sample number distributions for different levels of relative density enhancements for both satellites and changes of these numbers in percent. The value of 1.2 represents the balance of prominent density enhancements between the two altitudes (Kervalishvili and Lühr 2013). The number of anomaly events practically doubles at higher altitudes for the threshold values above 1.4 (Table 11.1). This can be observed especially clear in the midnight/premidnight region around 60–70° MLat.

The following conclusions are true for both the CHAMP (Fig. 11.5a) and GRACE (Fig. 11.5b) observations, but we should keep in mind that in the GRACE case density enhancements are more pronounced. The cusp-related density enhancement peaks show no significant seasonal dependence, but the locations of the density anomalies tend to expand equatorward from winter to summer. The confined dayside cusp pattern of the anomaly locations has a width of about 4 h in local time centered at 12:00 MLT, and it is clearly visible for all local seasons. There are also secondary maximum peaks in the midnight/premidnight time sector at about 70° MLat. The amplitude values of these peaks show seasonal dependence with decreasing intensities towards local summer. These secondary enhancements are related to the substorm process (Liu et al. 2005; Ritter et al. 2010). Magnetic activity is known to minimize around June solstice. Interestingly, there are also prominent density depletions, which are clearly visible in the dawn sector and at all Lloyd seasons. On the other hand, the depletions observed on the dusk side have a seasonal dependence: depletions in summer and combined equinoxes, and enhancements in winter.

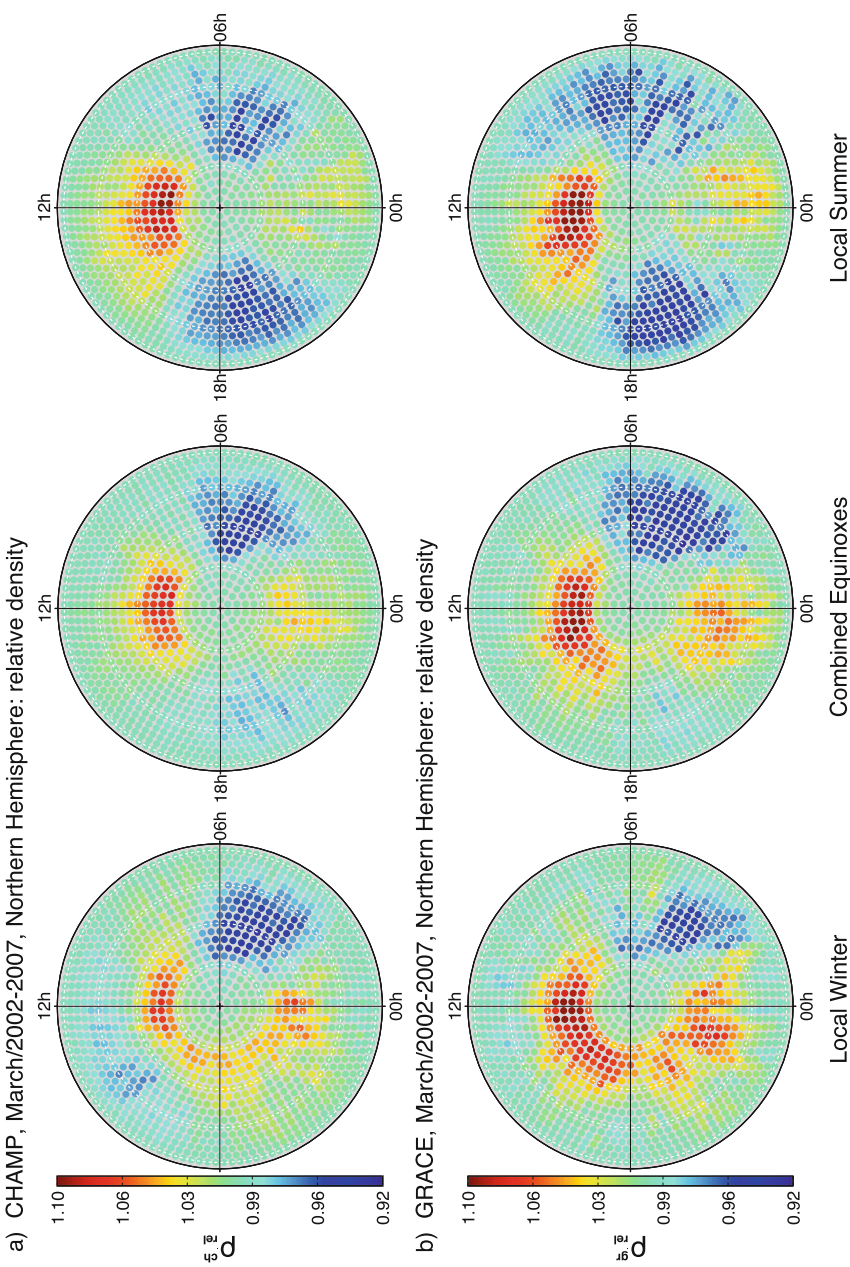


Fig. 11.5 The bin-averaged median values of relative density enhancements for local winter, combined equinoxes, and local summer, from left to right, respectively: (a) CHAMP and (b) GRACE. The white circles mark the 10° spacing starting from 50° MLat

Table 11.1 The sample number distribution of density enhancements at CHAMP and GRACE satellite altitudes for all seasons together

| $\rho_{\text{rel}}^{\text{threshold}}$ | CHAMP | GRACE | Change in % |
|--|--------|-------|-------------|
| $1.0 \leq \rho_{\text{rel}} < 1.2$ | 11,869 | 9138 | -23% |
| $1.2 \leq \rho_{\text{rel}} < 1.4$ | 8361 | 9183 | +10% |
| $1.4 \leq \rho_{\text{rel}}$ | 3488 | 5397 | +55% |

The results are listed separately for different threshold values. The last column shows the percentage change of the sample number from CHAMP to GRACE

11.4.2 The Spatial Distribution of ρ_{rel} , SSFAC, T_e , and V_z

The statistical distributions of the bin-averaged median values of the density enhancement $\rho_{\text{rel}}^{\text{ch}}$, electron temperature T_e , small-scale FAC, and vertical velocity V_z are shown in Fig. 11.6 from top to bottom, respectively. The survey results are presented for the three Lloyd seasons: local winter, combined equinoxes, and local summer from left to right, respectively. Data used here cover 4 years of CHAMP (March 2002–March 2006) and DMSP (March 2002–December 2005) satellite observations in the Northern Hemisphere.

The density enhancement peaks (Fig. 11.6a, top row) show practically no seasonal dependence in the northern cusp region having a width of about ± 2 h centered at noon MLT, but the locations of density anomaly tend to expand equatorward from winter to summer. The density anomalies clearly show the confined dayside cusp signatures for all three seasons. The location of density peaks is about 70 – 80° MLat in winter and about 64 – 80° MLat in equinoxes and summer.

The RMS values of SSFAC peaks (Fig. 11.6a, middle row) show strong seasonal dependence from weak in winter to strong in summer. These peaks are also located in the dayside cusp between 74° and 80° MLat and between 06:00 and 14:00 MLT spreading over 6–8 h in local time.

Electron temperature (Fig. 11.6a, bottom row) also shows strong seasonal dependence. The dayside cusp signature is visible here superposed onto the background temperature, which increases strongly from winter to summer.

Figure 11.6b shows merged (combined) values of ion vertical velocity from the DMSP F13 and F15 satellites. We have combined both DMSP spacecrafts to improve coverage of the dayside cusp region, because these satellites have sun-synchronous, fixed local time orbits and do not cover fully the MLat-MLT frame. Ion vertical velocity shows on average upward, seasonal dependent, positive flow in the northern dayside cusp region. The positive ion upflow intensities are strongest in winter and are decreasing towards summer. During winter a positive upflow is observed not only in the cusp but also in other regions. In the polar cap region the ion vertical velocities are downward (negative) at all seasons as expected (Coley et al. 2006).

The density anomaly, SSFAC, electron temperature, and ion vertical velocity have a clearly visible confined cusp signatures which can easily be identified from

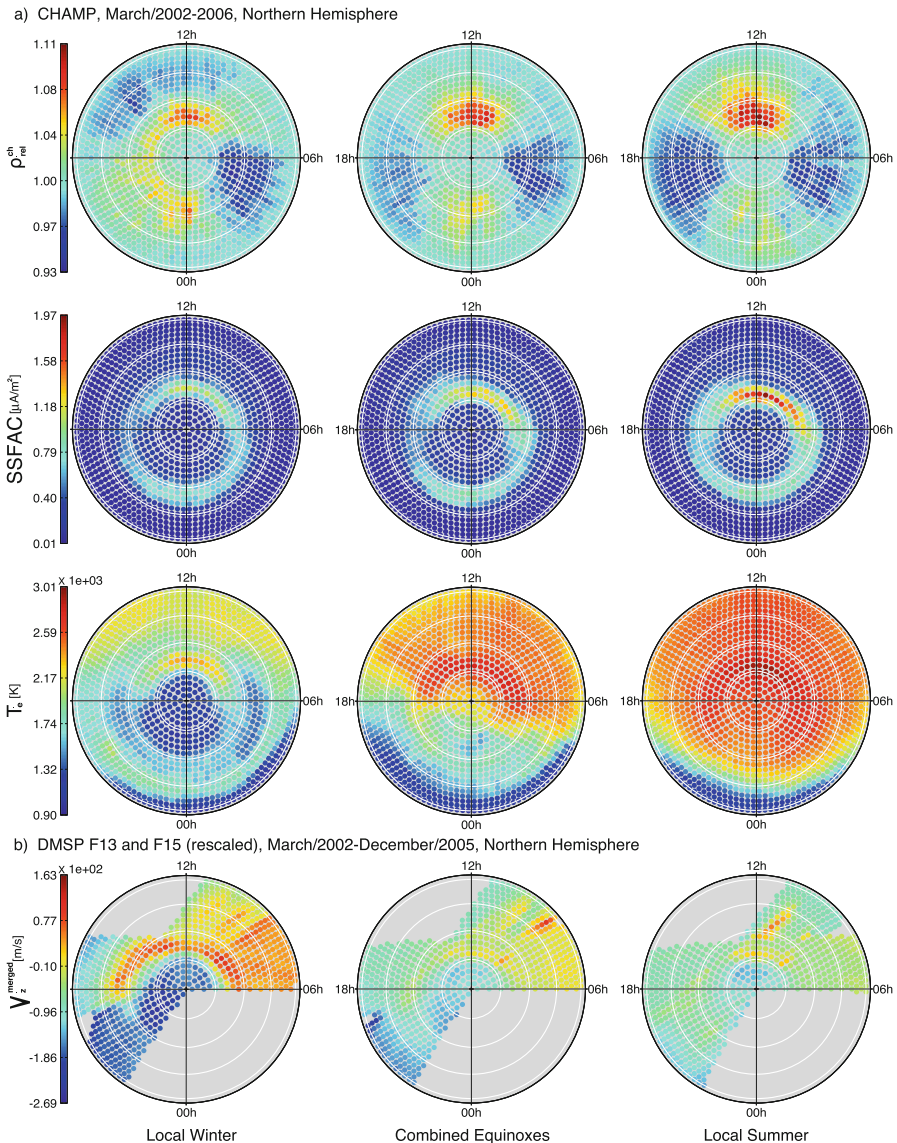


Fig. 11.6 Spatial distribution of bin-averaged median values of (a) relative density enhancement, small-scale FAC, and electron temperature *from top to bottom*, respectively, and (b) ion vertical velocity. The results are shown separately for local winter, combined equinoxes, and local summer *from left to right*, respectively. The white circles mark latitudes at 10° spacing, starting from 50° MLat. Modified after Figs. 3 and 4 from Kervalishvili and Lühr (2013)

Fig. 11.6. In the following sections possible relationships among these quantities in the northern dayside cusp region will be investigated in more details.

11.4.3 The Spatial Correlation of ρ_{rel} , SSFAC, T_e , and V_z

We have used the SEA method (Fig. 11.4) to investigate the spatial correlation between $\rho_{\text{rel}}^{\text{ch}}$, SSFACs, T_e , and V_z . The time and location of the peak values in mass density from CHAMP observations are used as zero epochs, where we only take into account $\rho_{\text{rel}}^{\text{ch}}$ with values larger than 1.2, which defines prominent density enhancements (for more details see Kervalishvili and Lühr 2014):

$$\rho_{\text{rel}}^{\text{ch}} > \rho_{\text{rel}}^{\text{threshold}} = 1.2. \quad (11.6)$$

The epoch window for $\rho_{\text{rel}}^{\text{ch}}$ is defined between 8:00–16:00 MLT and 60–80° MLat separately for northbound and southbound passes. Around every density peak reference time (zero epoch) a data interval of ± 4 min (about ± 1800 km arc length) was considered. Afterwards results for both passes were joined. In order to consider the ion drift measurements from DMSP satellites in the SEA analysis the close approach method has been used. This method demands two conditions: (1) DMSP passes the zero epoch latitude at a universal time within ± 30 min of the zero epoch; (2) V_z measurements must fall into the MLat-MLT window centered at the zero epochs and confined to $\pm 0.5^\circ$ MLat and ± 1 h MLT. Both DMSP satellite measurements of ion vertical velocities are used here for the SEA method. The average latitude profiles of $\rho_{\text{rel}}^{\text{ch}}$, SSFAC, T_e , and V_z , which are resampled at 1° in MLat, are shown in Fig. 11.7 separately for three Lloyd seasons: local winter, combined equinoxes, and local summer from left to right, respectively. The standard deviations at the 1° MLat bins are presented as vertical bars.

Pronounced peaks can be clearly identified in average latitude profiles of density enhancement, $\rho_{\text{rel}}^{\text{ch}}$, at zero epoch (as expected by design) for all three Lloyd seasons (Fig. 11.7a, top row). The peak values of density enhancement are about 1.33 and show no seasonal dependence.

The average latitude profiles of RMS values of small-scale FACs show strong seasonal dependence with increasing amplitudes towards local summer (Fig. 11.7a, middle row). The increase of intensity peak is about 19% in combined equinoxes and 36% in local summer. The pronounced peaks can also be observed here between -1° and zero epoch MLat for all three Lloyd seasons.

The expected dependence of the latitude profiles of electron temperature, T_e , on seasons emerges from Fig. 11.7a (middle row). The temperature peaks at zero epoch still can be identified at all seasons. The level of background temperature increases from winter to summer including the peak amplitude at zero epoch. However, the shape of temperature rise (peak) above the background changes from relatively high and narrow in winter to low and broad in summer.

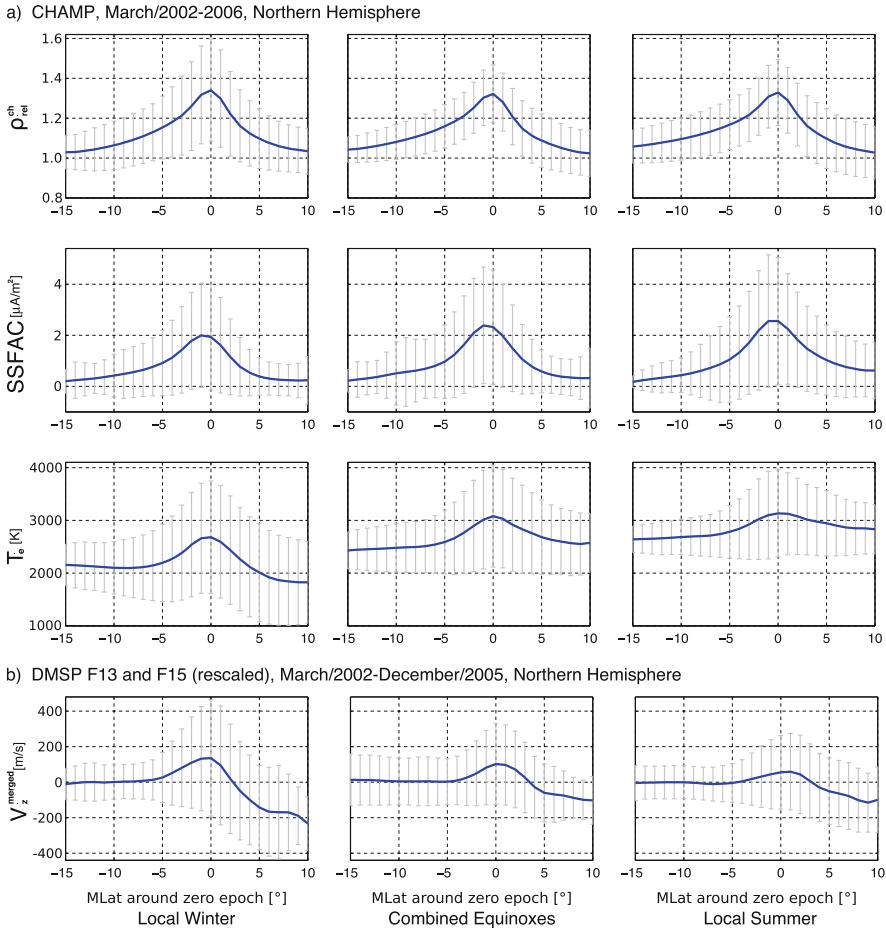


Fig. 11.7 The SEA results with respect to density anomaly peaks for MLat profiles of (a) $\rho_{\text{rel}}^{\text{ch}}$, small-scale FAC, and T_e from top to bottom, respectively; (b) vertical ion velocity V_z . The results are shown separately for local winter, combined equinoxes, and local summer from left to right, respectively, for $\rho_{\text{rel}}^{\text{threshold}} = 1.2$. The vertical bars represent the standard deviations of 1° MLat averages. Modified after Fig. 6 from Kervalishvili and Lühr (2013)

Figure 11.7b shows the latitude profiles of ion vertical velocity derived from the DMSP measurements. The velocity peak at zero epoch shows strong seasonal dependence. The amplitude values of V_z decrease towards local summer by more than 50%. The velocity peaks at zero epoch can be clearly identified at all seasons.

The peaks of $\rho_{\text{rel}}^{\text{ch}}$, SSFACs, T_e , and V_z centered at zero epoch (defined by $\rho_{\text{rel}}^{\text{ch}}$) are an important finding, which is clearly visible at all three Lloyd seasons (Fig. 11.7). Also, all considered variables show the same seasonal dependence, as was evident from the spatial distribution presented in Fig. 11.6. The possible relationship between electron temperature rise and ion vertical velocity is explored in the next section.

11.4.4 A Linear Relationship Between V_z and ΔT_e

Figure 11.8 shows the latitude profiles of electron temperature rise, ΔT_e , and ion vertical velocity, V_z , with removed background for the three local seasons. The clearly visible similarity in seasonal variations suggests a certain linear correlation between these two variables. The peak intensities at zero epoch decrease towards local summer by 20% and 25% in combined equinoxes and by 48% and 58% in local summer for ΔT_e and V_z , respectively. We can calculate the linear regression expression and correlation coefficients using the data around the zero epoch latitude between -5° and 5° MLat (Fig. 11.8):

$$V_z = a\Delta T_e + b, \quad (11.7)$$

where a is the slope and b is an offset of the regression line. Table 11.2 lists the derived linear regression expressions and correlation coefficients separately for each local season and for all seasons together (top row). The slope, a , and offset, b , values are quite similar for different local seasons: a varies between 0.22 and $0.24 \text{ K}^{-1}\text{m/s}$; b varies between -38 and -21 m/s . The corresponding correlation coefficients have also rather high values varying between 0.93 and 0.96. The highest value 0.96 is derived at local winter, when omitting the two outliers, which are shown in Fig. 11.9. The convincing linear regression expression can be derived for a combined correlation analysis using the data for all seasons together and omitting

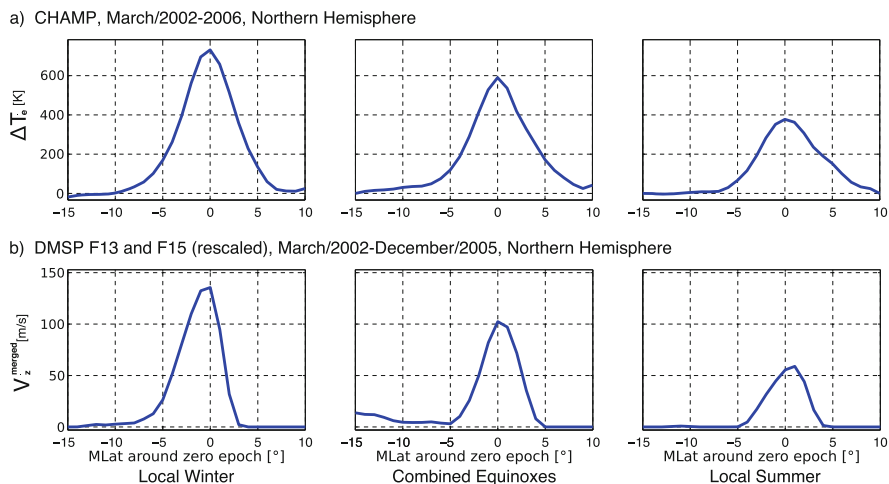


Fig. 11.8 The background removed latitude profiles of (a) electron temperature rise, ΔT_e and (b) ion vertical velocity, V_z . The results are derived from the same data as in Fig. 11.6 and are shown for the three Lloyd seasons. Modified after Fig. 7 from Kervalishvili and Lühr (2013)

Table 11.2 The linear regression functions and coefficients derived from the correlation analysis between V_z and ΔT_e

| Seasons | $V_z = a \Delta T_e + b$ (m/s) = (K^{-1} m/s) (K) + (m/s) | Correlation coefficients |
|----------------------|---|--------------------------|
| All seasons together | $a = 0.23; b = -31$ | 0.96 |
| Local winter | $a = 0.22; b = -21$ | 0.96 |
| Combined equinoxes | $a = 0.24; b = -38$ | 0.95 |
| Local summer | $a = 0.22; b = -27$ | 0.93 |

The results are listed separately for each season and for all seasons together. Here a is a slope and b is an offset. Modified after Table 2 from Kervalishvili and Lühr (2013)

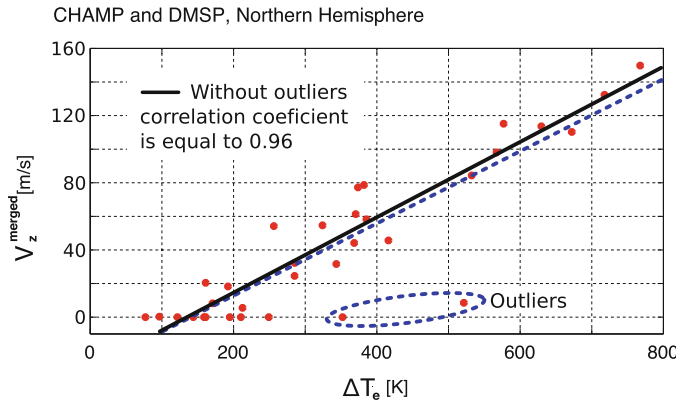


Fig. 11.9 Correlation analysis results between V_z and ΔT_e in the northern cusp region for the total data set independent of season. Modified after Fig. 8 from Kervalishvili and Lühr (2013)

the two outliers from the local winter

$$V_z = 0.23\Delta T_e - 31, \quad (11.8)$$

with the correlation coefficient value of 0.96 (Table 11.2). The regression lines with and without two outliers for all Lloyd seasons together are shown in Fig. 11.9.

11.4.5 The IMF B_y -Dependent Spatial Correlation of ρ_{rel} , U_{zon} , and LSFAC

To investigate the relationship between the neutral density enhancement $\rho_{\text{rel}}^{\text{ch}}$, neutral wind velocity U_{zon} , large-scale FAC, and electron temperature T_e , we have used the SEA method as described in Sect. 11.4.3 for the CHAMP satellite. Data used here cover 5 years of CHAMP (March 2002–March 2007) satellite observations in the Northern Hemisphere. The value of the relative density enhancement threshold,

$\rho_{\text{rel}}^{\text{threshold}}$, used here is equal to 1.2 (Eq. (11.6)) as before. Additionally, the calculated median values of the IMF B_y data (Sect. 11.2.4) at epoch zero are used here to sort $\rho_{\text{rel}}^{\text{ch}}$ according to the IMF B_y orientation. The IMF data used to calculate these median values are taken from the 1 h time interval before the zero epoch UT time.

Figure 11.10 presents the median profiles of IMF total field, B_t and the B_x , B_y , and B_z components for the ± 2 h time interval around zero epoch separately for IMF B_y^+ (red) and IMF B_y^- (green). The IMF data are from all seasons, because seasons are only relevant on Earth. The median temporal variations of the total field B_t show no dependence on the IMF B_y sign (top panel). An important finding is that all median components of IMF (B_x , B_y , and B_z) show no systematic sign change during the 4 h interval for both positive (red) and negative (green) components of IMF B_y . Also, the temporal variation (in terms of absolute value) of IMF B_x and B_y components

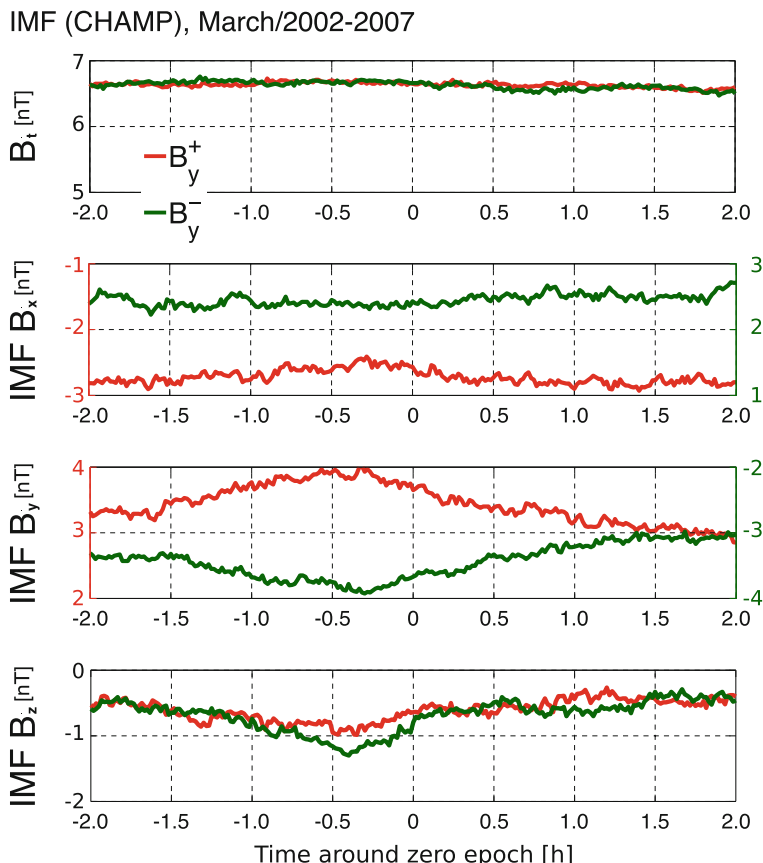


Fig. 11.10 Superposed median profiles of the total interplanetary magnetic field B_t and IMF B_x , B_y , and B_z components separately for IMF B_y^+ (red) and IMF B_y^- (green). The peak in density anomaly defines the zero epoch. Modified after Fig. 2 from Kervalishvili and Lühr (2014)

exhibits an anti-symmetry for both IMF B_y orientations. This is consistent with the notion of the Parker solar wind spiral. Additionally, there is a clear increase and decrease of the amplitude (third panel) for the IMF B_y^+ and B_y^- cases, respectively, at about half an hour before zero epoch. Interestingly, the IMF B_z component exhibits only a shallow minimum also about half an hour before zero epoch and stays on average negative (last panel) during times of density enhancements in the cusp region.

11.4.5.1 The Spatial Correlation of ρ_{rel} , U_{zon} , and LSFAC

Figure 11.11 shows the dependence on the IMF B_y orientation of median-latitude profiles as derived from a SEA for $\rho_{\text{rel}}^{\text{ch}}$, U_{zon} , LSFAC, and T_e for the three Lloyd seasons: local winter, combined equinoxes, and local summer from left to right, respectively. Here again zero epoch is defined by the peak in density anomaly, $\rho_{\text{rel}}^{\text{ch}}$. The average latitude profiles of the given variables are resampled at 1° MLat steps.

Pronounced peaks can be clearly identified in median-latitude profiles of $\rho_{\text{rel}}^{\text{ch}}$ at zero epochs (as expected) for both positive (red) and negative (green) IMF B_y (Fig. 11.11, top row). The peak values are about 1.32–1.35 and do not exhibit significant dependence on season or IMF B_y sign.

The latitude profiles of median zonal wind, U_{zon} , show pronounced negative (westward) peaks for both positive and negative IMF B_y signs (Fig. 11.11, second row). Therefore, the zonal wind has a westward component around noon for both IMF B_y cases. The spatial variations of U_{zon} exhibit a quite different character for the two signs of IMF B_y . We observe a practically identical behavior of U_{zon} curves in the MLat range between -15° and -5° (when approaching the cusp) for the IMF B_y^+ (red) and B_y^- (green) cases. For higher latitudes a clear dependence on IMF B_y direction appears. In case of positive IMF B_y strong westward winds peak around zero epoch and maintain this direction to high latitudes. Conversely, for negative IMF B_y the westward wind component maximizes at -3° MLat before reaching the zero epoch latitude, and it approaches zero speed a few degrees poleward. In case of this IMF orientation the meridional wind component (not shown here) seems to play the dominant role. The existence of a due poleward wind at high latitudes for negative IMF B_y is confirmed by studies of Thayer et al. (1987) and Förster et al. (2008). For both IMF B_y orientations high thermospheric wind speeds coincide with the density anomaly.

The latitude profiles of median LSFAC also show a clear dependence on the IMF B_y orientation (Fig. 11.11, third row). Here the upward current direction is positive. As expected, the maximum and minimum values of LSFAC amplitudes are increasing towards local summer for both positive (red) and negative (green) IMF B_y signs, but the spatial shape of LSFAC curves is of similar character. Starting around noon (-15° MLat) and moving towards the North Pole (10° MLat), in the case of positive (negative) IMF B_y , first we observe downward (upward) and then upward (downward) LSFACs. However, there is an imbalance feature between the amplitudes of LSFACs, which depends on the upward and downward

CHAMP, March 2002–2007, Northern Hemisphere

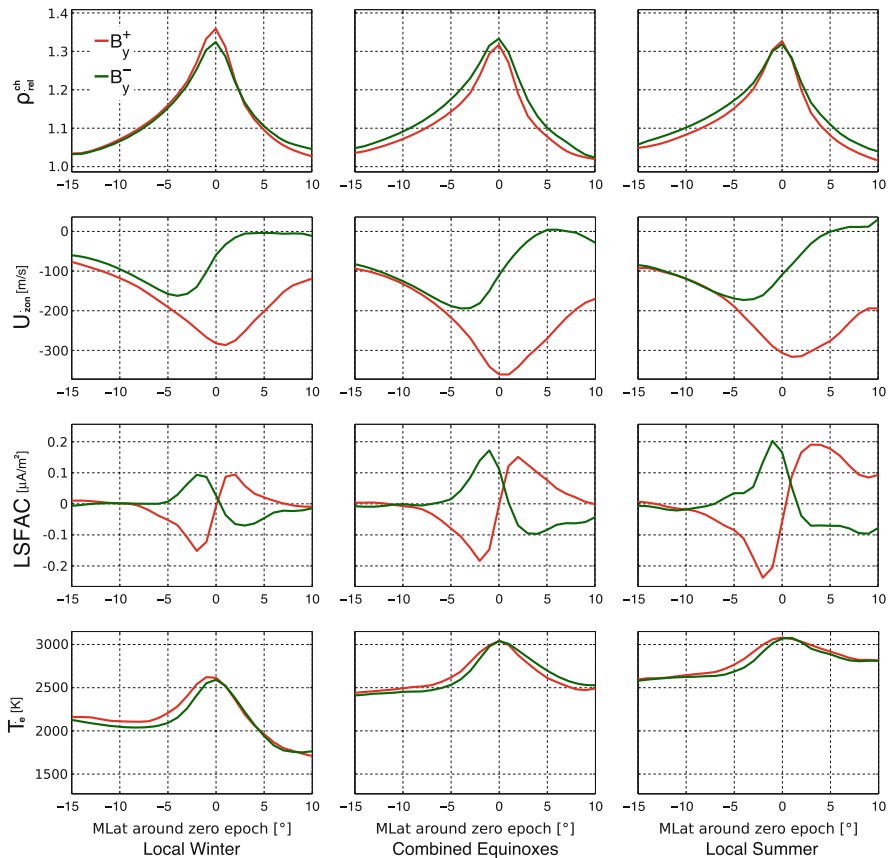


Fig. 11.11 The SEA results with respect to density anomaly peaks for MLat profiles of $\rho_{\text{rel}}^{\text{ch}}$, U_{zon} , LSFAC, and T_e from top to bottom, respectively, as functions of IMF B_y^+ (red) and IMF B_y^- (green). The results are shown separately for local winter, combined equinoxes, and local summer from left to right, respectively, for $\rho_{\text{rel}}^{\text{threshold}} = 1.2$. Modified after Fig. 1 from Kervalishvili and Lühr (2014)

current locations with respect to zero epoch latitude. The amplitudes of equatorward LSFACs are larger for downward ($\text{IMF } B_y^+$) and upward ($\text{IMF } B_y^-$) currents than the poleward ones for upward ($\text{IMF } B_y^+$) and downward ($\text{IMF } B_y^-$). We relate the stronger, equatorward currents to Region 1 (R1) FACs and the poleward ones to R0 FACs. Our findings about imbalance phenomena are in good agreement with results from He et al. (2012), which are based on 10 years of CHAMP data for noontime FAC distributions under positive (5 nT) and negative (-5 nT) IMF B_y .

The latitude distributions of median electron temperature for $\text{IMF } B_y^+$ (red) and B_y^- (green) are presented in Fig. 11.11 (bottom row). We can clearly identify that the amplitude of the electron temperature does not show a dependence on the orientation of IMF B_y .

11.4.5.2 A Parametric Study of Density Enhancement Values

To investigate the conditions that lead to larger thermospheric density anomalies in the cusp region, we have chosen four different thresholds of relative enhancements, which are listed in Table 11.3 together with the sample number distribution for both IMF B_y orientations. The sample number distributions are from combined seasons.

Figure 11.12 presents the averaged latitude profiles of $\rho_{\text{rel}}^{\text{ch}}$, U_{zon} , and LSFAC for IMF B_y^+ and different levels of $\rho_{\text{rel}}^{\text{threshold}}$ (Table 11.3) from top to bottom, respectively. An important observation, clearly identifiable in Fig. 11.12, is a change in characteristics of all variables for all seasons between $\rho_{\text{rel}}^{\text{threshold}}$ values 1.1 and 1.2 (a larger amplitude gap). This provides justification for the previously used value 1.2 of $\rho_{\text{rel}}^{\text{threshold}}$. As expected, the increased threshold values lead to increased peak amplitudes of $\rho_{\text{rel}}^{\text{ch}}$ at zero epoch (Fig. 11.12, top row). As before (Fig. 11.11, top row), there are no significant seasonal variations. The SEA curves of U_{zon} show the pronounced negative peaks around zero epoch for all seasons and $\rho_{\text{rel}}^{\text{threshold}}$ levels (Fig. 11.12, second row). The amplitude of zonal wind velocity peaks increases with increased levels of relative density threshold. The spatial variations of LSFAC latitude profiles for different levels of $\rho_{\text{rel}}^{\text{threshold}}$ (Fig. 11.12, bottom row) exhibit the same character of variations as for the threshold value 1.2 (Fig. 11.12, third row). This applies to the imbalance between upward and downward currents and for the seasonal dependence with increased amplitudes towards summer. The increased level of $\rho_{\text{rel}}^{\text{threshold}}$ that leads to larger peak amplitudes of $\rho_{\text{rel}}^{\text{ch}}$, U_{zon} , and LSFAC for all Lloyd seasons is an important observation.

Figure 11.13 shows similar results as Fig. 11.12, but for the IMF B_y^- case. All the conclusions drawn for IMF B_y^+ are also valid here for $\rho_{\text{rel}}^{\text{ch}}$ (Fig. 11.13, top row) and LSFAC (Fig. 11.13, bottom row). As before, this is true for all local seasons. Interestingly, in case of IMF B_y^- the increase of peak amplitude values of U_{zon} with increased level of $\rho_{\text{rel}}^{\text{threshold}}$ is barely significant (Fig. 11.13, second row) compared to the IMF B_y^+ case (Fig. 11.12, second row). This is true for all levels of threshold (Table 11.3) and seasons.

The increase of the more important meridional component is unfortunately not measured. Therefore we obtain only an incomplete picture of the wind response to an increased $\rho_{\text{rel}}^{\text{threshold}}$ for IMF B_y^- .

Table 11.3 The combined sample number distribution for all seasons

| $\rho_{\text{rel}}^{\text{threshold}}$ | IMF B_y^+ | IMF B_y^- |
|--|-------------|-------------|
| 1.0 | 9299 | 9627 |
| 1.1 | 6904 | 7290 |
| 1.2 | 3858 | 4052 |
| 1.3 | 2038 | 2122 |

The numbers are listed separately for both IMF B_y signs and for four different thresholds of $\rho_{\text{rel}}^{\text{ch}}$. Modified after Table 2 from Kervalishvili and Lühr (2014)

CHAMP, March/2002-2007, Northern Hemisphere: IMF $B_y > 0$

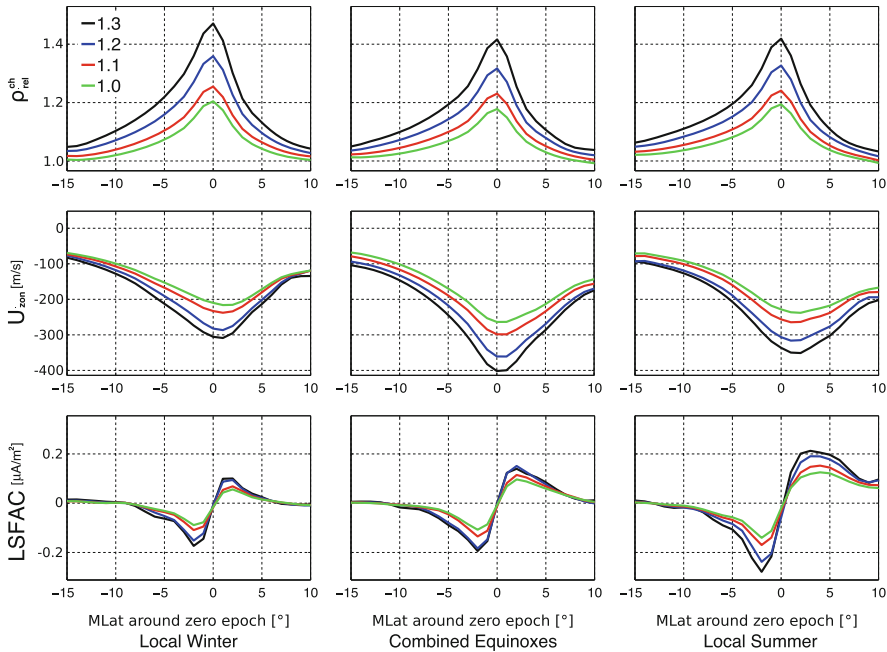


Fig. 11.12 The SEA curves of $\rho_{\text{rel}}^{\text{ch}}$, U_{zon} , and LSFAC for IMF B_y^+ in the northern cusp region from top to bottom, respectively. The results are presented for different levels of $\rho_{\text{rel}}^{\text{threshold}}$ (Table 11.3) and for three Lloyd seasons from left to right, respectively. Modified after Fig. 4a from Kervalishvili and Lühr (2014)

11.4.6 The IMF B_y -Dependent Spatial Correlation of $V_z N_i$ and LSFAC

For investigating the relationship between the vertical plasma flow $V_z N_i$ and large-scale FAC, we have used the similar SEA method as described in Sect. 11.4.3. But, here the time and location of the vertical plasma flow peaks from DMSP satellite measurements were used to define the zero epoch. CHAMP and DMSP (F13 and F15) data of the 5 years, March 2001–December 2005, are considered from the Northern Hemisphere. The values of the vertical plasma flow threshold, $(V_z N_i)^{\text{threshold}}$, used here are equal to 0.8×10^{14} , 1.0×10^{14} , and $1.2 \times 10^{14} \text{ m}^{-2} \text{ s}^{-1}$. To sort $V_z N_i$ according to the IMF B_z and IMF B_y orientation, the calculated median values of the IMF data (Sect. 11.2.4) around epoch zero are used. The relevant median values are calculated from the prevailing IMF B_z and IMF B_y data during the time interval 1 h before zero epoch. In case of IMF B_z , we consider two cases: (1) negative, less than -1.2 nT ; (2) zero, from -1.2 to 1.2 nT . The sample number distributions for all IMF B_z and B_y orientation cases and for three levels of

CHAMP, March/2002-2007, Northern Hemisphere: IMF $B_y < 0$

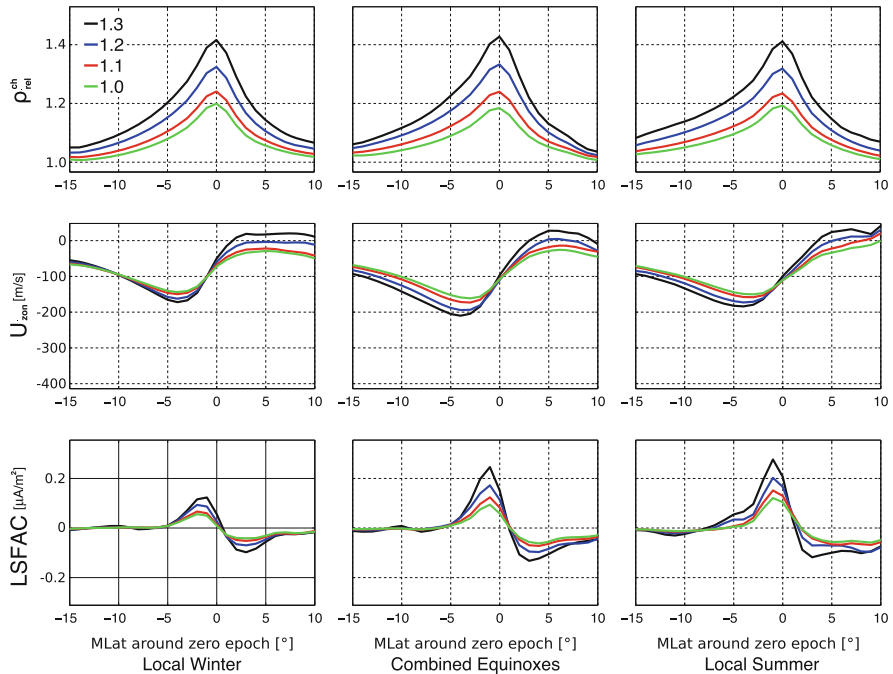


Fig. 11.13 The same as Fig. 11.12, but for the negative case of IMF B_y . Modified after Fig. 6a from Kervalishvili and Lühr (2014)

Table 11.4 The sample number distribution for all seasons is listed separately for all IMF B_z and IMF B_y cases and for three levels of $(V_z N_i)^{\text{threshold}}$

| $(V_z N_i)^{\text{threshold}} (\text{m}^{-2} \text{s}^{-1})$ | $\text{IMF } B_z \leq -1.2$ | | $-1.2 < \text{IMF } B_z < 1.2$ | |
|--|-----------------------------|---------------------|--------------------------------|---------------------|
| | $\text{IMF } B_y^+$ | $\text{IMF } B_y^-$ | $\text{IMF } B_y^+$ | $\text{IMF } B_y^-$ |
| 0.8×10^{14} | 10,766 | 11,713 | 10,358 | 10,432 |
| 1.0×10^{14} | 9680 | 10604 | 8731 | 8729 |
| 1.2×10^{14} | 8426 | 9705 | 7345 | 7205 |

$(V_z N_i)^{\text{threshold}}$ are listed in Table 11.4. The sample number distributions are given for all seasons.

The corresponding median profiles of IMF total field B_t and B_x , B_y , and B_z components for the IMF B_z negative and zero cases and for $(V_z N_i)^{\text{threshold}} = 10^{14} [\text{m}^{-2} \text{s}^{-1}]$ are shown in Fig. 11.14a, b, respectively. Combined results for all seasons are presented for the ± 2 h time interval around zero epoch separately for IMF B_y^+ (red) and IMF B_y^- (green). The behaviors of IMF total field B_t , B_x , and B_y are quite similar to the case described in Sect. 11.4.5 for both B_z conditions. Namely, B_t practically shows no dependence on the IMF B_y sign (top panels), and the temporal variation (in terms of absolute value) of IMF B_x and B_y components

IMF (DMSP), March/2001-December/2005

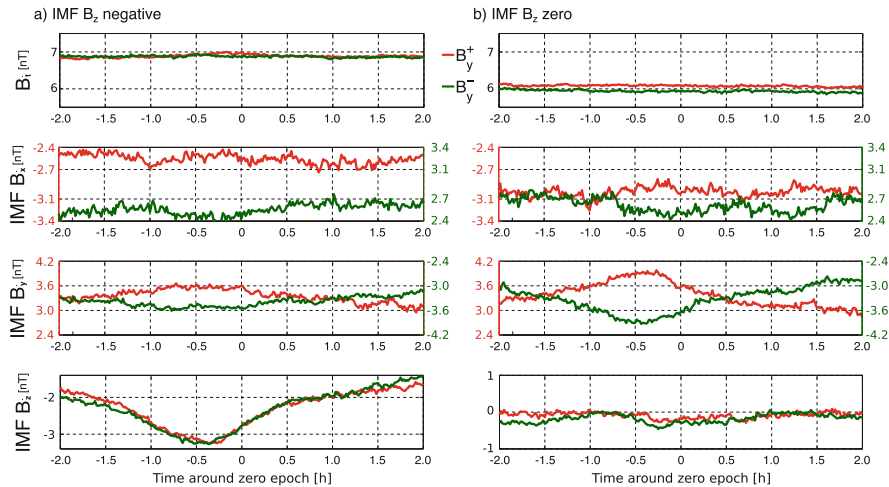


Fig. 11.14 Temporal evolution with respect to plasma upward flow peaks of the total interplanetary magnetic field B_t and IMF B_x , B_y , and B_z components as functions of IMF B_y^+ (red) and IMF B_y^- (green) for $(V_z N_i)^{\text{threshold}} = 10^{14} [\text{m}^{-2} \text{s}^{-1}]$ and: (a) $\text{IMF } B_z \leq -1.2$ and (b) $-1.2 < \text{IMF } B_z < 1.2$

exhibits the expected anti-symmetry for both IMF B_y orientations. Again, median IMF components show no systematic sign change during the 4 h interval time for both positive (red) and negative (green) components of IMF B_y . IMF B_z by design stays close to zero and is negative for IMF B_z zero and negative conditions, respectively (last panels). Also, IMF B_z exhibits no pronounced minimum about half an hour before zero epoch in case of zero IMF B_z (Fig. 11.14a, last panel). However, there is a very pronounced minimum about half an hour before zero epoch in case of negative IMF B_z (Fig. 11.14b, last panel). As before, IMF B_y curves show a clear increase and decrease about half an hour before zero epoch for IMF B_y^+ and B_y^- , respectively (third panels).

11.4.6.1 Conditions for IMF B_z -Negative Case

Results of the SEA centered on the peaks of vertical plasma flow for IMF conditions as shown in Fig. 11.14a are presented here. Figure 11.15 shows the dependence of $V_z N_i$ and large-scale FAC (LSFAC) on the IMF B_y component orientation for the three Lloyd seasons: local winter, combined equinoxes, and local summer from left to right, respectively. The results are presented for the IMF $B_z \leq -1.2$ case and for three different levels of $(V_z N_i)^{\text{threshold}}$ (Table 11.4). The median latitude profiles of $V_z N_i$ and LSFAC are resampled at 1° in MLat. Both $V_z N_i$ and LSFAC show no dependence on the value of $(V_z N_i)^{\text{threshold}}$. This implies that larger plasma flow peaks dominate the results.

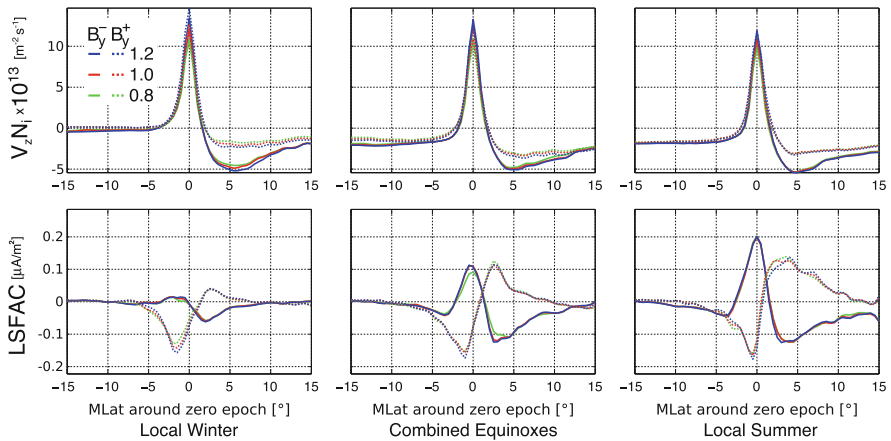
CHAMP, DMSP F13 and F15, March/2001–December/2005, Northern Hemisphere: $B_z \leq -1.2$ [nT]

Fig. 11.15 The SEA curves of $V_z N_i$ and LSFAC as functions of IMF B_y^+ (dotted lines) and IMF B_y^- (solid lines) for the IMF $B_z \leq -1.2$ case. The results are shown for different levels of $(V_z N_i)^{\text{threshold}}$ (Table 11.4) and for three Lloyd seasons *from left to right*, respectively

Pronounced peaks can be clearly identified in the latitude profiles of $V_z N_i$ at zero epochs (as expected) for both IMF B_y^+ (dotted lines) and IMF B_y^- (solid lines) cases and for all vertical plasma flow threshold levels (Fig. 11.15, top row). The peak values exhibit a slight dependence on local season and no dependence on the IMF B_y sign. The maximum values of $V_z N_i$ amplitudes are decreasing towards local summer for both orientations of IMF B_y . Interestingly, the vertical plasma flows exhibit a different character of spatial variations on the poleward side (positive MLat) for the two IMF B_y cases. There appears a pronounced negative peak at about 5° MLat for IMF B_y^- (solid lines), which is probably connected to the cusp location with respect to the noon sector depending on the IMF B_y orientation (Sect. 11.5.3). For negative IMF B_y , the cusp is shifted to earlier local times. In that case DMSP F15 passes through larger parts of the polar cap with downward flow (see Fig. 11.6b) than for events on the afternoon side (positive B_y).

The median-latitude profiles of LSFAC (the upward current is positive) show a clear dependence on the IMF B_y orientation and local season for all levels of $(V_z N_i)^{\text{threshold}}$ (Fig. 11.15, bottom row). As expected, the maximum and minimum values of LSFAC amplitudes are increasing towards local summer for both positive (dotted lines) and negative (solid lines) IMF B_y orientations. The LSFAC curves show a similar character of the spatial behavior as was described in Sect. 11.4.5.1. Namely, first we observe downward (upward) and then upward (downward) LSFACs in the case of positive (negative) IMF B_y . Also, there is a similar imbalance feature between the amplitudes of LSFACs. FACs located equatorward of zero epoch latitude (R1) are more intense than the corresponding poleward (R0) peaks.

11.4.6.2 Conditions for IMF B_z Around Zero Case

Figure 11.16 shows the dependence of $V_z N_i$ and LSFAC on the IMF B_y component orientation for the $-1.2 < \text{IMF } B_z < 1.2$ case as shown in Fig. 11.14b. Also here, both $V_z N_i$ and LSFAC show no dependence on the threshold value of $V_z N_i$.

The peak values of the median-latitude profiles of $V_z N_i$ show a slight dependence on local season and no dependence on the IMF B_y sign for all vertical plasma flow threshold levels (Fig. 11.16, top row). As before, for the negative IMF B_z case (Fig. 11.15, top row), the peak amplitudes are decreasing towards local summer for both IMF B_y^+ (dotted lines) and IMF B_y^- (solid lines) cases. We can still observe the differences in amplitude values of $V_z N_i$ poleward of about 5° MLat, which depends on the IMF B_y sign. But interestingly, these differences are much smaller than for the IMF B_z^- case and do not appear in combined equinoxes at all (Fig. 11.16, top middle).

The median-latitude profiles of LSFAC again show a clear dependence on the IMF B_y orientation and local season (Fig. 11.16, bottom row), as before for the IMF B_z^- case (Fig. 11.15, bottom row). Again, the maximum and minimum values of LSFAC amplitudes are increasing towards local summer for both IMF B_y^+ (dotted lines) and IMF B_y^- (solid lines) orientations. However, there is a difference in the latitudinal variation of LSFAC curves poleward of the zero epoch latitude. In particular during local summer LSFAC exhibits large amplitudes around 5° MLat. These can be related to the northward IMF B_z (NBZ) FACs poleward of the cusp. Interestingly, their amplitudes appear to be larger than the adjacent R1 FACs, which have been shown in previous cases to dominate the R0 FACs. We think that the mismatch in amplitude between the two adjacent FAC sheets is mainly due to the averaging process. NBZ FACs appear at rather fixed latitudes while the location of R1 shifts depending on geomagnetic activity.

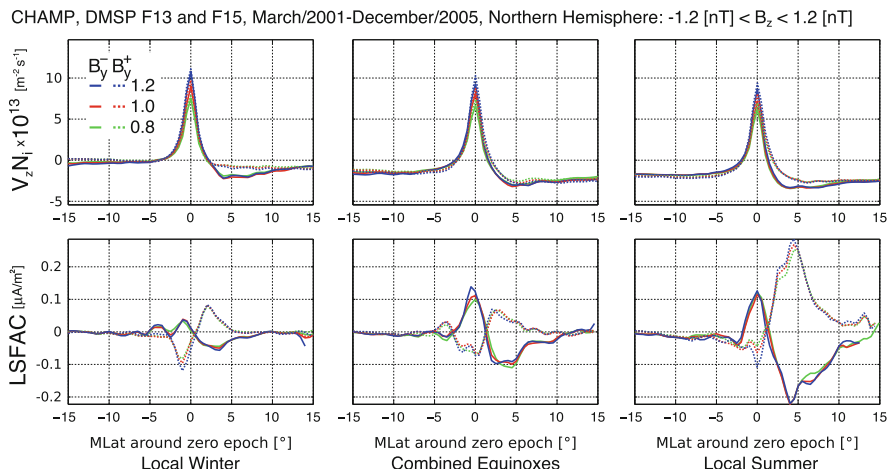


Fig. 11.16 The same as Fig. 11.15, but for the $-1.2 < \text{IMF } B_z < 1.2$ case

11.5 Discussion and Conclusion

In this chapter we have tried to identify processes that are responsible for lifting up ionospheric plasma and enabling ions like O⁺ to escape the atmosphere. From the thermodynamic point of view they should not be fast enough to leave the Earth. The atmosphere is gravitationally bounded to the planet. For estimating the escape flux, Φ_{es} , we can refer to *Jeans'* relation (e.g., Prölss 2004, p. 66):

$$\Phi_{\text{es}} = n(\text{EB}) \frac{c_t}{2\sqrt{\pi}} e^{-X} (1 + X), \quad (11.9)$$

where $n(\text{EB})$ is the number density at the exobase (~ 500 km altitude), c_t the typical thermal velocity of the gaseous species, and $X = (c_{\text{es}}/c_t)^2$ is the squared ratio of the escape velocity ($c_t = 11$ km/s) over the typical thermal velocity. When applying *Jeans'* relation to atomic oxygen ($T = 1000$ K, $n_0 = 4 \times 10^{13}$ m⁻³, $X_0 = 120$), there is practically no thermal escape possible ($\Phi_{\text{es},0} \approx 10^{-34}$ m⁻² s⁻¹). The actually observed substantial escape of oxygen is only possible if electrodynamics forces and the geometry of the geomagnetic field are taken into account. The cusp region with its almost vertical and diverging geomagnetic field lines is favorable for these processes.

One mechanism to energize oxygen ions is transverse heating by wave-particle interaction (e.g., Miyake et al. 1993). When the ions are fast enough, they can escape the Earth's atmosphere. However, this mechanism is not suitable to explain the large amount of cold oxygen ions that populate the magnetosphere. In this study we have focused on processes that may be able to lift up ions without a significant heating. In our opinion it is important to consider also the thermospheric dynamics accompanying outflow events. Most promising for such a comprehensive treatment is the polar cusp/cleft region. Here a lot of solar wind energy input is focused (see Thayer and Semeter 2004) onto a relatively small area in the upper atmosphere.

11.5.1 Conditions for Neutral Air Upwelling

In this chapter we have started with air upwelling events as a possible process supporting ion upflow. The temporal and spatial evolutions of a number of quantities, accompanying the air density anomaly at satellite height, have been investigated. It is interesting to see that also other quantities like small-scale field-aligned currents (SSFACs), electron temperature, and ion upflow show local peaks in the cusp (see Fig. 11.6). The preferential appearance in the cusp region has been reported before individually for each of these quantities (density peak: Lühr et al. 2004; SSFAC: Rother et al. 2010; electron temperature: Prölss 2006; ion upflow: Wahlund et al. 1992). We went one step further and showed the coincidence of occurrence with the help of a superposed epoch analysis. Here again the appearance of a density

anomaly in the cusp region defined the location and key time of an event. Concurrent observations of the other three quantities revealed on average very similar latitude profiles with peaks close to the reference position of the density anomaly (see Fig. 11.7). This result provides strong evidence for a functional relation between these quantities.

Already Lühr et al. (2004) suggested the important contribution of SSFACs for the generation of density anomalies. Although this is necessary, it is not a sufficient condition. In addition it obviously needs intense flows of precipitating soft electrons (<100 eV) for enhancing the ionospheric conductivity at the bottom-side F region (<200 km). This inference has been deduced from combined EISCAT-CHAMP measurements (see Lühr and Marker 2013) and verified by numerical model simulation (Deng et al. 2011). Under these conditions the Joule heating fueled by intense SSFACs is dumped into the neutral gas at an altitude where the density is much lower than at E-layer level and therefore significantly higher temperatures can be achieved. Unfortunately, we did not have an electron spectrometer on board CHAMP for directly confirming the close relation of density anomalies with soft electron precipitation. There is however quite some evidence for a frequent coincidence between SSFACs and low-energy electron precipitation. In a statistical study Watermann et al. (2009) confirmed the close correlation between SSFACs and electron precipitation by comparing magnetic field signatures from Ørsted and CHAMP with particle signatures from DMSP satellites. All these observations are consistent with density enhancements in the cusp region.

Another feature of the cusp is the elevated electron temperature. The cause for this can also be related to intense electron precipitation in that region. In the auroral acceleration region electrons are both heated and accelerated earthward. The clearly higher electron temperature than ion temperature in the cusp region creates an upward directed electric field that moves ions upward. Along the vertical magnetic field lines the ions can easily be transported. Support for the action of such an ambipolar electric field comes from the good linear relation between temperature enhancement and vertical ion drift, as shown in Figs. 11.8 and 11.9. Already small electric fields are sufficient to accelerate ions upward. For example, an E-field of $1.6 \mu\text{V/m}$ is sufficient to compensate for the gravity force acting on an oxygen ion ($eE = m_{\text{O}}^+ g$). From Fig. 11.9 we see that ions only start moving upward for temperature enhancements larger than 140 K . If we assume that this rise in T_e is needed to account for the Earth gravity, observed peak temperature enhancements of 800 K correspond then to field-aligned upward-directed E-fields of up to $9 \mu\text{V/m}$. This is observed at 840 km altitude in connection with vertical drift velocities of 150 m/s . Ion-neutral collisions every 4 s are sufficient at this height to maintain the observed velocity. These observations show which role ambipolar electric fields can play in lifting up ionospheric ions without significant heating.

The processes in the cusp region are closely controlled by the orientation of the interplanetary magnetic field. It is well known that a negative IMF B_z is in favor of dayside magnetic reconnection. But the IMF B_y component plays an important role for the topology of the current system in the cusp region. Our superposed epoch analysis reveals that we find for positive IMF B_y on average a downward FAC

on the equatorward side of the density anomaly and an upward on the poleward side (see Fig. 11.11). An oppositely directed (upward and downward) pair of FACs is bracketing the density anomaly in case of negative IMF B_y . Halfway between the upward and downward FAC pair we can assume fast westward plasma drift in the case of positive IMF B_y and eastward plasma drift for negative IMF B_y . These rapid plasma drifts may well be related with the cusp flow channels as introduced by Carlson et al. (2006). They are associated with flux transfer events and persist typically 15–20 min. IMF B_y tension forces can drive plasma velocities up to 1–3 km/s. This flow jet is expected to play a significant role in the formation of the density anomaly. Also the zonal wind exhibits peak velocities at the locations of the density anomaly. For positive IMF B_y westward winds of more than 300 m/s are observed (see Fig. 11.11). This is consistent with the expected plasma flow direction. Different from that, for negative IMF B_y the initially westward wind rotates towards higher latitudes into poleward direction. Förster et al. (2008) had reported about the wind directions in the cusp region and their dependence on the IMF B_y orientation. Neutral air forces, pressure gradient, and Coriolis force cause poleward and westward components. The additional influence of the plasma drift either enhances the westward wind component (B_y^+) or cancels it (B_y^-) and leaves only the poleward wind.

11.5.2 Conditions for Ion Upflow

In previous sections we have seen that ion upflow typically accompanies density anomalies in the cusp region. This may, however, just be a subset of upflow events in this region. In order to check that we performed a superposed epoch analysis controlled by peaks in ion upflow. Here we consider the product of ion density times ion velocity, which is more relevant for the atmospheric loss. As stated before, the orientation of the interplanetary magnetic field is expected to play also here an important role. For investigating the effect of IMF B_y we first consider only events from times when IMF B_z is negative ($B_z < -1.2$ nT) (Sect. 11.4.6.1). Interestingly, sizable upflow rates of $1.5 \cdot 10^{14} \text{ m}^{-2} \text{ s}^{-1}$ are observed by DMSP (840 km altitude) at the zero epoch location. And the peak values are largely independent of the IMF B_y orientation and only weakly of season (see Fig. 11.15). Flow rates of this order are somewhat higher than the rates reported by Pollock et al. (1990) based on DE-1 measurements at 1000 km altitude. Quite interesting is the comparison with the accompanying FACs. We find quite comparable with the SEA applied to the density anomaly, a pair of oppositely directed FACs equatorward and poleward of the upflow peaks. It confirms that the same current and plasma drift configuration in the cusp region is responsible for air upwelling and ion upflow. This provides clear evidence for the close relation between these two upward transport mechanisms.

Upflow events occurring during times when IMF B_z is close to zero ($-1.2 \text{ nT} < B_z < 1.2 \text{ nT}$) were also investigated for completeness (Sect. 11.4.6.2). In these cases the deflections of IMF B_y preceding the ion upflow peaks are larger (see

Fig. 11.14b). The ion upflows are quite similar to the cases of negative IMF B_z (see Fig. 11.16). Just the flow rates are somewhat smaller by about 30%. Overall it seems that the size of IMF B_y plays an important role for the ion upflow rate, at least comparable with the role of negative IMF B_z . In a recent study Li et al. (2011) have investigated the Joule heating rate dependence on the direction of IMF B_y for northward IMF conditions by means of satellite data (DMSP F15) and numerical modeling with the Open Geospace General Circulation Model (OpenGGCM). One of their conclusions is that the spatial size of the area in the cusp that is affected by Joule heating becomes smaller when the IMF B_y component becomes larger. This stronger focusing of the energy input may explain the observed influence of IMF B_y on the upwelling of neutral air and plasma in the cusp region.

11.5.3 Ion Upflow Locations with Respect to Auroral Plasma Flow Topology

In order to bring our observations of neutral gas and air upwelling into a context of auroral current systems, we present schematic patterns of the plasma flow, which are derived from FAC distributions as revealed from CHAMP observations (e.g., Wang et al. 2005; He et al. 2012; Kervalishvili and Lühr 2014).

Figure 11.17 depicts the plasma flow patterns in the Northern Hemisphere for the case of southward IMF B_z and the two orientations of IMF B_y (see also Cowley 2000). As expected for $\text{IMF } B_z < 0$, the two-cell convection pattern emerges with a spatial asymmetry between down and dusk cells, which depends on the orientation of IMF B_y . In case of positive (negative) IMF B_y , the dusk (dawn) cell is the large one of the two-convection patterns as can be seen in Fig. 11.17a (Fig. 11.17b). In the cusp region the plasma drift between Region 1 and Region 0 is mostly westward

Northern Hemisphere, IMF $B_z < 0$

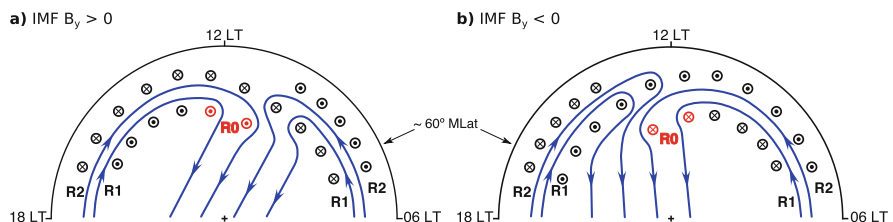


Fig. 11.17 Schematic of the plasma drift topology dependence on the IMF B_y orientation for the southward IMF B_z in the Northern Hemisphere: (a) $\text{IMF } B_y^+$; (b) $\text{IMF } B_y^-$. Arrowed solid lines represent plasma streamlines, circled crosses represent downward currents into the ionosphere, and circled dots represent upward currents out of the ionosphere. Plasma streams are perpendicular to the gradients of FAC density. The Region 0, Region 1, and Region 2 currents are labeled “R0” (red), “R1” (black), and “R2” (black), respectively. Modified after Fig. 10 from Kervalishvili and Lühr (2014)

for positive IMF B_y . In case of negative IMF B_y the opposite plasma drift direction is expected. This helps to understand the large differences in thermospheric wind velocity shown in Fig. 11.11, namely, the high westward zonal wind velocity for positive IMF B_y and the deflection towards poleward wind velocity for negative IMF B_y . We might expect a larger frictional heating for negative IMF B_y because of the larger differential velocity between ions and neutrals. However, no such systematic IMF B_y -dependent effect can be found on the relative density enhancements.

An important result of our investigations is that the upwelling of gas (both neutral and ionized) occurs preferably on the dayside halfway between R1 and R0 FAC sheets. This has been found to be valid for both signs of IMF B_y and also for northward and southward IMF B_z component (though effects are stronger for negative IMF B_z).

Even though air upwelling and ion upflow occur at the same location, we think that different processes are responsible. In case of neutral gas a temperature enhancement is required to start lifting up air parcels. This can be facilitated by the combined actions of field-aligned currents and precipitating electrons, enhancing the conductivity. Differently, in case of ion upflow we think that an enhanced electron temperature is the main driver, setting up an ambipolar electric field that accelerates the ions. Here again high fluxes of precipitating electrons are responsible for the elevated T_e values in the cusp region. Since precipitating electrons play an important role for both processes, it is no surprise that the air upwelling and ion upflow occur preferably in the cusp region where large flows of soft electrons are observed.

11.6 Summary

In this chapter we have investigated the processes that support the upflow and partly escape of air into space at high latitudes, as schematically shown in Fig. 11.18. For the first time the dynamics of neutral and charged particles are investigated together in this project “Role of the geomagnetic field in atmospheric escape from Earth” of the DFG Priority Programme “Planetary Magnetism.” Our studies are mainly based on satellite observations sampled, e.g., by CHAMP and the DMSP fleet.

In the first part we focus on the conditions that lead to an upwelling of neutral air. Most prominent for this phenomenon is the polar cusp region on the dayside. All the geomagnetic field lines reaching out to the magnetopause (boundary between magnetosphere and open space) have their ionospheric footprint in the cusp.

Air upwelling events are identified in CHAMP observations as local peaks in mass density data. With the help of a superposed epoch analyses we could reveal the typical evolution of other parameters during the events. We find peaks collocated with the density anomaly in small-scale field-aligned currents (SSFACs), electron temperature, and upward ion velocity. All these signals are particularly strong in the cusp region. But they show different dependencies on season. While the amplitude of density anomaly is practically constant over the year, most intense SSFACs are observed in summer. Conversely, electron temperature and ion upward drift

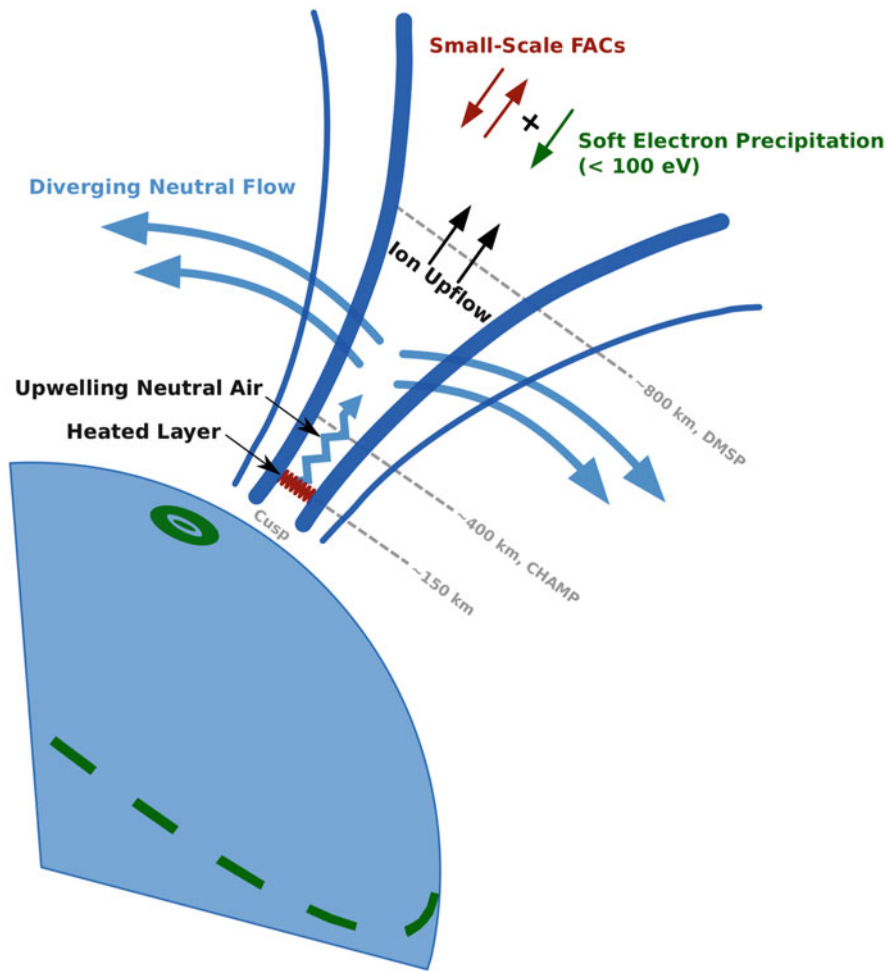


Fig. 11.18 Schematic drawing of the thermospheric heating, neutral air upwelling, and ion upflow, as suggested by the CHAMP and DMSP measurements. Modified after Fig. 4 from Lühr et al. (2004)

peaks are largest in winter. Interestingly, these two quantities show a high degree of correlation between their cusp-related peaks. This suggests that an ambipolar electric field set up by the hot electrons accelerates the ions upward.

We also checked a possible dependence on the IMF B_y component but could not find any effect on the density anomaly. This is quite different for large-scale field-aligned current (LSFAC) accompanying the density peaks. Generally the anomalies occur halfway between oppositely directed R1 and R0 FAC sheets. The direction of the R0 FAC is closely controlled by the IMF B_y orientation and at the same time the R1/R2 pattern is rotated in local time. We find downward R1 (upward R0) for

positive IMF B_y and upward R1 (downward R0) for negative IMF B_y associated with our events. This is the typical FAC configuration bracketing the cusp region. Also the thermospheric wind is strongly influenced by IMF B_y . For positive IMF B_y , peaks in westward wind velocity are accompanying the density anomalies. Conversely, for negative IMF B_y , poleward winds are dominating. All these observations infer a strong Joule heating as the driver for the density anomaly.

Likewise we also investigated the evolution of related quantities accompanying peak in major ion outflows. From a superposed epoch analysis, we revealed that either negative peaks in IMF B_z or enlarged IMF B_y values preceded about 30 min the appearance of upflow events. This again confirms the importance of magnetic reconnection for the escape. Similar to the air upwelling we find highest rates of ion upflow between the R1 and R0 FAC sheets. This qualifies again the cusp region as major source for the events. In case of vertical velocity a clear seasonal dependence emerged with highest value in winter and lowest in summer. But for the ion flow rate (density \times velocity) this dependence largely disappears. This latter quantity is more suitable for describing the atmospheric loss.

In our opinion Joule heating fueled by SSFACs is the major mechanism for driving the air upwelling. In case of ion upflow, we consider an ambipolar electric field set up by hot electrons as an important driver. In both cases intense precipitation of soft electrons (i.e., <100 eV) is needed in addition. These electrons enhance the ionospheric conductivity at the location of density anomaly, and in case of ion upflow facilitate the heating of electron gas. We think that the required contribution of precipitating electrons in both cases is the reason for the collocation of neutral air and ion upwelling.

Acknowledgements The CHAMP and GRACE missions were sponsored by the Space Agency of the German Aerospace Center (DLR) through funds of the Federal Ministry of Economics and Technology. The Center for Space Sciences at the University of Texas at Dallas and the US Air Force are gratefully acknowledged for making available the DMSP thermal plasma data. The authors gratefully acknowledge the use of NASA/GSFC's Space Physics Data Facility's OMNIWeb service and OMNI IMF and Solar wind data. The Deutsche Forschungsgemeinschaft (DFG) supported G. N. Kervalishvili through the Priority Programme "Planetary Magnetism" SPP 1488.

References

- André, M., Cully, C.M.: Low-energy ions: a previously hidden solar system particle population. *Geophys. Res. Lett.* **39**, L03101 (2012). doi:10.1029/2011GL050242
- André, M., Li, K., Eriksson, A.I.: Outflow of low-energy ions and the solar cycle. *J. Geophys. Res. Space Phys.* **120**, 1072–1085 (2015). doi: 10.1002/2014JA020714
- Axford, W.I.: The polar wind and the terrestrial helium budget. *J. Geophys. Res.* **73**, 6855–6859 (1968). doi:10.1029/JA073i021p06855
- Banks, P.M., Holzer, T.E.: The polar wind. *J. Geophys. Res.* **73**, 6846–6854 (1968). doi:10.1029/JA073i021p06846

- Carlson, H.C., Moen, J., Oksavik, K., Nielsen, C.P., McCrea, I.W., Pedersen, T.R., Gallop, P.: Direct observations of injection events of subauroral plasma into the polar cap. *Geophys. Res. Lett.* **33**, L05103 (2006). doi:10.1029/2005GL025230
- Carlson, H.C., Spain, T., Aruliah, A., Skjaeveland, A., Moen, J.: First-principles physics of cusp/polar cap thermospheric disturbances. *Geophys. Res. Lett.* **39**, L19103 (2012). doi:10.1029/2012GL053034
- Clemons, J.H., Hecht, J.H., Salem, D.R., Strickland, D.J.: Thermospheric density in the Earth's magnetic cusp as observed by the Streak mission. *Geophys. Res. Lett.* **35**, L24103 (2008). doi:10.1029/2008GL035972
- Coley, W.R., Heelis, R.A., Hairston, M.R.: Characteristics of high-latitude vertical plasma flow from the defense meteorological satellite program. *J. Geophys. Res.* **111**, A11314 (2006). doi:10.1029/2005JA011553
- Cowley, S.W.H.: Magnetosphere-ionosphere interactions: a tutorial review. In: Ohtani, S.-I., Fujii, R., Hesse, M., Lysak, R.L. (eds.) *Magnetospheric current systems*, pp. 91–106. American Geophysical Union, Washington, DC (2000). doi:10.1029/GM118p0091
- Crowley, G., Knipp, D.J., Drake, K.A., Lei, J., Sutton, E., Lühr, H.: Thermospheric density enhancements in the dayside cusp region during strong by conditions. *Geophys. Res. Lett.* **37**, L07110 (2010). doi:10.1029/2009GL042143
- Demars, H.G., Schunk, R.W.: Thermospheric response to ion heating in the dayside cusp. *J. Atmos. Sol. Terr. Phys.* **69**, 649–660 (2007). doi:10.1016/j.jastp.2006.11.002
- Deng, Y., Fuller-Rowell, T.J., Akmaev, R.A., Ridley, A.J.: Impact of the altitudinal Joule heating distribution on the thermosphere. *J. Geophys. Res.* **116**, A05313 (2011). doi:10.1029/2010JA016019
- Doornbos, E., van den IJssel, J., Lühr, H., Förster, M., Koppenwallner, G.: Neutral density and crosswind determination from arbitrarily oriented multiaxis accelerometers on satellites. *J. Spacecr. Rocket.* **47**, 580–589 (2010). doi:10.2514/1.48114
- Emmert, J.T., Richmond, A.D., Drob, D.P.: A computationally compact representation of magnetic-apex and quasi-dipole coordinates with smooth base vectors. *J. Geophys. Res.* **115**, A08322 (2010). doi:10.1029/2010JA015326
- Engwall, E., Eriksson, A.I., Cully, C.M., André, M., Torbert, R., Vaith, H.: Earth's ionospheric outflow dominated by hidden cold plasma. *Nat. Geosci.* **2**, 24–27 (2009). doi:10.1038/ngeo387
- Förster, M., Rentz, S., Köhler, W., Liu, H., Haaland, S.E.: IMF dependence of high-latitude thermospheric wind pattern derived from CHAMP cross-track measurements. *Ann. Geophys.* **26**, 1581–1595 (2008). doi:10.5194/angeo-26-1581-2008
- Hartman, W.A., Heelis, R.A.: Longitudinal variations in the equatorial vertical drift in the topside ionosphere. *J. Geophys. Res.* **112**, A03305 (2007). doi:10.1029/2006JA011773
- He, M., Vogt, J., Lühr, H., Sorbalo, E., Blagau, A., Le, G., Lu, G.: A high-resolution model of field-aligned currents through empirical orthogonal functions analysis (MFACE). *Geophys. Res. Lett.* **39**, L18105 (2012). doi:10.1029/2012GL053168
- Kervalishvili, G.N., Lühr, H.: The relationship of thermospheric density anomaly with electron temperature, small-scale FAC, and ion up-flow in the cusp region, as observed by CHAMP and DMSP satellites. *Ann. Geophys.* **31**, 541–554 (2013). doi:10.5194/angeo-31-541-2013
- Kervalishvili, G.N., Lühr, H.: Climatology of zonal wind and large-scale FAC with respect to the density anomaly in the cusp region: seasonal, solar cycle, and IMF B_y dependence. *Ann. Geophys.* **32**, 249–261 (2014). doi:10.5194/angeo-32-249-2014
- King, J.H., Papitashvili, N.E.: Solar wind spatial scales in and comparisons of hourly wind and ACE plasma and magnetic field data. *J. Geophys. Res.* **110**, A02104 (2005). doi:10.1029/2004JA010649
- Lemaire, J., Peterson, W.K., Chang, T., Schunk, R.W., Barakat, A.R., Demars, H.G., Khazanov, G.V.: History of kinetic polar wind models and early observations. *J. Atmos. Sol. Terr. Phys.* **69**, 1901–1935 (2007). doi:10.1016/j.jastp.2007.08.011
- Li, W., Knipp, D., Lei, J., Raeder, J.: The relation between dayside local Poynting flux enhancement and cusp reconnection. *J. Geophys. Res.* **116**, A08301 (2011). doi:10.1029/2011JA016566

- Liu, H., Lühr, H., Henize, V., Köhler, W.: Global distribution of the thermospheric total mass density derived from CHAMP. *J. Geophys. Res.* **110**, A04301 (2005). doi:10.1029/2004JA010741
- Liu, H., Lühr, H., Watanabe, S., Köhler, W., Henize, V., Visser, P.: Zonal winds in the equatorial upper thermosphere: Decomposing the solar flux, geomagnetic activity, and seasonal dependencies. *J. Geophys. Res.* **111**, A07307 (2006). doi:10.1029/2005JA011415
- Liu, R., Lühr, H., Ma, S.-Y.: Storm-time related mass density anomalies in the polar cap as observed by CHAMP. *Ann. Geophys.* **28**, 165–180 (2010). doi:10.5194/angeo-28-165-2010
- Lühr, H., Marker, S.: High-latitude thermospheric density and wind dependence on solar and magnetic activity. In: Lübben, F.-J. (ed.) *Climate And Weather of the Sun-Earth System (CAWSES): Highlights from a Priority Program*, pp. 189–206. Springer, Dordrecht (2013). doi:10.1007/978-94-007-4348-9
- Lühr, H., Warnecke, J., Rother, M.K.A.: An algorithm for estimating field-aligned currents from single spacecraft magnetic field measurements: a diagnostic tool applied to Freja satellite data. *Geosci. Remote Sens.* **34**, 1369–1376 (1996). doi:10.1109/36.544560
- Lühr, H., Rother, M., Köhler, W., Ritter, P., Grunwaldt, L.: Thermospheric up-welling in the cusp region: evidence from CHAMP observations. *Geophys. Res. Lett.* **31**, L06805 (2004). doi:10.1029/2003GL019314
- Lühr, H., Rentz, S., Ritter, P., Liu, H., Häusler, K.: Average thermospheric wind patterns over the polar regions, as observed by CHAMP. *Ann. Geophys.* **25**, 1093–1101 (2007). doi:10.5194/angeo-25-1093-2007
- Miyake, W., Mukai, T., Kaya, N.: On the evolution of ion conics along the field line from EXOS-D. *J. Geophys. Res.* **98**, 11127–11134 (1993). doi:10.1029/92JA00716
- Pollock, C.J., Chandler, M.O., Moore, T.E., Waite Jr., J.H., Chappell, C.R., Gurnett, D.A.: A survey of upwelling ion event characteristics. *J. Geophys. Res.* **95**, 18969–18980 (1990). doi:10.1029/JA095iA11p18969
- Prölss, G.W.: *Physics of the Earth's Space Environment: An Introduction* (translated by: Bird, M. K.). Springer, Berlin (2004). doi:10.1007/978-3-642-97123-5 .
- Prölss, G.W.: Electron temperature enhancement beneath the magnetospheric cusp. *J. Geophys. Res.* **111**, A07304 (2006). doi:10.1029/2006JA011618
- Reigber, Ch., Lühr, H., Schwintzer, P.: CHAMP mission status. *Adv. Space Res.* **30**, 129–134 (2002). doi:10.1016/S0273-1177(02)00276-4
- Rentz, S., Lühr, H.: Climatology of the cusp-related thermospheric mass density anomaly, as derived from CHAMP observations. *Ann. Geophys.* **26**, 2807–2823 (2008). doi:10.5194/angeo-26-2807-2008
- Rich, F.J., Hairston, M.: Large-scale convection patterns observed by DMSP. *J. Geophys. Res.* **99**, 3827–3844 (1994). doi:10.1029/93JA03296
- Ritter, P., Lühr, H., Doornbos, E.: Substorm-related thermospheric density and wind disturbances derived from CHAMP observations. *Ann. Geophys.* **28**, 1207–1220 (2010). doi:10.5194/angeo-28-1207-2010
- Rother, M., Schlegel, K., Lühr, H.: CHAMP observation of intense kilometer-scale field-aligned currents, evidence for an ionospheric Alfvén resonator, *Ann. Geophys.* **25**, 1603–1615 (2007). doi:10.5194/angeo-25-1603-2007
- Rother, M., Schlegel, K., Lühr, H., Cooke, D.: Validation of CHAMP electron temperature measurements by incoherent scatter radar data. *Radio Sci.* **45**, RS6020 (2010). doi:10.1029/2010RS004445
- Sadler, F.B., Lessard, M., Lund, E., Otto, A., Lühr, H.: Auroral precipitation/ion upwelling as a driver of neutral density enhancement in the cusp. *J. Atmos. Sol. Terr. Phys.*, **87–88**, 82–90 (2012). doi:10.1016/j.jastp.2012.03.003
- Tapley, B.D., Bettadpur, S., Watkins, M., Reigber, C.: The gravity recovery and climate experiment: mission overview and early results. *Geophys. Res. Lett.* **31**, L09607 (2004). doi:10.1029/2004GL019920
- Thayer, J.P., Semeter, J.: The convergence of magnetospheric energy flux in the polar atmosphere. *J. Atmos. Sol. Terr. Phys.* **66**, 807–824 (2004). doi:10.1016/j.jastp.2004.01.035

- Thayer, J.P., Killeen, T.L., McCormac, F.G., Tschan, C.R., Ponthieu, J.-J., Spencer, N.W.: Thermospheric neutral wind signatures dependent on the east-west component of the interplanetary magnetic field for northern and southern hemispheres, as measured from dynamics explorer-2. *Ann Geophys.* **5A**, 363–368 (1987)
- Wahlund, J.E., Opgenoorth, H.J., Haggstrom, I., Winser, K.J., Jones, G.O.L.: EISCAT observations of topside ionospheric ion outflows during auroral activity: revisited. *J. Geophys. Res.* **97**, 3019–3037 (1992). doi:10.1029/91JA02438
- Wang, H., Lühr, H., Ma, S.Y.: Solar zenith angle and merging electric field control of field-aligned currents: a statistical study of the southern hemisphere. *J. Geophys. Res.* **110**, A03306 (2005). doi:10.1029/2004JA010530
- Watermann, J., Stauning, P., Lühr, H., Newell, P.T., Christiansen, F., Schlegel, K.: Are small-scale field-aligned currents and magnetosheath-like particle precipitation signatures of the same low-altitude cusp? *Adv. Space Res.* **43**, 41–46 (2009). doi:10.1016/j.asr.2008.03.031
- Yau, A.W., Peterson, W.K., Shelley, E.G.: Quantitative parameterization of energetic ionospheric ion outflow. In: *Modeling Magnetospheric Plasma*, Geophysical Monograph, vol. 44, p. 211. American Geophysical Union, Washington, DC (1988)
- Yau, A.W., Abe, T., Peterson, W.K.: The polar wind: recent observations. *J. Atmos. Sol. Terr. Phys.* **69**, 1936–1983 (2007). doi:10.1016/j.jastp.2007.08.010

Chapter 12

Mars’ Crustal Magnetic Field

Achim Morschhauser, Foteini Vervelidou, Paul Thomas, Matthias Grott,
Vincent Lesur, and Stuart A. Gilder

Abstract Fossil magnetic fields within the Martian crust record the history of the planet’s ancient dynamo and hence retain valuable information on the thermal and chemical evolution of Mars. In order to decode this information, we have derived a spherical harmonic model of the crustal magnetic field. This model was derived from satellite vector magnetometer data, and allows to study the crustal magnetic field at high resolution down to surface altitudes. Based on this model, we calculate the required magnetization of the Martian crust, and discuss how the resulting strong magnetization might be explained. Further, we study the magnetization of impact craters and volcanoes, and conclude that the Martian core dynamo shut down most probably in the Noachian, at about 4.1 Gyr ago. Finally, we address the derivation of magnetic paleopole positions. In a first step, we use synthetic tests in order to outline under which constraints paleopole positions can be determined from satellite measurements. In a second step, we use these insights to present a scheme to estimate paleopole positions including an assessment of their underlying uncertainties.

12.1 Mars Magnetic Field

A wide variety of magnetic field configurations are observed for the planets in our Solar System (Schubert and Soderlund 2011). These configurations are intimately linked to the internal thermal and chemical state of the planet as well as its evolution.

A. Morschhauser (✉) • F. Vervelidou

GFZ German Research Centre for Geosciences, Telegrafenberg, 14473 Potsdam, Germany
e-mail: mors@gfz-potsdam.de; foteini.vervelidou@gfz-potsdam.de

P. Thomas • M. Grott

Institute of Planetary Research, German Aerospace Center, Berlin, Germany

V. Lesur

Institut de Physique du Globe de Paris, Sorbonne Paris Cité, Université Paris-Diderot, Paris, France

S.A. Gilder

Department of Earth and Environmental Sciences, Ludwig Maximilians Universität, Theresienstrasse 41, 80333 München, Germany

In this chapter, we focus on the magnetic field of Mars which is dominated by the field of its remanently magnetized crust. This type of magnetization is particularly useful, as it serves as a magnetic memory of a planet (e.g., Vine and Matthews 1963). Hence, many attempts have been made to decipher the magnetic signature of the Martian crust. In order to address some of the most important open questions related to the Martian magnetic field, our approach was to derive a model of the magnetic field of the Martian crust that can be downward-continued to the Martian surface without leading to spurious and unrealistic magnetic field signatures (Morschhauser et al. 2014). Such a stable model facilitates the interpretation of magnetic anomalies by allowing to study the magnetic field at altitudes below the satellite orbit, at least within the error and resolution limits of the model.

12.1.1 Current Knowledge

For decades, it was disputed whether Mars currently possesses a core dynamo (Dolginov 1978; Russell 1978). Eventually, this dispute was resolved in 1997 when the satellite orbiter Mars Global Surveyor (Albee et al. 1998) provided evidence for a very low global dipole moment in combination with relatively strong magnetic fields of crustal origin (Acuña et al. 1999). In consequence, it was concluded that Mars currently does not possess an active core dynamo and that its crust was magnetized in an ancient field of internal origin. Further, and with more data becoming available, it was observed that the distribution of crustal field intensities follows the topographic dichotomy (Connerney et al. 2001), with the strongest observed fields being located over the old Noachian (3.7–4.1 Gyr ago) terrain of Terra Cimmeria and Terra Sirenum in the Southern Hemisphere (Acuña et al. 1999). In addition, it was found that the largest visible impact basins (Hellas, Isidis, and Argyre) as well as the largest volcanic provinces (Tharsis and Elysium) cannot be related to any significant crustal fields (e.g., Acuña et al. 1999). Still, many questions remain unanswered, and some of these are summarized below.

12.1.2 Open Questions

Possibly the most disputed topic is the timing of the Martian core dynamo shutdown: On the one hand, it was suggested that the Martian core dynamo died at the end of the Noachian period, shortly after the largest visible impact craters formed (Acuña et al. 1999; Lillis et al. 2008, 2013a). This interpretation is supported mainly by the study of the magnetic fields related to impact craters, which may erase or create remanent magnetization, depending on the state of the core dynamo at the time of their formation (e.g., Lillis et al. 2013b). On the other hand, the magnetic field signature of some volcanoes is not in accordance with this scenario, and a later

shutdown of the dynamo has been suggested (Lillis et al. 2006; Langlais et al. 2004; Hood et al. 2010).

Finally, we address the question of Martian paleopoles. The study of paleopoles may reveal information about the dynamics of the ancient core dynamo, about true polar wander due to the emplacement of the massive Tharsis rise (e.g., Sprenke et al. 2005), or about apparent polar wander due to a suggested phase of early plate tectonics (e.g., Sleep 1994; Connerney et al. 1999). Indeed, many different paleopole locations have been suggested for Mars (c.f. Fig. 8 of Milbury et al. 2012), which support both pole reversals and polar wander. However, little effort has been made to address the robustness of these paleopole locations. Here, we investigate under which conditions the estimation of paleopole positions from satellite measurements of the magnetic field can be accurate, and we show that the accuracy of such estimations crucially depends on the validity of the implicit or explicit assumptions about the sources of the magnetic field. Based on these conclusions, we provide a scheme to estimate paleopole positions for Mars, along with their uncertainty.

12.2 Modeling the Crustal Magnetic Field of Mars

Although much has been learned from studying the Mars Global Surveyor magnetic field data, a model of the magnetic field of the Martian crust is necessary to better separate the crustal magnetic field from fields of external origin. In addition, a model of the crustal field allows one to project the field to a unique altitude, and to downward-continue the field to lower altitudes. This in turn enables one to better address many of the open questions related to the Martian magnetic field. However, downward-continuation is very sensitive to external field contributions leaking into the model, and dedicated techniques have to be used in order to handle these external fields as best as possible. Here, we have used such techniques to derive a stable model of the crustal magnetic of high resolution which is based on a selection of all Mars Global Surveyor data and which is based on an expansion of spherical harmonics. The derivation of this model is shortly presented below, and the interested reader may find further details in Morschhauser et al. (2014) and Morschhauser (2016).

12.2.1 Data Selection

Our model of the crustal magnetic field of Mars is based on a selection of the full dataset as recorded by the vector fluxgate magnetometers of Mars Global Surveyor (Albee et al. 2001). This dataset can be grouped according to different mission phases: the initial aerobraking and science phase (AB/SPO) and the mapping phase (MPO). For the AB/SPO phase, the orbit was highly elliptical, with a periapsis down

to 125 km (Albee et al. 2001). For this mission phase, we select only dayside data below 200 km altitude, and nightside data below the minimum mapping phase orbit altitude of 348 km, resulting in 0.29 million data points. The subsequent MPO phase was highly circular with a mean altitude of 400 km, sun synchronous, and almost polar. For this dataset, we reject all dayside data due to the increased influence of solar-wind-induced currents. Further, we select one data point every 80 km on a projected surface track, resulting in 2.58 million data points. This selection is necessary in order to decrease the computational cost of the inversion.

12.2.2 Model Description

We model the magnetic field of Mars in terms of its scalar potential due to internal and external sources. This is a valid approach, if no magnetic sources are present at the location of magnetic field measurements (Blakely 1995). Hence, our model is described by the scalar potential

$$V(r, \theta, \phi, t) = V_{\text{int}}(r, \theta, \phi) + \begin{cases} V_{\text{ext},n}(r, \theta, \phi), & t \in t_{\text{night}} \\ V_{\text{ext},d}(r, \theta, \phi), & t \in t_{\text{day}}. \end{cases} \quad (12.1)$$

and the magnetic field at any altitude can be calculated from (Blakely 1995, p. 2)

$$\mathbf{B} = -\nabla V. \quad (12.2)$$

Here, we expand Eq. (12.1) in terms of spherical harmonic (SH) functions Y_l^m of degree l and order m , i.e.,

$$V_{\text{int}} = R \sum_{l=1}^{L_{\text{int}}} \sum_{m=-l}^l \left(\frac{R}{r}\right)^{l+1} g_l^m Y_l^m(\theta, \phi), \quad (12.3)$$

and

$$V_{\text{ext},d/n} = R \sum_{l=1}^{L_{\text{int},d/n}} \sum_{m=-l}^l \left(\frac{r}{R}\right)^l h_l^m Y_l^m(\theta, \phi), \quad (12.4)$$

where g_l^m and h_l^m are the respective expansion coefficients, $R = 3393.5$ km is the model's reference radius, and (r, θ, ϕ) are spherical coordinates. Here, the spherical harmonic functions of negative order m are even in ϕ . Further, a different external potential is used for the day- and nightside as the characteristics of the respective external fields differ significantly (Olsen et al. 2010). Moreover, we have chosen

$L_{\text{int}} = 110$, $L_{\text{ext},d} = 5$, and $L_{\text{ext},n} = 10$ as maximum degree and order for the spherical harmonic expansion of the internal and external day- and nightside potentials, respectively. In addition, we assume a static internal potential V_{int} and ignore seasonal variations of the external potential V_{ext} . As a consequence, the respective expansion coefficients are constant.

We invert the Mars Global Surveyor data by minimizing the data misfit using an iteratively reweighted least-squares algorithm (Farquharson and Oldenburg 1998) in order to approximate a modified Huber norm (Huber 1964). Such a robust norm suppresses the influence of data outliers and improves the fit to more reliable data. However, a Huber norm could not be used for the AB/SPO data as some of the strong field variations cannot be fit by the model. Therefore, such variations would have been treated as data outliers by the Huber norm. Further, we weight the MPO data according to their temporal variations in dependence of their location. For the AB/SPO orbits, however, data density is too low for such an estimation. Therefore, these data are weighted based on their misfit to a preliminary model.

Apart from minimizing the misfit to the data, we additionally minimize the roughness of the surface field, measured by an approximation to the surface integral of the absolute horizontal gradient of the vertically down component of the crustal field at surface altitude. For this purpose, an L1 norm is used in combination with an iteratively reweighted least-squares algorithm (Farquharson and Oldenburg 1998). The magnetic field model derived using this norm supports locally strong field gradients which are supposed to be present on Mars. Regarding the trade-off between the minimization of the misfit and the model complexity, we used an L-curve (Aster et al. 2013) to determine a value that minimizes the model roughness and that minimally influences the misfit between model and data. With this approach, a sufficiently damped and stable model is obtained which still allows for comparatively strong local field gradients.

12.2.3 The Predicted Surface Magnetic Field

The crustal magnetic field of Mars as predicted by the model at the mean surface altitude of 3393.5 km is shown in Fig. 12.1 for the horizontal north (X), east (Y), and vertical down (Z) components as well as the total field intensity (F) (from bottom to top). According to this map, the major known characteristics of the Martian magnetic field are well reproduced. For example, the strongest fields are located in the Southern Hemisphere, and reach about $12 \mu\text{T}$ in field intensity. Also, the magnetic field over most of the Northern Hemisphere and over the largest visible impact craters (black dashed ellipses) is below the estimated noise level of 50nT at surface altitude.

Compared to previously published maps of the crustal magnetic field, which have usually been plotted at the satellite orbit altitudes (e.g., Langlais et al. 2004; Arkani-Hamed 2004; Whaler and Purucker 2005; Lillis et al. 2008), much more

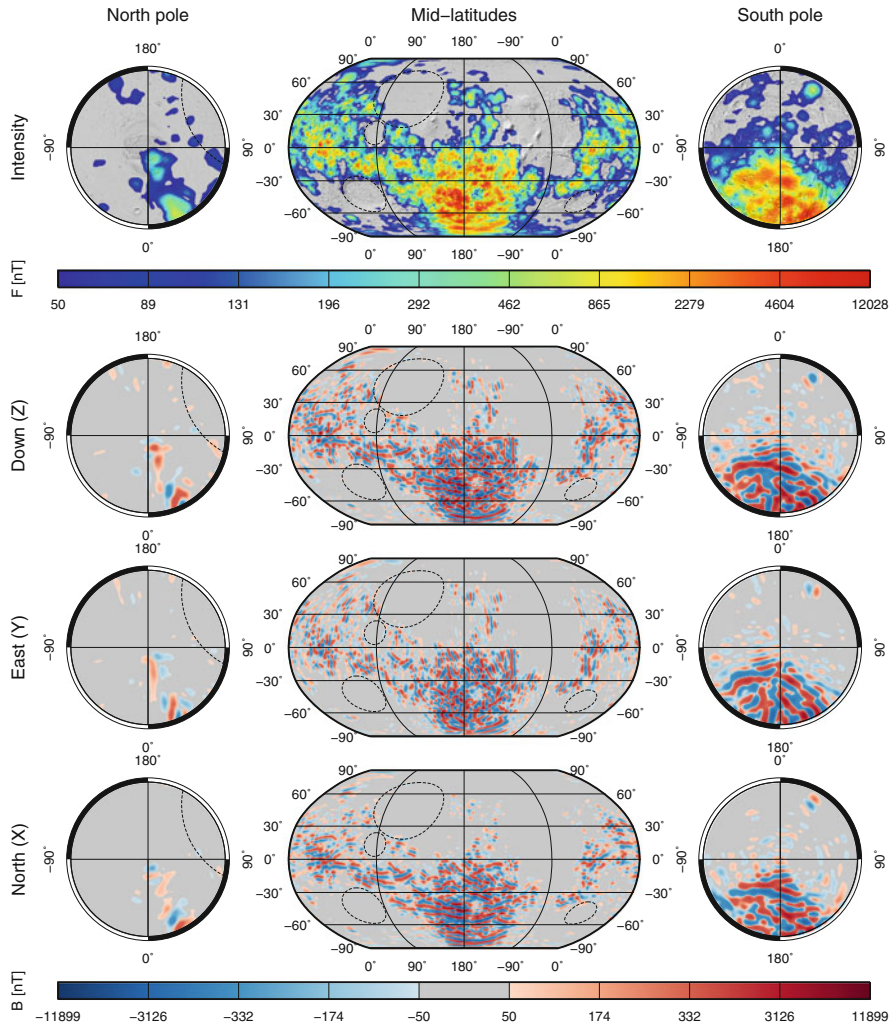


Fig. 12.1 Map of the downward-continued crustal magnetic field at the mean surface altitude, corresponding to a radius of 3793.5 km. *From bottom to top*, the horizontal north (X), east (Y), and vertical down (Z) components as well as the total field intensity (F) are shown. *From left to right*, the North Pole, midlatitudes, and the South Pole are presented. The polar views are in stereographic projection whereas the global maps are shown in Robinson projection. In addition, major impact basins are indicated by dashed lines (*from left to right*: Hellas, Isidis, Planitia, and Argyre), and the shaded Mars Orbiter Laser Altimeter (MOLA) topography is overlaid on the map of the field intensity (F) (*top*). Originally published as Fig. 7.4 of Morschhauser (2016)

small-scale features are visible. For example, a region of very low fields was discovered within Terra Sirenum (centered $166^{\circ}\text{W}/44^{\circ}\text{S}$) where the surface field intensity (F) decreases to about 70 nT. Interestingly, this area matches the location and extension of a previously proposed multiring basin (Schultz et al. 1982).

12.3 The Magnetization of Mars

As mentioned above, it is well known that inferring the magnetization distribution from magnetic field measurements suffers from inherent non-uniqueness (see, e.g., Runcorn 1975; Lesur and Jackson 2000; Maus and Haak 2002). Even perfect magnetic field measurements of infinite spectral content would not be sufficient for reconstructing the underlying magnetization. This is due to the fact that only part of the magnetization gives rise to an observable magnetic field. Therefore, the remaining part of the magnetization can only be reconstructed by means of a priori assumptions about the sources.

We have derived a map of the Martian crustal magnetization where the only assumptions on the sources are imposed by the limitations of magnetic field satellite measurements (Vervelidou et al. 2017b). In particular, these assumptions concern the truncation of the spectral content of the measurements to obtain an acceptable signal-to-noise ratio, and the fact that only the vertically integrated magnetization can be obtained from magnetic field data. In this way, we are able to recover specifically the part of the magnetization that can be reconstructed from the magnetic field measurements (Gubbins et al. 2011), whereas most previous studies did not distinguish between the part of the magnetization that gives rise to an observable magnetic field and the part that does not (see, e.g., Connerney et al. 1999; Langlais et al. 2004; Whaler and Purucker 2005).

12.3.1 Method

Following the work of Gubbins et al. (2011) (but see also, e.g., Mayer and Maier 2006; Gerhards 2011), we decompose the magnetization distribution \mathbf{M} into the part \mathcal{I} that generates an observable magnetic field and into the part $\mathcal{E} + \mathcal{T}$ that does not, i.e.,

$$\mathbf{M} = \mathcal{I} + \mathcal{E} + \mathcal{T}, \quad (12.5)$$

where \mathcal{E} and \mathcal{T} are the parts of the magnetization that produce a magnetic field observable only below and within the sources, respectively. This decomposition is based on an expansion of the magnetization in terms of real vector spherical harmonics with

$$\begin{aligned} \mathcal{I} &= \sum_{m,l} g_{\mathcal{I},l}^m \mathbf{Y}_{l,l-1}^m, \\ \mathcal{E} &= \sum_{m,l} g_{\mathcal{E},l}^m \mathbf{Y}_{l,l+1}^m, \\ \mathcal{T} &= \sum_{m,l} g_{\mathcal{T},l}^m \mathbf{Y}_{l,l}^m, \end{aligned} \quad (12.6)$$

where $\mathbf{Y}_{l,l-1}^m$, $\mathbf{Y}_{l,l+1}^m$, and $\mathbf{Y}_{l,l}^m$ are the three types of real vector spherical harmonics corresponding to \mathcal{I} , \mathcal{E} , and \mathcal{T} , respectively, and $g_{\mathcal{I},l}^m$, $g_{\mathcal{E},l}^m$, and $g_{\mathcal{T},l}^m$ are the corresponding real expansion coefficients of order m and degree l (Gubbins et al. 2011).

Now, the expansion coefficients $g_{\mathcal{I},l}^m$ which describe the magnetization giving rise to an observable magnetic field above the magnetic sources can be calculated from the expansion coefficients of a spherical harmonic model of the crustal magnetic field, such as the one proposed in Sect. 12.2 of this chapter. In order to do so, we use

$$\begin{aligned} V_{\text{int}}(\mathbf{r}) &= \frac{\mu_0}{4\pi} \int_{\Omega'} \mathbf{M}(\mathbf{r}') \nabla' \left(\frac{1}{|\mathbf{r} - \mathbf{r}'|} \right) d\Omega' \\ &= \frac{\mu_0}{4\pi} \int_{\Omega'} \mathcal{I}(\mathbf{r}') \nabla' \left(\frac{1}{|\mathbf{r} - \mathbf{r}'|} \right) d\Omega', \end{aligned} \quad (12.7)$$

(Blakely 1995; Gubbins et al. 2011) where μ_0 is the magnetic permeability of vacuum, and equate this equation to Eq.(12.3). The integration of Eq.(12.7) requires some assumptions on the magnetized volume Ω' and the behavior of the magnetization along the radial direction. Here, we assume that the magnetization \mathbf{M} is confined in a spherical layer of constant thickness, varies laterally but not vertically, and can be fully reconstructed by a truncated series of spherical harmonics. Then, we obtain

$$g_{\mathcal{I},l}^m = \frac{(l+2)}{\mu_0} \sqrt{\frac{2l+1}{l}} \left[1 - \left(1 - \frac{d}{R} \right)^{l+2} \right]^{-1} g_l^m \quad (12.8)$$

where $R - d$ and R define the lower and upper boundaries of the magnetized layer. This magnetization generates the observable magnetic field and associated potential of internal origin, V_{int} . It is hereafter called the visible magnetization.

12.3.2 Results

With the help of Eq.(12.8), we derive the visible magnetization according to our crustal field model of Mars (Sect. 12.2, Morschhauser et al. 2014). For this purpose, we assume that the magnetic minerals on Mars are located within a magnetic layer of 40 km thickness (see, e.g., Langlais et al. 2004; Whaler and Purucker 2005). The resulting magnetization distribution is shown in Fig. 12.2, and we observe that its main pattern follows closely that of the lithospheric magnetic field model (Fig.12.1). Still, regions do exist where the visible magnetization is significantly different from the crustal field. As an example, both the corresponding crustal magnetic field and the visible magnetization are shown in Fig. 12.3 over the westernmost part of Terra Sabaea.

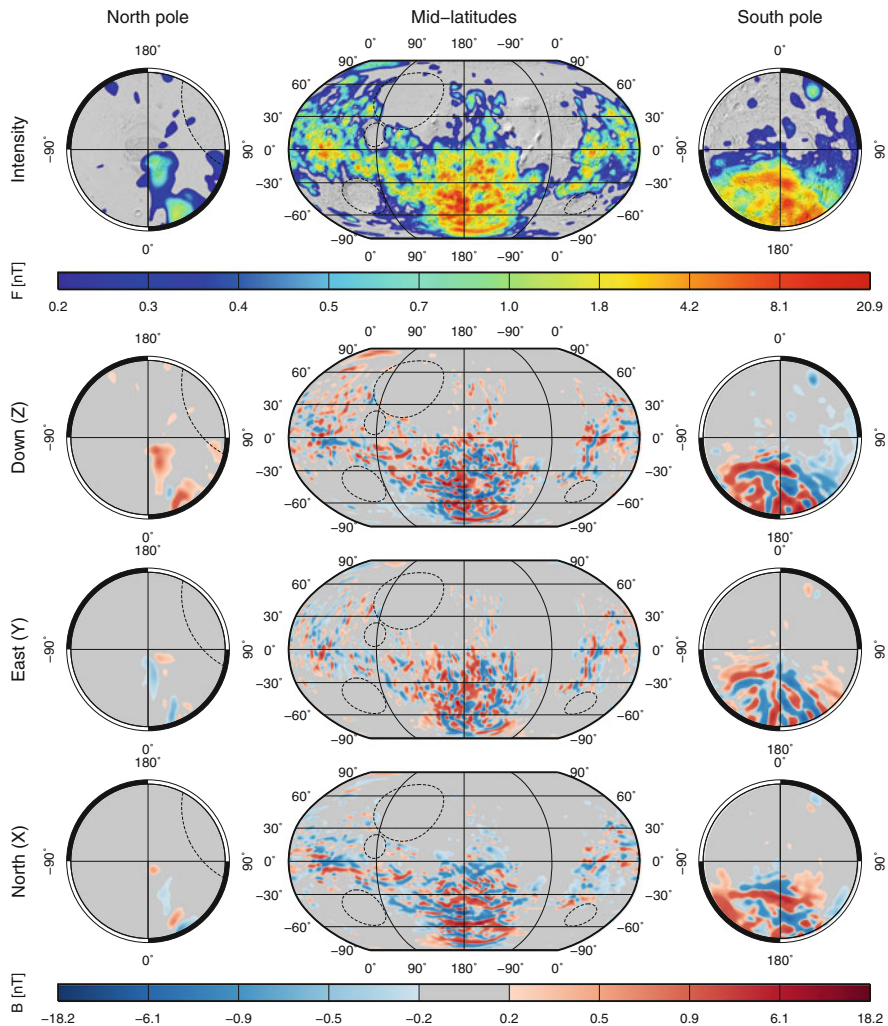


Fig. 12.2 The visible magnetization of Mars. *From bottom to top*, the horizontally north (X), east (Y), and vertically down (Z) components as well as the magnetization intensity (F) are shown. For more details, see caption of Fig. 12.1. Originally published as Fig. 11.1 of Morschhauser (2016)

Concerning the magnetization strength, we obtain a mean value of 0.7 A/m with a standard deviation of 1.3 A/m and a maximum value of 20 A/m . These values are very similar to the ones obtained by Whaler and Purucker (2005) who also assumed a magnetized thickness of 40 km . Further, the magnetizations of the horizontally north (X), east (Y), and vertically down (Z) components lie between -14.8 and 11.7 A/m , -6.7 and 9.5 A/m , and -18.2 and 12.5 A/m , respectively. These values are close to the -22 and 17 A/m of Purucker et al. (2000) who assumed a purely

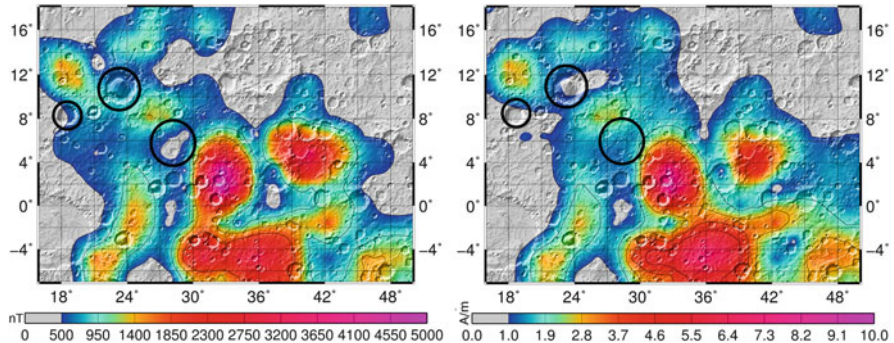


Fig. 12.3 *Left:* The intensity of the lithospheric magnetic field model of Morschhauser et al. (2014) over a selected region, plotted at the mean surface altitude of 3393.5 km. *Right:* The corresponding visible magnetization model over the same region, assuming a 40 km thick magnetized layer (Hammer projection). *Black circles* highlight impact craters that differ in their lithospheric magnetic field signatures and visible magnetizations

radial magnetization and a 50 km thick magnetized crust. Compared to the work of Langlais et al. (2004), we have found comparable, but slightly larger values.

12.3.3 Magnetic Minerals

The question arises as to which minerals carry the magnetic remanence and what is their extent in depth. Dunlop and Arkani-Hamed (2005) treated the problem using models of the thermal evolution of Mars and calculated the resulting magnetic layer thicknesses (Curie point isotherms) for different common magnetic minerals and their domain states. Then, Dunlop and Arkani-Hamed (2005) investigated which of these minerals can best account for an overall magnetization of 20 A/m (Sect. 12.3, Connerney et al. 1999). They found that a magnetic layer thickness of 40–50 km consisting of 0.3% by volume of single-domain magnetite is the most likely carrier of the remanence. Although pyrrhotite (iron sulfide) commonly occurs in Martian meteorites (Rochette et al. 2001), Dunlop and Arkani-Hamed (2005) favored magnetite over pyrrhotite because the saturation remanence of pyrrhotite is 80% weaker than magnetite and pyrrhotite's Curie temperature is 45% lower (325 °C for pyrrhotite, 580 °C for magnetite). Their conclusion was subsequently substantiated by Möbbauer and alpha particle X-ray spectroscopy from basement rocks in the Gusev crater on Mars that identified (titano)magnetite as the main ferrimagnetic mineral (Morris et al. 2006; McSween et al. 2008).

However, it is still uncertain as to how to account for the high remanent intensities. For example, Dunlop and Arkani-Hamed (2005) did not explain why single-domain ferrimagnetic minerals should be abundant at depth, where slow cooling will favor the growth of larger grains. One way around this problem is to

recall that pressure makes multidomain grains more single-domain like and that the higher the titanium concentration in titanomagnetite the greater the pressure enhancement effect on the magnetization (Gilder and Le Goff 2008). On the other hand, Mars has a relatively low pressure gradient (70 km/GPa), meaning that only the remanence of high-titanium titanomagnetite would become significantly amplified, with the trade-off that Curie temperature decreases with increasing titanium concentration. Another problem is that Dunlop and Arkani-Hamed (2005) assumed an Earth-like magnetic field of 50 μT at the surface (c.f. their Table 3) for Mars to produce the thermal remanent magnetizations in their models. They cited paleointensity results from non-Martian meteorites and estimates for Earth to derive this value. The problem is that the effect of even low pressures (<2 GPa) from shock or decompression will decrease paleointensity estimates by 10–20%/GPa (Volk and Gilder 2016) and that low-temperature cycling of remanence in space will further decrease paleointensity estimates (Dunlop 2003; Volk et al. 2016). Hence, paleointensity estimates derived from meteorites can only be taken as lower limits. In addition, simple scaling laws (Christensen et al. 2009; Laneuville et al. 2013) suggest that the field intensity depends on the heat flux at the core-mantle boundary, and this heat flux peaked at the time when the Martian core dynamo was probably active (e.g., Morschhauser et al. 2011). Another point to consider is that even if the dipole moment of Mars was only half as strong as Earth's present dipole moment, the surface field would still be three times that of Earth, simply due to the lower absolute distance to the core. Because thermal magnetic remanence acquisition is linear in ambient fields to 200 μT , intensities in the Martian crust could be two to four times higher than previously considered, which would serve to reduce the volume/depth distribution of the remanence carriers. Thus, it seems like the best explanation for the strong magnetic anomalies on Mars that higher surficial magnetic fields from the Martian dynamo had produced stronger magnetic remanences.

12.4 Timing of the Core Dynamo

The timing and dynamics of the Martian core dynamo have profound implications for the planetary evolution. For example, the thermal and chemical state of the core and heat transport mechanisms in the mantle directly influence the core dynamo. In turn, these parameters are a key in understanding the planet's formation and evolution. Furthermore, it has been suggested that the cessation of the Martian core dynamo triggered a climate change on Mars as the atmosphere could no longer be protected from atmospheric erosion (e.g., Jakosky and Phillips 2001; Chassefière and Leblanc 2004).

In order to constrain the timing of the Martian core dynamo, a process that at the same time resets the surface age as well as the magnetization of the crust needs to be considered. Both volcanism and impacts fulfill these constraints, and have extensively been studied for this purpose in many studies (e.g., Lillis et al.

2006; Johnson and Phillips 2005). In comparison to these studies, the stability and high resolution of our model of the Martian magnetic field allow us to study the magnetic field signature of volcanoes and impact craters at surface altitude. As a consequence, anomalies of smaller spatial scale can be analyzed, the corresponding visible magnetization as derived in Sect. 12.3 can be investigated, and the magnetic field and magnetization may directly be linked to the considered structures.

12.4.1 Impact Craters

Considering the magnetic field signature of impact craters as a proxy for their magnetization has led several studies to suggest that the Martian dynamo shut down at 4.1 Gyr ago (e.g., Lillis et al. 2008). For these studies, the main problems are the non-uniqueness issue of inferring the magnetization from magnetic field measurements, and the relatively high satellite orbit which damps the small-wavelength contributions to the field. As a solution, Lillis et al. (2013a) suggested a stochastic approach by using a forward model to assign magnetization probabilities to selected craters. In our study, we focus on the information that can be extracted by our visible magnetization model (Vervelidou et al. 2017b). Henceforth, by the term magnetization, we refer to the visible magnetization, \mathcal{I} (Sect. 12.3).

In a first step, we inspect the magnetization signature of the craters selected by Lillis et al. (2013a). As an example, the magnetization intensity of Isidis is shown in Fig. 12.4. The left panel of this figure shows a map of the magnetization intensity, and the right panel shows the normalized circumferential average of the magnetization intensity in dependence of the distance to the crater's center. This figure shows that the magnetization near the crater's center is demagnetized to 40% of the mean magnetization at the crater's edge.

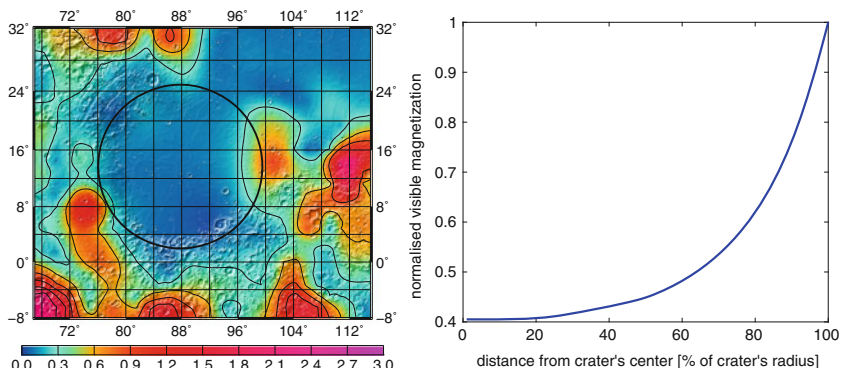


Fig. 12.4 *Left panel:* The visible magnetization, \mathcal{I} , in A/m, over the region around the Isidis impact basin. Projection is Mercator. *Right panel:* The normalized circumferential average of the visible magnetization intensity as a function of distance to the impact basin's center

In a second step, we combine the normalized magnetization circumferential profiles of the craters and their estimated crater ages. This is done separately for the craters dated by Frey (2008), Robbins et al. (2013), and Werner (2008). Then, we have rejected those craters whose magnetic signature is apparently affected by processes that are unrelated to the crater, e.g., other large craters or volcanoes. Finally, the results are shown in Fig. 12.5, where the ordinate shows age and the profiles are indicated by the vertical colored lines. Craters that are more magnetized (redder) at the crater's center than at their rim will be considered magnetized, and vice versa.

Looking at the compilation of craters dated by Frey (2008) (upper panel), we obtain both demagnetized craters (Acidalia (Ac), Chryse (Cr), CT3-F (F)) and magnetized craters (Hematite (Hm), Ares(Ar)) for ages between 4.1 and 4.2 Gyr ago. In particular, the craters Hematite (Hm) and Chryse (Cr) are both dated as 4.14 Gyr old, but show a reverse magnetization signature. This could be explained as resulting from dating uncertainties. In the middle panel, the craters dated by Robbins et al. (2013) are considered. In this case, all craters younger than Eta (Et) appear demagnetized. The database of Werner (2008) contains only the craters younger than 4 Gyr, which all appear demagnetized. Overall, this analysis confirms a correlation between a crater's magnetization and its age, and we agree with similar previous studies (Lillis et al. 2008, 2013a) with the conclusion that the dynamo shut down between 4.1 and 4.2 Gyr ago. In the future, a priori information about the sources might allow to additionally constrain the nonvisible part of the magnetization. Then, the above results should be revisited and expanded to account for the complete magnetization distribution.

12.4.2 Volcanoes

The most prominent regions of volcanic activity include Tharsis and Elysium. These large volcanic regions have been active throughout most of Mars' history (Hartmann et al. 1999; Werner 2009), and are largely demagnetized (Johnson and Phillips 2005; Lillis et al. 2009). In addition, there exist several volcanoes with ages of around 4 Gyr, including Hadriaca Patera, Apollinaris Patera, Syrtis Major, and Tyrrhena Patera (Werner 2009; Robbins et al. 2011). As it was previously found, Syrtis Major and Tyrrhena Patera show robust signs of demagnetization (Lillis et al. 2008, 2015), and our investigations are compatible with these results. However, we argue that Hadriaca Patera and Apollinaris Patera may be demagnetized, in contrast to previous findings (Lillis et al. 2006; Langlais and Purucker 2007; Hood et al. 2010). Here, we have a closer look at Apollinaris Patera, but similar conclusions can be drawn from studying Hadriaca Patera (Morschhauser 2016).

Apollinaris Patera is located near the dichotomy boundary in the vicinity of Elysium Planitia. The volcanic edifice extends to about 200 km in diameter and to 5 km in relative height (Plescia 2004), as shown in the topographic map in the upper left panel of Fig. 12.6. Further, the volcano was emplaced at around 3.8 Gyr ago

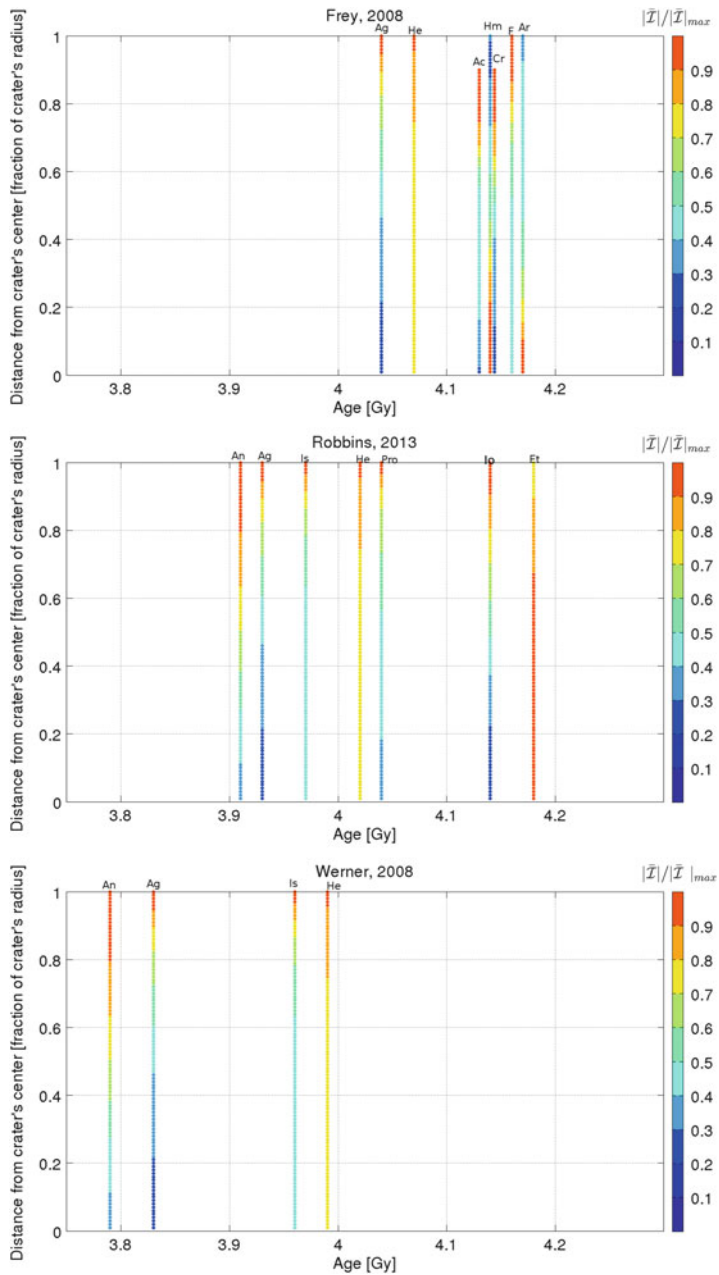


Fig. 12.5 The normalized circumferential average of the visible magnetization intensity is shown by colors for different distances to the crater's center. The ages given on the abscissa are based on estimates by Frey (2008) (upper row), Robbins et al. (2013), (middle row), and Werner (2008) (bottom row). The symbols Ag, He, Ac, Hm, Cr, F, Ar, An, Is, Pro, Io, and Et stand for the craters Argyre, Hellas, Acidalia, Hematite, Chryse, CT3-F, Ares, Antoniadi, Isidis, Prometheus, Iota, and Eta, respectively

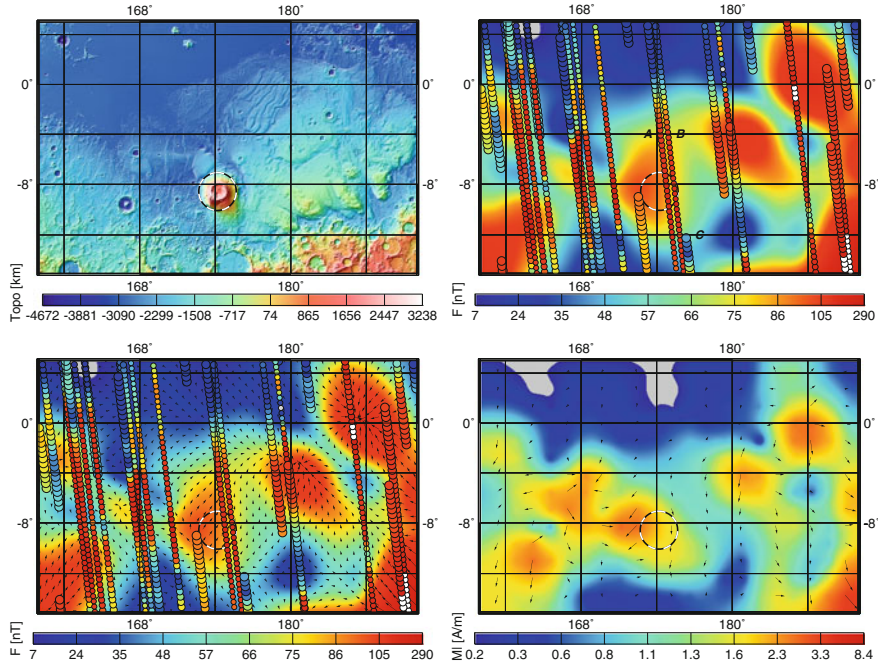


Fig. 12.6 *Upper left:* Topographic map of the region surrounding Apollinaris Patera. Apollinaris is located in the center of the figure and indicated by the black-white circle. *Upper right:* Magnetic field intensity as predicted by the model of Morschhauser et al. (2014) at 185 km altitude. Additionally, the aerobraking data within 30 km of this altitude are shown as indicated by the colored circles. Larger circles are closer to the map altitude. *Lower left:* magnetic field intensity as predicted by the model of Morschhauser et al. (2014) at the surface altitude. Here, the black arrows indicate the horizontal field direction and strength. *Lower right:* Visible magnetization over the same region for a 40 km thick magnetized layer. Part of this figure was originally published as Fig. 10.1 of Morschhauser (2016)

(Werner 2009; Robbins et al. 2011), and latest activity is dated to about 3.5 Gyr ago (Werner 2009; Robbins et al. 2011). Low-altitude magnetic field data is available over Apollinaris Patera from two AB/SPO dayside tracks, which are labeled A and B in the upper right panel of Fig. 12.6. These tracks have recorded an increased field intensity over the volcanic caldera which has been interpreted in terms of an active core dynamo at the time when Apollinaris formed (Hood et al. 2010). Indeed, the magnetic field as predicted from our model at an altitude of 185 km (also shown in the upper right panel) agrees with this interpretation. However, if the field is downward-continued to surface altitude (lower left panel), a much larger region of increased field intensity appears to the west of the caldera. This is further supported by the visible magnetization, as shown in the lower right panel of Fig. 12.6. The caldera clearly appears to be less magnetized than the region to its west. This region is older than the volcano, and corresponds to a Hesperian Noachian transition unit (Tanaka et al. 2014). Therefore, we argue that Apollinaris Patera may have

partially demagnetized a previously emplaced larger region of elevated magnetic field intensity. In consequence, the magnetic signature of Apollinaris does not necessarily contradict the implications on the timing of the Martian core dynamo which were made from studying the magnetic signature of impact craters.

12.5 Paleopoles

Paleopole positions can provide insight into the dynamics of the planet's core as well as on true and/or apparent polar wander. In consequence, many such studies have been published based on satellite magnetic field measurements of Mars (e.g., Hood and Zakharian 2001; Sprenke 2005; Langlais and Purucker 2007; Milbury and Schubert 2010; Plattner and Simons 2015). The underlying principle of these studies is that under the dipole field hypothesis, it is possible to reconstruct the location of the paleopoles from the magnetization direction (see, e.g., Butler 1992, Chap. 7). However, the same magnetic field can be generated by an infinite number of different magnetization distributions (Runcorn 1975; Lesur and Jackson 2000; Gubbins et al. 2011), all of them corresponding to different paleopole positions. Therefore, a priori information or assumptions about the sources are required in order to overcome this non-uniqueness issue.

Different studies have used a variety of different assumptions, leading to a large spectrum of possible solutions. For these studies, information on the robustness of the results is largely missing. Therefore, we investigate to which extent assumptions about the sources influence the estimated paleopole positions and under which conditions robust paleopole location estimations are feasible (Vervelidou et al. 2017a). Based on these findings, we propose a scheme to estimate robust paleopole positions along with their uncertainties.

12.5.1 *Limits of Estimating Paleopole Positions*

The decomposition of a magnetization distribution into vector spherical harmonics (SH) (Gubbins et al. 2011) provides us with a suitable framework for addressing the question under which circumstances paleopole positions can be recovered from magnetic field measurements. In a first step, we assume a distribution of susceptibility and an orientation of a central dipole. Based on this information, we generate a source magnetization and subsequently calculate the resulting magnetic field. In a second step, we represent this induced field in terms of a SH expansion and calculate the corresponding visible magnetization distribution \mathcal{I} (Eq. (12.8)). In a third step, we estimate the corresponding paleopole positions from this magnetization distribution, which are only based on the information that the induced magnetic field provides. Finally, we compare the estimated paleopole positions with

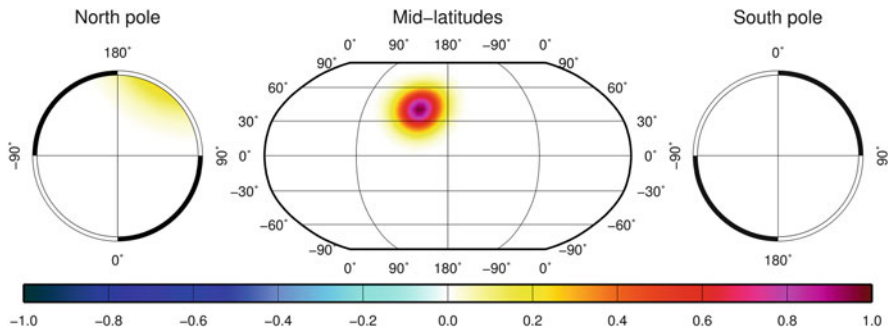


Fig. 12.7 The susceptibility distribution considered in the first synthetic case. Stereographic projections of the North and South Poles are shown on the left- and right-hand sides of the figure, respectively, along with a Robinson projection of all latitudes in the center of the figure

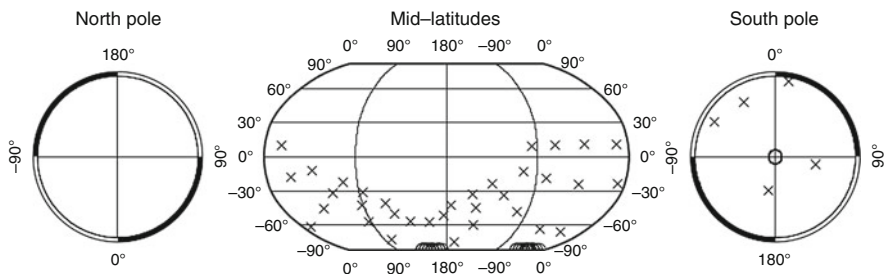


Fig. 12.8 The spatial distribution of paleopoles resulting from the visible magnetization \mathcal{I} (crosses), and the source magnetization (circles). Projection is the same as for Fig. 12.7

the true ones. In our study, we refer only to the South Pole of the inducing dipole when speaking of paleopole positions.

We apply this methodology to two distinct cases. In the first case, rocks of a very smooth susceptibility distribution (c.f. Fig. 12.7) are magnetized by a central dipole. In consequence, the resulting source magnetization gives rise to an induced magnetic field of low spectral content. As an example, Fig. 12.8 shows the paleopole for an inducing dipole that points to the North Pole. As expected, this paleopole is located at the South Pole (open circles). However, this paleopole position cannot be recovered from the visible magnetization alone. Even more, the paleopole positions recovered from the visible magnetization are scattered over a large area, as shown by the crosses in Fig. 12.8. The reason lies in our implicit assumption that the visible magnetization equals the source magnetization, i.e., that the null space of the source magnetization is zero. Indeed, the original paleopole position can be recovered if the full magnetization is considered, consisting of the sum of the \mathcal{I} , \mathcal{E} , and \mathcal{T} parts of \mathbf{M} (c.f. Eq. (12.5)). We conclude that the assumptions about the magnetization's null space, whether these are implicit or explicit, must be correct in order to correctly recover paleopole positions.

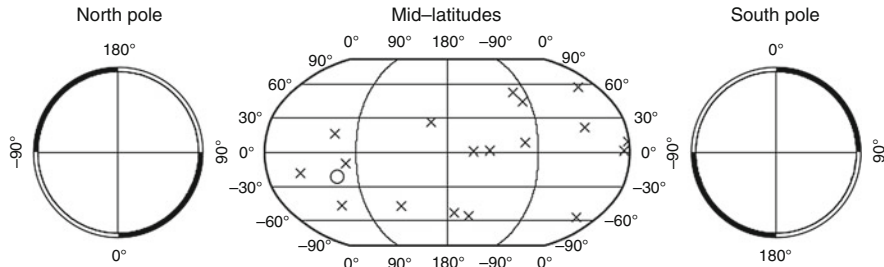


Fig. 12.9 The paleopole positions derived from the points of the visible magnetization \mathcal{I} that lie within a circle of 200 km around the location of the magnetized dipole are shown by crosses, and the true paleopole position is shown by the circle. Projection is the same as for Fig. 12.7

In a second synthetic test, the source magnetization is taken to be a single dipole on the surface of a sphere. The synthetic (true) paleopole position is marked by an open circle in Fig. 12.9. Now, the visible magnetization has been truncated at $l_{\max} = 110$, and the resulting paleopole positions within a circle of 200 km around the position of the source dipole are marked by crosses in Fig. 12.9. Again, the true paleopole cannot be recovered from the visible magnetization. However, the reason is different in this case: Now, the null space is zero, but the induced magnetic field is of almost infinite spectral content. Therefore, the complete reconstruction of \mathcal{I} and hence \mathbf{M} would require a SH magnetic field model of infinite maximum degree l_{\max} . In other words, an accurate estimation of the paleopole location requires that the full spectral content of the source magnetization is recovered. In real applications, this is possible either if the full spectral content is equal or smaller than the spectral content of the available magnetic field model or if the higher degree part of the source magnetization is correctly reconstructed, e.g., by means of independent information.

Now, we will examine whether there are cases for which both of the aforementioned conditions can be met. For this purpose, we insert Eq. (12.6) into Eq. (12.5), and obtain

$$\begin{aligned}\mathcal{I} &= \mathbf{M}(\theta, \phi) - \mathcal{E} - \mathcal{T} = \\ &= \mathbf{M}(\theta, \phi) - \sum_{m,l} g_{\mathcal{E},l}^m \mathbf{Y}_{l,l+1}^{m,c}(\theta, \phi) - \sum_{m,l} g_{\mathcal{T},l}^m \mathbf{Y}_{l,l}^{m,c}(\theta, \phi).\end{aligned}\quad (12.9)$$

This system of equations must not be underdetermined in order to recover the direction of \mathbf{M} correctly. As an example of an overdetermined system, we consider the case where a SH model of the lithospheric magnetic field is available up to a maximum degree l_{\max} . Then, we can generate N independent magnetic field vector observations, with $N = (l_{\max} + 1)(2l_{\max} + 1)$ (Lesur 2006). Now, let's assume that the source magnetization has the equal spectral content as the magnetic field model and, moreover, is everywhere uniform in direction. In this case, the number of unknowns is less than the number of equations. Therefore, the system

is overdetermined and can yield a solution. This reasoning can explain the validity of existing paleopole recovery methods, like that of Parker (1991). Still, it must be assured that the assumptions which allow to solve Eq. (12.9) are based on realistic considerations.

12.5.2 Estimating Paleopole Positions on Mars

In this section we present an approach to determine the magnetization orientation and associated paleopole position from a given set of magnetic field measurements over an isolated magnetic anomaly. As outlined in the previous section, additional information is needed to choose geophysically reasonable models from the infinite set of possible solutions. Here, we assume that the anomaly formed faster than the typical temporal timescales of main field changes. In consequence, a remanent magnetization of uniform orientation is present and we can apply the method of Parker (1991) to determine the best fitting magnetization orientation. With this method, no assumptions on the depth or lateral extent of the sources are required (Parker 1991; Mayhew 1979), and only weak constraints are placed on the spatial structure of the anomaly by distributing a regular grid of dipoles over the area of interest (c.f. Langlais and Purucker 2007; Oliveira and Wieczorek 2016). This approach differs from many other studies that make implicit assumptions about the center of the anomaly by assuming a single dipole, disks, or polygonal prisms as the source geometry for magnetic anomalies on Mars (e.g., Milbury et al. 2012; Hood and Zakharian 2001; Frawley and Taylor 2004; Boutin and Arkani-Hamed 2006; Hood et al. 2007).

In more detail, our implementation of Parker's method consists of distributing N dipoles at locations \mathbf{s}_i on the surface of the study area. These dipoles are set up with a uniform magnetization orientation $\hat{\mathbf{m}}$, leaving the magnetization strengths m_i as the unknown variables. Hence, the magnetic field resulting from the assumed magnetization is obtained from (Parker 1991; Blakely 1995)

$$\mathbf{B}_M(\mathbf{r}_j) = \frac{\mu_0}{4\pi} \sum_{i=1}^N m_i \left(\frac{3\hat{\mathbf{m}} \cdot (\mathbf{r}_j - \mathbf{s}_i)(\mathbf{r}_j - \mathbf{s}_i)}{|\mathbf{r}_j - \mathbf{s}_i|^5} - \frac{\hat{\mathbf{m}}}{|\mathbf{r}_j - \mathbf{s}_i|^3} \right) \quad (12.10)$$

where μ_0 is the magnetic permeability in vacuum, and \mathbf{r} is the vector of the $3K$ magnetic field elements at the K observation points. We invert for the magnetization strengths m_i by fitting the resulting magnetic field \mathbf{B}_M (Eq. (12.10)) at the K observation points at a certain altitude to the corresponding field predictions \mathbf{B}_{SH} as calculated from the spherical harmonic model of Morschhauser et al. (2014) (Sect. 12.2). Moreover, we impose the additional constraint that $m_i \geq 0$ for all i , since we are considering an area with uniform magnetization direction where no reversals occurred. Then, as Eq. (12.10) is linear with respect to m_i , we can solve for the magnetization intensity by using the nonnegative least-squares algorithm of

Lawson and Hanson (1995). Subsequently, this inversion is repeated for all possible orientations $\hat{\mathbf{m}}$. Then, assuming that the mean of the residuals $r_i = B_{M,i}(\hat{\mathbf{m}}) - B_{SH,i}$ is zero, the resulting standard deviation

$$\sigma_M(\hat{\mathbf{m}}) = \sqrt{\sum_i r_i^2 / K} \quad (12.11)$$

can be estimated for each orientation $\hat{\mathbf{m}}$. Hence, we neglect any correlations between the calculated magnetic field values $B_{M,i}$. The minimum of $\sigma_M(\hat{\mathbf{m}})$ then determines the best fitting orientation $\hat{\mathbf{m}}_{\text{fit}}$ from which the paleopole position can be determined using standard methods (Tarling 1983). It is worth mentioning that the above implementation of Parker's method (Parker 1991) slightly differs from the original approach for seamount magnetism where only the total field component aligned with the main field was considered. However, lacking a present-day core field on Mars, we choose to consider the full magnetic field vector when inverting for magnetization.

We have tested this method with various synthetic models, using different source and observation configurations. In a first test, we used a single dipole as the source of the anomaly whereas the observation points and the assumed source geometry were placed on a hexagonal grid. In a second test, a hexagonal grid of single dipoles was used for the source geometry while keeping the same observation points. In both test scenarios the prescribed magnetization orientation $\hat{\mathbf{m}}$ could be uniquely recovered with negligible standard deviation σ_M . In a last more complex test scenario we chose a quadratic area of $30^\circ \times 30^\circ$ as the source, spacing dipoles on a regular grid with one degree spacing. In order to simulate a non-isolated anomaly, this area was divided into a center square with the size of $10^\circ \times 10^\circ$ which included dipoles of uniform orientation only, and the remaining area which contained randomly oriented dipole sources. For this test scenario, the number of source dipoles and observation points was varied using 6/2, 18/6, and 60/20 dipoles and observation points, respectively. From this test we found that the achieved standard deviations $\sigma_M(\hat{\mathbf{m}})$ decreased for a smaller number of dipoles, but the results showed high uncertainties of up to 50° between the magnetic orientation of the input source and the calculated magnetic orientation. Calculated dipole locations could be recovered only when using a configuration of 60 dipoles which fully covers the magnetic anomaly at the surface. In conclusion, best results are achieved if the model dipoles fully cover the magnetic anomaly at the surface, and if they are equally distributed with a distance smaller than half the altitude of the observation points. In addition, the distribution of observation points should have a larger spatial extent than the model dipole distribution.

One of the problems when analyzing the resulting paleopole positions is the definition of an acceptable fit, and an objective criterion for such a threshold is usually missing in the literature (e.g., Milbury et al. 2012; Frawley and Taylor 2004; Boutin and Arkani-Hamed 2006). Therefore, most studies report either the best fitting paleopole position only, the mean paleopole position, or both. In the

future, we will approach this problem by taking the estimated uncertainties in the underlying magnetic field observations into account. For this purpose, we will apply the presented method to some selected crustal magnetic anomalies using the spherical harmonic model of the crustal magnetic field of Morschhauser et al. (2014) (Sect. 12.2) as a representation of the observed magnetic field. Then, the estimated covariance matrix of the Gauss coefficients can be used to calculate uncertainties of the magnetic field observations, which can then directly be compared to the modeled magnetic field given by Eq. (12.10). A robust criterion for acceptable models would then require the predicted magnetic field to fall within the uncertainty range spanned by the observations, and acceptable directions $\hat{\mathbf{m}}$ can then be determined. As these correspond to the locations of estimated paleopoles, a range of uncertainties for paleopole locations can then be directly derived.

12.6 Discussion and Summary

We have addressed some of the open questions related to the Martian magnetic field by deriving and investigating a spherical harmonic model of the Martian magnetic field based on vector satellite data of Mars Global Surveyor (Morschhauser et al. 2014). Compared to an analysis of raw satellite data, such a model provides several advantages: First, non-crustal field contributions can be minimized within a defined mathematical framework. Second, the interpretation of the data can be facilitated by projecting the satellite data to a unique altitude. Here, we have derived a model of the magnetic field of the Martian crust which is stable enough to be downward-continued to surface altitude, and which provides a high resolution of spherical harmonic degree and order 110, corresponding to a spatial resolution of about 190 km (Morschhauser et al. 2014; Morschhauser 2016).

In a first step, we have used this model to derive a model of the crustal magnetization of Mars. Here, we handle the well-known non-uniqueness issue (e.g., Runcorn 1975; Gubbins et al. 2011) by considering only the magnetization that is required to explain the observed magnetic field, i.e., the part of the actual crustal magnetization that produces a magnetic field which is visible outside of the planet. In doing so, we have slightly modified the formalism of Gubbins et al. (2011) to include real spherical harmonics and a finite thickness of the magnetized layer. For Mars, we have obtained a maximum magnetization of 20 A/m in the southern highlands when assuming a thickness of the magnetized layer of 40 km (Langlais et al. 2004; Dunlop and Arkani-Hamed 2005). On most parts of Mars, however, the obtained magnetization is below 8 A/m, and reaches 0.7 A/m on global average. Still, it remains difficult to explain such strong peak magnetizations on Mars. In particular, the most probable magnetic mineral candidate, single-domain magnetite (Dunlop and Arkani-Hamed 2005), is difficult to form in large amounts. Therefore, we point out that the Martian core dynamo might well have resulted in stronger surface fields than that of Earth.

Although it is accepted that the Martian crust was magnetized by an ancient core dynamo, it is disputed when this core dynamo shut down (e.g., Lillis et al. 2013a; Milbury et al. 2012; Schubert et al. 2000). On the one hand, the magnetic signature of impact craters consistently points to a shutdown in the late Noachian, at around 4.1 Gyr ago (e.g., Lillis et al. 2013a). On the other hand, the magnetic signature of some volcanoes points to a cessation in the Hesperian, less than about 3.8 Gyr ago (e.g., Langlais and Purucker 2007). With the help of the presented models of the Martian crustal magnetic field and magnetization, we have addressed the magnetic signatures of both impact craters and volcanoes. As a result, we agree with previous studies on the interpretation of the magnetic signature of impact craters, which point to a dynamo cessation at around 4.1 Gyr ago (e.g., Lillis et al. 2013a). However, we show that the magnetic signature of Apollinaris Patera (c.f. Sect. 12.4.2 and Morschhauser (2016)) and Hadriaca Patera (Morschhauser 2016) can be interpreted as being partially demagnetized instead of being magnetized. Therefore, we conclude that the interpretation of the magnetic signature both of volcanoes and impact craters allows for a Martian core dynamo shutdown in the late Noachian, at around 4.1 Gyr ago.

The dynamics of the ancient core dynamo on Mars can be assessed by investigating positions of paleopoles. In addition, paleopole positions contain information on true and apparent polar wander. For Mars, paleopole positions can only be estimated from satellite magnetic field measurements, and many studies based on Mars Global Surveyor data have been published (Milbury et al. (2012) and references therein). Here, we have shown that the accuracy of paleopole position estimates is strongly limited for two reasons: First, we lack knowledge of the full spectral content of the magnetic field, and second, the presence of magnetization that does not result in an observable field may influence the results. Still, paleopole positions may be recovered under specific assumptions, given that these assumptions are correct. As an example, we consider the method of Parker (1991), where it is assumed that magnetization is unidirectional over a certain area. In our approach, we additionally consider the confidence limits of our magnetic field model in order to provide estimates for the range of possible paleopole positions.

Overall, we believe that using a model of the Martian crustal magnetic field improves and facilitates the interpretation of magnetic anomalies on Mars. With this approach, we addressed some of the open questions related to the Martian magnetic field. Further progress may be made by improving the involved investigation techniques. However, significant progress must await new low-altitude data of good quality that will lead to a much better model of the Martian magnetic field. This may be provided by the MAVEN mission, which is currently in orbit around Mars.

Acknowledgements This work was funded by the Deutsche Forschungsgemeinschaft (DFG, German Research Foundation) within the priority program “Planetary Magnetism” (SPP 1488) under grants LE2477/3-1, LE2477/3-2 (F.V. and V.L.), GR3751/1-1 (A.M. and M.G.), GR3751/1-2 (A.M., M.G., and P.T.), and GI712/6-1 (S.G.).

References

- Acuña, M.H., Connerney, J.E.P., Ness, N.F., Lin, R.P., Mitchell, D., Carlson, C.W., McFadden, J., Anderson, K.A., Reme, H., Mazelle, C., Vignes, D., Wasilewski, P., Cloutier, P.: Global distribution of crustal magnetization discovered by the Mars Global Surveyor MAG/ER experiment. *Science* **284**(5415), 790–793 (1999). doi:10.1126/science.284.5415.790
- Albee, A.L., Palluconi, F.D., Arvidson, R.E.: Mars global surveyor mission: overview and status. *Science* **279**(5357), 1671–1672 (1998). doi:10.1126/science.279.5357.1671. <http://dx.doi.org/10.1126/science.279.5357.1671>
- Albee, A.L., Arvidson, R.E., Palluconi, F., Thorpe, T.: Overview of the Mars Global Surveyor mission. *J. Geophys. Res.* **106**, 23291–23316 (2001). doi:10.1029/2000JE001306
- Arkani-Hamed, J.: A coherent model of the crustal magnetic field of Mars. *J. Geophys. Res.* **109**, E09005 (2004). doi:10.1029/2004JE002265. <http://dx.doi.org/10.1029/2004JE002265>
- Aster, R.C., Borchers, B., Thurber, C.H.: Parameter Estimation and Inverse Problems, 2nd edn. Elsevier—Academic, New York (2013). ISBN:978-0-12-385048-5
- Blakely, R.J.: Potential Theory in Gravity & Magnetic Applications. Cambridge University Press, Cambridge (1995). ISBN:0-521-57547-8
- Boutin, D., Arkani-Hamed, J.: Pole wandering of Mars: evidence from paleomagnetic poles. *Icarus* **181**(1), 13–25 (2006). doi:10.1016/j.icarus.2005.10.025. <http://dx.doi.org/10.1016/j.icarus.2005.10.025>
- Butler, R.F.: Paleomagnetism: Magnetic Domains to Geologic Terranes. Blackwell Scientific Publications, Hoboken (1992). ISBN:978-0865420700
- Chassefière, E., Leblanc, F.: Mars atmospheric escape and evolution; interaction with the solar wind. *Planet. Space Sci.* **52**(11), 1039–1058 (2004). doi:10.1016/j.pss.2004.07.002. <http://dx.doi.org/10.1016/j.pss.2004.07.002>
- Christensen, U.R., Holzwarth, V., Reiners, A.: Energy flux determines magnetic field strength of planets and stars. *Nature* **457**(7226), 167–169 (2009). doi:10.1038/nature07626. <http://dx.doi.org/10.1038/nature07626>
- Connerney, J.E.P., Acuna, M.H., Wasilewski, P.J., Ness, N.F., Reme, H., Mazelle, C., Vignes, D., Lin, R.P., Mitchell, D.L., Cloutier, P.A.: Magnetic lineations in the ancient crust of Mars. *Science* **284**, 794–798 (1999). doi:10.1126/science.284.5415.794
- Connerney, J.E.P., Acuña, M.H., Wasilewski, P.J., Kletetschka, G., Ness, N.F., Rème, H., Lin, R.P., Mitchell, D.L.A.: The global magnetic field of Mars and implications for crustal evolution. *Geophys. Res. Lett.* **28**, 4015–4018 (2001). doi:10.1029/2001GL013619
- Dolginov, S.S.: On the magnetic field of Mars - Mars 5 evidence. *Geophys. Res. Lett.* **5**, 93–95 (1978). doi:10.1029/GL005i001p00093
- Dunlop, D.J.: Stepwise and continuous low-temperature demagnetization. *Geophys. Res. Lett.* **30**(11) (2003). doi:10.1029/2003gl017268. <http://dx.doi.org/10.1029/2003GL017268>
- Dunlop, D.J., Arkani-Hamed, J.: Magnetic minerals in the Martian crust. *J. Geophys. Res.* **110**(E12), E12S04 (2005). doi:10.1029/2005JE002404. <http://dx.doi.org/10.1029/2005JE002404>
- Farquharson, C.G., Oldenburg, D.W.: Non-linear inversion using general measures of data misfit and model structure. *Geophys. J. Int.* **134**, 213–227 (1998). doi:10.1046/j.1365-246X.1998.00555.x
- Frawley, J.J., Taylor, P.T.: Paleo-pole positions from martian magnetic anomaly data. *Icarus* **172**(2), 316–327 (2004). doi:10.1016/j.icarus.2004.07.025. <http://dx.doi.org/10.1016/j.icarus.2004.07.025>
- Frey, H.: Ages of very large impact basins on Mars: implications for the late heavy bombardment in the inner solar system. *Geophys. Res. Lett.* **35**, L13203 (2008). doi:10.1029/2008GL033515
- Gerhards, C.: Spherical decompositions in a global and local framework: theory and an application to geomagnetic modeling. *Int. J. Geomath.* **1**(2), 205–256 (2011). doi:10.1007/s13137-010-0011-9. <http://dx.doi.org/10.1007/s13137-010-0011-9>

- Gilder, S.A., Le Goff, M.: Systematic pressure enhancement of titanomagnetite magnetization. *Geophys. Res. Lett.* **35**(10) (2008). doi:10.1029/2008gl033325. <http://dx.doi.org/10.1029/2008GL033325>
- Gubbins, D., Ivers, D., Masterton, S.M., Winch, D.E.: Analysis of lithospheric magnetization in vector spherical harmonics. *Geophys. J. Int.* **187**, 99–117 (2011). doi:10.1111/j.1365-246X.2011.05153.x
- Hartmann, W.K., Malin, M., McEwen, A., Carr, M., Soderblom, L., Thomas, P., Danielson, E., James, P., Veverka, J.: Evidence for recent volcanism on Mars from crater counts. *Nature* **397**(6720), 586–589 (1999). doi:10.1038/17545. <http://dx.doi.org/10.1038/17545>
- Hood, L.L., Zakharian, L.L.H.: Mapping and modeling of magnetic anomalies in the northern polar region of Mars. *J. Geophys. Res.* **106**(E7), 14601–14619 (2001). doi:10.1029/2000JE001304
- Hood, L.L., Richmond, N., Harrison, K., Lillis, R.: East-west trending magnetic anomalies in the Southern Hemisphere of Mars: modeling analysis and interpretation. *Icarus* **191**(1), 113–131 (2007). doi:10.1016/j.icarus.2007.04.025. <http://dx.doi.org/10.1016/j.icarus.2007.04.025>
- Hood, L.L., Harrison, K.P., Langlais, B., Lillis, R.J., Poulet, F., Williams, D.A.: Magnetic anomalies near Apollinaris Patera and the Medusae Fossae formation in Lucus Planum, Mars. *Icarus* **208**, 118–131 (2010). doi:10.1016/j.icarus.2010.01.009
- Huber, P.J.: Robust estimation of a location parameter. *Ann. Math. Stat.* **35**(1), 73–101 (1964)
- Jakosky, B.M., Phillips, R.J.: Mars' volatile and climate history. *Nature* **412**, 237–244 (2001)
- Johnson, C.L., Phillips, R.J.: Evolution of the Tharsis region of Mars: insights from magnetic field observations. *Earth Planet. Sci. Lett.* **230**(3–4), 241–254 (2005). doi:10.1016/j.epsl.2004.10.038. <http://dx.doi.org/10.1016/j.epsl.2004.10.038>
- Laneuville, M., Wieczorek, M.A., Breuer, D., Tosi, N.: Asymmetric thermal evolution of the moon. *J. Geophys. Res.-Space* **118**(7), 1435–1452 (2013). doi:10.1002/jgre.20103. <http://dx.doi.org/10.1002/jgre.20103>
- Langlais, B., Purucker, M.: A polar magnetic paleopole associated with Apollinaris Patera, Mars. *Planet. Space Sci.* **55**, 270–279 (2007). doi:10.1016/j.pss.2006.03.008
- Langlais, B., Purucker, M.E., Mandea, M.: Crustal magnetic field of Mars. *J. Geophys. Res.* **109**(E2), E02008 (2004). doi:10.1029/2003JE002048. <http://dx.doi.org/10.1029/2003JE002048>
- Lawson, C.L., Hanson, R.J.: Solving least squares problems. In: Applied Mathematics. Society for Industrial & Applied Mathematics (SIAM), Jan 1995. ISBN:978-0-89871-356-5. doi:10.1137/1.9781611971217
- Lesur, V.: Introducing localized constraints in global geomagnetic field modelling. *Earth Plan. Space* **58**(4), 477–483 (2006). doi:10.1186/BF03351943
- Lesur, V., Jackson, A.: Exact solutions for internally induced magnetization in a shell. *Geophys. J. Int.* **140**, 453–459 (2000). doi:10.1046/j.1365-246X.2000.00046.x
- Lillis, R.J., Manga, M., Mitchell, D.L., Lin, R.P., Acuna, M.H.: Unusual magnetic signature of the Hadriaca Patera Volcano: implications for early Mars. *Geophys. Res. Lett.* **33**, L03202 (2006). doi:10.1029/2005GL024905
- Lillis, R.J., Frey, H.V., Manga, M.: Rapid decrease in Martian crustal magnetization in the Noachian era: implications for the dynamo and climate of early Mars. *Geophys. Res. Lett.* **35**(14), L14203 (2008). doi:10.1029/2008GL034338. <http://dx.doi.org/10.1029/2008GL034338>
- Lillis, R.J., Frey, H.V., Manga, M., Mitchell, D.L., Lin, R.P., Acuña, M.H., Bougner, S.W.: An improved crustal magnetic field map of Mars from electron reflectometry: highland volcano magmatic history and the end of the martian dynamo. *Icarus* **194**(2), 575–596 (2008). doi:10.1016/j.icarus.2007.09.032. <http://dx.doi.org/10.1016/j.icarus.2007.09.032>
- Lillis, R.J., Dufek, J., Bleacher, J.E., Manga, M.: Demagnetization of crust by magmatic intrusion near the Arsia Mons volcano: magnetic and thermal implications for the development of the Tharsis province, Mars. *J. Volcanol. Geotherm. Res.* **185**(1–2), 123–138 (2009). doi:10.1016/j.jvolgeores.2008.12.007

- Lillis, R.J., Robbins, S., Manga, M., Halekas, J.S., Frey, H.V.: Time history of the Martian dynamo from crater magnetic field analysis. *J. Geophys. Res.* **118**, 1488–1511 (2013a). doi:10.1002/jgre.20105
- Lillis, R.J., Stewart, S.T., Manga, M.: Demagnetization by basin-forming impacts on early Mars: contributions from shock, heat, and excavation. *J. Geophys. Res.* **118**, 1045–1062 (2013b). doi:10.1002/jgre.20085
- Lillis, R.J., Dufek, J., Kiefer, W.S., Black, B.A., Manga, M., Richardson, J.A., Bleacher, J.E.: The Syrtis Major volcano, Mars: a multidisciplinary approach to interpreting its magmatic evolution and structural development. *J. Geophys. Res.* 1476–1496 (2015). doi:10.1002/2014je004774. <http://dx.doi.org/10.1002/2014JE004774>
- Maus, S., Haak, V.: Is the long wavelength crustal magnetic field dominated by induced or by remanent magnetisation. *J. Ind. Geophys. Union* **6**(1), 1–5 (2002)
- Mayer, C., Maier, T.: Separating inner and outer Earth's magnetic field from CHAMP satellite measurements by means of vector scaling functions and wavelets. *Geophys. J. Int.* **167**, 1188–1203 (2006). doi:10.1111/j.1365-246X.2006.03199.x
- Mayhew, M.A.: Inversion of satellite magnetic anomaly data. *J. Geophys. - Z. Geophys.* **45**(2), 119–128 (1979)
- McSween, H.Y., Ruff, S.W., Morris, R.V., Gellert, R., Klingelhöfer, G., Christensen, P.R., McCoy, T.J., Ghosh, A., Moersch, J.M., Cohen, B.A., Rogers, A.D., Schröder, C., Squyres, S.W., Crisp, J., Yen, A.: Mineralogy of volcanic rocks in gusev crater, Mars: reconciling mössbauer, alpha particle x-ray spectrometer, and miniature thermal emission spectrometer spectra. *J. Geophys. Res.* **113**(E6) (2008). doi:10.1029/2007je002970. <http://dx.doi.org/10.1029/2007JE002970>
- Milbury, C., Schubert, G.: Search for the global signature of the Martian dynamo. *J. Geophys. Res.* **115**, E10010 (2010). doi:10.1029/2010JE003617
- Milbury, C., Schubert, G., Raymond, C.A., Smrekar, S.E., Langlais, B.: The history of Mars' dynamo as revealed by modeling magnetic anomalies near Tyrrhenus Mons and Syrtis Major. *J. Geophys. Res.* **117**, E10007 (2012). doi:10.1029/2012JE004099
- Morris, R.V., Klingelhöfer, G., Schröder, C., Rodionov, D.S., Yen, A., Ming, D.W., de Souza, P.A., Fleischer, I., Wdowiak, T., Gellert, R., Bernhardt, B., Evlanov, E.N., Zubkov, B., Foh, J., Bonnes, U., Kankeleit, E., Gülich, P., Renz, F., Squyres, S.W., Arvidson, R.E.: Mössbauer mineralogy of rock, soil, and dust at gusev crater, mars: spirit's journey through weakly altered olivine basalt on the plains and pervasively altered basalt in the Columbia hills. *J. Geophys. Res.* **111**(E2) (2006). doi:10.1029/2005je002584. <http://dx.doi.org/10.1029/2005JE002584>
- Morschhauser, A.: A model of the crustal Magnetic Field of Mars. PhD thesis, University of Muenster (2016). <http://nbn-resolving.de/urn:nbn:de:hbz:6-62269665189>
- Morschhauser, A., Grott, M., Breuer, D.: Crustal recycling, mantle dehydration, and the thermal evolution of Mars. *Icarus* **212**(2), 541–558 (2011). doi:10.1016/j.icarus.2010.12.028
- Morschhauser, A., Lesur, V., Grott, M.: A spherical harmonic model of the lithospheric magnetic field of Mars. *J. Geophys. Res.* **119**, 1162–1188 (2014). doi:10.1002/2013JE004555
- Oliveira, J.S., Wieczorek, M.A.: Testing the axial dynamo hypothesis for the moon by modeling the direction of crustal magnetization. In: Lunar and Planetary Science Conference, vol. 47 (2016)
- Olsen, N., Glassmeier, K.-H., Jia, X.: Separation of the magnetic field into external and internal parts. *Space Sci. Rev.* **152**, 135–157 (2010). doi:10.1007/s11214-009-9563-0
- Parker, R.L.: A theory of Ideal bodies for seamount magnetism. *J. Geophys. Res.-space* **96**, 16101–16112 (1991). doi:10.1029/91JB01497
- Plattner, A., Simons, F.J.: High-resolution local magnetic field models for the martian south pole from Mars global surveyor data. *J. Geophys. Res.* **120**(9), 1543–1566 (2015). doi:10.1002/2015je004869. <http://dx.doi.org/10.1002/2015JE004869>
- Plescia, J.B.: Morphometric properties of Martian volcanoes. *J. Geophys. Res.* **109**, E03003 (2004). doi:10.1029/2002JE002031
- Purucker, M., Ravat, D., Frey, H., Voorhies, C., Sabaka, T., Acuña, M.: An altitude-normalized magnetic map of Mars and its interpretation. *Geophys. Res. Lett.* **27**, 2449–2452 (2000). doi:10.1029/2000GL000072

- Robbins, S.J., Achille, G.D., Hynek, B.M.: The volcanic history of Mars: High-resolution crater-based studies of the calderas of 20 volcanoes. *Icarus* **211**, 1179–1203 (2011). doi:10.1016/j.icarus.2010.11.012
- Robbins, S.J., Hynek, B.M., Lillis, R.J., Bottke, W.F.: Large impact crater histories of Mars: the effect of different model crater age techniques. *Icarus* **225**, 173–184 (2013). doi:10.1016/j.icarus.2013.03.019
- Rochette, P., Lorand, J.-P., Fillion, G., Sautter, V.: Pyrrhotite and the remanent magnetization of SNC meteorites: a changing perspective on Martian magnetism. *Earth Planet. Sci. Lett.* **190**, 1–12 (2001). doi:10.1016/S0012-821X(01)00373-9
- Runcorn, S.K.: On the interpretation of lunar magnetism. *Phys. Earth Planet. Int.* **10**, 327–335 (1975). doi:10.1016/0031-9201(75)90059-X
- Russell, C.T.: The magnetic field of Mars - Mars 5 evidence re-examined. *Geophys. Res. Lett.* **5**, 85–88 (1978). doi:10.1029/GL005i001p00085
- Schubert, G., Soderlund, K.M.: Planetary magnetic fields: observations and models. *Phys. Earth Planet. Int.* **187**(3–4), 92–108 (2011). doi:10.1016/j.pepi.2011.05.013. <http://dx.doi.org/10.1016/j.pepi.2011.05.013>
- Schubert, G., Russell, C.T., Moore, W.B.: Geophysics: timing of the Martian dynamo. *Nature* **408**, 666–667 (2000). doi:10.1038/35047163
- Schultz, P.H., Schultz, R.A., Rogers, J.: The structure and evolution of ancient impact basins on Mars. *J. Geophys. Res.* **87**, 9803–9820 (1982). doi:10.1029/JB087B12p09803
- Sleep, N.H.: Martian plate tectonics. *J. Geophys. Res.* **99**(E3), 5639–5655 (1994). doi:10.1029/94JE00216
- Sprenke, K.F.: Martian magnetic paleopoles: a geostatistical approach. *Geophys. Res. Lett.* **32**(9), L09201 (2005). doi:10.1029/2005GL022840. <http://dx.doi.org/10.1029/2005GL022840>
- Sprenke, K.F., Baker, L.L., Williams, A.F.: Polar wander on Mars: evidence in the geoid. *Icarus* **174**, 486–489 (2005). doi:10.1016/j.icarus.2004.11.009
- Tanaka, K.L., Skinner, J.A., Dohm, J.M., Irwin, R.P., Kolb, E.J., Fortezzo, C.M., Platz, T., Michael, G.G., Hare, T.M.: Geologic Map of Mars. Scientific Investigations Map, Jul 2014. ISSN:2329-132X. doi:10.3133/sim3292. <http://dx.doi.org/10.3133/sim3292>
- Tarling, D.H.: Palaeomagnetism. Springer Science and Business Media, Berlin (1983). ISBN:978-94-009-5957-6. doi:10.1007/978-94-009-5955-2. <http://dx.doi.org/10.1007/978-94-009-5955-2>
- Vervelidou, F., Lesur, V., Morschhauser, A., Grott, M., Thomas, P.: On the accuracy of paleopole estimations from magnetic field measurements. *Geophys. J. Int.* (2017a). doi:10.1093/gji/ggx400
- Vervelidou, F., Lesur, V., Grott, M., Morschhauser, A., Lillis, R.: Constraining the date of the Martian dynamo shutdown by means of crater magnetization signatures. *J. Geophys. Res. Planets* (2017b). doi:10.1002/2017JE005410
- Vine, F.J., Matthews, D.H.: Magnetic anomalies over oceanic ridges. *Nature* **199**, 947–949 (1963). doi:10.1038/199947a0
- Volk, M.W.R., Gilder, S.A.: Effect of static pressure on absolute paleointensity recording with implications for meteorites. *J. Geophys. Res.* **121**(8), 5596–5610 (2016). doi:10.1002/2016jb013059. <http://dx.doi.org/10.1002/2016JB013059>
- Volk, M.W.R., Gilder, S.A., Feinberg, J.M.: Low temperature magnetic properties of monoclinic pyrrhotite with particular relevance to the Besnus transition. *Geophys. J. Int.* **ggw376** (2016). doi:10.1093/gji/ggw376. <http://dx.doi.org/10.1093/gji/ggw376>
- Werner, S.C.: The early martian evolution - constraints from basin formation ages. *Icarus* **195**, 45–60 (2008). doi:10.1016/j.icarus.2007.12.008
- Werner, S.C.: The global martian volcanic evolutionary history. *Icarus* **201**, 44–68 (2009). doi:10.1016/j.icarus.2008.12.019
- Whaler, K.A., Purucker, M.: A spatially continuous magnetization model for Mars. *J. Geophys. Res.* **110**(E9) (2005). doi:10.1029/2004JE002393. <http://dx.doi.org/10.1029/2004JE002393>

Chapter 13

Magnetic Signatures of Terrestrial Meteorite Impact Craters: A Summary

Stuart A. Gilder, Jean Pohl, and Michael Eitel

Abstract This chapter summarizes the magnetic characteristics of meteorite impact craters. Magnetic mineralogies of both impact melts and target rocks are described, as are the paleomagnetic signals they retain and the magnetic field anomalies they produce. Particular emphasis is given to five craters studied under the umbrella of the Deutsche Forschungsgemeinschaft's Schwerpunktprogramm, Planetary Magnetism: Manicouagan (Canada), Mistastin (Canada), Ries (Germany), Rochechouart (France), and Vredefort (South Africa), with a synthesis from other craters worldwide. A special problem addressed here is whether shock waves generated during impact influence the geodynamo. We conclude that the seismic energy released during the formation of craters up to 90 km in diameter is insufficient to disturb the dynamo process in a way that would provoke observable changes in field direction or intensity at the Earth's surface. We show that shock can permanently modify magnetic properties of the target rocks; however, it is difficult to assess the relative influence between thermal and pressure effects on their remanent magnetizations. Distinguishing between shock and thermal overprinting and then unraveling these signals from the original remanence remain important problems that bear on the interpretation of magnetic anomalies in impact craters as well as our understanding of heat production from collision. Paleomagnetic directions from impact melts and suevites are well clustered at each crater, which suggests that building of the structures was completed before the ferrimagnetic minerals cooled through their Curie temperatures.

S.A. Gilder (✉) • J. Pohl • M. Eitel

Department of Earth and Environmental Sciences, Ludwig Maximilians Universität,
Theresienstrasse 41, 80333 München, Germany

e-mail: gilder@lmu.de; pohl@geophysik.uni-muenchen.de; eitel@geophysik.uni-muenchen.de

13.1 Brief Description of an Impact Event with Relevance to Magnetism

Meteorite impact craters are ubiquitous throughout our solar system and mark important events in planetary evolution (Shoemaker 1977; French 1998). To date around 190 impact craters have been identified on the surface of Earth (French 1998; Earth Impact Database: www.unb.ca/passc/ImpactDatabase/) (Fig. 13.1). When a bolide hits the Earth with enough energy, some of the terrestrial material may be vaporized. A larger part, up to several times the volume of the impactor, will be melted (Pierazzo et al. 1997; Pierazzo and Melosh 2000; Barr and Citron 2011; Quintana et al. 2015). The melt can form massive impact melt sheets within the structure, smaller isolated melt bodies within and around the crater, and/or minor melt pockets within breccias (suevites) and dikes inside or outside the structure. Friction between rock masses during crater formation can result in micromelts (pseudotachylite). A small volume of melt is thrown airborne where it is rapidly quenched into glass, called tektite, that can be transported up to hundreds of kilometers away from the crater.

Impact melt thicknesses are low in small impact craters and, on Earth, thicker melt sheets are often eroded in larger craters such that melt thickness greater than 100 m is rare. The close resemblance in chemistry and petrology between impact melts and volcanic rocks was one of the arguments against an external origin for the craters (e.g., Currie and Larochelle 1969 for Mistastin)—a debate that persisted to the early 1990s for the Vredefort crater (Antoine et al. 1990). This resemblance is also seen in magnetic mineralogy, with both containing iron oxides predominantly within the magnetite-ulvöspinel solid solution series. Moreover, the relatively rapid cooling rates produce grain sizes toward the single to pseudo-

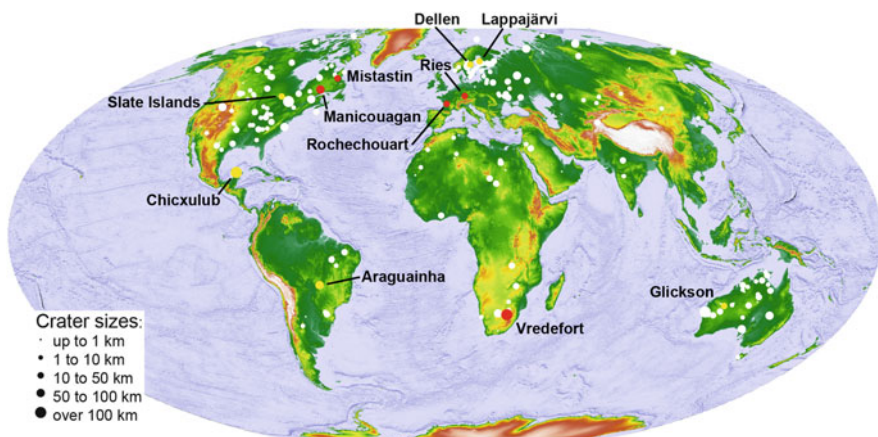


Fig. 13.1 Recognized terrestrial meteorite impact craters. Craters studied by us discussed in this chapter are indicated in red; craters whose data are used in some figures are in yellow

single domain range associated with stable and strong remanent magnetizations that are favorable for paleomagnetic studies. Such ideal magnetic carriers record the magnetic field when they cool through their blocking (Curie) temperatures, thereby enabling paleomagnetists to study geomagnetic effects like secular variation or deformation related to crater formation.

Impact craters produce distinctive magnetic and gravity anomalies (e.g., Pilkington and Grieve 1992; Plado et al. 1999; Ugalde et al. 2005). While the interpretation of gravity anomalies is rarely contentious, the opposite is true for magnetic anomalies. The complexity of the geometry and polarity of the sources make magnetic anomalies more difficult to model due to the confluence of whether a crater contains impact melt, the volume of melt, and the nature of the basement rock. As permanent magnetizations tend to dominate aeromagnetic expressions, the polarity recorded in the impact melts and suevites, if present, typically dictates the sign of the anomalies. However, in several cases it is difficult to unravel whether the signal from the target rocks is primary, a thermal overprint, or influenced by shock. For the latter, there is confusion whether shock demagnetizes the target material or remagnetizes it parallel to the ambient field direction. Other ambiguities are whether hydrothermal systems create new magnetic minerals or provide heat to overprint existing remanence directions, and how long the hydrothermal process lasts, all which bear on the timing when the lock-in of magnetic remanence occurs after impact.

In this contribution, we discuss the magnetic carriers found in melt-bearing rocks in various craters, as well as the influence of shock on the target rocks. We give some examples of the intriguing magnetic anomalies produced by the impact structures. Paleomagnetic directions from several craters are presented to draw conclusions on the formation rate and subsequent tectonic modification of the structures. Finally, the energy transferred to the Earth during impact can be so high that several workers postulated whether impacts can perturb the geodynamo process (e.g., Glass and Heezen 1967; Durrani and Khan 1971). This topic and the others mentioned above are discussed here in light of our findings at five impact craters, Manicouagan (Canada; Eitel et al. 2016), Mistastin (Canada; Hervé et al. 2015), Ries (Germany; Koch et al. 2012), Rochechouart (France; Eitel et al. 2014), and Vredefort (South Africa; Carporzen et al. 2012), and by comparing with published data from several other craters.

13.2 Link Between Crater Structure and Local Aeromagnetic Signatures

The ca. 15 Ma Ries (Germany) impact structure serves as a good example of a well-preserved crater, whose subsurface is well characterized through drilling and seismic exploration, and it has abundant magnetic data (Fig. 13.2) (e.g., Pohl et al. 1977; Pohl 1977). The suevite deposits attain up to 400 m in thickness within the

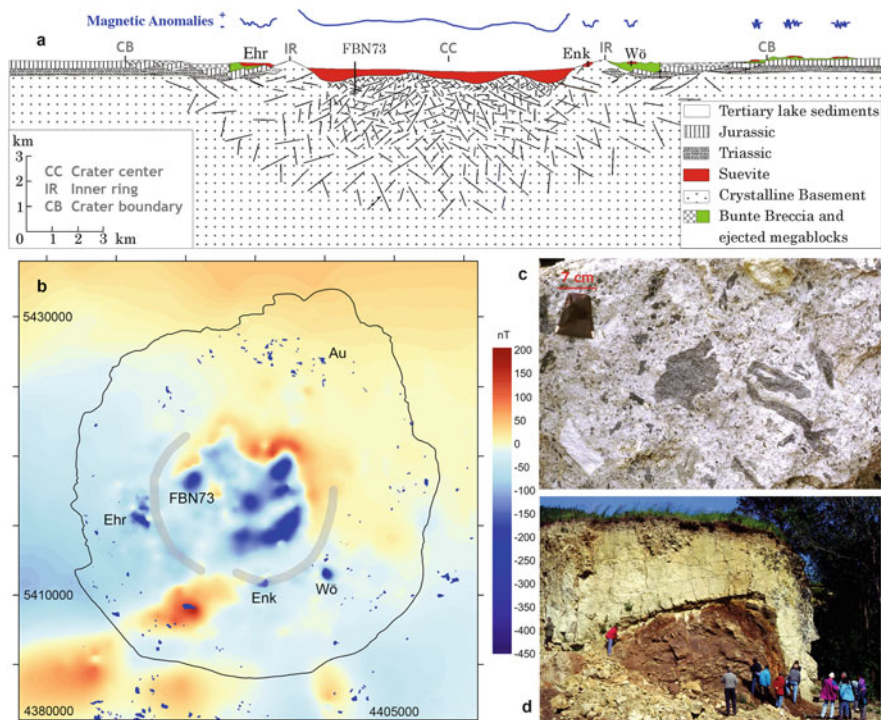


Fig. 13.2 Schematic geologic cross section of the Ries (Germany) impact structure (a). Impact-created lithologies are colored. Impact breccia and melt were emplaced when the field was reversed, which produce negative magnetic field anomalies in today's normal polarity field. Thick deposits inside the inner ring (indicated in grey in the magnetic anomaly map [b]) produce long-wavelength anomalies while isolated patches of suevite and impact melt produce erratic, short-wavelength anomalies as sketched above the cross section. Drill holes FBN73, Wö (Wörnitzostheim) and Enk (Enkingen) reached 1200 m, 180 m, and 100 m depth, respectively. (b) Magnetic anomaly map of the Ries impact structure. Small dark blue spots represent suevite and impact melt outcrops. Thin black line demarcates the crater rim; Ehr stands for Ehringen. (c) Photo of suevite from Öttingen containing grey impact melt and crystalline rock clasts in a fine-grained matrix. Key holder in upper left is 7 cm in length. (d) Photo from the Aumühle (Au) quarry showing suevite (yellow-grey) lying on top of the Bunte Breccia ejecta (red-brown)

inner ring, while several, thinner, isolated pockets crop out near the inner ring and beyond. The impact happened while the Earth's magnetic field was in the reversed polarity state, opposite of today's normal polarity field, so that the combination led to lower than average (negative) magnetic anomalies. The thicker and more laterally extensive the melts, the longer the wavelength of the negative anomalies. Isolated patches of suevite yield complex, short-wavelength anomalies as sketched above the cross section in Fig. 13.2a. The short-wavelength positive anomalies in the SW part of the aeromagnetic map are generated by the underlying basement rocks, unrelated to the impact (Pohl et al. 1977).

Magnetic anomaly maps of impact craters are quite diverse, yet most reveal the circular nature of the structures (Fig. 13.3). The 19 km diameter Dellen (Sweden) structure contains a melt sheet 9 km in diameter, up to 500 m thick, with normal magnetic polarity (Bylund 1974) that produces fairly small-wavelength positive anomalies up to a few 100 nT (Henkel 1992; Geological Survey of Sweden, www.sgu.se). The Glikson structure possesses a distinct, 14 km diameter magnetic ring anomaly that was interpreted by Macdonald et al. (2005) to result from the truncation and folding of mafic sills into a circular-symmetric syncline. The exposed rocks in the Glikson structure consist entirely of sandstone (Shoemaker and Shoemaker 1997).

The 215 Ma Manicouagan (Canada) crater, whose rim-to-rim diameter of 90 km ranks it as one of the ten largest impact craters on Earth, possesses an exceptionally thick impact melt sheet, with >1 km of clast-free, differentiated impact melt and a further 400 m of clast-laden impact melt at the center (Spray and Thompson 2008). The melt rock is so thick in the center that it underwent differentiation, where titanomagnetite enrichment occurred in the lower portion of the melt (Eitel et al. 2016). The central magnetic anomaly high is partially produced from the titanomagnetite-enriched deeper levels in the thick impact melt; however, meta-gabbroic rocks within the central anomaly region have susceptibility values equal to or greater than the deep differentiated impact melts (L. Thompson, unpublished data), so they likely contribute to the anomaly's presence; further work is required to solve the origin of the magnetic anomalies from Manicouagan. One obstacle is that the rocks from the drill cores that access the deeper levels of the structure have drilling-induced overprints that both reoriented the original directions and changed the magnetization intensities (Eitel et al. 2016); these potential affects are often not considered when interpreting the magnetizations of rocks drilled in other craters.

The 2 Ga Vredefort structure is likely the largest crater on Earth (>250 km original diameter). Up to 8 km of erosion since its formation has exposed a complete cross section of Archean crust: going from upper mantle facies (harzburgite) in the center, grading to highly depleted granulite typical of the lower crust, a ductilely deformed metamorphic suite, undeformed granites, and then folded Witwatersrand basin sediments whose fold axes parallel the circular structure of the crater. Corner et al. (1990) proposed that the upturned ferruginous shales of the West Rand Group give rise to the prominent negative anomalies marking the perimeter of the Vredefort dome (Fig. 13.3). A “horseshoe-shaped” region of strong (<-1000 nT) negative anomalies lies near the amphibolite to granulite metamorphic facies transition, analogous to the Conrad discontinuity (Corner et al. 1990; Muundjua et al. 2007), where impact-related thermal and shock metamorphism are significantly higher than in other parts of the structure (Hart et al. 1991). Muundjua et al. (2007) suggested that focusing and defocusing of shock waves at this rheologic interface during impact enhanced the magnetic signature at this boundary from a combination of both thermal and shock effects.

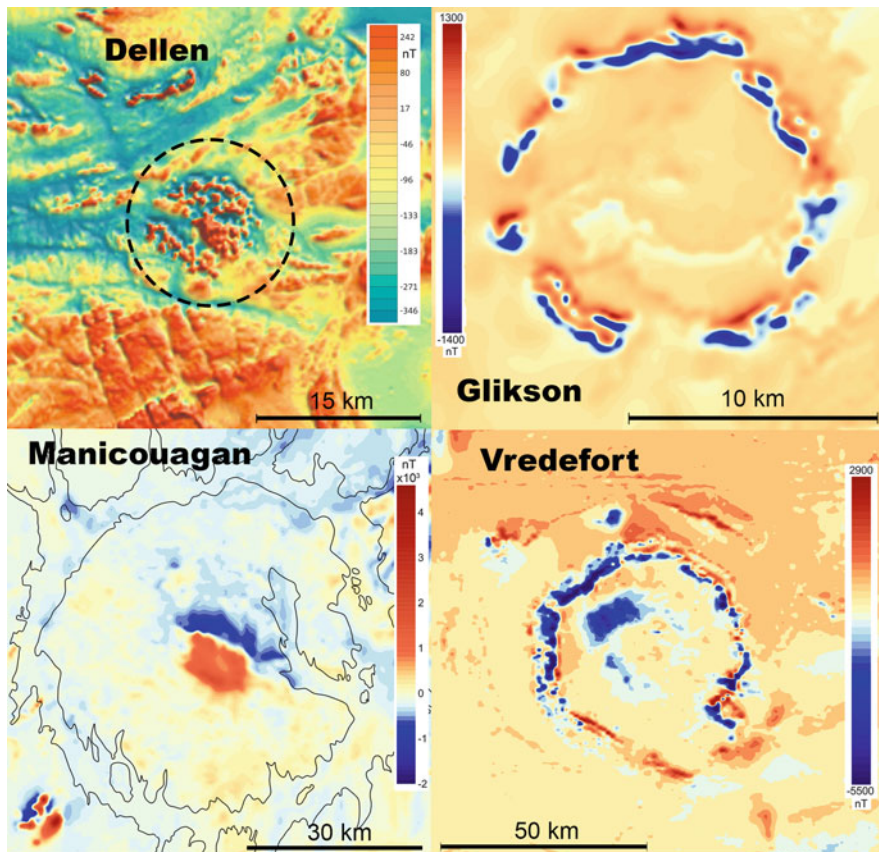


Fig. 13.3 Magnetic anomaly maps of the Dellen (Sweden), Glikson (Australia), Manicouagan (Canada) and Vredefort (South Africa) craters. The image for Dellen is courtesy of the Geological Survey of Sweden, www.sgu.se: 61.8°N, 16.8°E, diameter ca. 15 km, age ca. 89.0 Ma, anomaly range +250 to −1750 nT, erosion level 5 (crater-fill breccias/melt rocks partly preserved). Data for Glikson are courtesy of Geoscience Australia: 24.0°S, 121.6°E, diameter ca. 19 km, age <508 Ma, anomaly range +1280 to −1330 nT, erosion level 5. Data for Manicouagan are courtesy of the Natural Resources of Canada, Geoscience Data Repository for Geophysical Data, 2014 (<http://gdr.agg.nrcan.gc.ca/gdrdap/dap/search-eng.php>), 51.4°N, 68.7°W, diameter ca. 90 km, age 214 Ma, anomaly range +4200 to −1900 nT, erosion level 4 (rim largely eroded, crater-fill breccias/melt rocks preserved). Vredefort (data from the Geological Survey of South Africa—see Corner et al. (1990) and Antoine et al. (1990)), 27.0°S, 27.5°E, diameter ca. 250 km, age 2023 Ma, anomaly range +3000 to −5500 nT, erosion level 6 (crater-fill breccias/melt rocks eroded, isolated breccia dikes). Erosion levels from Osinski and Ferrière (2016)

Key to these interpretations is that shock from the impact created single-domain magnetite within the planar deformation features in quartz (Cloete et al. 1999). That two generations of magnetite existed in Vredefort basement rocks was substantiated by Carporzen et al. (2006), who found two distinct Verwey transitions that were clearly linked to >2.7 Ga multidomain magnetite and to single-domain magnetite that was thought to be created during the impact event at 2 Ga. However, this latter interpretation was proved false by Carporzen et al. (2012), who drilled two 10 m deep cores in the negative anomaly region. They found that the single-domain magnetite that carried the lower of the two Verwey transition temperatures disappeared about a half meter below the surface. Coupled with a wide range of magnetic experiments, Carporzen et al. (2012) concluded that the majority of the single-domain magnetite was created by lightning strikes. Salminen et al. (2013) arrived at a similar conclusion from laboratory experiments that produced artificial lightning strikes on Vredefort rocks. Hence, the most likely explanation for the negative “horseshoe” anomaly comes from thermal overprinting during impact when the field was in a reversed polarity state (Hargraves 1970; Jackson 1982; Carporzen et al. 2005). Rocks closer to the center of the crater are relatively magnetite poor (Hart et al. 1995; Carporzen 2006), which explains the lack of negative anomalies there.

Several other notable examples of magnetic anomalies exist. For example, concentric circular anomalies with amplitudes ranging from 50 to 4 nT are described for the Foelsche, Yallalie, and Wolfe Creek craters (Australia; Hawke 2003, 2004). Hawke (2003) interpreted the anomaly pattern at Yallalie to be due to remanently magnetized impact melt or post-impact hydrothermal activity. Indeed, hydrothermal activity is occasionally evoked as the cause of magnetic anomalies, such as at Chicxulub (Mexico; Pilkington and Hildebrand 2000) and Haughton (Canada; Quesnel et al. 2013). The Haughton anomaly map contains a particularly spectacular positive spike of ca. 700 nT in the center (Pohl et al. 1985; Glass et al. 2002, 2005). Pohl et al. (1985, 1988) ascribed the anomaly to magnetite-bearing, shocked crystalline basement with vertically downward inclinations. Quesnel et al. (2013) found that pyrrhotite-bearing melt rocks also possessed downward-directed inclinations; their magnetic models suggest that the source of the central anomaly is a magnetized body with a 1 km deep root that was created by post-impact hydrothermal alteration of the basement.

Scott et al. (1997) reviewed the magnetic anomalies of four Canadian craters: West Hawk, Deep Bay, and Clearwater (East and West). All four impact structures exhibit reduced magnetizations that extend beyond their morphologically defined limits. Scott et al. (1997) concluded that the target rocks beneath the crater floors must reflect an impact-induced reduction in NRM intensity and susceptibility to account for discrepancies between observed and modeled data. While shock has clearly been shown to modify the magnetic properties of ferromagnetic minerals, experimental results indicate that shock can either magnetize a rock parallel to the ambient field or demagnetize a rock in a manner analogous to alternating field demagnetization (Dunlop et al. 1969; Hargraves and Perkins 1969; Cisowski and Fuller 1978; Pohl et al. 1975; Gattacceca et al. 2007). For example, an alternative

explanation for the negative anomalies in the West Clearwater structure is that impact melt and basement rocks have reverse polarities, consistent with their deposition during the Kiaman reversed superchron (Zylberman et al. 2015), thus giving rise to negative magnetic anomalies. Shock effects on magnetization are discussed further below.

A final point concerns the role of faulting and the circular expression of magnetic anomalies. Chicxulub (Mexico) serves as a good example where a system of regional vertical faults surrounding the central portion of the crater explain the magnetic high and lows of the aeromagnetic anomalies over the southern sector of the crater (Rebolledo-Vieyra et al. 2010). Circular fault systems, predicted in structural models of formation and evolution of complex multi-ring craters, are well documented in Manicouagan where intensive drilling for mineral exploration indicates that the distribution of the impact melt is controlled by vertical faults with 100s to 1000s of meters of offset surrounding the central uplift (Spray and Thompson 2008; Spray et al. 2010). Ring faults likely facilitated the transport of fluids that led to the creation of massive sulfide ore deposits at Sudbury, where anisotropy of magnetic susceptibility reveals strongly developed lineations in the fault zones (Hirt et al. 1993; Scott and Spray 1999).

13.3 Magnetic Mineralogy

13.3.1 Melt Rocks

Titanomagnetite ($\text{Fe}_{3-x}\text{Ti}_x\text{O}_4$), mostly with low Ti concentration ($\text{Ti} < \text{ca. } 5\%$ with corresponding Curie temperatures from 525 to 580 °C), is the dominant magnetic mineral found in melt rocks, followed by pyrrhotite (Fe_{1-x}S) and then titanohematite ($\text{Fe}_{2-x}\text{Ti}_x\text{O}_3$). Fregerslev and Carstens (1976) and Kukkonen et al. (1992) (Lappajärvi) and El Goresy (1968) (Ries) report the presence of FeNi spherules or nickel-bearing native iron. Although definitive magnetic evidence such as Curie temperatures $>680^\circ\text{C}$ is not provided, the presence of FeNi inclusions in impact glasses seems well established (El Goresy et al. 1968). Badjukov et al. (1989) report metallic Fe ($>2\%$ Ni) in suevite in the Kara (Russia) crater, while Öhman et al. (2003) report Curie temperatures of fresh impact glasses from Kara solely within the magnetite range. Perhaps the greatest obstacle in drawing conclusions on magnetic mineralogy stems from the relatively low number of observations compared to the enormous volume and heterogeneity of available material.

Little attention has been paid to the importance of the iron oxide composition on the temperature, oxygen activity, and cooling time of the melts produced by impacts. For example, Eitel et al. (2014) found that the impact melt-bearing rocks in the Rochechouart crater contain distinctly different titanohematite compositions at three different places—ranging from nearly pure hematite (Curie temperatures of $673 \pm 9^\circ\text{C}$) in the Montoume quarry which contains the rocks with the highest melt

degrees, followed by Curie temperatures of 656 ± 5 °C and 630 ± 4 °C at the Valette and Chassenon localities, respectively. The unique magnetic mineralogy at Valette produces self-reversal behavior stemming from magnetic exchange interaction. Steiner (1996) also reported self-reversal-like behavior from the Manson (USA) and Chicxulub (Mexico) craters, although the evidence is fairly equivocal.

A noteworthy observation comes from the Chesapeake Bay (USA) structure where Mang et al. (2012) reported the existence of an anomalous ferrimagnetic pyrrhotite with Curie temperatures between 350 and 365 °C, significantly higher than the known Curie temperature of 325 °C for monoclinic pyrrhotite [Fe₇S₈]. Moreover, it lacks the 34 K Besnus transition characteristic of monoclinic pyrrhotite. This species has a metal-to-sulfur ratio of 0.81, which indicates a distinctly higher vacancy concentration than monoclinic pyrrhotite with a composition closer to smythite (Fe₉S₁₁). Mang et al. (2012) suggested that this phase was produced by shock metamorphism and carries a stable natural remanent magnetization. On the other hand, shock experiments on monoclinic pyrrhotite to 12 GPa found no change in the Curie or Besnus temperatures and no evidence for iron depletion (Louzada et al. 2010). Figure 7c in Mang et al. (2012) shows sub-micron-sized nickel-rich phases within a shocked pyrrhotite, which leads us to speculate whether the anomalously high Curie temperatures are rather due to Ni metal inclusions, since pure Ni has a Curie temperature of ca. 358 °C (Wei et al. 2014). Confirming the existence of an anomalous ferrimagnetic pyrrhotite phase warrants further investigation.

Whether the ferromagnets in impact melt rocks are inherited or crystallized in the melt yields further information on the formation temperature of the system. Clear examples exist for shocked magnetite or pyrrhotite phases existing in impact melts and suevites (Chesapeake Bay: Mang et al. 2012; Bosumtwi: Kontny et al. 2007; Ries: Koch et al. 2012). Others contain euhedral grains with no shock features (Manicouagan: Eitel et al. 2016; Mistastin: Hervé et al. 2015). That shocked ferrimagnets in melt-poor suevites record the field direction acting at the time of impact suggests that they were heated above their Curie temperatures. On the other hand, if the temperatures did not exceed the Curie temperature, the rocks would tend to have low magnetization intensities with erratic demagnetization directions due to the randomized vectors of the inherited clasts. Such results would likely be considered spurious and discarded. Alternatively, if a single inherited clast dominated the volume of the sample, it could contain a high magnetization intensity with stable demagnetization directions that would likely differ from the ambient field direction at the time of impact. Such samples might be disregarded as outliers.

Pilkington et al. (2004) documented the creation of iron hydroxide (limonite-goethite) in an impactite sequence from the Yax-1 drill hole in the Chicxulub crater. Concentrically zoned, botryoidal limonite-goethite is abundant as an interstitial phase in the matrix of reworked suevite. It occurs ubiquitously in the impactite sequence, mostly as open-space fillings in lithic basement fragments. These phases, as well as secondary magnetite, formed as a result of low-temperature (<150 °C) alteration—they likely serve as the best examples of magnetic phases created by hydrothermal processes (see also Urrutia-Fucugauchi et al. 2004). Botryoidal tex-

ture of hematite-rich impact bombs from the Araguainha structure led (Jovane et al. 2011) to speculate that the hematite was produced by post-impact hydrothermal circulation. Hydrothermal alteration of the host rock was proposed to explain the origin of the magnetic anomalies at the Lake St. Martin crater (Coles and Clark 1982). Yokoyama et al. (2015) proposed that fluid migration along faults altered the basement rock and created the circular magnetic anomaly pattern at the Vargeao structure. On the other hand, the spatial distribution of the iron oxides in the impact melts at Manicouagan is better explained by a model of degassing and oxygen diffusion in the upper few hundred meters of the impact melt, rather than an advecting system associated with hydrothermal activity (Eitel et al. 2016).

Pseudotachylite, a glass-bearing, pulverized rock, can be found in impact craters in quantities far exceeding pseudotachylite from non-impact-related faults. Relatively few studies have focused on the magnetic properties of pseudotachylite from impact structures. Elming and Bylund (1991) found that hematite carries the magnetization in two pseudotachylite sites from the Siljan (Sweden) crater and magnetite in another site. Pseudotachylite in the 45 km long, 10 to 500 m wide, South Range breccia belt in the Sudbury crater contains pyrrhotite (Scott and Spray 1999). To our knowledge, only Nakamura and Iyeda (2005) have performed paleointensity experiments on pseudotachylite. Their petrologic observations on samples from Sudbury reveal abundant fine-grained magnetite inclusions and coarse-grained multidomain magnetite and exsolved titanomagnetite.

Salminen et al. (2009) found that pseudotachylitic breccia from Vredefort contains two distinct magnetite phases: grains in the micrometer size range that are interpreted to carry remanence from the time of the impact and larger, altered ($>50\text{ }\mu\text{m}$) grains that carry a viscous remanence. Carporzen et al. (2006) identified single-Verwey transitions in eight pseudotachylite samples from four localities in Vredefort. The lower right image in Fig. 13.4 shows an electron microprobe image of the magnetite from sample V0111A extracted a few 10s of cm from sample V0112 reported in Carporzen et al. (2006) that has a Verwey transition temperature of 94 K based on a field cooling experiment using a Quantum Design, magnetic property measurement system and 100 K from a Lake Shore Cryotronics alternating current susceptometer. Chemical analyses indicate that this mineral is Ti-free titanomagnetite, which suggests the relatively low Verwey transition temperatures stem from oxidation and not from cation (titanium) substitution. Because the pseudotachylite from this quarry yields paleomagnetic directions consistent with the impact at 2 Ga (Carporzen et al. 2005), the oxidation occurred during genesis. The formation temperature of the pseudotachylite must have exceeded the melting temperature of magnetite (1500–1600 °C), and have been likely higher if the formation depth was 20 km. The fascinating texture could have developed during rapid decompression when magnetite micromelts agglomerated to form larger crystallites.

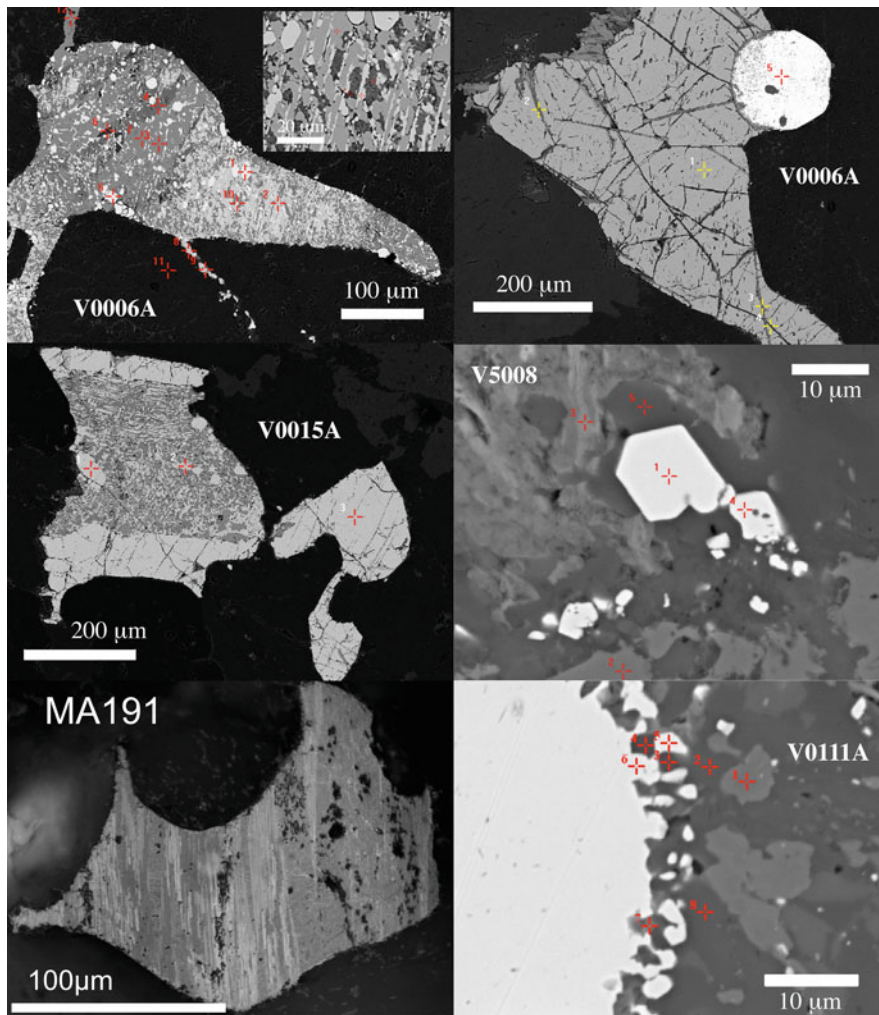


Fig. 13.4 Electron microprobe images of rocks from the Vredefort (V) and Manicouagan (MA) craters. The image on the *upper right* is Ti-poor magnetite showing fractures interpreted to be shock induced. The round bright mineral is monazite (rare earth element-bearing phosphate). The image on the *upper left* is highly exsolved titanomagnetite that comes from the same 1-in. core as that on the upper right. Bright (dark) grains are Ti-poor (rich) titanomagnetite. *Middle left image* of sample V0015A contains a combination of the two examples from V0006A. Margins are Ti-poor, fractured magnetite, while the interior is highly exsolved titanomagnetite with no cracks. V5008 contains euhedral Ti-poor magnetite with no evidence for shock. V0111A comes from a pseudotachylite in the Otavi quarry in Vredefort. The bright mineral is Ti-poor magnetite. MA191 shows an exsolved iron-titanium oxide from a gneissic diorite (Eitel et al. 2016)

13.3.2 Target Rocks

How meteorite impacts modify the magnetic signals of the target rocks is as complex as the diverse petrology existing in the myriad of craters. Images of fractured grains are published for Bosumtwi (Kontny et al. 2007), Keurusselkä (Raiskila et al. 2011), and Sudbury (Giroux and Benn 2005). Figure 13.4 shows a few curious examples (V0006A and V0015A) from the granulite facies rocks in Vredefort collected in the “horseshoe” region containing the most negative magnetic anomalies inside the crater (Fig. 13.3). The image on the upper right is Ti-poor magnetite showing evidence for shock. Darker material in the cracks is likely sphene (Ca, Ti silicate). The image on the upper left comes from the same 1-in. core as that on the right. This grain consists of highly exsolved iron-titanium oxide whose morphology is highly rounded. The bright regions are Ti-poor magnetite while the darker material is Ti-rich magnetite. Some titanomagnetite from the main body appears to have been injected into surrounding minerals.

Sample V0015 (middle left image in Fig. 13.4) was collected a few meters from V0006. This sample shows a combination of the two examples above whose margins are composed of Ti-poor, shocked magnetite, while the interior is highly exsolved titanomagnetite with no cracks. Sample V5008 comes from a granite quarry in the northwest part of the Vredefort crater, about 1.5 km from the contact with the sediments, outside the region with distinctive negative anomalies. It contains euhedral Ti-poor magnetite with no evidence for shock. In comparison, the lower right image (MA191) from Manicouagan shows an exsolved iron-titanium oxide from a gneissic diorite (Fig. 3 in Eitel et al. 2016). Its non-euhedral morphology mimics that of the exsolved titanomagnetite from Vredefort, except that MA191 shows only one preferred exsolution plane, whereas V0006A has multiple planes. We think that the shock texture in V0006A stems from the 2 Ga meteorite impact whereas the multiplanar exsolution texture might be due to partial melting from lightning strikes. More work is needed to understand the shock textures and morphologies of iron oxides from target rocks.

13.3.3 Shock Remanent Magnetization

Static and dynamic pressures have the potential to drastically change the magnetic properties of the ferromagnetic minerals in rocks (Hargraves and Perkins 1969; Pohl et al. 1975; Cisowski and Fuller 1978; Gattaccea et al. 2010; Louzada et al. 2010; Tikoo et al. 2015; Bezaeva et al. 2016). A natural remanent magnetization (NRM) acquired in the Earth magnetic field can be appreciably reduced by weak shock waves as low as 1 GPa. On the other hand shock waves can generate new remanent magnetizations in an ambient field on par with the strength of that of the Earth ($\sim 50 \mu\text{T}$) and thus overprint the preexisting NRM. Experiments show that these shock remanent magnetizations (SRMs) primarily affect the grains with relatively

low coercive forces that can be removed by alternating field demagnetization. Thermal effects can be neglected for pressures less than a few GPa. Higher pressures lead to irreversible changes of the mineralogical and magnetic properties, such as susceptibility or coercive force, and thermal effects can no longer be neglected, which leads to an ambiguity whether the remanence in target rocks is due to an SRM (shock remagnetization in the absence of a thermal overprint) or whether they are complete or partial thermal overprints that potentially erased an SRM. Distinguishing an SRM from a thermal (TRM) or chemical (CRM) remanent magnetization is a complex problem (Halls 1979).

Among the earliest investigations for shock remanent magnetization (SRM) was a study at the Barringer (USA) impact structure. There, Hargraves and Perkins (1969) found no evidence for modification of the magnetic remanence at four, hematite-bearing red bed sites around the rim of the crater when compared to the changes measured from shock created by underground nuclear explosions on magnetite+hematite-bearing tuff or compared to laboratory ballistic shock experiments on magnetite-bearing basalt. Further work by Cisowski and Fuller (1978) suggested that dolomite and sandstone in the crater underwent changes in remanence and hysteresis properties with increasing degrees of shock metamorphism. Remanent directions in deformed Ordovician sediments at the Kentland structure (USA) are solely of normal polarity and fail the fold test, which led (Jackson and Van der Voo 1986) to conclude that the magnetization directions do not stem from a shock remanence since the directions post-date deformation, but they could be related to heat generated from the impact. Deformed carbonate rocks at the Weaubleau (USA) structure possess post-folding magnetizations that cannot be an SRM, but are possibly related to fluids generated from the impact event that created a chemical remanent magnetization (Dulin and Elmore 2008). Agarwal et al. (2015) found no evidence for shock-related reorientation of the magnetic principal axes in the magnetite-bearing basement rocks 4–8 km from the center of the Lockne (Sweden) crater where shock pressures were relatively low (<0.5 and >0.2 GPa). In a borehole 4 km from Lockne's center, Melero-Asensio et al. (2015) found that the magnetic properties of rocks affected by the impact show a slight weakening in the coercivity of magnetic minerals in comparison with rocks not affected by the impact.

Evidence for shock remanent magnetization at the Lonar (India) crater is hotly contested. Rao and Bhalla (1984) claimed that systematic variations in magnetization intensity and susceptibility could be detected over a radial distance of 150 m in the target basalt flows. Cisowski and Fuller (1978) suggested that shock influenced the remanence and the coercivity of the basalts. Nishioka and Funaki (2008) imparted ballistic shock on Lonar basalts—the magnetic remanence and susceptibility were reduced and the principal axes of magnetic anisotropy ellipsoid became reoriented and distorted. Consistent with these experimental results, Misra et al. (2010) found a lowering of the degree of anisotropy compared to unshocked rocks as well as widely scattered principal axes of the magnetic anisotropy ellipsoid directions from basalts collected around the rim. However, Misra et al. (2010) and a subsequent study by Arif et al. (2012) failed to apply a tilt correction

for folding around the rim. Louzada et al. (2008) did apply a tilt correction and found that viscous (and/or chemical) remanent magnetization acquired in the ca. 50 kyr subsequent to crater formation obscured any evidence of shock remanent magnetization, which calls into question the interpretations of the anisotropy data. Moreover, Agarwal et al. (2016) found no significant differences in the magnetic fabrics of the Lonar basalts in the deformed rim or farther away.

Halls (1979) argued that the magnetic directions of a magnetization component isolated in the low-coercivity part of the alternating field unblocking spectrum of target rocks from the Slate Islands crater were reoriented by the passage of a shock wave within 2–3 s following meteorite impact. The main evidence for the overprint being acquired as a shock remanent magnetization was that the low-coercivity magnetization component clustered more tightly after making a structural correction based on shatter cone directions. The magnetization of the matrix of clastic breccia dikes that formed during the impact event had a similar direction, which led (Halls 1979) to interpret it to have formed as a thermal remanent magnetization due to frictional heating during their emplacement. A subsequent study by Fairchild et al. (2016) on Slate Islands breccia dikes confirmed this thermal remanent magnetization interpretation by demonstrating that clasts within the dikes were overprinted as well. This work found a tight grouping of paleomagnetic directions in breccia dikes throughout the Slate Islands structure in the absence of a tectonic correction, which implies that the dikes cooled and locked in magnetic remanence over a time interval in which the impact structure was not deforming. These results indicate that the crater reached a stable geometry within 6 min of the impact based on thermal modeling of the thinnest dikes. The overprint component in the target rocks away from the dikes unblocks mostly between 275 and 325 °C, which may indicate that the overprint is thermal in origin (Tikoo et al. 2015; Fairchild et al. 2016), in contrast with the SRM interpretation of Halls (1979).

At Mistastin, thermally remagnetized anorthositic basement rocks near the contact with impact melts have higher remanent magnetizations and higher coercivities than non-thermally remagnetized anorthositic basement rocks (Hervé et al. 2015) (compare red and blue curves in Fig. 13.5a, b). Hence, the thermally remagnetized samples with the heightened coercivities could be mistaken as a shock product. This highlights the ambiguity whether an SRM is due to remagnetization solely by passage of shock waves through the target rock, or whether heat from the impact thermally overprinted the target rock (Bezaeva et al. 2016), which also increased the coercivity and unblocking spectra as is the case for Mistastin. The Day plot (Fig. 13.5c; Day et al. 1977) yields information on the domain state from magnetic hysteresis parameters. Mistastin basement rocks exhibit a progression from multidomain towards increasingly single-domain-like behavior approaching the crater's center (Hervé et al. 2015). We think this pattern arises from the strain due to shock and not thermal effects from shock, consistent with laboratory experiments (Carporzen and Gilder 2010; Reznik et al. 2016), although the samples from the central uplift (Horseshoe Island) might also be thermally influenced.

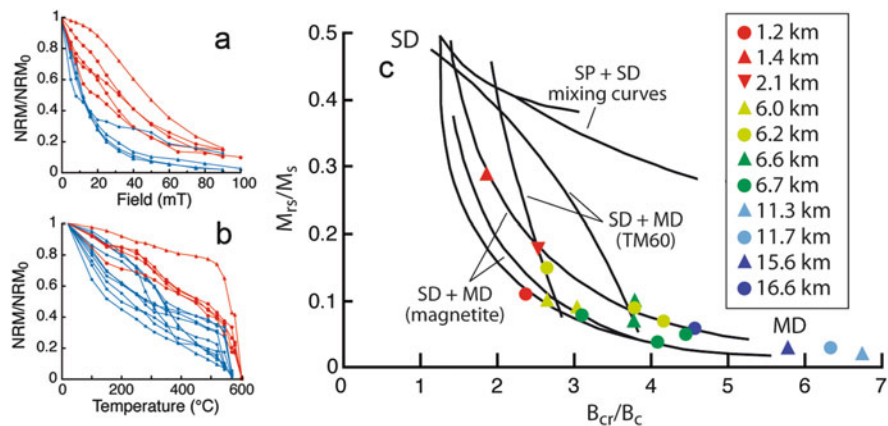


Fig. 13.5 Rock magnetic data from anorthositic basement rocks from the Mistastin impact structure (from Hervé et al. 2015). (a) and (b) Normalized alternating field and thermal magnetization intensity curves comparing samples in red that were thermally remagnetized by 36 Ma impact melts with those in blue that were not thermally remagnetized. (c) Day plot (Day et al. 1977) of the remanence ratio (remanent saturation magnetization [M_{rs}]/saturation magnetization [M_s]) versus the coercivity ratio (coercivity of remanence [B_{cr}]/bulk coercive force [B_c]) with single-domain (SD)-multidomain (MD) and superparamagnetic (SP)-SD mixing curves for pure magnetite and titanomagnetite from Dunlop (2002). Samples are color coded as a function of radial distance from the crater's center

13.4 Paleomagnetism

13.4.1 Crater Formation Processes

Paleomagnetic studies in impact craters can shed light on crater formation processes. The transient crater becomes filled with impact melts and breccias, and then rebound occurs, which might cause displacement of the crater fill material. Larger craters have central uplifts and even larger craters have multiple rings. Questions arise as to how fast these processes occur and how the structural features form kinematically. Paleomagnetism can help answer these questions by examining the dispersion in directions from rocks sampled around the crater (Fig. 13.6), noting that one needs to unravel the effect of geomagnetic secular variation, which creates directional dispersion through dipole wobble, from directional reorientation due to kinematic readjustment. One must keep in mind that the “paleomagnetic clock” starts ticking only after the ferromagnets in the studied rocks cool through their Curie temperatures. The clock in craters <30 km in diameter with melt thicknesses generally <100 m (e.g., Ries or Rochechouart) likely begins within days to 10s or 100s of years of formation; however, it can be as long as a few 10^4 years in larger craters like Manicouagan where impact melts reach several 100s of meters

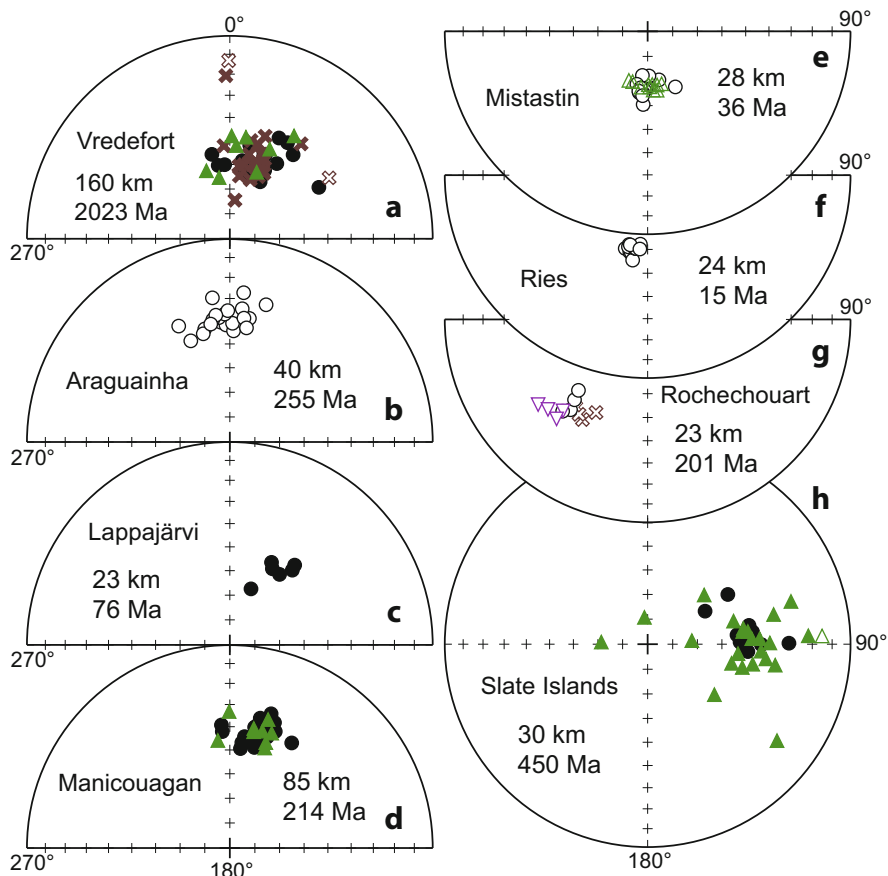


Fig. 13.6 Site mean paleomagnetic directions from impact melt-bearing rocks from eight craters. Age and diameter data from <http://www.passc.net/EarthImpactDatabase/index.html>. Open symbols upper hemisphere, solid symbols lower hemisphere. (a) Vredefort: circles from Salminen et al. (2009), triangles from Hargraves (1970), crosses from Carporzen et al. (2005); (b) Araguainha: Yokoyama et al. (2014); (c) Lappajärvi: Pesonen et al. (1992); (d) Manicouagan: circles from Eitel et al. (2016), triangles from Laroche and Currie (1967); (e) Mistastin: circles from Hervé et al. (2015), triangles from Currie and Laroche (1969); (f) Ries: Pohl (1965); (g) Rochechouart: circles from Eitel et al. (2014), triangles from Pohl and Soffel (1971), crosses from Carporzen and Gilder (2006) (two data points inverted to reversed polarity); (h) Slate Islands: circles from Fairchild et al. (2016), triangles from Halls (1979)

thick. To a first order, Fig. 13.6 shows that structural modifications related to crater formation completely ceased over these time scales. The general impression is that the smaller the crater, the less the dispersion, which makes sense recalling that smaller craters likely have thinner impact melts that cool quicker, so they record less time and smaller secular variation amplitudes.

13.4.2 Do Meteorite Impacts Influence the Geodynamo?

Because the energy released during an impact can exceed that of the strongest terrestrial earthquakes by several orders of magnitude, several workers have questioned whether impact events can perturb the magnetohydrodynamic regime in planetary interiors and influence the magnetic field generation process. Testing this has been our overriding motivation over the last several years. Here we summarize our findings and give additional evidence from other craters.

Glass and Heezen (1967) were among the first to link changes in the geomagnetic field to a meteorite impact event by claiming that the Australasian microtektite field was deposited during the period coinciding with the last known reversal (Brunhes-Matuyama). Durrani and Khan (1971) then suggested that the slightly older Ivory Coast microtektite field was deposited just above the base of a brief magnetic chron known as the Jaramillo event. Further drilling in the Atlantic Ocean led (Glass and Zwart 1979) to conclude that the Ivory Coast microtektite field was four times larger than previously thought. They correlated the tektite layer with the beginning of the Jaramillo event.

The association of meteorite impacts with geomagnetic field reversals led several workers to explore how an impact event could perturb the geodynamo (e.g., Schwarzschild 1987). Muller and Morris (1986) postulated that the link between impacts and geomagnetic perturbation occurred through climate change. They calculated that if sea-level fluctuations were large (>10 m) and rapid (a few 100 years) enough before adjustments in the moment of inertia could take place, then shear would occur between the Earth's mantle and solid core, which would deform convection cells in the liquid outer core, thereby influencing the magnetic field. Their scenario predicted that the dipole component of the geodynamo would diminish with a concomitant increase in higher order components, which are characteristics of field reversals and transitions. Pal and Creer (1986) performed a statistical analysis of field reversals and found a correlation with episodes of bombardment. Like Muller and Morris (1986), and later Burek and Wänke (1988), Pal and Creer (1986) postulated that meteorite impacts would create turbulence in the outer core leading to lower field strength and a departure from axial symmetry, consistent with reversal models.

Won and Kuo (1973) worked out the conditions for which the solid inner core begins oscillating from translational motion due to an earthquake. They found that a magnitude 8.8 earthquake (10^{18} J of energy released) would provoke an inner core oscillation with an amplitude of 58 cm. The amount of inner core oscillation required to modify the magnetohydrodynamic regime in the outer core is unknown, although Roberts et al. (2009) and Arkani-Hamed and Olson (2010) proposed that bombardment by very large meteorites producing craters >2500 km in diameter could stop the Martian dynamo.

Loper and McCartney (1990) computed that dynamical coupling between the core and mantle is too strong to allow large angular displacements to occur and thus refuted an extraterrestrial origin for field reversals. Rice and Creer (1989) calculated that shock spallation, either at the core-mantle or inner-outer core boundaries, would not provide enough energy to significantly disturb the geomagnetic field. More detailed work on the Australasian and Ivory Coast microtektite fields, including a more detailed examination of sedimentation rates, provided evidence that deposition of the tektite fields was shifted by 8–15 kyr from the nearest geomagnetic event (Burns 1990; DeMenocal et al. 1990; Schneider and Kent 1990; Schneider et al. 1992; Glass et al. 1991). Hartl and Tauxe (1996) subsequently found a global decrease in paleointensity approximately 15 kyr prior to the Brunhes-Matuyama reversal, suggesting that it may have commenced earlier than previously thought—precisely at the time when the Australasian microtektites were deposited. Two suevite sites associated with the Bosumtwi crater that produced the Ivory Coast microtektite field yielded normal polarity directions consistent with emplacement during the Jaramillo chron (Plado 2000). Polarity designations of directions from unoriented drill cores (Elbra et al. 2007) cannot be assigned with confidence; given the crater’s proximity to the geographic equator, latitudinal variations in the position of the geomagnetic equator obscure polarity designation based on inclination-only data.

Tektite production represents only a small fraction of the material created during a meteorite impact, whereas a much larger volume of the target rocks is heated, often melted, and deposited near the crater. For this reason, a more straightforward test for a relationship between meteorite impacts and geomagnetic field changes can be performed by examining the thermal remanent magnetization of the melt rocks and impact breccias (suevites) acquired during cooling through the Curie temperatures of the magnetic minerals after the impact. We thus initiated a paleomagnetic study of rocks within meteorite craters whose ferromagnetic minerals cooled through their Curie temperatures after impact. The objective was to sample impact lithologies as a function of cooling time, e.g., from the margins toward the interior of impact melt sheets, to identify potential changes in magnetic field direction and/or intensity.

We carried out such work in the Ries (Germany: Koch et al. 2012), Rochechouart (France: Eitel et al. 2014), Mistastin (Canada: Hervé et al. 2015), and Manicouagan (Canada: Eitel et al. 2016) craters. In the first three, we found no evidence for aberrant directions or for paleointensity values outside the range of expected values. That anomalous field behavior was not observed in any of them could result from insufficient amounts of energy released during these impact events, or because the rocks cooled too fast after impact and “missed” the event. The amount of time captured by the magnetic record in these craters did not exceed 400 years. At the Manicouagan structure, we sampled stratigraphic thicknesses corresponding to several hundred to several thousand or even tens of thousands of years of cooling time following the impact. These time scales exceed normal overturn times (3000–5000) in the outer core, i.e., the time needed for a geomagnetic reversal (Bogue and Merrill 1992; Leonhardt and Fabian 2007; Valet et al. 2012), so we should have observed an effect had the Manicouagan impact perturbed the dynamo process. Our

overall conclusion is that the seismic energy released from terrestrial impacts that create craters <90 km in diameter is insufficient to disturb the dynamo process (such as through oscillation of the inner core) in a way that results in observable changes in geomagnetic field direction or intensity on the Earth's surface.

The 180 km diameter Chicxulub crater should be a candidate for further research. In the Yucatan-6 exploratory well, about 60 km from the crater's center, paleomagnetic research on impact melts and breccias yielded inclinations of -40° to -45° , indicating a reverse polarity field during impact around the Cretaceous-Tertiary boundary (Urrutia-Fucugauchi et al. 1994). These inclinations lie within the range of expected values predicted by the apparent polar wander path for North America, which suggest that the rocks were not overprinted during drilling and extraction. Subsequent paleomagnetic work by Rebolledo-Vieyra and Urrutia-Fucugauchi (2004) on a different borehole (Yax-1) confirmed that impact breccias have reverse polarities and that carbonates deposited up to 56 cm over the impact breccias also contain reverse polarity. Above this, four samples from 20 cm of carbonate have normal polarity, which leads us to wonder whether the polarity flip could represent a link between impact and reversal. However, there is room for doubt as the data in Fig. 3 of Rebolledo-Vieyra and Urrutia-Fucugauchi (2004) indicate that demagnetization was sometimes incomplete and that some samples with downward-pointing inclinations could be drilling-induced overprints. Urrutia-Fucugauchi et al. (2004) presented a much more complicated stratigraphic profile of inclinations from the same core. They interpreted the reverse magnetization as the primary component in the breccias, with the rest of the remanences being acquired during an extended interval where secondary partial or total remagnetization occurred. The latter seems well substantiated by magnetic mineralogy studies by Pilkington et al. (2004). Further paleomagnetic work on the impactite sequence in Yax-1 yielded an even more complicated pattern of inclination variation with depth (Velasco-Villareal et al. 2011). Future drilling should shed more light on this intriguing problem.

13.5 Conclusions

Meteorite impact structures are among the most dominant topographic expressions in the Solar System. They commonly possess distinct magnetic anomalies. Magnetic expressions of impact craters have been used on Mars to date the history of its dynamo (Hood et al. 2003; Lillis et al. 2013). Shock waves from impact were proposed to influence the geodynamo and even to stop the Martian dynamo (Roberts et al. 2009; Arkani-Hamed and Olson 2010). Our data indicate that the impact events producing the Manicouagan, Ries, Rochechouart, and Mistastin structures had no observable affect on Earth's dynamo (Koch et al. 2012; Eitel et al. 2014; Hervé et al. 2015; Eitel et al. 2016); hence geodynamo disturbances from impacts should be considered improbable during the Phanerozoic when impact frequency and meteorite sizes were lower than in the Precambrian (French 1998). Other places

in the Solar System host craters much larger than on Earth, such as the South Pole Aitken crater on the Moon (2400 km) or Hellas Planitia on Mars (2300 km), so the influence could be significantly different in those cases.

Paleomagnetic directions in the impact melts and suevites from all studied craters show limited dispersion regardless of size. This suggests that tectonic adjustments, including the formation of central peaks, should be faster than it took the impactites to cool to ca. 600°, which is true even for very thin bodies that cooled within 10–100 days of impact. Further work is needed to unravel how shock pressures and thermal effects related to shock influence the magnetic remanence and rock magnetic characteristics of the target rocks. A dichotomy exists in that strain has a disproportionate influence on grains with low unblocking temperatures, yet produces systematically more single-domain-like grains whose unblocking spectra should be shifted higher as observed from thermal effects in Mistastin (Fig. 13.5). While shock experiments in Earth-like fields show that the magnetization vector can reorient parallel to the ambient field (e.g., Pohl et al. 1975; Gattaccea et al. 2008), static compression experiments do not, despite comparable changes in rock magnetic parameters (e.g., Hamano 1983; Valeev and Absalyamov 2000; Gilder et al. 2006).

Acknowledgements We thank the many collaborators and friends that contributed to this work: Ian Garrick-Bethell, Jennifer Buz, Laurent Carporzen, Armand Galdeano, Joshua Gilder, Rodger, Craig and Jarred Hart, Gwenaël Hervé, Joseph Hodich, Joe Kirschvink, Stephan Koch, Thomas Kunzmann, Maxime Le Goff, Eduardo Lima, Claude Marchat, Cassandra Marion, Manfried Muundjua, Francois Mazeaufroid, Gordon Osinski, Nikolai Petersen, Anne Pommier, John Spray, Paul Sylvester, Lucy Thompson, Claudia Trepmann, Ben Weiss, and Marie-France Yserd. This work was made possible through funding by Deutsche Forschungsgemeinschaft's Schwerpunktprogramm, Planetary Magnetism grant GI712/6-1. A thorough review by Nicolas Swanson-Hysell is greatly appreciated.

References

- Agarwal, A., Kontny, A., Greiling, R.: Relationship among magnetic fabrics, microfractures and shock pressures at an impact crater: a case study from Lockne crater, Sweden. *J. Appl. Geophys.* **114**, 232–243 (2015)
- Agarwal, A., Kontny, A., Srivastava, D., Greiling, R.: Shock pressure estimates in target basalts of a pristine crater: a case study in the Lonar crater, India. *Geol. Soc. Am. Bull.* **128**, 19–28 (2016)
- Antoine, L., Nicolaysen, L., Niccol, S.: Processed and enhanced gravity and magnetic images over the Vredefort structure and their interpretation. *Tectonophysics* **171**, 63–74 (1990)
- Arif, M., Basavaiah, N., Misra, S., Deenadayalan, K.: Variations in magnetic properties of target basalts with the direction of asteroid impact: Example from Lonar crater, India. *Meteorit. Planet. Sci.* **47**, 1305–1323 (2012)
- Arkani-Hamed, J., Olson, P.: Giant impacts, core stratification, and failure of the Martian dynamo. *J. Geophys. Res.* **115**(E7), E12021 (2010)
- Badjukov, D., Bazhenov, M., Nazarov, M.: Paleomagnetism of impactites of the Kara impact crater: preliminary results. In: *Lunar and Planetary Science Conference*, vol. 20 (1989)

- Barr, A., Citron, R.: Scaling of melt production in hypervelocity impacts from high-resolution numerical simulations. *Icarus* **211**, 913–916 (2011)
- Bezaeva, N., Swanson-Hysell, N.L., Tikoo, S., Badyukov, D., Kars, M., Egli, R., Chareev, D., Fairchild, L., Khakhalova, E., Strauss, B., Lindquist, A.: The effects of 10 to >160 GPa shock on the magnetic properties of basalt and diabase. *Geochem. Geophys. Geosyst.* **17**, 1–19 (2016)
- Bogue, S., Merrill, R.: The character of the field during geomagnetic reversals. *Ann. Rev. Earth Planet. Sci.* **20**, 181 (1992)
- Burek, P., Wänke, H.: Impacts and glacio-eustasy, plate-tectonic episodes, geomagnetic reversals: a concept to facilitate detection of impact events. *Phys. Earth Planet. Int.* **50**(2), 183–194 (1988)
- Burns, C.: The Australasian microtekite layer: implications concerning its source area and its relationship to the Brunhes/Matuyama geomagnetic reversal. PhD thesis, University of Delaware (1990)
- Bylund, G.: Paleomagnetism of a probable meteoritic impact, the Dellen structure. *Geologiska Föreningens i Stockholm Förhandlingar* **96**, 275–278 (1974)
- Carporzen, L.: Magnétisme des cratères d'impact de météorite à Vredefort (Afrique du Sud) et Rochechouart (France). Thesis, Université Paris VII - Denis Diderot (2006)
- Carporzen, L., Gilder, S.: Evidence for coeval Late Triassic terrestrial impacts from the Rochechouart (France) meteorite crater. *Geophys. Res. Lett.* **33**, L19308, 1–6 (2006)
- Carporzen, L., Gilder, S.: Strain memory of the Verwey transition. *J. Geophys. Res.* **115**(B05103), 17 (2010)
- Carporzen, L., Gilder, S., Hart, R.: Paleomagnetism of the Vredefort meteorite crater and implications for craters on Mars. *Nature* **435**, 198–201 (2005)
- Carporzen, L., Gilder, S., Hart, R.: Origin and implications of the Verwey transitions in the basement rocks of the Vredefort meteorite crater, South Africa. *Earth Planet. Sci. Lett.* **251**, 305–317 (2006)
- Carporzen, L., Weiss, B., Gilder, S., Pommier, A.: Lightning remagnetization of the Vredefort impact crater: no evidence for impact-generated magnetic fields. *J. Geophys. Res.* **117**(E01007) (2012)
- Cisowski, S., Fuller, M.: The effect of shock on the magnetism of terrestrial rocks. *J. Geophys. Res.* **83**, 3441–3458 (1978)
- Cloete, M., Hart, R., Schmidt, H., Drury, M., Demanet, C., Sankar, K.: Characterization of magnetite particles in shocked quartz by means of electron- and magnetic force microscopy: Vredefort, South Africa. *Contrib. Miner. Petrol.* **137**, 232–245 (1999)
- Coles, R., Clark, J.: Lake St. Martin impact structure, Manitoba, Canada: magnetic anomalies and magnetizations. *J. Geophys. Res.* **87**, 7087–7095 (1982)
- Corner, B., Durrheim, R., Nicolaysen, L.: Relationships between the Vredefort structure and the Witwatersrand basin within the tectonic framework of the Kaapvaal craton as interpreted from regional gravity and aeromagnetic data. *Tectonophysics* **171**, 49–61 (1990)
- Currie, K., Larochelle, A.: A paleomagnetic study of volcanic rocks from Mistastin Lake, Labrador. *Earth Planet. Sci. Lett.* **6**, 309–315 (1969)
- Day, R., Fuller, M., Schmidt, V.: Hysteresis properties of titanomagnetites: grain-size and compositional dependence. *Phys. Earth Planet. Int.* **13**(4), 260–267 (1977)
- DeMenocal, P., Ruddiman, W., Kent, D.: Depth of post-depositional remanence acquisition in deep-sea sediments: a case study of the Brunhes-Matuyama reversal and oxygen isotopic stage 19.1. *Earth Planet. Sci. Lett.* **99**, 1–13 (1990)
- Dulin, S., Elmore, R.: Paleomagnetism of the Weaubleau structure, southwestern Missouri. In: Evans, K., Horton, J., King, J., Morrow, D. (eds.) *The Sedimentary Record of Meteorite Impacts*, volume special paper 437, pp. 55–64. Geological Society of America, Boulder (2008)
- Dunlop, D.: Theory and application of the Day plot (Mrs/Ms versus Hcr/Hc) 2. Application to data for rocks, sediments, and soils. *J. Geophys. Res.* **107**(B3), EPM 5-1 - EPM 5-15 (2002)
- Dunlop, D., Ozima, M., Kinoshita, H.: Piezomagnetization of single-domain grains: a graphical approach. *J. Geomagnet. Geoelectr.* **21**(2), 513–518 (1969)
- Durrani, S., Khan, H.: Ivory coast microtekites: fission track age and geomagnetic reversals. *Nature* **232**(5309), 320–323 (1971)

- Etet, M., Gilder, S., Kunzmann, T., Pohl, J.: Rochechouart impact crater melt breccias record no geomagnetic field reversal. *Earth Planet. Sci. Lett.* **387**, 97–106 (2014)
- Etet, M., Gilder, S., Spray, J., Thompson, L., Pohl, J.: A paleomagnetic and rock magnetic study of the Manicouagan impact structure: implications for crater formation and geodynamo effects. *J. Geophys. Res.* **121**, 1–19 (2016)
- Elbra, T., Kontny, A., Pesonen, L., Schleifer, N., Schell, C.: Petrophysical and paleomagnetic data of drill cores from the Bosumtwi impact structure, Ghana. *Meteorit. Planet. Sci.* **42**, 829–838 (2007)
- El Goresy, A.: Electron microprobe analysis and ore microscopic study of magnetic spherules and grains collected from the Greenland ice. *Contrib. Miner. Petrol.* **17**(4), 331–346 (1968)
- El Goresy, A., Fechtig, H., Ottemann, T.: The opaque minerals in impactite glasses. In: French, B., Short, N. (eds.) *Shock Metamorphism of Natural Materials*, pp. 531–554. Mono Book Corporation, Baltimore (1968)
- Elming, S., Bylund, G.: Paleomagnetism of the Siljan impact structure, central Sweden. *Geophys. J. Int.* **105**, 757–770 (1991)
- Fairchild, L., Swanson-Hysell, N., Tikoo, S.: A matter of minutes: breccia dike paleomagnetism provides evidence for rapid crater modification. *Geology* **44**(9), 723–726 (2016)
- Fregerslev, S., Carstens, H.: FeNi metal in impact melt rocks of Lake Lappäjärvi, Finland. *Contrib. Miner. Petrol.* **55**(3), 255–263 (1976)
- French, B.: *Traces of Catastrophe: A Handbook of Shock-Metamorphic Effects in Terrestrial Meteorite Impact Structures*, LPI Contribution, vol. 954, p. 120. Lunar and Planetary Institute, Houston, TX (1998)
- Gattacceca, J., Lamali, A., Rochette, P., Boustie, M., Berthe, L.: The effects of explosive-driven shocks on the natural remanent magnetization and the magnetic properties of rocks. *Phys. Earth Planet. Int.* **162**(1–2), 85–98 (2007)
- Gattacceca, J., Berthe, L., Boustie, M., Vadeboin, F., Rochette, P., De Resseguier, T.: On the efficiency of shock magnetization processes. *Phys. Earth Planet. Int.* **166**, 1–10 (2008)
- Gattacceca, J., Boustie, M., Lima, E., Weiss, B., Lamali, A., De Resseguier, T., Cuq-Lelandais, J.: Unraveling the simultaneous shock magnetization of rocks. *Phys. Earth Planet. Int.* **182**, 42–49 (2010)
- Gilder, S., Le Goff, M., Chervin, J.: Static stress demagnetization of single and multidomain magnetite with implications for meteorite impacts. *High Pressure Res.* **26**, 539–547 (2006)
- Giroux, L., Benn, K.: Emplacement of the Whistle dike, the Whistle embayment and hosted sulfides, Sudbury impact structure, based on anisotropies of magnetic susceptibility and magnetic remanence. *Econ. Geol.* **100**, 1207–1227 (2005)
- Glass, B., Heezen, B.: Tektites and geomagnetic reversals. *Nature* **214**(5086), 372 (1967)
- Glass, B., Zwart, P.: The Ivory Coast microtektite strewnfield: new data. *Earth Planet. Sci. Lett.* **43**(2), 336–342 (1979)
- Glass, B., Kent, D., Schneider, D., Tauxe, L.: Ivory Coast microtektite strewn field: description and relation to the Jaramillo geomagnetic event. *Earth Planet. Sci. Lett.* **107**, 182–196 (1991)
- Glass, B., Lee, P., Osinski, G.: Airborne geomagnetic investigations at the Haughton impact structure, Devon Island, Nunavut, Canada: New results. In: *Lunar and Planetary Science Conference*, vol. 33, p. 2008 (2002)
- Glass, B., Domville, S., Lee, P.: Further geophysical studies of the Haughton impact structure. In: *Lunar and Planetary Science Conference*, vol. 36, p. 2398 (2005)
- Halls, H.: The Slate Islands meteorite impact site: a study of shock remanent magnetization. *Geophys. J. R. Astron. Soc.* **59**, 553–559 (1979)
- Hamano, Y.: Experiments on the stress sensitivity of natural remanent magnetization. *J. Geomagn. Geoelectr.* **35**, 155–172 (1983)
- Hargraves, R.: Paleomagnetic evidence relevant to the origin of the Vredefort ring. *J. Geol.* **78**, 253–263 (1970)
- Hargraves, R., Perkins, W.: Investigations of the effect of shock on natural remanent magnetism. *J. Geophys. Res.* **74**, 2576–2589 (1969)

- Hart, R., Andreoli, M., Reimold, W., Tredoux, M.: Aspects of the dynamic and thermal metamorphic history of the Vredefort cryptoexplosion structure: implications for its origin. *Tectonophysics* **192**(3–4), 313–331 (1991)
- Hart, R., Hargraves, R., Andreoli, M., Tredoux, M., Doucoure, C.: Magnetic anomaly near the center of the Vredefort structure: implications for impact-related magnetic signatures. *Geology* **23**, 277–280 (1995)
- Hartl, P., Tauxe, L.: A precursor to the Matuyama/Brunhes transition-field instability as recorded in pelagic sediments. *Earth Planet. Sci. Lett.* **138**, 121–135 (1996)
- Hawke, P.: Geophysical Investigation of the Wolfe Creek Meteorite Crater. Geological Survey of Western Australia, Perth (2003)
- Hawke, P.: The geophysical signatures and exploration potential of Australia's meteorite impact structures. Thesis, University of Western Australia (2004)
- Henkel, H.: Geophysical aspects of meteorite impact craters in eroded shield environment, with special emphasis on electric resistivity. *Tectonophysics* **216**, 63–89 (1992)
- Hervé, G., Gilder, S., Marion, C., Osinski, G., Pohl, J., Petersen, N., Sylvester, P.: Paleomagnetic and rock magnetic study of the Mistastin Lake impact structure (Labrador, Canada): implications for geomagnetic perturbations and shock effects. *Earth Planet. Sci. Lett.* **417**, 151–163 (2015)
- Hirt, A., Lowrie, W., Clendenen, W., Kligfield, R.: Correlation of strain and the anisotropy of magnetic susceptibility in the Onaping formation: evidence for a near-circular origin of the Sudbury Basin. *Tectonophysics* **225**, 231–254 (1993)
- Hood, L., Richmond, N., Pierazzo, E., Rochette, P.: Distribution of crustal magnetic fields on Mars: shock effects of basin-forming impacts. *Geophys. Res. Lett.* **30**, 1281 (2003)
- Jackson, G.: Paleomagnetic study and magnetic modeling of the Vredefort Dome. PhD dissertation, University of Witwatersrand (1982)
- Jackson, M., Van der Voo, R.: A paleomagnetic estimate of the age and thermal history of the Kentland, Indiana cryptoexplosion structure. *J. Geol.* **94**, 713–723 (1986)
- Jovane, L., Yokoyama, E., Seda, T., Burmester, R., Trindade, R., Housen, B.: Rock magnetism of hematitic “bombs” from the Araguainha impact structure, Brazil. *Geochem. Geophys. Geosyst.* **12**, 14 p. (2011)
- Koch, S., Gilder, S., Pohl, J., Treppmann, C.: Geomagnetic field intensity recorded after impact in the Ries meteorite crater, Germany. *Geophys. J. Int.* **189**, 383–390 (2012)
- Kontny, A., Elbra, T., Just, J., Pesonen, L., Schleicher, A., Zolk, J.: Petrography and shock-related remagnetization of pyrrhotite in drill cores from the Bosumtwi impact crater drilling project, Ghana. *Meteorit. Planet. Sci.* **42**, 811–827 (2007)
- Kukkonen, I., Kivekäs, L., Paananen, M.: Physical properties of kärnäite (impact melt), suevite and impact breccia in the Lappajärvi meteorite crater, Finland. *Tectonophysics* **216**, 111–122 (1992)
- Larochelle, A., Currie, K.: Paleomagnetic study of igneous rocks from the Manicouagan structure, Quebec. *J. Geophys. Res.* **72**, 4163–4169 (1967)
- Leonhardt, R., Fabian, K.: Paleomagnetic reconstruction of the global geomagnetic field evolution during the Matuyama/Brunhes transition: iterative Bayesian inversion and independent verification. *Earth Planet. Sci. Lett.* **253**(1–2), 172–195 (2007)
- Lillis, R., Robbins, S., Manga, M., Halekas, J., Frey, H.: Time history of the Martian dynamo from crater magnetic field analysis. *J. Geophys. Res. Planets* **118**, 1–24 (2013)
- Loper, D., McCartney, K.: On impacts as a cause of geomagnetic field reversals or flood basalts. In: Geological Society of America Special Papers, vol. 247, pp. 19–26. Geological Society of America, Boulder (1990)
- Louzada, K., Weiss, B., Maloof, A., Stewart, S., Swanson-Hysell, N., Soule, S.: Paleomagnetism of Lonar impact crater, India. *Earth Planet. Sci. Lett.* **275**, 308–318 (2008)
- Louzada, K., Stewart, S., Weiss, B., Gattacceca, J., Bezaeva, N.: Shock and static pressure demagnetization of pyrrhotite and implications for the Martian crust. *Earth Planet. Sci. Lett.* **290**(1–2), 90–101 (2010)

- Macdonald, F., Wingate, M., Mitchell, K.: Geology and age of the Glikson impact structure, Western Australia. *Aust. J. Earth Sci.* **52**, 641–651 (2005)
- Mang, C., Kontny, A., Harries, D., Langenhorst, F., Hecht, L.: Iron deficiency in pyrrhotite of suevites from the Chesapeake Bay impact crater, USA. A consequence of shock metamorphism? *Meteorit. Planet. Sci.* **47**, 277–295 (2012)
- Melero-Asensio, I., Martín-Hernández, F., Ormö, J.: A rock magnetic profile through the ejecta flap of the Lockne impact crater (central Sweden) and implications for the impact excavation process. *J. Appl. Geophys.* **112**, 91–105 (2015)
- Misra, S., Arif, M., Basavaiah, N., Srivastava, P., Dube, A.: Structural and anisotropy of magnetic susceptibility (AMS) evidence for oblique impact on terrestrial basalt flows: Lonar crater, India. *Geol. Soc. Am. Bull.* **122**, 563–574 (2010)
- Muller, R., Morris, D.: Geomagnetic reversals from impacts on the Earth. *Geophys. Res. Lett.* **13**(11), 1177–1180 (1986)
- Muundjua, M., Hart, R., Gilder, S., Carporzen, L., Galdeano, A.: Magnetic imaging of the Vredefort impact crater, South Africa. *Earth Planet. Sci. Lett.* **261**, 456–468 (2007)
- Nakamura, N., Iyeda, Y.: Magnetic properties and paleointensity of pseudotachylites from the Sudbury structure, Canada: petrologic control. *Tectonophysics* **402**, 141–152 (2005)
- Nishioka, I., Funaki, M.: Irreversible changes in anisotropy of magnetic susceptibility. Study of basalts from lunar crater and experimentally impacted basaltic andesite. In: *Meteoritics & Planetary Science*, vol. 43, p. A116. Meteoritical Society, Chantilly (2008)
- Öhman, T., Lorenz, K., Pesonen, L., Badjukov, D., Raitala, J., Elo, S., Ojala, K., Nishioka, I., Funaki, M.: Kara impact structure, Russia: Recent developments in petrophysical and geochemical studies. In: *Large Meteorite Impacts*, p. 4071 (2003)
- Osinski, G., Ferriere, L.: Shatter cones: (mis)understood? *Sci. Adv.* **2**(8), e1600616 (2016)
- Pal, P., Creer, K.: Geomagnetic reversal spurts and episodes of extraterrestrial catastrophism. *Nature* **320**(6058), 148–150 (1986)
- Pesonen, L., Marcos, N., Pipping, F.: Palaeomagnetism of the Lappajärvi impact structure, western Finland. *Tectonophysics* **216**, 123–142 (1992)
- Pierazzo, E., Melosh, H.: Melt production in oblique impact. *Icarus* **145**, 252–261 (2000)
- Pierazzo, E., Vickery, A., Melosh, H.: A reevaluation of impact melt production. *Icarus* **127**, 408–423 (1997)
- Pilkington, M., Grieve, R.: The geophysical signature of terrestrial impact craters. *Rev. Geophys.* **30**, 161–181 (1992)
- Pilkington, M., Hildebrand, A.: Three-dimensional magnetic imaging of the Chicxulub crater. *J. Geophys. Res.* **105**, 23479–23491 (2000)
- Pilkington, M., Ames, D., Hildebrand, A.: Magnetic mineralogy of the Yaxcopoil-1 core, Chicxulub. *Meteorit. Planet. Sci.* **39**, 831–841 (2004)
- Plado, J.: The Bosumtwi meteorite impact structure, Ghana: a magnetic model. *Meteorit. Planet. Sci.* **35**, 723–732 (2000)
- Plado, J., Pesonen, L., Puura, V.: Effect of erosion on gravity and magnetic signatures of complex impact structures: geophysical modeling and applications. In: Dressler, B., Sharpton, V. (eds.) *Large Meteorite Impacts and Planetary Evolution II*, volume special paper 339, pp. 229–239. Geological Society of America, Boulder (1999)
- Pohl, J.: Die Magnetisierung der Suevite des Rieses. *Neues Jahrb. Miner. Monatsh.* **1965**, 268–276 (1965)
- Pohl, J.: Paläomagnetische und gesteinsmagnetische untersuchungen an den kernen der forschungsbohrung Nördlingen 1973. *Geol. Bavarica* **75**, 329–348 (1977)
- Pohl, J., Soffel, H.: Paleomagnetic age determination of the Rochechouart impact structure (France). *Z. Geophys.* **37**, 857–866 (1971)
- Pohl, J., Bleil, U., Hornemann, U.: Shock magnetization and demagnetization of basalt by transient stress up to 10 kbar. *J. Geophys.* **41**, 23–41 (1975)
- Pohl, J., Stoffler, D., Gall, H., Ernstson, K.: Impact and explosion cratering. In: Roddy, D., Pepin, R., Merrill, R. (eds.) *Impact and Explosion Cratering*, pp. 343–404. Pergamon Press, Oxford (1977)

- Pohl, J., Eckstaller, A., Robertson, P., Hajnal, Z.: First results of a multidisciplinary analysis of the Haughton Dome impact structure, Devon Island, Canada. In: *Lunar and Planetary Science Conference*, vol. 16, pp. 669–670 (1985)
- Pohl, J., Eckstaller, A., Robertson, P.: Gravity and magnetic investigations in the Haughton impact structure, Devon Island, Canada. *Meteoritics* **23**, 235–238 (1988)
- Quesnel, Y., Gattacceca, J., Osinski, G., Rochette, P.: Origin of the central magnetic anomaly at the Haughton impact structure, Canada. *Earth Planet. Sci. Lett.* **367**, 116–122 (2013)
- Quintana, S., Crawford, D., Schultz, P.: Analysis of impact melt and vapor production in CTH for planetary applications. *Proc. Eng.* **103**, 499–506 (2015)
- Raiskila, S., Salminen, J., Elbra, T., Pesonen, L.: Rock magnetic and paleomagnetic study of the Keurusselkä impact structure, central Finland. *Meteorit. Planet. Sci.* **46**(11), 1670–1687 (2011)
- Rao, G., Bhalla, M.: Lonar Lake: palaeomagnetic evidence of shock origin. *Geophys. J. Int.* **77**(3), 847–862 (1984)
- Rebolledo-Vieyra, M., Urrutia-Fucugauchi, J.: Magnetostratigraphy of the impact breccias and post-impact carbonates from borehole Yaxcopoil-1, Chicxulub impact crater, Yucatan, Mexico. *Meteorit. Planet. Sci.* **39**, 821–829 (2004)
- Rebolledo-Vieyra, M., Urrutia-Fucugauchi, J., López-Loera, H.: Aeromagnetic anomalies and structural model of the Chicxulub multiring impact crater, Yucatan, Mexico. *Rev. Mex. Cienc. Geol.* **27**, 185–195 (2010)
- Reznik, B., Kontny, A., Fritz, J., Gerhards, U.: Shock-induced deformation phenomena in magnetite and their consequences on magnetic properties. *Geochem. Geophys. Geosyst.* **17**, 393–396 (2016)
- Rice, A., Creer, K.: Geomagnetic polarity reversals: can meteor impacts cause spall disruption into the outer core. In: *Geomagnetism and Palaeomagnetism*, pp. 227–230. Springer Science, Berlin (1989)
- Roberts, J., Lillis, R., Manga, M.: Giant impacts on early Mars and the cessation of the Martian dynamo. *J. Geophys. Res.* **114**(E4), E04009 (2009)
- Salminen, J., Pesonen, L., Reimold, W., Donadini, F., Gibson, H.: Paleomagnetic and rock magnetic study of the Vredefort impact structure and the Johannesburg Dome, Kaapvaal craton, South Africa - implications for the apparent polar wander path of the Kaapvaal craton during the Mesoproterozoic. *Precambrian Res.* **168**, 167–184 (2009)
- Salminen, J., Pesonen, L., Lahti, K., Kannus, K.: Lightning-induced remanent magnetization - the Vredefort impact structure, South Africa. *Geophys. J. Int.* **195**, 117–129 (2013)
- Schneider, D., Kent, D.: Ivory Coast microtektites and geomagnetic reversals. *Geophys. Res. Lett.* **17**, 163–166 (1990)
- Schneider, D., Kent, D., Mello, A.: A detailed chronology of the Australasian impact event, the Brunhes-Matuyama geomagnetic polarity reversal, and global climate change. *Earth Planet. Sci. Lett.* **111**, 395–405 (1992)
- Schwarzschild, B.: Do asteroid impacts trigger geomagnetic reversals? *Phys. Today* **40**(2), 17 (1987)
- Scott, R., Spray, J.: Magnetic fabric constraints on friction melt flow regimes and ore emplacement direction within the South Range breccia belt, Sudbury impact structure. *Tectonophysics* **307**, 163–189 (1999)
- Scott, R., Pilkington, M., Tanczyk, E.: Magnetic investigations of the West Hawk, Deep Bay and Clearwater impact structures, Canada. *Meteorit. Planet. Sci.* **32**, 293–308 (1997)
- Shoemaker, E.: Why study impact craters? In: Roddy, D., Pepin, R., Merrill, R. (eds.) *Impact and Explosion Cratering*, pp. 1–10. Pergamon Press, New York, NY (1977)
- Shoemaker, E., Shoemaker, C.: Glikson, a probable impact structure, western Australia. In: *Lunar and Planetary Science XXVIII*, p. 1669 (1997)
- Spray, J., Thompson, L.: Constraints on central uplift structure from the Manicouagan impact crater. *Meteorit. Planet. Sci.* **43**(12), 2049–2057 (2008)
- Spray, J., Thompson, L., Biren, M., O'Connell-Cooper, C.: The Manicouagan impact structure as a terrestrial analogue site for lunar and Martian planetary science. *Planet. Space Sci.* **58**(4), 538–551 (2010)

- Steiner, M.: Implications of magneto-mineralogic characteristics of the Manson and Chicxulub impact craters. In: Ryder, G., Fastovski, D., Gartner, S. (eds.) *The Cretaceous-Tertiary Event and Other Catastrophes in Earth History*, volume special paper 307, pp. 89–104. Geological Society of America, Boulder (1996)
- Tikoo, S., Gattacceca, J., Swanson-Hysell, N., Weiss, B., Suavet, C., Courrière, C.: Preservation and detectability of shock-induced magnetization. *J. Geophys. Res.* **120**(9), 1461–1475 (2015)
- Ugalde, H., Artemieva, N., Milkereit, B.: Magnetization on impact structures - constraints from numerical modelling and petrophysics. In: Kenkmann, T., Hörz, F., Deutsch, A. (eds.) *Large Meteorite Impacts III*, volume special paper 384, pp. 24–42. Geological Society of America, Boulder (2005)
- Urrutia-Fucugauchi, J., Marin, L., Sharpton, V.: Reverse polarity magnetized melt rocks from the Cretaceous/Tertiary Chicxulub structure, Yucatan peninsula, Mexico. *Tectonophysics* **237**, 105–112 (1994)
- Urrutia-Fucugauchi, J., Soler-Arechalde, A., Rebolledo-Vieyra, M., Vera-Sánchez, P.: Paleomagnetic and rock magnetic study of the Yaxcopoil-1 impact breccia sequence, Chicxulub impact crater (Mexico). *Meteorit. Planet. Sci.* **39**, 843–856 (2004)
- Valeev, K., Absalyamov, S.: Remanent magnetization of magnetite under high pressures and shear loads. *Izv. Phys. Solid Earth* **36**, 241–245 (2000)
- Valet, J., Fournier, A., Courtillot, V., Herrero-Bervera, E.: Dynamical similarity of geomagnetic field reversals. *Nature* **490**(7418), 89–93 (2012)
- Velasco-Villareal, M., Urrutia-Fucugauchi, J., Rebolledo-Vieyra, M., Pérez-Cruz, L.: Paleomagnetism of impact breccias from the Chicxulub crater: implications for ejecta emplacement and hydrothermal processes. *Phys. Earth Planet. Inter.* **186**, 154–171 (2011)
- Wei, Q., Gilder, S., Maier, B.: Pressure dependence on the remanent magnetization of Fe-Ni alloys and Ni metal. *Phys. Rev. B* **90**(14), 144425-1 - 144425-8 (2014)
- Won, I., Kuo, J.: Oscillation of the Earth's inner core and its relation to the generation of geomagnetic field. *J. Geophys. Res.* **78**(5), 905–911 (1973)
- Yokoyama, E., Brandt, D., Tohver, E., Trindade, R.: Palaeomagnetism of the Permo-Triassic Araguainha impact structure (central Brazil) and implications for Pangean reconstructions. *Geophys. J. Int.* **198**, 154–163 (2014)
- Yokoyama, E., Nédélec, A., Baratoux, D., Trindade, R., Fabre, S., Berger, G.: Hydrothermal alteration in basalts from Vargeao impact structure, south Brazil, and implications for recognition of impact-induced hydrothermalism on Mars. *Icarus* **252**, 347–365 (2015)
- Zylberman, W., Gattacceca, J., Quesnel, Y., Rochette, P., Osinski, G., Demory, F.: Paleomagnetism in complex impact structures: examples from the Haughton and West Clearwater impacts, Canada. *LPI Contributions* **1861**, 1101 (2015)

Chapter 14

Magnetic Properties of the Iron–Nickel System: Pressure, Composition, and Grain Size

Michael Wack, Michael Volk, and Qingguo Wei

Abstract We present an introduction to FeNi alloys as they appear in nature and how their magnetic properties can be studied in the laboratory. Meteorites provide natural samples which can carry information about our early Solar System and the magnetic fields present at that time. Grain size, and therefore domain state, of magnetic particles is the key to understanding their ability to record magnetic information on geological time scales. Material specific properties can be easier studied and optimized for technological applications from synthetic samples. We present common synthesis methods as well as analytical procedures to analyze the composition, crystal structure, grain size, and magnetic properties of FeNi alloys. We present data compiled from the literature together with our own results from samples synthesized by mechanical alloying and melting. In particular, we demonstrate changes in hysteresis and backfield parameters as well as Curie temperatures linked to composition, pressure, and alloying. The single-domain (SD) threshold in FeNi alloys remains unknown due to methodical limits in grain size and strong magnetic interactions between individual particles.

14.1 Introduction

Iron forms the basis of many technologically important alloys (e.g., steel and cast iron). Therefore iron is omnipresent in everyday life (e.g., kitchen equipment, cars, bridges, power poles, railways, and reinforcements in buildings). Its discovery and usage for tools gave rise to the “iron age.” It is one of the most abundant elements on Earth and forms a plethora of minerals in the Earth’s crust. Some of those minerals can record the Earth’s magnetic field with a stability that lasts over billions of years. It is this unique property that allows the extraction of magnetic information from rocks which was acquired during their formation. The latter helps us to understand the behavior of the Earth’s dynamo and the movement of the continents in the past.

M. Wack (✉) • M. Volk • Q. Wei

Department of Earth and Environmental Sciences, LMU Munich, Theresienstr. 41, 80333
Munich, Germany

e-mail: wack@geophysik.uni-muenchen.de; volk@geophysik.uni-muenchen.de;
wei@geophysik.uni-muenchen.de

Technologically, magnetic studies gave rise to the development of magnetic tape recording systems as well as modern hard disk technology.

Nickel is also an important industrial material due to its resistance to oxidation and high melting point (1453 °C). Most stainless steels contain a few percent of nickel. Many coins are made from nickel alloys. This gave rise to the well-known name ‘nickel’ for the US five-cent coin.

Combining iron and nickel in a crystal lattice results in FeNi alloys that exhibit specific properties depending on the ratio. Mu-metal ($\text{Fe}_{19}\text{Ni}_{81}$) is the best known material for passive shielding of magnetic fields due to its high magnetic permeability which concentrates magnetic field lines inside the material and therefore rarefies them in ambient space. It has a wide range of technological applications in medical magnetic resonance imaging, navigational fluxgate sensors, and cathode ray tubes. Invar ($\text{Fe}_{65}\text{Ni}_{35}$) exhibits little thermal expansion, which is attributed to magnetovolume effects that compensate thermal expansion. Therefore it’s an ideal material for high-precision instruments, especially for measuring length scales.

Due to their abundance, high density, and good miscibility, gravitational forces concentrate iron and nickel in planetary cores (Wood et al. 2006). This is also true for the Earth. The liquid outer core is believed to act as a geodynamo, creating Earth’s magnetic field by motion of the electrically conducting fluid. Static compression experiments showed that the solid inner core probably consists of hexagonal close-packed (hcp) iron (Tateno et al. 2010). High-energy collisions with differentiated bodies can result in the formation of FeNi-rich fragments which can be found as iron meteorites on Earth (Weisberg et al. 2006).

The investigation of the natural state of the magnetization can be impeded by remagnetization due to strong permanent magnets used by professional meteorite hunters (mostly working in hot deserts) to identify meteorites by their high iron content (Weiss et al. 2010). The strong gradients produced by a magnet that was held to the rock’s surface can be detected and therefore potentially removed from the paleomagnetic signal for large enough fragments (Weiss et al. 2010). However, many samples are not contaminated by magnets such as meteorites collected in Antarctica for scientific studies.

Upon entry into the Earth’s atmosphere a thermally remagnetized fusion crust of a few millimeter forms (Weiss et al. 2008). The inner part, however, is usually unaltered and therefore suitable to study primordial properties.

Meteorites can serve as windows to the early Solar System. Their natural remanent magnetizations (NRM) potentially contain information concerning the magnetic fields present during the initial stages of proto-planetary formation and the extinct dynamos once present in planets or moons. The strength of the magnetic field at the time of acquisition is referred to as paleointensity. Several methods, both absolute and relative, are available to study the remanent magnetization of a meteorite. Many studies found a wide scatter of values on the order of magnitude of Earth’s magnetic field or smaller (Gattaccea and Rochette 2004).

14.2 Magnetic Properties

The physical properties of FeNi alloys are controlled by their composition, crystal structure, pressure, and temperature. The response of FeNi alloys to external magnetic fields also depends on crystallite size, magnetic interactions, domain state, and magnetic ordering. The instantaneous response can be accessed by magnetometry (see Sect. 14.2.1). From theoretical considerations (Néel 1949) and studies on other minerals like magnetite, it is known that only single-domain (SD) and possibly pseudo-single-domain (PSD) grains can retain a stable magnetic state for billions of years. Butler and Banerjee (1975) showed that at room temperature there is no stable SD range for spherical iron particles. For prolate shapes (elongation = 1.67) SD behavior is observed for particle sizes of 15–36 nm. Smaller particles are in a superparamagnetic (SP) state and do not retain any magnetic remanence. Particles above the stable (pseudo) single-domain range are in a multidomain (MD) state, where several magnetic domains separated by domain walls are produced to minimize the energy of the system. Multidomain particles typically carry very little remanent magnetization. The existence and size boundaries for stable SD FeNi particles are still unknown, but such knowledge is crucial to the interpretation of paleointensity experiments on FeNi meteorites.

14.2.1 Magnetometry

Magnetic properties of materials are typically measured in vibrating sample magnetometers (VSM). By vibrating a sample inside a set of pickup coils while applying a magnetic field, the VSM is capable of recording the magnetic moment and or susceptibility of the material in question. Due to the movement of the sample in the coil system, an induced voltage proportional to the magnetic moment of the sample can be measured. We have used a VSM to characterize the samples discussed in this chapter.

The most common measurement is the hysteresis loop. A hysteresis loop (Fig. 14.1) starts at zero applied field with a sample in the demagnetized state ($B = 0, M \approx 0$). The field is successively ramped up to a maximum value while the magnetic moment of the sample is recorded in predefined field steps. Once reading the maximum field, the field is ramped back down to zero. Then the polarity of the field is switched and ramped to a negative maximum field. Finally the field is changed back to the positive maximum. Several magnetic parameters can be inferred from a hysteresis loop. Provided that the ferromagnetic moment of the sample reached saturation, the mass-normalized maximum magnetic moment ($B \rightarrow \infty$) (corrected for the high field slope) is the saturation magnetization M_s which is a material constant. For nanoparticles however, it was shown that M_s can decrease with decreasing particle size due to surface effects (Huber 2005). The magnetization at $B = 0$ after reaching saturation is called saturation remanent magnetization (M_{rs})

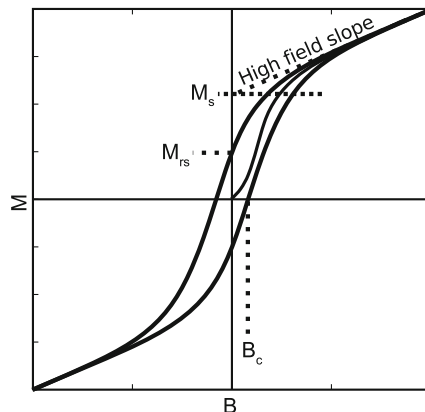


Fig. 14.1 Synthetic hysteresis loop of single domain-dominated sample. Magnetic moment M of the sample (typically mass normalized to Am^2/kg) is plotted versus the applied field (typically measured in mT). Saturation magnetization (M_s), saturation remanent magnetization (M_{rs}), and coercivity (B_c) can be calculated from the hysteresis loop. Because of the uniaxial SD character of the sample, M_{rs} is close to $0.5 \cdot M_s$ and coercivity is large (visible opening of the loop)

and the field at which the magnetization disappears ($M = 0$) is the bulk coercivity (B_c).

Another important parameter can be determined from a backfield curve. In this measurement a saturating magnetic field (e.g., 2 T) is applied in one direction. Then a small field in the opposite direction is applied, and switched off, and the remanent magnetization of the sample is measured (M_{rs}). This procedure is made stepwise with incrementally increasing fields. The field that completely demagnetizes the remanence of the specimen is called the coercivity of remanence (B_{cr}).

These four easily accessible rock magnetic parameters can be used to estimate the domain state (i.e., single or multidomain) of the material by evaluating the remanence (M_{rs}/M_s) and coercivity ratios (B_{cr}/B_c) (Day et al. 1977; Dunlop 2002). Theoretical calculations show that a randomly oriented assemblage of uniaxial single-domain particles should have an $M_{rs}/M_s = 0.5$ ratio and a coercivity ratio close to 1 (Stoner and Wohlfarth 1948). Large multidomain grains have much smaller remanence ratios, because the domains, which minimize the energy of the system, are arranged in such a way that the remanence is also minimized. Furthermore, domain walls have to be moved through the crystal, thereby increasing the remanence coercivity compared to single-domain particles. Thus, the ratio of B_{cr}/B_c increases with increasing grain size.

The Curie temperature (T_c) of a material is defined as the temperature at which a ferromagnetic material loses the capacity to carry a remanent magnetization and behaves like a paramagnetic substance. T_c is a material constant and is often used to identify minerals in a rock (e.g., Dunlop and Özdemir 1997). To measure T_c , the magnetic moment is recorded during heating and cooling. Typically a small magnetic field is applied. The mineral becomes paramagnetic at the Curie

temperature and loses most of its magnetization. Thus, the thermomagnetic curve shows a sharp drop in magnetization. This technique is especially useful since it is able to distinguish between several ferromagnetic minerals in a sample within a single measurement.

Data in this study were obtained by magnetometric measurements consisting of hysteresis loops and backfield curves with a *Lake Shore* PMC MicroMag 3900 Series vibrating sample magnetometer (VSM). High-temperature measurements were done using a Ar-flow furnace in the VSM and in a Peterson Instruments variable field translation balance (VFTB) in air.

14.3 Studies on Synthetic Samples

We present various ways to synthesize FeNi samples and exemplary magnetic studies on the obtained material in the following paragraphs.

14.3.1 Structure

The iron–nickel system forms a binary alloy with two stable unordered phases. Kamacite denotes the low nickel (up to 7%) α phase which crystallizes in a body-centered cubic (bcc) iron structure (Fig. 14.2a) (Nagata 1983). When Ni content exceeds 7%, kamacite alone is not stable anymore and the crystal unmixes into a

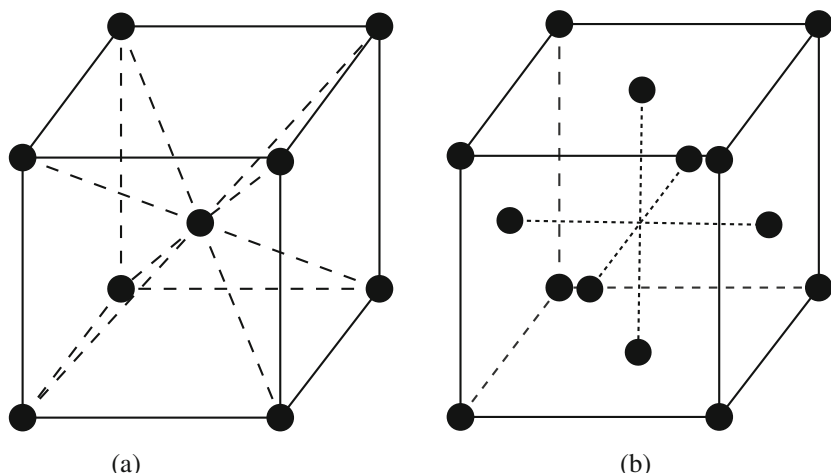


Fig. 14.2 Schematic of the different crystal structures for kamacite (bcc) and taenite (fcc). Lines are guides for the eye. (a) Body-centered cubic (bcc) structure. (b) Face-centered cubic (fcc) structure

mixture of α and taenite, which is a face-centered cubic (fcc) γ -phase (Fig. 14.2b) with more than 30% nickel (Buchwald 1977; Nagata 1983). After reaching a critical Ni content (25–45%) only the γ phase is stable and can exist on its own.¹

Thermodynamic equilibrium of FeNi alloys depends on the heating/cooling rates. Fast cooling (quenching) an alloy through the taenite+kamacite stability boundary can suppress the formation of kamacite and converts taenite into martensite, a bcc alloy with a distorted lattice (e.g., Gilbert and Owen 1962; Inokuti and Cantor 1982). Since this transformation can occur below the Curie temperature of the alloy, interpretation of the natural remanent magnetization (NRM) can be complicated. In this case the material acquires a chemical or martensitic remanence instead of a thermal remanence (TRM) (Wasilewski 1988). The martensitic transformation is affected by several variables, such as grain size, pressure, and composition (Wood 1967).

Ordered taenite in a tetragonal structure is exclusively found in meteorites and is known as tetrataenite (\approx 50% nickel content). It is formed in meteorites due to very slow cooling rates (\approx 0.1 °C/m.y.) (Clarke and Scott 1980; Santos et al. 2015) which can't be reproduced in the lab. However it can be synthesized by irradiation of FeNi alloys with neutrons or electrons (Néel et al. 1964). Its magnetic properties are largely dependent on grain size and microstructure. The so-called cloudy zone in iron meteorites consists of nano-sized tetrataenite precipitates embedded in a Ni-poor matrix (Yang et al. 2007; Uehara et al. 2011). The actual sizes and compositions are cooling rate dependent (Yang et al. 1997; Goldstein et al. 2009, 2014). The smallest tetrataenite grains (SD range) exhibit very high coercivity (Wasilewski 1988; Uehara et al. 2011) and are considered a candidate to develop advanced rare-earth-free permanent magnets (Lewis et al. 2014). Awaruite FeNi_3 comprises another known ordered FeNi phase in meteorites (Howald 2003).

14.3.2 Grain and Crystallite Size

Most inorganic solids including FeNi alloys have a polycrystalline structure which means that they are composed of multiple crystallites (grains) of varying sizes and shapes.

Grain size plays an important role when characterizing magnetic properties. As discussed in Sect. 14.2.1 the size determines whether a particle will be in a superparamagnetic, single-domain, pseudo-single-domain, or multidomain state (Néel 1949, 1955; Dunlop and Özdemir 1997). Special methods have to be used to synthesize nano-structured materials (see following sections). The study of dusty olivines in several meteorite types has shown that inclusions in the nm range may be in a single-domain state and thus carry a stable magnetization (e.g., Van de Moortèle

¹For a more in depth discussion of the structures and a full phase diagram see Swartzendruber et al. (1991).

et al. 2007; Lappe et al. 2011; Uehara and Nakamura 2006). Measuring grain sizes in the nm range can be difficult, especially when dealing with strongly magnetic powders that easily form agglomerates.

The most straightforward methods to determine grain size are imaging techniques, such as scanning or transmission electron microscopy (SEM, TEM). Here the size of the particles can be directly measured by hand or software algorithms. Difficulties in the interpretation of these images can be due to agglomeration of particles and insufficient observations (i.e., low counting statistics). Another frequently used measurement technique for nm-sized particles is laser diffraction to determine the size distribution of a large number of particles. By measuring the scattering intensity as a function of the scattering angle particles of only few nm can be detected and counted. Most machines require the suspension of the sample in liquid. Similar to conventional imaging techniques with SEM and TEM, agglomeration can cause apparent grain sizes several times larger than the actual particle size. X-ray diffraction (XRD) allows one to study crystal structures. With Rietveld refinement (Rietveld 1969), the composition, crystallite sizes, and microstrain can be recovered (see Sect. 14.3.5). Evaluating size-dependent magnetic properties is further complicated by strong interactions between the individual particles which can potentially be overcome by use of surfactants (see Sect. 14.3.5).

14.3.3 Chemical Synthesis

A variety of methods to chemically synthesize FeNi alloys exist. Some will be briefly discussed in the following paragraphs. Selected methods with exemplary studies and obtained compositions are listed in Table 14.1.

The most common and simple method is to chemically reduce Fe^{2+} and Ni^{2+} present in the desired ratio in an aqueous solution. Such solutions are prepared by dissolving Fe and Ni salts (e.g., FeCl_3 and NiCl_2) in deionized water. Hydrazine (N_2H_4) or sodium borohydride (NaBH_4) is a common reducing agent. The composition of the precipitation usually corresponds to the initial ratio of metal salts.

Electrodeposition is the process of aggregating positively charged metal ions from a solution on the surface of a negatively charged electrode (cathode) by an electric current. Depending on the solution, current density, and duration, thin coatings as well as bulk material can be produced. Simultaneous electrodeposition of nickel and iron results in higher-than-expected iron content in the deposit due to anomalous co-deposition, which inhibits the reduction of nickel, while the deposition of iron is enhanced compared to their individual electrodeposition rates (Kieling 1997). Composition is controlled by the applied current density and the ion ratio in the bath (Kieling 1997; Li and Ebrahimi 2003).

Other approaches include evaporation of FeNi alloys in an inert gas followed by condensation on a cold surface and spraying of fine-sized droplet mist into an oven by ultrasonic atomization.

Table 14.1 Selected methods and studies to chemically synthesize FeNi alloys

| Method | Studies | Composition [%Ni] |
|------------------------------------|-----------------------------|----------------------|
| Reduction from solution | Bolsoni et al. (2002) | 50 |
| | Vitta et al. (2008)* | 0,26,51,81,100 |
| | McNerny et al. (2010)* | 12,14,15,20,25 |
| | Mohamed et al. (2013) | 50 |
| Electrodeposition | Cheung et al. (1995) | 78,86,93,96,100 |
| | Li and Ebrahimi (2003) | 49,57,65,75,79,94,95 |
| Electroless deposition | Moustafa and Daoush (2007)* | 80 |
| Polyol process | Viau et al. (1996) | 79,82,88 |
| | Kodama et al. (2010)* | 80 |
| Hydrothermal reduction | Liao et al. (2006)* | 75 |
| | Chen et al. (2012)* | 75 |
| Microwave plasma | Chau (2007) | fcc |
| Hydrogen plasma reaction | Li et al. (1997)* | 0,20,40,60,80,100 |
| | Dong et al. (1999)* | 0,5,12,19,28,49,100 |
| Coprecipitation | Davarpanah et al. (2008)* | 60 |
| Ultrasonic spray pyrolysis | Gurmen et al. (2009) | bcc |
| Gas evaporation method | Kaito et al. (1989) | 25,50,75 |
| | Scorzelli et al. (1994)* | 38–50 |
| Inert gas condensation | Djekoun et al. (2009a) | 50 |
| Nanoparticles on carbon nano-tubes | Wu et al. (2010)* | fcc+bcc |
| | Zhang et al. (2013)* | 68,72,85,86,90 |
| Sol-gel combustion | Cao et al. (2014)* | fcc |

Studies marked with * include magnetic data

14.3.4 Bulk Samples

High-temperature melting is the most common and widely used alloying method in the metal industry. Usually induction furnaces are used to melt FeNi alloys in alumina crucibles above 1538 °C to get FeNi into liquid state (Swartzendruber et al. 1991). Composition is controlled by weighing out the starting materials.

We synthesized bulk FeNi alloys of low Ni content (<20%) by melting the correct mixture of Fe and Ni powders at 1600 °C in an argon atmosphere. The liquid of Fe and Ni was mixed in an alumina crucible for more than 1 h, and then quenched by ice water with the alumina crucible. Electron probe analyses were carried out to check the composition and homogeneity. Three synthesized Fe–Ni alloys show atomic Ni percentage of 8.4 ± 0.7 , 12.7 ± 0.9 , and $16.4 \pm 0.8\%$. Powder X-ray diffraction identifies solely bcc structure for the three alloys. Since Ni composition is over 8%, the three alloys are probably in martensitic bcc phase (Gilbert and Owen 1962; Inokuti and Cantor 1982). Magnetic properties obtained from those samples are included in the compositional study in Sect. 14.3.6.

14.3.5 Mechanical Alloying

Mechanical alloying (MA) or mechanochemical synthesis is a method for producing homogeneous powdered alloys from elemental powder mixtures. The technique involves repeated cold welding, fracturing, and re-welding of particles to create very fine powders. It is commonly used in industry and, in contrast to most conventional techniques, can produce nonequilibrium phases (Suryanarayana 2001). The kamacite phase, if produced by mechanical alloying, has been shown to be stable up to $\approx 25\%$ nickel content (Djekoun et al. 2009b).

The planetary ball mill is commonly used for mechanical alloying. It consists of a planetary disk where the milling bowls are attached. The elementary powders together with milling balls are filled into the bowls. Disk and bowls rotate in opposite directions, thereby creating strong centrifugal forces that accelerate the grinding balls. Whenever two balls collide, a small amount of powder is trapped in between them and is fractured and cold welded (Suryanarayana 2001). The repeated shocks cause a rapid grain size reduction of the particles and the transformation of the different starting powders into a single-crystal structure. This method can produce homogeneous alloys with crystallites of a few nm (Suryanarayana 2001).

The results of the milling process rely on many factors (Moys 2015). Higher rotation speeds generate stronger centrifugal forces and the milling medium is accelerated to higher velocities. The ratio of planetary disk rotation speed (Ω) compared to that of the bowls (ω) can change the energy regime from more friction towards more shock energy (Gaffet et al. 2004). The size of the milling balls as well as the powder-to-ball weight ratio will also influence the resulting sample (Suryanarayana 2001; Koch 1997). When the powder is suspended in liquid (e.g., water or ethanol) during milling the process is referred to as wet milling. Surfactants can be added (surfactant-assisted milling) (e.g., Chakka et al. 2006; Akdogan et al. 2009; Yue et al. 2009) to create a layer of material between individual particles and thus increase their mean distance and reduce interactions between particles. Finally, also the material of the milling balls and bowls can influence the purity of the sample so that materials should be used that are abrasion resistant and do not contain the elements of interest (Koch 1997).

We synthesized mechanically alloyed samples with a Fritsch Pulverisette Premium (P7) planetary ball mill (Fig. 14.3a) at rotation speeds of 400 rpm. Elementary powders of Fe (Sigma Aldrich $\geq 99.5\%$) and Ni (Sigma Aldrich $\geq 99.7\%$) were used as received. Several different powder mixtures were produced with Ni concentrations ranging from 2 to 20%. Ten grams of powder mixture was filled into a 80 mL bowl (Fig. 14.3b) together with 100 g yttrium-stabilized zirconium oxide ceramic beads with 3 mm diameter (Fig. 14.3c) giving a powder-to-ball ratio of 1:10. All sample-handling steps were done under argon atmosphere in a glovebox (Fig. 14.3d). The oxygen level in the glovebox was constantly monitored using an oxygen gas sensor and never exceeded 2%.

Figure 14.4 shows the XRD pattern of a 80% iron and 20% nickel powder mixture before ball milling and after milling at several different times (rpm = 400)



Fig. 14.3 Milling setup: (a) Mill. (b) Beakers. (c) Grinding medium. (d) Glovebox

recorded with a STOE Stadi P diffractometer in Debye-Scherrer geometry at LMU Munich. The XRD patterns ($\text{Mo-}k\alpha_1$) were corrected for instrument broadening and analyzed using the Rietveld method (Rietveld 1969). The unmilled powders show no resolvable sample broadening for both phases, i.e., Fe (bcc) and Ni (fcc star in Fig. 14.4). Through Rietveld refinement it is possible to extract an estimated composition, which is calculated to be $18.7 \pm 2\%$ Ni for the unmilled powder.

The widths of the reflections increase with increasing milling time. A wider full width at half maximum is indicative of the reduction of grain size and/or the introduction of stress in the sample which can be resolved by Rietveld refinement. Figure 14.5 shows that particle size follows an approximately exponential function

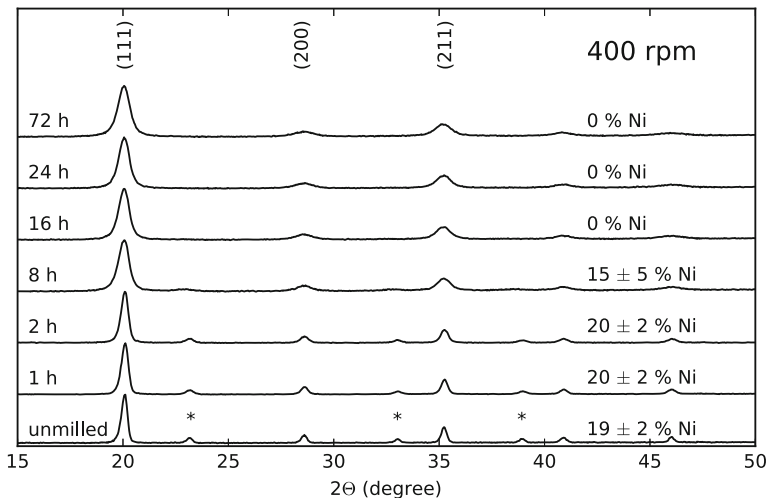


Fig. 14.4 X-ray powder diffraction of Fe₈₀Ni₂₀ at several stages of the milling process. Ni reflections are marked by the star and completely disappear after milling times greater than 16 h. Miller indices shown for iron only. Amount of fcc Ni-phase determined by Rietveld refinement

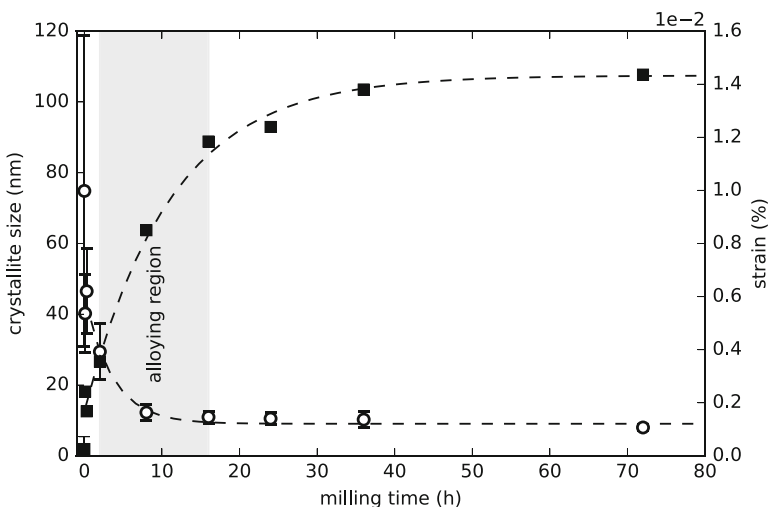


Fig. 14.5 Crystallite sizes (circles) and microstrain (squares) as determined from X-ray diffraction. Dashed lines represent exponential fit of the data. Shaded zone shows the alloying region

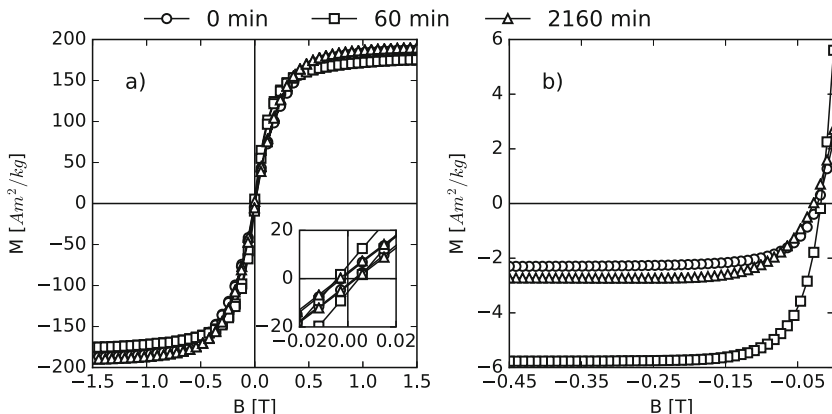


Fig. 14.6 Hysteresis loops (a) and backfield (b) measurements at different stages of milling/alloying. Circles show data for unmilled powder, squares after milling for 60 min, and triangles after milling for 36 h. Every 20th data point shown in hysteresis for clarity

with the main decrease within the first 10 h of milling. The mean crystallite size can be reduced to ≈ 10 nm after milling for 16 h. In contrast, the strain in the crystal increases at a slower rate and reached values of $1.2 \pm 2\%$ (16 h). During the first 2 h of milling the calculated Ni concentration stays largely the same (Fig. 14.4); therefore the sizes of the elementary powders are reduced without alloying. At milling times longer than 2 h the Ni reflections become less pronounced and ultimately disappear after 16 h of milling. This shows that for our setup, a minimum of 16 h of milling is needed to alloy the particles into a homogeneous sample with a mean crystallite size of ≈ 10 nm and 1% microstrain.

Changes in magnetic properties due to alloying of the powders were monitored by subsampling the alloy at several times during the milling process. Figure 14.6 shows hysteresis loops at three different milling times for $\text{Fe}_{80}\text{Ni}_{20}$. The loops of the unmilled powders (i.e., mixture of elemental powders) are almost closed, with low coercivity ($B_c = 2.7$ mT) and saturation remanence ($M_{rs} = 2.2 \text{ Am}^2/\text{kg}$). The saturation magnetization ($M_s = 182.7 \pm 3 \text{ Am}^2/\text{kg}$) is within error of the calculated value $M_s(\text{Fe}_{80}\text{Ni}_{20}) = 183.9 \text{ Am}^2/\text{kg}$ for a mixture of 80 at.% Fe ($217.7 \text{ Am}^2/\text{kg}$) and 20 at.% Ni ($55.1 \text{ Am}^2/\text{kg}$) (Crangle and Goodman 1971).

The three phases of the milling process can be monitored by changes in magnetic properties (Fig. 14.7).

1. Grain size reduction of the individual elementary powders. As long as the particles are above the superparamagnetic threshold, potential stable single-domain particles are superior remanence carriers compared to their larger counterparts. Decreasing grain size from a multidomain state, therefore, leads to an increase in remanence ratio (M_{rs}/M_s). Furthermore, the coercivity increases and coercivity of remanence decreases with decreasing grain size due to the decreasing size of the particles (approaching SD threshold).

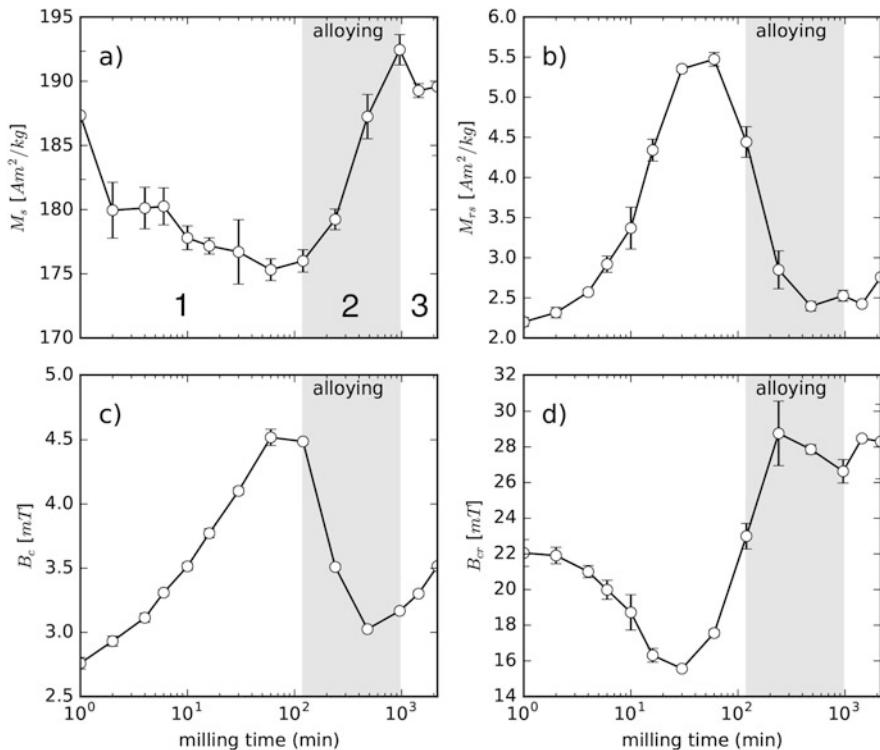


Fig. 14.7 Average rock magnetic parameters (a) M_s ; (b) M_r ; (c) B_c ; (d) B_{cr} , at several stages of the milling process for $\text{Fe}_{80}\text{Ni}_{20}$ milled at 400 rpm. Error bars show one standard deviation ($n = 3$). Alloying region (shaded) was determined by XRD measurements and Rietveld refinement. 1, 2, and 3 denote stages of milling

2. Alloying = incorporation of the Ni atoms into the iron crystal structure, thereby increasing the lattice parameter (Hamzaoui et al. 2003). Saturation magnetization rises from 177 to 190 Am²/kg the M_s value of the final alloy. The remanence decreases as does the coercivity of the particles, while coercivity of remanence increases reflecting changes in Ni content. However, the interpretation is further complicated by a possible change in SD-MD threshold during alloying of the powder.
3. Alloyed particles are further reduced in size. However, since the main size reduction takes place during the first 10 h of milling, very long milling times are needed to substantially reduce the grain size. On the other hand strain in the material is still increasing (see Fig. 14.5) and can influence the magnetic properties of the material further. The crystallite size is estimated to be on the order of 10 nm after 16 h of milling.

Further milling has only a minor effect on grain size but increases microstrain.

Once the alloying process is complete, the particles are already reduced to ≈ 10 nm. Therefore crystallite sizes produced by mechanical alloying are limited to a narrow range. A possible method for increasing particle sizes was demonstrated by Eastman et al. (1995). By annealing nanocrystalline nickel samples they were able to show stress reduction and grain size growth. This approach can hopefully be adopted to FeNi alloys in the future.

The SD-MD threshold size for nonspherical iron particles has been estimated to be in a similar range to powders prepared by mechanical alloying (Butler and Banerjee 1975; Muxwworthy and Williams 2015). However our parameters determined from hysteresis and backfield curves suggest that the samples are still in a multidomain configuration. More detailed investigation of the magnetic properties (FORC, Henkel diagrams, not shown) reveals that the individual particles are strongly interacting with their neighbors and thus behave like larger, more MD particles. Adding surfactants and diluting the resulting powder by milling with sand did not overcome those interactions in our experiments. Thus grain size-dependent magnetic properties of FeNi particles are still a scientific challenge.

14.3.6 Composition

Meteorites contain a wide variety of FeNi compositions; thus understanding the variability of the magnetic properties with increasing Ni content is vital to the interpretation of the magnetic signal. Here we present thermomagnetic and rock magnetic measurements on bulk and mechanically alloyed samples described above in conjunction with values from other studies.

We measured Curie temperatures for compositions ranging from 2 to 50 at.% Ni on a VFTB. Heating in air yields slightly underestimated Curie points ($\Delta T_c \approx 20$ °C) for compositions <10% Ni. For bcc FeNi alloys with Ni concentrations of more than 12% Ni, the Curie temperatures in air are increasingly underestimated with increasing Ni concentration when compared to literature values. Since the Curie temperatures for several terrestrial iron oxide minerals lie in the same temperature range ($\text{Fe}_2\text{O}_3 \approx 680$ °C, $\text{Fe}_3\text{O}_4 \approx 580$ °C), an erroneous measurement of the Curie point can lead to a wrongful interpretation of the magnetic mineralogy. Measuring thermomagnetic curves in a nonoxidizing atmosphere (e.g., in Ar) significantly increases the Curie temperature (see gray and white symbols in Fig. 14.8). Alloys with low Ni concentration and a bcc structure have Curie temperatures close to that of iron (770 °C). Increasing Ni content lowers T_c only slightly up to 20% Ni (Fig. 14.8) and more significantly with higher Ni concentrations. When FeNi is in a fcc structure (>30% Ni), the Curie temperature rises with increasing Ni from ≈ 100 °C at 30% to $T_c(\text{Fe}_{50}\text{Ni}_{50}) \approx 500$ °C.

Saturation magnetization, saturation remanent magnetization, and coercivity were determined from hysteresis loops, while remanent coercivity was calculated from a backfield measurement (see Sect. 14.2.1). The saturation magnetization of pure iron is 217.6 Am²/kg (Crangle and Goodman 1971). Adding a few percent

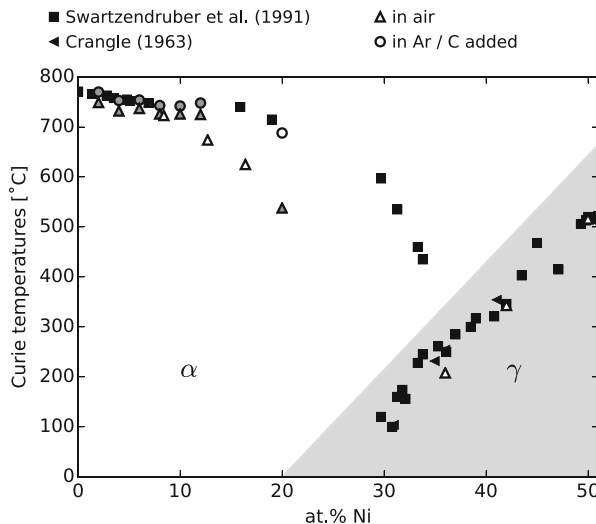


Fig. 14.8 Curie temperatures determined from the second derivative method for several different compositions. Additional data taken from Crangle and Hallam (1963) and Swartzendruber et al. (1991, and references within). Open symbols are for our samples, with gray symbols indicating those prepared by mechanical alloying

of nickel (12%) lowers M_s slightly to 212.6 Am²/kg in our experiments. When previous studies are considered, an overall reduction of saturation magnetization with increasing nickel content can be seen (Fig. 14.9a). Strong scattering in the M_s data can be caused due to the nano character of the grains. Particles of only several nm have a very large surface-to-volume ratio and the atoms on the surface are not properly aligned in the crystal structure (Huber 2005). Therefore, these grains can have a lower saturation magnetization compared to bulk samples and M_s values determined from nanostructured alloys should only be considered as a lower limit.

Little data is available for the remanent saturation magnetization. At low nickel concentrations M_{rs} varies by an order of magnitude (Fig. 14.9b) and no trend can be found in the data. Coercivity (Fig. 14.9c) of the samples is similarly scattered. The mechanically alloyed samples (gray open circles in Fig. 14.9) show higher coercivity when compared to the samples produced by melting techniques in our study. Milling of the powder introduces stress (see Sect. 14.3.5) that can lead to an increase in coercivity due to pinning of domain walls at crystal defects. However, coercivity can be influenced by the measurement protocol as well. The coercivity of the alloys in the iron–nickel system is only a few mT compared to hematite $B_c > 100$ mT (Dunlop 1981). Thus, it is crucial to choose small field steps within the coercivity region for hysteresis as well as backfield measurements. Otherwise, small overshoots of the field due to imperfect control (precise to within a few 100 µT for our VSM) can influence the outcome.

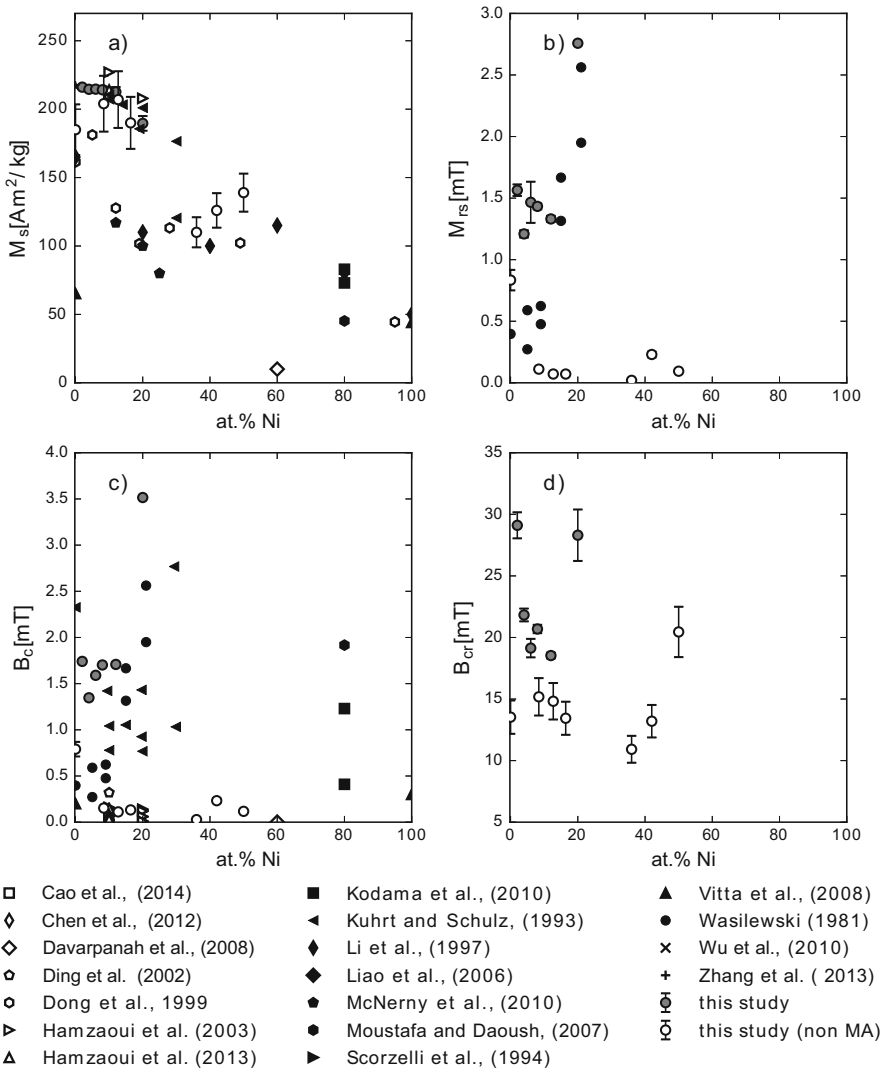


Fig. 14.9 Hysteresis parameters determined from the data presented in this chapter as well as data compiled from several studies concerning FeNi alloys with compositions ranging from pure iron to pure Ni

To our knowledge, the remanent coercivity data presented here are the first to be presented as a function of Ni content in FeNi alloys. Starting at large remanent coercivities ($B_{\text{cr}} \approx 29$ mT) for Ni concentrations of 2%, an increase in Ni lowers B_{cr} to ≈ 13 mT at 16% Ni. The opposite behavior can be seen when further increasing the Ni content ($B_{\text{cr}} \approx 20$ mT at 50% Ni). Small values can be seen for intermittent compositions (Fig. 14.9d). Similar to the hysteresis parameters B_c and M_{rs} , the

remanent coercivity is also strongly influenced by crystal defects. This dependency complicates comparing mechanically alloyed and thermally synthesized samples.

14.3.7 Pressure Cycling

To study FeNi alloys under pressure a diamond anvil cell (DAC) can be used (Bassett 2009). It operates on small sample volumes (Fig. 14.10) and can provide pressure up to hundreds gigapascal (GPa), even terapascal (Dubrovinskaia et al. 2016). Diamond is transparent in the optical range, which makes it suitable for in situ observation and measurements like optical, Raman, or X-ray spectroscopy.

Hardened beryllium-copper alloy (Fig. 14.10) with high mechanical strength is the preferred material to build nonmagnetic DACs. Diamonds anvils usually are around 0.1–0.4 carat. To support the small diamonds, back seats made of hard materials are needed. While back seats made of tungsten carbide usually used in ordinary DAC are often magnetic, moissanite (Mohs scale 9.5) or sapphire (Mohs scale 9.0) can be used to build the diamond back seat or for lower pressures even replace the diamond anvils for magnetic applications. As moissanite and sapphire are much cheaper than diamond, moissanite and sapphire anvils can be made much larger (>1 carat) without support. Maximum pressures of a moissanite anvil cell (MAC) can be up to 60 GPa (Xu et al. 2002). Generally there is a trade-off between pressure and magnetic moment. The maximum achievable pressure is inversely proportional to the sample size. On the other hand, the minimum sample size – and the maximum pressure—is limited to the sensitivity of the magnetometer [10^{-11} Am^2]. We performed our measurements by inserting the DAC into a superconducting quantum interference device (SQUID).

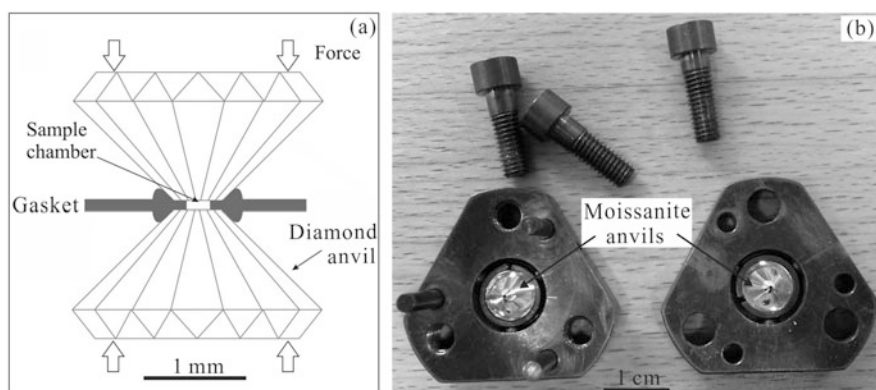


Fig. 14.10 (a) Principle of a diamond anvil cell. (b) Nonmagnetic moissanite anvil cell made of working hardened beryllium-copper alloy

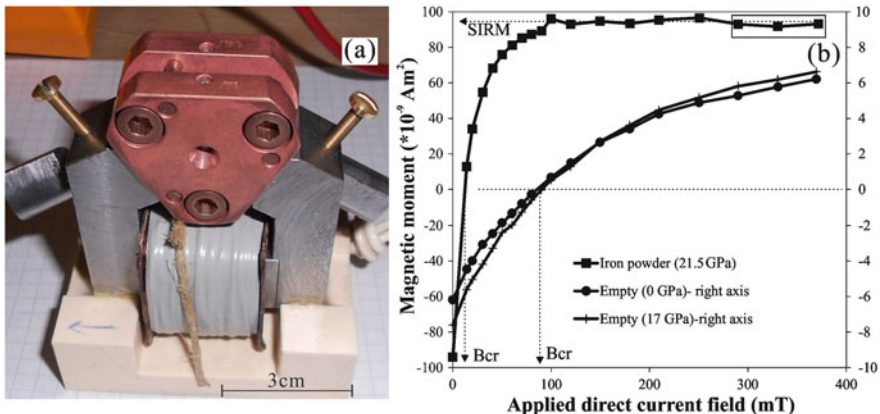


Fig. 14.11 Isothermal remanent magnetization. (a) Give IRM to sample in the diamond anvil cell. (b) Backfield curves of diamond anvil cell. Remanent magnetization of empty cell at pressures of 0 and 17 GPa, and iron powder at 21.5 GPa, has been subtracted from the empty cell. Bcr: coercivity of remanence; SIRM: saturation isothermal remanent magnetization

To impart an isothermal remanent magnetization (IRM), a specifically designed electromagnet (Fig. 14.11a) was used on the diamond anvil cell (Gilder et al. 2011). Magnetization contributed from the diamond anvil cell is constant with pressure and can be subtracted. Backfield curves can be acquired by applying stepwise increasing of IRMs. Coercivity of remanence (Bcr) and saturation isothermal remanent (SIRM) can be deduced from those curves (Fig. 14.11b).

We prepared bulk fcc FeNi samples with 36, 42, and 50% nickel by high-temperature alloying and measured those samples within a DAC under pressure by a superconducting quantum interference device (SQUID magnetometer) at room temperature (Wei et al. 2014). In general, their magnetization is enhanced by compression and decompression. The magnetization (Fig. 14.12a) decrease for $\text{Fe}_{64}\text{Ni}_{36}$ between 5 and 7 GPa is consistent with the pressure-induced Curie temperature decrease (Hausch 1973; Kouvel and Wilson 1961; Leger et al. 1972; Patrick 1954). Three independent experiment runs on $\text{Fe}_{64}\text{Ni}_{36}$ with different maximum pressures show that the higher the pressure the higher the magnetization when decompressed to ambient condition. It indicates that the enhanced magnetization is related to structural distortion or defects. Magnetic coercivity (Fig. 14.12c, d) for all Fe–Ni compositions remains fairly constant at relatively low values (5–20 mT).

Curie temperature measurements (Fig. 14.13) on pressure-cycled $\text{Fe}_{64}\text{Ni}_{36}$ to different peak pressures (4.0, 7.1, 11.1, and 16.3 GPa) show that the Curie temperature decreases with increasing pressure (Wei et al. 2014).

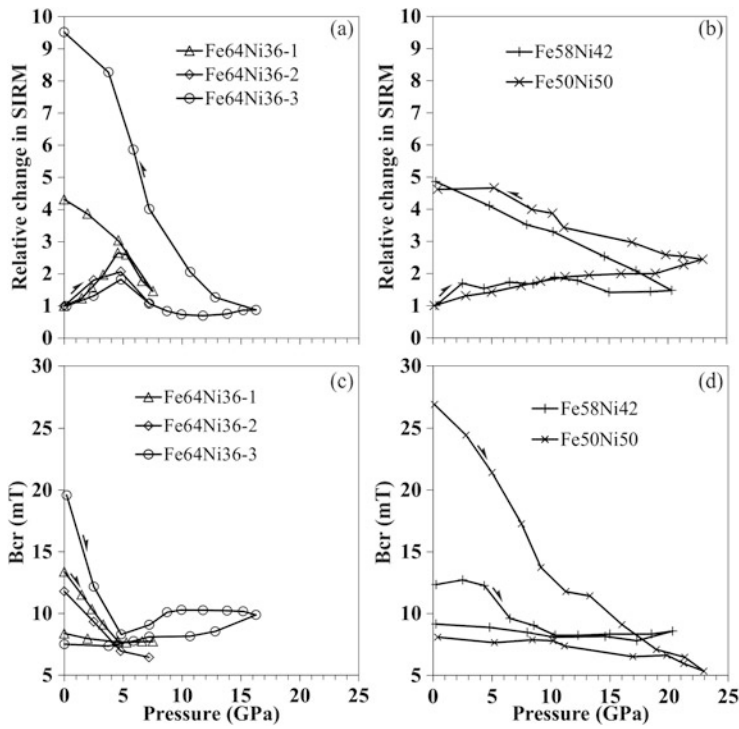


Fig. 14.12 (a) and (b) Saturation isothermal remanent magnetization (SIRM) of Fe–Ni alloys as a function of pressure. (c) and (d) Coercivity of remanence (B_{cr}) of Fe–Ni alloys as a function of pressure. Arrows show the pressure path. After Wei et al. (2014)

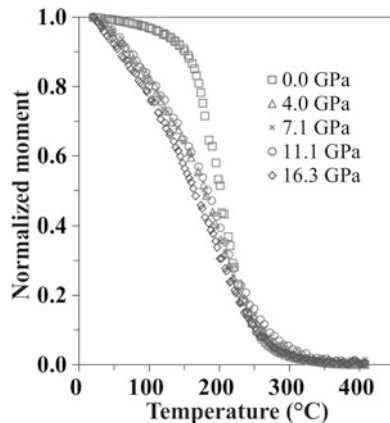


Fig. 14.13 Curie temperature of pressure-cycled Fe₆₄Ni₃₆. Remanent magnetization double normalized and measured after decompression from the indicated peak pressure. Data from Wei et al. (2014)

14.4 Conclusions

The binary system of FeNi alloys has technological and scientific interesting properties due to a complex interplay of magnetic and structural characteristics. Those can be studied by the combination of compositional and structural (e.g., X-ray) with magnetic measurements (e.g., VSM).

Low and high nickel phases exhibit pure bcc and fcc structures. Structure and mixture of phases for midrange compositions depend strongly on the synthesis method which complicates their characterization. Iron meteorites contain FeNi minerals with varying amounts of Ni and sometimes complicated microstructures of fine intergrowths of different phases (plessite and cloudy zone) which strongly control the magnetic properties. Thus understanding the magnetic properties of the iron–nickel system is crucial to understand the remanent magnetization of meteorites. Due to their origin in the early Solar System they can provide valuable primordial information.

Creating synthetic samples in the laboratory is possible by chemical processes, melting and mixing, as well as mechanical alloying. The latter proved to provide high-quality, homogeneous samples. The obtainable crystallite size range ($\approx 10\text{ nm}$) is limited by the particle size needed for alloys to form and the natural lower size limit of the methodology. Magnetic properties of individual particles are obscured by high magnetic interactions due to small distances and high magnetic moments. Special attention has to be paid to avoid oxidation during the synthesis process and at high-temperature measurements (esp. at compositions in the $\alpha + \gamma$ stability field). Mechanical alloying introduces high levels of microstrain in the individual particles. To overcome the restrictions in crystallite size and microstrain heat treatment (sintering) is a good option for further experiments.

The available magnetic data are rather scattered. This demonstrates how sensitive the magnetic parameters are to crystal structure and crystallite size which may vary for each synthesis method although the Fe–Ni ratio is the same. Surface effects can especially affect M_s on nanoparticles. When analyzing our samples we found that it is especially important to measure fine-stepped hysteresis loops to obtain reliable estimates for the small values of M_{rs} and B_c . For future comparative studies, a precise characterization of the analyzed material and error estimates based on different independent samples are crucial.

Pressure cycling FeNi alloys makes them better magnets. With increasing peak pressure the SIRM is increased significantly. The Curie temperature is lowered with increasing peak pressure which complicates its interpretation.

Acknowledgements Funding was provided through the Deutsche Forschungsgemeinschaft (DFG) projects WA 3402/1-1 and GI712/7-1. We thank Martin Leberer and Johannes Heinbuch for assistance in the laboratory and Bernd Maier for supplying X-ray data. FRITSCH GmbH provided technical support for the ball mill. A review by Jérôme Gattacceca helped to improve the manuscript.

References

- Akdogan, N.G., Hadjipanayis, G.C., Sellmyer, D.J.: Anisotropic Sm-(Co,Fe) nanoparticles by surfactant-assisted ball milling. *J. Appl. Phys.* **105**(7), 07A710 (2009)
- Bassett, W.A.: Diamond anvil cell, 50th birthday. *High Pressure Res.* **29**(2), 163–186 (2009). doi:10.1080/08957950802597239
- Bolsoni, R., Drago, V., Lima, E. Jr.: Chemical synthesis and characterization of a nanometric Fe50Ni50 alloy. *Mater. Sci. Forum* **403**, 51–56 (2002). doi:10.4028/www.scientific.net/MSF.403.51
- Buchwald, V.F.: The mineralogy of iron meteorites. *Philos. Trans. R. Soc. Lond. Ser. A Math. Phys. Sci.* **286**(1336), 453–491 (1977)
- Butler, R.F., Banerjee, S.K.: Single-domain grain-size limits for metallic iron. *J. Geophys. Res.: Solid Earth* **80**(2), 252–259
- Cao, J., Qin, Y., Li, M., Zhao, S., Li, J.: Sol–gel combustion synthesis of magnetic MnFe₂O₄ oxide and FeNi alloy: product dependence on the reduction ability. *Appl. Phys. A* **117**(4), 2019–2023 (2014) doi:10.1007/s00339-014-8611-0
- Chakka, V.M., Altunccevahir, B., Jin, Z.Q., Li, Y., Liu, J.P.: Magnetic nanoparticles produced by surfactant-assisted ball milling. *J. Appl. Phys.* **99**(8), 08E912 (2006)
- Chau, J.L.H.: Synthesis of Ni and bimetallic FeNi nanopowders by microwave plasma method. *Mater. Lett.* **61**(13), 2753–2756 (2007). doi:10.1016/j.matlet.2006.04.125
- Chen, Y.C., Zheng, F.C., Min, Y.L., Wang, T., Zhao, Y.G.: Synthesis and properties of magnetic FeNi₃ alloyed microchains obtained by hydrothermal reduction. *Solid State Sci.* **14**(7), 809–813 (2012). doi:10.1016/j.solidstatesciences.2012.04.006
- Cheung, C., Djuanda, F., Erb, U., Palumbo, G.: Electrodeposition of nanocrystalline Ni–Fe alloys. *Nanostruct. Mater.* **5**(5), 513–523 (1995). doi:10.1016/0965-9773(95)00264-F
- Clarke, R.S., Scott, E.R.D.: Tetraetaenite; ordered FeNi, a new mineral in meteorites. *Am. Miner.* **65**(7–8), 624–630 (1980)
- Crangle, J., Goodman, G.M.: The magnetization of pure iron and nickel. *Proc. R. Soc. A: Math. Phys. Eng. Sci.* **321**(1547), 477–491
- Crangle, J., Hallam, G.C.: The magnetization of face-centred cubic and body-centred cubic iron + nickel alloys. *Proc. R. Soc. Lond. A: Math. Phys. Eng. Sci.* **272**(1348), 119–132 (1963)
- Davarpanah, A.M., Mirzae, A.A., Sargazi, M., Feizi, M.: Magnetic properties of Fe–Ni nanoparticles prepared by co-precipitation method. *J. Phys.: Conf. Ser.* **126**(1), 012065 (2008). doi:10.1088/1742-6596/126/1/012065
- Day, R., Fuller, M.D., Schmidt, V.: Hysteresis properties of titanomagnetites: grain-size and compositional dependence. *Phys. Earth Planet. Inter.* **13**(4), 260–267 (1977)
- Ding, J., Li, Y.Y., Shi, Y., Chen, L.F., Deng, C.R., Fuh, S.H., Li, Y.: A structural, magnetic and microwave study on mechanically milled Fe-based alloy powders. *J. Magn. Magn. Mater.* **247**(3), 249–256 (2002)
- Djekoun, A., Boudinar, N., Chebli, A., Otmani, A., Benabdeslem, M., Bouzabata, B., Grenache, J.M.: Characterization of Fe and Fe50Ni50 ultrafine nanoparticles synthesized by inert gas-condensation method. *Physica B: Condens. Matter* **404**(20), 3824–3829 (2009a). doi:10.1016/j.physb.2009.07.074
- Djekoun, A., Boudinar, N., Chebli, A., Otmani, A., Benabdeslem, M., Bouzabata, B., Grenache, J.M.: Structure and magnetic properties of Fe-rich nanostructured Fe_{100-x}Ni_x powders obtained by mechanical alloying. *Phys. Proc.* **2**(3), 693–700 (2009b)
- Dong, X.L., Zhang, Z.D., Zhao, X.G., Chuang, Y.C., Jin, S.R., Sun, W.M.: The preparation and characterization of ultrafine Fe–Ni particles. *J. Mater. Res.* **14**(2), 398–406 (1999). doi:10.1557/JMR.1999.0058
- Dubrovinskaia, N., Dubrovinsky, L., Solopova, N.A., Abakumov, A., Turner, S., Hanfland, M., Bykova, E., Bykov, M., Prescher, C., Prakapenka, V.B., Petitgirard, S., Chuvashova, I., Gasharova, B., Mathis, Y.L., Ershov, P., Snigireva, I., Snigirev, A.: Terapascal static pressure generation with ultrahigh yield strength nanodiamond. *Sci. Adv.* **2**(7) (2016). doi:10.1126/sciadv.1600341. <http://advances.sciencemag.org/content/2/7/e1600341.full.pdf>

- Dunlop, D.J.: The rock magnetism of fine particles. *Phys. Earth Planet. Inter.* **26**(1-2), 1–26 (1981)
- Dunlop, D.J.: Theory and application of the Day plot (Mrs/Ms versus Hcr/Hc) I. Theoretical curves and tests using titanomagnetite data. *J. Geophys. Res.: Solid Earth* **107**(B3), 2056 (2002)
- Dunlop, D.J., Özdemir, Ö.: Rock Magnetism. Fundamentals and Frontiers. Cambridge University Press, Cambridge (1997)
- Eastman, J.A., Beno, M.A., Knapp, G.S., Thompson, L.J.: X-ray diffraction characterization of defect behavior in nanocrystalline nickel during annealing. *Nanostruct. Mater.* **6**(5), 543–546 (1995). doi:10.1016/0965-9773(95)00116-6
- Gaffet, E., Hamzaoui, R., Elkédim, O.: Milling conditions effect on structure and magnetic properties of mechanically alloyed Fe–10% Ni and Fe–20% Ni alloys. *Mater. Sci. Eng. A* **381**(1–2), 363–371 (2004)
- Gattacceca, J., Rochette, P.: Toward a robust normalized magnetic paleointensity method applied to meteorites. *Earth Planet. Sci. Lett.* **227**(3–4), 377–393 (2004). doi:10.1016/j.epsl.2004.09.013
- Gilbert, A., Owen, W.: Diffusionless transformation in iron–nickel, iron–chromium and iron–silicon alloys. *Acta Metall.* **10**(1), 45–54 (1962). doi:10.1016/0001-6160(62)90185-2
- Gilder, S.A., Egli, R., Hochleitner, R., Roud, S.C., Volk, M.W.R., Le Goff, M., de Wit, M.: Anatomy of a pressure-induced, ferromagnetic-to-paramagnetic transition in pyrrhotite: implications for the formation pressure of diamonds. *J. Geophys. Res.: Solid Earth* **116**(B10), B10101 (2011). doi:10.1029/2011JB008292
- Goldstein, J.I., Yang, J., Kotula, P.G., Michael, J.R., Scott, E.R.D.: Thermal histories of IVA iron meteorites from transmission electron microscopy of the cloudy zone microstructure. *Meteorit. Planet. Sci.* **44**(3), 343–358 (2009). doi:10.1111/j.1945-5100.2009.tb00737.x
- Goldstein, J.I., Yang, J., Scott, E.R.D.: Determining cooling rates of iron and stony–iron meteorites from measurements of Ni and Co at kamacite–taenite interfaces. *Geochim. Cosmochim. Acta* **140**, 297–320 (2014). doi:10.1016/j.gca.2014.05.025
- Gurmen, S., Ebin, B., Stopić, S., Friedrich, B.: Nanocrystalline spherical iron–nickel (Fe–Ni) alloy particles prepared by ultrasonic spray pyrolysis and hydrogen reduction (USP-HR). *J. Alloys Compd.* **480**(2), 529–533 (2009). doi:10.1016/j.jallcom.2009.01.094
- Hamzaoui, R., Elkédim, O.: Magnetic properties of nanocrystalline Fe–10%Ni alloy obtained by planetary ball mills. *J. Alloys Compd.* **573**, 157–162 (2013)
- Hamzaoui, R., Elkédim, O., Fenineche, N., Gaffet, E., Craven, J.: Structure and magnetic properties of nanocrystalline mechanically alloyed Fe–10% Ni and Fe–20% Ni. *Mater. Sci. Eng. A* **360**(1–2), 299–305 (2003)
- Hausch, G.: Magnetovolume effects in invar alloys: spontaneous and forced volume magnetostriction. *Phys. Status Solidi (A)* **18**(2), 735–740 (1973). doi:10.1002/pssa.2210180236
- Howald, R.A.: The thermodynamics of tetrataenite and awaruite: a review of the Fe–Ni phase diagram. *Metall. Mater. Trans. A* **34**(9), 1759–1769 (2003). doi:10.1007/s11661-003-0142-9
- Huber, D.L.: Synthesis, properties, and applications of iron nanoparticles. *Small* **1**(5), 482–501 (2005). doi:10.1002/smll.200500006
- Inokuti, Y., Cantor, B.: Overview 15 the microstructure and kinetics of martensite transformations in splat-quenched Fe and FeNi alloys—II. FeNi alloys. *Acta Metall.* **30**(2), 343–356 (1982). doi:10.1016/0001-6160(82)90214-0
- Kaito, C., Saito, Y., Fujita, K.: Ordered structure in alloy grains of iron–nickel produced by the gas evaporation technique. *Jpn. J. Appl. Phys.* **28**, L694–L696 (1989). doi:10.1143/JJAP.28.L694
- Kieling, V.C.: Parameters influencing the electrodeposition of Ni–Fe alloys. *Surf. Coat. Technol.* **96**(2–3), 135–139 (1997). doi:10.1016/S0257-8972(97)00078-9
- Koch, C.C.: Synthesis of nanostructured materials by mechanical milling: problems and opportunities. *Nanostruct. Mater.* **9**(1–8), 13–22 (1997)
- Kodama, D., Shinoda, K., Kasuya, R., Tohji, K., Doi, M., Balachandran, J.: Synthesis of submicron sized Fe₂₀Ni₈₀ particles and their magnetic properties. *J. Appl. Phys.* **107**(9), 09A320 (2010). doi:10.1063/1.3334170
- Kouvel, J.S., Wilson, R.H.: Magnetization of iron–nickel alloys under hydrostatic pressure. *J. Appl. Phys.* **32**(3), 435 (1961). doi:10.1063/1.1736020

- Kuhrt, C., Schultz, L.: Formation and magnetic properties of nanocrystalline mechanically alloyed Fe-Co and Fe–Ni. *J. Appl. Phys.* **73**(10), 6588 (1993). doi:10.1063/1.352573
- Lappe, S.C.L.L., Church, N.S., Kasama, T., da Silva Fanta, A.B., Bromiley, G., Dunin-Borkowski, R.E., Feinberg, J.M., Russell, S., Harrison, R.J.: Mineral magnetism of dusty olivine: A credible recorder of pre-accretionary remanence. *Geochem. Geophys. Geosyst.* **12**(12), 1525–2027 (2011). <http://dx.doi.org/10.1029/2011GC003811>
- Leger, J.M., Loriers-Susse, C., Vodar, B.: Pressure effect on the curie temperatures of transition metals and alloys. *Phys. Rev. B* **6**(11), 4250–4261 (1972). doi:10.1103/physrevb.6.4250
- Lewis, L.H., Mubarok, A., Poirier, E., Bordeaux, N., Manchanda, P., Kashyap, A., Skomski, R., Goldstein, J., Pinkerton, F.E., Mishra, R.K., Kubic, R.C. Jr., Barmak, K.: Inspired by nature: investigating tetrataenite for permanent magnet applications. *J. Phys.: Condens. Matter* **26**(6), 064213 (2014). doi:10.1088/0953-8984/26/6/064213
- Li, H., Ebrahimi, F.: Synthesis and characterization of electrodeposited nanocrystalline nickel–iron alloys. *Mater. Sci. Eng. A* **347**(1–2), 93–101 (2003). doi:10.1016/S0921-5093(02)00586-5
- Li, X., Chiba, A., Takahashi, S.: Preparation and magnetic properties of ultrafine particles of Fe–Ni alloys. *J. Magn. Magn. Mater.* **170**(3), 339–345 (1997). doi:10.1016/S0304-8853(97)00039-5
- Liao, Q., Tannenbaum, R., Wang, Z.L.: Synthesis of FeNi3 alloyed nanoparticles by hydrothermal reduction. *J. Phys. Chem. B* **110**(29), 14262–14265 (2006). doi:10.1021/jp0625154, 00062
- McNerny, K., Kim, Y., Laughlin, D., McHenry, M.: Chemical synthesis of monodisperse γ -Fe–Ni magnetic nanoparticles with tunable Curie temperatures for self-regulated hyperthermia. *J. Appl. Phys.*, p. 09A312 (2010). doi:10.1063/1.3348738
- Mohamed, M.A., El-Maghriby, A.H., El-Latif, M.M.A., Farag, H.A.: Optimum synthesis conditions of nanometric Fe50Ni50 alloy formed by chemical reduction in aqueous solution. *Bull. Mater. Sci.* **36**(5), 845–852 (2013). doi:10.1007/s12034-013-0539-z
- Moustafa, S.F., Daoush, W.M.: Synthesis of nano-sized Fe–Ni powder by chemical process for magnetic applications. *J. Mater. Process. Technol.* **181**(1–3), 59–63 (2007). doi:10.1016/j.jmatprotec.2006.03.008
- Moys, M.H.: Grinding to nano-sizes: effect of media size and slurry viscosity. *Miner. Eng.* **74**(C), 64–67 (2015)
- Muxworthy, A.R., Williams, W.: Critical single-domain grain sizes in elongated iron particles: implications for meteoritic and lunar magnetism. *Geophys. J. Int.* **202**(1), 578–583 (2015)
- Nagata, T.: Meteorite magnetization and paleointensity. *Adv. Space Res.* **2**(12), 55–63 (1983). doi:10.1016/0273-1177(82)90288-5
- Néel, M.L.: Théorie du trainage magnétique des ferromagnétiques au grains fin avec applications aux terres cuites. *Ann. Géophys.* **5**(2), 99–136 (1949)
- Néel, M.L.: Some theoretical aspects of rock-magnetism. *Adv. Phys.* **4**(14), 191–243 (1955)
- Néel, L., Pauleve, J., Pauthenet, R., Laugier, J., Dautreppe, D.: Magnetic properties of an iron–nickel single crystal ordered by neutron bombardment. *J. Appl. Phys.* **35**(3), 873–876 (1964). doi:10.1063/1.1713516
- Patrick, L.: The change of ferromagnetic curie points with hydrostatic pressure. *Phys. Rev.* **93**(3), 384–392 (1954). doi:10.1103/physrev.93.384
- Rietveld, H.M.: A profile refinement method for nuclear and magnetic structures. *J. Appl. Crystallogr.* **2**(2), 65–71 (1969)
- Santos, E.D., Gattacceca, J., Rochette, P., Fillion, G., Scorzelli, R.: Kinetics of tetrataenite disordering. *J. Magn. Magn. Mater.* **375**, 234–241 (2015). doi:10.1016/j.jmmm.2014.09.051
- Scorzelli, R.B., Silva, E.G., Kaito, C., Saito, Y., McElfresh, M., Elmassalami, M.: Mössbauer spectroscopy, X-ray diffraction and magnetic measurements of iron–nickel ultrafine particles. *Hyperfine Interact.* **94**(1), 2337–2342 (1994). doi:10.1007/BF02063785
- Stoner, E.C., Wohlfarth, E.P.: A mechanism of magnetic hysteresis in heterogeneous alloys. *Philos. Trans. R. Soc. Lond. A: Math. Phys. Eng. Sci.* **240**(826), 599–642 (1948). doi:10.1098/rsta.1948.0007
- Suryanarayana, C.: Mechanical alloying and milling. *Progr. Mater. Sci.* **46**(1–2), 1–184 (2001)
- Swartzendruber, L.J., Itkin, V.P., Alcock, C.B.: The Fe–Ni (iron–nickel) system. *J. Phase Equilib.* **12**(3), 288–312 (1991)

- Tateno, S., Hirose, K., Ohishi, Y., Tatsumi, Y.: the structure of iron in earth's inner core. *Science* **330**(6002), 359–361 (2010). doi:10.1126/science.1194662
- Uehara, M., Nakamura, N.: Experimental constraints on magnetic stability of chondrules and the paleomagnetic significance of dusty olivines. *Earth Planet. Sci. Lett.* **250**(1–2), 292–305 (2006)
- Uehara, M., Gattacceca, J., Leroux, H., Jacob, D., van der Beek, C.J.: Magnetic microstructures of metal grains in equilibrated ordinary chondrites and implications for paleomagnetism of meteorites. *Earth Planet. Sci. Lett.* **306**(3–4), 241–252 (2011). doi:10.1016/j.epsl.2011.04.008
- Van de Moortèle, B., Reynard, B., Rochette, P., Jackson, M.J., Beck, P., Gillet, P., McMillan, P.F., McCammon, C.: Shock-induced metallic iron nanoparticles in olivine-rich Martian meteorites. *Earth Planet. Sci. Lett.* **262**(1–2), 37–49 (2007)
- Viau, G., Fiévet-Vincent, F., Fiévet, F.: Nucleation and growth of bimetallic CoNi and FeNi monodisperse particles prepared in polyols. *Solid State Ionics* **84**(3), 259–270 (1996). doi:10.1016/0167-2738(96)00005-7
- Vitta, S., Khuntia, A., Ravikumar, G., Bahadur, D.: Electrical and magnetic properties of nanocrystalline Fe100xNix alloys. *J. Magn. Magn. Mater.* **320**(3–4), 182–189 (2008). doi:10.1016/j.jmmm.2007.05.021
- Wasilewski, P.: Magnetization of small iron–nickel spheres. *Phys. Earth Planet. Inter.* **26**(1–2), 149–161 (1981). doi:10.1016/0031-9201(81)90106-0
- Wasilewski, P.: Magnetic characterization of the new magnetic mineral tetrataenite and its contrast with isochemical taenite. *Phys. Earth Planet. Inter.* **52**(1), 150–158 (1988)
- Wei, Q., Gilder, S.A., Maier, B.: Pressure dependence on the remanent magnetization of Fe–Ni alloys and Ni metal. *Phys. Rev. B* **90**(14) (2014). doi:10.1103/physrevb.90.144425
- Weisberg, M.K., McCoy, T.J., Krot, A.N.: Systematics and evaluation of meteorite classification. In: *Meteorites and the Early Solar System II*. University of Arizona Press, Tucson, pp. 19–52 (2006)
- Weiss, B.P., Fong, L.E., Vali, H., Lima, E.A., Baudenbacher, F.J.: Paleointensity of the ancient martian magnetic field. *Geophys. Res. Lett.* **35**(23) (2008) doi:10.1029/2008gl035585
- Weiss, B.P., Gattacceca, J., Stanley, S., Rochette, P., Christensen, U.R.: Paleomagnetic records of meteorites and early planetesimal differentiation. *Space Sci. Rev.* **152**(1–4), 341–390 (2010). doi:10.1007/s11214-009-9580-z
- Wood, J.A.: Chondrites: their metallic minerals, thermal histories, and parent planets. *Icarus* **6**(1–3), 1–49 (1967)
- Wood, B.J., Walter, M.J., Wade, J.: Accretion of the Earth and segregation of its core. *Nature* **441**(7095), 825–833 (2006)
- Wu, H., Qian, C., Cao, Y., Cao, P., Li, W., Zhang, X., Wei, X.: Synthesis and magnetic properties of size-controlled FeNi alloy nanoparticles attached on multiwalled carbon nanotubes. *J. Phys. Chem. Solids* **71**(3), 290–295 (2010). doi:10.1016/j.jpcs.2009.12.079
- Xu, J., Mao, H., Hemley, R.J., Hines, E.: The moissanite anvil cell: a new tool for high-pressure research. *J. Phys.: Condens. Matter* **14**(44), 11543 (2002)
- Yang, C.W., Williams, D.B., Goldstein, J.I.: A new empirical cooling rate indicator for meteorites based on the size of the cloudy zone of the metallic phases. *Meteorit. Planet. Sci.* **32**(3), 423–429 (1997). doi:10.1111/j.1945-5100.1997.tb01285.x
- Yang, J., Goldstein, J.I., Scott, E.R.D.: Iron meteorite evidence for early formation and catastrophic disruption of protoplanets. *Nature* **446**(7138), 888–891 (2007). doi:10.1038/nature05735
- Yue, M., Wang, Y.P., Poudyal, N., Rong, C.B., Liu, J.P.: Preparation of Nd–Fe–B nanoparticles by surfactant-assisted ball milling technique. *J. Appl. Phys.* **105**(7), 07A708 (2009)
- Zhang, X., Zhang, H., Wu, T., Li, Z., Zhang, Z., Sun, H.: Comparative study in fabrication and magnetic properties of FeNi alloy nanowires and nanotubes. *J. Magn. Magn. Mater.* **331**, 162–167 (2013). doi:10.1016/j.jmmm.2012.11.033

Index

A

ACRONYM, 232
ACRONYM-PIC code, 218
Additional magnetic field, 276, 280, 289
 calculation, 291
Age-depth model, 89
Air upwelling, 322, 323, 326
Alfvén, 255
 velocity, 155
 wings, 155
Alfvén Mach number M_A , 155, 204
Alloying, 395
 α^2 -dynamo, 55, 69, 72
 α -mechanism, 55
 $\alpha\Omega$ -dynamo, 55, 56, 69, 74
Anelastic, 20, 21, 24–26, 34, 37, 38, 42, 52,
 55, 70
Annulus model, 42, 47, 48
Apollinaris Patera, 352
Araguainha, 366
Archeological artefacts, 87
Archeomagnetic data, 85
Aspect ratio, 28, 50, 55–57, 60, 62
Auroral electrojets, 282
Auroral latitudes, 296
Auroral ovals, 170
Australasian microtektite field, 373
Azimuthal MRI (AMRI), 127, 128,
 137–139

B

Backfield curves, 386, 400
Background state, 16, 21, 23–24, 26–28,
 30–34, 57, 60, 61

density, 16, 31
ideal gas, 30, 57, 60
temperature, 16, 24
Background temperature, 307
Barringer (USA), 369
Bayesian age-depth modeling, 90
BEPI COLOMBO, 209, 232
Besnus transition, 365
 β -effect, 38–41, 47, 49–52, 71, 74
Bilharz' stability criterion, 131
Biot-Savart law, 275
Bistability, 55–57
Boltzmann equation, 174
Bosumtwi, 365
Bottom heating, 60, 65, 67
Boundary conditions, 167
 entropy, 27
 magnetic, 30
 rigid, 29
 stress-free, 29, 44, 50, 54–56, 60
Boussinesq, 20, 37–42, 44, 45, 50–52, 54, 58,
 60, 66
Bow shock, 155, 203
Breakdown of corotation, 164
Breccias (suevites), 358
Brunhes-Matuyama reversal, 374
B-spline, 112
Buneman, 232
Busse annulus, 41, 42

C

Callisto's, 173–179
 atmosphere, 174
interaction, 177

- ionosphere, 174–177
 plasma interaction, 177–179
- Cassini, 242, 243, 245, 249, 251, 253, 255, 258, 260
 mission, 8
- Centrifugal forces, 160
- C³FM2, 113
- CHAllenging Minisatellite Payload (CHAMP)
 satellite, 295, 296, 307, 315, 323, 324
 electron temperature, 297
 field-aligned current (FAC), 297
 thermospheric mass density, 296
 zonal wind, 297
- Chandrasekhar, 133
- Chemical remanent magnetization (CRM), 369
- Chesapeake Bay (USA), 365
- Chicxulub (Mexico), 364
- Clearwater, 363
- Close approach method, 307
- Coercivity, 385, 396
- Coercivity of remanence, 386, 400
- Collective effects, 252
- Combined equinoxes, 299, 305, 312, 319
- Combined kinetic and fluid model, 176
- Complex multi-ring craters, 364
- Compressible β -effect, 38–41, 47, 49
- Conductivity, 324
- Conductivity elements, 257
- Conductivity tensor for the Earth ionosphere, 267
- Continuity equation, 22, 24, 27, 35, 38
- Convection, 8, 21, 29, 35, 37, 41–50, 60, 71, 73–75
- Convective bursts, 49
- Core angular momentum (CAM), 112
- Core dynamo, 332, 341–346
- Core dynamo shut down, 352
- Core-mantle boundary, 84
- Corotation breakdown, 161
- Correlation analysis, 184, 309
- Covariance matrix, 184
- COV-OBS, 113
- Craters, 342
- Crustal magnetic field, 335
- Crustal magnetization, 337, 351
- Crystallite size, 402
- Curie temperatures, 386, 396, 401
- Current sheets, 217
- Current volume element, 276
- Cusp region, 295, 312, 320–322, 326
- D**
- Day night asymmetry, 177
- Dayside cusp region, 305
- Debye length, 252
- Deep Bay, 363
- Deep zonal wind models, 9, 10, 29
- Defense Meteorological Satellite Program (DMSP), 298, 300, 315, 318, 324
 ion vertical flows, 298
 measurements, 296
 plasma density data, 298
 satellites, 321
 vertical plasma flow, 298
- Dellen, 361
- Demagnetized, 343
- Density
 anomalies, 305, 314, 320, 322, 324
 enhancement peaks, 305
 enhancements, 312, 321
 functional theory, 12–13
 profile, 16, 31, 32
 scale height, 31, 41, 47
 stratification, 37, 40, 42–44, 47, 49, 51, 53–56, 58, 59, 71, 75
- Determination coefficient, 197
- Diamond anvil cell (DAC), 399
- Diffusivities
 molecular, 25
 turbulent, 25
- Dipolarity, 19, 54, 56, 58
- Dipolar solution, 54–56, 58–60, 64
- Dipole coordinate system, 270
- Dipole moment, 92, 98
- Dissipation number, 28, 31
- Domain walls, 397
- Double-diffusive instabilities, 133
- Downward-continued crustal magnetic field, 336
- DRESDYN, 128, 146
- DTS experiment, 127
- Dusty plasma(s), 242, 243, 261
- Dynamo effect, 125
- Dynamo equation, 21, 33, 35
- Dynamo magnetic field, 168
- E**
- Eigenvectors, 184
- EISCAT, 295
- Ekman friction, 49
- Ekman number, 28, 33, 34, 50, 51, 55, 57, 58, 60–62, 64, 67, 73, 74

- E-layer, 295, 321
Electrical conductivity, 9, 15, 16, 22, 27, 32,
33, 55–59, 61, 63, 64, 67, 68, 70, 72,
75
profile, 9, 32, 33, 56–59, 61, 63, 64, 70
Electrically non-conductive, 158
Electric field potential distribution, 272
Electrodeposition, 389
Electromagnetic obstacle, 157
Electron
acceleration, 217, 225, 227, 233
distribution function, 174
microscopy, 389
precipitation, 321
spectra, 218
temperature, 305, 310, 313, 320
EMVIM, 185
Enceladus, 242, 243, 245, 246, 251, 252, 255,
260, 261
plume, 245, 248, 253
Entropy
diffusion, 25, 30, 42
equation, 42
Equation of state, 23, 70, 71
Equatorial and polar electrojets, 273
Equatorial electrojet, 280
Equatorial jet, 35, 36, 46, 55, 58, 67, 68, 71, 72
Escape flux, 320
Euhedral Ti-poor magnetite, 368
Excursions, 85, 100–103
Exobase, 320
Exsolution texture, 368
Exsolved titanomagnetite, 368
Extrasolar planets, 156, 179
- F**
FACs, *see* Field-aligned currents (FACs)
Fast Mach number M_f , 155
F2COSMIC, 185
Fermi acceleration, 222, 227
Fermi-type acceleration, 231, 234
Field aligned auroral current systems, 164
Field-aligned currents (FACs), 161, 264, 294,
323, 324
Fluctuating dust charges, 247
Flux ropes, 233–234
Foelsche, 363
Frozen-flux induction equation, 114
- G**
G12, 31, 63, 64, 67–70, 73
Ganymede, 166, 179
- Gauss coefficients, 112
Gaussian probability distribution, 248
GEOMAGIA48, 84, 87–88
Geomagnetic field models, 95–98
Geomagnetic jerks, 112
Geostrophic, 37–39, 41, 45, 55, 71–74
Glikson, 361
Global electric field, 266
Global inverse models, 84
Global ionosphere thermosphere model
(GITM), 295
Global structure of the ionospheric current
system, 289
GOEMHD3 code, 223
Grain size, 394, 395
Granite, 368
Granulite facies, 368
Gravitational harmonics, 16, 17
Gravity field, 8, 36
Gravity profile, 30
Gravity Recovery And Climate
Experiment (GRACE) satellites,
296, 297
thermospheric mass density, 298
GRIMM3, 113
gufm1, 113
Guide-field, 233
- H**
Hadriaca Patera, 343
Hall and Pedersen conductivities, 270
Hall conductivity, 255, 256, 258, 259
Hall effect, 259
Hartmann number, 129
Haughton, 363
Havnes parameter, 257
Heat equation, 25, 26, 30, 35
HEDGEHOG, 143, 144
Helical MRI (HMRI), 127, 128
Helium sedimentation, 19, 71
Hematite, 366
Hermean magnetopause, 217, 221
reconnection, 233
Hermean magnetotail, 222–231
Hermean tail, 234
High-latitude electric field, 273
High pressure experiments, 11
Historical observations, 92–93
Holocene field reconstructions, 95–100
Hubble Space Telescope (HST), 170
Huber norm, 335
Hybrid simulations, 210
Hydrogen-helium

demixing, 8, 9, 14, 20, 74
 mixture, 13–15, 71
 Hydrostatic condition, 24
 Hydrothermal alteration, 366
 Hysteresis loop, 385

I
 IMF, *see* Interplanetary magnetic field (IMF)
 Impact melt, 358
 Induce electric currents, 173
 Initial and boundary conditions, 158
 Inner core oscillation, 373
 Insulating nature, 159
 Integrated ionospheric current density, 285
 Intensity spikes, 84, 94
 Interior structure model, 16, 71
 Internal magnetic fields, 159
 Internal mass sources, 160
 Interplanetary magnetic field (IMF), 204, 296,
 298, 311, 312, 316–319, 322, 323,
 325, 326
 total magnetic field, 298
 Interplanetary shocks, 205, 209–217
 waves, 231–233
 Invar, 384
 Ion kinetic scales, 223
 Ionosphere, 184
 Ionospheric current
 density, 267
 layer, 265
 system, 279
 Ionospheric F2 region and protonosphere
 block, 266
 Ionospheric generator, 269
 Ion outflow, 294, 295
 Ion upflow, 320, 322, 324, 326
 Ion vertical velocity, 305
 Irregular numerical grid, 279
 Isothermal remanent magnetization (IRM), 400
 Ivory Coast microtektite field, 373

J
 JCF, 61–65
 Joule heating, 295, 326
 Juno mission, 16, 18, 67, 68, 72, 73
 Jupiter, 179
 interior structure, 10–20
 ionosphere, 160
 magnetic field model, 74
 magnetosphere, 160
 rocky core, 74

K
 Kamacite, 387
 Kamacite phase, 391
 Kara (Russia), 364
 Karlsruhe dynamo, 125
 Kentland (USA), 369
 Keurusselkä, 368
 Kohn-Sham equations, 12

L
 Lake St. Martin, 366
 Lappajärvi, 364
 Large-scale FACs (LSFACs), 300, 310, 312,
 314, 315, 317–319
 Laschamp excursion, 101
 Least-squares inversion, 114
 Length-of-day (LOD), 112
 Limonite-goethite, 365
 Linear regression, 309
 Local summer, 299, 305, 312
 Local-time asymmetries, 163
 Local winter, 299, 305, 312
 Lockne (Sweden), 369
 Lonar (India), 369
 Long current sheets, 223
 Lorentz force, 26, 56, 58–60, 64, 71–73, 252
 Lower ionosphere, 266
 LSFACs, *see* Large-scale FACs (LSFACs)
 Luminosity, 19, 20, 71, 72
 Lundquist number, 134, 223

M
 Mach-numbers, 204, 232
 MagIC database, 21, 31, 34, 35, 53, 70, 71, 88
 Magnetic anomalies, 360
 Magnetic domains, 385
 Magnetic field model, 333
 Magnetic field of Mars model, 334
 Magnetic-field-parallel electric fields, 231
 Magnetic latitude (MLat), 301
 Magnetic local time (MLT), 301
 Magnetic Prandtl number, 28, 34, 60, 64, 129
 Magnetic reconnection, 205–206, 217
 Magnetic Reynolds number, 64, 67, 72
 critical, 66
 Magnetic Rossby number, 130
 Magnetic spectrum, 72
 Magnetic stresses, 164
 Magnetite, 340, 363
 Magnetization signature, 342
 Magnetization strength, 339

- Magnetized spherical Couette flow (MSCF), 142
Magnetohydrodynamic (MHD), 155
Magnetohydrodynamic waves, 155
Magnetopause, 205
Magneto-rotational instability (MRI), 126
Magnetosphere, 293
Magnetosphere-ionosphere (MI) coupling, 160
Magnetospheric generator, 269
Magnetospheric plasma, 242, 255
Magnetotail, 206
Main auroral oval, 163
Main field, 84
Mariner-8, 202, 203, 207
Mars', 331–352
Mars Global Surveyor, 333
Martian paleopoles, 333
Mauersberger-Lowes spectrum, 64, 65
Mechanical alloying (MA), 391, 402
Mechanical obstacle, 157
Mechanochemical synthesis, 391
Mercury's magnetosphere, 220
MErcury Surface, Space ENvironment,
 GEOchemistry and Ranging
 (MESSENGER), 202, 203,
 205–209, 233
Metallization of hydrogen, 11, 71
Meteorites, 384
MFACE, 185
 MgSO_4 , 173
MHD approach, 157
Microstrain, 395, 402
Mid-to-high latitude jets, 72
Minerals, 339
Minimum electrical conductivity, 173
MLat-MLT frame, 305
Molecular dynamics, 12–13
Mono Lake excursion, 101
Multidomain, 370, 388
Multiple reconnection, 224
Multipolar solution, 55–58, 62, 64
Mu-metal, 384
- N**
Nanograins, 242, 247, 253, 255
Naval Research Laboratory Mass
 Spectrometer and Incoherent
 Scatter (NRLMSISE-00) model,
 300
Navier-Stokes equation, 21, 22, 24, 25, 27, 35,
 45
Neptune, 52, 75
Neutral atmosphere block, 265
Neutral density enhancement, 310
Neutral wind dynamo, 264
Neutral wind velocity, 310
New electric field block, 265
Non-modal growth, 132
Non-uniqueness, 346
Number, 212
Numerical method, 10, 34–35
Numerical scheme, 277
- O**
Observable magnetic field, 338
Ohmic heating, 22, 29
Ohm's law, 270
 Ω -mechanism, 55, 69
Open-closed field line boundary (OCFL), 170
Orbital-motion-limited (OML) approximation,
 246
- P**
Paleointensity, 384
Paleopole positions, 346, 349, 350, 352
Parallel conductivity, 257, 258
Parker dynamo wave, 69
Parker's method, 349
Pedersen conductivity, 256, 258
Planar deformation features, 363
Planetary ball mill, 391
PlanetMag, 8
Plasma
 beta, 212
 conductivity, 243, 255, 260
 drift, 322, 324
 interaction, 177
 interactions, 154, 155
 turbulence, 233
Plasmoid, 160
Plasmoid-unstable current sheets, 223
Plume, 242, 243, 246, 251, 252, 260
Polar cap, 294
Polar wind, 294
Poloidal, 30, 34, 35
 field, 55, 58, 59, 70
 and toroidal coefficients, 159
Polytropic index, 31
Positive shear instabilities, 147–148
Potential structure, 253
Power-law, 220
 electron distribution, 233
 part of the spectrum, 221
Prandtl number, 26, 28, 30, 33, 34, 44, 53, 60,
 62, 64

- Precipitating electrons, 324
 Predictor variables, 184
 Pressure, 399
 Primary dynamo, 68
 Prominent density enhancements, 307
 PROMISE, 136–138
 Pseudo-single-domain (PSD), 385, 388
 Pseudotachylite, 358
 Pyrrhotite, 340, 364
- Q**
 Quadrupole moments, 168
 Quasi-geostrophy (QG), 114
 Quasi-parallel, 209
 Quasi-perpendicular, 215
 shocks, 209
- R**
 Radiocarbon dating, 89
 Random fluctuations, 248
 Rayleigh number, 28, 33, 43–46, 52, 55,
 59–61, 64, 67
 Reconnection, 229, 233, 234
 Region 1 (R1) FACs, 313, 319, 324, 325
 Region 0 (R0) FAGs, 313, 324, 325
 Regression expression, 309
 Regularization, 194
 Relative density
 anomaly, 303
 enhancements, 300, 303
 Relative density threshold, 314
 Relative paleointensity (RPI), 87
 Relaxation oscillations, 45
 Remanent coercivity, 396
 Response variable, 184
 Reynolds number, 43, 46, 64, 66, 67, 72, 129
 Reynolds stress, 71, 74
 Rhines length, 49, 50
 Rhines scaling, 49, 50, 52, 71
 Rietveld refinement, 392
 Riga, 125
 Rocking angle α , 171
 Rocky core, 16, 17, 20, 33, 71, 72, 74
 Rossby number, 130
 local, 54, 55
 Rossby waves, 38, 39, 42, 48, 49
- S**
 Saturation magnetization, 385, 396
 Saturation remanent magnetization, 385, 396
 Saturn, 8–20, 29, 35, 36, 71, 74, 242

- corotating plasma, 245
 interior structure, 10–20
 magnetic field, 9, 19, 71, 74
 magnetosphere, 246, 251
 thermal evolution, 18–20
Schatzman factor, 135
 Schmidt numbers, 135
 Screening length, 252
 SEA method, *see* Superposed epoch analysis
 (SEA) method
 Seasonal dependence, 303
 Secondary dynamo, 69
 Secular acceleration (SA), 113
 Secular cooling, 20, 26, 74
 Secular variation (SV), 98, 113
 Sediments, 87
 Self-consistent kinetic approach, 231
 Self-consistent PIC simulations, 234
 Self-reversal behavior, 365
 Shallow zonal wind models, 36
 Shielding, 384
 Shielding lengths, 253
 Shock acceleration, 215, 232
 Shock remanent magnetizations (SRMs), 368
 Siljan (Sweden), 366
 Single dipole, 348
 Single-domain (SD), 340, 385, 388
 Six-year oscillation, 112
 Slate Islands, 370
 Slow mode Mach number M_s , 155
 Small-scale field-aligned currents (SSFACs),
 300, 305, 320, 321, 326
 Smoothing, 89
 Smooth susceptibility, 347
 Solar wind, 183, 204, 212
 South Atlantic Anomaly (SAA), 84, 93–94
 Specific entropy, 22, 23, 29
 Spherical Couette experiment, 126
 Spherical Couette flow, 142
 Spherical harmonics (SH), 112, 334
 basis functions, 197
 model, 351
 Spiralling convection, 44
 Sq current system, 274
 SSFACs, *see* Small-scale field-aligned currents
 (SSFACs)
 Stochastic charge fluctuations, 248
 Stochastic dust charge fluctuations, 260
 Stochastic equilibrium model, 251
 Sub-Alfvénic, 155, 167, 179
 conditions, 156
 Subsurface oceans, 159, 168, 173, 179
 Sudbury, 364, 366
 Super-fast interactions, 179

Superparamagnetic (SP), 385, 388
Superposed epoch analysis (SEA) method, 302, 307, 312, 314, 315, 317, 320, 322, 324
Supra-thermal electron population, 174
Surface altitude, 335
Surfactants, 391
Synthetic models, 350

T
Tachocline, 148
Taenite, 388
Tangent cylinder, 38, 40–43, 50–52, 71, 74
Tangential geostrophy (TG), 114
Tangential magnetostrophy (TM), 114
Taylor instability (TI), 127, 128, 140
Taylor-Spruit dynamo, 127, 140
Taylor-Couette experiment, 127
Taylor-Couette flow, 136
Taylor-Proudman theorem, 37–38
Test particle acceleration, 223–228
Tetraenite, 388
Themagnotosphere, 183
Thermal remanent magnetization (TRM), 369
Thermal Rossby wave, 38, 42
Thermal velocity, 320
Thermomagnetic curve, 387
Thermoremanent magnetization (TRM), 85
Thermospheric heating, 325
3D and equivalent current systems, 285
Three-layer model, 17
Time-periodic magnetic fields, 168
Time-variability, 163
Timing, 332, 341–346
Titanohematite, 364
Titanomagnetite, 361
Topographic β -effect, 38–41, 49–52, 74
Toroidal, 30, 34, 35, 55, 69, 70
Torsional oscillations, 112
Total field, 311
Turbulent cascade, 164
Turbulent reconnection, 233

U
Ultrasonic Doppler Velocimetry (UDV), 137
Uniform orientation, 349
Uranus, 52, 75
UV emission, 174

V
Vargeao, 366
Vertical plasma flow, 315, 318, 319
Vertical velocity, 300
Vibrating sample magnetometers (VSM), 385
VIP4, 10, 61–65, 67, 68, 73
Virtual axial dipole moment, 103
Virtual geomagnetic pole, 103
Viscosity, 13, 15, 16, 22, 26, 27, 33, 48, 71
Viscous friction, 50
Viscous heating, 22, 29
Visible magnetization, 338, 339
Volcanics, 85–87
Volcanism and impacts, 341
Volumetric heating, 22, 29
Volumetric heat source, 26, 28, 30
von Kármán Sodium (VKS) experiment, 126

W
wave-4, 196
Wavelet analysis, 188
Weaubleau (USA), 369
West Hawk, 363
Wolfe Creek, 363

X
X-ray diffraction (XRD), 389

Y
Yallalie, 363

Z
Zero epoch, 307
Zonal winds, 9, 29, 35, 36, 47–50, 52, 55, 56, 58, 60, 64, 71, 74, 312